European Commission
Research Directorate General

NOTES ON NUMERICAL FLUID MECHANICS AND MULTIDISCIPLINARY DESIGN · VOLUME 103

DESider – A European Effort on Hybrid RANS-LES Modelling

Results of the European-Union Funded Project, 2004–2007

Werner Haase
Marianna Braza
Alistair Revell (Eds.)

Springer

DESider – A European Effort on Hybrid RANS-LES Modelling

Results of the European-Union Funded Project, 2004–2007

Werner Haase
Marianna Braza
Alistair Revell
(Editors)

Springer

Dr. Werner Haase
Höhenkirchener Str. 19D
D-85662 Hohenbrunn
Germany
E-mail: office@haa.se

Dr. Marianna Braza
Institut de Mécanique
des Fluides de Toulouse
UMR CNRS/INPT N° 5502
Allée du prof. Camille Soula
F-31400 Toulouse
France
E-mail: Marianna.Braza@imft.fr

Dr. Alistair Revell
School of Mechanical Aerospace
and Civil Engineering
C40, George Begg Building
The University of Manchester
P.O. Box 88
Manchester M60 1QD
UK
E-mail: alistair.revell@manchester.ac.uk

ISBN 978-3-540-92772-3 e-ISBN 978-3-540-92773-0

DOI 10.1007/978-3-540-92773-0

Notes on Numerical Fluid Mechanics
and Multidisciplinary Design ISSN 1612-2909

Library of Congress Control Number: applied for

Typeset & Cover Design: Scientific Publishing Services Pvt. Ltd., Chennai, India.

Printed in acid-free paper
5 4 3 2 1 0
springer.com

NNFM Editor Addresses

Prof. Dr. Wolfgang Schröder
(General Editor)
RWTH Aachen
Lehrstuhl für Strömungslehre und
Aerodynamisches Institut
Wüllnerstr. zw. 5 u. 7
52062 Aachen
Germany
E-mail: office@aia.rwth-aachen.de

Prof. Dr. Kozo Fujii
Space Transportation Research Division
The Institute of Space
and Astronautical Science
3-1-1, Yoshinodai, Sagamihara
Kanagawa, 229-8510
Japan
E-mail: fujii@flab.eng.isas.jaxa.jp

Dr. Werner Haase
Höhenkirchener Str. 19d
D-85662 Hohenbrunn
Germany
E-mail: office@haa.se

Prof. Dr. Ernst Heinrich Hirschel
(Former General Editor)
Herzog-Heinrich-Weg 6
D-85604 Zorneding
Germany
E-mail: e.h.hirschel@t-online.de

Prof. Dr. Bram van Leer
Department of Aerospace Engineering
The University of Michigan
Ann Arbor, MI 48109-2140
USA
E-mail: bram@engin.umich.edu

Prof. Dr. Michael A. Leschziner
Imperial College of Science
Technology and Medicine
Aeronautics Department
Prince Consort Road
London SW7 2BY
U.K.
E-mail: mike.leschziner@ic.ac.uk

Prof. Dr. Maurizio Pandolfi
Politecnico di Torino
Dipartimento di Ingegneria
Aeronautica e Spaziale
Corso Duca degli Abruzzi, 24
I-10129 Torino
Italy
E-mail: pandolfi@polito.it

Prof. Dr. Jacques Periaux
38, Boulevard de Reuilly
F-75012 Paris
France
E-mail: jperiaux@free.fr

Prof. Dr. Arthur Rizzi
Department of Aeronautics
KTH Royal Institute of Technology
Teknikringen 8
S-10044 Stockholm
Sweden
E-mail: rizzi@aero.kth.se

Dr. Bernard Roux
L3M – IMT La Jetée
Technopole de Chateau-Gombert
F-13451 Marseille Cedex 20
France
E-mail: broux@l3m.univ-mrs.fr

Prof. Dr. Yurii I. Shokin
Siberian Branch of the
Russian Academy of Sciences
Institute of Computational
Technologies
Ac. Lavrentyeva Ave. 6
630090 Novosibirsk
Russia
E-mail: shokin@ict.nsc.ru

Preface

"In aircraft design, efficiency is determined by the ability to accurately and reliably predict the occurrence of, and to model the development of, turbulent flows. Hence, the main objective in industrial computational fluid dynamics (CFD) is to increase the capabilities for an improved predictive accuracy for both complex flows and complex geometries". This text part taken from Haase et al (2006), describing the results of the DESider predecessor project "FLOMANIA" is still - and will be in future valid.

With an ever-increasing demand for faster, more reliable and cleaner aircraft, flight envelopes are necessarily shifted into areas of the flow regimes exhibiting highly unsteady and, for military aircraft, unstable flow behaviour. This undoubtedly poses major new challenges in CFD; generally stated as an increased predictive accuracy whist retaining "affordable" computation times. Together with highly resolved meshes employing millions of nodes, numerical methods must have the inherent capability to predict unsteady flows. Although at present, (U)RANS methods are likely to remain as the workhorses in industry, the DESider project focussed on the development and combination of these approaches with LES methods in order to "bridge" the gap between the much more expensive (due to high Reynolds numbers in flight), but more accurate (full) LES.

Therefore the primary objective of the DESider project, amongst several key goals, was to demonstrate the capabilities of these so-called hybrid RANS-LES approaches in the application to industrially relevant test cases with a focus on aerodynamic flows characterised by separation, wakes, vortex interaction and buffeting, i.e. flow features with the central common theme; inherent unsteadiness.

An additional aspiration that has been met was to demonstrate the extent to which hybrid RANS-LES methods can be applied to multi-disciplinary topics such as aero-acoustics (noise reduction) and aero-elastics (reduced A/C weight, unsteady loads, fatigue issues, improved A/C safety), thus enabling further tools towards a cost-effective and more accurate design.

All the goals achieved during the DESider project and described in this book have resulted from what has been a highly successful co-operation between European industries, research establishments and universities, leading to much improved knowledge dissemination and achieving cross-fertilisation between different the various represented engineering industries; airframe, helicopters, power generation, car and train industries.

This close collaboration, stimulated by the financial support from the European Union, can quite genuinely claim to have promoted and accelerated the enhancement

of CFD approaches of each DESider partner to a far greater extent than would have otherwise been possible with the partners functioning individually in isolation.

The present book undertakes to describe the outcomes of the DESider project in their entirety and the editors keenly hope that this book clearly and effectively contributes to the area of accurate flow prediction in the form of new and innovative results and methods.

Moreover, we hope that the chapter on hybrid RANS-LES methods, the newly developed turbulence models and the assessment and validation of methods based on a variety of test cases will help seed and motivate further and extended future investigations and validation work.

Acknowledgments are due to each and all DESider partners who have contributed in a remarkably open and collaborative manner to ensure success and in doing so, making it such a pleasure for the editors to summarize the programme's technical achievements in the present book.

Thanks are also due to A. Podsadowski and D. Knörzer, the European Commission's Scientific Officers of the DESider project, who have provided every help at every corner along to route to making this programme a success. Moreover, the financial support received for this book from the European Union via the KATnet-II network is very much appreciated.

Last but not least, the editors of this book would like to express their gratitude to W. Schröder, the General Editor of the Springer series 'Notes on Numerical Fluid Mechanics and Multidisciplinary Design', as well as to his colleague A. Hartmann for their help and editorial advice.

January 2009

Werner Haase München
Marianna Braza Toulouse
Alistair Revell Manchester

Contents

I The DESider Project……. 1

1 Summary……... 1

2 Introduction……... 2

2.1 The ‘Aeronautics and Space’ Priorities as a Background for DESider…… 2

2.2 State of the Art……... 3

3 Technical Project Description……. 6

3.1 Research Approach and Technical Achievements…… 6

3.2 Dissemination and Exploitation…….. 7

3.2.1 General Plans According to the Technical Annex……... 7

3.2.2 An Attempt to Structure Dissemination and Exploitation Work…… 7

3.2.3 Publication of Results…….. 8

3.3 Description of Tasks……... 9

4 List of Partners and Addresses……..……... 15

5 Conclusion……..…… 18

6 The DESider Web Site and How to Access It……..……... 18

II Presentation of Modelling Approaches……. 19

1 DES and Its Modifications and Enhancements…… 19

1.1 Introduction……. 19

1.2 DES97 Formulation and General Principles of Building DES Models Based on Different RANS Models…… 20

1.3 DDES……..…… 23

1.3.1 Motivation and Objective……..……. 23

1.3.2 DDES Formulation……..……... 24

1.4 IDDES……..…….. 26

1.4.1 Motivation and Objective……..……. 26

1.4.2 IDDES Formulation……..…… 26

2 The X-LES Method……..…….. 32

3 A Hybrid URANS-LES Strategy for Large Eddy Simulation at High Reynolds Numbers…...……..…….. 33

3.1 Introduction……..……. 33

3.2 Model Formulation……..…….. 33

3.3 Illustrative Results……..……... 36

4 University of Manchester Hybrid RANS LES Method……. 38

4.1 Introduction……..……. 38
4.2 Hybrid RANS - LES Method……..……. 38
4.2.1 Channel Flows……..…….. 39
4.2.2 Trailing Edge Computations……... 40
5 Zonal Detached Eddy Simulation, ZDES, ONERA……... 41
5.1 Motivations……..…….. 41
5.2 Formulation……..……. 41
5.2.1 ZDES Length Scale……..…….. 42
5.2.2 Subgrid Length Scale……..……... 42
5.2.3 Treatment of the Damping Functions……. 42
6 University of Manchester Embedded LES Method…… 44
6.1 Introduction……... 44
6.2 Synthetic Eddy Method……. 44
6.2.1 Motivations……. 44
6.2.2 Description of the Method…….. 44
7 Isotropic Synthetic Fluctuations as Inlet Boundary Conditions… 47
7.1 Introduction……... 47
7.2 Synthesized Turbulence……. 47
8 Formulation of the Scale-Adaptive Simulation (SAS) Model during the DESIDER Project……. 51
8.1 Introduction……... 51
8.2 Rotta's kL Model…….. 52
8.3 The KSKL Model…….. 52
8.4 The SST-SAS Model……. 54
8.5 Numerical Treatment…….. 55
8.5.1 Convective Terms……... 55
8.5.2 High Wave Number Treatment…….. 56
8.6 Scale-Adaptive Simulation (SAS) Capability……... 59
9 RANS/URANS Modelling……..…… 63
9.1 The Stress-Strain Lag Model……..…… 63
9.2 The SST-Cas Model……..…… 64
10 URANS/OES Tensorial Eddy-Viscosity Modelling……..... 65
10.1 Tensorial Eddy-Viscosity Concept in the Turbulence Behaviour Law……..……..…….. 65
10.2 Summary of the OES Anisotropic First-Order Model…… 66

III DESider Measurements……... 69
1 The DESider Bump Experiment…… 69
1.1 Motivation……. 69
1.2 Model Desin…… 69
1.3 Wall Measurements…… 71
1.4 LDV Measurements…… 72
1.5 PIV Measurements…….. 74
1.5.1 Accuracy Estimation…… 76
1.5.2 Main Statistics of the Flow…….. 77

1.6 Coherent Structures……. 82
1.6.1 Introduction…….. 82
1.6.2 Characteristics of the Extracted Vortices……. 84
1.7 Unsteadiness Characterization…… 87
1.8 Conclusion……..……... 88
2 The IMFT Circular Cylinder Experiment…… 90
2.1 Experimental Set-Up……... 90
2.1.1 Configuration……... 90
2.1.2 Measurements……..... 91
2.1.3 Reynolds Averaging……. 93
2.1.4 Phase Averaging and Proper Orthogonal Decomposition……. 93
2.2 Experimental Results……...……... 94
2.2.1 Flow Regime…… 94
2.2.2 Time Independent Reynolds Averaged Fields……. 95
2.2.3 Instantaneous Motion……... 95
2.2.4 Coherent Structure Identification by Means of the POD…….. 97
2.3 Conclusions……. 103

IV Applications – Test Cases……. 105
1 Circular Cylinder Flow……. 105
1.1 Turbulence Models Used by the Related Partners…… 105
1.2 Numerical Parameters…… 106
1.3 Results……... 106
1.3.1 Comparison of Global Parameters……... 106
1.3.2 Comparison of Statistically Averaged Fields…… 107
1.3.3 Comparison of Unsteady Fields……... 110
1.3.4 Coherent Structures Identification by Means of the POD……..……. 112
1.4 Conclusions……..……. 114
2 TU Munich Delta Wing……. 115
2.1 Test Case Description……... 115
2.2 Description of the Computations…….……. 116
2.2.1 Grids...……. 116
2.2.2 Numerical Methods and Turbulence Models……..... 116
2.3 Results……... 117
2.4 Conclusions……..……. 126
3 NACA0021 at 60^{o} Incidence……..…….. 127
3.1 Introduction……... 127
3.2 General Flow Description……..……... 127
3.3 Participants and Some Details of Simulations…….. 128
3.4 DES Results and Discussion……. 129

3.4.1 Effect of Time Sample, Span Size of the Domain, and Wind-Tunnel Walls……. 129
3.4.2 Effect of Background RANS Model for DES…… 131
3.4.3 Effect of Grid-Refinement……. 133
3.4.4 Cross-Plotting of Results……... 133
3.5 SAS and TRRANS Results and Discussion…….. 135
3.6 Integral Forces…….. 138
3.7 Concluding Remarks……. 139
4 Ahmed Car Body (25° and 35° Slant Angle)…….……... 140
4.1 Introduction…….. 140
4.2 Geometry Description and Flow Conditions……. 141
4.3 Participants Overview……... 141
4.4 Results……... 142
4.4.1 Ahmed Body with 25° Slant Angle……... 142
4.4.2 Ahmed Body with 35° Slant Angle……... 144
4.5 Concluding Remarks……. 145
5 Decay of Isotropic Turbulence……... 147
5.1 Background and Motivation……. 147
5.2 Flow and Test Case Description……... 148
5.3 Table of Participants and Methods…… 150
5.4 Results and Discussion……. 150
5.5 Conclusion……. 155
6 Three-Element Airfoil……. 156
6.1 Test Case Description……... 156
6.1.1 Geometry and Conditions……..…. 156
6.1.2 Grid…… 157
6.2 Computations and Models…….…... 158
6.2.1 Zonal-Detached Eddy Simulation (ZDES)…… 158
6.2.2 Delayed-Detached Eddy Simulation (DDES)…… 159
6.3 Results and Discussion……..... 160
6.3.1 ZDES…….. 160
6.3.2 DDES……. 162
6.4 Conclusions……... 163
7 Simpson's 3D Hill Test-Case……. 164
7.1 Test-Case Description……... 164
7.2 The Computations……. 164
7.2.1 Chalmers University……... 164
7.2.2 FOI……. 165
7.2.3 Imperial College……. 166
7.2.4 EDF…… 166
7.3 Discussion……. 166
7.4 Conclusions……... 173
8 Fully Developed Channel……..…….. 174
8.1 Low Reynolds Number Models…… 174
8.2 Wall Functions……..… 174
8.3 Technical Description……..…….. 175

8.3.1 Mandatory Low-Re Grid, Re ≈4000……... 175
8.3.2 Recommended Low-Re Grids, Re = 8000 and 16000… 175
8.3.3 Recommended Wall-Model Grids, Re = 4000 , 8000 and16000……. 175
8.4 Participants and Methods……..… 176
8.4.1 Chalmers……..... 176
8.4.2 EDF……. 176
8.4.3 FOI……...……... 176
8.4.4 ICSTM……. 176
8.4.5 NTS……. 176
8.4.6 TUB……. 176
8.4.7 UMIST…… 177
8.5 Results…… 178
8.6 Concluding Remarks…….. 183
9 Bump in Square Channel (ONERA Experiment)…….. 184
9.1 Introduction…… 184
9.2 Physical Properties and Boundary Conditions…….. 185
9.3 Grid Information…… 186
9.4 Participating Partners, Turbulence Models, and Simulation Details……. 186
9.5 Results of Simulations…… 187
9.5.1 Mean Pressure Distribution along the Bottom Wall….. 188
9.5.2 Mean Velocity Profiles…… 188
9.5.3 Profiles of the Reynolds Stresses…… 189
9.5.4 Two- and Three-Dimensional Visualisation……... 193
9.6 Discussion…….. 195
9.7 Conclusions…… 196
10 Supersonic Base Flow…… 197
10.1 Introduction……..... 197
10.2 Test Case Presentation……..... 197
10.3 Participants and Methods Used……..... 198
10.4 Results and Discussion……..... 200
10.4.1 RANS Solutions……...…… 200
10.4.2 Turbulence-Resolving Simulations…….. 201
10.5 Conclusions……...……..... 206
11 Separated Flow behind an Aerofoil Trailing Edge without Camber……..……..... 207
11.1 Description of Test Case……..... 207
11.2 Partner-Specific Practices……..... 208
11.2.1 Imperial College London (ICL) ……..... 208
11.2.2 New Technologies and Services (NTS)……..... 209
11.2.3 University of Manchester (UMan)……..... 210
11.3 Results and Discussion……..... 211
11.4 Conclusions……...……... 215
12 FA-5 Configuration……...…… 217
12.1 Introduction……...……..……. 217

12.2 Experimental Setup and Data……..... 218
12.3 Structured Grid……..……..... 218
12.4 Unstructured Grid Computations……..... 224
12.5 Conclusion……..……..... 230
13 Circular Cylinder on a Ground Plate……..... 232
13.1 Overview……..……..... 232
13.2 Flow Geometry……..……... 232
13.3 Participants……..……..... 233
13.4 Results……..……..... 235
13.4.1 Pressure Coefficient……..……..... 235
13.4.2 Velocity Profiles……..……..... 237
13.4.3 Turbulent Intensity……..……..... 237
13.4.4 Streamlines……..……..……. 239
13.5 Conclusions……..……..…… 240
14 Fuel Assembly Industrial Test-Case……..……... 242
14.1 Introduction……..……..…… 242
14.2 The Computational Domain……..…….. 243
14.3 Turbulence Modeling……..……..…. 244
14.4 Grid Generation……..……..…….. 244
14.5 URANS and LES Computations……..…… 244
14.6 High Performance Computation (HPC) Tests (100 MCells)……..……..…… 247
14.7 Conclusions and Perspectives……..…… 248
15 EC145 Helicopter Fuselage – An Industrial Case……..... 250
15.1 Test Case Description……..……..…….. 250
15.1.1 Geometry……..……..…… 250
15.1.2 Flight Conditions……..……..... 250
15.2 Computation Challenges……..……..... 251
15.3 Experiment……..……..…….. 252
15.4 Partners, Numerical Tools, Grids and Computations…… 252
15.4.1 Partners and Numerical Tools……..…… 252
15.4.2 Grids……..……..……..... 252
15.4.3 Computations……..……..…….. 253
15.5 Results……..……..……. 255
15.5.1 Global Loads……..……..……... 255
15.5.2 Cp-Distribution……..……..... 255
15.5.3 Oil Flow……..……..…….. 258
15.6 Conclusion……..……..…….. 260
16 Oscillating Airfoil NACA0012 at 15° – A Basic Case for Aero Elasticity……..……..……... 261
16.1 Test Case Description……..……..……... 261
16.1.1 Dynamic Stall……..……..…….. 261
16.1.2 Flow Conditions……..……..……. 261
16.1.3 Experimental Data……..……..……. 262
16.2 Computations……..……..……..…., 263
16.2.1 Computational Grids……..…….. 263

16.2.2 Computational Details……..……..... 264
16.2.3 Results for URANS……..……..... 264
16.2.4 Results for DES……..……... 265
16.3 Conclusion……..……..…… 268
17 M219 Cavity Flow……..……..…… 270
17.1 Introduction……..……..…….. 270
17.2 Description of Test Case……..……..... 270
17.3 Information of Modelling Methods……..……. 272
17.4 Results and Discussion……..……..……. 273
17.4.1 Unsteady Flow Features……..…….. 273
17.4.2 Time-Averaged Mean Flow Features……. 275
17.4.3 Acoustic Tonal Modes Due to Pressure Oscillations……..……..…….. 279
17.5 Concluding Remarks……..……..……. 284
18 Appendix for M219 Cavity Flow: Computations with and without Bay Doors……..……..……. 286
18.1 Introduction……..……..……. 286
18.2 Results and Discussion……..……..…… 288
18.2.1 Rossiter Mode Frequencies……..……. 288
18.2.2 Sound Pressure Levels (SPL) ……..…… 289
18.3 Summary of Conclusions……..…… 291
19 Car Side-Mirror – An Aero-Acoustics Case……..……... 292
19.1 Background and Motivation……..……..... 292
19.2 Flow and Test Case Description……..…….. 292
19.3 Summary of the FLOMANIA Study……..……... 293
19.4 Partners Contributing, Numerical and Modelling Setup..... 294
19.5 Results……..……..…….. 296
19.5.1 Processing of the SPL Spectra…..……..... 296
19.5.2 Comparison of LES, DES and SAS in the Wake Region…..……..……..... 296
19.5.3 Effect of Grid Resolution…..…… 297
19.5.4 The Upstream Horseshoe Vortex…..…… 298
19.6 Conclusions…..……..……. 300
20 Simplified Landing Gear Test Case…..……. 302
20.1 Introduction…..……..…….. 302
20.2 Computational Setup…..……..……..... 302
20.3 Results…..……..……..……... 304
20.4 Conclusions…..……..…….. 308

V Technical, Partner-Related Reports – Methods, Models and Applications Performed……..……... **309**
1 Contribution of Alenia Aeronautica: Main Results Obtained within the Project…… 309

1.1 Description of Numerical Techniques and Turbulence Models Implemented in Code UNS3D……. 309
1.1.1 The Code UNS3D…… 309
1.1.2 URANS Turbulence Model…….. 310
1.1.3 DES Turbulence Model……. 310
1.2 Decay of Isotropic, Homogeneous Turbulence…… 311
1.3 TC 02, Delta Wing at High Incidence……. 312
1.4 TC E2 – Oscillating NACA0012 Airfoil……. 312
1.5 TC A1, M219 Cavity Flow…….. 313
2 SAS Model Development and Validation Activity of the ANSYS Group in the DESider Project……. 316
2.1 Model Development…… 316
2.2 Model Validation……. 317
3 Chalmers' Contribution…… 320
3.1 Inlet Boundary Conditions…….. 320
3.2 Channel Flow: Direct Numerical Simulations…… 321
3.3 3D Hill Flow…… 321
3.4 Onera Bump……. 324
3.5 The SAS Model……..... 324
3.6 The Turbulence Model…… 325
3.7 Channel Flow……... 326
3.8 LES of the Flow around a 3D Hill……..... 327
3.9 LES of the Flow over a Finite Cylinder…….. 329
4 Contribution of Dassault to DESider……... 332
4.1 Introduction……. 332
4.2 Presentation of Navier-Stokes Solver…… 333
4.3 Validation of Numerics on DIHT Test-Case…….. 333
4.4 Implementation and Validation of DES Modelisation…… 334
4.4.1 Spalart-Allmaras Based DES……... 334
4.4.2 k-ε SST Based DES…….. 334
4.4.3 Calibration on DHIT Case…… 335
4.5 Implementation and Validation of Wall "Blending" Function……..... 335
4.5.1 Spalart Based DES……..... 335
4.5.2 k-ε SST Based DES…….. 336
4.5.3 Validation on 3D Generic Flat Plate…… 336
4.5.4 Validation on Generic S-Duct…….. 336
4.6 Application to Aero-Acoustics…… 338
4.7 Conclusions……. 340
5 Contributions of DLR in DESider…… 341
5.1 Numerical Method - The DLR TAU Code…….. 341
5.2 Work Undertaken during the DESider Project……. 341
5.2.1 DIT……..... 342
5.2.2 NACA0021……..... 342
5.2.3 NACA 0012 (Oscillating at 15° AoA) – Basic Aero-Elasticity Case……. 342

5.2.4 Supersonic Base Flow at M=2.49……. 343
5.2.5 Ahmed Body……. 343
5.2.6 FA5 Aircraft……. 343
5.3 Additional Work Performed by DLR…….. 343
5.3.1 Grid Convergence Study for NACA0021 at 60° AoA…….. 343
5.3.2 High Wave Number Dissipation Reduction in the TAU Code……... 343
6 EADS-MAS Methods and Applications…….. 347
6.1 Methods and Turbulence Models…… 347
6.2 NACA 0021……. 348
6.3 Delta Wing…….. 349
6.4 FA5 Generic Airplane……. 349
6.5 M219 Cavity…… 351
7 A Look Back on DESider at Eurocopter Germany…….. 355
7.1 Numerical Aerodynamics at ECD……..... 355
7.1.1 Potential Applications……..... 355
7.1.2 Methods……..... 356
7.1.3 Models……. 356
7.2 Facts and Lessons Learnt…….…….…….... 356
7.3 Notes…….…….…….... 357
7.3.1 Test-Cases…….…… 357
7.3.2 Models…….…… 358
7.4 Conclusion…….…… 358
8 EDF Achievements in Desider……... 359
8.1 Introduction…….…… 359
8.2 General Overview of the Overset Grid Technique……. 359
8.2.1 Coupling Boundary Faces……..... 360
8.2.2 Coupling with a Body Force in the Overlapping Region……..... 360
8.3 RANS/LES Coupling Examples……. 361
8.3.1 The Back-Step Facing Step Test-Case – Normal RANS/LES Coupling……..... 361
8.3.2 Tangential Coupling – Channel Flow……..... 363
8.3.3 Use of Code/Code Coupling for Wall Treatment (RALEWA Method)……. 364
8.4 Conclusions……. 365
9 Towards Efficient and Accurate Hybrid RANS-LES Modeling for Aerodynamic Applications……. 366
9.1 Introduction……. 366
9.2 DES and Hybrid RANS-LES Modelling……. 367
9.2.1 DES Based on the k-Equation Model (k-DES Model)……. 367
9.2.2 Hybrid RANS-LES Modelling……. 369
9.3 Examples of Application Using the HYB0 Model…….. 371
9.3.1 Flow over a Three-Dimensional Hill…… 372

9.3.2 Supersonic Base Flow…….. 373
9.3.3 M219 Cavity Flow…… 374
9.4 Summary and Outlook……. 376
10 Approximate Near-Wall Treatments Based on Hybrid RANS-LES and Zonal Methods for LES at High Reynolds Numbers…….. 377
10.1 Description of Schemes…….. 377
10.1.1 Hybrid RANS-LES Scheme……..... 377
10.1.2 Zonal Scheme…… 378
10.2 Performance in Channel Flow…….. 379
10.3 Separated Flow from a Hydrofoil…… 380
10.4 Separated Flow over a Three-Dimensional Hill……..... 381
10.5 Conclusions…… 383
11 Statistical and Hybrid Turbulence Modelling for Strongly Detached Flows Around Fixed/Oscillating Bodies…… 384
11.1 Anisotropic OES Modelling – Tensorial Eddy-Viscosity Concept…….. 384
11.1.1 DES Associated with OES…… 386
11.2 Results……... 387
11.2.1 NACA0012 at Re=10^5, a=20° - “in House” Test Case……..... 387
11.2.2 NACA021 beyond Stall Test Case……... 389
11.2.3 Pitching NACA0012 Airfoil……. 389
11.2.4 The Ahmed Car Body……..... 391
11.3 Conclusions…….. 391
12 Hybrid RANS–LES Simulations at NLR Using X-LES and a High-Order Finite-Volume Method……..... 392
12.1 X-LES Method…….. 392
12.2 High-Order Finite-Volume Method……... 392
12.3 Grid Convergence…….. 394
12.4 Shear Layer Instability…….. 395
12.5 Application……... 397
12.6 Conclusion……..... 398
13 Contribution of NTS……. 399
13.1 General Overview……. 399
13.2 DES Enhancements…….. 399
13.2.1 Delayed DES (DDES) …… 399
13.2.2 DDES with Improved Wall-Modelling Capability (IDDES) ……..... 401
13.3 Digest of the Validation Activity……..... 403
14 Contribution by NUMECA…….. 407
14.1 Introduction……. 407
14.2 Code Description……. 407
14.3 Turbulence Modelling……. 408
14.4 Selected Results……... 408
14.4.1 Calibration and Validation……..... 408

14.4.2 Aerofoil at a High Angle of Attack……..... 409
14.4.3 The DESider Bump…..……. 410
14.4.4 The Ahmed Body…..……. 410
14.5 Concluding Remarks, Observations and Recommendations…. 412
15 Contribution by ONERA…..…….. 413
15.1 Task 2.2: Measurements of Separating/Re-attaching Flows….. 413
15.2 Task 3.2: DES with Improved Modelling…..…… 413
15.3 Task 3.3: Embedded LES – The Near-Future Approach…….. 414
15.4 Task 3.4: Hybrid LES – A Step Forward…..…….. 415
15.5 Task 4.1.2: Application Challenges…..…….. 418
16 DES Implementation, Validation and Application at TU-Berlin…..…….……..……... 420
16.1 Modelling Developments…..…….……. 420
16.2 Test Cases…..…….……..…….. 421
16.3 DES Investigations……..…….. 421
16.3.1 DES Validation for Massively-Separated Flows…….. 421
16.3.2 Time Step Sensitivity of DES…..…….……. 422
16.3.3 Dependency of DES on the Underlying RANS Model…..…….……..……..... 422
16.3.4 Assessment of the Numerical Scheme……..... 422
16.3.5 Additional Length Scale Substitutions and the Grey Area Problem…..…….……..... 423
16.3.6 Correction of RANS Model Damping Term Behaviour in LES Mode…..…….……..... 424
16.3.7 The IDDES Method for Wall-Modelled LES and Combination with Adaptive Wall Functions……. 424
16.4 Conclusions and Outlook…..…….……. 425
17 University of Manchester Contribution……..……. 426
17.1 Introduction…….……..…….. 426
17.2 The Stress-Strain Lag Model…….…… 426
17.3 Synthetic Eddy Method…….……..... 428
17.4 Hybrid RANS - LES Method…….……..... 428
17.5 Conclusions…….……..…….. 431

VI Summary of Experience with Hybrid RANS-LES Methods and a Look Ahead…..…….……..……..... 433

References…….. 437

I The DESider Project

1 Summary

The DESider project was motivated by the increasing demand of the European aerospace industries to improve their CFD-aided design procedures and analyses on turbulent unsteady aerodynamic flows. Recent modelling approaches such as DES, hybrid RANS-LES, embedded LES (summarised as "RANS-LES Methods") but also URANS had not yet – at the beginning of the project - reached the same or a comparable maturity for becoming general predictive tools for industrial CFD with a "sensible" reliability.

Thus the major aim was to overcome known weaknesses in the different approaches - in order to support the European aeronautics industry with simulation methods that offer an improved predictive accuracy for unsteady flows exhibiting (massive) separation. Hence, emphasis was placed on the enhancement of both the modelling capabilities of RANS-LES methods and at the same time an alleviation of computational costs.

In that respect, the DESider project denoted a considerable step forward in closing the gap between (U)RANS and LES by investigating and validating known hybrid RANS-LES methods. However, LES was not treated as a stand-alone method as it is well known that full LES for practical (and therefore industrial) use, i.e. for flows with high Reynolds numbers, will not be usable in the next decades. Therefore, the main objectives of the DESider project gathering expertise from European experts in the field of aerodynamics, turbulence modelling and numerical analysis up to multi-disciplinary (aero-elastic and aero-acoustic) design, were laid out as follows:

1. Based on the previously developed DES approach, investigate and develop advanced modelling approaches for unsteady flow simulations as a compromise between URANS and LES, which are able to produce LES-comparable results for real aeronautical applications (in industrial design environments), yet with less costly computational resources than using LES.
2. Demonstrate the capabilities of hybrid RANS-LES approaches in solving industrially relevant applications with a focus on aerodynamic flows characterised by separation, wakes, vortex interaction and buffeting, i.e. flow features all of which are inherently unsteady.
3. Investigate further that hybrid RANS-LES methods can be well and with improved predictive accuracy applied to multi-disciplinary topics as there are aero-acoustics (noise reduction) and aero-elastics (reduced A/C weight, unsteady loads, fatigue issues, improved A/C safety), improving by this a cost-effective design.
4. Facilitate a co-operation between European industries, research establishments and universities. Foster co-operation, improve dissemination, and achieve cross-fertilisation between different industries as there are airframe, turbo-machinery, helicopters, power generation as well as turbo-engines and ground transportation (cars, trains) by setting up a so-called "observer group", that is linked to the project.

W. Haase et al. (Eds.): DESider – A Euro. Effort on Hyb. RANS-LES, NNFM 103, pp. 1–18.
springerlink.com

2 Introduction

2.1 The 'Aeronautics and Space' Priorities as a Background for DESider

It is the European Vision-2020 report (issued by the "Group of Personalities") in preparing for the global challenges, which documents why the DESider project was positively contributing to the general objectives of the aeronautics priority. When the new vision for future aircraft is aiming at "more affordable, safer, cleaner and quieter" aircraft, enhanced design processes are playing an important role and future design processes very much rely on complete "design chains" in a multi-disciplinary environment where computational fluid dynamics (CFD) with increased predictive accuracy is playing a major role. Hence, future air transport systems will have to support European growth and attract and foster business, whilst meeting the needs of European citizens for travel and transport, as well as the requirements to preserve the environment and quality of life. With an estimated average growth of 5% per year air traffic volume will triple by 2020 – and is addressing demanding aims:

1. Five fold reduction in accidents,
2. Halving perceptive aircraft noise,
3. 50% cut in CO_2 emission per passenger kilometre (halving fuel consumption)
4. 80% cut in NO emissions,
5. Air traffic system capable of handling 16 million flights a year with 24h operation at airports and more comfort for passengers.

As mentioned above, improved aerodynamics – and all multi-disciplinary designs with aerodynamics involved, in the DESider case aero-elasticity and/or aero-acoustics need CFD simulation tools which offer the best ever achievable accuracy in the shortest design time.

DESider, as an active part of the European Commission's 6^{th}-Framework programme (2002-2006), with its thematic priority on 'aeronautics and space', did address the general objectives for aeronautics:

1. Strengthening competitiveness,
2. Improving environmental impact with regard to noise and emission,
3. Improving aircraft safety and security,
4. Increasing operational capacity and safety of air transport systems.

When considering the primary objectives of the DESider project to provide the European Aerospace Industry with approach(es) to exploit substantial advances made on the research side in the area of simulating turbulent unsteady aerodynamic flows exhibiting large areas of separation and strong vortices (equivalent to noise sources), a direct impact on aircraft design aiming at less fuel consumption due to reduced weight, improved flight trajectories, and indirectly a positive impact on environmental issues is straightforward.

2.2 State of the Art

When dealing with complex (e.g. high angle of attack) turbulent separated and hence vortical flows, (U)RANS modelling, the today's workhorse in industrial aerodynamics, has frequently appeared or proven to be a poorly adapted approach. While LES has shown viable capabilities of resolving the flow structures and achieving more accurate predictions, it is still too costly to be used at present in aeronautical applications - even for a single airfoil at high Reynolds numbers. To close the gap between RANS and LES, a class of hybrid RANS-LES methods has been previously developed, among which the so-called detached eddy simulation, DES, which – at a first glance - serves as an industrially relevant approach.

Enormous efforts of numerous researches all over the world have driven the development, verification and validation of Reynolds-Averaged Navier-Stokes (RANS) turbulence models for a multitude of flow problems. In many cases these models have been even applied to Unsteady Reynolds-Averaged Navier-Stokes (URANS) computations in cases where the flow is either forced to be unsteady because of body movement or where large flow-separating areas naturally lead to large-scale unsteady flow behaviour.

Currently available experimental data suggest that the latest generation of (U)RANS models is able to accurately predict flows under adverse pressure gradients, including flows with (small) separation bubbles, but it has been observed that turbulence levels in the shear-layers emanating from the separation line are often under-predicted by RANS turbulence models. On the other hand, and due to industrial needs, the advances in predictive capabilities in this area have significantly expanded the range of applications of RANS methods into off-design conditions. Much of this effort was focused in the European Commission's FLOMANIA project (Haase et al, 2006), that was aiming at an improvement of (industrially used) turbulence models and a first employment of full Reynolds stress models in (external) aerodynamics.

Concerning now DES it is well known that the dominant, "detached", eddies in massively separated flows are highly geometry-specific and have not much in common with the "standard" eddies of the thin shear flows RANS models are designed to model. In particular, the RANS modelling theories start off with a "local homogeneity" hypothesis. This is clearly not the case in many industrially relevant applications. As a direct consequence, performing Reynolds averaging over the entire spectrum of the turbulent eddies, and trying to include those geometry-sensitive vortices that are typical for the separated flows is more than an industrial "wish", it is a future demand.

As mentioned, modelling in RANS has to be pursued because the method is (still) the backbone for industry. Nevertheless, RANS has its counterpart in LES, which is assumed being the only "defensible" tool that has a real promise for accurately predicting separated flow regions. A considerably high effort has been put to LES investigations so far but the resolution needed in boundary layers and wakes makes LES unaffordable in many industrial applications in the foreseeable future, see Table 1 below. In that table, Spalart (2000) compares the aforementioned strategies of turbulence simulation in terms of their major features/capabilities, computer power needed and "availability". Obviously, the (highlighted) DES method denotes the (industrial) basis for further direct research/development on all "RANS-LES" methods.

Table 1 Methods according to needs, performance, and readiness, (Spalart, 2000)

Method	Aim*)	Grid: Re-no. Dependence	Empiricism	Grid-Size	Number of time steps	Readiness
2D URANS	Numerical	Weak	Strong	10^5	$10^{3.5}$	1980
3D-URANS	Numerical	Weak	Strong	10^7	$10^{3.5}$	1995
LES	Hybrid	Weak	Weak	$10^{11.5}$	$10^{6.7}$	2045
DNS	Numerical	Strong	None	10^{16}	$10^{7.7}$	2080
DES	**Hybrid**	**Weak**	**Strong**	$\mathbf{10^8}$	$\mathbf{10^4}$	**2000**

* "Numerical" means that grid-refinement does not add any new physics to the solution and its only goal is to improve its numerical accuracy while "Hybrid" means that both numerical and physical improvements occur with grid-refinement.

Although Spalart has issued this table already in the year 1999, it has nothing lost in its meaning, and the recognition of the conflict between RANS/URANS and LES makes it very tempting to create an approach that combines the fine-tuned RANS technology in the attached boundary layers with the power of LES in the separated regions. The general idea of such an approach has first been proposed by Spalart in the year 1997, implying that in the "attached" boundary layer eddies should be modelled in the RANS mode, while the larger "detached" eddies should be simulated - with small eddies in the LES region being also modelled, however with much less influence compared to boundary-layer eddies. Finally, the so-called "detached" eddies have thus inspired the name of Detached Eddy Simulation, DES (Spalart et al, 1997), which was at that time based on a specific formulation of the Spalart-Allmaras (1994) turbulence model.

Most of all, US colleagues together with researchers in St. Petersburg, Russia, (M. Strelets et al.) have used DES and have provided impressive results for complex aerodynamic applications. While the so-called 1997-DES introduced significant grid dependency into the RANS portion of the simulations, which required a grid spacing for the wall grid in both tangential directions that is larger than the boundary layer thickness at that wall location, further grid refinement below this limit often led to Grid Induced Separation (GIS), an issue that was thoroughly investigated in DESider – and the first problem that was solved entirely.

It should be noted that URANS is not a simple transposition of RANS (steady-state flows in statistical equilibrium) into unsteady flows, but unfortunately this was the case in many previous studies in the state of the art. Thus, an alternative to DES is the Scale Adaptive Simulation (SAS) approach recently proposed by Menter (2003). SAS is mainly a URANS model, which is capable to resolve turbulent structures in highly separated regions. At a start of DESider, the SAS method in use was based on a simple one-equation turbulence model. As part of

the DESider project, this was extended to more advanced models. The SAS approach was evaluated in detail against current and improved DES formulations for a variety of test cases and results can be found in the corresponding chapters of this book.

In the range of RANS-LES approaches, another method known as the "embedded LES" approach, carries out a "local" LES simulation in a region of particular interest (for acoustics, complex flow separation, fluid-structure coupling) while the rest of the flow domain "remains" a RANS area. As an example, a local LES would be applied to a wing pod, fuel tank, landing gear or engine inlet with the aerodynamics of the whole aircraft computed by RANS. The advantage over DES is that optimal time-steps and numerical methods can be used for each simulation and the exchange between LES and RANS is based on the provision of synthetic turbulent structures corresponding to statistical characteristics provided by the RANS (rms velocities and length-scales). Results based on the DESider test case matrix are demonstrated below.

The objective of generating synthetic turbulence is common to another approach called hybrid LES-RANS, which has the more ambitious objective of computing the whole flow domain with LES, but introducing a RANS model in the attached boundary layer zones, thus providing huge savings and paving the way to industrial applications. Hence, hybrid LES-RANS is an approach to circumvent the extreme requirement on near-wall grid resolution in LES (Temmermann et al, 2002, Davidson et al, 2003). While DES can be regarded as a method which is an extension of RANS to treat unsteady separated regions, hybrid LES-RANS is an approach which extends LES to make it possible to also treat attached boundary layers. One approach to this is to superimpose instantaneous velocity fluctuations to the LES region along the interface. These fluctuations can be taken from a generic boundary layer, i.e. instantaneous DNS data (Dahlström 2003, Dahlström & Davidson, 2003) or using vortex methods (Sergent, 2002).

Another attempt to make LES useful for industrial applications is to combine LES with wall functions aiming at "realistic" computation times. Although for aerodynamic flows with accuracy requirements of about 1 drag count (equivalent to 0.0001 of the drag coefficient), wall functions are not really applicable. This is different for example for process-industry flows where 10-20% margins are allowed. Thus LES with wall functions were not considered in DESider. However, another alternative for the already mentioned hybrid RANS-LES models are LES formulations with significantly reduced grid resolution requirements which allow the gradual introduction of LES into real life industrial applications. One of those is the "immersed boundary layer" approach, a step beyond the restrictive wall-functions.

Last but not least, additional novel approaches were tested and evaluated in DESider. Amongst them is the "zonal" approach, a hybrid RANS-LES method, where "zones" of RANS and LES are pre-defined according to a pre-investigation of the expected flow field.

3 Technical Project Description

3.1 Research Approach and Technical Achievements

As shown above, the innovative elements of the DESider project are concerned with the improvement and enhancement of flow-physics modelling in general by taking care of current (and future) industrial needs and requirements. This was achieved by an approach giving rise to a validation of different hybrid RANS-LES methods on standardised test cases – which is enabling future investigations by means of comprehensive data base.

The main achievements and studies performed in the course of the DESider project in terms of development and assessment of the turbulence-resolving approaches include:

1. Investigation of the role of the background RANS model in DES in terms of accuracy and robustness,
2. Improvement of RANS-LES switching in DES and, particularly, elimination of premature switching which may occur inside the boundary layer with a grid that is not sufficient for the well-resolved LES,
3. Extension of SAS modelling to two-equation turbulence models and a thorough assessment of the SAS approach against standard URANS and DES methods,
4. Development of DES-based approaches for the near-wall treatment in LES to enable DES application to flows without any separation zone,
5. Assessment of DES, RANS-LES hybrids, and SAS capabilities in aero-acoustics and aero-elastics analysis, i.e., proof-of-applicability of new models in multi-disciplinary design environments,
6. Development of a new experimental data base for channel flow, with measurements carried out by ONERA and data post-processing by University Lille. Experimental results have been used to validate the hybrid RANS-LES methods investigated in the DESider project.
7. Furthermore, as a so-called added value experiment (i.e. work not funded by DESider but used by the partners), a cylinder flow in the critical regime was directed by IMFT.

All findings made in the course of the above studies were supported by applying different (hybrid RANS-LES) approaches to a wide range of thoroughly selected generic and industrial test cases. Based on this, the model limitations were established, best practice recommendations were formulated and, most important, predictive capabilities of CFD codes used by the DESider partners were significantly enhanced.

To conclude this achievements chapter, the DESider project was making Europe and hence the European research community in the area of aeronautics, a world-leading group on (improvement) and application of hybrid RANS-LES methods.

3.2 Dissemination and Exploitation

3.2.1 General Plans According to the Technical Annex

The DESider project, incorporating industry, research institutes and universities focused on the solution of accurate, reliable and robust computational fluid dynamics (CFD) applications in the framework of hybrid RANS-LES methods.

The main topic in that respect denoted the goal to use the new and innovative methods in an industrial framework. All partners, with their highly skilled personnel were given access to highly improved aerodynamics simulation tools, fostering and exploiting their expertise in CFD both on a local and a trans-national basis. Moreover, this was directly improving a dissemination of highly advanced computational tools and giving rise to close the gap between European countries/partners with different levels of potential or technologies. Additionally, the corresponding know-how will be disseminated by young scientists and engineers, which are currently educated in these organisations.

Apart from directly using the experience gained for teaching and training of students and young researchers at research laboratories and also universities, those persons have been – and will be in future - educated in a way making them more competitive for a professional market in which expertise in the numerical simulation of unsteady turbulent flows is getting more and more important for a large variety of applications (interior flows in engines, chemical facilities, exterior flows around cars, trains, aircraft, etc.). Thus, the project outcome will allow universities to pursue their goals in the field of aerodynamics both in research and in teaching.

Last but not least, the “group of observers”, Airbus, Peugeot, Volvo Cars and the University of Liverpool, with their access to all technical information, are promoting dissemination and even exploitation by applying the new/advanced tools in their own environment.

3.2.2 An Attempt to Structure Dissemination and Exploitation Work

In Fig. 1, the dissemination and exploitation structure of the DESider project is sketched. In more detail, the following explanations might lead the reader to an improved understanding:

1. Dissemination and exploitation is represented by the yellow left hand part of the figure, while exploitation activities are related to the green right hand part of the figure.
2. Intentionally, the observer activities, represented by the blue box, are split into dissemination and exploitation activities, in the exploitation case, direct and immediate exploitation is enabled.
3. All partners in the DESider project have exchanged knowledge and expertise in an interactive way, as indicated by the red DESider box.
4. “Links to other projects” are seen to be activities related to dissemination.
5. Red arrows indicate activities dedicated to DESider as a whole; no specific inter-partner activities are meant here.

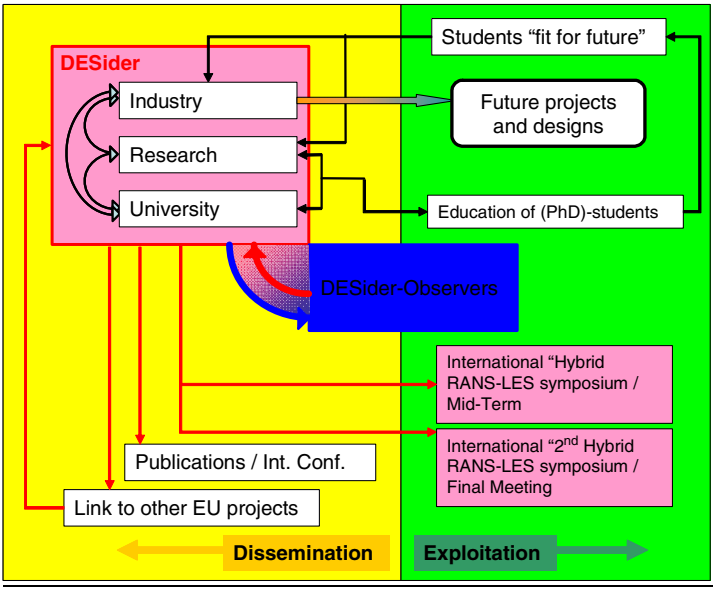

Fig. 1 Sketch of dissemination and exploitation activities

6. The black arrows are seen to be more partner-wise or to be at least organisational (industry-research- university) activities that are clear exploitation related.
7. Research labs and universities are providing additional means for educating students (pre- or post-diploma/PhD). Because of its future consequences, education of students is seen as an exploitation activity.
8. The main industrial exploitation is linked to the use of the new and by the end of DESider well validated hybrid RANS-Les methods for future design aspects.
9. DESider has set up a first conference on “Hybrid RANS-LES Methods”, an event that was 14/15 July 2005 at FOI in Stockholm in association with ER-COFTAC and sponsored by EADS-MAS, ANSYS, FOI and NUMECA.
10. A second symposium followed on Corfu, 17/18 June 2007. 4 invited lectures were accomplished by 26 contributed presentations, with the majority of presentations coming from non-DESider researchers. Sponsors were again EADS-MAS, ANSYS, FOI and NUMECA, accompanied by EUROCOPTER Deutschland GmbH, and Airbus Deutschland GmbH via the European KAT-net-II project.

3.2.3 Publication of Results

Concerning results obtained from DESider, two books are published.

The first book comprises results from the Hybrid RANS-LES Symposium that took place on Corfu in June 2007 as part of the final meeting. This was an open conference presenting all presentations, together with an overview article by

P. Spalart. As it can be seen from the book layout provided in Figure 2 below, the symposium contributions have been published in the Springer series on “Notes on Numerical Fluid Mechanics and Multidisciplinary Design”, Vol. 97, 2008.

The second book/publication is this present publication.

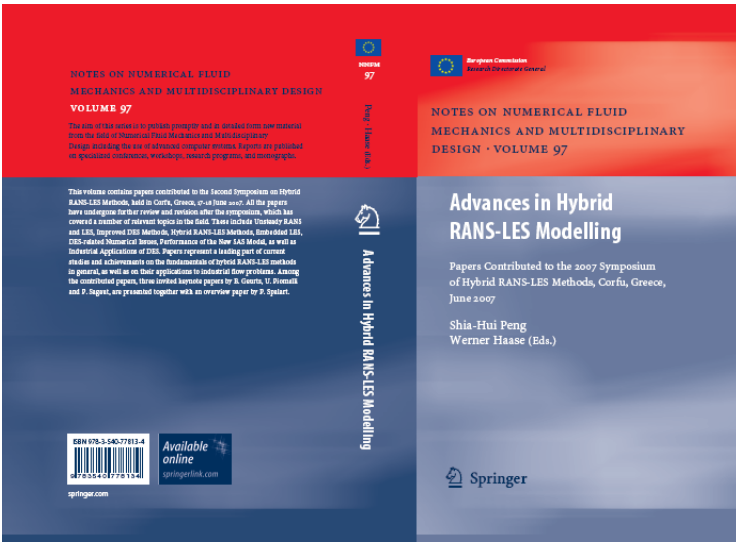

Fig. 2 Hybrid RANS-LES Symposium - Publication of the Corfu conference

3.3 Description of Tasks

A graphical overview describing the DESider project can be taken from Fig. 3, see next page.

Task 1.1 – Project Management

The overall objective of this task was to provide a sound and thorough basis for the technical work going to be carried out and to provide all relevant tools for a successful management and administration of the DESider project, tools that ensured that all partners were contributing to these "administrative aspects" in a comparable way. This included all aspects from meeting preparation versus project monitoring to taking care of successful exploitation.

Task 1.2 - Web Server

AWeb site was set up for the DESider project and maintained during the runtime of the project in order to better disseminate results, knowledge and information in the consortium. This Web site was split into a “public” and a “private” (consortium confidential) part, the latter password protected. The Web site is still maintained and can be visited under http://cfd.mace.manchster.ac.uk/desider. The reader is also referred to Section 6 below.

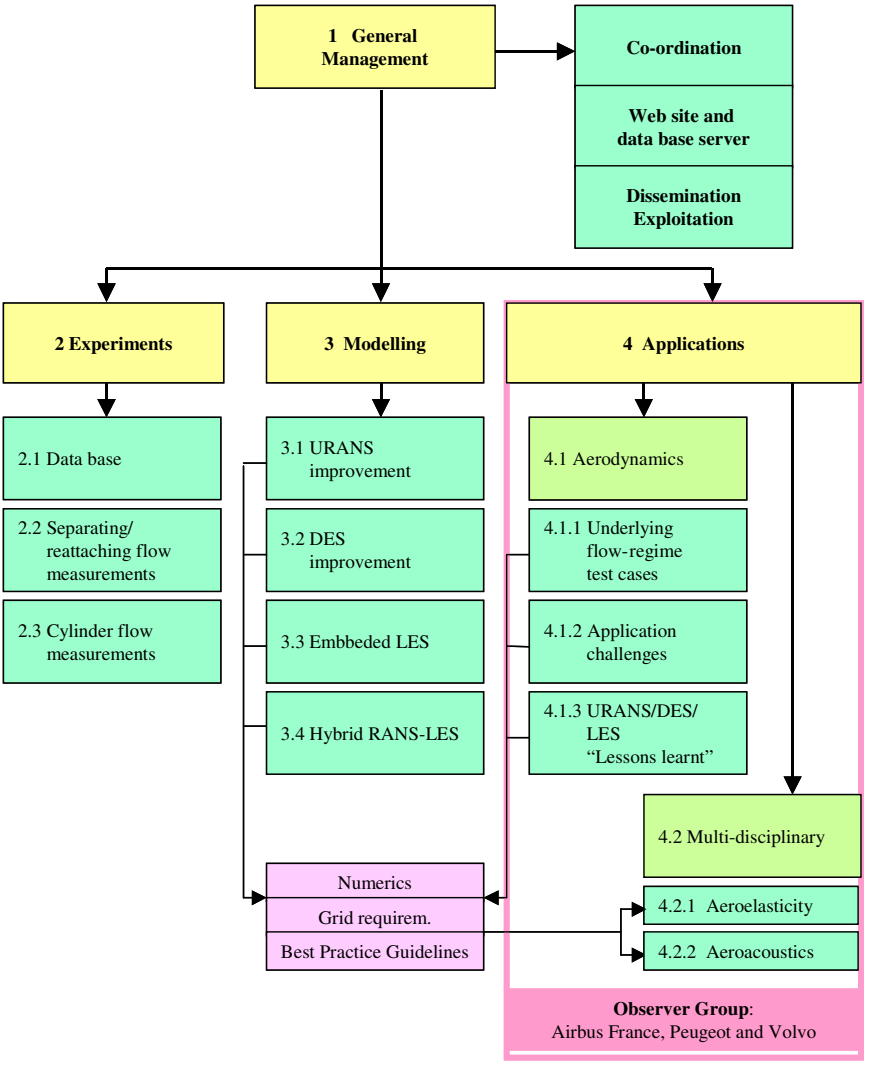

Fig. 3 The DESider work plan - an overview

Task 1.3 - Dissemination/Exploitation

Besides dissemination of knowledge during run-time of the DESider project, exploitation of the achieved expertise was of utmost importance. The latter can be underlined by recognising the impact of DESider on all future industrial projects where CFD is involved. A specific dissemination/exploitation action was initiated including the above mentioned "observer group" consisting of Airbus France, Peugeot-PSA, Volvo Cars and Liverpool University (at a later stage).

Task 2.1 - Data Base

The objective of this task was to set up a data base for test cases and to specify test cases for modelling calibration, validation and verification, which should cover both fundamental baseline test cases and test cases relevant to industrial applications. This has been carried out successfully.

A test-case group has been formed, including ANSYS, EADS-MAS, FOI, ICL, IMFT, ONERA, and UMIST. At the first group meeting, all the proposed test cases had been discussed and reviewed. This meeting concluded 22 test cases (with two mandatory cases) as relevant for DESider. An important focus was put on the specification of the geometry and flow conditions of the DESider bump measurement carried out by ONERA, see chapter III.1.

The test-case data base has spanned widely, ranging from "underlying-flow regime" cases, new experimental measurements to application-challenge cases (including aero-acoustic and aero-elastic cases) with one co-ordinator assigned for each test case.

Task 2.2: Measurements of Separating/Re-attaching Flows

The goals of the new DESider measurements – the ONERA channel-bump experiment - were to investigate separated flow and its reattachment in order to:

1. Provide statistical data to validate computations, especially on critical points such as the prediction of the separation, its unsteady behaviour and the recovery of the boundary layer downstream of reattachment,
2. Provide information on the turbulent structures to compare them to the ones predicted by the computations.

The experiment was first designed by ONERA and pre-investigated by ANSYS by means of CFD methods. Information about the water tunnel was provided by ONERA while ANSYS tried to define a bump with a smooth turning to avoid geometry driven separation. As the tunnel has a rectangular section, a horizontal bump was preferred to have a higher aspect ratio. Attention was also paid to have a rather long separated region as well as a long enough recovery region - to be able to probe both regions easily. Finally, a bump shape has been proposed by ANSYS. With this shape the preliminary simulations have shown a noticeable mid-span separation zone. Flow visualizations confirmed the obtained CFD results. The separation on the bump has a nearly two-dimensional character, except of course very close to the side walls, the side vortices are unsteady but not flapping, the reattachment occurs about five to six bump heights downstream and the wall streamlines rapidly align with the tunnel axis downstream of reattachment.

For the wall measurements, liquid crystals (LC) were used to get information about the location of separated and reattached regions, while LDV measurements were performed first to document the whole entry plane, to be taken as the inflow condition for the computations.

The main part of the experiment though, was devoted to PIV measurements. A stereo PIV system, with four cameras was used to cover a large field of view.

Moreover, IMFT has carried out own measurements (cylinder flow), an "added value" as it was only partially supported by DESider funds. These experiments were carried out in the S1 and S4 wind tunnels of IMFT, by using Three-Component PIV, PIV-3C, two-component *time-resolved* PIV, TR-PIV, as well as a combination of both techniques - that constitutes a new approach. Appropriate and detailed signal processing techniques have been applied to capture the organised and chaotic turbulence processes and their non-linear interaction for the strongly detached unsteady flow around a circular cylinder at Reynolds number ranges entering the critical regime. For the majority of the experiments, the vertical and spanwise confinement of the flow was fixed by transparent walls to allow taking into account the exact boundary conditions within a realistic CPU time for the CFD simulations. The complete data base is available on the DESider Web, see section 6 of this chapter.

Task 3.1 - Improved URANS Modelling

URANS simulations based on the "classic" turbulence models have shown a very limited range of unsteady flow features and are therefore not optimal for the simulation of the turbulent structures in highly separated flows. So the goal of this task was to develop innovative URANS models, where – compared to DES - no explicit grid dependency is introduced into the equations. Therefore, within the current project, first of all turbulence models were considered with good predictive capabilities for URANS applications. The models have in common that they resolve unsteady features of the flow to a more extent than the classic ones and permit to account for the influence of turbulent structures on aerodynamic flows - without the high computing requirements of standard LES formulations.

In other words, the objective of this task was to develop more sophisticated RANS turbulence models that must be further away from equilibrium and in many cases also strongly affected by streamline curvature (e.g. vortices) but, in contrast to DES, do not involve LES-like explicit grid-dependence of the solution.

Task 3.2 - DES with Improved Modelling

The goal of this task was to investigate and develop modelling approaches in the context similar to, yet more feasible/sophisticated than, the original DES approach by Spalart et al. Thus, the aim was to incorporate advanced turbulence models in DES to cope with "more sophisticated" approaches. A major item was also related to "rotation corrected" turbulence models, emphasising on modelling vortices more correctly. The latter includes accurate prediction of vortex breakdown as well as modelling of non-dissipative vortices (trailing vortices) caused by wing-tip, flap devices, etc.

Specifically, the objectives read:

1. Improvement of the RANS-LES switching procedure in DES to avoid a grid-sensitive switching from the wall region to an off-wall LES.

2. Development of DES-based approaches for the near-wall treatment in LES.
3. Investigation of the effect of grid arrangement on the standard/original and improved DES models for aeronautical applications.
4. Improvement of coupling DES methods to support multi-disciplinary applications.
5. Investigation of trip-less approach suggested by Shur et al. (1996) for the prediction of transition onset in the transitional separated bubbles in the framework of RANS/URANS.

Task 3.3 - Embedded LES

This task aimed at establishing a methodology for embedding a local LES in a global RANS simulation, which requires numerical and modelling developments, for cases where, in opposition to DES, separation is not triggered by a geometric singularity, or where the upstream or free-stream turbulence matters.

A first and simpler objective is the one-way coupling where the RANS is trusted to provide the inlet and far-field conditions for the LES, e.g. noise generation or fluid-structure coupling of a small protruding obstacle that does not affect the global flow parameters. A challenging task, however, lies in the de-averaging process, generating synthetic turbulent structures using only the RANS data available: rms of velocity fluctuations and a length-scale. Various techniques can be used: vortex method, Langevin equations, wavelet transforms, optimal control of stochastic noise injection. This aim is somewhat similar to reproducing backscatter in SGS modelling where energy is transferred from smaller scales to resolved scales or when the flow is from a coarse grid to a fine grid, some SGS models can be applied (Taylor expansions, deconvolution techniques…).

A further step consists in a two-way coupling, whereby the RANS simulation is regularly updated using LES results where these are deemed more reliable and affect the global flow, such as significant flow separation on a smooth surface. This requires running the RANS and LES simultaneously (each one with their own characteristic time scales) and updating the exchanges at regular intervals.

Task 3.4 - Hybrid LES – A Step Forward

An undesirable feature of the original DES method was that the layer in which the RANS model is used is dictated by the wall-parallel mesh characteristics - that is, there is no explicit control over the thickness of the RANS layer. The solution becomes very sensitive to the RANS-LES switching location, which is usually required to occur out of the wall boundary layer to render reasonable DES (Spalart, 2001).

This has encouraged the development of a variety of RANS-Hybrid (zonal) methodologies beyond traditional wall-function approaches and the original DES. These and other new hybrid modelling methods were investigated and/or developed in this task to show their applicability to industrial requirements.

Consequently, the objective of this task was to develop hybrid modelling approaches combining unsteady RANS to model the near-wall region in a large eddy

simulation with the focus on the development of reasonable matching methodologies between the near-wall RANS region and the off-wall LES region. Several approaches, like the DDES, IDDES, XLES, zonal methods, or LES with wall-modelling have been applied. Descriptions of these methods, including inlet boundary condition treatments, can be taken from chapter II.

Task 4.1.1 - Applications- Aerodynamics: Underlying Flow-Regime Test Cases)

The objective of the complete work package (WP) 4 was to apply models developed in WP 3 to different test cases relevant to industrial flow problems and to test whether the given guidelines acquired in previous tasks still hold. The capabilities of these modelling approaches were demonstrated and investigated through cross-comparison and in comparison to RANS/URANS, available data and/or fully resolved LES, for a number of fundamental flows and real-world aerodynamic flows relevant to aeronautical applications. Work in this task spanned from testing and calibrating the chosen modelling approaches with basic, but relevant test cases over challenging real-world industrial test cases to even multi-disciplinary applications.

The ultimate purpose of this work package was to fully assess their potential of application in an industrial environment. This means to individuate in what practical situations the new technologies can give an improved prediction with respect to RANS modelling. Moreover, it proved necessary to identify the modelling advantages and disadvantages in comparison with other modelling approaches (URANS, existing DES or hybrid models and/or full LES). Hence, to accumulate a reliable data-base on the original and modified DES applications to the generic test cases that permitted to establish certain ranges of the DES applicability to aerodynamic flows and to assess the impact of the accuracy order of the numerical method on the physical order of accuracy.

Task 4.1.2 - Applications- Aerodynamics: Application Challenges

The main objective was to both take advantage and support credibility of the generic, underlying-flow-regime test cases, and to apply findings on real-life, industrially relevant, “real world” test cases in terms of ranges of validity, robustness, numerical efficiency, and affordability for industrial needs.

It is evident that the outcome of this task was supporting best-practice aspects and provided clear recommendations for industry on the performance of different methods and approaches.

Task 4.1.3 - Best Practice: URANS/DES/LES & Range of Validity

The objective of this task was to analyse and demonstrate the capabilities of the modelling approaches covered in this project and, consequently, to give implementation guidelines for industrial end-users, i.e. to generalise experience accumulated in the course of the work of tasks 4.1.1 and 4.1.2 in the form of recommendations on the optimal usage of different approaches in the industrial environment.

Task 4.2.1 - Multi-Disciplinary Applications: Aero-Elasticity

Modern transport aircraft have to become more economic and safe while at the same time being less environmentally intrusive in order to have a high market potential. This leads to high aspect ratio wings with supercritical airfoils optimised for high Mach number cruise and at the same time to high by-pass engines. However, the price to be paid for this may be a lower, unacceptable aero-elastic stability (not only) at high transonic speeds. Thus flutter becomes a limiting factor for further improvement of aircraft, and its accurate prediction for systems (such as wing–pylon–nacelle) becomes more and more important in the aircraft design.

Here, especially design points near the "transonic dip" are very critical where the complex interaction of the structure with a flow with shock boundary-layer interaction and eventually separation can lead to both flutter, which would be disastrous for an aircraft and Limit Cycle Oscillations (LCO) which do not lead to destruction immediately but to fatigue problems in the long run. Due to their inherently unsteady behaviour this is an area where unsteady methods have to be employed anyway and as such the additional effort using the methods to be developed and implemented in DESider was limited but most probably very worthwhile.

Task 4.2.2 - Multi-disciplinary Applications: Aero-Acoustics

One of the major difficulties of aero-acoustic predictions is related to the broadband noise, conditioned by the turbulent fluctuating field. Within an acoustic analogy approach, the DES simulation of a rotor configuration will allow defining both the tone noise contribution from the average blade loading (dipole contribution) and its broadband noise components, arising from the interactions between the wakes, boundary layers and the rotating blades. The resulting acoustic source identification can be connected to a far field wave propagation solution for the far field noise intensity prediction.

It must be noted that a pre-requisite for aero-acoustic simulations is the computation of the source terms in the acoustic field equations (Lighthill (1952, 1954), Ffowcs Williams & Hawkings (1969)). These terms can only be computed if information on the unsteady turbulent structures is available from the CFD simulation and accurate enough. They cannot be obtained – or very limited - from RANS simulations. The methods investigated and optimised within DESider were an essential step forward in terms of computation of aircraft noise and its reduction. Thus, the objective of this subtask was to test and to assess the new models/methods in aero-acoustic applications, and to make turbulence-generated noise source analysis so as to identify the capability of such turbulence modelling approaches in reproducing the range of frequencies for the acoustic pressure spectrum.

4 List of Partners and Addresses

In the following please find the list of partners (industry, research labs, and universities). Participant names in bold denote the official point-of-contact.

Organisation	Participants	Address
EADS Military Air Systems	**W. Haase**	Hoehenkirchener Str. 19d 85662 Hohenbrunn, Germany
	S. Leicher	Dept. MEG91 / Build. 362 Rechliner Str. 1 D-85077 Manching, Germany
Alenia Aeronautica	**N. Ceresola**	C.P. 432 Corso Marche, 41 I- Turino, Italy
ANSYS/CFX	Y. Egorov **F. Menter**	Staudenfeldweg 12 D-83624 Otterfing, Germany
Chalmers University	**L. Davidson** S. Krajnovic	Department of Applied Mechanics Division of Fluid Dynamics Horsalsvagen 7A SE-41296 Gothenburg, Sweden
Dassault	G. Petit **M. Mallet**	DTIAE/AERAV 78, quai Marcel Dassault F-92214 Saint Cloud, France
DLR	B. Eisfeld T. Knoop **D. Schwamborn** K.Weinman	Institut für Aerodynamik und Strömungstechnik Bunsenstr. 10 D-37073 Göttingen, Germany
EDF	S. Benhamadouche **Yvan Fournier** D. Laurence	EDF R&D 6 quai Watier F-78400 Chatou, France
EUROCOPTER Deutschland GmbH	A. D'Alascio **F. Le Chuiton**	Aeronautics, Aeroacoustics & Performance D-81663 Munich, Germany
FOI	**S-H Peng** S. Wallin	Division of Systems Technology Gullfossgatan 6 SE-164 90 Stockholm, Sweden
Imperial College	**M. Leschziner** F. Tessicini	Aeronautics Department Prince Consort Road London SW7 2AZ, England
IMFT	**M. Braza**	EMT2 Group Avenue du Professeur Camille Soula F-31400 TOULOUSE, France
LML	M. Stanislas **J-P. Laval**	UMR 8107 Bv P. Langevin Cite Scientifique F59655 Villeneuve d'Ascq, France
NLR	**B. Soemarwoto**	Anthony Fokkerweg 2 NL_1059 CM Amsterdam, The Netherlands
NUMECA	**C. Hirsch** B. Leonard L. Temmerman	5 Av. Franklin Roosevelt B-1050 Brussels, Belgium

NTS	A. Garbaruk M. Shur **M. Strelets** A. Travin	14 Dobrolyubov Ave. 197198 St.-Petersburg, Russia
ONERA	**B. Aupoix** **G. Pailhas** **P. Barricau** **Y. Touvet**	ONERA DMAE 2? Avenue E. Belin BP 74025 F-31055 Toulouse Cedex 04, France
	S. Deck	ONERA Applied Aerodynamics Department 8, Rue des Vertugadins F 92190 Meudon, France
	Y. Mary V. Gleize	ONERA DSNA BP72 – 29 Avenue de la Division Leclerc 92322 Chatillon Cedex, France
	J.C. Monnnier A. Gilliot C. Geiler	ONERA DAAP 5, boulevard Paul Painlevé 59045 Lille Cedex, France
TU Berlin	C. Mockett **F. Thiele**	Institut für Strömungsmechanik und Technische Akustik, TU-Berlin, Sekr. MB1 Mueller-Breslau-Str. 8 D-10623 Berlin, Germany
The University of Manchester	**D. Laurence** A. Revell	Department of Mechanical, Aerospace & Manufactoring Engineering PO Box 88 Manchester, M60 1QD, UK

Observers		
Airbus France	**L. Tourrette**	316 Route de Bayonne EDGAMTD, B.P. M0131/1 F-31060 Toulouse cédex 9, France
PSA Peugeot Citroen	**F. Perot** S. Depardon	DRIA/SARA/STEV/ARCT Case Courrier: VV013 2, route de Gisy 78943 Velizy-Villacoublay Cedex, France
University of Liverpool	**G. Barakos**	Dept. of Engineering Brownlow Hill Liverpool L69 3GH, UK
Volvo Car Corporation	**J. Ask**	Environment & Fluid Dynamics Center Computational Fluid Dynamics Dept. 91780 PVT3 SE-40531 Gothenburg, Sweden
Bombardier Transportation	**A. Orellano**	Center of Competence for Aerodynamics & Thermodynamics Am Rathenaupark D-16761 Berlin, Germany

5 Conclusion

The European Commission funded the DESIDER project, with 18 partner organisations, running for 36 months with a 6-months prolongation. The project has proven to be very successful as it has enabled the European partners to improve and enhance their knowledge on flow physics modelling, in particular on hybrid RANS-LES methods. Results achieved were very promising and paved the way for new hybrid RANS-LES approaches and presenting ways for making them usable in industry.

Technical achievements apart, the DESider project offered a sound organisational framework promoting understanding and co-operation between partners as well as with third parties that have been supported by expertise that arose from DESider's dissemination and exploitation policy.

The collaboration within DESider was based on tightly controlled information-exchange protocols, clear descriptions of test cases, provision of mandatory meshes, model implementation support, centralised collection of results, a comprehensive collection of information via deliverables, and most of all by a fruitful co-operation between all partners.

All test case/application results are provided in chapter IV of this book, together with brief method descriptions of approaches and methods used by partners in chapter V, the presentation of modelling approaches in chapter II, and – summarising the findings - an attempt to give some advices and best-practice guidelines on the usage of these models in chapter VI.

To conclude, it can be stated (again) that the collective outcome of European projects – as DESider - is seen to be by far greater than what could have been expected to arise from partners working on their own resources only. Evidently, the DESider project – as a European "network" - tended to be far richer and more diverse in approach, in new and challenging ideas, as well as in the different partner-related ways looking at the same problems.

And all partners now hope that the present publication will be of extended value for all those interested in hybrid RANS-LES approaches.

6 The DESider Web Site and How to Access It

As pointed out above, the DESider Web site provided two areas, a public area that is accessible to any web user and, after the welcome page, consists mainly of pages which outline the aims, purpose and work content of the DESider project and, secondly, a private area that requires a project username and password. For dissemination purposes, the DESider consortium has decided to release appropriate information on demand, i.e. to shift documents from the private to the public part of the Web site if it is required by the reader. For reasons of efficiency, and to maximise the usage of existing facilities, the project web site will be maintained on the web server of the CFD/Turbulence Modelling Research Group at The University of Manchester. The web site is (still) available at: http://cfd.mace.manchster.ac.uk/desider.

II Presentation of Modelling Approaches

This chapter contains details of the hybrid modelling approaches used by partners for their work performed in and for the DESider project. It is not intended as a complete review of all currently available hybrid RANS-LES methods, but instead proposes to the reader a set of methods worth noting, validating and even improving.

The complete chapter can be split into three categories,

- *non-zonal hybrid methods* are covered in sections 1-4,
- *zonal hybrid methods* with sections 5-7 and
- *URANS methods*, see sections 8-9 of the present chapter.

1 DES and Its Modifications and Enhancements

A. Garbaruk, M. Shur, M. Strelets, and A. Travin

NTS

Abstract. The present chapter briefly summarises a progress in DES modelling reached in the course of DESider. In the introduction we outline a motivation for development of the hybrid RANS-LES methods, in general, and a place of DES and DES-like models within this rather wide group of turbulence resolving approaches, particularly. Then, in Section 1.2, the original DES formulation is presented together with a general approach to building DES versions based on different background RANS models and a list of such versions used or developed in DESider. Finally, Sections 1.3 and 1.4 describe two more general modifications not related to any specific background model and touching upon the basics of DES. They are Delayed DES (DDES) and Improved DDES (IDDES), which permit respectively to eliminate major flaws of the "standard" DES found in the course of its intensive use both within and outside DESider and to widen an area of DES applicability.

1.1 Introduction

It is currently commonly accepted that a wide range of wall bounded flows with massive separation being of primary importance for aeronautic industry cannot be quantitatively predicted in a reliable way by classical (RANS) models of *any level of complexity*, including non-linear eddy viscosity models and DRSM. On the other hand, approaches based on "first principles", i.e., DNS and LES, which are now considered as quite capable of facing these challenges, are still computationally non-affordable at practical Reynolds numbers and will probably remain such during a major part of this century, even based on a very optimistic prognosis regarding computer power increase. This situation stimulated intensive work on development of hybrid, RANS-LES, approaches whose appearance at the end of

W. Haase et al. (Eds.): DESider – A Euro. Effort on Hyb. RANS-LES, NNFM 103, pp. 19–67.
springerlink.com

the 20th century can be considered to a certain extent as a "turning-point" in a view on turbulence modelling and simulation strategies. These approaches plausibly combine the advantages of RANS and LES and serve as a valuable addition to pure RANS in the arsenal of industrial computational tools until LES and DNS become manageable.

DES proposed by Spalart et al. (1997) is historically the first approach of such a type. Its general idea is to combine the fine-tuned RANS technology in the attached boundary layers with the "raw power" of LES in the separated flow regions populated with relatively large and more geometry-specific "detached" eddies whose representation is beyond the capabilities of the traditional RANS models. Implementation of this idea is gratifyingly simple. It is based on using the same background RANS model with different length scales (RANS and sub-grid ones respectively) depending on the local grid-resolution. Exactly this simplicity and also impressive results obtained in the first uses of DES for the complex aerodynamic applications by its authors (see, for example, Shur et al. (1999), Travin et al. (2000), Strelets (2001)) and positive experience accumulated in the course of FLOMANIA project (Haase et al. (2006)) have motivated further development and assessment of this approach in DESider.

In Sections 1.3 and 1.4 below we present a major outcome of this effort, namely, newly proposed modifications of DES (Delayed DES or DDES and Improved DDES or IDDES). The first one eliminates the odd reaction of the original DES (hereafter DES97) to a grid-refinement beyond some limit ("Model-Stresses Depletion" (MSD) or "Grid-Induced Separation" (GIS)), whereas the second extends the DES-like formalism to Wall Modelling LES (WMLES) and, therefore, significantly broadens DES ranges of applicability. However before this, in Section 1.2, we concisely outline the DES97 formulation and a general methodology used for building its versions based on other than Spalart-Allmaras background turbulence models.

1.2 DES97 Formulation and General Principles of Building DES Models Based on Different RANS Models

DES97 combines the S-A RANS model with its Sub-Grid Scale (SGS) "counterpart" by means of the "DES limiter" defined by

$$l_{DES} = \min\{d_w, C_{DES}\Delta\}, \tag{1}$$

where l_{DES} is the model length scale, d_w is the distance to the wall involved in the destructive term of the S-A model, C_{DES} is the only additional empirical model constant, and Δ is defined as the largest local grid-spacing:

$$\Delta = \max\{\Delta_x, \Delta_y, \Delta_z\} \tag{2}$$

Substituting of the length scale (equ. 1) in place of the distance to the wall in the eddy-viscosity transport equation of the S-A RANS model directly results in the DES97 model, which performs as the background RANS model in the attached

boundary layer near the wall (at $d_w < C_{DES}\Delta$) and as an SGS model with implicit filter $C_{DES}\Delta$ in the separation flow region away from the walls ($d_w > C_{DES}\Delta$).

A more general definition of the DES limiter (equ. 1) compatible with any RANS model given by Travin et al. (2002) reads as

$$l_{DES} = \min\{l_{RANS}, l_{LES}\}, \tag{3}$$

where l_{RANS} is the RANS length scale explicitly or implicitly involved in any RANS model (e.g., for the *k*-ω model this length scale is defined as $l_{RANS} = k^{1/2}/(C_\mu \omega)$, and for the *k*-ε model $l_{RANS} = k^{3/2}/\varepsilon$) and $l_{LES} = C_{DES}\Delta$ is the LES length scale.

Note that in accordance with the definition according to equ. 1, location of the RANS-LES interface depends only upon the grid used in the simulation, whereas with the definition (3) it may become also solution-dependent. Other than that, the latter definition provides some "freedom of choice" regarding specific terms of RANS model equations in which the RANS length scale should be replaced by the DES one. The only "guideline" in this process suggested by Travin et al. (2002) is that at the equilibrium ("generation is equal to dissipation"), resulting SGS model should reduce to the Smagorinsky model. This question was thoroughly studied by TUB in the course of DESider and is discussed in detail by Yan et al. (2005). Leaving aside these "subtleties", (3) suggests a straightforward procedure for building a DES model based on arbitrary RANS model. This resulted in a wide range of DES versions based on RANS models ranging from one- and two-equations linear eddy viscosity models (e.g., S-A and Menter SST *k*-ω models) to algebraic Reynolds stress models (e.g., CEASM of Lübcke et al. (2002)). A list of such models used/developed in DESider is presented in Table 1. Their formulations can be found in the FLOMANIA final report (Haase et al. (2006)) and in the original publications.

The DES models with the low Reynolds number correction appeared in the Table include a modified expression for the LES length scale needed to compensate activation of the low-Reynolds number terms of a background RANS models in the LES mode. It reads as:

$$l_{LES} = \Psi C_{DES}\Delta \tag{4}$$

where the function Ψ depends on the ratio of the eddy and molecular viscosities and deviates from the value of 1.0 only at low sub-grid viscosities (see Shur et al. (2003), Spalart et al. (2006), Mockett et al. (2007)). For RANS models not containing any low-Reynolds number terms (e.g., the Menter SST model), Ψ is equal to 1.

As of today, no strong evidences of noticeable DES model-sensitivity for the wall bounded flows are known (this is supported also by new results presented in

Table 1 DES versions based on different RANS models used/developed in DESider

Acronym	Background RANS model	References
S-A DES (DES97)	S-A model, Spalart and Allmaras (1994)	Spalart et al. (1997)
SAE-DES	S-A model with Edwards and Chandra (1996) modification	
SALSA DES	Strain-Adaptive Linear S-A model, Rung et al. (2003)	Bunge et al. (2007)
S-A DES with low-Re correction	S-A model	Shur et al. (2003), Spalart et al. (2006)
SAE and SALSA DES with low-Re correction	SAE and SALSA models	Mockett et al. (2007)
M-SST DES	k-ω Shear Stress Transport model, Menter (1993)	Travin et al. (2002)
WCX k-ω DES	k-ω model, Wilcox (1988)	Yan et al. (2005)
LLR k–ω DES	Linear Local Realisable k–ω model, Rung and Thiele (1996)	Bunge et al. (2007)
X-LES	TNT k-ω model, Kok (2000)	Kok et al. (2004)
k-DES	Modified Chen-Patel k-equation model, Chen and Patel (1988)	Peng (2006)
k-ε DES	Two-Layer SST k-ε, Chalot et al. (1994)	
CEASM DES	Compact Explicit Algebraic Stress model, Lübcke et al. (2002)	Bunge et al. (2007)
OEM DES	k-ω model, Wilcox (1988)	Braza et al. (2006) Elakoury et al. (2007)
Zonal S-A DES	S-A model	Deck (2005)
DDES	Any background model	Spalart et al. (2006)
S-A and M-SST ID-DES	S-A, Menter SST models	Travin et al. (2006) Shur et al. (2008)
SAE and CEASM IDDES	SAE and CEASM models	Mockett et al. (2007)

Chapter IV of this book). This is naturally considered as an essential advantage of DES. Nonetheless, its versions based on different RANS models are still of interest, at least for two reasons. The first one is that some of these versions still may provide for a higher accuracy, especially when accurate prediction of the separation point (line) is of crucial importance. Second and may be more important motivation for development of such models is caused by "personal affections" of different research groups and aeronautical industries to this or that RANS turbulence model. Whether objective or not, this makes it logical to have DES versions based exactly on those models which are used in the RANS context. A straight example of this practice is the DES version developed in the course of DESider by Dassault Aviation and based on two-layer SST k-ε RANS model: this model is routinely used by the company as a reference RANS model providing for a fairly good accuracy in most of typical applications it deals with.

1.3 DDES

1.3.1 Motivation and Objective

DES97 is well understood in thin boundary layers with flattened grid cells, where it functions in the RANS mode, and in regions of massive separation with grid cells close to isotropic, where DES functions in its LES mode. However it can exhibit an incorrect behaviour in thick boundary layers and shallow separation regions. This behaviour begins when the grid spacing parallel to the wall, $\Delta_{||}$, becomes less than the boundary-layer thickness. The grid spacing is then fine enough for the DES length-scale to follow the LES branch in accordance with (1) and, therefore, lower the eddy viscosity below the RANS level, but resolved Reynolds stresses deriving from velocity fluctuations ("LES content") have not replaced the modelled Reynolds stresses. The depleted stresses reduce the skin friction, which can even lead to premature or Grid Induced Separation (GIS).

To elucidate this issue, Fig. 1 displays three types of grid in a boundary layer. Recall that DES97 is designed to treat the *entire* boundary layer using a RANS model and to apply LES *only* to separated regions.

In the Type I grid, typical of RANS and of DES with a thin boundary layer, the wall-parallel spacings, $\Delta_{||}$, set Δ via (2) and exceed δ, so that the DES length-scale is on the "RANS branch" ($l_{DES} = d_w$) throughout the boundary layer. The model functions as intended, since DES was created precisely to by-pass LES in large areas of thin boundary layer.

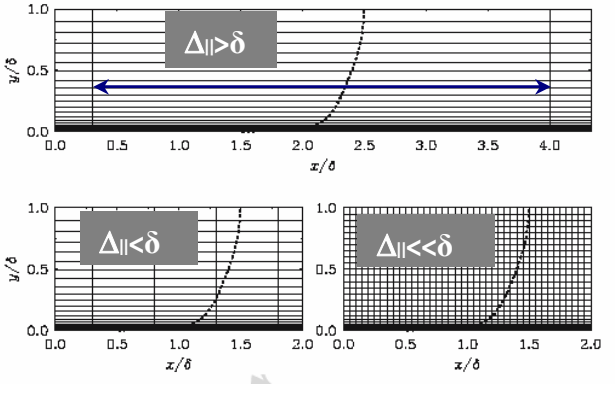

Fig. 1 Grids in a boundary layer. Top – Type 1, natural DES; left - Type II, ambiguous spacing; right - Type III, LES grid. Dashed lines – mean velocity profile. δ is the boundary layer thickness. Assume $h_z \sim h_x$

The other extreme is the Type III, LES grid, with all spacings much smaller than δ. The model functions as an SGS model (i.e., $l_{DES} = C_{DES}\Delta$) over the bulk of the boundary layer, and as a RANS-like model $l_{DES} = d_w$ very near the wall, with a "grey" layer in-between. This regime presents using the DES formalism for WMLES and is considered in sub-section 4 below.

The "ambiguous" grid of the Type II unfortunately activates the LES mode of DES ($l_{DES} = C_{DES}\Delta$) deep inside the boundary layer, but is patently not fine enough to support resolved velocity fluctuations, i.e., LES content. This results in a reduction of the eddy viscosity, and therefore the modelled Reynolds stresses, without any sizeable resolved stresses to restore the balance. The effect is referred to as Modelled Stress Depletion (MSD). It may occur either when the grid is gradually refined starting from the Type I, typically when a user is justifiably seeking grid convergence, or when geometry features demand a fine wall-parallel grid, or when a boundary layer thickens and nears separation. For instance, over an airfoil, the same grid may be of the Type I near its leading edge and of the Type II close to the trailing edge.

The MSD was predicted by Spalart et al. (1997) from the origin of DES97, though anticipated only with "excessive" grid refinement and therefore not perceived as a major issue. However, later on it was encountered in studies of Caruelle (2000) and Deck (2002), and strongly emphasized by Menter and Kuntz (2004) who showed how severe cases of MSD lead to GIS, although with 2D examples which were somewhat artificial. Further studies have shown that 3D grids quite affordable today can lower $\Delta_{\|}$ sufficiently to result in MSD. This motivated a search of the ways to eliminate the MSD.

1.3.2 DDES Formulation

The first proposal on eliminating MSD was that of Menter and Kuntz (2004), who suggested using the F_1 or F_2 functions of the SST *k*-ω model of Menter (1993) to identify the boundary layer and prevent a premature switch of DES to LES mode within it. Then a more general approach, Delayed DES or DDES, was developed (Spalart et al. (2006)), which is a derivative of the Menter and Kuntz proposal applicable to any RANS model. Its formulation is presented below.

The argument of the blending functions F_1 and F_2 of the SST *k*-ω model, $\sqrt{k}/(\omega d_w)$, is the ratio between the internal length scale $\sqrt{k}/\omega$ of the *k*-ω turbulence model and the distance to the wall. Both functions equal 1 in the boundary layer, and fall to zero rapidly at its edge. One-equation models, such as the S-A one, do not have an internal length-scale, but involve the parameter *r*, which is also the ratio (squared) of a model length-scale to the wall distance. Exactly this, slightly modified, parameter is used for building DDES approach:

$$r_d \equiv \frac{\nu + \nu_t}{\sqrt{U_{i,j}U_{i,j}}\,\kappa^2 d_w^2}, \tag{5}$$

where ν is the molecular kinematic viscosity, ν_t is the eddy viscosity, $U_{i,j}$ are the velocity gradients, and κ is the von Kármán constant. Similar to r in the S-A model, this parameter equals 1 in a logarithmic layer, and falls to 0 gradually towards the edge of the boundary layer. The addition of ν in the numerator of (5) corrects the very near-wall behavior by ensuring that r_d remains away from 0. The subscript "*d*" represents "delayed."

The quantity r_d is used in the function:

$$f_d = 1 - \tanh[(8r_d)^3], \tag{6}$$

which is designed to be 1 in the LES region, where $r_d << 1$, and 0 elsewhere (and to be insensitive to r_d exceeding 1 very near the wall). It is similar to F_2, and rather steep near $r_d = 0.1$. The values 8 and 3 for the constants in (6) are based on intuitive shape requirements for f_d, and on tests of DDES in the flat-plate boundary layer (see Spalart et al. (2006)). These values ensure that the solution is essentially identical to the RANS solution, even if Δ is much less than δ (it is conceivable that models very different from S-A would make r_d approach 0 at d_w=δ differently enough to require a modest adjustment of f_d). The application of the above procedures to S-A DES proceeds by re-defining the DES length scale l_{DES} (1):

$$l_{DES} \equiv d_w - f_d \max(0, d_w - C_{DES}\Delta)., \tag{7}$$

Although very simple in terms of coding, this new definition does not represent a minor adjustment within DES97 in terms of physics. Indeed, without it, l_{DES} (1) depends only on the grid, whereas the modified length-scale also depends on the eddy-viscosity field, which is time-dependent. The crucial effect is that RANS function is self-perpetuating, i.e., the model using (7) for l_{DES} can "refuse" LES mode if the function f_d indicates that the point is well inside a boundary layer, as judged from the value of r_d. However, if massive separation occurs, f_d does rise from 0, and LES mode takes over. In fact, the switch from RANS to LES takes place more abruptly following separation than in the DES97, which is desirable, since the grey area between RANS and LES becomes narrower. Although this does not in itself create LES content, it accelerates its growth following natural instabilities, closer to the region where modelled Reynolds stresses are still at full strength. This behaviour is confirmed by the numerical examples presented in Chapter IV.

1.4 IDDES

1.4.1 Motivation and Objective

As already mentioned, both the DES97 and DDES approaches are aimed at computing of massively separated turbulent flows. However, an attempt to apply DES formalism for WMLES in the developed channel flow undertaken by Nikitin et al. (2000) turned out generally successful in the sense that the approach enabled LES predictions at unlimited values of grid-spacing parallel to the wall (in wall units) with no impractical, "channel-friendly", steps. On the other hand, the simulations produced two logarithmic layers: the "inner" log-layer, which arises because the RANS model is constructed to provide it and the "outer" log-layer, which arises since LES is functioning well once all local grid-sizes are much smaller than the distance to the wall. Unfortunately, these two log-layers turn out to be mismatched (have different intercept) resulting in lowering the skin-friction by up to 15%-20%, by far missing up-to-date demands for simple flows. Considering the crucial importance of WMLES which provides huge savings of computer resources compared to the full LES of the wall bounded flows and, thus, paves the way to its industrial applications, creating a model which would plausibly combine DDES capabilities for natural DES uses with WMLES is very tempting and gives a strong motivation for development of a model which would not only provide a remedy of the LLM but present a single set of formulas for both natural DES applications and their WMLES uses, so that different flows or different regions inside a single simulation over a complex geometry could be automatically treated by an optimal model. An approach, which seems to match these objectives developed in the course of DESider was called Improved DDES or IDDES (Travin et al. (2006), Shur et al. (2008)). It includes several new elements, which are presented in the next section one by one.

1.4.2 IDDES Formulation

Sub-Grid Length-Scale

An issue of the optimal definition of SGS length scale in an LES is far from trivial, especially when the computational grid is significantly anisotropic, which is typical of real life simulations of wall-bounded flows. Historically, the most widely employed definition has been the cube root of the cell volume. Although it was challenged in DES97, where the maximum of the three cell dimensions was advocated instead (see (2)), neither definition is successful, if judged by a straightforward application to well-resolved LES of wall-bounded flows: the values of the SGS constants, which work well in free turbulent flows with cubic cells, are then too large. For instance, the optimal value of the Smagorinsky constant for LES of channel flow is about 0.1 if the cube root is used, or roughly half its optimal value of 0.2 for Decaying Isotropic Homogeneous Turbulence (DIHT). Using the maximum grid spacing, as in (D)DES, the difference between the optimal model constants for channel flow and DIHT is even larger. This motivated a search for a more physically justified definition of the sub-grid length-scale, which would not demand different subgrid model constants for the wall-bounded and free turbulent flows.

Considering that wall-proximity effects, primarily inviscid blocking, are involved, the new definition of the sub-grid length scale proposed by Shur et al. (2008) relies not only on the cell sizes, but also explicitly includes a wall-distance dependency, i.e., has the form:

$$\Delta = f(\Delta_x, \Delta_y, \Delta_z, d_w), \tag{8}$$

where Δ is the needed sub-grid length-scale, Δ_x, Δ_y, and Δ_z are the local streamwise, wall-normal, and lateral cell sizes respectively, and d_w is the distance to the wall.

Let Δ_{free} be the infinite-d_w limit of the function $f(\Delta_x, \Delta_y, \Delta_z, d_w)$. Then, following the concept in the DES, it is set equal to the maximum local grid spacing (away from the walls, the grid for an LES should be fairly isotropic anyway, and so the impact of this specific choice is not crucial)

$$\Delta_{free} = \Delta_{\max} \equiv \max\{\Delta_x, \Delta_y, \Delta_z\}, \tag{9}$$

As for the behaviour of Δ in very close vicinity of the wall, it should not follow the drastic decrease of the wall-normal step typical of this region and, therefore, should depend on the wall-parallel steps only:

$$\Delta_{wall} = const(d_w) = f(\Delta_x, \Delta_z), \tag{10}$$

Assuming, finally, that between these two limiting cases Δ is a linear function of d_w and that at any distance to the wall it varies within the range $\Delta_{\min} \le \Delta \le \Delta_{\max}$, a definition of the sub-grid length-scale satisfying all the above demands is formulated as follows:

$$\Delta = \min\{\max[C_w d_w, C_w \Delta_{\max}, \Delta_{wn}], \Delta_{\max}\}, \tag{11}$$

where Δ_{wn} is the grid step in the wall-normal direction and C_w is an empirical constant set equal to 0.15 based on a well-resolved LES of the developed channel flow (see Shur et al. (2008)).

Figure 2 shows two possible types of variation of the sub-grid length-scale Δ defined by (11), normalized by the maximum grid step, across a plane channel with half-width H. The first type (solid line in Fig.2) takes place if $\Delta_{wn} \le C_w d_w$ and, therefore, in accordance with (11), as long as $d_w < \Delta_{\max}$, the length scale Δ remains constant equal to $C_w \Delta_{\max}$. Then, once $d_w > \Delta_{\max}$, it grows linearly ($\Delta = C_w d_w$) until reaching the value of $\Delta_{\max}$, and stays constant after that. The second type of Δ variation (dashed line in Fig.2) corresponds to a strong wall-normal step stretching. In this case, Δ

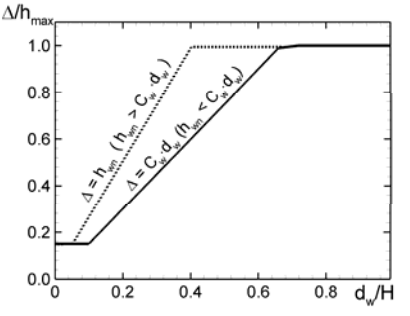

Fig. 2 Two possible types of variation of the sub-grid length-scale (11) across the plane channel

remains constant equal to $C_w\Delta_{\max}$ as long as $h_{wn} < C_w\Delta_{\max}$. Then, it grows with a rate higher than C_w until reaching the value of $\Delta_{\max}$ and after that, just as in the first case, remains constant. Note that this scenario is undesirable, but with any rate of wall-normal step stretching that is acceptable for an accurate LES, it still is not a disaster. For instance, for a wall-normal step varying in accordance with a geometric series, it takes place only if the series index $k > (1 + C_w)$, i.e., if k >1.15, which is very close to the maximum k values 1.2÷1.3 that still provide sufficient accuracy in LES. Therefore, with any acceptable rate of growth of the wall-normal step, the difference between the two branches of (11) is not large.

An example demonstrating a convincing performance of the sub-grid length-scale (11) in the framework of pure LES is presented in Shur et al. (2008).

WMLES Branch

This branch is intended to be active only when the inflow conditions used in the simulation are unsteady and impose some turbulent content. It couples RANS and LES approaches via introducing the following blended RANS-LES length-scale:

$$l_{WMLES} = f_B(1 + f_e)l_{RANS} + (1 - f_B)l_{LES}\,. \tag{12}$$

In accordance with the general DES concept, in order to create a seamless hybrid model, the length-scale l_{WMLES} defined by (12) should be substituted into the background RANS model in place of the RANS length scale, l_{RANS}.

As far as the LES length-scale is concerned, it is defined via the sub-grid length-scale Δ (11) just as it is done in (D)DES (4).

Let us now consider two other ingredients of the length-scale (12), namely, the functions f_B and f_e.

The empirical blending function f_B is a function of $d_w / h_{\max}$ defined by

$$f_B = \min\{2\exp(-9\alpha^2), 1.0\}\,,.\,\alpha = 0.25 - d_w / h_{\max}\,. \tag{13}$$

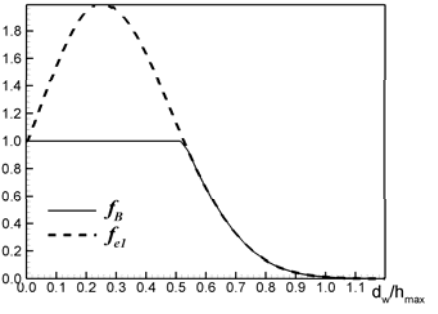

Fig. 3 Profiles of the functions f_{step} and f_{e1} in plane channel

This function varies from 0 to 1 and provides a fast switching of the model from the RANS mode (f_B =1.0) to the LES mode (f_B =0) within the range of wall-distance $0.5h_{\max} < d_w < h_{\max}$ (see solid line in Fig. 3).

The second empirical function involved in (12), elevating function f_e, is aimed at preventing an excessive reduction of the RANS Reynolds stresses as could be caused by the interaction of the RANS and LES regions in the vicinity of their interface. It is instrumental in combating log-layer mismatch and should be close to zero in two cases:

1. when the grid used in the simulation is sufficient for a well-resolved LES (the RANS-LES interface is located very close to the wall, at y^+ >15-20, so that the Reynolds stresses near the interface are negligible);
2. when the final IDDES model (see eqn. (22) below) effectively performs as the background RANS model (otherwise, the activation of the function f_e would corrupt the correct RANS behaviour).

The function built to satisfy these demands reads

$$f_e = \max\{(f_{e1} - 1),\ 0\}\Psi f_{e2} \tag{14}$$

Here the functions f_{e1} is defined by

$$f_{e1}(d_w / h_{\max}) = \begin{cases} 2\exp(-11.09\alpha^2) & if \quad \alpha \geq 0 \\ 2\exp(-9.0\alpha^2) & if \quad \alpha < 0 \end{cases} \tag{15}$$

It provides a "predefined" (depending on the grid but not on the solution) "elevating" device for the RANS component of the WMLES length-scale (12). As seen in Fig. 3, where f_{e1} is plotted together with f_B, it coincides with f_B when $f_B < 1$, i.e., in the transitional RANS-LES region, then, with d_w decrease, grows up to 2.0, and then gradually falls to 1.0 on the wall.

The function f_{e2} reads as

$$f_{e2} = 1.0 - \max\{f_t, f_l\}. \tag{16}$$

It controls the intensity of "elevating" of the RANS component of the model (12) through the functions f_t and f_l:

$$f_t = \tanh[(c_t^2 r_{dt})^3], \quad f_l = \tanh[(c_l^2 r_{dl})^{10}], \tag{17}$$

where the quantities r_{dt} and r_{dl} are defined as

$$r_{dt} = \nu_t / \max\{[\sum_{i,j}(\partial u_i / \partial x_j)^2]^{1/2}, 10^{-10}\}\kappa^2 d_w^2, \tag{18a}$$

$$r_{dl} = \nu / \max\{[\sum_{i,j}(\partial u_i / \partial x_j)^2]^{1/2}, 10^{-10}\}\kappa^2 d_w^2, \tag{18b}$$

and c_l and c_t are additional model constants depending on the background RANS turbulence model. These constants should be adjusted so that the function f_{e2} is virtually zero when either r_{dt} or r_{dl} is close to 1.0. As mentioned above, r_{dt} is close to 1.0 in the logarithmic part of the turbulent boundary layer, and its laminar analogue, the new parameter r_{dl}, is close to 1.0 in the laminar sublayer. So, with the properly chosen constants c_t and c_l, one of the functions, f_t or f_l is close to 1.0, and therefore the functions f_{e2} and f_e are close to zero, which ensures satisfaction of the demands 1) and 2) formulated above. Based on simulations of channel flow, the values of the constants are set to 3.55 and 1.63 for the SA-IDDES and 5.0 and 1.87 for the MSST-IDDES respectively.

Note that, in contrast to f_{e1}, f_{e2} depends on the solution via the quantity $\sum_{i,j}(\partial u_i / \partial x_j)^2$ in the denominator of r_{dt} and r_{dl}. As for introducing of the function Ψ (see equ. 4) into the definition of f_e (14), it is unrelated to the low-Re correction role this function plays in the LES mode of (D)DES, and is purely empirical. A better function to enforce the effect of f_e when the background RANS model has the low-Re terms could probably be devised. However, as shown in Section 9 of Chapter IV, even with this choice, the IDDES performance turns out quite satisfactory, so that a search for another function does not seem to be crucial.

DDES Branch and its Blending with the WMLES Branch

This branch responsible for the DDES-like functionality of IDDES becomes active only when the inflow conditions do not have any turbulent content.

The original DDES formulation (7) may be presented in the following more general (applicable not only to the S-A but for any RANS background model) form:

$$l_{DDES} = l_{RANS} - f_d \max\{0, (l_{RANS} - l_{LES})\}. \tag{19}$$

Unfortunately, no way was found to blend this length-scale with that of the WMLES-branch (12), which would ensure an automatic choice of the WMLES or DDES mode by the final (combined) model, depending on the type of the simulation (with or without turbulent content). However this turned out to be possible with a modified version of (19), namely,

$$\tilde{l}_{DDES} = \tilde{f}_d l_{RANS} + (1 - \tilde{f}_d) l_{LES}, \tag{20}$$

where the blending function $\tilde{f}_d$ is defined by

$$\tilde{f}_d = \max\{(1 - f_{dt}), f_B\} \text{ with } f_{dt} = 1 - \tanh[(8r_{dt})^3]. \tag{21}$$

As shown in Shur et al. (2008), this definition of the length-scale is effectively equivalent to the original one in DDES (19).

With the use of (20), the required IDDES length-scale combining the WMLES and DDES scales (12) and (20) can be defined by:

$$l_{hyb} = \tilde{f}_d (1 + f_e) l_{RANS} + (1 - \tilde{f}_d) l_{LES}. \tag{22}$$

Indeed, in the simulations with an inflow turbulent content, $r_{dt} << 1$, f_{dt} is close to 1.0, and $\tilde{f}_d$ defined by (21) is equal to f_B so that (22) automatically reduces to (12). Otherwise, f_e becomes zero, and so (22) reduces to (20).

Note in conclusion that, provided that the DDES model is already available in a code, implementation of the IDDES approach, i.e., embedding the length scale (22) instead of DDES length-scale (7) is very simple. Also, the approach can be easily coupled with other than S-A and M-SST DES models as demonstrated by Mockett et al. (2007) who implemented SAE and CEASM IDDES versions. However, in theoretical terms, the difference between DDES and IDDES is rather significant. Unlike the usual LES and (D)DES practice, the IDDES employs a new definition of the sub-grid length-scale that includes explicit wall-distance dependence. Other than that, IDDES includes an additional, WMLES, branch and a set of empirical functions designed to provide for both a correct performance of this branch itself and its coupling with the DDES branch.

2 The X-LES Method

Johan C. Kok, Bambang I. Soemarwoto, and Harmen van der Ven

National Aerospace Laboratory NLR

The X-LES formulation (Kok *et al*., 2004) is a particular DES method (Spalart *et al*., 1997) that consists of a composition of a RANS *k*–*ω* turbulence model and a *k*-equation SGS model. In developing the method, the main idea was to extend the DES approach from the Spalart–Allmaras model to the TNT *k*–*ω* model (Kok, 2000), which is the standard RANS model used at NLR. Furthermore, a formulation was sought that maintains the independence from the wall distance of the TNT model and that is based on an existing, clearly defined SGS model. This latter goal was obtained by following the approach of Bush and Mani (2001), in which the *k*-equation SGS model is obtained in LES regions by replacing the length scale in the *k*–*ω* model with the LES filter width both in the dissipation of turbulent kinetic energy and in the eddy-viscosity coefficient. This approach may be contrasted with the SST DES method (Travin *et al*., 2002) in which the length scale is only replaced in the dissipation of turbulent kinetic energy, so that in LES mode the subgrid stresses are still dependent on the *ω*-equation through the eddy viscosity.

Both the RANS *k*–*ω* model and the *k*-equation SGS model use the Boussinesq hypothesis to model the Reynolds or subgrid-scale stress tensor, which depends on the eddy-viscosity coefficient, ν_t. Furthermore, both models are based on the equation for the modelled turbulent kinetic energy *k*, which depends on its dissipation rate *ε*. Both the eddy viscosity and the dissipation rate are modelled using the turbulent kinetic energy as velocity scale together with a length scale l_t,

$$\nu_t = l_t\sqrt{k} \qquad \text{and} \qquad \varepsilon = \beta_k \frac{k^{3/2}}{l_t},$$

where l_t is defined as a combination of the RANS length scale $l = \sqrt{k}/\omega$ and the SGS filter width Δ,

$$l_t = \min\{l, C_1\Delta\},$$

with $C_1 = 0.05$. The RANS *k*–*ω* model is completed by an equation for the specific dissipation rate *ω* and uses the TNT set of coefficients. The X-LES method will be in LES mode when the filter width (times C_1) is small compared to the RANS length scale. Note that in that case the SGS model is completely independent of *ω*.

To define the SGS filter width Δ, there are two options. Either it is defined proportional to a measure of the local mesh width, as in the original DES method, or a constant value is used throughout the flow domain. The latter option has the advantage that it makes the method independent of the grid. It does require a grid that is consistent with the chosen filter width, with mesh widths equal to or smaller than the filter width in the desired LES region.

3 A Hybrid URANS-LES Strategy for Large Eddy Simulation at High Reynolds Numbers

M. Leschziner and F. Tessicini

Imperial College London

3.1 Introduction

The best-known realisation of the (broadly-interpreted) hybrid RANS/LES concept is Spalart et al's (1997) DES method, and the present Chapter contains a detailed article about this method and its two more recent off-shoots, referred to as "Delayed DES (DDES)" and "Improved Delayed DES (IDDES)". However, within a more differentiated classification of near-wall approximations for LES, DES falls into the category of "seamless methods". Such schemes are characterised by the fact that a single turbulence model is used within a single mesh and numerical process to treat both the outer and inner regions; the transition from one to the other being effected, essentially, by grid-dependent modifications to the length scale or related model constants as the model switches from its subgrid-scale form to its RANS form. In the case of DES, attached flow regions upstream of separation are forced, through a deliberate choice of mesh characteristics (e.g. aspect ratio), to operate purely as a steady-state RANS model, with switching to LES effected by the rapid thickening of the shear layer provoked by separation. This is a behaviour that is fundamentally different from one in which the RANS solution is confined to an explicitly prescribed near-wall layer, irrespective of whether it is within an attached or separated region. This then leads to a stricter interpretation of hybrid RANS-LES models as a group in which the RANS-LES interface is prescribed, and in which (usually) two different models, appropriately interfaced, operate, respectively, in the LES and near-wall RANS regions. The designation "Wall-Modelled LES (WMLES)" has also been applied to this type of approach, and the recently formulated IDDES framework contains a WMLES branch that is, in fact, a hybrid RANS-LES model in the sense defined above.

This contribution summarises a particular form of a hybrid RANS-LES method that has been applied by the authors within the DESIDER project. The method, documented in detail in Temmerman et al (2004) and Tessicin et al (2006), involves the prescription of the RANS-LES interface and a particular practice for interfacing the subgrid-scale LES model to (an entirely different) near-wall RANS, within a single mesh and numerical process. A particular feature of the method is the manner in which the RANS is adjusted dynamically, by reference to the LES solution at the interface, in an effort to avoid the well-known problem of "double-counting of turbulence". The manner in which this is done is outlined in the following section.

3.2 Model Formulation

The present formulation is based on the use of one- and two-equation models for the RANS layer and a variety of algebraic subgrid-scale models in the LES

domain, including the dynamic Smagorinsky and WALE models. In all cases, the interface is prescribed to conveniently align with a selected grid line close to the wall. Hence, in general, the y^+ distance of the interface from the wall varies, except for fully-developed channel flow, which is statistically streamwise and spanwise homogeneous. There is no reason, however, why a prescribed y^+ value cannot be adopted in a general implementation; this is merely a question of coding complexity. A single mesh is used, which is progressively refined towards the wall down to a y^+ value of order 1. The savings offered by the hybrid approach, relative to pure LES arises from the fact that spanwise and streamwise refinements do not go hand-in-hand with the wall-normal refinement, so as to ensure low values for the cell-aspect ratios. Hence, in the case of the hybrid scheme, the cell-aspect ratios close to the wall are much higher than normally used in LES.

A study by Temmerman et al (2003) illustrates that, unless special steps are taken to modify the RANS model close to the interface, the RANS model returns turbulence energy, viscosity and shear-stress levels which are substantially higher than those resulting from the LES solution at the interface. This is the result of superposition of the modelled turbulence activity, designed to reflect the entire turbulence spectrum, and the high level of resolved turbulence due to the imposition of unsteady conditions onto the RANS model by the LES solution. This clearly suggests a potentially serious incompatibility at the interface, which requires resolution by the imposition of some limiting criteria. This must be such that disparate approaches to modelling the RANS and SGS viscosities can be accommodated.

In the present formulation in which a one-equation RANS model is used in conjunction with the dynamic Smagorinsky (or similar algebraic) SGS model, it is clear that very large differences in the modelled viscosities can arise, especially when the interface is placed at a freely chosen position. Here, we propose to secure continuity of <u>total</u> eddy viscosity across the interface:

$$\nu_{LES}^{mod} + \nu_{LES}^{res} = \nu_{RANS}^{mod} + \nu_{RANS}^{res}, \tag{1}$$

where the resolved LES viscosity may be extracted from:

$$\nu_{LES}^{res} = \frac{\left\langle (\overline{u_i u_j}^{res}) \bar{S}_{ij} \right\rangle}{\left\langle \bar{S}_{ij} \bar{S}_{ij} \right\rangle}, \tag{2}$$

with the overbar identifying filtered quantities, lower-case u denotes a turbulent velocity fluctuations and $\langle\ \rangle$ signifying some local smoothing operator or averaging over a wall-parallel interface segment. Equation (1) is a form satisfying the minimum mean-square error between the resolved stress anisotropy and the eddy-viscosity. On the RANS side, the total is the modelled turbulent viscosity plus resolved components ν_{RANS}^{res} in the RANS layer (it is noted here that the a-priori tests showed that last is a substantial contributor to the total), the latter evaluated in a manner analogous to (5). Because the resolved stresses are required to be continuous across the interface, equations (1) and (2) imply, at the interface:

$$\nu_{LES}^{mod} = \nu_{RANS}^{mod} . \tag{3}$$

Assuming that a $k-\varepsilon$ model is used in the RANS layer,

$$\nu_{RANS}^{mod} = C_\mu f_\mu \frac{k^2}{\varepsilon} , \tag{4}$$

With the r.h.s. quantities pertaining to the RANS layer, the continuity constraint expressed by equation (4) can be imposed by modifying C_μ:

$$C_{\mu,int}^{av} = \frac{\left\langle \nu_{LES}^{mod} \right\rangle}{\left\langle f_\mu \left(k^2 / \varepsilon \right) \right\rangle} . \tag{5}$$

An analogous approach is taken in the case of a one-equation RANS model, in which the eddy viscosity is represented by:

$$\nu_{RANS}^{mod} = C_\mu f_\mu k l_\mu \tag{6}$$

Simulations for channel flow for bulk Reynolds numbers ranging between 10600 and 42000 show that the level of C_μ extracted from the LES solution at the interface is of order 0.02, as compared to 0.09 usually used. This level arises from the Smagorinsky model, subject to the estimate $k_{LES}^{mod} = \frac{1}{2}\overline{u}_i\overline{u}_i$, where $\overline{u}_i = \overline{U}_i - \hat{\overline{U}}_i$, with ^ denoting a test filter over 2Δ, but other models give similar values. In the case of a one-equation model, ε can simply be replaced by the appropriate length scale expression linking ε, k and l_ε, the last being the dissipation length scale. What remains is to provide a smooth transition, within the RANS layer, from the value derived from (5) to the standard value of C_μ.

Two proposals are made in Temmerman et al (2004), of which the more elaborate is:

$$C_\mu = \begin{cases} \dfrac{15}{40 - y^+}\left[0.09 + (C_{\mu,int} - 0.09)\dfrac{(1-e^{-y/\Delta})}{(1-e^{-y_{int}/\Delta_{\text{int}}})} \right]; & y^+ < 25 \\ 0.09 + (C_{\mu,int} - 0.09)\dfrac{(1-e^{-y/\Delta})}{(1-e^{-y_{int}/\Delta_{\text{int}}})}; & y^+ > 25 \end{cases} \tag{7}$$

where y is the distance from the wall and the subscript '*int*' identifies the interface. This variation has been found to agree well with the interface values extracted from wall-resolved LES for channel flow in which the interface position was systematically varied.

Without the averaging adopted in equation (5), the value for C_μ varies greatly in time and space. The averaging (or filtering) process is thus designed to return a relatively smooth variation of the interface value and the distribution given by

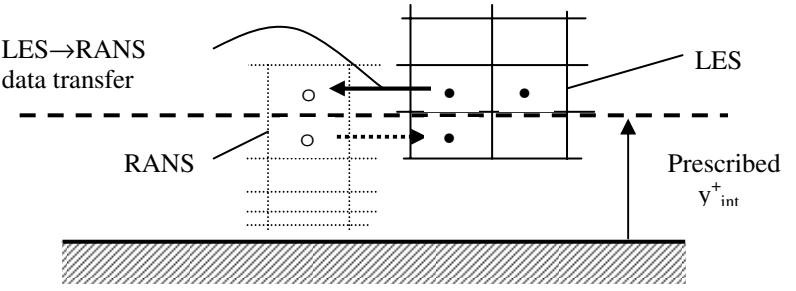

Fig. 1 Two-layer near-wall region with LES-RANS overlap

equation (7), for this is computationally advantageous. However, the penalty paid is the loss of small-scale features, which then leads to an under-estimate of turbulence activity (e.g. shear stress) in the LES region close to the interface. One way of counteracting this effect is to impose at the interface the instantaneous value $C_{\mu,int}^{inst}$. This has been done in several applications to channel flow and found to reduce the "log-law mismatch" often observed in hybrid RANS-LES approximations.

The numerical implementation of the coupling is straightforward and conveyed in Fig. 1. The solution within the near-wall layer is identical to that of the outer LES domain. The LES field at nodes nearest to the interface provide the 'boundary conditions' for the inner layer. Also, at these nodes, C_μ is computed from (5).

3.3 Illustrative Results

Applications of the present method to various flows are documented in Temmerman et al (2004) and Tessicini et al (2006). Sample results are shown in Figures 2 and 3. The former merely illustrates, for channel flow at Re_τ=560 that the

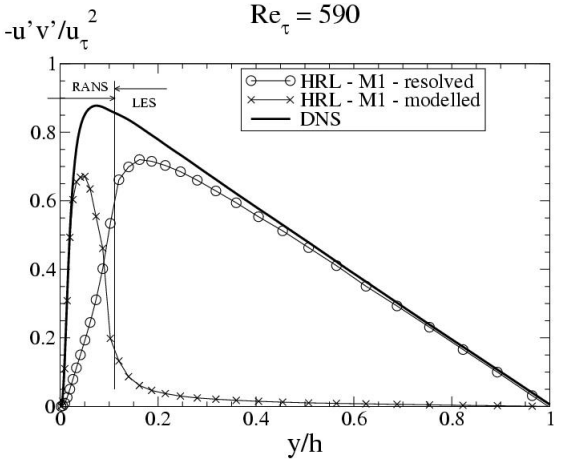

Fig. 2 Modelled vs. resolved shear-stress contributions in channel flow

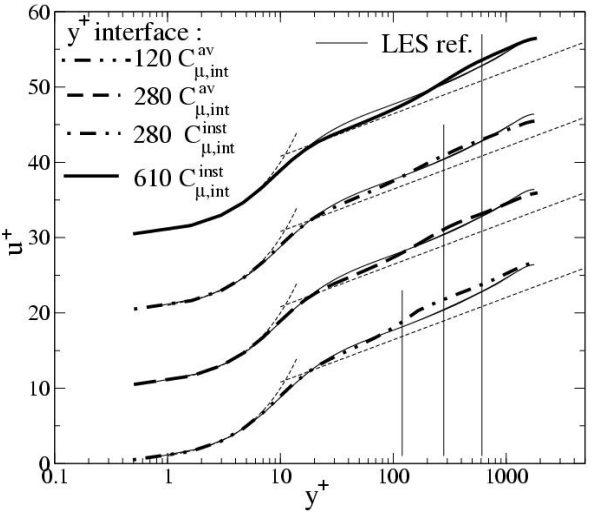

Fig. 3 Velocity distributions in channel flow at Re_τ=2000 – dependence on interface position and manner in which the interface value of C_μ is prescribed

modelled turbulence activity is tightly limited to the prescribed RANS region, diminishing rapidly as the interface is approached.

Figure 3 provides the results of four simulations for a channel flow at Re_τ=2000. These illustrate the dependence of the velocity resolution for interface positions y^+ varying between 120 and 610 and the benefits arising from the imposition of the instantaneous relative to the averaged value of C_μ at the interface.

4 University of Manchester Hybrid RANS LES Method

J. Uribe, D. Laurence, A. Revell, and N. Jarrin

University of Manchester

4.1 Introduction

The final approached developed by the University of Manchester during the course of the DESider project is the hybrid RANS-LES method based on two velocity fields in the same mesh. This approach is based on dividing the contribution of the fluctuating and the averaged velocity fields in the subgrid tensor and modelling each one with its corresponding turbulent viscosity.

4.2 Hybrid RANS - LES Method

The work done on hybrid RANS-LES methods starts by revisiting an idea of Schumann (1975) who proposed to split the residual stress tensor coming out of the filtered momentum equations into a "locally isotropic" part and an "inhomogeneous" part. The isotropic part is proportional to the fluctuating strain and does not affect the mean flow equations but determines the rate of energy dissipation. The inhomogeneous part is proportional to the mean strain and controls the shear stress and mean velocity profile:

$$\tau_{ij}^{r} - \frac{2}{3}\tau_{kk}\delta_{ij} = \underbrace{-2\nu_r\left(\overline{S}_{ij} - \left\langle \overline{S}_{ij} \right\rangle\right)}_{\text{locally isotropic}} - \underbrace{2\nu_a\left\langle \overline{S}_{ij} \right\rangle}_{\text{inhomogeneous}} \tag{1}$$

where $\langle . \rangle$ denotes ensemble averaging of the filtered equations. The viscosities ν_r and ν_a are based on fluctuating and mean strains respectively. The isotropic part of the residual stress tensor has a zero time mean value. By refining the grid the residual stresses must tend to zero, therefore the inhomogeneous part must have a grid dependence parameter in the turbulent viscosity ν_a.

In the context of hybrid LES-RANS, a blending function, f_b, can be used to introduce a smooth transition between the resolved and the ensemble averaged turbulence parts. We write the total residual stress as:

$$\tau_{ij}^{r} - \frac{2}{3}\tau_{kk}\delta_{ij} = -2\nu_r f_b\left(\overline{S}_{ij} - \left\langle \overline{S}_{ij} \right\rangle\right) - 2(1-f_b)\nu_a\left\langle \overline{S}_{ij} \right\rangle \tag{2}$$

In this way the averaged stress would be:

$$\left\langle \tau_{ij}^{r} - \frac{2}{3}\tau_{kk}\delta_{ij} \right\rangle = 2(1-f_b)\nu_a\left\langle \overline{S}_{ij} \right\rangle \tag{3}$$

Which represents just the RANS stress, and the total shear stress would be $2(1-f_b)\nu_a\left\langle \overline{S}_{ij} \right\rangle + \left\langle u'v' \right\rangle$. It is therefore necessary that the blending function f_b

tends to value of unity in the region where $\langle u'v' \rangle$ is resolved correctly and to a value of zero in the region near the wall where the shear stress is under resolved due to the coarse grid.

For the isotropic viscosity the standard Smagorinsky model based on the fluctuating strain is used:

$$\nu_r = (C_s \Delta)^2 \sqrt{2 s'_{ij} s'_{ij}} \tag{4}$$

with $s'_{ij} = \overline{S}_{ij} - \langle \overline{S}_{ij} \rangle$. In the frame of unstructured codes, the filter width is taken as twice the cell volume ($\Delta = 2Vol$).

In this study, the elliptic relaxation model $\varphi - f$ of Laurence et al (2004) is used to calculate the RANS viscosity. This model solves for the ratio $\varphi = \overline{v^2}/k$ used in the turbulent viscosity as:

$$\nu_a = C_\mu \varphi k T \tag{5}$$

where $T = \max\left(\frac{k}{\varepsilon}, C_T \sqrt{\frac{\nu}{\varepsilon}}\right)$. For the channel flow calculations performed during the course of the DESider project, the choice of the RANS models hardly makes a difference but the elliptic relaxation method has been shown to perform well on separating and impinging flows; the aim of the present case is only to show the robustness of the coupling even with a sophisticated RANS model.

The blending function has been parameterised by the ratio of the turbulent length scale to the filter width:

$$f_b = \tanh\left(C_l \frac{L_t}{\Delta} \right)^n \tag{6}$$

Here $C_l = 1$ and $n = 1.5$ are empirical constants. These values were chosen to match the shear stress profile based on channel flow results at $Re_\tau = 395$ with DNS data. When using the $\varphi - f$ model, the wall distance is not a desirable parameter and the blending function can be formulated using $L_t = \varphi k^{3/2} / \varepsilon$. The blending function allows a higher contribution from the LES part as the grid is refined. Different coefficients have been used in the optimisation of the blending function and although the results are not greatly affected, they nevertheless are always better than standard LES on the same mesh. In equation 2 the averaged velocity has been calculated as a running average with an averaging window of about 10 times the eddy turnover time.

4.2.1 Channel Flows

Channel flow computations have been carried out at different Reynolds numbers and the full results can be seen in chapter IV section 8 and in chapter V section 17. The meshes used are too coarse for a standard LES to capture all the small scales and

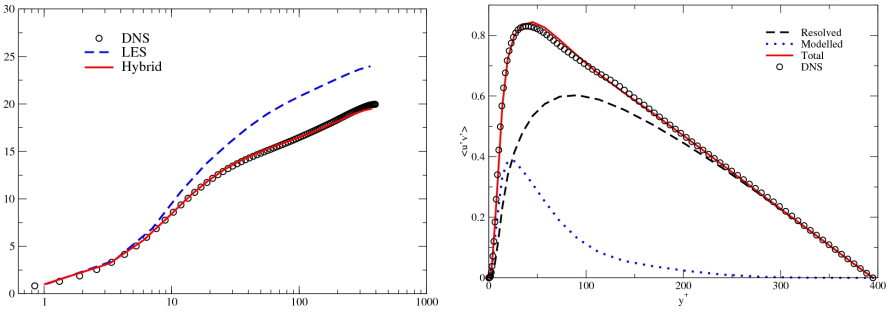

Fig. 1 Channel flow results at $Re_\tau = 395$. Velocity profiles (left) and shear stress (right)

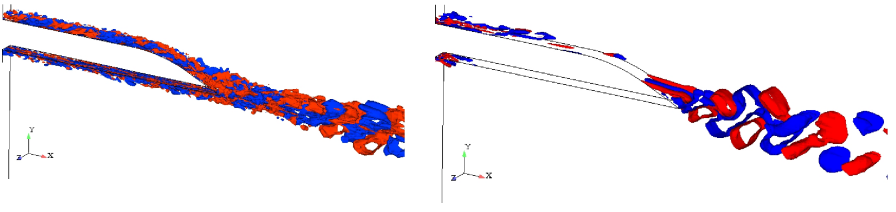

Fig. 2 Iso-Q surfaces on the trailing edge case: Hybrid model (left) DES (right)

therefore the shear stress is under-predicted which, in turn, produces an overestimation of the velocity magnitude. The hybrid model successfully blends the average shear stress and with the resolved one to produce the correct magnitude and therefore a better prediction of the velocity profile. The usual behaviour of overestimating the stream-wise normal stress on coarse meshes by LES is corrected by the hybrid model.

4.2.2 Trailing Edge Computations

In the course of the project, we performed various hybrid simulations of the flow past an axi-symmetric bevelled trailing edge. The case is described fully in chapter IV section 12. In this case the model performs better than the standard DES on the same mesh. The hybrid model is able to sustain the turbulent fluctuations at the inlet and gives a separation zone similar to the reference LES. See chapter V section 18 for more.

5 Zonal Detached Eddy Simulation, ZDES, ONERA

S. Deck

ONERA, Applied Aerodynamics Department

5.1 Motivations

Detached Eddy Simulation is quite well understood in thin boundary layers where the model acts in RANS mode as well as in massive separation regions where the model degenerates toward a subgrid-scale model. The region corresponding to $d \approx \Delta$ where the model needs to switch from fully modelled turbulence (attached boundary layer) to almost fully resolved turbulence (massive separation) is recognized as more delicate. This situation happens when the switching to LES mode occurs inside the boundary layer, e.g., when the grid brings the $\tilde{d} = C_{DES}\Delta$ branch to intrude into the boundary layer. This practically results in lower eddy viscosity, usually not weak enough to allow eddies to form; this consequently yields lower Reynolds stress levels compared to those provided by the RANS model. Note that this issue was already addressed in the original paper presenting the method by Spalart et al. (1997).

For complex geometries, the building of a DES grid appears to be a dilemma for the user. On one hand, the RANS part of the simulation requires a near wall grid spacing in tangential direction much larger than the boundary layer thickness at that location in order to avoid Modelled-Stress-Depletion (MSD, see Spalart et al. (2006)). On the other hand, there is no reason why a DES calculation should accept a coarser grid than a LES calculation. Especially, a LES grid is locally refined in all directions since strongly anisotropic grids are inefficient. As a result, the grid is also refined in regions not supposed to be handled by LES. This situation is practically unavoidable when using structured grids which require refinements in regions of high geometry curvature or in presence of thick boundary layers.

To avoid this problem, Deck (2005a, 2005b) developed a "zonal-DES" approach where attached boundary layer regions are explicitly treated in URANS mode no matter how fine the grid is. That means that, following the example of RANS/LES coupling methods, the user explicitly marks different regions as RANS, or as DES. The motivation is to avoid MSD and GIS and to clarify the role of each region. As a counterpart, the user decision load is significantly increased compared to an 'automatic' approach like DDES.

In effect, the interest of this approach is that the user can focus his grid refinement on regions of interest without corrupting the boundary layer properties farther upstream or downstream.

5.2 Formulation

The formulas of ZDES differ from those of DES97 or DDES in the definition of the ZDES length scale, the subgrid length scale and the treatment of the near wall function in LES mode.

5.2.1 ZDES Length Scale

Let us a consider a multi-domain mesh made of N blocs and let $ides(ndom)_{1 \le ndom \le N}$ be a label such as:

$$\begin{aligned} ides[ndom]=0 &\text{ if domain } ndom \text{ is in RANS mode} \\ ides[ndom]=1 &\text{ if domain } ndom \text{ is in DES mode} \end{aligned} \quad (1)$$

The ZDES length scale becomes:

$$\tilde{d} = (1 - ides[ndom]).d_w + ides[ndom].\min(d_w, C_{DES}\Delta) \quad (2)$$

where d_w and Δ denote respectively the distance to the wall and the subgrid length scale. RANS mode is the default mode so that the user has to mark the DES domains. If necessary, the switching into LES mode within a DES domain can be prescribed by the user (for example, if the boundary layer thickness is known). Note also that eq. (2) can be extended to any RANS model by substituting d_w by the length scale of the underlying turbulence model.

5.2.2 Subgrid Length Scale

In DES mode, the subgrid length scale is given by the cube root of the cell like in classical subgrid scale models:

$$\Delta = \left(\Delta_x \Delta_y \Delta_z\right)^{1/3} \quad (3)$$

The latest evolution of ZDES aims at solving the slow LES development in mixing layers where the following definition proposed by Chauvet et al. (2007) is retained:

$$\Delta = \sqrt{N_x^2 \Delta_y \Delta_z + N_y^2 \Delta_z \Delta_x + N_z^2 \Delta_x \Delta_y} \quad (4)$$

where $\vec{N} = \dfrac{\vec{\omega} + \varepsilon}{\left\|\vec{\omega} + \varepsilon\right\|}$ is the unit vector defined by the vorticity $\vec{\omega}$ and ε is a small value (typically 10^{-8}) that stands for preventing zero divide when the vorticity vanishes. Note that in the early stages of a plane shear layer of spanwise direction is $\vec{z}$, eq (4) becomes $\Delta = \sqrt{\Delta_x \Delta_y}$ which takes into account the local orientation of the vorticity. This new definition prevents a delayed development of instabilities in the shear layer and a subsequent late transition to fully turbulent flow.

5.2.3 Treatment of the Damping Functions

We also chose to remove the near wall functions in LES mode formulation:

$$f_{v1} = 1,\ f_{v2} = 0,\ f_w = 1 \quad (5)$$

This choice also avoids that the damping functions of the RANS model interpret the low eddy viscosity levels typical of resolved LES regions as closeness to the wall with corresponding fast non-linear drop of sub-grid viscosity.

In practice, ZDES switches very quickly to the LES mode, thus limiting the grey area, responsible for the delay in the formation of instabilities.

The ZDES approach has been successfully used to predict the transonic buffet phenomenon over a supercritical airfoil (Deck, 2005a) and on a civil aircraft Brunet et al, 2008, the flow around a high lift configuration (Deck, 2005b), as well as to investigate both subsonic (Deck and Thorigny, 2007), (Simon et al, 2007a) and supersonic ((Simon et al, 2006, 2007b) base flows aerodynamics under highly compressible conditions and the mixing enhancement process in a supersonic mixing layer (Chauvet et al, 2007). In these last references, ZDES is thoroughly validated and compared with the available experimental data including spectral and second-order analysis.

6 University of Manchester Embedded LES Method

N. Jarrin, J. Uribe, D. Laurence, and A. Revell

University of Manchester

6.1 Introduction

During the course of the DESider project the University of Manchester focused the efforts in the development of two new approaches for the use of RANS and LES. The first method is the Synthetic Eddy Method (SEM) in which synthetic turbulence is created from averaged profiles. This is useful for coupling RANS and LES domains where there is a need to impose fluctuations on the RANS field to prevent the LES field from loosing fluctuating components. It also can be used for inlet boundary conditions thus saving computational time devoted to run a precursor simulation. Another important use of the method is the initialisation of a LES calculation where the SEM can create turbulent structures that will help the rapid convergence of the calculation.

6.2 Synthetic Eddy Method

6.2.1 Motivations

This research was motivated by the growing interest of the engineering community in LES and hybrid RANS-LES methods, and the lack of a cost effective, robust and accurate method of generation of inflow data for LES.

The Synthetic Eddy Method (SEM) is a stochastic algorithm that generates instantaneous velocity fluctuations with prescribed mean velocity, Reynolds stresses, length and time scales distributions. The method is based on the classical view of turbulence as a superposition of eddies. The velocity signal is thus expressed as a sum of synthetic eddies with random position and intensity. The characteristics of the synthetic eddies are calculated from input statistical quantities typically available from a RANS solution, and determine the characteristics of the synthesized signal.

A brief description of the method as it is implemented in its latest form is provided below.

6.2.2 Description of the Method

We begin by taking a finite set $S \subset R^3$ of points $S = \{\mathbf{x}_1, \mathbf{x}_2, \cdots, \mathbf{x}_s\}$ on which we want to generate synthetic velocity fluctuations with the SEM. We assume for now that the mean velocity $\mathbf{U}$, the Reynolds stresses R_{ij} and a characteristic length scale of the flow σ are available for the set of points considered.

Definition of the Box of Eddies

The first step is to create a box of eddies B which is going to contain the synthetic eddies. It is defined by

$$B = \{(x_1, x_2, x_3) \in R^3 : x_{i,\min} < x_i < x_{i,\max}, i = \{1,2,3\}\}$$

where $x_{i,\min} = \min_{\mathbf{x}\in S}(x_i - \sigma(\mathbf{x}))$ and $x_{i,\max} = \max_{\mathbf{x}\in S}(x_i + \sigma(\mathbf{x}))$

The volume of the box of eddies is denoted V_B.

Computation of the Velocity Signal

In the synthetic eddy method, the velocity fluctuations generated by N eddies have the representation

$$u_i = U_i + \frac{1}{\sqrt{N}} \sum_{k=1}^{N} a_{ij} \varepsilon_j^k f_{\sigma(\mathbf{x})}(\mathbf{x} - \mathbf{x}^k).$$

where $\mathbf{x}^k = (x^k, y^k, z^k)$ denote the location of the N eddies, ε_j^k is their respective intensities and a_{ij} is the Cholesky decomposition of the Reynolds stress tensor

$$\begin{pmatrix} \sqrt{R_{11}} & 0 & 0 \\ R_{21}/a_{11} & \sqrt{R_{22} - a_{21}^2} & 0 \\ R_{31}/a_{11} & (R_{32} - a_{21}a_{31})/a_{22} & \sqrt{R_{33} - a_{31}^2 - a_{32}^2} \end{pmatrix},$$

$f_{\sigma(\mathbf{x})}(\mathbf{x} - \mathbf{x}^k)$ is the velocity distribution of the eddy located at $\mathbf{x}^k$. We assume that the difference in the distributions between the eddies depends only on the length scale σ and thus define f_σ by

$$f_\sigma(\mathbf{x} - \mathbf{x}_k) = \sqrt{V_B}\sigma^{-3} f\left(\frac{x - x^k}{\sigma}\right) f\left(\frac{y - y^k}{\sigma}\right) f\left(\frac{z - z^k}{\sigma}\right)$$

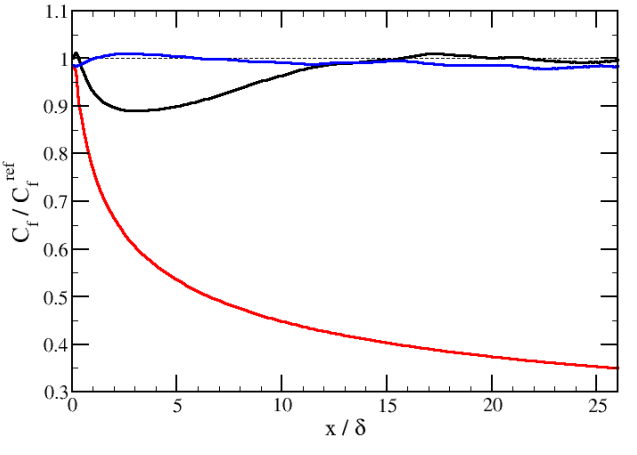

Fig. 1 Channel flow $\mathrm{Re}_\tau = 395$. Evolution of the error in the skin friction coefficient downstream of the inlet for optimal inflow boundary conditions: optimal SEM (black line), uncorrelated random numbers (red line), precursor simulation (blue line)

where the shape function f is common to all eddies. f has compact support $[-\sigma,\sigma]$ and has the normalization $\|f\|_2 = 1$. In the most recent form, the shape function is taken as a tent function, $f(x) = rt\frac{3}{2}(1-|x|)$, if $x<1$ and 0 otherwise.

Before the first time step, the eddies are located independently from one other and taken from a uniform distribution $U(B)$ over the box of eddies; B and ε_j^k are independent random variables taken from any distribution with zero mean and unite variance. In all simulations carried out we choose $\varepsilon_j^k \in \{-1,1\}$ with equal probability to take one value or the other. We choose this distribution because it has a lower flatness than any other distribution. The advantages of this argument will become clearer later on, when some exact results concerning the intermittency of the signal are established.

Convection of the Population of Eddies

The eddies are convected through the box of eddies B with a constant velocity $\mathbf{U}_c$ characteristic of the flow. In our case it is straight forward to compute $\mathbf{U}_c$ as the averaged mean velocity over the set of points S. At each iteration, the new position of eddy k is given by

$$\mathbf{x}^k(t+dt) = \mathbf{x}^k(t) + \mathbf{U}_c dt.$$

where dt is the time step of the simulation. If an eddy k is convected out of the box through face F of B, then it is immediately regenerated randomly on the inlet face of B facing F with a new independent random intensity vector ε_j^k still taken from the same distribution.

In Figure 1 the evolution of the friction coefficient along a channel flow for different synthetic turbulence generation methods can be seen. The SEM recovers the correct level much faster that the use of uncorrelated random numbers.

7 Isotropic Synthetic Fluctuations as Inlet Boundary Conditions

L. Davidson

Chalmers University

7.1 Introduction

In this section we describe a method to prescribe synthesized turbulent inlet boundary conditions. When making LES, DES or hybrid LES-RANS a precursor channel DNS is often used. The disadvantage of this method is that it is difficult to re-scale the DNS fluctuations to higher Reynolds numbers. Here synthesized isotropic turbulent fluctuations are generated at the inlet plane with a prescribed turbulent length scale and energy spectrum. A large number of independent realizations are generated. A correlation in time between these realization is introduced via an asymmetric, non-truncated time filter. In this way the turbulent time scale of the synthesized isotropic turbulent fluctuations is prescribed. The method has been used for channel flow (Davidson 2007a), the 3D hill flow (Davidson 2007b,c), the asymmetric plane diffuser (Davidson 2008) and the Onera bump (Davidson 2008).

7.2 Synthesized Turbulence

A turbulent velocity field can be simulated using random Fourier modes. This was proposed by Kraichnan (1970) and later developed further by Karweit et al. (1991), Lee et al. (1992), Bechara et al. (1994) and Bailly and Juve (1999).. The velocity field is given by N random Fourier modes as

$$u'_i(x_j) = 2\sum_{n=1}^{N} \hat{u}^n \cos(\kappa_j^n x_j + \psi^n)\sigma_i^n \tag{1}$$

where $\hat{u}^n$, ψ^n and σ_i^n are the amplitude, phase and direction of Fourier mode n. The notation used here follows that in Billson (2004), Billson et al. (2993) and Davidson and Billson (2006) and more information is given in these papers. The synthesized turbulence at one time step is generated as follows.

1. For each mode n, create random angles φ^n, α^n and θ^n (see Figs. 1 and 2) and random phase ψ^n. The probability distributions are given in Table 1.
2. Define the highest wave number based on mesh resolution $\kappa_{max} = 2\pi/(2\Delta)$, where Δ is the grid spacing. The fluctuations are generated on a grid with equidistant spacing, $\Delta\eta = y_{max}/N_j$, $\Delta z = z_{max}/N_k$, where η denotes the wall-normal direction and N_j and N_k denote the number of cells in the y and z direction, respectively. The fluctuations are set to zero at the wall and are then interpolated to the inlet plane of the CFD grid (the $y-z$ plane).

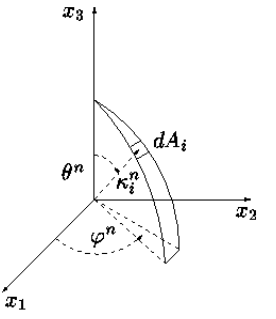

Fig. 1 The probability of a randomly selected direction of a wave in wave-space is the same for all dA_i on the shell of a sphere

3. Define the smallest wave number from $\kappa_1 = \kappa_e / p$, where $\kappa_e = \alpha 9\pi/(55L_t)$, $\alpha = 1.453$. Factor p should be larger than one to make the largest scales larger than those corresponding to κ_e. In the present work $p = 2$.
4. Divide the wavenumber space, $\kappa_{max} - \kappa_1$, into N modes, equally large, of size $\Delta\kappa$.
5. Compute the randomized components of κ_j^n according to Fig. 1.
6. Continuity requires that the unit vector, σ_i^n, and κ_j^n are orthogonal. σ_3^n is arbitrarily chosen to be parallel with κ_i^n (see Fig. 2), and α^n and the requirement of orthogonality give the remaining two components.

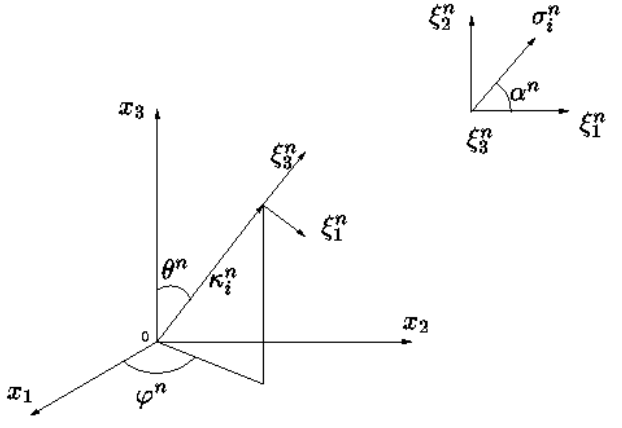

Fig. 2 The wave-number vector, κ_i^n, and the velocity unit vector, σ_i^n, are orthogonal (in physical space) for each wave number n. The unit vector, σ_i^n, is defined such that $\sigma_i^n \kappa_i^n = 0$ (superscript n denotes Fourier mode n). Furthermore, σ_3^n is parallel to κ_i^n (i.e. $\sigma_3^n = \xi_3^n$). The direction of σ_i^n in the $\xi_1^n - \xi_2^n$ plane is randomly chosen through α^n

Table 1 Probability distributions of the random variables

$$
\begin{aligned}
p(\varphi^n) &= 1/(2\pi) \qquad 0 \le \varphi^n \le 2\pi \\
p(\psi^n) &= 1/(2\pi) \qquad 0 \le \psi^n \le 2\pi \\
p(\theta^n) &= 1/2\sin(\theta) \qquad 0 \le \theta^n \le \pi \\
p(\alpha^n) &= 1/(2\pi) \qquad 0 \le \alpha^n \le 2\pi
\end{aligned}
$$

7. A modified von Kármán spectrum is chosen, see Eq. 2 and Fig. 3. The amplitude $\hat{u}^n$ of each mode in Eq. 1 is then obtained from $\hat{u}^n = (E(|\kappa_j^n|)\Delta\kappa)^{1/2}$.
8. Having $\hat{u}^n$, κ_j^n, σ_i^n and ψ^n, allows the expression in Eq. 1 to be computed.

$$
\begin{aligned}
E(\kappa) &= \alpha \frac{u_{rms}^2}{\kappa_e} \frac{(\kappa/\kappa_e)^4}{[1+(\kappa/\kappa_e)^2]^{17/6}} e^{[-2(\kappa/\kappa_\eta)^2]} \\
\kappa &= (\kappa_i \kappa_i)^{1/2}, \quad \kappa_\eta = \varepsilon^{1/4} \nu^{-3/4}
\end{aligned}
\tag{2}
$$

In this way inlet fluctuating velocity fields (u', v', w') are created at the inlet $y-z$ plane.

A fluctuating velocity field is generated each time step as described above. They are independent of each other, however, and their time correlation will thus be zero. This is unphysical. To create correlation in time, new fluctuating velocity fields, U', V', W', are computed based on an asymmetric time filter, as in Billson (2004) and Billson et al. (2003)

$$
\begin{aligned}
(U')^m &= a(U')^{m-1} + b(u')^m \\
(V')^m &= a(V')^{m-1} + b(v')^m \\
(W')^m &= a(W')^{m-1} + b(w')^m
\end{aligned}
\tag{3}
$$

where m denotes the time step number and $a = \exp(-\Delta t/T)$. This asymmetric filter resembles the spatial digital filter presented by Klein et al. (2003). The second coefficient is taken as $b = (1-a^2)^{0.5}$ which ensures that $<U'^2> = <u'^2>$ ($<\cdot>$ denotes averaging). The time correlation of, say, U'_i, will be equal to $\exp(-\Delta t/T)$, and thus Eq. 3 is a convenient way to prescribe the turbulent time scale of the fluctuations. The inlet boundary conditions are prescribed as

$$
\begin{aligned}
\bar{u}(0, y, z, t) &= U_{in}(y) + u'_{in}(y, z, t) \\
\bar{v}(0, y, z, t) &= V_{in}(y) + v'_{in}(y, z, t) \\
\bar{w}(0, y, z, t) &= W_{in}(y) + w'_{in}(y, z, t)
\end{aligned}
\tag{4}
$$

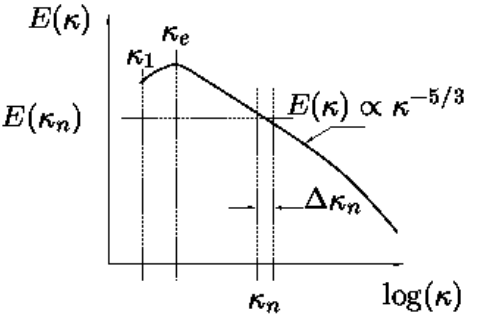

Fig. 3 Modified von Kármán spectrum

where $u'_{in} = (U')^m$, $v'_{in} = (V')^m$ and $w'_{in} = (W')^m$ (see Eq. 3). The mean velocity inlet profile is usually taken from experimental data. If no experimental data are available, the mean velocities can be taken from the wall law (Welty et al, 1984).

$$U_{in}^{+} = \begin{cases} y^{+} & y^{+} \leq 5 (5) \\ -3.05 + 5\ln(y^{+}) & 5 < y^{+} < 30 (6) \\ \dfrac{1}{\kappa}\ln(y^{+}) + B & y^{+} \geq 30 \end{cases} \tag{5}$$

where $\kappa = 0.4$ and $B = 5.2$.

8 Formulation of the Scale-Adaptive Simulation (SAS) Model during the DESIDER Project

F.R. Menter and Y. Egorov

ANSYS Germany GmbH

Abstract. At the start of the DESIDER project, an early version of the SAS model existed which was based on a one-equation model for the eddy-viscosity. During the project, the theoretical basis for the model formulation was substantially broadened using Rotta's length-scale equation as foundation. In addition, several modelling venues have been explored and significant insight into the model behaviour and applicability was gained. Numerous testcases have been computed leading to a validation basis, which allows promoting SAS as a viable industrial turbulence modelling concept.

8.1 Introduction

Historically, the scale-equation of two-equation RANS models (typically ε- or ω) has been derived using dimensional reasoning based on a formulation analogous to the k-equation. A more consistent approach for formulating a scale-equation has been developed by Rotta (1968, 1972). Instead of using purely heuristic and dimensional arguments, Rotta formulated an exact transport equation for kL, where L is an integral length-scale of turbulence. Rotta's equation represents the large scales of turbulence and can therefore serve as a basis for term-by-term modelling. The distinguishing factor of the model proposed by Rotta is the appearance of a natural length-scale in the source terms of the kL-equation, involving a higher derivative of the velocity field. This resulted from the analysis of one of the terms in the exact transport equation. The availability of a natural length-scale is an attractive feature, because it allows a more subtle reaction of the model to resolved and unresolved flow features. However, the third derivative proposed by Rotta has turned out to be problematic and was never actually used in any of the kL-variants. By avoiding this term, the model lost its main distinguishing feature compared to the ε-equation. As a result, the model did not make its way into mainstream aerodynamics and later industrial CFD codes.

During the DESIDER project steps of modernizing the kL-equation have been taken (Menter and Egorov 2004, 2005a, 2005b, 2005c). It is argued that Rotta's assumptions, leading to the term with the third derivative of the velocity field in his kL-equation is not consistent with the nature of the underlying term in the exact equation. As a result, the second derivative appears in the model formulation, satisfying the log-law without the need for additional terms. Furthermore, the model lends itself much easier to the introduction of robust low-Re (viscous sublayer model) terms than the k-ε model (Menter et al, 2006). Within the DESIDER project the model has been re-formulated as a one- and a two-equation model using $\Phi = \sqrt{k}L$ as the new scaling variable. While the resulting KSKL

($k-\sqrt{k}L$) and SKL ($\sqrt{k}L$) offer interesting alternatives to existing RANS models, the more important aspect from the DESIDER project standpoint is their ability of resolving unsteady turbulent structures similar to the behaviour of Detached Eddy Simulation (DES) models, but without an explicit influence of the grid resolution on the RANS part of the model.

During the project, the KSKL model has also been transformed into a *k-ω* framework. This was motivated by the desire to apply the scale-resolving aspects of the model in the established SST model framework. In fact, most of the project testcases have been computed with this version of the SST-SAS model formulation.

As has to be expected with emerging techniques, several details in the model formulation have been modified and optimized in the course of the project. One modification was to use the square of L_{vK} instead of a linear formulation. While this has very limited effects from a practical standpoint in the SST-SAS model, the quadratic form is better in line with the nature of the term in Rotta's original derivation. A second change was made to the formulation of the SST version of the model. This was motivated by a better understanding of the behaviour of the model in the limit of the cut-off range (grid resolution limit of small scales). Finally, the numerical treatment of the equations has been optimized, using modified functions for switching between the second-order upwind and the second order central schemes in the RANS and LES regions respectively.

8.2 Rotta's kL Model

Starting point of the formulation of the SAS modelling concept is an exact equation of Rotta (1968, 1972) for $\Psi = kL$. This equation is then modelled term by term and results in the following equations:

$$\frac{\partial k}{\partial t} + U_j \frac{\partial k}{\partial x_j} = P_k - c_\mu^{3/4} \frac{k^{3/2}}{L} + \frac{\partial}{\partial x_j}\left(\frac{\nu_t}{\sigma_k}\frac{\partial k}{\partial x_j}\right)$$

$$\frac{\partial \Psi}{\partial t} + \frac{\partial \left(U_j \Psi\right)}{\partial x_j} = \frac{\Psi}{k} P_k \left[\hat{\zeta}_1 - \hat{\zeta}_2 \frac{L^2}{L_{Rotta}^2}\right] - \hat{\zeta}_3 k^{3/2} + \frac{\partial}{\partial x_j}\left(\frac{\nu_t}{\sigma_\Psi}\frac{\partial \Psi}{\partial x_j}\right) \qquad (1)$$

$$\Psi = kL; \quad \nu_t = c_\mu^{1/4} \frac{\Psi}{\sqrt{k}}$$

$$\nu_t = \tilde{c}_\mu \frac{\Psi}{\sqrt{k}}; \qquad L_{Rotta}{}^2 = 2\kappa^2 \frac{\partial U / \partial y}{\partial^3 U / \partial y^3}$$

The principle difference of the *kL*-equation to other scale equations is the appearance of the third derivative of the velocity field. All other terms are equivalent to corresponding terms in the *ω* - or the *ε*-equation.

8.3 The KSKL Model

There are several reasons why the inclusion of the third derivative is undesirable. The first one is that it is physically non-intuitive. There is no good reason, why the third derivative should have a strong influence on the definition of a turbulent length-scale.

The second reason why the length-scale as introduced through the third derivative is problematic is that it produces the incorrect sign in a logarithmic layer.

The final reason why the third derivative term should be avoided is that it is difficult to compute in a general purpose CFD code and that it is most likely erratic in a three-dimensional flow field. This is the main reason, why the term has never been used in any published implementation of the model. However, without any higher derivative term, the model has no advantage compared to the scale-equations derived solely on dimensional arguments. As mentioned above, it actually has a disadvantage as it does not allow satisfying the logarithmic layer.

In the referenced publications Menter and Egorov have reformulated Rotta's model. The main change is that instead of the third derivative, a second derivative of the velocity field was introduced into the model. The physical reasoning for this modification can be found in Menter and Egorov (1994). In addition, instead of $\Psi = kL$, the variable $\Phi = \sqrt{k}L$ was used as a scale variable (Menter et al, 2006). This allows the formulation of a on-e and a two-equation model.

The final formulation of the KSKL (K-Square-root-K-L) model reads:

$$\frac{\partial \rho k}{\partial t} + \frac{\partial \left(\rho U_j k\right)}{\partial x_j} = P_k - c_\mu^{3/4} \rho \frac{k^{3/2}}{L} + \frac{\partial}{\partial x_j}\left(\frac{\mu_t}{\sigma_k}\frac{\partial k}{\partial x_j}\right)$$

$$\frac{\partial \rho \Phi}{\partial t} + \frac{\partial \left(\rho U_j \Phi\right)}{\partial x_j} = \frac{\Phi}{k} P_k \left[\zeta_1 - \zeta_2 \left(\frac{L}{L_{vK}}\right)^2\right] - \zeta_3 \rho k + \frac{\partial}{\partial x_j}\left(\frac{\mu_t}{\sigma_\Phi}\frac{\partial \Phi}{\partial x_j}\right) \tag{2}$$

$$\Phi = \sqrt{k}L; \quad \mu_t = c_\mu^{1/4} \rho \Phi$$

$$L_{vK} = \kappa \left|\frac{U'}{U''}\right|; \quad with \quad U'' = \sqrt{\frac{\partial^2 U_i}{\partial x_k^2}\frac{\partial^2 U_i}{\partial x_j^2}}; \quad U' = \sqrt{2 \cdot S_{ij} S_{ij}}$$

In order to satisfy the logarithmic law, the constant ζ_2 has to satisfy:

$$\zeta_2 = \zeta_1 + \kappa^2 / \sigma_\Phi / \sqrt{c_\mu} - \zeta_3 / c_\mu^{3/4}; \quad with \quad c_\mu = 0.09; \kappa = 0.41 \tag{3}$$

Table 1 Model constants $k - \sqrt{k}L$ model

ζ_1	ζ_2	ζ_3	σ_k	σ_Φ
0.80	1.47	0.0288	2/3	2/3

The constants are those given in Menter et al. (2006) – it is likely that they will be further optimized in the future mainly for improved RANS coverage of free shear flows. Experience shows however, that slight variations of constants do not affect the unsteady behavior of the model, which is the main subject of the DESIDER project.

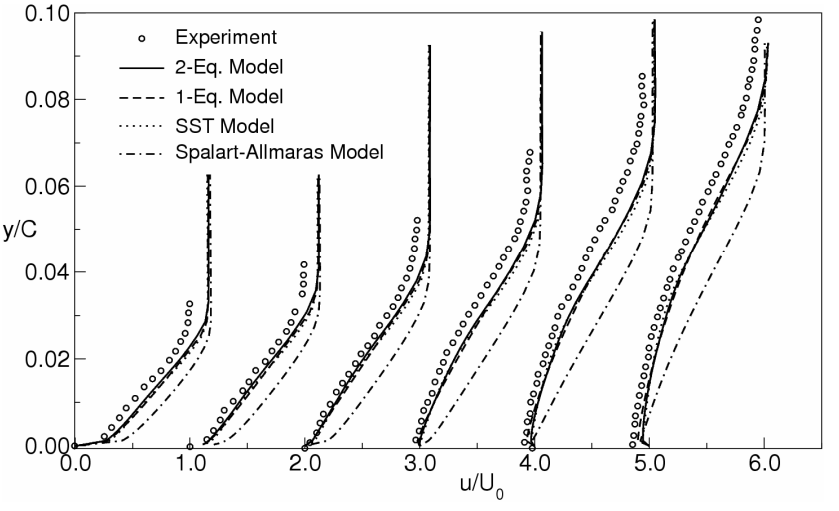

Fig. 1 Velocity profiles at the upper surface around the trailing edge separation zone for NACA 4412 airfoil

It is interesting that an equilibrium transformation of the k-ε model to a one-equation model for the eddy viscosity does actually produce a term equivalent to $-\zeta_2\left(\frac{L}{L_{vK}}\right)^2\frac{\Phi}{k}P_k$ (see Menter 1994, 1997). This discussion is however beyond the scope of the current report. Furthermore in Menter et al. (2006) the formulation of a one-equation model based on the above KSKL model can be found. This reference contains also a viscous sublayer model for both formulations.

As an example of the potential of this new models in RANS mode, Figure 1 shows a comparison of the KSKL (2-Eq), SKL (Square-root-K-L) (1-Eq), SST and the Spalart and Allmaras (1994) model for the NACA 4412 airfoil of Coles and Wadcock (1979) at 13.9° and Re=1.5x10^6 using the model formulation given in Menter et al. (2006).

8.4 The SST-SAS Model

As will be shown below, the KSKL model offers an attractive behavior for certain unsteady flows, which results from the term involving the von Karman length scale. It is therefore desirable to also include this term into other modeling frameworks like the k-ε or the k-ω formulations. The transformation of one scale-equation into another is a straightforward step, requiring little more than the application of the chain rule:

$$\omega = \frac{1}{c_\mu^{1/4}}\frac{k}{\Phi} \rightarrow \frac{D\omega}{Dt} = \frac{1}{c_\mu^{1/4}}\left(\frac{1}{\Phi}\frac{Dk}{Dt} - \frac{k}{\Phi^2}\frac{D\Phi}{Dt}\right) \tag{4}$$

This transformation gives formally (assuming $\sigma_k = \sigma_\Phi$):

$$\frac{\partial \rho\omega}{\partial t}+\frac{\partial \rho U_j\omega}{\partial x_j}=\frac{\omega}{k}P_k\left(1-\zeta_1+\zeta_2\left(\frac{L}{L_{vK}}\right)^2\right)-\rho\omega^2\left(c_\mu-c_\mu^{1/4}\zeta_3\right)$$
$$+\frac{\partial}{\partial x_j}\left(\frac{\mu_t}{\sigma_\Phi}\frac{\partial\omega}{\partial x_j}\right)+\frac{2\rho}{\sigma_\Phi}\left(\frac{1}{\omega}\frac{\partial k}{\partial x_j}\frac{\partial\omega}{\partial x_j}-\frac{k}{\omega^2}\frac{\partial\omega}{\partial x_j}\frac{\partial\omega}{\partial x_j}\right) \tag{5}$$

or in terms of the k-ε model (for completeness):

$$\frac{\partial \rho\varepsilon}{\partial t}+\frac{\partial \rho U_j\varepsilon}{\partial x_j}=\frac{\varepsilon}{k}P_k\left(2-\zeta_1+\zeta_2\left(\frac{L}{L_{vK}}\right)^2\right)-\rho\frac{\varepsilon^2}{k}\left(2-\frac{\zeta_3}{c_\mu^{3/4}}\right)$$
$$+\frac{\partial}{\partial x_j}\left(\frac{\mu_t}{\sigma_\Phi}\frac{\partial\varepsilon}{\partial x_j}\right)-\frac{2c_\mu\rho}{\sigma_\Phi}\left(\frac{k^4}{\varepsilon^2}\frac{\partial}{\partial x_j}\left(\frac{\varepsilon}{k}\right)\frac{\partial}{\partial x_j}\left(\frac{\varepsilon}{k}\right)\right) \tag{6}$$

These equations (in high Re number) form are equivalent to the KSKL model.

In order to recover the performance of the SST model for boundary layer flows, the SAS extension was formulated as an extra term to the ω-equation, which does not disturb the SST models performance for boundary layer flows, but allows for SAS behaviour in unsteady situations. The final additional term to the right hand side of the ω-equation reads:

$$Q_{SAS}=\rho\cdot\max\left[\zeta_2\kappa S^2\left(\frac{L}{L_{vK}}\right)^2-C_c\frac{2}{\sigma_\Phi}k\cdot\max\left(\frac{1}{\omega^2}\frac{\partial\omega}{\partial x_j}\frac{\partial\omega}{\partial x_j},\frac{1}{k^2}\frac{\partial k}{\partial x_j}\frac{\partial k}{\partial x_j}\right),0\right] \tag{7}$$

with $C_c = 2$. The Q_{SAS} term is essentially zero for boundary layer flows (due to $C_c=2$) while it activates the term with L_{vK} in unsteady situations. It should be noted that the additional modification of the above term is only a result of the desire of preserving the SST model. It is not inherent to the SAS approach.

8.5 Numerical Treatment

8.5.1 Convective Terms

The most interesting aspect of SAS models is their ability to resolve turbulent structures in certain flow situations. Figure 2 shows the instantaneous solution computed with the KSKL model (right) compared to the SST-URANS model (left) for a cylinder in crossflow for $Re=3.6x10^6$. The ability of the SAS formulation to resolve the turbulent spectrum for unstable flow is a result of the usage of the von Karman length scale, which allows the model to adjust to already resolved scales. In contrast, SST-URANS models produce single-mode structures which are of the size of the cylinder (similar to a von Karman vortex street). The SAS model allows the original flow instability to develop into a turbulent spectrum down to the resolution limit of the grid. The behaviour of the SAS model is therefore similar to that of a DES model: the attached boundary layers are solved like in a RANS model and the "detached" unsteady-state flow behind the cylinder

results in a LES-like solution. As already discussed above, the advantage of the SAS model compared to DES is that the grid spacing does not explicitly affect the RANS model, as will be discussed below.

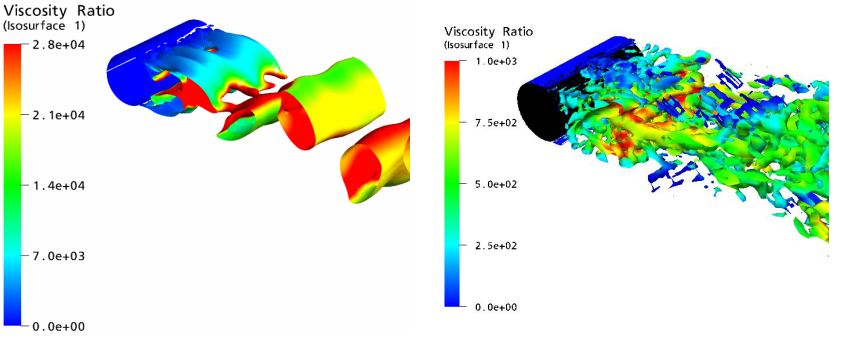

Fig. 2 Circular cylinder in a cross flow at Re=3.6·10^6, Left: SST-URANS, Right: KSKL model. Isosurface of Q=S^2-Ω^{2}Color shows the ratio "Eddy Viscosity/ Molecular Viscosity" (note different scales. Left 0-2.8e4, right 0-1.0e3)

Similar to the DES formulation, the SAS model also benefits from a switch in the numerical treatment between the steady and unsteady regions. In DES, this is achieved by a blending function as proposed by Strelets (2001), which allows with solver the use of a second order upwind scheme in RANS regions and a second order central scheme in unsteady regions. The blending functions are based on several parameters, including the grid spacing and the ratio of vorticity and strain rate (Strelets 2001).

No effort has currently been made for reformulating these functions for the SAS model. A future development could be the formulation of numerical blending functions without the explicit use of the grid spacing. Instead of that the numerical switch could be based on $R = \left| L_{vk} / \Delta \right|$. If R~1 the central difference scheme should be activated. However, this is not urgent, as the current functions have proven adequate for a range of geometrically and physically diverse flows.

8.5.2 High Wave Number Treatment

The treatment of the SAS model at the high wave number limit has undergone several iterations (Menter et al. 2003, 2004, 2005abc). In this limit, the resolved turbulence is of the same scale as the grid spacing Δ. In this limit, the energy which is transported down the turbulent spectrum through vortex stretching and break-up has to be dissipated. This situation is similar to standard LES methods, where the main effect of the subgrid eddy-viscosity is the dissipation of energy from the smallest resolved scales. Since the SAS modelling concept automatically adjusts to the resolved scales (meaning to the smallest scales in the simulation) it was first thought that the model does not require any special provisions for damping small scales, but could provide an adequate level of eddy-viscosity without modification. This was

actually the case with the implementation in CFX, which used a specific numerial treatment for the strain rate, *S*. After some contemplation it became however clear that URANS models which allow the formation of a turbulent spectrum need special treatment at the cut-off limit. As such models are based on partial differential equations, with no information on the grid spacing, they will attempt to transfer the energy through the entire cascade down to the Kolmogorov limit (dissipative scales). However, like in LES, this is not possible as the resolution is not sufficient for this transfer. Information on the grid spacing (in some form or another) will therefore have to be supplied to such methods. In principle, this must be true for all URANS-like methods with scale-resolving capability (e.g. Revell et al., 2008).

In a first implementation of the SAS model in ANSYS-CFX, the information on the grid resolution was implicitly provided by the discretization of the source terms. This can best be explained in a 1D scenario. Assuming the smallest scales possible on a given 1D grid is an odd/even oscillation. Considering two different discretizations of the strain rate:

$$S_N = \left| \frac{U_{i+1} - U_{i-1}}{2\Delta y} \right| \qquad \overline{S} = \frac{1}{2}\left(\left| \frac{U_{i+1} - U_i}{\Delta y} \right| + \left| \frac{U_i - U_{i-1}}{\Delta y} \right| \right) \tag{8}$$

both of which are second order in space and equivalent in a resolved flow field. For the high wave number limit of grid oscillation $U_i = \pm U_0$ with the + sign for odd and the – sign for even indices, one gets:

$$S_N = 0; \qquad \overline{S} = \frac{2U_0}{\Delta} \tag{9}$$

It is heuristically clear that using S_N in L_{vK} would result in reduced damping for grid oscillations, as:

$$S_N = 0 \quad \rightarrow \quad L_{vK} = 0 \tag{10}$$

whereas the element-averaged $\overline{S}$ value gives (assuming a central difference representation of U''):

$$L_{vK} = \frac{1}{2}\kappa\Delta \tag{11}$$

From a physical standpoint, the second result is more in line with expectations, as a given grid cannot resolve scales smaller than the grid spacing. Therefore the *physical* lower limit on L_{vk} has to be $L_{vK} \geq c \cdot \Delta$. It was found that the usage of a 3D equivalent to $\overline{S}$ within the ANSYS-CFX code provided sufficient damping of the smallest scales. While this is a viable option for providing the required damping, it was felt that it lacks generality and does not offer an independent way of calibration for the high wave number limit.

There are numerous other ways of achieving the same goal. One would be the usage of a dissipative scheme for the convective fluxes similar to MILES. Another approach, which was actually followed within the DESIDER project, is the explicit limitation of L_{vK} by the grid spacing Δ in the SST-SAS model:

$$L_{vK} = \max\left(\kappa \left| \frac{U'}{U''} \right|, C_S \Delta \right) \tag{12}$$

where Δ is the cubic root of the cell volume. C_S can be used for calibrating the model for decaying isotropic turbulence (DIT). A value of C_S~0.26 proved adequate in combination with a S_N representation for the strain rate. It is interesting to compare this value to the value of 0.205 which would result from the $\overline{S}$ discretization for grid oscillations. The two numbers are of the same order – and it is therefore understandable that the $\overline{S}$ discretization can implicitly provide the correct damping without an explicit limiter.

Figure 3 shows the results for the DIT testcase at time t=2 for a 32^3 grid for the SST-SAS model. The most interesting curve is the dashed blue one using vortex gradients (S_N) and no lower limit on L_{vK}. In this case, insufficient damping is provided to the smallest scales, leading to increased energy content in the high wave number limit. This is contrary to the expectations for RANS models which are known to damp out small scales very quickly, as shown for the k-ε model. The element gradients ($\overline{S}$) are obviously sufficient for providing enough damping to avoid the energy concentration near the cut-off limit without limiter, although a bit less dissipative than the reference LES.

There is a subtle but important aspect concerning the C_S limiter. When used inside the SST-SAS term Q_{SAS}, it is without problems even for very coarse grids. In this limit, L_{vK} will be increased, which in turn will reduce the impact of Q_{SAS} (Eq. 7) – thereby keeping the model in RANS mode. In other words, the grid limiter would not affect the RANS limit of the model.

This is not the case if Eq. 12 would be applied directly to the KSKL model of Eq. 2. In this case, a large value for Δ would change the behaviour of the RANS

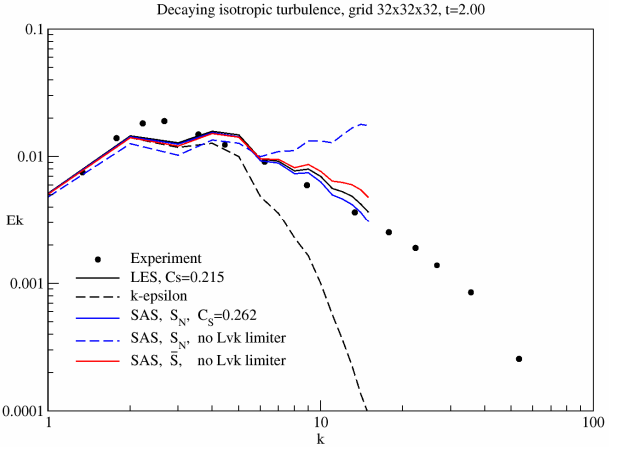

Fig. 3 DHIT results calculated with the SST-SAS model version 2

model. This is problematic as such situations can easily exist in nominally 2D flows computed on 3D grids. L_{vK} is then determined by the 2D physics, whereas the value of Δ can be arbitrarily increased by increasing the grid spacing in the third direction. This will eventually impact the RANS model, which is undesirable.

In order to avoid this potential influence of the grid limiter, another option can be employed. It consists of supplying a lower limit for the eddy-viscosity:

$$\tilde{\nu}_t = \max\left(\nu_t^{SAS}, \nu_t^{LES}\right) \tag{13}$$

where ν_t^{LES} comes from a suitable LES model. ν_t^{LES} should be zero for the RANS situation described above. A suitable model is the WALE model (Nicoud and Ducros, 1999), which produces zero eddy-viscosity for 2D shear flows avoiding any impact of this limiter on typical RANS situations (especially near walls). Another advantage of this limiter is that it allows a clear identification of "LES"-zones within a SAS simulation. In case the LES limiter is activated, the code will use the underlying LES model, invalidating any questions concerning the viability of SAS in the LES limit. Instead of the WALE model, one could also use a dynamic Smagorinsky model, which would also produce an essentially zero LES-eddy-viscosity in RANS regions.

Finally, the interaction within the project partners has shown that it is important to discretize the second derivative of the velocity field with a compact stencil, which reduces to 3 grid nodes in a 1D situation.

8.6 Scale-Adaptive Simulation (SAS) Capability

In the previous chapters, the expression "Scale-Adaptive Simulation - SAS" has been used several times without a proper explanation of its meaning. The terminology is essentially based on a URANS models ability to adjust to resolved structures in a flowfield through its source terms (source term equilibrium). While two-equation models are used routinely for many decades now, their mechanism for determining the turbulent length scale is not fully appreciated. As only the strain-rate, *S*, of the mean flow is provided to the source terms of standard two-equation models, only one scale can be obtained from the equilibrium of source terms. As *S* has dimension *1/T*, the source terms determine only the turbulent frequency, ω. The turbulence length scale cannot be obtained from the source terms alone. It requires the inclusion of diffusion terms. Estimating the diffusion term for a generic variable as:

$$\frac{\partial}{\partial y}\left(\frac{\nu_t}{\sigma}\frac{\partial \Theta}{\partial y}\right) \propto \nu_t \frac{\Theta}{\delta^2} \tag{14}$$

where δ is the thickness of the shear layer, one obtains:

$$L \sim \delta \tag{15}$$

for standard RANS models. This means that independent of any resolved content inside the layer, the model will always return the layer thickness as the appropriate length scale. It is clear that this will result in an over-prediction of the length-scale and the eddy-viscosity for flows with resolved structures. This is turn will result in damping out these resolved flow features as observed in conventional RANS models (see Figure 2). As they use the same scale-equation, this argument also applies to Reynolds Stress models.

The KSKL model and other variants of SAS formulation provide an eddy-viscosity small enough to allow a break-up of large scales into smaller ones under unstable flow situations. Unfortunately, there is no theoretical criterion with respect to when a flow is sufficiently unstable to produce such a mode. It is very likely that this will depend on the specific formulation of the SAS model (e.g. a combination of an SAS scale equation with a Reynolds stress model might be less stable than a simple eddy-viscosity formulation). Nevertheless, there are classes of flows for which a resolution down to the grid limit is typically achieved. Examples are massively separated flows on the leeward side of bluff bodies or strongly swirling flows etc. The industrial applications of the model already cover a significant range of flows:

- Combustion chambers with strong swirl
- Highly stalled airfoils wings
- Flow in chemical mixers
- Flow past valves of combustion engines
- Acoustics simulation of obstacles (mirror etc.)
- Cavity flows

In order of avoiding multiple definitions and naming conventions, as observed in DES, the following definition is given for SAS models, (Menter and Egorov, 2006c).

1. SAS modelling is based on the use of a second mechanical scale in the source/sink terms of the underlying high-Re turbulence model. In addition to the standard input from the momentum equations in the form of first velocity gradients (strain rate tensor, vorticity tensor, …) SAS models rely on a second scale, typically in the form of higher velocity derivatives (typically second derivatives).
2. SAS models satisfy the following requirements:
    a. Provide proper RANS performance in stable flow regions (boundary layer, channel flow, etc.)
    b. Allow the break-up of large turbulent structures into a turbulent spectrum for unstable flow regimes (cylinder in crossflow, airfoil at 60º angle of attack, flow in cavities, …)
    c. Provide proper damping of resolved turbulence at the high wave number end of the spectrum (resolution limit of the grid) (DIT).

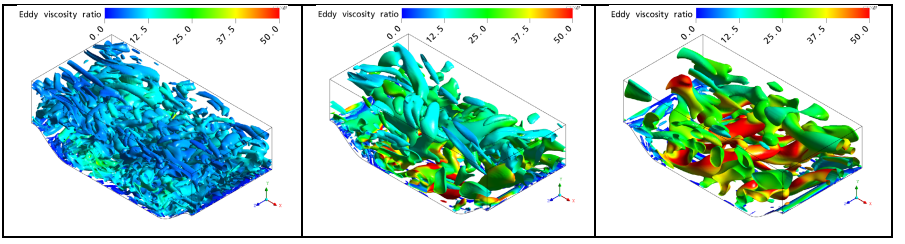

Fig. 4 Turbulent structures for periodic hill flow. Iso-surface for $Q=S^2-W^2$. Color gives ratio of (eddy-viscosity/molecular viscosity). Left $\Delta t=0.045U_B/h$ Middle, $\Delta t=0.09U_B/h$, Right, $\Delta t=0.18U_B/h$

3. Contrary to DES and related methods, 2.a and 2.b are achieved without an explicit grid or time step dependency in the model. Only function 2.c has to be based on information on the grid spacing, other information concerning the resolution limit (dynamic LES model, etc.), or the numerical method (MILES damping etc.).

Figure 4 shows a visual example for scale-adaptivity for the periodic hill flow. The three pictures show the Q-criterion for three simulations of this flow. The left picture was computed with a time step of $\Delta t=0.045U_B/h$ (U_B – bulk velocity, h-height of hill) which corresponds to an LES time resolution. The middle and the left pictures where obtained using a factor 2 and 4 larger Δt on the same numerical mesh ($2.5\text{x}10^6$ nodes). The colour of the figures depicts the ratio of eddy-viscosity to molecular viscosity. The larger time steps do not allow the same spatial resolution as the small ones, resulting in significantly larger turbulent structures. The important aspect is that the eddy-viscosity adjusts accordingly and increases from left to right. It thereby compensates for the non-resolved portion of the spectrum. Further increasing the time step will result in a steady RANS solution for the SST-SAS model. It is interesting to consider the behaviour of a classical Smagorinsky LES model for this situation. As the grid is the same in all three simulations, and as the strain rate is lower for large scales than for small scales, one would obtain actually the opposite behaviour. The Smagorinsky model would predict a lower eddy-viscosity for the under-resolved spectrum and is therefore not scale-adaptive. This behaviour would also carry over to DES methods, as they scale similarly to the Smagorinsky model once the DES limiter is activated.

It is this robust behaviour with respect to space and time resolution which makes the SAS concept a powerful and attractive model for engineering simulations. In many technical flows, the quality of the grid and a proper LES time step cannot be maintained in the entire domain. The SAS model will however always have a fall-back URANS or RANS solution if the resolution is not sufficient for resolving the turbulent scales. In contrast, LES and DES models can return undefined model formulations and potential numerical instabilities under those conditions, as the eddy-viscosity can be unphysically reduced.

The limitation of SAS is that it will not switch into scale-resolving mode if the flow is not sufficiently unstable. In this case, the user has no means of enforcing an unsteady behaviour. If this is the case, the next step is switching to DES, which allows a reduction of the RANS eddy-viscosity by reducing the grid spacing. This in turn is often sufficient for rendering the simulation unsteady. As stressed before however, the grid and time step will then have to be crafted carefully to avoid stress-depletion and or grey zones (meaning undefined model behaviour somewhere between RANS and LES).

If the flow instability is still not sufficient for producing the required unsteady structures, an interface or forcing terms need to be activated between the RANS and LES zones. In that respect all the modelling concepts investigated in DESIDER will find their proper range of applications. From an engineering standpoint, the question is not “which model is better?”, but ”which model is better for a given class of applications?”. For strongly unstable flows the pendulum will likely swing towards the SAS model, for less unstable flows towards DES or even further to more advanced embedded LES models.

9 RANS/URANS Modelling

A. Revell, T. Craft, and D. Laurence

University of Manchester

9.1 The Stress-Strain Lag Model

Substantial development of the Stress-Strain Lag Model was undertaken at UniMAN during the course of the DESider project. Coupling of the Lag model with the popular $k-\omega$ SST model, to form the so-called SST-*Cas* model, has been shown to incorporate some of the advantages of a full Reynolds Stress transport Model (RSM), whilst retaining the efficiency and stability benefits of a eddy viscosity model (EVM) (Revell et al., 2006, 2007).

Motivated by work on cyclic piston engines by Hadžić et al. (2002), the Lag model builds upon existing two equation models with a third transport equation that is sensitive to the local stress-strain misalignment of mean unsteady turbulent flow. The key parameter, C_{as} is defined to represent the dot product of the strain tensor S_{ij}, and the turbulent stress anisotropy tensor a_{ij} as follows:

$$C_{as} = -\frac{a_{ij}S_{ij}}{\|S\|},$$

where $a_{ij} = \overline{u_i u_j} / k - 2/3\delta_{ij}$ is the turbulent stress anisotropy tensor, $\overline{u_i u_j}$ is the Reynolds stress tensor, $k = 0.5\overline{u_i u_i}$ is the turbulent kinetic energy, δ_{ij} the Kronecker delta and the strain invariant $\|S\| = \sqrt{2S_{ij}S_{ij}}$.

The quantity C_{as} projects the six equations of the Reynolds stress transport model onto a single equation. The anisotropy tensor has zero trace and is dimensionless by definition, whereas the strain rate tensor is an inverse time scale and has zero trace only in the condition of incompressibility, which is assumed for this work. An EVM assumes that these two tensors are aligned.

The strategy adopted for this scheme was to develop a transport equation that could be solved to obtain values for the parameter C_{as}. The resulting values could then be used in the evaluation of the production of turbulence kinetic energy P_k, in order to capture some of the features of stress-strain misalignment, but at a much smaller computational cost than employing a full stress transport model. For details on the derivation see Revell (2006). The final implemented form of the transport equation is given as follows:

$$\frac{DC_{as}}{Dt} = \alpha_1 \frac{\varepsilon}{k} C_{as} + \alpha_1^* \|S\| C_{as}^2 + \left(\alpha_3 + \alpha_3^* \sqrt{a_{ij}a_{ij}}\right)\|S\| + \frac{S_{ij}a_{ik}}{\|S\|}\left(\alpha_4 S_{jk} + \alpha_5 \Omega_{jk}\right)$$
$$- \frac{S'_{ij}}{\|S\|}\left(a_{ij} + \frac{2S_{ij}C_{as}}{\|S\|}\right) + \frac{\partial}{\partial x_k}\left[\left(\nu + \sigma_c \nu_t\right)\frac{\partial C_{as}}{\partial x_k}\right],$$

where ε is the rate of dissipation of turbulent kinetic energy and the model constants are given as $\{\alpha_1,\alpha_1^*,\alpha_3,\alpha_3^*,\alpha_4\,\alpha_5,\sigma_c\}$={-0.7, -1.9, 0.267, 0.1625, 0.75, 1.6, 0.5}. The transport equation is derived directly from an RSM, so the constants of the selected underlying pressure-strain model are retained and, in general, there is no requirement to calibrate these constants. The advection of the rate of strains is calculated explicitly.

The transport equation for C_{as} is not in closed form as a model for a_{ij} is still required. This can be obtained from any existing Non-Linear EVM, and in the present work the model of Craft et al (1996) has been selected for this purpose.

9.2 The SST-Cas Model

The fully implemented SST model requires only small modifications to incorporate the C_{as} model. The modification was originally intended to be applied to the production rate of turbulence kinetic energy term only, but it can be applied in a more coherent manner by means of a simple modification to the turbulent eddy viscosity as follows:

$$\nu_t = k\ min\left(\frac{1}{\omega};\frac{0.31}{\|S\|F_2};\frac{C_{as}}{\|S\|}\right),$$

where ω is the turbulent frequency and F_2 is a blending function which takes a value ~1 across most of the boundary layer, dropping to 0 near the top and in the free-stream (Menter, 1994). The value of C_{as} is limited to ±0.31 for the calculation of the production terms, while when evaluating diffusion terms, the absolute value, $|C_{as}|$, is used.

The current version requires special treatment in the near-wall region as a consequence of the modelling of the pressure-strain terms, which are used in the derivation of the transport equation. For high Reynolds number flows of the kind considered in the present work, the simplest treatment consists of preventing the model from acting in regions where viscous effects are expected to be dominant.

10 URANS/OES Tensorial Eddy-Viscosity Modelling

R. Bourguet[1], M. Braza[1], G. Harran[1], A. Sevrain[1], and Y. Hoarau[2]

[1] Institut de Mécanique des Fluides de Toulouse, UMR CNRS 5502
[2] Institut de Mécanique des Fluides et de Solides de Strasbourg (present address)

Abstract. IMFT has contributed in the context of URANS modelling with a directional anisotropy tensor transport modelling in the Organised Eddy Simulation (OES), (Braza, Perrin, Hoarau, (2006)), by means of URANS/DRSM. A tensorial eddy-viscosity concept for the eddy-viscosity has been derived, directionally sensitized to capture non-equilibrium turbulence physics. The turbulence anisotropy tensor in the DRSM model has been projected according to the principal directions of the strain-rate, by transporting a directional criterion of stress-strain misalignment, (Bourguet et al, (2007)). This modelling is also useful in modifying the RANS turbulence length scale in DES.

10.1 Tensorial Eddy-Viscosity Concept in the Turbulence Behaviour Law

This modelling takes into account modification of the turbulence spectrum in the inertial range, due to the non-linear interaction between the coherent and random turbulence processes (Perrin et al, FLOMANIA book, 2006). Therefore, modified turbulence scales are required for flow physics modelling of the turbulent stresses. The equations of motion in the time-domain are the phase-averaged (or ensemble – averaged) Navier-Stokes equations, (Dervieux, Braza, Dussauge, (1998), Jin & Braza, (1994), Cantwell & Coles, (1983)). It is recalled that by using Differential Reynolds Stress transport Modelling (DRSM) the eddy-diffusion coefficient C_μ used in OES two-equation modelling (Bourdet et al., 2007) was evaluated, by adopting the Boussinesq behaviour law as a first approximation. However, this tends to reinforce isotropic character especially in the near wall region. In DESIDER program, the first order turbulence behaviour law (in the sense of the strain rate expressions) has been reconsidered by means of a *directional* eddy viscosity tensor that aims at reinforcing turbulence anisotropy within non-equilibrium regions. This anisotropic constitutive law involves the elements of a spectral decomposition applied to the mean strain-rate tensor, whose respective 'weights' are the components of the eddy-viscosity tensor.

The IMFT's circular cylinder test-case (TC01) allowed quantification of the afore mentioned anisotropy character in the near region of a strongly detached turbulent flow, thanks to an ensemble of advanced measurements technique involving especially time-resolved 3C-PIV (Perrin et al, 2007), as described in the experimental contributions in the present book. These results allowed quantification of a *directional* misalignment between the turbulence anisotropy tensor and the strain rate. This has been used as a criterion for the projection of DRSM anisotropy tensor on the principal directions of the strain rate. This approach is complementary to modifications of turbulence constitutive laws by means of scalar

eddy-viscosity (Non Linear Eddy-Viscosity Models, NLEVM, (Gatski and Speziale, (1993), among other) and to the C_{as} model, (Revell et al, 2005, 2007) that suggested a scalar criterion of stress-strain misalignment derived from DRSM.

10.2 Summary of the OES Anisotropic First-Order Model

Three transport equations have been derived from DRSM to close the anisotropic constitutive law previously described. The corresponding anisotropic first-order closure scheme thus involves five equations in addition to the three momentum equations in the general three-dimensional case: two transport equations for k and ε, as well as three corresponding to each component of directional misalignment coefficient, CV_i. The scalar eddy-viscosity is replaced by the tensorial one in the whole system. The OES turbulence damping function (Jin & Braza, 1994) is used. The modelling consists therefore of solving the following set of equations:

$$-\langle u_i u_j \rangle + \frac{2}{3} k \delta_{ij} = 2 (\nu_{td})_\alpha S_{ij}^\alpha$$

with $S_{ij}^{mi} = \lambda_m^S V_{ij}^m$ and λ_m^S are the eigenvalues of the strain rate, S. Contrary to linear EVM, projection, the coefficients CV_i are no more modelled but predicted exactly as new state variables by DRSM transport equations. The SSG model has been adopted to derive the related transport equations.

$$(\nu_{td})_i = \frac{C_{V\,i}}{2\lambda_i^S} k$$

with

$$\frac{DC_{V\,i}}{Dt} = \left(\frac{4}{3} + c_3^* II_a^{\frac{1}{2}} - c_3\right) V_{\alpha\beta}^i S_{\alpha\beta} + (2 - 2c_4) V_{\alpha\beta}^i a_{\alpha\gamma} S_{\beta\gamma} - \frac{c_2 \varepsilon}{k} V_{\alpha\beta}^i a_{\alpha\gamma} a_{\gamma\beta} + (2 - 2c_5) V_{\alpha\beta}^i a_{\alpha\gamma} \Omega_{\beta\gamma}$$

$$+ (1 - c_1) \frac{\varepsilon}{k} C_{V\,i} + (1 + c_1^*) C_{V\,i} a_{\alpha\beta} S_{\alpha\beta} + \frac{c_2 II_a \varepsilon}{3k} + \frac{2(c_4 - 1)}{3} a_{\alpha\beta} S_{\alpha\beta} - a_{\alpha\beta} \frac{DV_{\alpha\beta}^i}{Dt} + D^{C_{V\,i}}$$

The diffusion term $D^{C_{V\,i}}$ combines viscous and turbulent diffusion contributions and approximated by:

$$D^{C_{V\,i}} = \frac{\partial}{\partial x_\alpha} \left(\left(\nu \delta_{\alpha\beta} + \frac{(\nu_{tt})_{\alpha\beta}}{\sigma_{C_{V\,i}}} \right) \frac{\partial C_{V\,i}}{\partial x_\beta} \right)$$

$\sigma_{C_{V\,i}}$-coefficients are set to the value of one. Moreover the second term issued from the derivation of CV_i, vanishes if the anisotropy tensor is replaced by its approximation, $\hat{a}$: $-\hat{a}_{\alpha\beta} DV_{\alpha\beta}^i / Dt = 0$.

The above equations are joined to the turbulence kinetic energy and dissipation transport equations in case of a two-equation model:

$$\frac{Dk}{Dt} = \frac{\partial}{\partial x_\alpha}\left(\left(\nu\delta_{\alpha\beta} + \frac{(\nu_{tt})_{\alpha\beta}}{\sigma_k}\right)\frac{\partial k}{\partial x_\beta}\right) + P_k - \varepsilon - \frac{2\nu k}{{y_n}^2},$$

$$\frac{D\varepsilon}{Dt} = \frac{\partial}{\partial x_\alpha}\left(\left(\nu\delta_{\alpha\beta} + \frac{(\nu_{tt})_{\alpha\beta}}{\sigma_\varepsilon}\right)\frac{\partial \varepsilon}{\partial x_\beta}\right) + c_{\varepsilon_1} f_1 \frac{\varepsilon}{k} P_k - c_{\varepsilon_2} f_2 \frac{\varepsilon^2}{k} - \frac{2\nu\varepsilon}{{y_n}^2}\exp\left(-0.5y^+\right)$$

The damping functions and constants are provided in the following table:

Table 1 Damping functions and constants for the tensorial-eddy-viscosity anisotropic URANS/OES modelling

f_μ	f_1	f_2	c_{ε_1}	c_{ε_1}	σ_k	σ_ε
$1-\exp\left(-0.0002\ y^+ - 0.000065\ y^{+2}\right)$	1	$1-0.22\exp\left(-\frac{k^2/(\varepsilon\nu)^2}{36}\right)$	1.44	1.92	1	1.3

A detailed description of the above developments can be found in Bourguet et al (2007), Bourguet (2008). A brief description of the present modelling approach and of results can be found in the partnerwise contribution (IMFT) in the present book.

III DESider Measurements

This chapter contains a description of the measurements carried out during the DESider project. It should be mentioned that the bump experiment was financed as part of the Technical Annex of the DESider project, while the IMFT circular cylinder experiment was what is called an "added-value", i.e. it was to a great deal funded by IMFT - but data were made available to all DESider partners. Hence, several partners calculated that case and results are given in chapter IV, section 1.

1 The DESider Bump Experiment

B. Aupoix[1], P. Barricau[1], C. Geiler[1], A. Gilliot[1], J.C. Monnier[1], G. Pailhas[1], Y. Touvet[1], Y. Egorov[2], F. Menter[2], J.M. Foucaut[3], J.P. Laval[3], L. Perret[3,*], and M. Stanislas

[1] ONERA
[2] ANSYS
[3] LML UMR CNRS 8107

1.1 Motivation

This experiment was planned to provide information relevant to hybrid approaches, which couple RANS and LES approaches, investigated in the EU-funded DESider project. Flow situations in which RANS models are known to fail were looked for, which led to investigate a massively separated flow, with a separation point not imposed by the geometry, as well as reattachment and recovery after reattachment in a highly three-dimensional situation. Not only mean values were looked for but also information about the characteristic flow frequencies, which can be predicted by hybrid approaches. Moreover, as some doubts were raised about the validity of the solutions in the transition region (or grey zone) between the RANS and the fully developed LES regions, an attempt was made to identify turbulent structures which develop in the separated region, in order to compare them with those predicted by hybrid approaches.

1.2 Model Design

A two-dimensional, highly confined, bump shape, with a contoured backward shroud on which separation is not fixed by the geometry, was chosen. The geometry was selected, with the help of a preliminary numerical study performed by ANSYS, using the commercial CFD solver CFX. A series of simulations was performed to optimise the geometry parameters, in particular the slope angle of the backward facing part, using RANS as well as URANS computations. With the final shape, the time-averaged URANS solution reveals the 3-D separation pattern with a distinct recirculation zone in the middle and the two corner zones. The final shape was analytically defined as

[*] Now at École Centrale de Nantes, Laboratoire de Mécanique des Fluides.

W. Haase et al. (Eds.): DESider – A Euro. Effort on Hyb. RANS-LES, NNFM 103, pp. 69–103.
springerlink.com

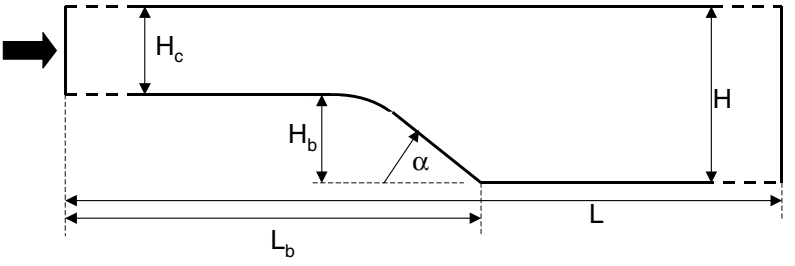

Fig. 1 Sketch of the bump geometry

$$h = H_b \left[\tanh\left(\tan(\alpha) \frac{(L_b - x)}{H_b} \right)^{\beta} \right]^{1/\beta}$$

and is given in figure 1 where

H = 0.30m total channel height,
H_b = 0.14m bump height
L = 3.0m total channel length
L_b = 1.0m bump length
$\alpha = 35^\circ$ slope angle of the bump contour
$\beta = 5$ shape contour exponent

All experiments were conducted in the ONERA/Toulouse water tunnel THALES which has been designed for easy optical access. The test section is 50cm wide, 30cm high and 3m long. Water speed was 4 ms^{-1}.

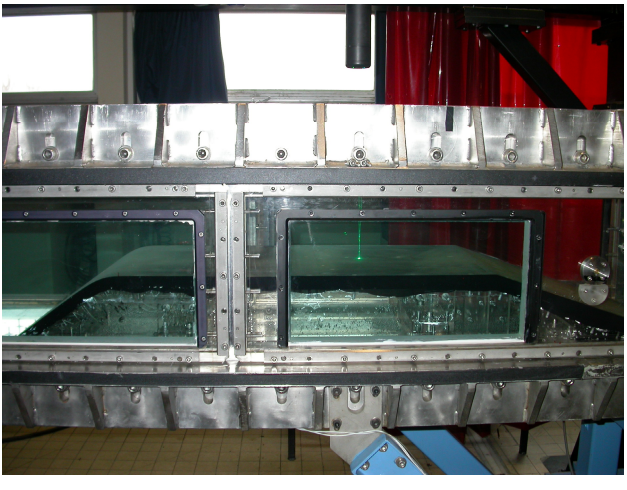

Fig. 2 Model in the water tunnel

A first model was used to quickly check the concept by only performing flow visualisations. It evidenced a nearly two-dimensional separation and a highly unsteady, but not flapping, separated region. The final model was then built and installed in the water tunnel, as shown in figure 2. In this figure, the flow is from right to left.

The model was equipped with 90 pressure taps distributed over three equally spaced parallel lines, one on the centreline, the other two at one-third and two-thirds of the half test section width. Moreover, two unsteady pressure transducers were implanted on the sloping region of the bump and two on the downstream bottom wall.

In the following, the X-axis is along the tunnel axis direction, Y is the vertical direction and Z is spanwise. X=0 corresponds to the downstream junction of the bump with the bottom wall, Y=0 to the test section lower wall and Z=0 to the test section centreline.

1.3 Wall Measurements

Steady pressure measurements show a pressure plateau from X=-0.20m to X=0.35m. Moreover, the wall pressure distribution is nearly two-dimensional.

Liquid crystals (LC) were used to get information about the location of separated and reattached regions. They were deposited on the bump and on the bottom test section wall. The change in colour of the LC on the bump (not shown here) clearly indicated the location of the separation line at the beginning of the bump expansion and confirmed a nearly two-dimensional separation. LC deposited on the plexiglass test section wall did not work as a shear-sensitive paint but rather as a visualization coat and so revealed an unexpected highly three-dimensional secondary separation behind the foot of the bump, as shown in figure 3. They also evidenced the relaxation of the flow towards a two-dimensional flow.

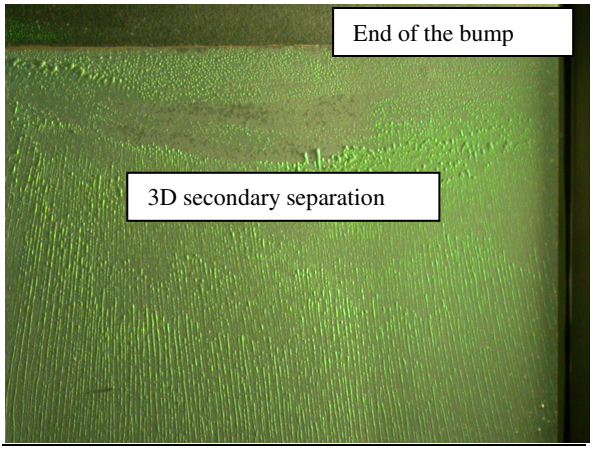

Fig. 3 Visualisation of the secondary separation near the foot of the bump

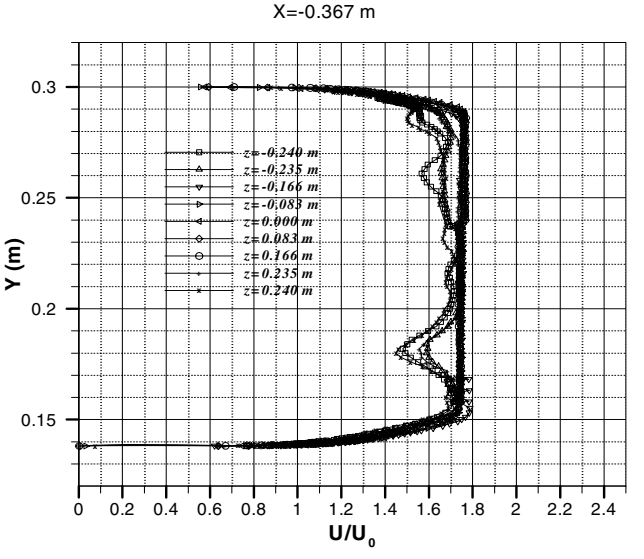

Fig. 4 Streamwise velocity profiles across the test section

1.4 LDV Measurements

LDV measurements were performed first to document the whole entry plane, to be taken as the inflow condition for the computations. It appeared that because of the ramp on the upstream side of the bump, the initially planned location did not correspond to equilibrium boundary layers so that a complete mapping of the flow on the flat part of the bump was performed to determine the convenient entry plane location for CFD purpose, i.e. a region where boundary layers exhibit a canonical character.

A complete probing of this entry plane was undertaken. The streamwise velocity profiles throughout the vertical lines joining the bump to the test section ceiling are presented in figure 4. Regardless of the boundary layer evolution, it can be noted that, in a general way, the flow exhibits a quite similar pattern in the whole investigated section excepted in the vicinity of the lateral walls. As a matter of fact, along the farthest lines from the vertical centre line, the velocity evolution is no more linear. A pocket of velocity defect is well observable close to the bump surface; the peak of deficit is located at a distance of about 40 mm from the wall. Close to the test section ceiling, the velocity profiles are also disturbed.

The turbulence level (figure 5) is remarkably constant in the central part of the test section. The turbulence profiles become somewhat chaotic along lines drawn near the lateral test section walls. A peak of turbulence is detected at the same location than the mean velocity defect. These mean and turbulent velocities evolution might be connected to a corner vortex formation.

In order to get more information about the previous evocated distortion of mean and turbulent velocity profiles in the vicinity of the lateral walls, LDV measurements in the corner region (formed with the bump surface and the lateral test section wall) in the reference and upstream *YOZ* planes respectively located at X=-0.367 m and X=-0.745 m were performed.

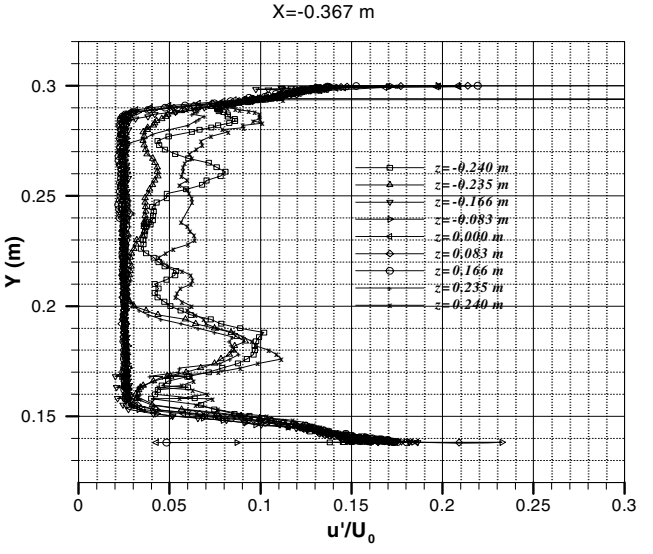

Fig. 5 Turbulent velocity profiles across the test section

Contours of axial mean velocity (figure 6) seem to be distorted in a manner indicative of corner secondary flow. The iso-level velocity lines deep close to the walls along the corner bisector whereas they exhibit a pronounced bulge in the lateral boundary layer about 40 mm away from the bump surface. This conjectured behaviour evidenced a corner vortex the origin of which was not identified.

LDV measurements were also performed to map the whole symmetry plane, with special attention to the reattachment region. High resolution allowed a precise description of the mixing layer in the separated region and of the flow reattachment and recovery downstream of reattachment, in terms of mean and

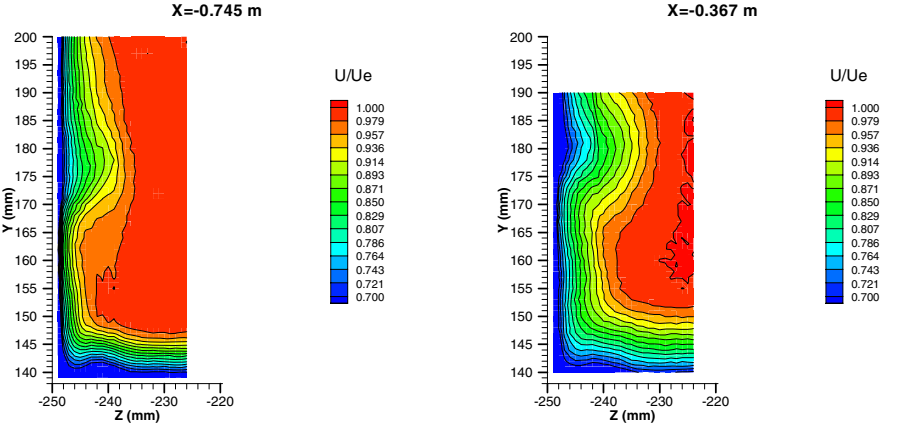

Fig. 6 Axial mean velocity contours in the corner region

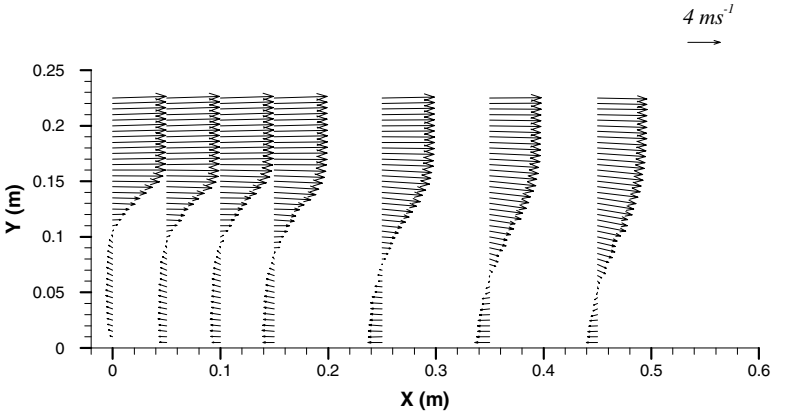

Fig. 7 LDV Probing of the symmetry plane: mean velocity vectors; separated region

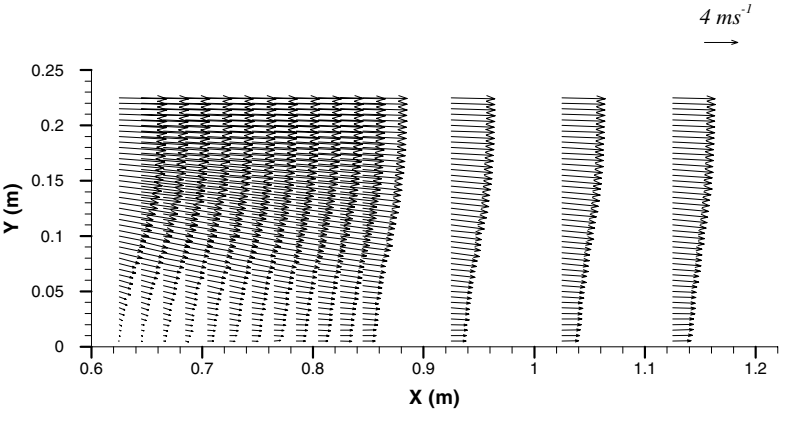

Fig. 8 LDV Probing of the symmetry plane: mean velocity vectors; reattachment and recovery regions

fluctuating quantities, as shown in figures 7 and 8. These measurements allow a determination of the mean reattachment point at X=0.630m.

1.5 PIV Measurements

The main part of the experiment was devoted to PIV measurements. A stereo PIV system, with four cameras was used to cover a large field of view (figure 9). All components of the mean velocity vector and Reynolds stress tensor were measured.

In order to cover both the separated region and the reattachment region, measurements have been performed in:

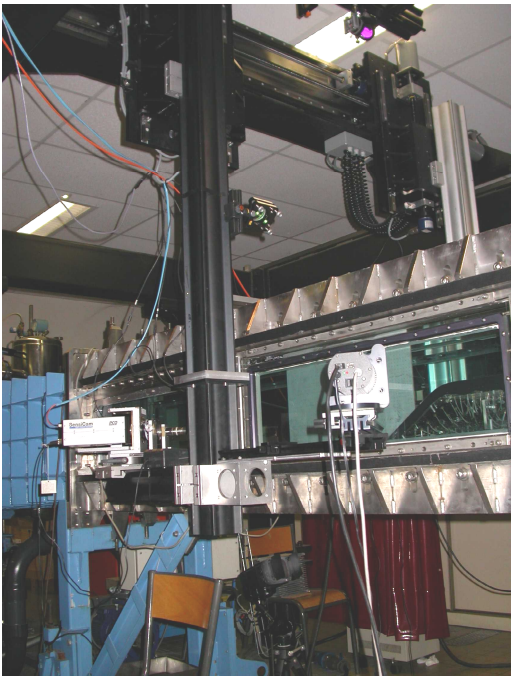

Fig. 9 PIV set-up showing two cameras on one side of the water tunnel and the calibration plane (white)

- 3 longitudinal planes L11, L21-L22 and L31-L32 located on the centreline of the test-section (z = 0),
- 1 longitudinal plane L41-L42 located at z = -125 mm,
- 1 longitudinal plane L51-L52 at z = +125 mm.

The longitudinal distribution of these planes is presented in figure 10.

In the following, these planes will always be referred to as Ln1 and Ln2 (n = 1.., 5) for the upstream and downstream part, respectively. As planes Ln1 and Ln2, for n=3 to 5, spatially overlap, the turbulent statistics have been combined in common planes L3M, L4M and L5M by interpolating-extrapolating these statistics on a common grid.

The PIV data were processed by ONERA/Lille and post-processed by LML.

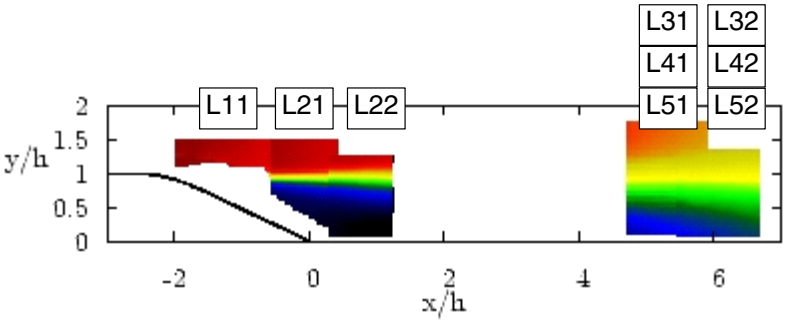

Fig. 10 Longitudinal planes investigated by PIV

1.5.1 Accuracy Estimation

It should be noted here that some technical issues occurred during the experiment and may have affected the final accuracy of the provided vector fields. The main problems turned out to be optical access difficulties due to the water tunnel geometry (as can be seen in figure 10, a large gap exists between the group of measurement planes in the separated region and those obtained just downstream of the reattachment region (x/h = 5.5)), correctly seeding the water, avoiding light reflection on the wall, especially in the separated region. Furthermore, the presence of strong velocity gradients and high turbulence levels (as in planes L11, L21 and L22, figure 10) can lead to some difficulties to optimize the PIV analysis parameters in the entire measurement domain. For these reasons, the plane L11 presented in figure 10 has not been taken into account in the present study. As a matter of fact, the only reliable domain remaining in this plane does not bring any additional information on the flow. Consequently, in the following of the present work, only planes L21-L22, L31-L32, L41-L42 and L51-L52 will be processed and analysed.

In this section, an attempt to evaluate the accuracy of the presented PIV measurements is proposed. It relies on the fact that the upstream and downstream fields of view, acquired by the two independent PIV systems, spatially overlap in a small region. It must be underlined here that the absence of temporal synchronization between the two systems prevents from evaluating the instantaneous difference between the velocity fields measured by the two systems and, consequently, the classical least square error for instance.

To overcome this issue, statistics such as the temporal average and the r.m.s of each velocity component are first computed independently in each plane over the Nt time samples. The difference between the statistics is then calculated in the region of spatial overlap and spatially integrated over this common domain to provide an estimation of the error of the measurement technique. This estimated error for the mean and the r.m.s of each velocity component is given in table 1. One should keep in mind that this computed error only provides a rough estimate of the measurement precision by comparing the statistics obtained with two different PIV systems.

Table 1 Estimation of measurement error

Planes	**U** **m/s - %**	**V** **m/s - %**	**W** **m/s - %**	σ_u **m/s - %**	σ_v **m/s - %**	σ_w **m/s - %**
L21-L22	0.12 - 13%	0.01 – 14%	0.06 -	0.05 11%	0.02 - 7.0%	0.13 - 18%
L31-L32	0.04 - 1.5%	0.04 – 20%	0.09 -	0.02 - 1.9%	0.05 - 6.5%	0.05 - 5.8%
L41-L42	0.06 - 2.1%	0.05 – 14%	0.07 -	0.03 - 3.0%	0.04 - 5.8%	0.10 - 12%
L51-L52	0.04 - 1.6%	0.05 – 15%	0.09 -	0.03 - 3.6%	0.06 - 8.9%	0.05 - 5%

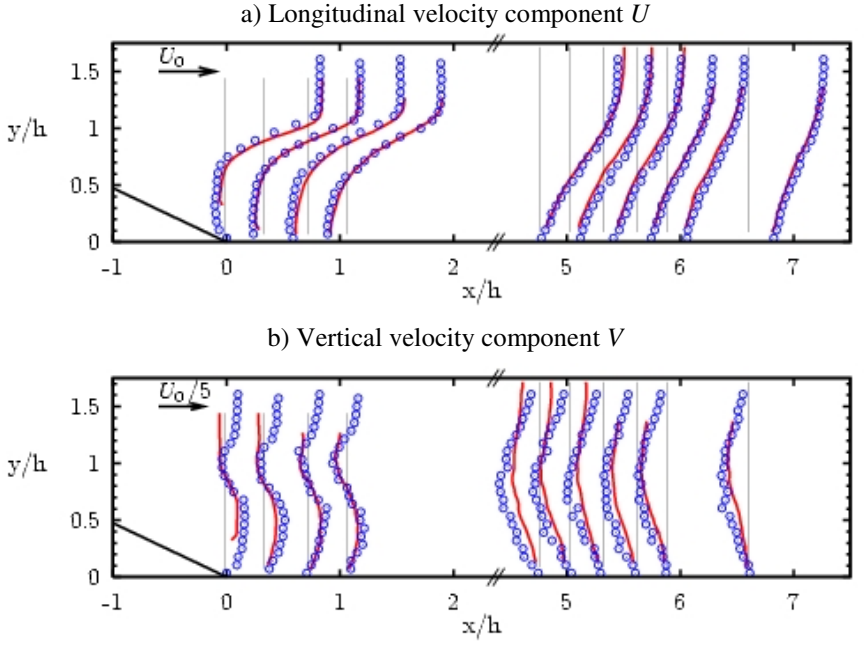

Fig. 11 Longitudinal evolution of the mean flow velocity profiles on the centreline of the test-section: lines, PIV measurements; symbols, LDV measurements

From the results presented in table 1 it is noticeable that the absolute error in m/s is rather homogeneous over all the considered planes and velocity components and remains small (below 0.13 m/s) when compared to the higher velocity levels that exist in this flow (about 8 m/s). When the relative error is considered, it can reach higher levels as the considered quantity can be small. In particular, the mean value of the vertical and transverse components V and W, respectively, are almost zero in such a flow and thus lead to high relative error levels whereas the measurement error in physical unit remains reasonable.

1.5.2 Main Statistics of the Flow

Figure 11 provides the evolution of the streamwise and transverse mean velocity components compared to the LDV measurements. The agreement is fairly good on the streamwise component, a bit less on the transverse one which is much smaller. The streamwise evolution of the mean streamwise velocity component U (figure 11a) shows in the upstream region the presence of a shear layer, the axis of which is near y/h ~ 1. Below this shear layer, a recirculation zone where U<0 can be seen. Further downstream, as the flow reattaches to the wall, the location of the maximum of mean shear moves toward the wall, the flow decelerates and the region of reverse flow (U<0) disappears, confirming the progressive redevelopment of the boundary layer near x/h ~ 5.5. On the bump, the flow shows an upward motion (figure 11b) whereas it is downward near the axis of the shear layer

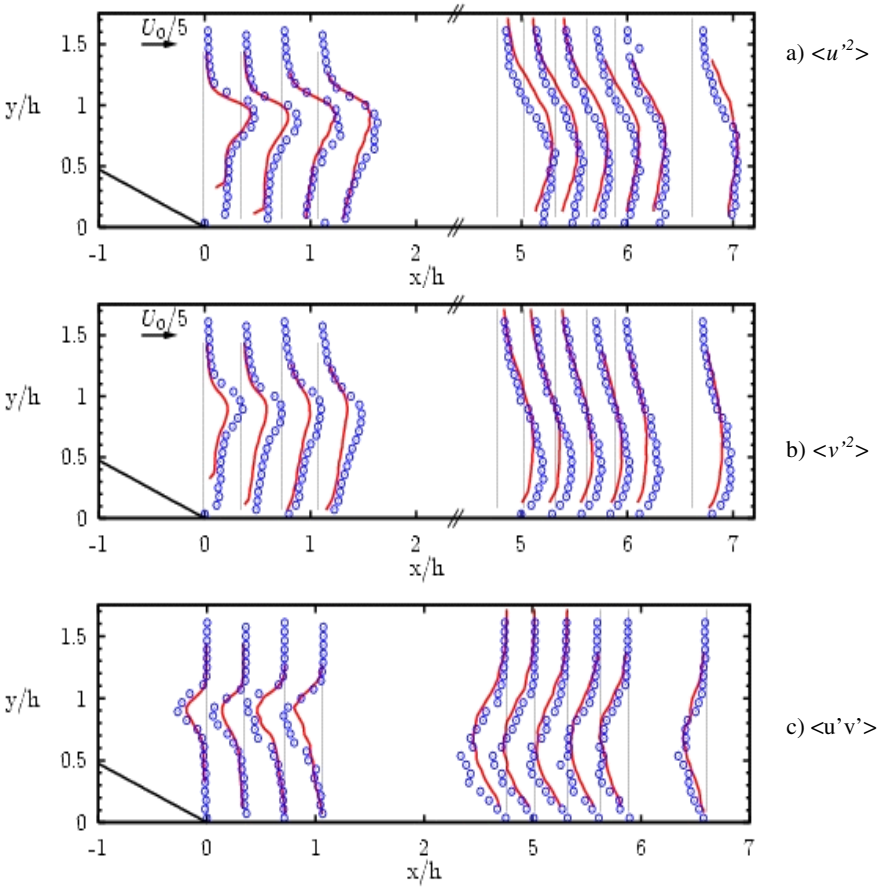

Fig. 12 Longitudinal evolution of the longitudinal and vertical turbulent intensity components as well as the Reynolds shear stress on the centre line of the test-section: From top to bottom <u'2>, <v'2> and <u'v'> Lines, PIV measurements; symbols, LDV measurements

due to the mean swirling motion in the recirculation region. Near the reattachment point, the flow exhibits a motion toward the wall, compatible with the reattachment and the deceleration of the flow and the redevelopment of the boundary layer. In these planes, the mean spanwise component W is almost zero, in agreement with the symmetry of the flow on its centreline.

For the three components, and despite the experimental uncertainty that exists, profiles obtained at different spanwise locations (planes L3, L4 and L5) are in good agreement, showing the good spanwise homogeneity of the flow in the range $-0.9 < z/h < 0.9$. Thus, if steady corner vortices exist, they are confined to the region near the sidewalls of the test-section and cannot be detected in the present dataset.

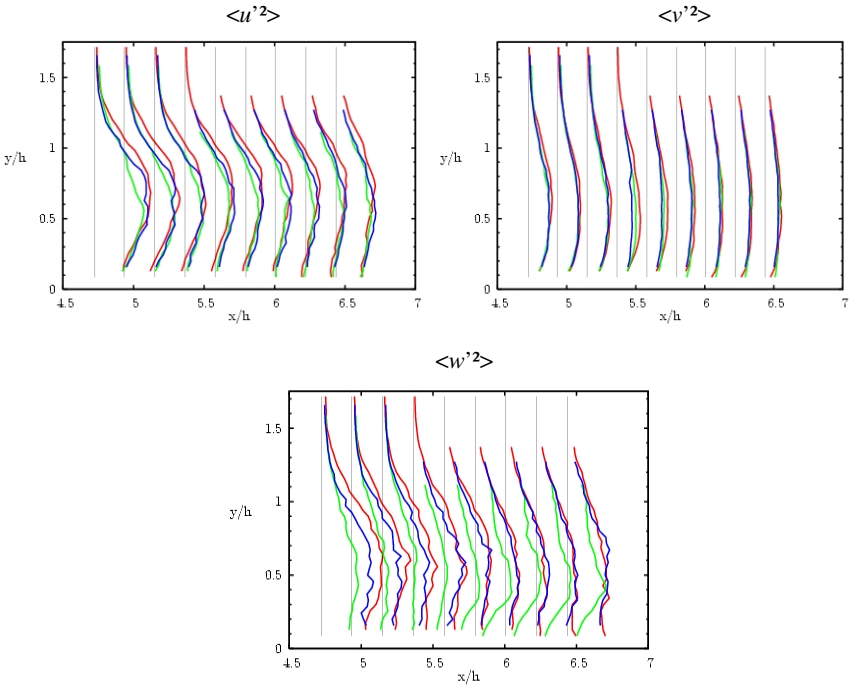

Fig. 13 Longitudinal evolution of the normal Reynolds stresses in the reattachment region at three different spanwise locations: red lines, L3M plane; blue lines, L4M plane; green lines, L5M planes

Figure 12 shows a comparison of LDV and PIV results for three components of the Reynolds stress tensor, $\langle u'^2 \rangle$, $\langle v'^2 \rangle$ and the correlation $\langle u'v' \rangle$. In the separated region, the flow shows high levels of turbulent fluctuation on the axis of the shear layer that develops downstream of the bump. The streamwise and spanwise components exhibit comparable levels of fluctuation which are higher than those of the vertical component. In the longitudinal range of measurements, it is noticeable that the maximum value of these profiles increases with the streamwise location. That may be due to the strong three dimensional unsteady character of the flow that develops downstream of the separation.

In the reattachment region, the fluctuation levels remain high for all the components and slowly decrease as the flow reattaches and the boundary layer redevelops on the bottom wall. In this region, the vertical location of the maximum value of the profiles is well below the shear layer axis, near y/h ~ 0.5, in agreement with the global downward motion detected in the analysis of the mean flow.

Some differences between LDV and PIV measurements exist especially in regions of high turbulence levels. However, the differences remain in agreement with the estimated PIV uncertainties.

Figure 13 shows profiles of the three normal Reynolds stresses obtained at three different spanwise locations. These profiles are in relatively good agreement

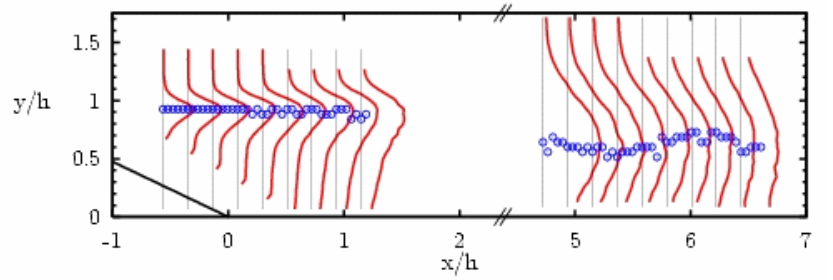

Fig. 14 Longitudinal evolution of the turbulent kinetic energy k in the symmetry plane of the test-section. Symbols: location of the maximum of *k*

with each other except for <w'²>, for which some discrepancies between profiles measured in the symmetry plane and on each side exist. Given the values of the measurement error estimated in section 1.5.1, these differences can be attributed to experimental uncertainties rather than to particular spanwise organization of the flow in this region.

Figures 14 and 15a present the longitudinal evolution of the turbulent kinetic energy $k=0.5(<u'^2>+<v'^2>+<w'^2>)^{1/2}$ in the plane of symmetry and the two other spanwise locations in the test-section. Again, the analysis of this quantity shows how the turbulence develops downstream of the shear layer with increasing levels of energy with the longitudinal location until the flow reattaches and the boundary layer starts to redevelop on the bottom wall.

Analysis of the Reynolds shear stress profiles <u'v'> (figures 15b) are also in good agreement with the previous conclusions, exhibiting negative values, characteristic in a shear layer, with increasing amplitude while the flow develops in the channel until its reattachment.

In a general way, overall agreement is good between the PIV and LDV data in these planes. Measurements in planes normal to the flow were also tried with PIV but the optical distortions and the unsteadiness of the flow did not allow obtaining good quality records.

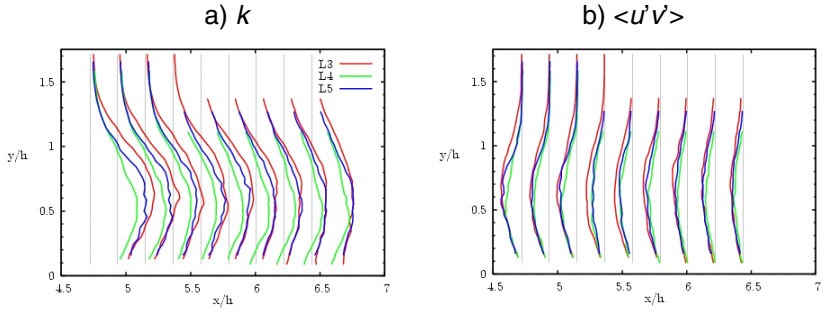

Fig. 15 Longitudinal evolution of the profiles of a) the kinetic turbulent energy *k* and b) the Reynolds shear stress <*u*'*v*'> in the reattachment region at three different spanwise locations: red lines, L3M plane; blue lines, L4M plane; green lines, L5M planes

In this section, we further investigate the evolution of the turbulent kinetic energy within the flow and more particularly its production. Focus is put on this term as its relationships with the coherent structures present in the flow and the development and the evolution with the streamwise location can bring additional information and can be directly compared with numerical predictions. Moreover, given the available data in the present study and their accuracy, it is the only term of the turbulent kinetic energy budget that can be reliably evaluated. Indeed, the velocity/pressure-gradient and the triple product terms are not accessible or cannot be computed accurately. Furthermore, as the scale at which dissipation occurs is not resolved in the present experiment, the turbulent dissipation term cannot be evaluated. Therefore, only the production term P_k is evaluated here:

$$-P_k = \overline{u_1 u_1}\frac{\partial \overline{U_1}}{\partial x_1} + \overline{u_1 u_2}\frac{\partial \overline{U_2}}{\partial x_1} + \overline{u_2 u_1}\frac{\partial \overline{U_1}}{\partial x_2} + \overline{u_2 u_2}\frac{\partial \overline{U_2}}{\partial x_2}$$

As can be seen, terms containing spanwise derivatives have been neglected as the data are computed in the symmetry plane of the flow. Figure 16 shows the spatial distribution of P_k in the plane of symmetry of the water tunnel. Maximum levels of this term are obtained on the shear layer axis, near $x/h \sim 1$, where the shear layer instability, responsible for the roll-up phenomenon and the creation of Kelvin-Helmoltz structures of z-axis, induces strong kinetic energy transfer from the mean flow to the primary vortices.

As the computation of the production term involves quantities such as gradients and second-order moments that are more affected by the experimental uncertainties, spatial distributions of P_k obtained at different spanwise locations show slight differences. Consequently, as far as the energy production is concerned, spanwise homogeneity of the flow is not as good as already mentioned.

The evolution of the turbulent kinetic energy within the flow and more particularly its production P_k was further investigated. The spatial distribution of P_k in the plane of symmetry and at two different spanwise locations in the reattachment region is given in figure 17.

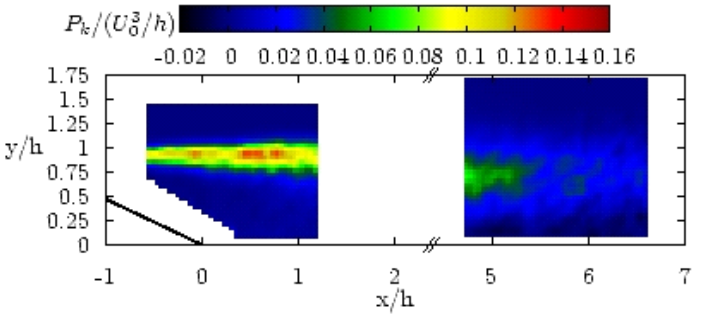

Fig. 16 Normalized turbulent kinetic energy production $P_k/(U_0^3/h)$ in the plane of symmetry of the channel

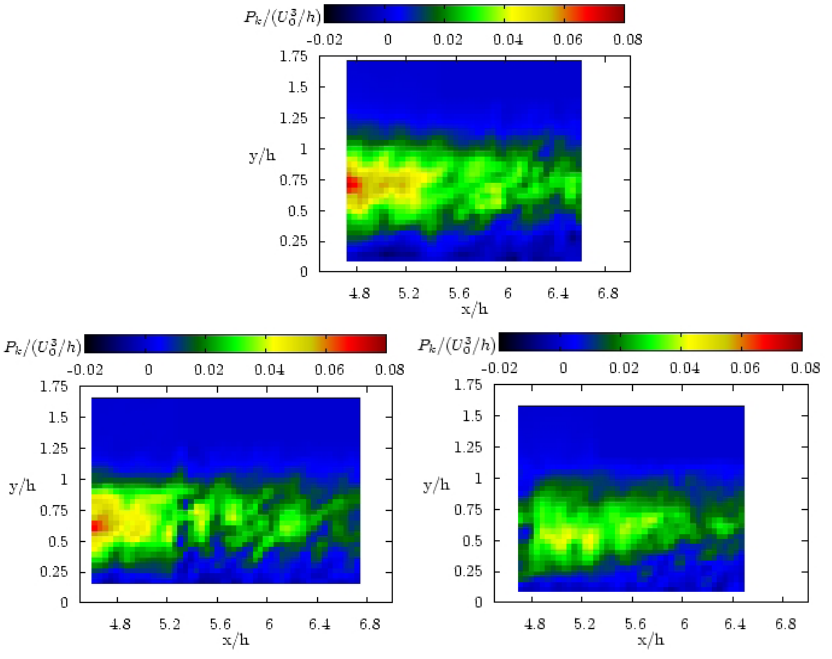

Fig. 17 Normalized turbulent kinetic energy production in the reattachment region at three spanwise locations

As far as the energy production is concerned, spanwise homogeneity of the flow is not as good as observed from the mean velocity distribution. Moreover, it can be noticed that the maximum of turbulent kinetic energy production occurs far from the wall.

Mean Vorticity Field

In agreement with the analysis of the mean flow conducted in the previous section, the spanwise vorticity distribution (figure 18) shows the footprint of the shear layer. As the above discussed production term, this quantity is dominated by strong vertical gradients of streamwise velocity. In the reattachment region, the location of the maximum level of spanwise vorticity also corresponds to the location of the maximum of turbulent kinetic energy and energy production. Thus, the flow turns out to be dominated by the shear induced by the separation in the upstream region and then downstream by the presence of the wall.

1.6 Coherent Structures

1.6.1 Introduction

The following sections are devoted to the coherent structures that exist within a turbulent flow and to the large-scale structure organization of the present

separated turbulent flow over a rounded bump. The goal of the methods employed here is to take advantage of the spatial information provided by PIV to describe the spatial features, such as the spatial distribution, the size, the intensity and direction of rotation, of the coherent vortices of the flow as well as their relationships with each other and other flow features.

For that purpose, two distinct methods have been employed. The first one is based on the use of a detection algorithm that enables the extraction of vortices from instantaneous PIV velocity fields. Classical statistical and conditional approaches can then be used to characterize the detected vortices. The other method is the now well-known Proper Orthogonal Decomposition (POD) that provides a statistical view of the most energetic structures of the flow by decomposing the velocity fields into a set of uncorrelated temporal and spatial modes.

When dealing with identification and characterization of vortices in turbulent flows, the problem of properly defining the basic properties of a vortex to be able to detect it arise. Several studies (see Jeong & Hussain (1995) for a review) have already been devoted to that issue. Most of the existing methods are based on the computation of velocity gradients to evaluate the vorticity or invariants of the tensor of velocity gradients for instance. These approaches can be difficult to use when experimental velocity field with limited spatial resolution and the presence of experimental noise are considered. To avoid problems related to the gradient estimation, Graftieaux et al. (2001) proposed a method based on the evaluation of a scalar function representative of the solid body rotating character of the flow surrounding each point of the instantaneous velocity field. This approach, able to locate the centre of the large-scale vortices, is only based on the topology of the velocity field, not its magnitude. Moreover, thank to its global character, this method tends to remove the small-scale turbulent fluctuations and the noise effect, thus improving its robustness. For further details, the reader is referred to the work of Graftieaux et al. (2001).

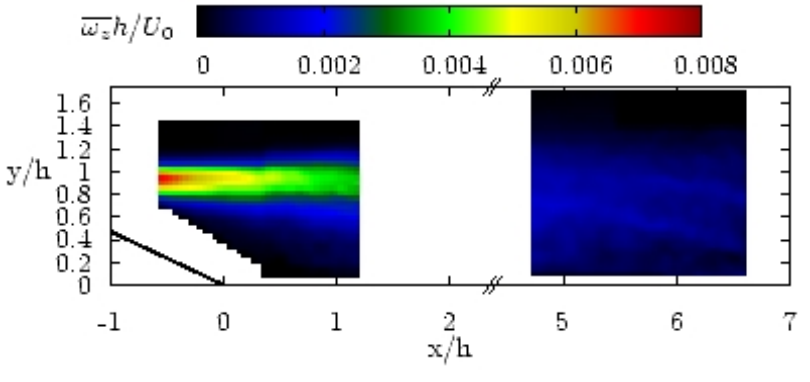

Fig. 18 Mean spanwise vorticity distribution obtained in the plane of symmetry

The POD which is now fairly well known will not be described here. Details can be found in Berkooz et al. (1993) and Sirovich (1987). The velocity field is decomposed in the following manner:

$$u_i(\mathbf{x},t) = \sum_{n=1}^{\infty} a^{(n)}(t)\Phi_i^{(n)}(\mathbf{x})$$

In the above equation, $a^{(n)}(t)$ are the temporal coefficients driving the temporal dynamics and $\Phi_i^{(n)}(\boldsymbol{x})$ the spatial eigenmodes. Using the present database containing N_t = 1020 instantaneous velocity maps, the number of modes is limited to N_t modes. The snapshot method described by Sirovich (1987) is employed here to solve the corresponding eigenvalue problem. Modes are sorted in descending order so that the first modes capture the largest energy fraction. Reconstruction of the velocity field can be performed with a limited number of POD modes in order to analyse the dynamics of the dominating large-scale structures. Consequently, complexity of flows can be measured and compared by analysing the energy captured by the same subset of eigenmodes.

1.6.2 Characteristics of the Extracted Vortices

Figure 19 shows an example of the spatial distribution of the detected vortices as a function of their intensity, in the planes L21 and L22 located in the separated region downstream of the bump. It can be seen that clockwise (positive vorticity) and counter-clockwise (negative vorticity) vortices are extracted. Most of the counter-clockwise vortices (referred as to CCRV in the following) are found near the wall, at the end of the bump. On the contrary, clockwise vortices (referred to as CRV), which are the most numerous, are detected in the entire measurement region. Moreover, vortices with higher vorticity amplitude are located near the axis of the shear layer. From this plot, two populations of vortices can be distinguished: vortices which are directly related to the shear layer instability and the existence of a strong mean shear due to the separation, and vortices that are part of more random turbulent motion.

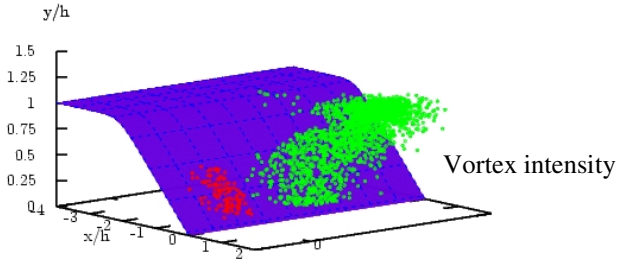

Fig. 19 Intensity of the detected vortices in the planes L21 and L22 as the function of the coordinates of the centre of the detected vortex core. Green clockwise, Red counter-clockwise

Results as those presented in figure 19 enable the computation of probability density functions (pdf) of the spatial location of the detected vortices. In the present case, these distributions have been computed as a function of the sign of the vortices and have been integrated over the entire longitudinal extent of each measurement plane in order to improve statistical convergence.

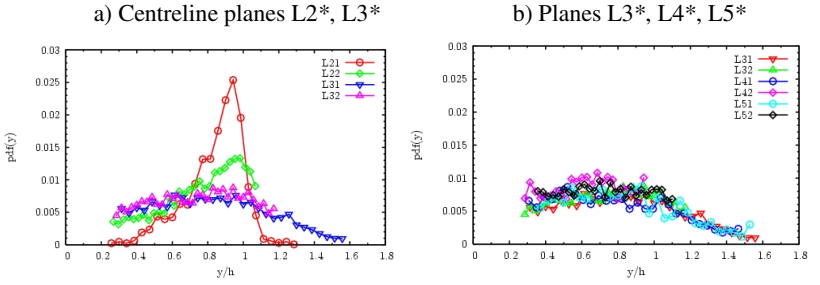

Fig. 20 Probability density functions of the vertical location within each plane of measurement of the detected clockwise rotating vortices (CRV)

As far as the CRV are concerned (figure 20a), in the separated region, most of them are found near the shear layer axis. As the flow moves downstream, the pdf flattens and widens showing, first, the expansion of the shear layer and then, the spreading out and the homogenization of the flow as it reattaches the bottom wall. Conversely, CCRV are detected in majority in the near-wall region, the pdfs of which exhibit totally different shape, being almost zero for y/h > 0.8. These vortices remain rare even at the most downstream location, showing that the flow is still strongly dominated by the mean shear first imposed by the separation and then by the presence of the wall.

Figures 20b and 21b show the pdfs obtained at different spanwise locations in the reattachment region. No significant differences are noticeable between results obtained in planes located on each side of the test-section centreline. This comforts the hypothesis of relative spanwise homogeneity of the flow in the investigated spanwise range.

Figure 22 shows the evolution of the energy associated to each mode of the POD decomposition performed in the planes L21, L22, L31 and L32. It should be noted here that some systematic differences occur between the modes obtained in the upstream plane and the downstream plane of each pair L21-L22 and L31-L32 (e.g. the convergence rates in the planes L22 and L32 is lower than those obtained in the planes L21 and L31). This is attributed to the fact that, as two different

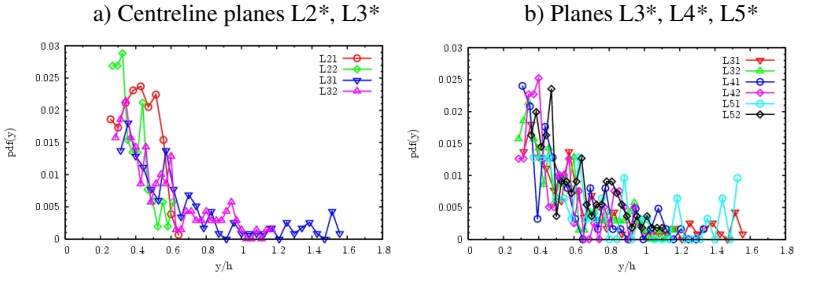

Fig. 21 Probability density functions of the vertical location within each plane of measurement of the detected counter-clockwise rotating vortices (CCRV)

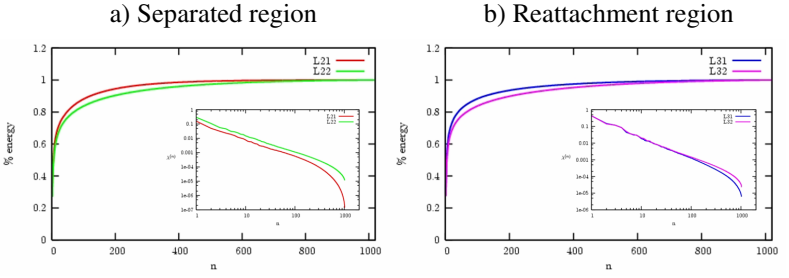

Fig. 22 Energy convergence and energy content (enclosed diagrams) of the POD eigenmodes computed in a) the separated region and b) the reattachment region

PIV systems were employed to perform the measurements, velocity fields are affected by different noise levels and do not resolve exactly the same spatial turbulent scales, the spatial resolution of the two systems being different.

Despite this point, the rate of convergence of the POD modes energy is comparable between the separated region and the reattachment region. Consequently, the longitudinal evolution of the structure of the flow has no significant influence on the energy distribution among the POD modes. However, the fast rate of convergence of the decomposition (~70% of the total energy contained in the first 20 modes) indicates the presence of well-organized coherent motions.

To further investigate the evolution of the large-scale structures of the flow, an analysis of the topology of the first POD modes obtained in the plane of symmetry of the flow is proposed. The first three of these modes in planes L21 and L22 are presented in figure 23. In this separated region, it is remarkable that the first mode that contains approximately 27% of energy does not show any vortical structure. It appears indeed that this mode is a flapping mode, which can be related to the vertical flapping motion of the shear layer. If higher order modes are considered, it can be seen that they contain vortical structures of z-axis, mostly located on the axis of the shear layer.

Moreover, combination of these modes via the use of the temporal coefficients leads to the reconstruction of velocity fields containing vortices rotating in the same direction and travelling downstream. Thus, analysing the most energetic POD modes obtained in the separated region reveals that the flow is dominated by the mixing layer that develops downstream of the separation point.

Conversely, the first POD modes obtained in the reattachment region (not presented) show a completely different spatial organization. They exhibit very large-scale motion of the size of the measurement domain and do not exhibit any vortices of the same or comparable size as those found upstream. Reconstruction of instantaneous velocity fields (not shown here) shows that these modes (containing up to 50% of the total kinetic energy) correspond to very large-scale vertical motions, with a size of the order of the height of the bump. Smaller-scale vortices are represented by the higher order modes. When analysing these modes, distributed vortices are found in the entire measurement domain, confirming the finding based on direct vortices detection.

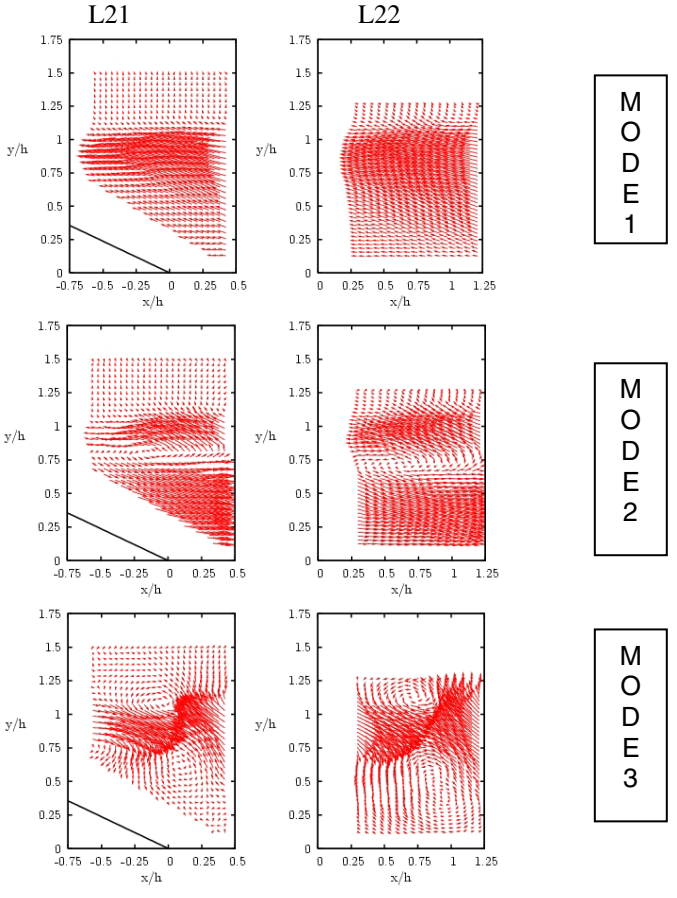

Fig. 23 First three eigenmodes in planes L21 and L22

The analysis of the topology of the spatial POD modes reveals that, in spite of a very similar energetic content, the upstream and downstream investigated regions present a totally different dynamics: the separated region is clearly dominated by shear instabilities leading to the formation of primary vortices of Kelvin-Helmholtz type, whereas the reattachment region is dominated by very large-scale motions and contain more randomly distributed vortical structures of size comparable to those detected in the upstream region.

1.7 Unsteadiness Characterization

At last, unsteady wall pressure were measured. Pressure spectra, measured at various locations, are shown in figure 24. They exhibited a different character in the vicinity of separation (X= -0.10m and -0.20m), in the detached region and recovery region (X=0.30m and X = 0.60m), with a large and higher energy plateau in the detached and recovery region. However, no peak in the spectrum was

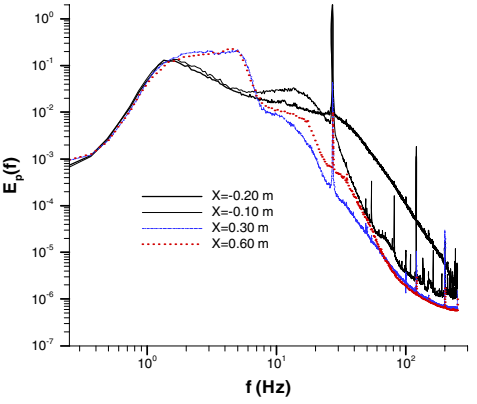

Fig. 24 Wall pressure energy spectra at four locations in the separated and recovery regions

determined which could be linked to a resonance frequency. The energy peaks (with the main one close to 27 Hz), which are still present when the bump is removed, should be attributed to the natural frequency of the impeller rotating blades.

1.8 Conclusion

An experimental study of a turbulent separated flow through a channel with a bump was performed in the THALES water tunnel of ONERA. From LDV measurements, mean velocity values and turbulence statistics were obtained in a section perpendicular to the streamwise direction along vertical and horizontal lines. Boundary layer profiles were also documented in order to provide complete flow characteristics in the computational entry plane. The characterization of the flow along lines perpendicular to the horizontal part of the bump showed the presence of velocity defect area close to the bump wall; this could be connected to the vortex corner formation. A spectral analysis of the pressure fluctuation was undertaken; it did not reveal particular feature that could be connected to large convective structures.

Results of the post-processing of the instantaneous vector fields obtained in the longitudinal planes with PIV have been presented. For each longitudinal plane, the accuracy of the PIV measurements has been estimated. This error analysis shows that the experimental uncertainty, when considered in physical units (e.g. in m/s) remains reasonable and in agreement with the error that can be expected in flows presenting such high levels of turbulence fluctuations and strong velocity gradients in the measurement domain. The main statistics of the flow have been computed and analysed. The mean velocities obtained agree fairly well with the LDV measurements. Comparison of statistics obtained at three different spanwise locations in the reattachment region do not show significant differences which could be attributed the corner vortices detected in some numerical simulations.

In addition, information on the characteristics of the turbulent coherent structures was provided, using a vortex identification methods as well as the Proper Orthogonal Decomposition. These analyses reveal that in the separated region, the

flow is dominated by a shear layer, both from an energetic point of view and for its spatio-temporal organization. Indeed, stronger vortices are located near the axis of the shear layer and most of the detected eddies have a sign imposed by the mean shear. Further downstream, as the flow re-attaches, its dynamics changes and the imprint of the mixing layer vanishes. The flow is composed of more randomly distributed vortices that do not represent the most energetic motion in the flow which is there at the scale of the bump height.

The whole of these experimental results constitutes an interesting database useful for computational works as detailed flow information is given in a referenced entry plane and flow events are described in some detail in the separated or reattached regions. This data base was widely used by the DESider partners to assess their hybrid approaches.

As PIV measurements in the transverse planes were not successful, these measurements will be performed in the near future with LDV.

2 The IMFT Circular Cylinder Experiment

R. Perrin[1,2], M. Braza[1], E. Cid[1], S. Cazin[1], A. Sevrain[1], and G. Harran[1]

[1] Institut de Mécanique des Fluides de Toulouse, UMR-CNRS-INPT N°5502
[2] Laboratoire d'Etudes Aérodynamique (LEA), Université de Poitiers, ENSMA, CNRS, SP2MI

Abstract. The DESIDER IMFT's circular cylinder experiment was carried out in the S1 and S4 wind tunnels of IMFT, using Three-Component PIV (3C-PIV), two-component *time-resolved* PIV (TR-PIV), as well as Time Resolved 3C PIV (3C-TR-PIV). Appropriate and detailed signal processing techniques have been applied to capture the organised and chaotic turbulence processes and their non-linear interaction for the strongly detached unsteady flow around a circular cylinder at Reynolds numbers entering the critical regime. For the majority of the experiments, the vertical and spanwise confinement of the flow was fixed by transparent walls, to allow taking into account the exact boundary conditions within a realistic CPU time for the CFD simulations. The complete data bases are available in the DESIDER web site. The experimental uncertainties were appropriately assessed and ensured a high-quality data-base for physical analysis and turbulence modelling validation of strongly detached flows characterised by non-equilibrium turbulence. Among the post-treatments, phase-averaging, linear stochastic estimation (LSE) and Proper Orthogonal Decomposition (POD), have been carried out in three dimensions. The coherent structures dynamics as well as the chaotic turbulence structural properties are analysed by means of the aforementioned techniques. The phase-averaged Reynolds stresses, the strain-rate and vorticity fields, the *turbulence production and 3D kinetic energy,* as well as *the turbulence spectrum* are determined. The modification of the structural properties of the present non-equilibrium turbulence has been evaluated, compared to turbulence scales in case of statistical equilibrium. The overall physical quantities quantified, not measured in this detail up to now to our knowledge, are believed useful for the development of advanced turbulence modelling techniques for unsteady flows, especially concerning Detached Eddy Simulation approaches.

2.1 Experimental Set-Up

2.1.1 Configuration

The major part of the experiment has been carried out in the low subsonic wind tunnel S1 of IMFT. The cylinder was mounted in a channel which has a 670x670 mm^2 square cross section. The cylinder spans the width of the channel without endplates and has a diameter of 140 mm, giving an aspect ratio L/D=4.8 and a blockage coefficient D/H=0.208. The upstream velocity U_0 at the centre of the channel is 15 ms^{-1}, so the Reynolds number based on the upstream velocity and the cylinder diameter D is 140,000. The free stream turbulence intensity, measured by hot wire technique in the inlet was found 1.5%. All the quantities have been non-dimensionalised using U_0 and D.

An additional set of measurements have been carried out in the wind tunnel S4 of IMFT, having a cross section of 61×71 cm. To keep the same blockage coefficient as in the previous measurements, the diameter of the cylinder was chosen 12.5 cm, which results in a blockage coefficient of 0.21 and an aspect ratio of 5.7. The main exploitations of the S4 results concern Reynolds number 140 000, using an inlet velocity U0 = 16.8 ms−1. Although the aspect ratio is different from the previous one and therefore the flow was not expected to be rigorously the same, it has been seen that a good agreement with the S1 measurements is achieved for the mean flow and the velocity spectra.

2.1.2 Measurements

Pressure

Measurements were carried out using a pressure transducer Validyne DP15-20. The sensor was mounted so that the frequency response is flat up to about 500 Hz. Measurements were carried out at angles from 0° to 360° in steps of 10° for each considered Reynolds number. The acquisitions were achieved during 2 to 5mn at a sampling frequency of 1 kHz. The uncertainty on the mean *Cp* coefficient is estimated to 3.5%.

2C- and 3C- PIV

A double-pulsed Nd-YAG laser Quantel (2x200mJ) and PCO-sensicam cameras (1280x1024 pixels) were used. The seeding particles used were DEHS (the typical size of the particle is 1μm). The cameras were equipped with a 35mm objective lens at a diaphragm aperture of 11. The system, both camera and laser, operated at a frequency of 4Hz. The measurements were carried out in the near wake of the cylinder and near the separation in *(x, y)* planes located at the middle span position *z=0* (Figure 1a). The size of the measurement area was 238 x 188 mm (1.34D x 1.7D) for the largest plane.

The software used to analyse images is a product of IMFT ("service signaux-images"). The algorithm is based on a 2D FFT cross-correlation function implemented in an iterative scheme with a sub-pixel image deformation, according to Lecordier & al. (2003). The flow has been analysed by cross-correlating 50% overlapping windows of 32×32 pixels. This yielded fields of 77 x 61 vectors with a spatial resolution of 3.13mm (0.0224*D*). Although the smallest scales of the flow cannot be captured with this resolution, as it is generally the case for in a PIV experiment, it has been shown that it is sufficient for the evaluation of the major part of the turbulent stresses, according to test carried out using smaller PIV planes and evaluation of vectors using 16x16 pixels interrogation windows.

For 3C measurements, the Scheimpflug angular configuration was used (Figure 1b) with the cameras placed on each side of the light sheet. Details of the procedure used for the reconstruction of the three components can be found in Perrin et al (2007). The achieved resolution is similar to that of the 2C measurements.

In S1, TR-PIV measurements were also carried out in a previous study, but the optical access to the wind tunnel and the low energy of the laser used restricted the size of the domain. To carry out time resolved measurements in a domain of similar size to that of the low frequency measurements, complementary data sets have been acquired in the S4 wind tunnel of IMFT.

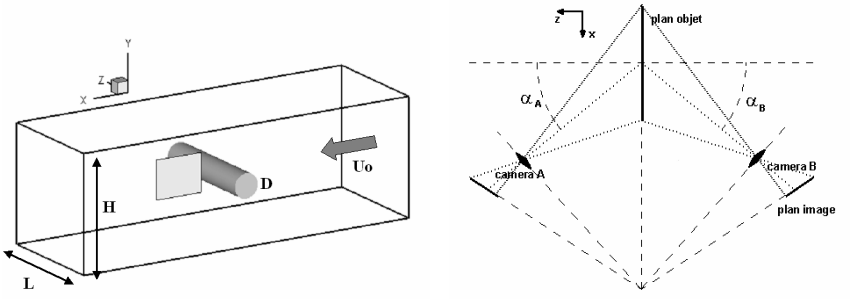

Fig. 1 Left: flow configuration, right: Scheimpflug configuration

2C- and 3C- TR-PIV

The TRPIV measurements were carried out using a laser Darwin 2 × 20 mJ from Excel Technology, a camera CMOS APX (PHOTRON) with a resolution of 1024x1024 pixels, and DEHS as seeding particles. The system allowed acquisition of image pairs at a rate of 1 kHz. The image pairs were analysed using the same 'in-house' code 'PIVIS', described in the previous paragraph. 2C-TRPIV was carried out in a *(x, y)* plane of similar size to that of the low data rate PIV, in the near wake of the cylinder. The flow was analysed by cross-correlating 50% overlapping windows of 32x32pixels, yielding fields of 61x57 vectors with a spatial resolution of 3mm (0.0238D). Approximately 2% of the calculated vectors were detected as outliers using a sort based on the norm, the signal-to-noise ratio, and a median test filter, and these vectors were replaced using a second order least square interpolation scheme. Six temporal series of 3072 images pairs have been acquired and analysed, each series containing approximately 85 vortex shedding periods.

3C-TR-PIV were performed using a Pegasus laser from New-Wave which delivers 2*10 mJ at 1kHz and two cameras CMOS RS3000 (Photron) with a resolution of 1024*1024 pixels used in the Scheimpflug angular configuration. These measurements were carried out in *(x, z)* planes in the near wake, with the aim of studying the three-dimensionality of the instantaneous flow. The PIV images are analysed using 'PIVIS'. For these measurements, the so-called pinhole based model was considered. The achieved resolution is 0.015*D*. Details of these last measurements can be found in Perrin & al (2008).

Comparisons between these new TRPIV measurements in S4 and the S1 measurements have been made in Perrin et al. (2007), given the small differences in the experimental set-up. Although not shown here, the recirculation length is found to be 1.25 and agrees well with the value of 1.28 found with low data rate PIV. Comparison of velocity spectra at the same points issued from the new TRPIV measurements and TRPIV performed in the S1 wind tunnel have also shown good agreement. Therefore, the influence of the aspect ratio slightly modified compared with the previous studies of us, was found to not have an important effect in the middle span plane.

2.1.3 Reynolds Averaging

About 3000 pairs of images were analysed to generate converged turbulence statistics with the 2C-PIV. The uncertainties are estimated, using a 95% confidence interval. They are 0.02 for *U*, 0.03 for *V* mean components, and 0.015 for $\overline{u^2}$, 0.02 for $\overline{v^2}$ and 0.01 for $\overline{uv}$ correlations. For the 3C-PIV, 2570 instantaneous flow fields were acquired. The differences between the 2C-PIV and 3C-PIV results are lower than 0.03 for the mean components and lower than 0.04 for the correlations.

2.1.4 Phase Averaging and Proper Orthogonal Decomposition

The nearly periodic nature of the flow, due to the von Kármán vortices, allows the definition of a phase and the calculation of phase averaged quantities. The flow is classically decomposed into a mean component, a periodic fluctuation and a random fluctuation as $U_i = \overline{U_i} + \tilde{U}_i + u_i'$ (Hussain and Reynolds (1972)). The phase average quantity is then $\langle U_i \rangle = \overline{U_i} + \tilde{U}_i$.

In a previous study of us (Perrin & al, 2007), the phase averaged quantities were measured using 2D PIV and a procedure based on a trigger signal. The trigger signal was the wall pressure on the cylinder at an angle $\theta=70°$ with the upstream stagnation point. The shedding phase angle was determined from this pressure signal using the Hilbert transform, and the averaging operation was performed both by averaging the ensemble of PIV fields acquired in a phase interval around a given phase angle, and by using an adapted version of Linear Stochastic Estimation, both techniques giving results in good agreements. The noticeable advantage of using LSE is that it is based on unconditionally acquired PIV fields, and therefore requires practically less efforts to compute phase averaged quantities.

A Proper Orthogonal Decomposition (for details on POD, see Berkooz & al, 1993) was then performed on the fluctuating instantaneous velocity. Denoting $\vec{\phi}^n(\vec{x})$ the POD modes, and $a_n(t)$ the coefficients associated with each POD modes, the instantaneous fields can be reconstructed as:

$$U_i(x,t) = \overline{U_i}(x) + \sum_{n=1}^{N} a_n(t)\vec{\phi}_i^n(\vec{x})$$

When choosing appropriately the number *N* of modes for the reconstruction, the POD acts as a convenient filter which extracts the coherent motion that is dominant in the flow from an energetic point of view.

The von Kármán vortices extracted by POD were then compared to the phase averaged fields. It was shown by considering an ensemble of fields acquired in a same phase interval, that a significant dispersion of the vortices at a given phase angle occurs, and therefore that the von Kármán vortices issued from phase averaging were significantly smoothed by the averaging procedure. This observation was confirmed from the spectral point of view, using the first TRPIV measurements. Velocity spectra classically exhibit a continuous part related to the

turbulent motion and a strong peak at the Strouhal frequency, related to the shedding motion. By estimating the spectra of the coherent part $\tilde{U}_i$, and of the chaotic one u'_i, it was shown that a significant residual peak remains in the continuous part, hence evidencing that a part of the coherent motion was let in the chaotic fluctuation. This effect was attributed to a phase jitter occurring between the pressure signal and the velocity signal in the wake. The consequences are an overestimation of the turbulent stresses and an underestimation of the coherent motion.

To alleviate this effect, phase averaging was then performed using a definition of the phase angle of the shedding based on the POD coefficients, as first suggested by BenChiekh et al. (2004) and van Oudheusden et al. (2005). As the two first POD coefficients have a quasi sinusoidal evolution, with a phase shift of a quarter of period, the phase angle can defined as:

$$\varphi_{a_1-a_2} = \arctan\left(\frac{a_1/\sqrt{2\lambda_1}}{a_2/\sqrt{2\lambda_2}}\right) \tag{1}$$

where α_1 and α_2 are the two first POD coefficients and λ_1 and λ_2 their corresponding eigenvalues. Using this definition of the phase angle, phase averaged quantities have been re-evaluated using LSE, and a significant enhancement was obtained, as will be shown in the results section. More details on this phase averaging procedure can be found in Perrin & al (2007).

2.2 Experimental Results

2.2.1 Flow Regime

From the wall pressure measurements on the cylinder at Re numbers from 65,000 to 190,000 (Figure 2a), the mean pressure drag coefficient is evaluated by integration of the pressure (Figure 2b). The base-pressure coefficient, $(-C_{pb})$ is found higher than in non-confined flow conditions, because of the blockage ratio. This yields a drag coefficient higher than in a non-confined case.

The drag decrease shows that the flow is at *the beginning of the critical regime.* This regime occurs at lower Reynolds number than reported in Roshko (1961), because of the free-stream turbulence intensity (1.5%).

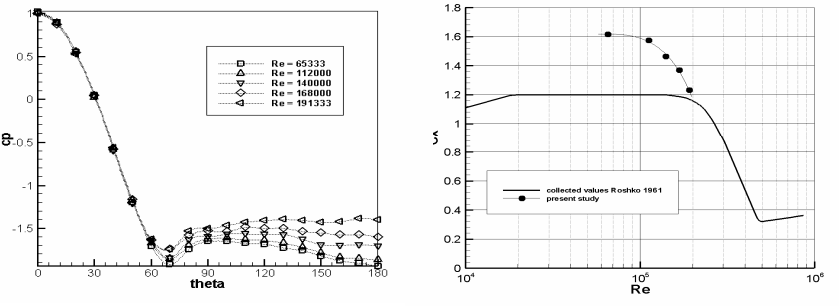

Fig. 2 Mean wall pressure coefficient around the cylinder (left); mean pressure drag coefficient versus Reynolds number

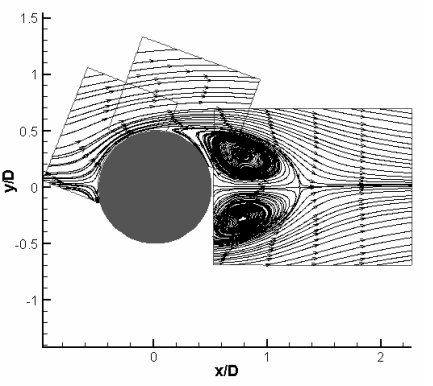

Fig. 3 Streamlines showing in detail the near-wall separation region

2.2.2 Time Independent Reynolds Averaged Fields

Before analysing the instantaneous motion and the coherent structures, the topology of the mean flow at Re=140,000 has been studied according to Reynolds averaging decomposition. As expected, a two symmetric eddies pattern is obtained, due to the averaging of the passage of the alternating vortices. Although not shown here due to space limitation, the U and V components present a symmetric and anti-symmetric topology, respectively, the mean spanwise component W, measured by 3C-PIV is found to be null. The dimensionless recirculation length l_c is found 1.28 ±0.03 with 2C-PIV and 1.23 ±0.03 with 3C-PIV. Values between 1.1 and 1.4 are found by several authors (Cantwell & Coles (1983), Norberg (1998),...) in the same Re number range. Given the difference in the boundary conditions (blockage, aspect ratio and inlet turbulence intensity) and experimental details having an important influence especially in the critical regime, where the global parameters vary rapidly with Re number, the present results appear to be reasonable. A detailed description of the mean motion, time independent Reynolds stresses, kinetic energy and production term can be found in Perrin & al, 2007.

2.2.3 Instantaneous Motion

The instantaneous motion is analysed in this section. Figure 4 shows a sequence of instantaneous superimposed vorticity and velocity, corresponding approximately to one third of period (one picture every three is represented as well as one velocity vector every two). The vortex shedding is clearly shown, together with smaller eddies in the separated shear layer which are wrapped around the von Kármán vortices. This behaviour is in good agreement with the measurements of Leder and Brede (2004) at a lower Reynolds number, although the flow is more irregular, as could be expected at this high Reynolds number. Although not shown here, another interesting point is that the vortex shedding becomes very irregular at some short instants occurring randomly. These instants and their description by a POD analysis have been studied in Perrin & al, 2008.

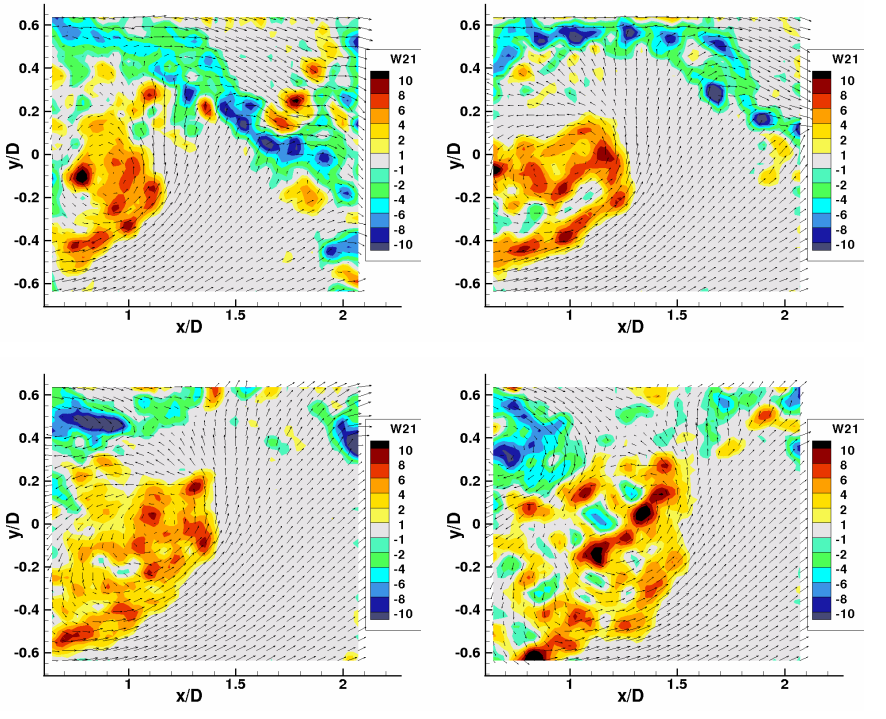

Fig. 4 Sequences of instantaneous fields

Figure 5 shows instantaneous fields in the *(x, z)* plane at *y*=0. The instantaneous fields are shown together with a phase averaged flow reconstruction in the *(x, y)* plane, at the phase angle at which the *(x, z)* field is acquired. The phase angle in

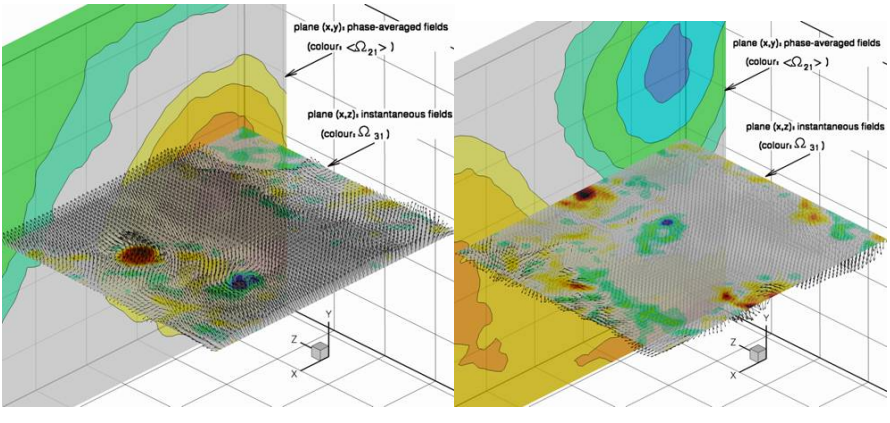

Fig. 5 3CTRPIV in the *(x, z)* plane in the cylinder wake. Vertical plane shows phase- averaged fields in the (x, y) plane phased with the 3C acquisition

this case is determined from the velocity at the intersecting line of both planes. Details of this reconstruction can be found in Perrin & al, 2008. One can recognise pairs of counter rotating vortices in the *(x, z)* plane, which are the signature of longitudinal vortices located between the main von Kármán vortices. To our knowledge, these counter-rotating longitudinal vortices have been studied only at lower Reynolds number, using DNS (e.g. Braza et al. (2001)), and experiments (e.g. Lin et al. (1995), Williamson, (1992), Hussain & Hayakawa, (1987)), and it has been shown that they are issued from a secondary instability. The present experiment demonstrates their persistence at high Reynolds number, although they are found much more irregular. A characterisation of these longitudinal vortices, with respect to the main von Kármán vortices, has been conducted in Perrin & al, 2008, using a pattern recognition technique based on wavelets, combined with conditional averaging.

2.2.4 Coherent Structure Identification by Means of the POD

POD is applied in this section to the TRPIV data sets acquired in the *(x, y)* plane. The access to spatiotemporal data allows an analysis of the POD by giving access to the temporal evolution of the coefficients associated with each mode. Fig 6 shows the cumulative sum (percentage) of energy of the POD modes, as well as the shape of the first 3 modes, obtained from the TRPIV measurements. It is recalled here that the POD modes do not represent vortices, but their combination through a POD reconstruction provides the most energetic vortex structures. In agreement with other wake studies at lower Reynolds number (Noack et al. (2003); Deane et al. (1991); and others), the two first modes can be associated with the von Kármán vortices. Their topology is found to be very similar to that found at low Re. The higher order modes however are more difficult to analyse. While, at low Reynolds number, the modes can be grouped by pairs and are related to the harmonics of the Strouhal frequency, it appears that higher order modes, in our case, present different topologies to that observed at low Re and cannot be directly related to the harmonics of the Strouhal frequency.

To analyse these modes, time traces and spectra of the coefficients associated with each modes have been plotted. Figure 8 shows the spectra of the coefficients a_1 to a_{10}. As expected, the spectra of the first two coefficients are mainly dominated by a peak at the Strouhal frequency. The time traces of these two coefficients present a quasi sinusoidal behaviour, a_1 and a_2 being shifted by a phase angle $\pi/2$ (Figure 7). This quasi sinusoidal evolution is however modulated both in frequency and amplitude and the spectral peak displays a width. The higher-order coefficients show a more complex behaviour. Although not shown for all modes here, their time traces appear very chaotic and their spectra present a non negligible continuous part. Some coefficients present distinct peaks at frequencies multiple of the Strouhal number, but it is not possible to clearly identify pairs of modes associated with the harmonics. Even if the higher order modes are not clearly identifiable, the behaviour of the third mode can be analysed, especially with respect to the instants of irregularities. The spectrum of a_3 indicates that this mode is

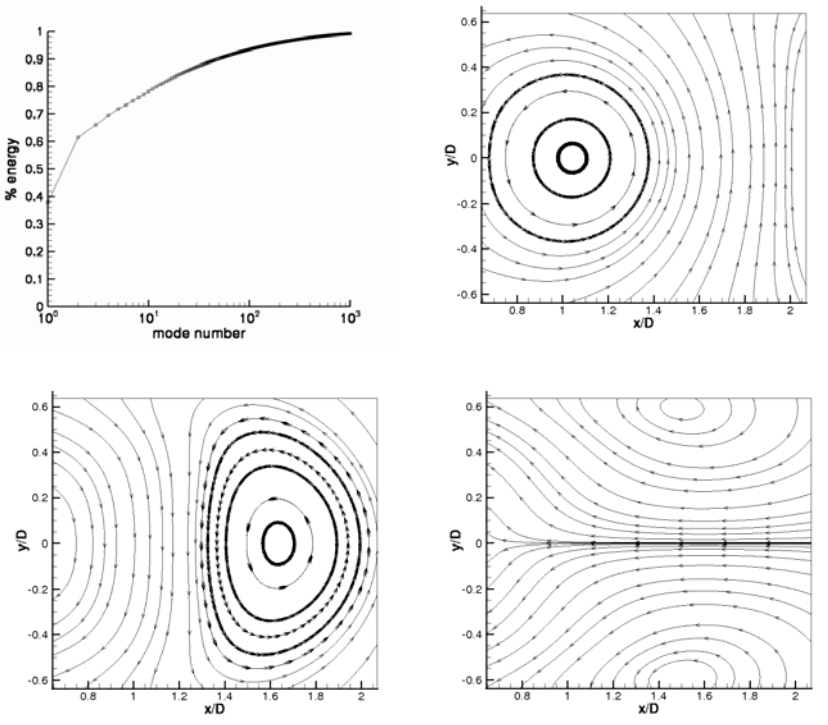

Fig. 6 POD: cumulative % of energy of POD modes (top left); mode 1 (top right); mode 2 (bottom left); mode 3 (bottom right)

mainly characterised by low frequencies. Furthermore, looking at its time trace, its amplitude seems to increase during the instants where the shedding is irregular (Fig. 7a at t~ 190). This increase of a_3 is also associated with a diminution of the amplitude of a_1 and a_2. Although not shown here, it has been shown in Perrin & al, 2008, that during these instants, the formation of the von Kármán vortices occurs farther downstream in the wake, and that the very near wake is mainly characterised by a chaotic motion. The topology of the 3rd mode is found very similar to that of the shift mode introduced by Noack & al, 2003, which is constructed as the difference between the steady motion (with a long recirculation zone) and the mean motion (with a short recirculation zone). Therefore, the role played by the third mode in the POD reconstruction of these instants is believed to be significant, owing to the behaviour of a_3, and to the topology of the mode.

The time evolution of the first two coefficients confirms the possibility to define a phase angle representative of the shedding using eq. (1). Fig. 7b shows the time evolution of the phase together with that of the first two coefficients. Using this definition of φ, the phase averaged quantities have been re-evaluated. It is noticeable that the instants where the shedding is irregular, as discussed just above, were not taken into account in the averaging operation. As it has been seen

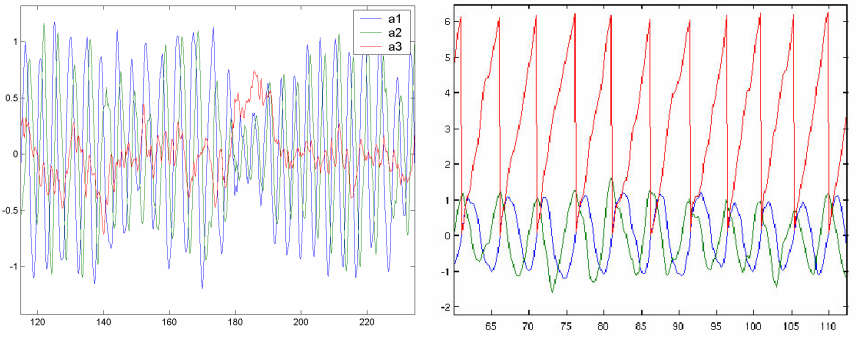

Fig. 7 left: Time evolution of POD coefficients a1, a2 and a3; right: phase angle of the shedding determined from a1 and a2

that a significant reduction of the amplitude of the coefficients is observed during these instants, a simple way to exclude these events from the averaging is to impose a threshold on $\sqrt{a_1^{\,2}+a_2^{\,2}}$. In Perrin & al (2007), it was shown that the resulting vortices were less smoothed by the averaging operation, and that the level of the turbulent stresses was reduced compared to phase averaging using pressure as a trigger signal. The time resolved PIV data allow checking this enhancement from a spectral point of view. Fig 9 shows the spectra of the fluctuating velocity *v*, together with both the phase averaged component and the random component, determined using pressure as trigger and using POD coefficients. Considering phase averages with pressure, it is seen that a residual peak remains in the continuous part, as explained in the previous section. On the other side, it is seen that this residual peak is significantly reduced, using POD coefficients, hence confirming the enhancement of phase averaging. This alleviation of the effect of phase jitter is mainly due to the fact that the phase angle is in this case determined directly from the velocity fields to be averaged.

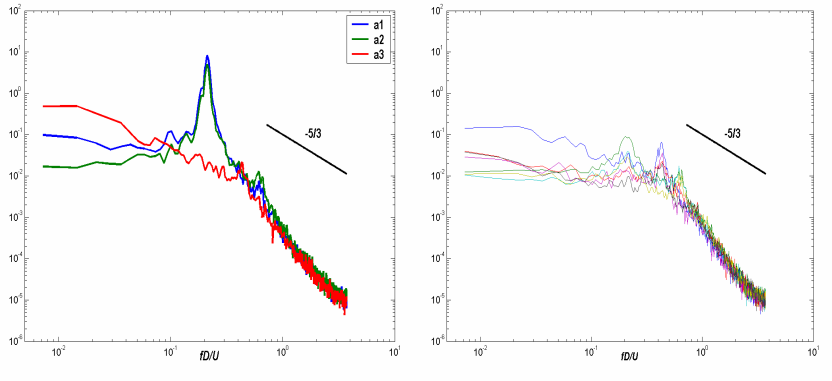

Fig. 8 Spectra of the POD coefficients (left: a1, a2 and a3; right: a4 to a10)

The experimental phase averaged fields are presented in Fig. 10. The phase averaged $<\Omega_{21}>$ component of the rotation rate tensor, the turbulent stresses issued from 2C-PIV and 3C-PIV, are shown, as well as the turbulent kinetic energy and the production term at phase angle φ=45°. On each figure, the red line corresponds to the iso-contour 0.5 of the Q criterion, used to identify the vortices. $<\Omega_{21}>$ clearly exhibits vortex shedding. The maximum value at the centre of the vortices is of order 3 at x/D=1 during their formation and decreases to 2 at x/D=2 at the beginning of their convection. $\langle u^2 \rangle$ and $\langle uv \rangle$ have their highest values in the shear regions near the separation. When the vortices are formed, the two lobes of high values of are $\langle u^2 \rangle$ transported towards the rear axis, and the centre of the vortices. At the beginning of the convection of the vortices, the highest values of $\langle uv \rangle$ are located in the shear regions near the saddle points between the vortices, where the strain rate is important. Concerning the normal stresses in the near wake, they all exhibit their highest values near the centres of the vortices when they start to be convected. High values of $\langle v^2 \rangle$ and $\langle w^2 \rangle$ are also present between the vortices, and can be supposed to be linked to the presence of longitudinal vortices connecting the primary one (cf. Figure 5). Finally, regions of low turbulent stresses values are identified in front of the vortices, corresponding to external fluid entering in the wake. It is also noticeable that a strong anisotropy is observed.

Fig. 11 illustrates the enhancements of the phase averaging and the influence it has on the topology of the stresses with respect to the mean motion. Iso-contours of the normal turbulent stress $\langle u^2 \rangle$ are represented with respect to the von Kármán vortices, which are delimited by the iso line 0.5 of the Q criterion (red line), for phase averaging with pressure (top), and phase averaging using POD (bottom). It can be seen, first, that the level of the stress is reduced when phase averaging

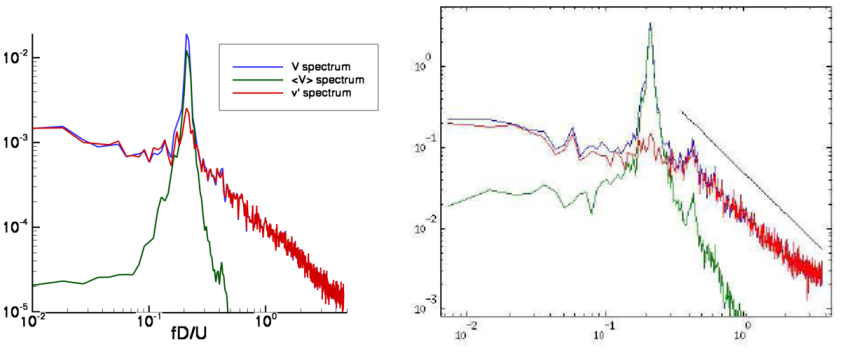

Fig. 9 Comparison of phase averaging using pressure *(left)* and phase averaging using POD coefficients *(right)*. The spectrum of the fluctuating v component at *(x/D, y/D)=(1, 0.5)* is represented. *blue line:* spectrum of the total fluctuating v-component; *green line:* phase averaged component; *red line:* chaotic v' component

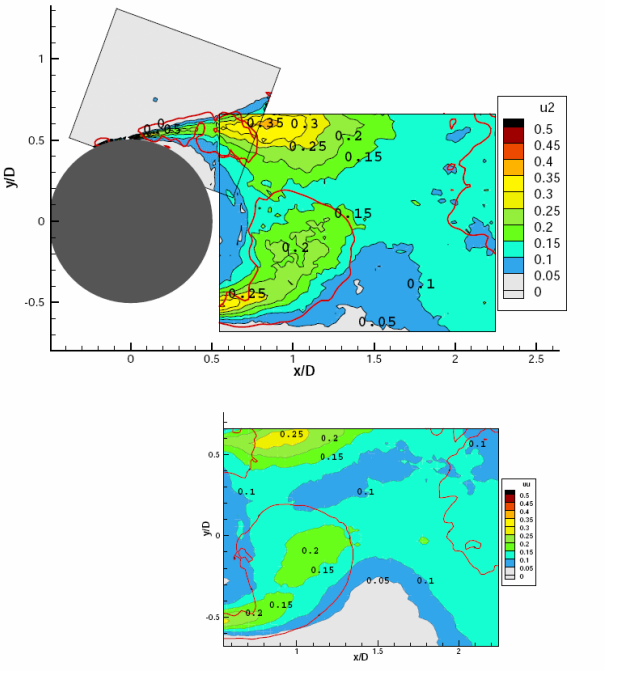

Fig. 10 Phase-averaged $\langle u^2 \rangle$ turbulent stress ; top: with pressure trigger, bottom: with POD phase angle. Red line iso-contour illustrates vortex structure by means of Q criterion.

using POD, in agreement with the discussion above. The topology of the stress is also found in better agreement with that of the coherent motion. Especially, the high levels of the stress are more concentrated near the centre of the vortices (on the lower side in the figure), and the regions of low turbulence intensity on the side of the wake, where the low turbulent motion is entrained toward the centre of the wake, are more pronounced.

The general topology of the stresses is found in good agreement with previous studies in wakes (Cantwell and Coles (1983), Leder (1991), Hussain and Hakayawa (1987), among other). With the use of stereoscopic PIV, the turbulent kinetic energy k can be evaluated without assumption on $\langle w^2 \rangle$. Its topology is compared to the production term that appears in the k transport equation $P = -\langle u_i u_j \rangle \dfrac{\partial \langle U_i \rangle}{\partial x_j}$. It appears, in agreement with the aforementioned studies, that while the production is mainly located near the saddle points in the shear regions, where the deformation rate and $\langle uv \rangle$ are important, the turbulent kinetic energy is mainly located near the centre of the vortices, suggesting a transport of the turbulent energy.

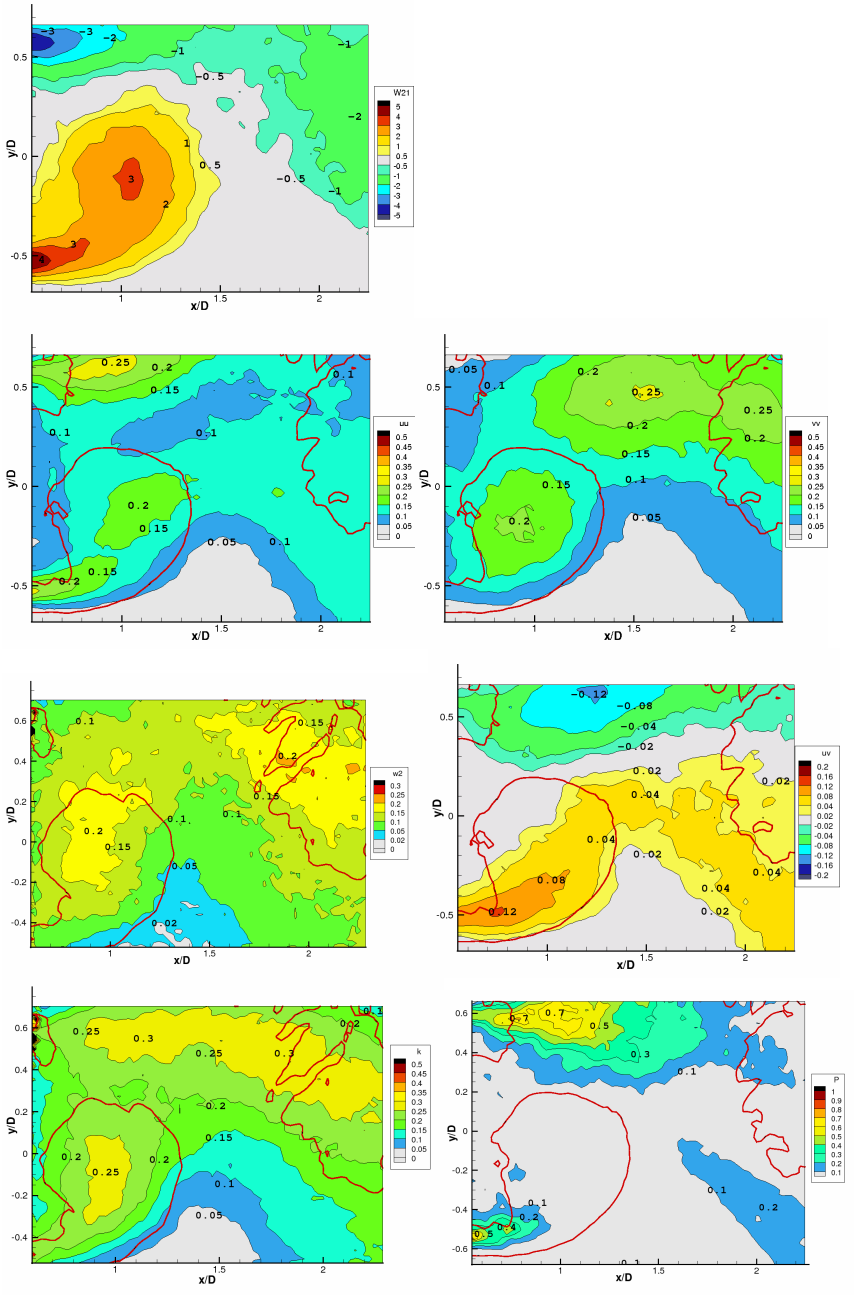

Fig. 11 Phase averaged quantities in near wake at φ=45°: from top to bottom and left to rigth: $<\Omega_{21}>$, turbulent stresses $\langle u^2 \rangle$, $\langle v^2 \rangle$, $\langle w^2 \rangle$, $\langle uv \rangle$, turbulent kinetic energy k and production P

2.3 Conclusions

Pressure measurement and different versions of PIV (3C-PIV, TR-PIV, 3C-TR-PIV) have been used to characterise the flow past a circular cylinder at Reynolds numbers from 65,000 to 190,000, this range corresponding to the beginning of the critical regime. Emphasis is given at the Reynolds number 140,000. After having quantified the mean motion and turbulent quantities, in a time independent Reynolds averaging sense, the main effort was devoted to the characterisation of the different coherent structures which occur in the flow and their interactions with the turbulent motion. Especially, the main von Kármán vortices were analysed using an appropriate phase averaging procedure which use POD coefficients to alleviate the phase jitter effects, that generally occurs in case of phase averaging. The topology of these alternating vortices, as well as the phase averaged turbulent quantities, were quantified and analysed. The present data base also allowed the analysis of different features occurring in the wake, like shear layer vortices, longitudinal vortices, and also instants of irregular shedding. As it is expected that hybrid simulations, especially DES approaches, are able to predict these features, the present analysis is believed to constitute a solid base for improvements and validations of turbulence modelling by hybrid approaches, for strongly detached flows around bodies.

IV Applications – Test Cases

1 Circular Cylinder Flow

R. El Akoury[1], M. Braza[1], C. Mockett[2], R. Perrin[1,4], T. Reimann[2], A. Revell[3], T. Craft[3], D. Laurence[3], Y. Hoarau1[1,5], and F. Thiele[2]

[1] Institut de Mécanique des Fluides de Toulouse, UMR CNRS 5502
[2] Technical University Berlin
[3] University of Manchester
[4] LEA Poitiers (present address)
[5] Institut de Mécanique des Fluides et de Solides de Strasbourg (present address)

Abstract. This test-case is based on the DESIDER IMFT's circular cylinder experiment described in a previous section. The flow around a circular cylinder with a low aspect ratio (L/D=4.8) and a high blockage coefficient (D/H=0.208) is investigated. This confined environment is used in order to allow direct comparisons with realisable 3D Navier-Stokes computations avoiding 'infinite' spanwise conditions. The flow is investigated in the critical regime at *Reynolds number 140,000.* The results are compared with statistically averaged wall pressure measurements, statistically averaged and *phase-averaged* three-component PIV, (3CPIV), two component *time-resolved* PIV, (TRPIV), as well as by Stereoscopic Time Resolved PIV (3C-TR-PIV). The present test-case offers a proper basis for comparison and validation of advanced statistical and hybrid (especially DES) turbulence modelling for strongly detached flows around bodies. The computations are carried out by the partners TUB, UMAN and IMFT. Previously obtained results by NTS in the FLOMANIA program are also reported. A discussion on the ability of the used turbulence modelling to capture the complex flow physics in respect on the present non-equilibrium turbulence is addressed, based on comparison with the present detailed data base: global parameters, resolved unsteady vortex structures, POD modes extracting the most energetic coherent structures.

1.1 Turbulence Models Used by the Related Partners

A detailed description of the present test-case can be found in Chapter "Experiments" of the present book. Advanced DES and URANS models have been employed and compared. TUB performed DES on the basis of a compact explicit algebraic Reynolds stress (CEASM) RANS model (Lübcke et al, 2000), which employs the Lien and Leschziner (1993) $k-\varepsilon$ formulation as a background model.

W. Haase et al. (Eds.): DESider – A Euro. Effort on Hyb. RANS-LES, NNFM 103, pp. 105–308.
springerlink.com

IMFT applied the DES/OES – Organised Eddy Simulation that involves modified turbulence length scale in the RANS k-ω part of DES, (El Akoury et al, 2007). UMAN applied the standard DES-SST as well as 2 URANS models, the standard SST model and the stress-strain lag version, the SST-*Cas* model (Revell et al, 2005, 2007). For the sake of completeness, results of NTS with the DES/SA (Spalart Allmaras) model are also presented, referenced in the FLOMANIA book. Concerning the above turbulence models, please refer also to the individual partners contributions.

1.2 Numerical Parameters

The numerical grid used by IMFT were of order N-total=2 345 952 nodes in structured 3D blocks (N-block=34) and the NSMB ((Navier-Stokes MultiBlock) code including the OES modelling version. TUB used a grid of 5M points and their in house ELAN code. UMAN used the unstructured finite volume Code_Saturne with a 3D mesh of 2.1M points.

1.3 Results

The results discuss first the global parameters as well as the statistically averaged flow quantities compared with the experiment. Secondly, comparisons and physical analysis with the instantaneous flow quantities, especially phase-averaging and POD (Proper Orthogonal Decomposition) are presented. It is recalled that the free-stream turbulence intensity is 1.5%.

1.3.1 Comparison of Global Parameters

Table 1 shows comparisons of averaged drag coefficient, Strouhal number and of recirculation length. A good agreement with the experiment is achieved.

Figure 1 shows comparison of the statistically averaged wall pressure coefficient with the experiment. TUB, NTS and IMFT modelling takes into account the transition starting downstream of the separation point by using trip-less

Table 1 Statistically averaged global parameters

	UMAN (SST)	UMAN (SST-Cas)	UMAN (DES-SST)	NTS (DES)	TUB (DES) (fine time step)	IMFT-CFD (OES)	IMFT-Exp
CD	-	-	1.49	1.38	1.48	1.44	1.45
St	0.235	0.23	0.225	0.22	0.225	0.19	0.21
lrec	1.07	1.35	1.38	≈1.35	1.35	1.28	1.28 ±0.03

approach according to NTS, (Strelets et al, Flomania book, Aupoix *et al*, 2006). UMAN calculates the upstream boundary layer and the downstream of the separation regions directly from the turbulence modelling. For this reason, the pressure 'plateau' is higher in this case.

1.3.2 Comparison of Statistically Averaged Fields

Figure 2a shows the mean iso-velocity (*U* and *V* components) fields, as well as streamlines compared with the experiment. A good overall agreement is achieved for DES. Concerning URANS, the SST-Cas model provides improved results for the recirculation length. Figure 2b compares the normal and shear Reynolds stresses. A good agreement is also achieved.

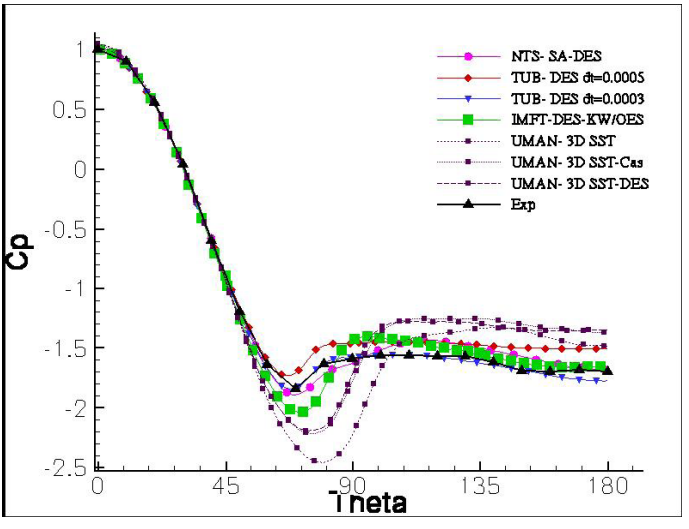

Fig. 1 Statistically averaged wall pressure coefficient

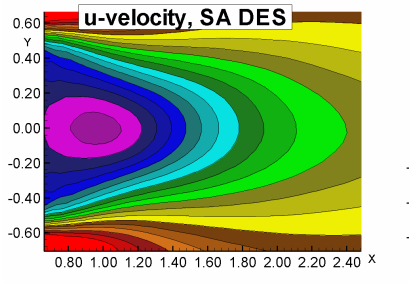

NTS – Iso-*U*

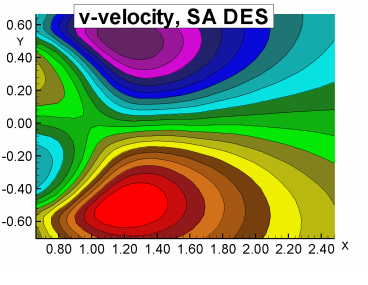

NTS – Iso-*V*

Fig. 2a Iso-longitudinal velocity components

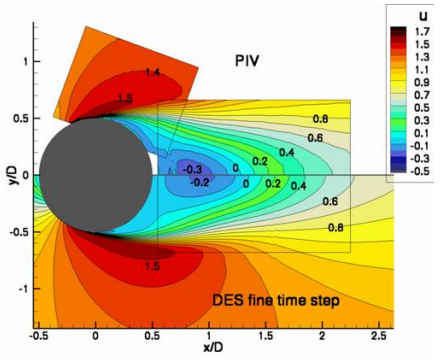

TUB – Iso-*U*

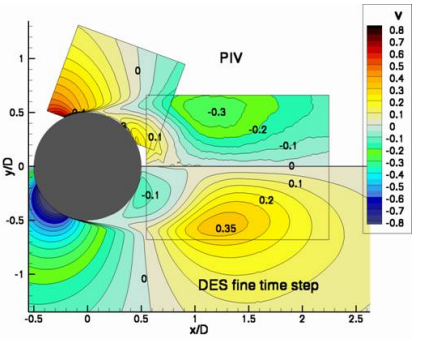

TUB – Iso-*V*

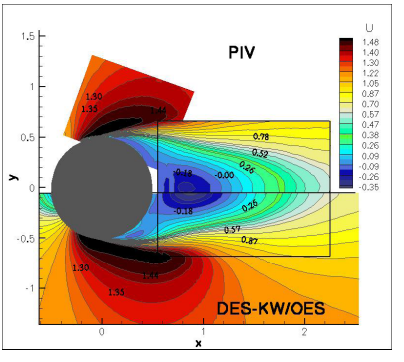

IMFT – Iso-*U*

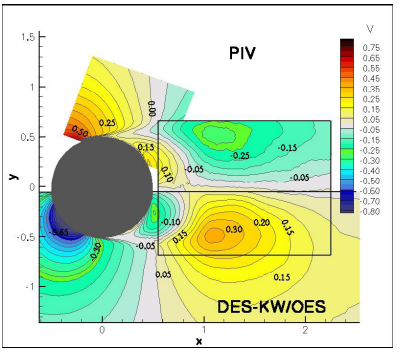

IMFT – Iso-*V*

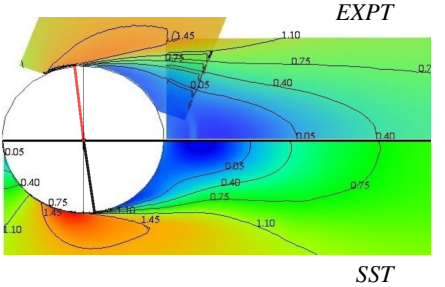

UMAN – Iso-U -SST

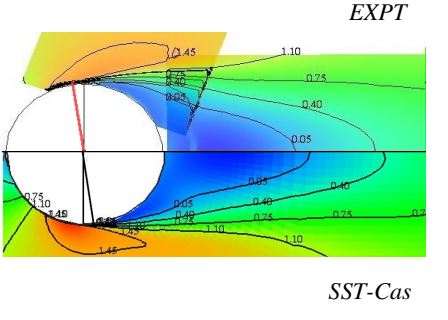

UMAN – Iso-U – SST-Cas

Fig. 2a (*continued*)

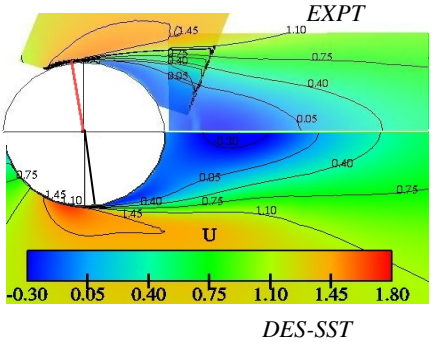

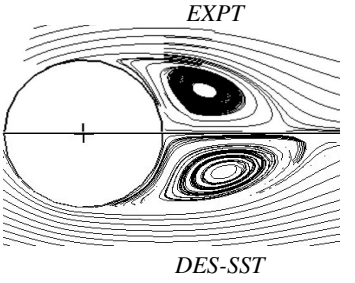

UMAN – Iso-U - DES

UMAN – Iso-streamlines -DES

Fig. 2a (*continued*)

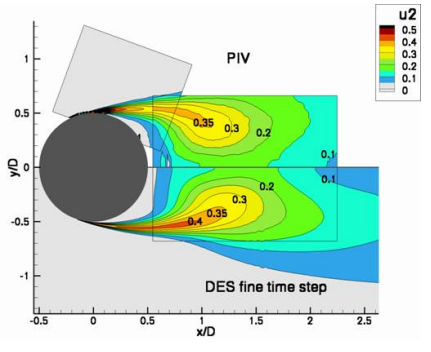

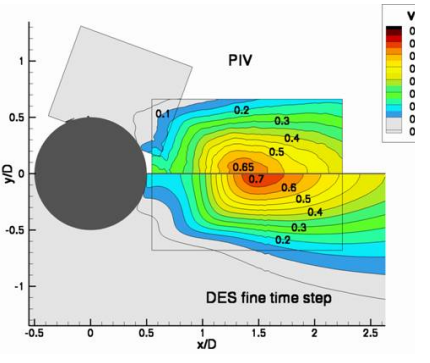

TUB – Iso-*u2*

TUB – Iso-*v2*

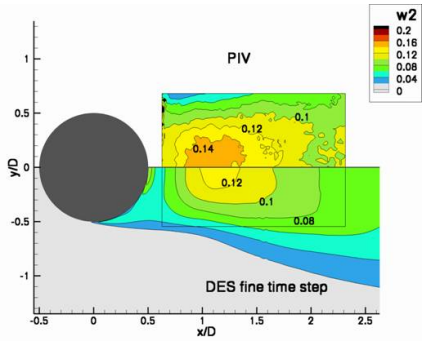

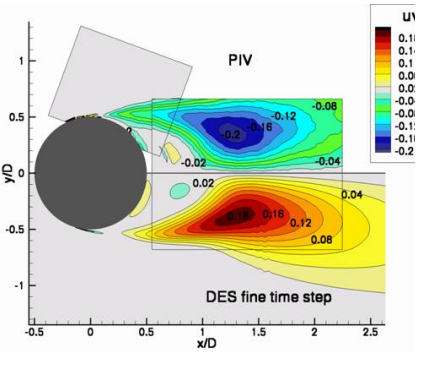

TUB – Iso-*w2*

TUB – Iso-*uv*

Fig. 2b Iso-contours of Reynolds stresses compared with the experiment

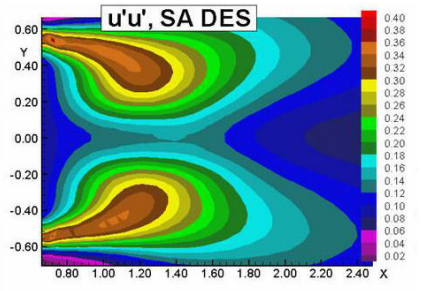

NTS – Iso-*u2*

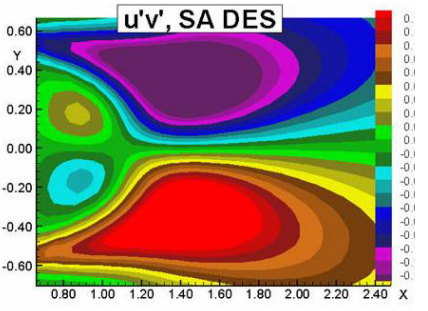

NTS – Iso-*uv*

Fig. 2b (*continued*)

1.3.3 Comparison of Unsteady Fields

The topology of different classes of vortices is provided by each partner's contribution. Figure 3 shows indicatively instantaneous views of the complex vortex structures in the near wake, especially illustrated by the $\lambda 2$ criterion (Jeon et al, 1995). The advanced URANS and DES approaches are able to capture not only the Bénard -von Kármán vortices but also smaller-scale structures as the Kelvin-Helmholtz vortices downstream of the separation. The non-linear interaction among these kinds of structures has been also produced by the simulations.

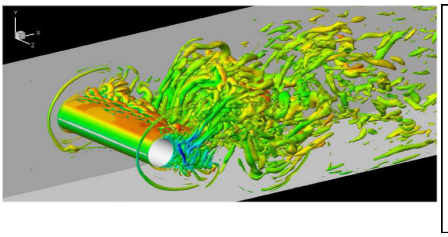

TUB

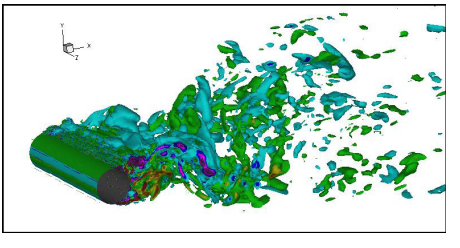

IMFT

Fig. 3 Iso-λ_2 surfaces shaded with streamwise velocity, DES/CEASM (left); Iso-vorticity component ω_z, DES/OES (right)

Phase-Averaged Fields

The present experiments allow direct comparison of the flow quantities at the same phase-angles, according to the phase-averaged decomposition, Cantwell & Coles (1983). TUB performed a detailed parametric study showing the influence of the numerical time-step to capture correctly the unsteady shearing regions and the Kelvin-Helmholtz vortices (Figures 4 and 5). The DRSM – SSG model is able to better capture this kind of smaller structures.

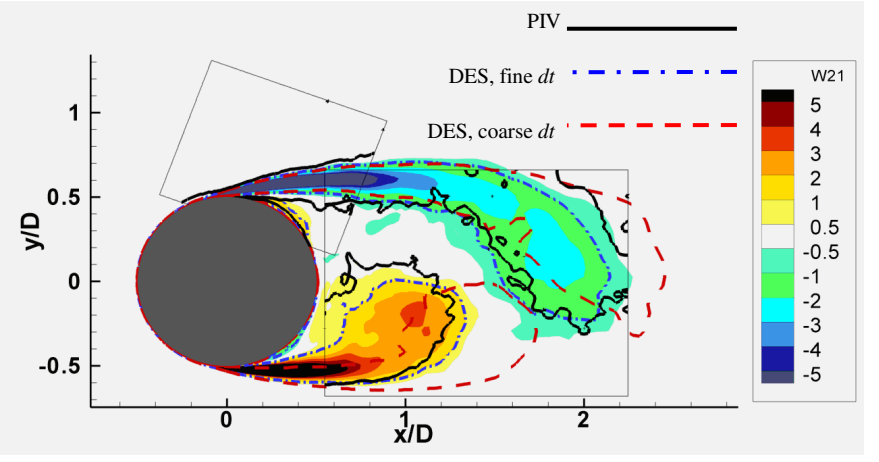

TUB – Phase-averaged iso-vorticity field versus experiment

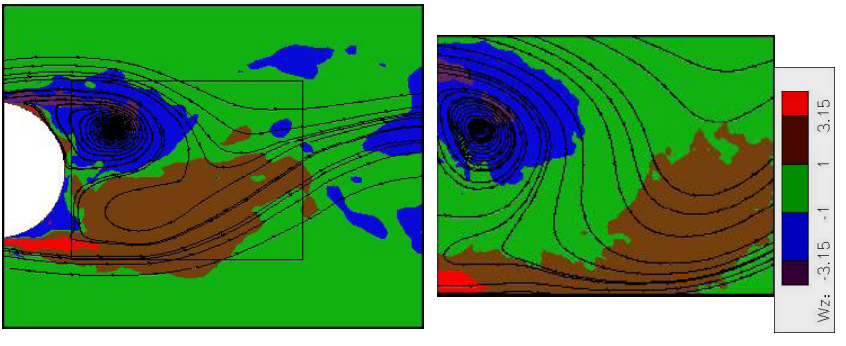

IMFT – Phase-averaged iso-vorticity field versus experiment

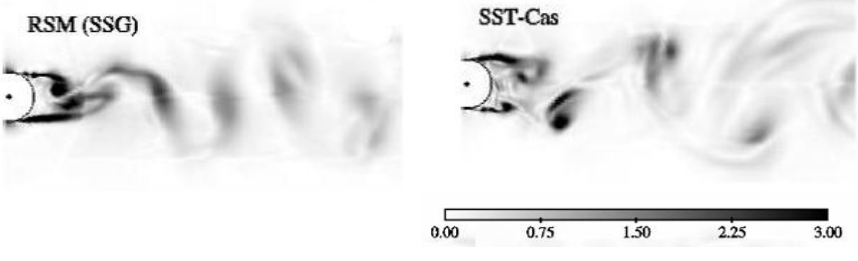

UMAN – Phase-averaged iso-vorticity fields

Fig. 4 Comparison of phase-averaged iso-vorticity fields

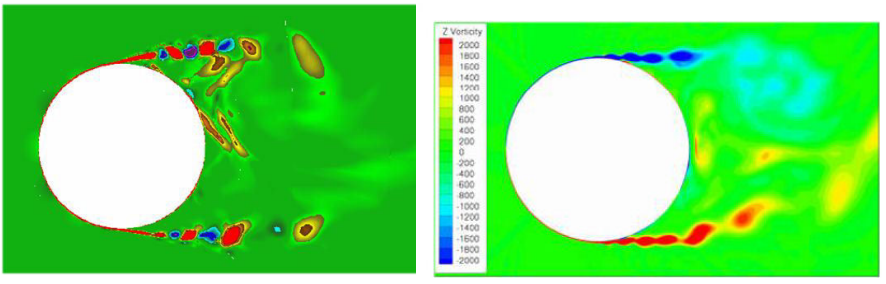

IMFT – DES/OES TUB - CEASM

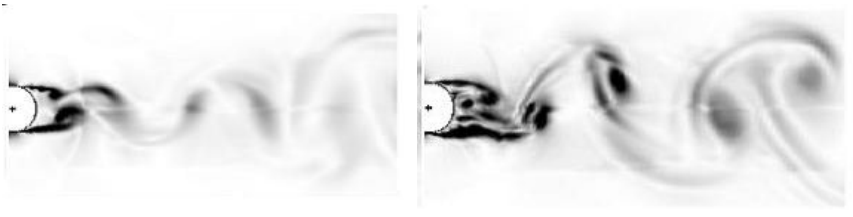

UMAN - SSG UMAN- *Cas*

Fig. 5 Mixing layer Kelvin-Helmholtz instability eddies downstream of separation point

Fig 5 shows an example of Kelvin-Helmholtz vortices formation simulated by DES and URANS. The SSG model captures this kind of structures although it provides a narrower wake expansion downstream. It is recalled that standard URANS usually lead to a complete damping of these smaller-scales organised structures.

1.3.4 Coherent Structures Identification by Means of the POD

The application of the Proper Orthogonal Decomposition, as well as a brief description of its principles can be found in the chapter "Experiments", concerning the circular cylinder. A detailed description can be found in Berkooz et al (1993). The purpose of this section is to analyse the coherent structures by means of the POD modes that are combined to perform the flow field reconstruction by retaining only the most energetic modes. It is recalled that the modes are not the vortex structures. A discussion about 3D reconstruction can be found in El Akoury et al, 2008. The present TRPIV experiment allows providing the POD modes as well as the temporal evolution of the shape functions coefficients as described in the experimental section. In the present, a direct comparison of the POD experimental and DES/TUB modes is performed and shows a good agreement. As the currently available physical experiments provide spatio-temoral fields with a significant detail, this kind of comparisons is now possible. Furthermore, the POD reconstruction is proven able to provide the Kelvin-Helmholtz instability and related

vortices by using an order of 49 first energetic modes (DES/IMFT). The energy diagram is provided in the IMFT's partnerwise contribution.

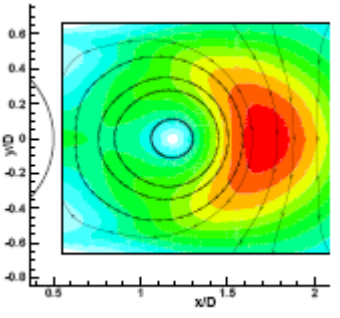

1st POD mode – TRPIV IMFT exp

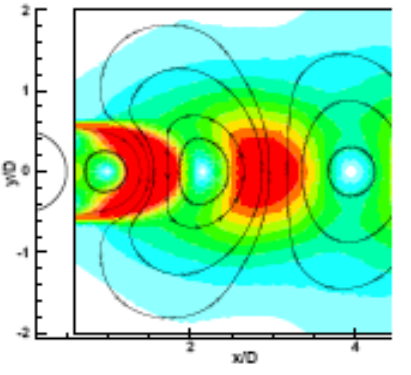

1st POD mode – DES/CEASM TUB

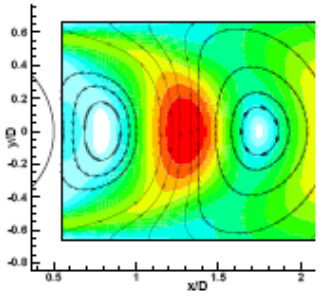

2nd POD mode – TRPIV IMFT exp

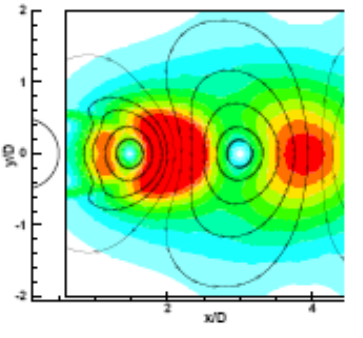

2nd POD mode – DES/CEASM TUB

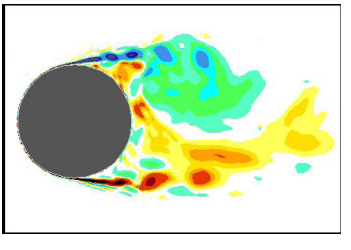

POD reconstruction – 49 modes; von Kármán and Kelvin-Helmholtz eddies IMFT DES/OES

von Kármán and Kelvin-Helmholtz eddies; UMAN- *Cas*

Fig. 6 Comparison of POD modes (experiment and simulations), POD reconstructions of the principal coherent structures compared to the simulations

1.4 Conclusions

The presented DES and advanced URANS models are able to simulate the present complex 3D strongly detached flow around a cylinder. The DES approach seems to give a more detailed vortex structure for the present flow. The URANS SST-Cas model provides an improved flow structure with respect to the SST, thus offering an interesting compromise between DRSM and two-equation modelling, in respect of capturing the present complex flow physics.

2 TU Munich Delta Wing

N. Ceresola

Alenia Aeronautica

Abstract. This test case concerns vortical flow simulation past a delta wing at a high angle of attack. The testcase has been studied experimentally at TU Munich, and the configuration is the same that was used in FLOMANIA. The participants to this exercise were Alenia, EADS-M and ANSYS. The DES simulations carried out by participants allowed a satisfactory prediction of vortex breakdown at α=35° and of mean flow quantities. The same conclusion cannot be drawn as the prediction of fluctuating quantities is concerned. The importance of a proper, isotropic grid refinement to correctly resolve the physics is evidenced in this respect.

2.1 Test Case Description

The test case considered in this chapter is a sharp leading edge delta wing with an aspect ratio of 1 as it is shown in Figure 1. Measurements were carried out by Breitsamter (1997) at Technical University of Munich, in an open wind tunnel with a circular test section of 1.5 m diameter.

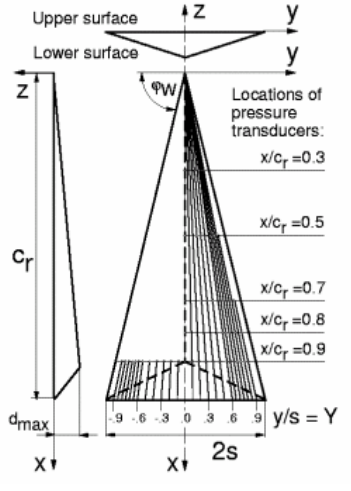

Cr = 0.670 m. (chord length of wing)
Dmax = 0.057 m. (max.thickness at 90% chord)
lμ = 0.670 m. (mean aerodynamic chord)
2s = 0.335 m. (full span)
φ_w = 76° (leading edge sweep angle)
Λ = 1. (aspect ratio)

Fig. 1 Geometry of the delta wing

The tests were conducted at four angles of attack, namely 12.5°, 25°, 30° and 35°. Only two of them have been taken under consideration in DESider project, namely 25° (optional) and 35° (mandatory). The first one is characterized by the

presence of a compact leading edge vortex, while vortex breakdown at about 50% chord is present in the second case.

Only the results referring to the case α=35° are considered in the present chapter, being the most significant test case to assess the possible benefits arising from an applications of DES modelling.

A large amount of steady and unsteady experimental data is available for this test case.

Carried-out measurements include mean and rms pressure distributions at 5 streamwise stations, namely at x/C=0.3, 0.5, 0.7, 0.8 and 0.9. Hot wire measurements were used to get detailed insight in the structure of the flow, providing mean and rms uvw velocity components on five x=const planes corresponding to the same stations. In addition, flow visualizations using the laser light sheet and liquid crystal techniques were performed.

The free-stream velocity was constant and equal to 37m/s. Experimental conditions include ambient static pressure and room temperature. The experimental Reynolds number, based on the mean aerodynamic chord, is approximately 10^6. No specific treatment for the transition was applied.

2.2 Description of the Computations

2.2.1 Grids

EADS-M used FLOWer and TAU code for the cases at 25 and 35 degrees angle of attack. The structured grid was derived from that used in FLOMANIA, with additional grid blocks added in the leading edge region. It consists of 16 blocks, made of 81x97x41 grid points each, for a total of 5.2 10^6 points. 281x161 points stay on the surface while 97 lines are normal to it. The unstructured grid was made of 13 million nodes.

Alenia generated an unstructured, hybrid grid with 600 000 points in total, and 5000 points on the surface, that was flow adapted with point enrichment in the regions of vortex core and vortex sheet.

ANSYS used the same unstructured grid generated by EADS for TAU computations.

2.2.2 Numerical Methods and Turbulence Models

EADS used the FLOWer code that operates on block-structured grids and is cell centred. The results obtained, using the TAU, code are omitted in this report. All the computations were done with SA DES turbulence model.

Alenia employed the code UNS3D, a finite-volume, node-centred operating code on unstructured grids and using the k-ω-EARSM DES turbulence model.

ANSYS simulations were carried out with the CFX code on the EADS unstructured grid, using the SST-SAS turbulence model, with the curvature correction procedure of the SST model.

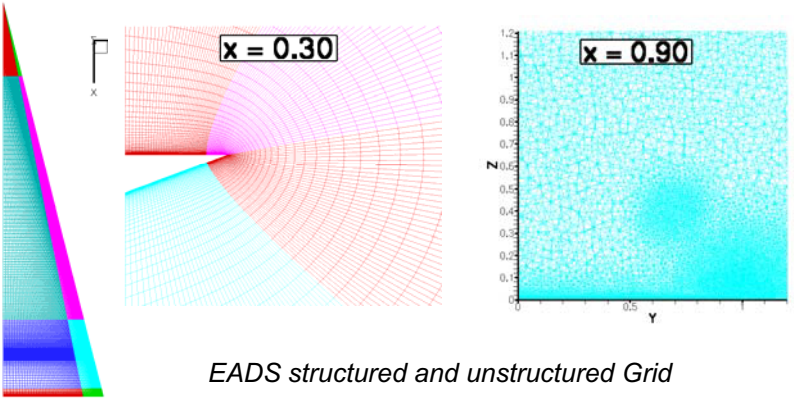

EADS structured and unstructured Grid

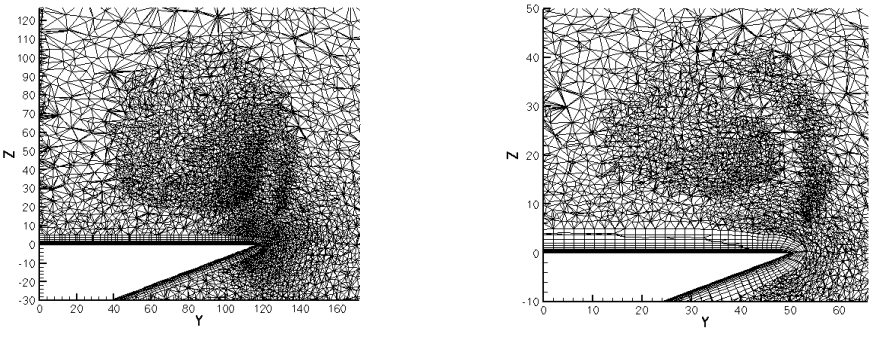

Alenia grid at x/c=0.3 and x/c=0.9

Fig. 2 Grids used for the computations

The integration in time was performed by all participants using a second order backward Euler scheme and the dual time stepping technique. Different time step lengths were adopted for the integration:

EADS	$\Delta t = 1\ 10^{-3}$ sec
Alenia	$\Delta t = 1.5\ 10^{-4}$ sec
ANSYS	$\Delta t = 3\ 10^{-5}$ sec

2.3 Results

In Figure 3 the mean surface pressure distribution for the case at α=35° on spanwise cuts at x/c=0.3, 0.5, 0.7, 0.8 are shown. Satisfactory results have been obtained by the participants with respect to the experiment: the location and extent of the secondary vortex and of the vortex breakdown were in general correctly predicted. A slight inboard displacement of the pressure peak due to the main vortex can be observed at x/c=0.3. This is due to an over-prediction of the effect of the secondary vortex, that probably is not originating exactly at the apex in the

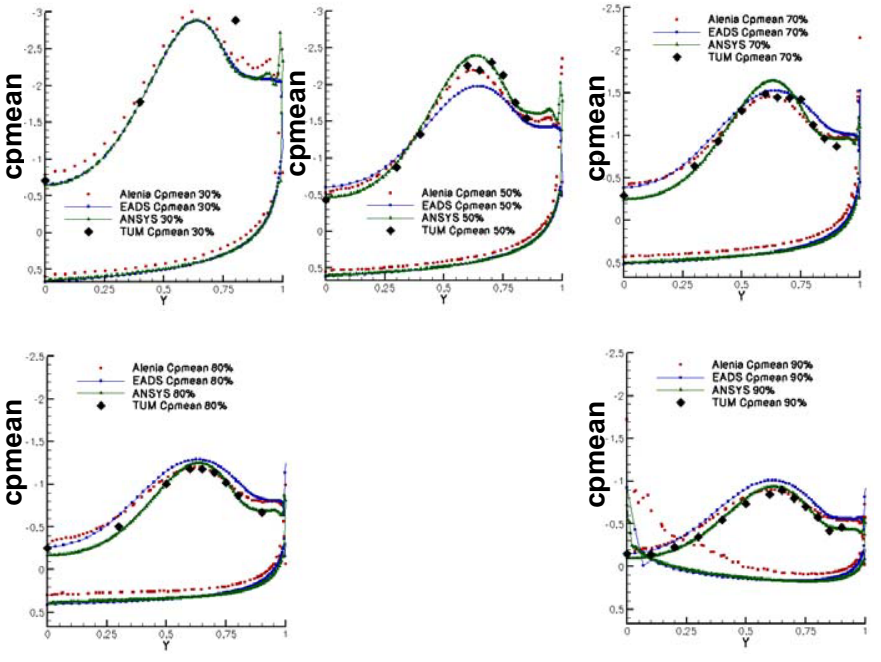

Fig. 3 Mean Cp distributions at x/c=0.3, 0.5, 0.7, 0.8 and 0.9

experiment, as it does in the computations An earlier prediction of breakdown may be present in the EADS results, as it can be seen from the pressure distribution at x/c=0.5. The ANSYS results were obtained on the finest grid (EADS unstructured) and showed the best agreement with experimental data due to the better grid resolution of the main pressure peak. In Figure 4, the mean Cp contours on wing surface are compared to the wind tunnel data.

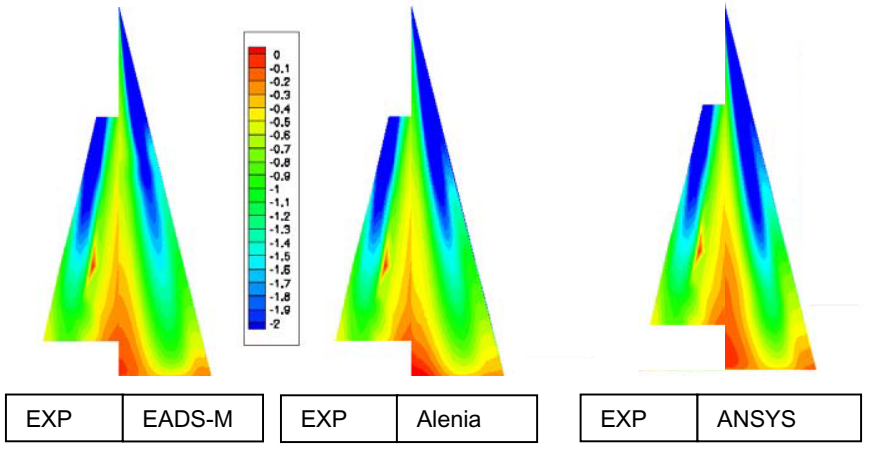

Fig. 4 Mean wall Cp contours

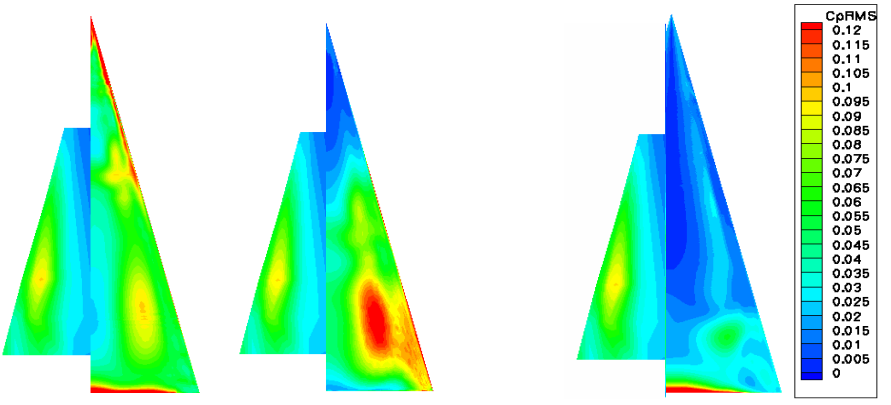

Fig. 5 Rms wall Cp contours, EADS (left), Alenia (middle), ANSYS (right); experiment (left parts), computations (right parts)

In Figure 5, the surface rms pressure distributions are compared versus the experimental data, while the rms Cp-distribution on five surface cuts is compared in Figure 6. Acceptable rms pressure distributions have been predicted by EADS and Alenia up to x/c=0.7. On the contrary, fluctuation levels much higher than in

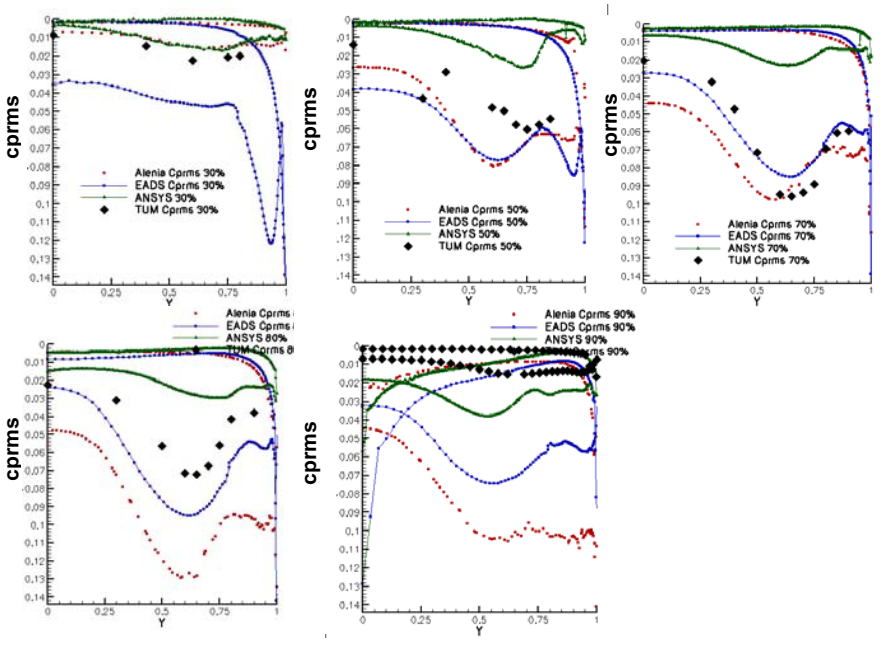

Fig. 6 RMS Cp distributions at x/c=0.3, 0.5, 0.7 0.8, and 0.9

the experiment were predicted toward t.e., particularly in Alenia results. The point seems to be the excess of energy predicted in the region of the breakdown and downstream to it, where the experimentally measured fluctuation decay to a low level, that is not predicted by the numerical models. It can be deduced that an energy dissipation mechanism must be present, that is not taken in account by the simulations and can be related to the decrease in mesh resolution common to the two grids as the flow is approaching the trailing edge.

ANSYS low Cp_{rms} levels may be an effect of the very short time integration period so that unsteady fluctuation were not allowed to grow up to their physical levels.

Anyway, the different fluctuating components predicted by the participants seemed not to have a relevant influence on the respectively computed mean values. More than the features of sub-grid modelling, it is the grid resolution in the vortex core that appears to be the most relevant issue to be addressed in order to correctly simulate the mean flow quantities.

The Cp_{rms} contours computed by Alenia and EADS on spanwise cuts at x/c=0.3, 0.5, 0.7, 0.8 are shown in Figure 7. The structure is roughly axial-symmetric with respect to the axis of the main vortex, and the maximum level of fluctuations occurs at a fixed radial distance from the its centre. The predicted level is significantly higher in Alenia results than in EADS computations, except upstream of the breakdown location where Alenia computation predicts a very low level of unsteadiness. This fact may be related to the grid resolution in the region of the main vortex, being lower for the Alenia grid and leading to an over-estimation of the amplitude of the fluctuations.

The interpretation of the computed results and the comparison with the experiment is much more difficult as rms contours of velocity are concerned.

The experimental and computed rms contours of the u-component of velocity (roughly the axial vortex direction) are shown in Figure 8. Following the experimental data, low levels of fluctuations are present upstream the location of vortex breakdown, that is reproduced in Alenia results. The different behaviour in EADS data may be due to a grid-related numerical vorticity generation arising at the sharp leading edge, near the wing apex. Proceeding toward the trailing edge, the Alenia results show at least a qualitative agreement with experiment, as the maximum of fluctuations is located at some radial distance from the vortex core, while strongly overpredicting the fluctuation amplitude. At the breakdown location (x/c=0.5), the vortical structure appears to be broken and the unsteadiness is located mainly in the core region. The levels of unsteadiness predicted by EADS are on the contrary underpredicted.

A somewhat different picture is given in Figs. 9 and 10, where the experimental and computed rms contours of the v and w components (roughly in the azimuthal plane) are shown, respectively. The EADS simulation seems to qualitatively better representing the experimental data, as a similar distribution of the fluctuation levels with respect to the vortex axis is reproduced. At least one conclusion may be obtained, that to increase the grid resolution in the axial direction is equally important than refining the grid in the radial plane, unlike it is usually done generating grids for (U)RANS computations.

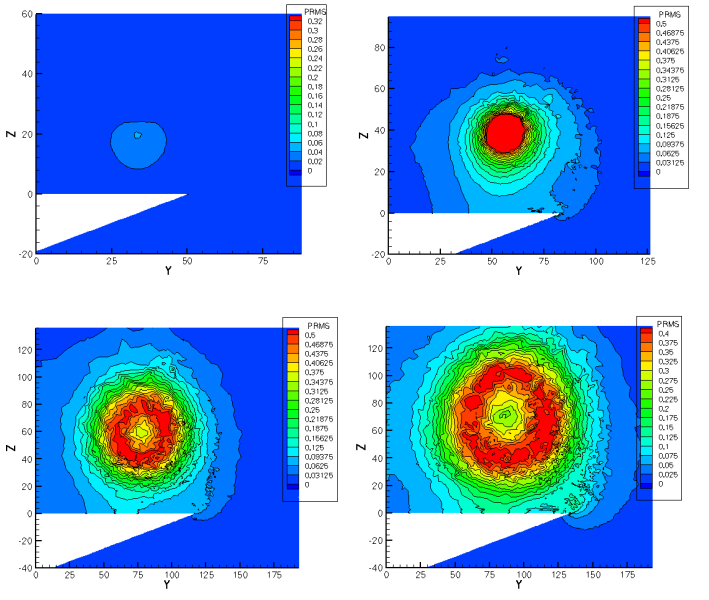

Alenia

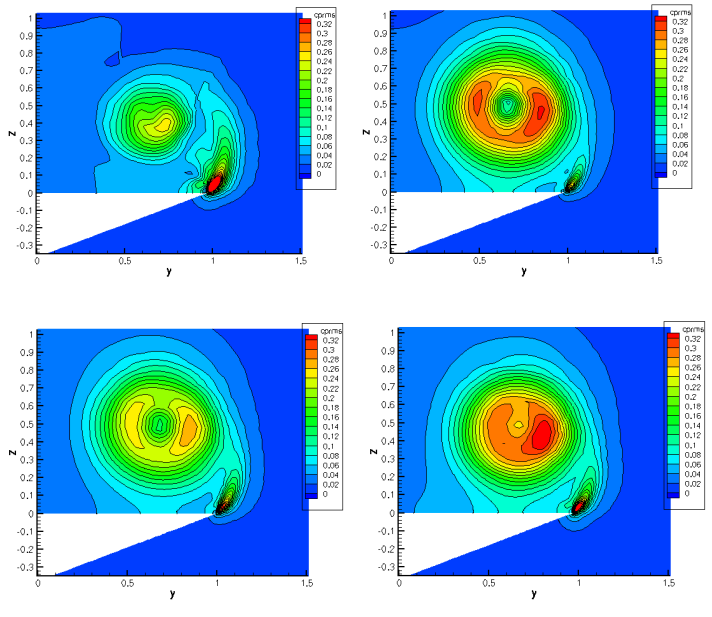

EADS-M

Fig. 7 Cp-rms at x/c=0.3, 0.5, 0.7, 0.8 (upper left, upper right, lower left, lower right)

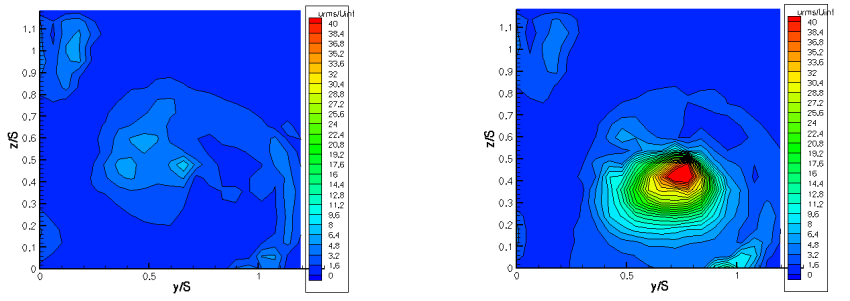

Experiment

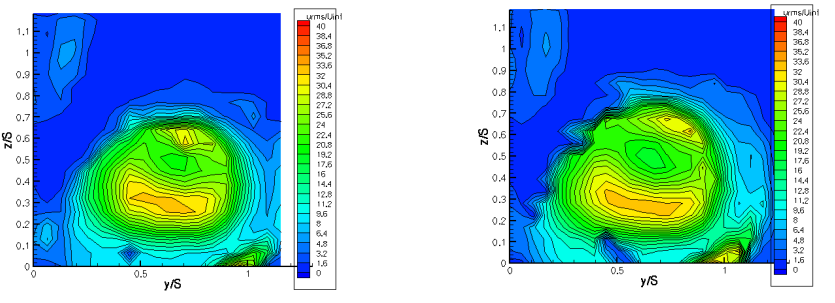

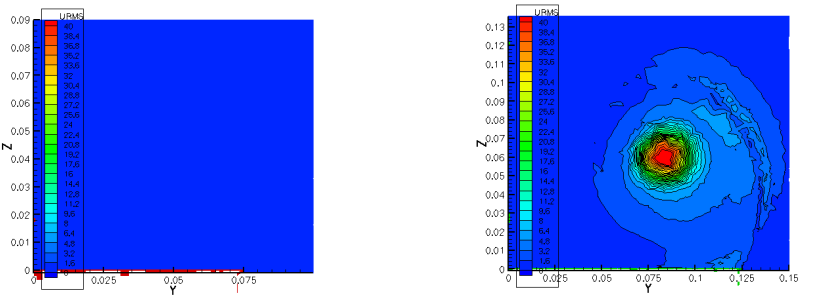

Alenia

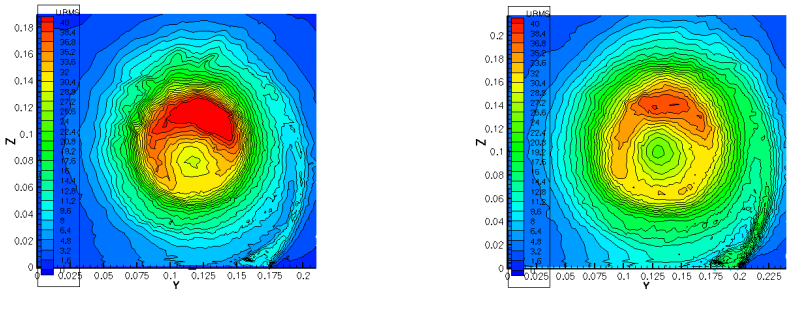

Fig. 8 u-rms at x/c=0.3, 0.5, 0.7, 0.8 (upper left, upper right, lower left, lower right)

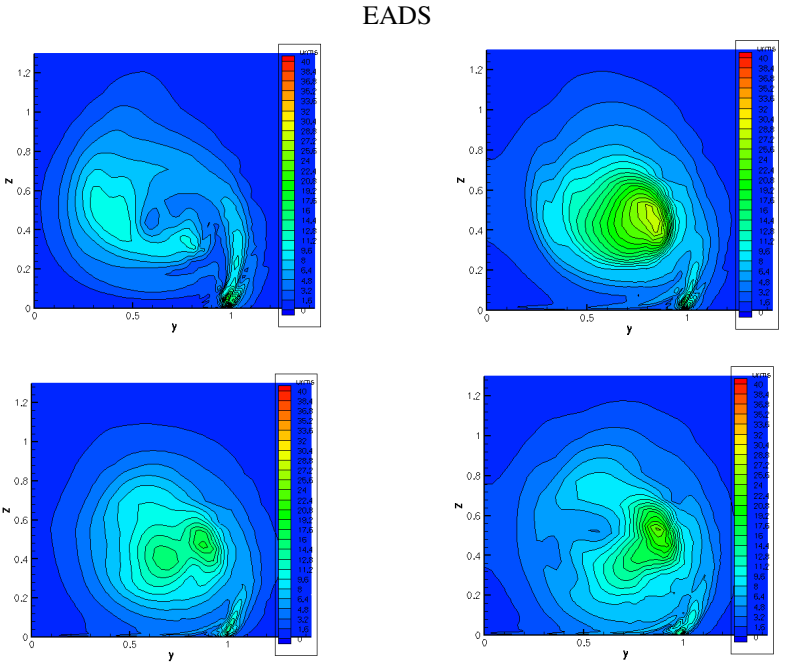

Fig. 8 (*continued*)

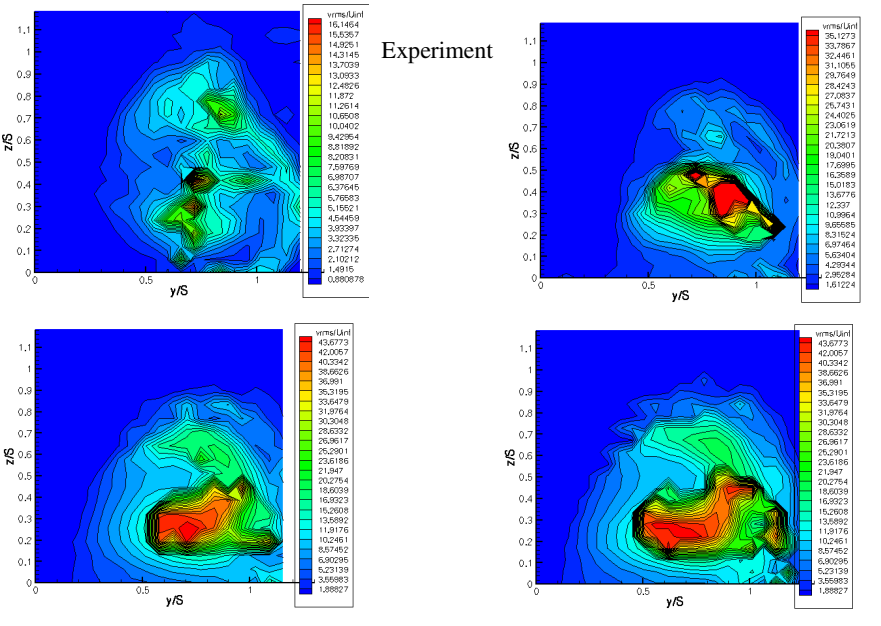

Fig. 9 v-rms at x/c=0.3, 0.5, 0.7, 0.8 (upper left, upper right, lower left, lower right)

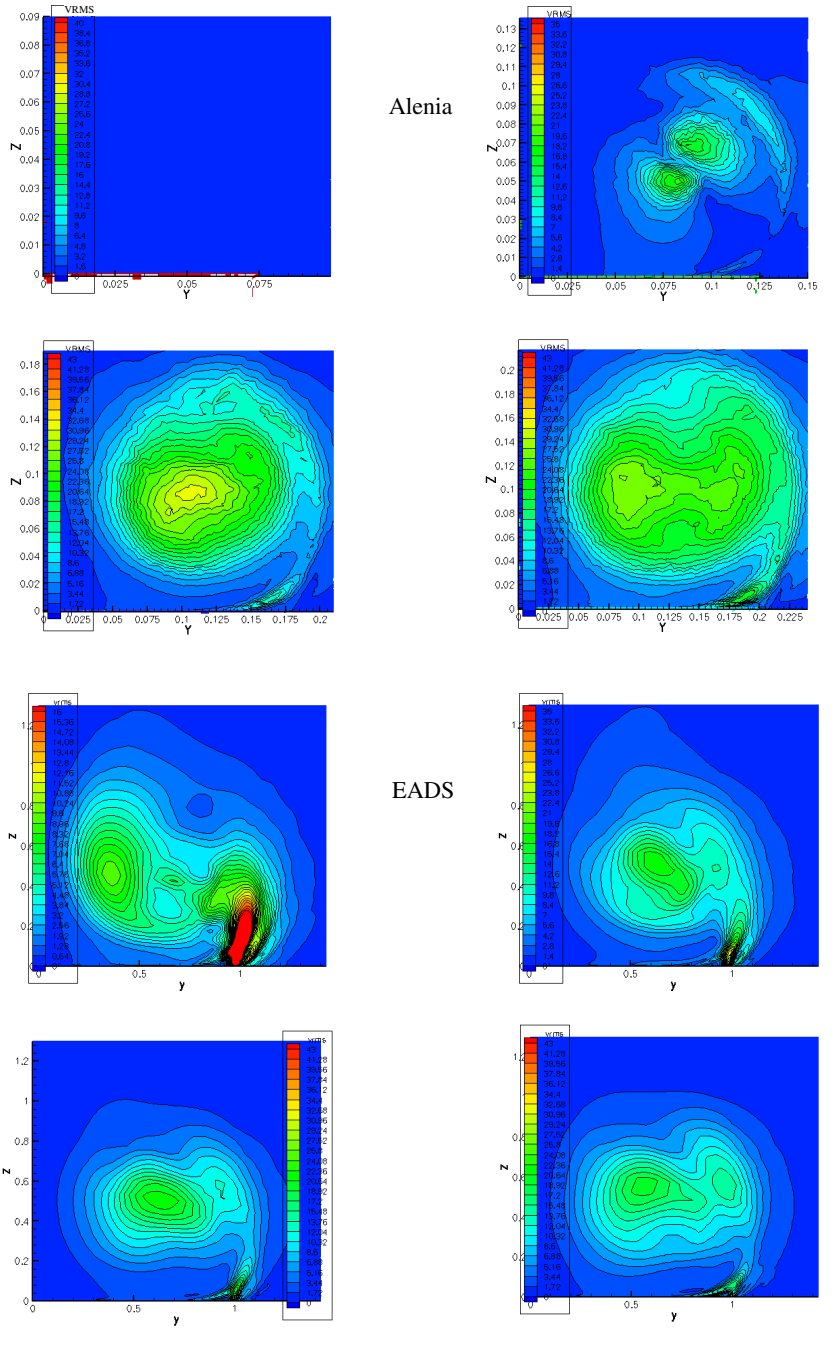

Fig. 9 (*continued*)

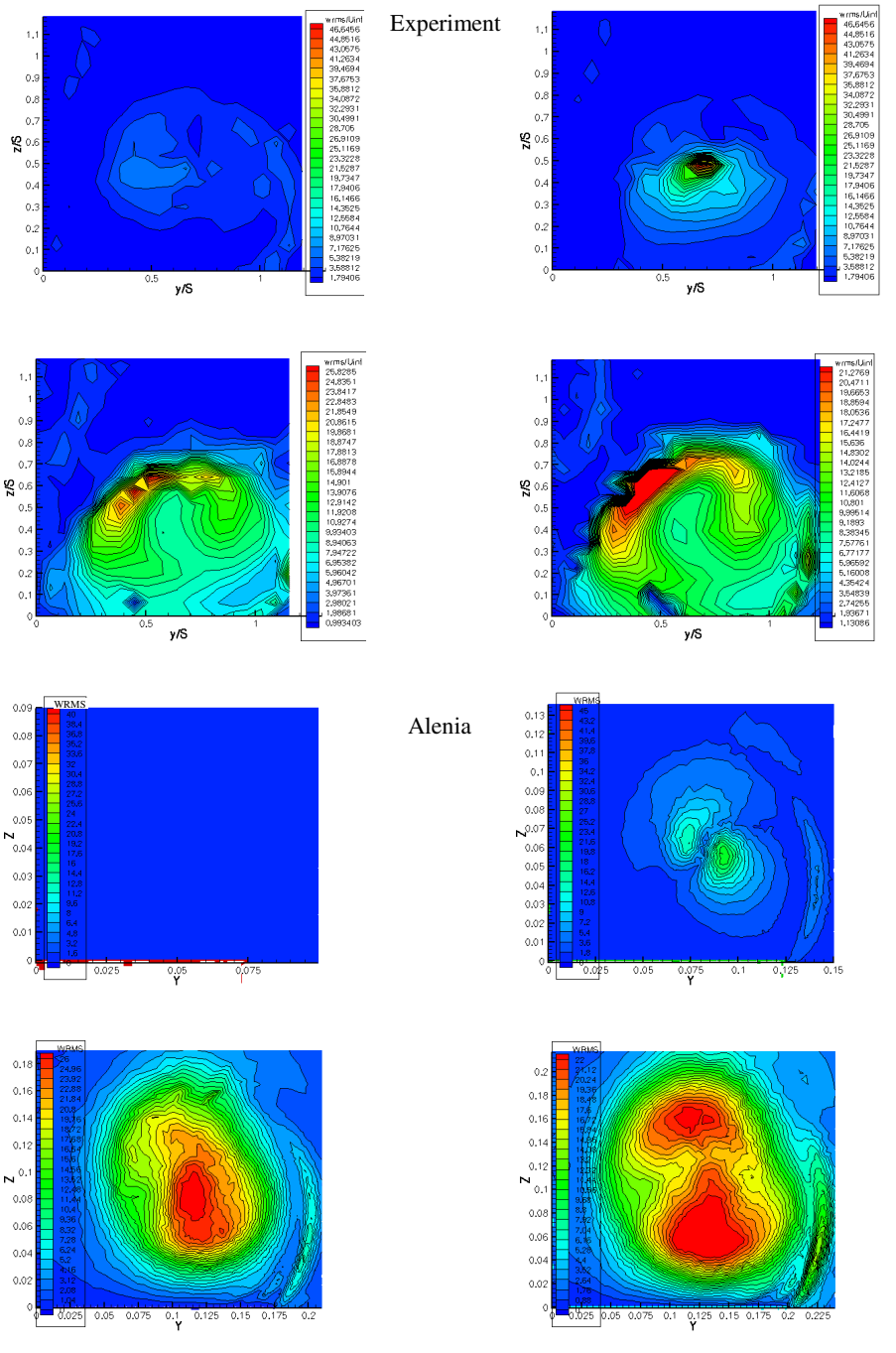

Fig. 10 w-rms at x/c=0.3, 0.5, 0.7, 0.8 (upper left, upper right, lower left, lower right)

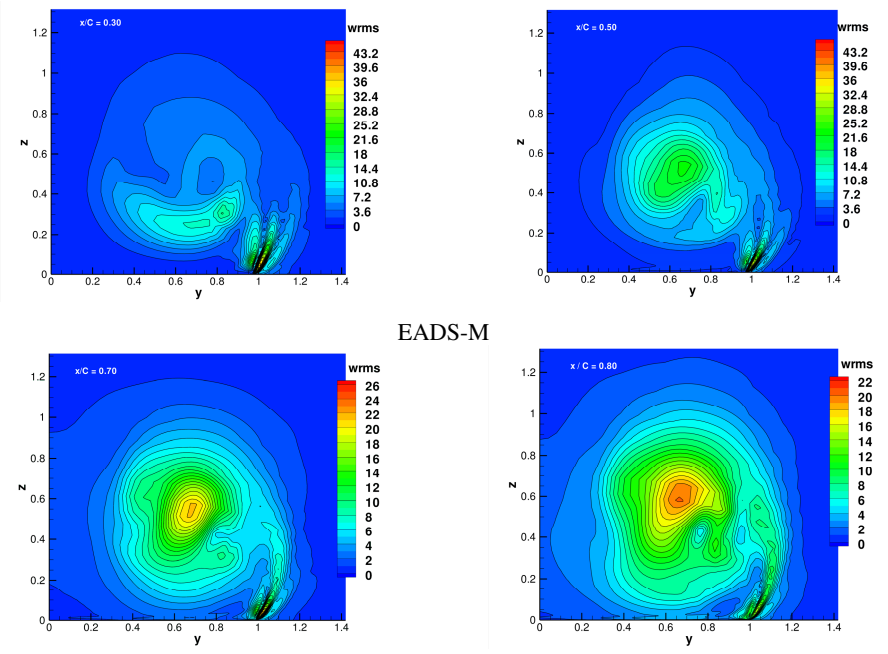

Fig. 10 (*continued*)

2.4 Conclusions

The following main lessons have been learned from the present exercise:

As the prediction of mean flow quantities is concerned, satisfactory results have been obtained by the participants with respect to the experiment: the location and extent of the secondary vortex and of the vortex breakdown were in general correctly predicted. Accuracy is increased compared to RANS modelling - with the partial exception of results obtained using WJ-EARSM model including vortex correction (see FLOMANIA results). The interpretation of results concerning the fluctuating quantities is more difficult. The rms pressures at the wall behave differently depending on what codes and what grids have been used. The ANSYS results show the best mean pressure field, with fluctuation levels being one order of magnitude smaller. Hence, the different fluctuating components predicted by the participants do not have a relevant influence on the respectively computed mean values. More than the features of sub-grid modelling, the grid resolution in the vortex core appears to be the most relevant issue in order to correctly simulate the mean flow quantities. Concerning rms velocities, the radial components w.r. to the main vortex seem to be better predicted than the axial one in the EADS results; the opposite happens for Alenia results. This is probably due to the fact that both grids have a different resolution in both axial and radial directions, while the fluctuating eddies are isotropic in nature. A possible conclusion is that for a correct simulation of rms quantities it is equally important to use isotropic grids with the same resolution in axial and radial direction - unlike it is usually done generating grids for (U)RANS computations.

3 NACA0021 at 60° Incidence

A. Garbaruk, M. Shur, M. Strelets, and A. Travin

NTS

3.1 Introduction

A flow over an airfoil in a deep stall is a typical example of the flows DES was designed for. Not surprisingly, exactly such flow (NACA0012 airfoil at large angles of attack) was the first real 3D application of DES (Shur et al. (1999)), and a success of this simulation to a considerable extend influenced the fast spreading of the DES technology. Note, however, that in this first DES application and also in the subsequent studies of this flow in the framework of FLOMANIA EU project, a comparison with experimental data was rather restricted, since only the integral lift and drag values are available. Also, because of the limited computer power, the computations were carried out with the use of relatively coarse grids and narrow domains in the spanwise direction. In the recent experimental study of Swalwell et al. (2003), Swalwell (2005) carried out for the NACA0021 airfoil at 60° angle of attack a much more informative database has been accumulated which includes not only mean flow characteristics but also lift and drag time histories and corresponding spectra. This and, also, a significant increase of the computer power since 1999, permits to perform a more reliable validation of different versions of DES and, also, of new, non-conventional, URANS approaches (SAS of Menter and Egorov (2005) and TRRANS of Travin et al. (2004)) developed in the course of DESider. These considerations have motivated including of the NACA 0021 flow in the list of DESider test cases.

3.2 General Flow Description

The airfoil geometry normalized with the chord length, c, is defined by:

$$y = \pm\frac{0.21}{0.2}\left(0.2969\sqrt{x} - 0.126x - 0.3516x^2 + 0.2846x^3 - 0.1015x^4\right)$$

Experimental flow parameters, needed to set up appropriate numerical simulations are presented in Table 1.

Table 1 Flow parameters

Parameter	Notation	Value
Reynolds number	$\mathrm{Re}=U_\infty c/\nu$	$2.7\mathrm{x}10^5$
Chord length	c	0.125 m
Angle of attack	α	60^0
Free stream Mach number	M	0.1
Free stream streamwise turbulence intensity	l_u	0.6%

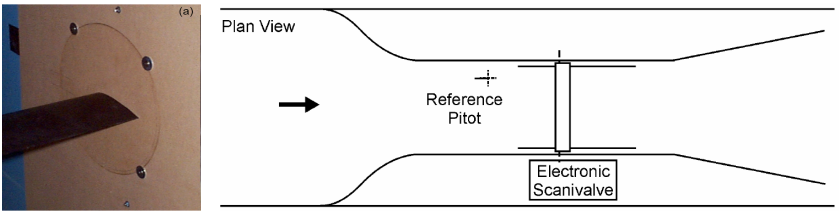

Fig. 1 NACA0021 airfoil in the wind tunnel (left), and a plan view of the wind tunnel (right)

The experiments were carried out in the wind tunnel of Monash University (see Fig.1), which experimental section width is $7.2c$ and height is $16c$.

The flow parameters measured in the experiments and kindly provided to the DESider consortium by K. Swalwell are:

1. Time-averaged pressure coefficient distribution over the airfoil surface, $C_p(x)$;
2. Time- and span-averaged drag and lift coefficients, C_D, C_L;
3. Time histories of the sectional lift and drag coefficients (32,000 points total over the time interval $T \approx 9000(c/U_0)$).

3.3 Participants and Some Details of Simulations

A list of participants and key information on turbulence modelling approaches and computational grids they used are presented in Table 2.

All the simulations, except for that of the EADS-M, were carried out without accounting the wind tunnel walls ("in free air"). Most of them used O-type grids ("coarse" and "fine") built by NTS and provided to all the interested partners. Along with this, NLR has built three (coarse, medium, and fine) structured grids, which were also used by DLR and TUB, and EADS-M generated its own unstructured grid (examples of the grids are presented in Fig.2.) In the spanwise direction all the grids are uniform (information about the span-size of the domain, L_z, and the grid step Δz in different simulations is presented in Table 2).

All the simulations were conducted in the "fully-turbulent" mode, i.e., with prescription of relatively high eddy viscosity ($\nu_t \approx \nu$) at the inflow boundary,

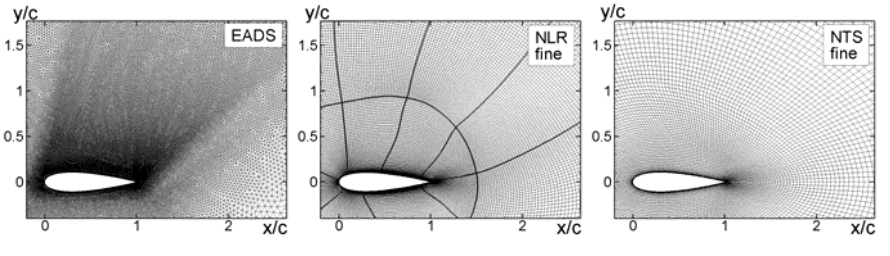

Fig. 2 Zoomed fragments of different grids in *XY*-plane

Table 2 Summary of simulations

Partner	Model	Grid size (M nodes)	z-grid		Δt	Time Sample
			L_z	Δz		
ANSYS	SAS 2	1.9	4	0.03	0.03	400
DLR	S-A DDES	0.5	1	0.03	0.0125	320
		1.6	1	0.02	0.0125	345
		5.2	1	0.014	0.0125	280
EADS-M	S-A DES	19.2	7.2	0.025	0.07	429
IMFT	S-A DES	0.5	1	0.03	0.0024	48
	k-ω DES	0.5	1	0.03	0.0024	50
	k-ω OEM DES	0.5	1	0.03	0.0024	41
		2	4	0.03	0.0024	20
NLR	X-LES	0.5	1	0.03	0.0125	212
		1.6	1	0.02	0.0125	195
		5.2	1	0.014	0.0125	188
NTS	S-A DES	0.5	1	0.03	0.03	2500
		0.7	1.4	0.03	0.03	2000
		1	2.0	0.03	0.03	2000
		1.4	2.8	0.03	0.03	2000
		2	4	0.03	0.03	2000
		1.4	2	0.02	0.03	2000
		1	2	0.03	0.02	2000
		2	2	0.03	0.02	2000
	SAS 2	1	2	0.03	0.03	2000
	TRRANS	1	2	0.03	0.03	2000
NUMECA	S-A DES	0.5	1	0.03	0.0125	177
TUB	SALSA DES	0.5	1	0.03	0.025	1000
	CEASM DES	0.5	1	0.03	0.025	1620
		1.6	3.24	0.03	0.025	730
	LLR DES	0.5	1	0.03	0.025	1230
		0.5	1	0.03	0.0125	790
		1.6	1	0.02	0.0125	650
		5.2	1	0.014	0.0125	535

which ensures turbulent flow starting virtually from the leading edge of the airfoil. Other than that, in order to ensure a consistency of the comparison of the lift and drag spectra, all the partners computed these spectra with the use of the common Fourier transform tool provided by TUB.

3.4 DES Results and Discussion

3.4.1 Effect of Time Sample, Span Size of the Domain, and Wind-Tunnel Walls

Starting from FLOMANIA it became clear that in order to obtain mean characteristics of the flows around nominally 2D bluff bodies, time samples the

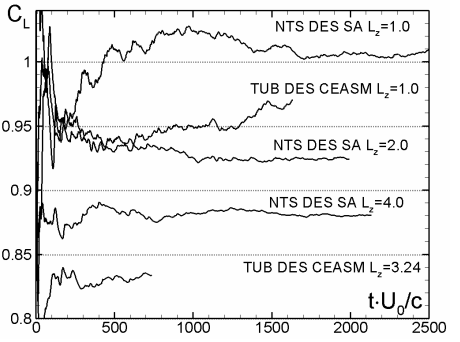

Fig. 3 Running time-average of the span-averaged lift coefficient predicted by DES on NTS coarse grid at different span size values

averaging is carried out over should be rather long. To get a quantitative information about the time-samples ensuring reliable averaging needed for a formulation of clear guidelines on DES of such flows, NTS and TUB performed special numerical studies whose results are presented in Fig. 3 in the form of running average of the lift coefficient as a function of time at different span sizes of the domain from DES based on the S-A (NTS) and CEASM (TUB) RANS models.

One can see that for both considered DES versions very long time-samples are needed to get a statistically reliable lift value. Because of the span-averaging, with the span size increase the demands to the time-sample for obvious reason become less severe but even for the largest of the considered span-sizes, 4*c*, the time-sample has to be not shorter than ~300-400 convective units. Therefore, some of the simulations (see Table 2) have insufficient time-samples. This circumstance should be kept in mind when comparing predictions of the mean forces with the experimental data.

Another observation from Fig.3 is that the effect of the span size of the domain on the mean lift is rather strong and that saturation occurs at L_z about as large as 4*c*. This is more clearly seen in Fig. 4, where the mean pressure distributions and power spectral density (PSD) of the lift are presented from the simulations with different L_z. The figure suggests also that the span-independent mean pressure worse agrees with the data than that obtained with the narrower domains, 1*c* and 1.4*c*. The same conclusion can be drawn based on Fig.5 where a comparison is presented of the mean pressure predicted by NTS at $L_z = 4c$ with that of EADS-M obtained for the full span size of the experimental model (L_z=7.2*c*) with account of the walls of the experimental section. This finding is somewhat frustrating. Indeed, provided that the experimental data are accurate, this, in fact, suggests that the earlier conclusions about a very high accuracy of DES as applied to the massively separated 2D airfoil flows, which were based on the simulations carried out in relatively narrow domains, are somewhat too optimistic. On the other hand, as seen from the lift spectra in Fig.4, there is a clear trend to a better agreement of the spectra with the data with the span-size increase.

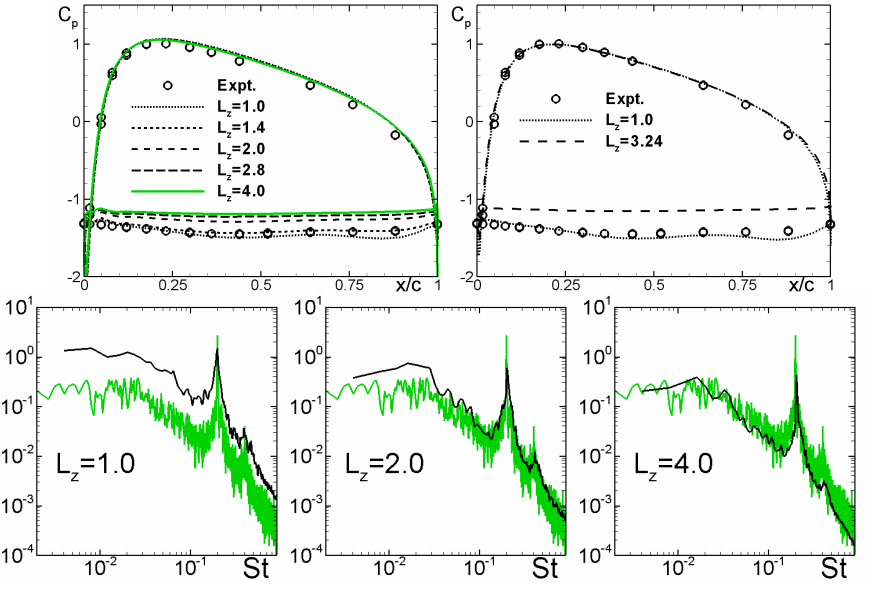

Fig. 4 Upper row: mean pressure at different span-sizes of domain from S-A DES (left frame, NTS simulation) and by CEASM DES (right frame, TUB simulation). Lower row: PSD of lift coefficient (NTS, S-A DES). Simulations on coarse NTS grid

Fig. 5 Comparison of Cp computed by NTS with periodic boundary conditions at $L_z=4c$ and EADS-M results obtained for the full span-size of the model

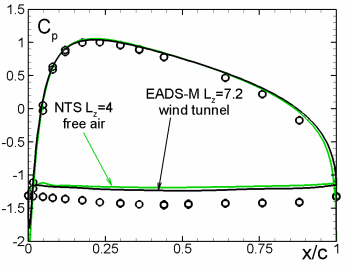

Note also, that as seen in Fig.5, the effect of the walls of the experimental section is marginal: once the span-size of the domain is large enough, the simulation under the free-air conditions (with periodic boundary conditions in the spanwise direction) virtually coincide with those obtained with account of the walls.

This is true not only with respect to the mean C_P distribution but also for the lift spectra shown in Fig.6 (EADS-M spectrum is more "noisy" because it is a sectional spectrum, whereas the NTS one is span-averaged) and for the resolved turbulent kinetic energy shown in Fig.7.

3.4.2 Effect of Background RANS Model for DES

A relatively weak sensitivity of DES to the background RANS model demonstrated in the literature is an essential DES feature naturally considered as

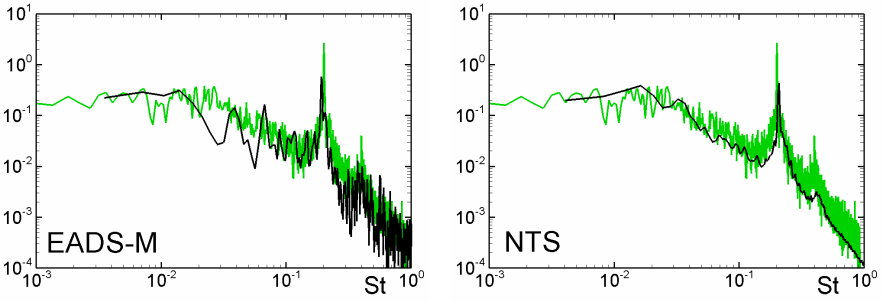

Fig. 6 Comparison of the computed (black lines) and experimental (grey lines) PSD of lift coefficient. Left: EADS-M simulation with account of the wind-tunnel walls, sectional spectrum; right: NTS simulation with the use of the periodic boundary conditions in the spanwise direction (L_z=4.0), span-averaged spectrum

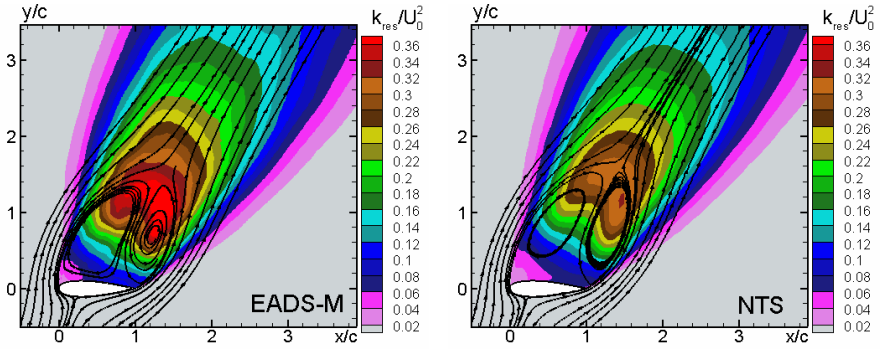

Fig. 7 Mean-flow streamlines and resolved TKE fields (same simulations as in Fig.6)

one of its serious advantages over RANS turbulence modelling. Results of the studies of the effect of the background RANS model on the DES predictions of the NACA 0021 flow are summarized in Figs. 8-10. One can see that, indeed, the effect is marginal: the results obtained with the use of DES versions based on very different RANS models are close to each other in terms of both turbulence resolution and mean flow thus supporting this feature of DES at least in the

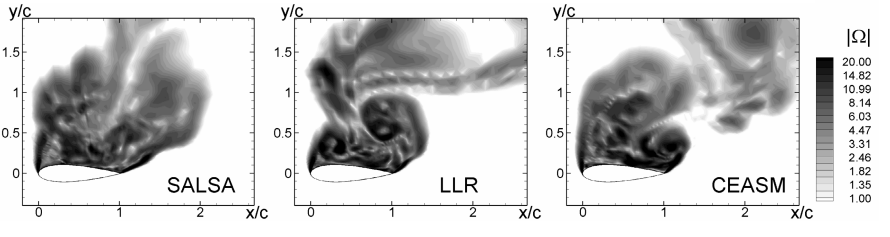

Fig. 8 Snapshots of vorticity from DES based on different RANS models (simulations of TUB, coarse NTS grid, L_Z=1)

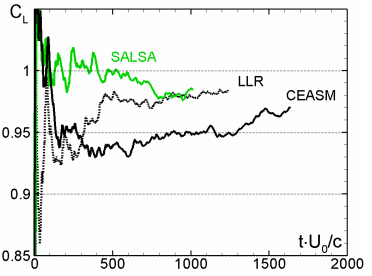

Fig. 9 Running time-average of span-averaged lift coefficient from DES based on different RANS background models (same simulations as in Fig.8)

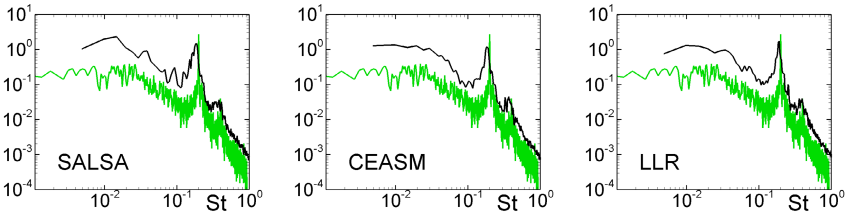

Fig. 10 PSD of the lift coefficient from DES based on different RANS background models (same simulations as in Fig.8; black: simulations, grey: data)

situations when an accurate prediction of the separation point being responsibility of RANS mode of DES is not difficult.

3.4.3 Effect of Grid-Refinement

As far as the mean flow characteristics are concerned, the simulations carried out on the very different grids (see Table 2) have given virtually identically results thus suggesting that even the coarse NTS grid provides for a sufficiently accurate mean flow prediction. This is illustrated by Fig.11, which compares the time- and span-averaged distributions of the pressure coefficients computed by NTS on its coarse (1 M nodes) and fine (2 M nodes) structured grids and by EADS-M on the very fine (19.2M nodes) unstructured grid.

3.4.4 Cross-Plotting of Results

In this section we present a comparison of the available results. Considering the strong effect of the span-size of the domain L_z discussed above, in order to perform this comparison consistently, only results obtained in the simulations with the same L_z should be taken into account. A maximum number of such simulations is available at L_z=1.0. So the comparison is carried out exactly for this L_z value.

Figures 12-14 present respectively the mean pressure distributions, spectra of the lift coefficient, and streamlines and resolved turbulent kinetic energy computed by different partners with different codes and different DES versions.

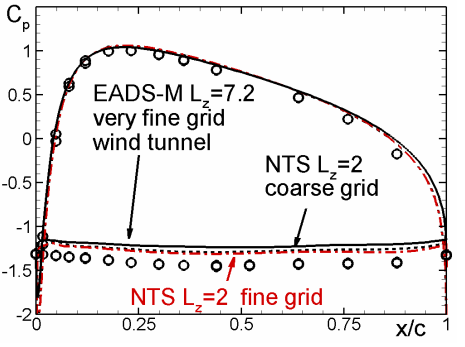

Fig. 11 Effect of grid refinement on time- and span-averaged Cp distributions predicted by S-A DES

Note that the experimental data for pressure and lift spectra are shown in the figures just as a reference: considering the strong effect of the span-size of the domain on the results of the simulations, at the span-size as low as L_z=1 comparison with the data is not quite representative. Also, when analysing these results, one should keep in mind that in the simulations of IMFT and NUMECA the time samples used for the mean flow and spectra computation are too short (see Table 2), and that the DLR and NLR results are obtained with the use of the "frozen filter" (see the discussion in the previous section). Other than that, similar to what has been done in the experiments, NTS and TUB computed the lift spectra by span averaging of the sectional spectra, whereas DLR, NLR, and NUMECA computed the spectra of the span-averaged lift, which is not quite the same. Nonetheless, even with all these differences, the results of different partners shown in Figs.12-14 are, in general, close to each other, which suggest a correct implementation of all the DES versions involved and a relatively weak sensitivity of the simulations to subtleties of the numerics.

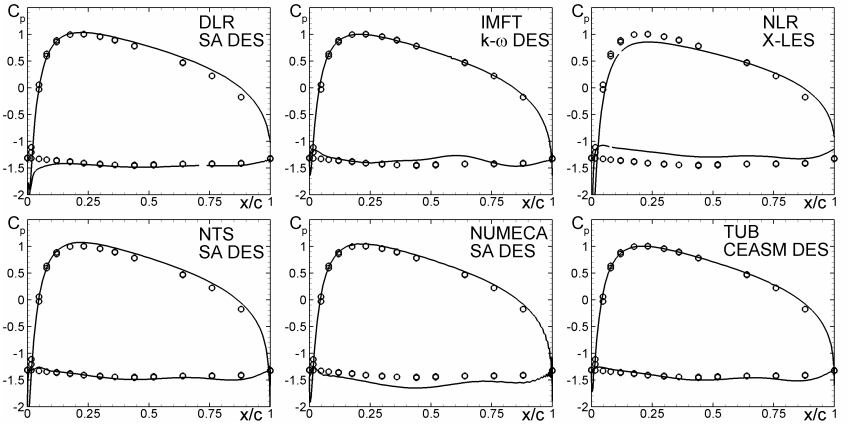

Fig. 12 Pressure distributions computed by different partners. DLR, NLR: coarse NLR grid; other partners: coarse NTS grid

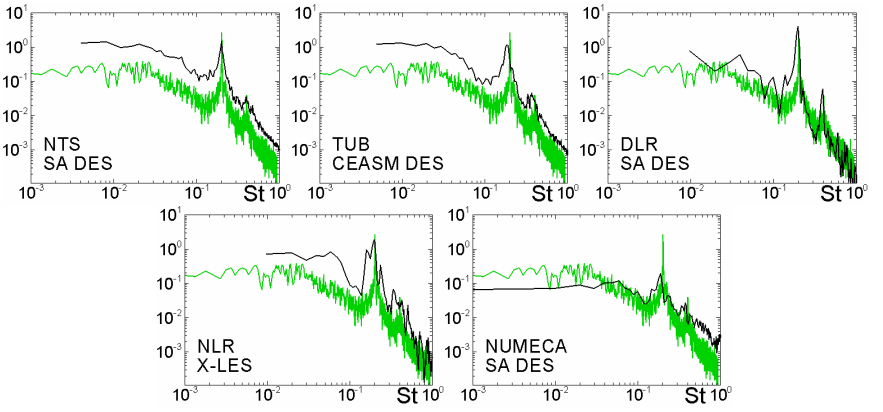

Fig. 13 Lift spectra computed by different partners (same simulations as in Fig.12). Upper row: span-averaged sectional spectra; lower row: spectra of span-averaged C_L

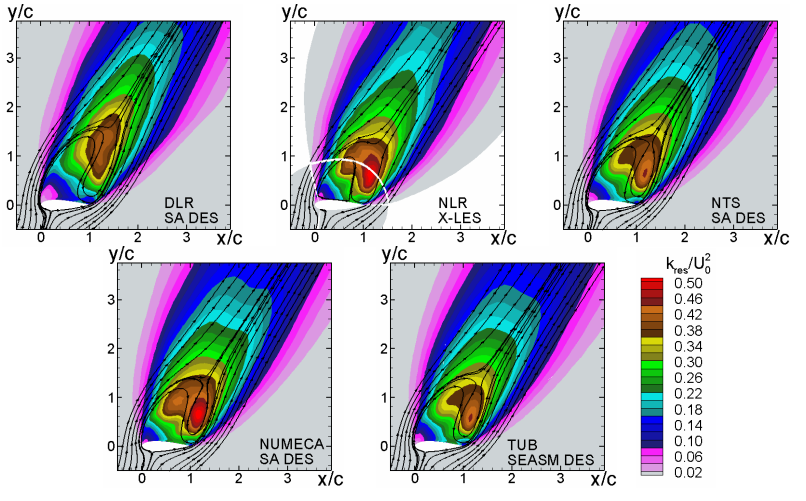

Fig. 14 Comparison of mean flow streamlines and resolved turbulent kinetic energy computed by different partners (same simulations as in Fig.12)

3.5 SAS and TRRANS Results and Discussion

Although formulations of these approaches are quite different, their common feature is that both are of URANS-type, i.e., that they do not rely upon a size of computational cell as a model length-scale. Nonetheless, at least in massively separated flows, both approaches claim to possess a key LES feature, namely, a capability of resolving more and more fine turbulent structures with grid refinement.

Simulations presented below are carried out by ANSYS (SAS) and NTS (SAS and TRRANS), and both partners used the Version 2 of SAS based on the

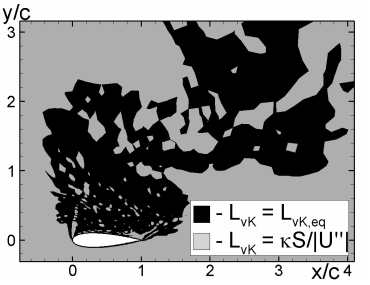

Fig. 15 Snapshot of the von-Karman lengths-scale from SAS on NTS coarse grid

Menter-SST RANS model (see Section 1 of Chapter II for more detail). Recall that this version involves a grid size in the "max limiter" in the "equilibrium" branch of the length-scale, which strictly speaking makes it not a pure URANS model (as seen in Fig.15 where a snapshot is shown of the von-Karman length-scale from the NTS coarse grid SAS, this branch turns out active in a significant part of the separation area and wake of the airfoil).

Figure 16 compares vorticity snapshots from SAS, TRRANS, and SA DES at L_z=2c and, also, from SAS and SA DES at L_z=4c. The figure suggests that turbulence resolution provided by all the three modelling approaches is nearly the same. Also, no qualitative difference of the resolved vortical structures in *XY*-plane is observed between the simulations performed at L_z=2 and 4.

A similar conclusion can be drawn based on Fig.17, where the mean flow topology and resolved turbulence kinetic energy fields are shown as predicted by all the simulations. Still some difference between the modelling approaches does exist. Namely, SAS seems to predict somewhat higher resolved turbulence kinetic energy than TRRANS and DES do.

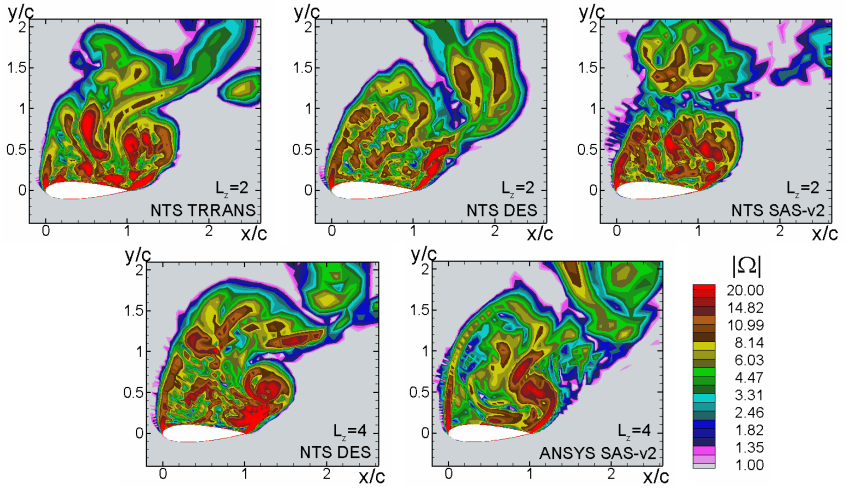

Fig. 16 Vorticity snapshots from SAS, TRRANS, and SA DES. Upper row: L_z=2; lower row: L_z=4. Simulations on the NTS coarse grid

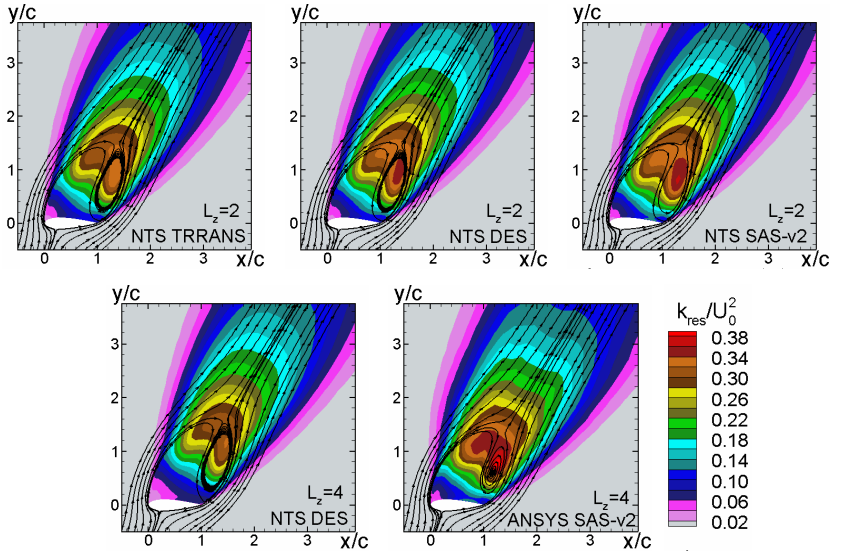

Fig. 17 Mean streamlines and resolved kinetic energy (same simulations as in Fig.16)

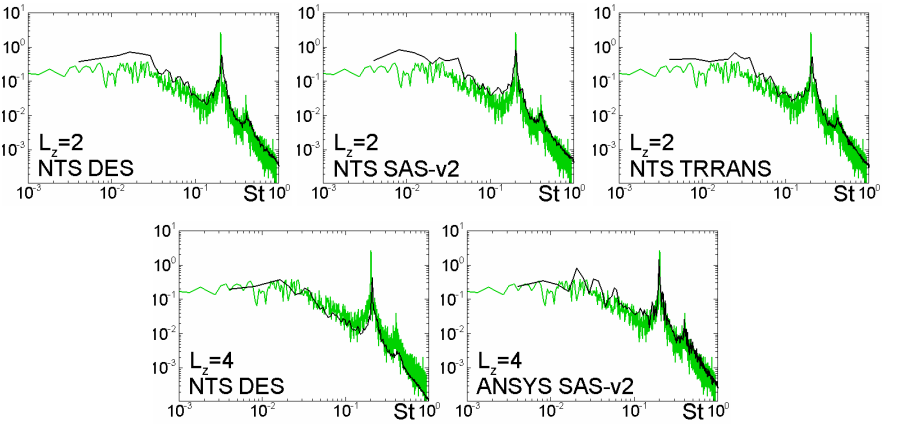

Fig. 18 PSD of the lift coefficient (same simulations as in Fig.16)

Figure 18 compares the PSD of the lift coefficient from the simulations. One can see that, again, the different modelling approaches are in line with each other and predict both the broadband part of the spectra and the frequencies of the main and secondary peaks of C_L fairly well.

Finally, Fig.19 compares distributions of the mean pressure coefficient over the airfoil predicted by SAS, TRRANS, and DES at different L_z. One can see that all the distributions from the NTS simulations at L_z=2c are virtually identical and that, as repeatedly mentioned above, an increase of L_z up to 4c results in somewhat worse agreement of the computed pressure with the data. In contrast to this, the distribution from ANSYS SAS at L_z=4c agrees with the data fairly well.

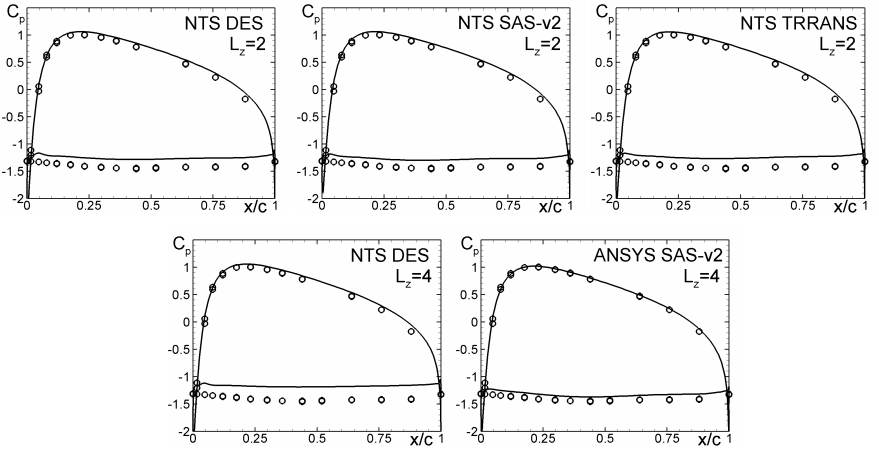

Fig. 19 Mean pressure coefficient distributions (same simulations as in Fig.16)

Unfortunately, neither SAS results of ANSYS at L_z=2c nor those of NTS at L_z=4c are available, which does not permit to tell whether the trend to an increase of the pressure on the suction side of the airfoil with L_z increase typical of DES holds on for SAS or not.

3.6 Integral Forces

Table 3 summarizes values of the integral lift and drag forces obtained by different partners in their simulations performed with the longest time sample, largest span size, and finest grid. Unfortunately, even some of these values (bold entries in the Table) are actually not sufficiently reliable in this sense (are obtained in the simulations with insufficient span-size or with too short time-samples). If not take these values into consideration, the discrepancy of the lift and drag predictions

Table 3 Summary of integral forces

Partner and approach	Lift, C_L	Drag, C_D
ANSYS (SST-SAS version 2, L_z=4, coarse NTS grid)	0.915	1.484
NTS (SST-SAS version 2, L_z=2, coarse NTS grid)	0.915	1.475
NTS (TRRANS, L_z=2, coarse NTS grid)	0.912	1.445
DLR (SA DDES with frozen filter, L_z=1, coarse NLR grid)	**1.001**	**1.548**
EADS-M (SA DES, fine EADS-M grid in wind-tunnel)	0.889	1.425
IMFT (k-ω OEM DES, L_z=1, coarse NTS grid)	**1.093**	**1.796**
NLR (X-LES with frozen filter, L_z=1, coarse NLR grid)	**1.082**	**1.567**
NTS (SA DES, L_z=4, coarse NTS grid)	0.879	1.381
NUMECA (SA DES, L_z=1, coarse NTS grid)	**1.026**	**1.688**
TUB (SALSA DES, L_z=1, coarse NTS grid)	**0.984**	**1.592**
TUB (LLR DES, L_z=1, coarse NTS grid)	**0.985**	**1.620**
TUB (CEASM DES, L_z=3.24, coarse NTS grid)	0.834	1.354
Experiment	0.931	1.517

with the data is within the range from ~2% (SST SAS at L_z=4c) up to ~10% (CEASM DES at L_z=3.24), which can be considered as reasonably good, especially keeping in mind that the best RANS results for this kind of flow differ from the data by at least 25%.

3.7 Concluding Remarks

As far as the DES is concerned, in the course of DESider a representative database is accumulated on its performance as applied to this test case. Major findings from the simulations carried out by the partners are as follows.

A significant DES superiority over RANS in terms of the mean flow prediction and a marginal sensitivity of DES to a background RANS model are convincingly demonstrated, which supports similar observations based on the previous DES studies of airfoils in a deep stall. It is shown also that even relatively coarse grids of about 2M nodes are quite sufficient for getting virtually grid-independent mean flow characteristics. Also in line with the previous studies, it is shown that for getting a reliable statistics, very long time samples are needed (300–400 convective time units, at least).

An important finding of the performed study is a strong sensitivity of DES predictions to the span-size of the computational domain and some worsening of the agreement of the predicted mean pressure and integral forces with the data when the span-size increases. Considering that a correct solution is that obtained in the wide enough domain, this means that DES prediction is somewhat worse than it was believed earlier, provided of course that the experimental data used are quite accurate. In particular, the best (carried out with the very fine grid and accounting for the real geometry of the test section) simulation carried out by EADS-M underestimates the experimental integral lift and drag by 4.5% and 6% respectively. Although these errors are much less than those one would get with the use of (U)RANS modelling, this discrepancy with the data is still tangible and its reasons are not established. On the other hand, agreement with the experimental spectra of the forces, in some contradiction with the mean values behaviour, improves with the span-size increase.

For the SAS and TRRANS approaches, although the accumulated computational database is restricted by only two contributions (ANSYS and NTS), it still permits to make some important conclusions.

In particular, it is shown that as applied to this test case, the approaches significantly surpass corresponding conventional RANS and URANS models and are quite competitive with DES. Also, based on the NTS experience, it can be concluded that the second version of the M-SST SAS is less numerics-sensitive and is compatible with “non-CFX” numerics.

Just as for DES, long time samples and large span-size of the domain are needed for an accurate prediction of the flow. In this respect all the turbulence-resolving approaches are quite similar.

It should be noted also that the wide-domain (L_z=4c) SAS of ANSYS resulted in a somewhat better agreement with the data on the mean pressure distribution than both DES and TRRANS. Unfortunately these results were obtained in the very end of the project, which did not permit to carry out additional simulations that could help to understand a reason of the observed difference.

4 Ahmed Car Body (25° and 35° Slant Angle)

L. Temmerman and Ch. Hirsch

NUMECA

4.1 Introduction

The Ahmed body, shown in Fig. 1, is a generic car geometry with a slanted back at two different angles (25° and 35°). The configuration was first studied by Ahmed et al (1984), then, more recently, by Lienhart and Becker (2003). The data can be obtained from the *Ercoftac Classic Collection* database (http://cfd.mace.manchester.ac.uk/ercoftac/).

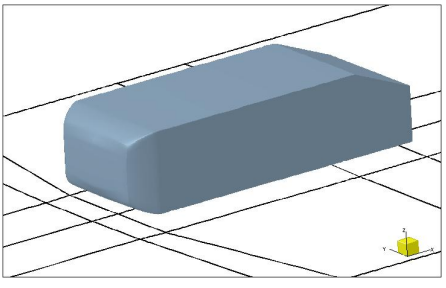

Fig. 1 General view of the Ahmed car body

While the present configuration is geometrically simple, the flow-field generated is very similar to the one found in real-life cars. Important features include a complex separation and reattachment on the slant and a wake development behind the body. These features strongly depend of the slant angle. For the 25° case, the flow is three-dimensional at the rear of the body with a separation bubble appearing on the upper part of the slant. The flow then reattaches midway through the slant. On its edges, two counter-rotating vortices are generated. The 35° case is gentler and virtually two-dimensional, the flow separating from the top of the slant over the whole of the body rear. The side vortices are somewhat weaker. The complexity of the flow features poses severe problems to numerical predictions and, with detailed experimental data available, it is no surprise that the Ahmed body has been extensively used as reference test case for the testing and validation of numerical methods and turbulence models (see the recent 9th and 10th ERCOFTAC/IAHR workshops on refined turbulence modelling held in Darmstadt and Poitiers, respectively, or the EC-funded FP5 Flomania project (Haase et al, 2006)). These workshops, as well as the Flomania project, showed that a correct prediction of this flow was difficult with the RANS approach with results strongly depending on the turbulence model considered and the details of implementation. These results also hinted that a successful computation of this case may require to take into account the flow unsteadiness. This is the reason behind the choice of this case for the DESider project.

The following section will briefly describe the geometry and the flow conditions. Section 5.3 lists the DESider partners computing this test case. It also briefly describes the computations performed. Results, compared with the experimental data from Lienhart and Becker (2003), are then shown and discussed in Section 5.4. The final section summarizes the main findings for this test case.

4.2 Geometry Description and Flow Conditions

In the experiment, the body was mounted on four stilts with a diameter of 30 mm. The distance from the floor to the bottom of the body is equal to 50 mm. In order to simplify the mesh generation process and because their influence on the main solution was negligible, the stilts are removed for the computations, the body thus floating 50 mm above the floor. The body height is 288 mm while its length is equal to 1044 mm. The body width is equal to 389 mm. The Reynolds number, based on the body height and a freestream velocity of 40 m/s, is equal to 768,000.

From a computational point of view, the inflow is located at 2.1 m upstream of the body front and the inflow velocity is set to 40 m/s. No slip conditions are used to represent the bottom wall while the side walls are treated as slip wall.

4.3 Participants Overview

Table 1 gives the list of participants and describes the computations performed by each of them (slant angle considered, Reynolds number used if different from the nominal one, type of mesh, model used). Table 2 gives more details on the computational parameters and models used by each participant. A detailed description of the DES models can be found in Chapter II of the present book.

Table 1 Participants list and methods description

Participant	Slant angle computed	Reynolds number	Mesh	Model
Chalmers	35°	200,000	Structured	LES (Smagorinsky)
DLR	25°	768,000	Unstructured	SA-DDES, X-LES
IMFT	25°	768,000	Structured	SA-DES, SA-DDES
NUMECA	25°	768,000	Structured	SA-DES, SST-DES

Table 2 Computational parameters

Participant	Model	Δt	Mesh size	Averaging time
Chalmers	LES	n.a.	16.5 10^6 cells	n.a.
DLR	SA-DDES 2	2 10^{-4} s	4.6 10^6 cells	1.008 s (5040 Δt)
	XLES	2 10^{-4} s	4.6 10^6 cells	0.3 s (after a run of over 1 s)
IMFT	SA-DES	5 10^{-2} s	2.8 10^6 cells	n.a.
	SA-DDES	5 10^{-2} s	2.8 10^6 cells	n.a.
NUMECA	SA-DES	10^{-4} s	3 10^6 cells	0.0567 s (after a run of over 1 s)
	SST-DES	10^{-3} s	4.5 10^6 cells	0.512 s (after a run of about 1 s)

Chalmers performed a LES computation of the Ahmed car body for the 35° slant angle on a structured mesh made of 16,500,000 cells and at a reduced Reynolds number of 200,000 selected to alleviate the computational cost of the simulation.

All three other partners used the nominal Reynolds number of 768,000 in conjunction with a 25° slant angle. DLR performed SA-DDES and XLES computations on a hybrid structured mesh, shown in Figs 2a and 2b. The near-wall regions are meshed with prisms while, in the other regions, tetrahedrons are used. Particular attention was given during the grid generation process to the mesh symmetry. In the areas above the slant and in the wake, special care was taken to obtain an isotropic cells distribution. IMFT performed SA-DES and SA-DDES simulations for the 25° slant angles on a structured mesh shown in Fig. 2c. NUMECA also worked on a structured grid (see Fig. 2d) using both SA-DES and SST-DES models.

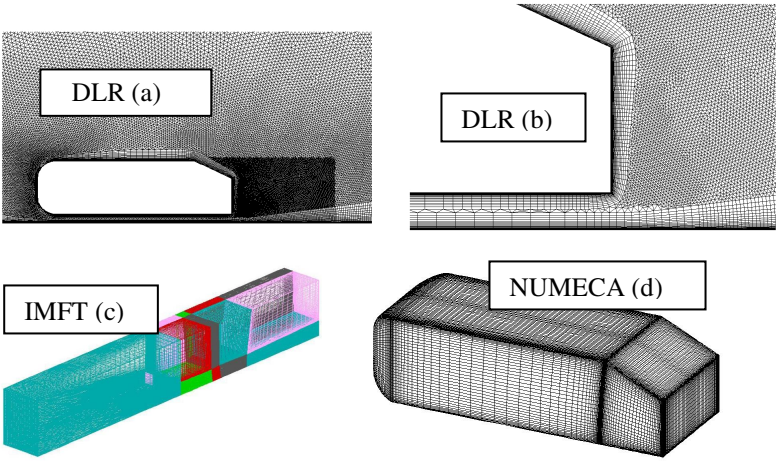

Fig. 2 Meshes used by the different partners

4.4 Results

4.4.1 Ahmed Body with 25° Slant Angle

Three out of the four partners involved in this test case (see Table 2) chose to compute the case with the 25° slant angle. Fig. 3 shows a comparison of the stream-wise velocity profiles on centre plane on the slant with the experimental data while Fig. 4 shows the same profile behind the slant.

On one side, the computations performed with SA-DDES (DLR) and SA-DES (NUMECA) show the flow not separating on the slant. On the contrary, the experiments indicate a separation occurring on the upper part of the slant down to the middle. On the other side, the SA-DES (IMFT) computation separates. It however fails to reattach on the slant.

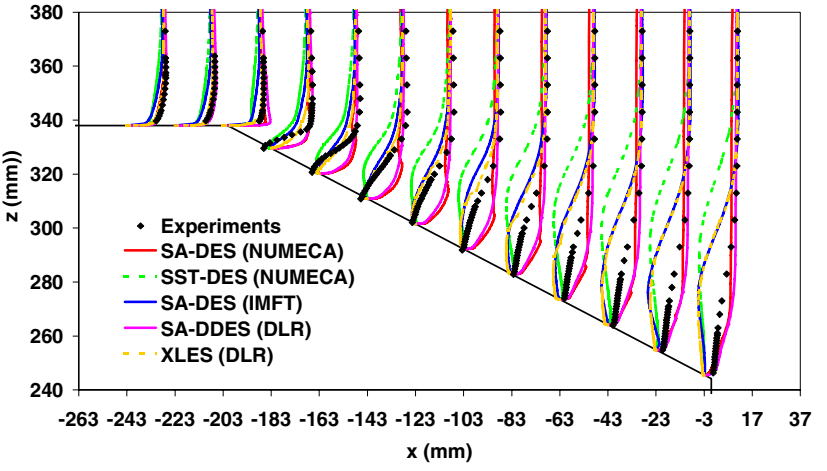

Fig. 3 Velocity profiles at y = 0 mm on the slant for all computations

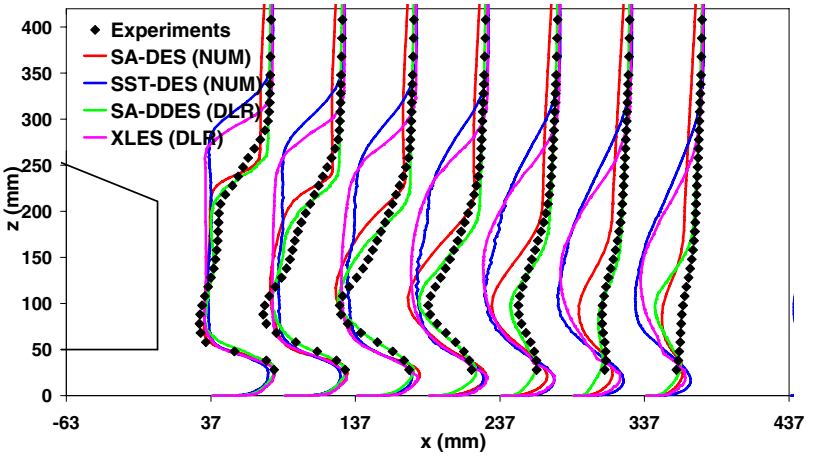

Fig. 4 Velocity profiles at y = 0 mm behind the slant for all computations

Both, DLR and NUMECA also used a DES model based on a two-equation RANS model, XLES for DLR and SST-DES for NUMECA. Both computations feature this time a large recirculation zone. This zone remains detached beyond the slant end as shown on Fig. 4.

Putting aside the results obtained from SA-DES (IMFT) for a moment, it would seem that the choice of the underlying RANS model in the DES model is very influential for this particular test-case. Indeed, when used in steady RANS mode, the Spalart-Allmaras model fails to predict the recirculation zone on the slant while the SST and k-ω models (used in XLES) overpredict it. If the SA-DES

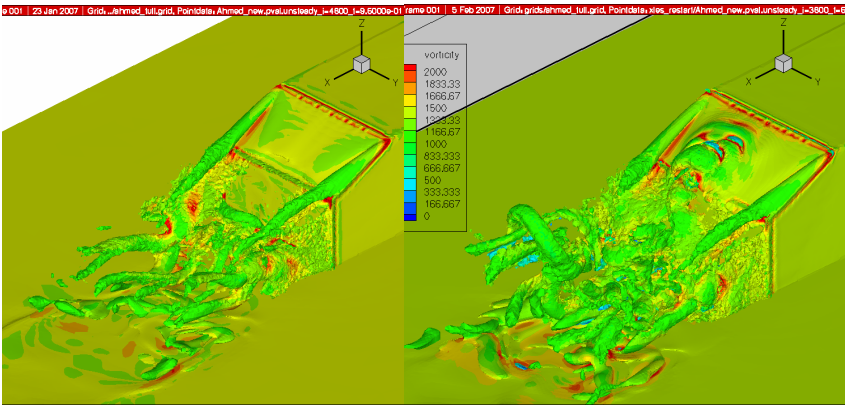

Fig. 5 Iso-surfaces of the Q-criterion coloured by the vorticity. Left: SA-DDES (DLR), Right: XLES (DLR)

(IMFT) computation is now taken into account, this conclusion does not seem valid any more and other factors may also play an important role.

Looking at the profiles at the three first locations, upstream and around the start of the slant, it can be noted that the simulations that predict an attached flow on the slant are the ones over-predicting the velocity at the start of the slant while the simulations that either correctly predict or under-predict it are the ones that separate. This further indicates that modelling and, also maybe, implementations issues could justify these differences.

Fig. 5 shows instantaneous snapshots of flow structures on the body slant and behind. It seems as if the model behaves as a RANS model for some time after the slant where the separation is supposed to occur. Indeed, on the slant, the computation using SA-DDES does not show any activity while the XLES computation does. Very similar pictures (not shown here) were obtained for the other computations.

4.4.2 Ahmed Body with 35^o Slant Angle

One partner, Chalmers, has focused on the case with the 35^o slant angle, computing it with LES and the Smagorinsky model, on a mesh made out of 16.5 millions cells. The Reynolds number based on body height and freestream velocity was taken equal to 200,000 instead of the nominal 768,000 in order to alleviate computing requirements.

Fig. 6 shows a comparison of the mean stream-wise velocity profiles in the center plane on the body slant. A similar comparison is shown on Fig. 7 for the wake. On the slant, the computational results agree poorly with the experimental data. Not surprisingly, with the flow over the slant not correctly predicted, the comparison in the wake is also poor. A possible reason for this strong difference could be that boundary conditions in the LES and in the experiment are different. Indeed, trip wires were used on the front of the body in the experiment. Another possible

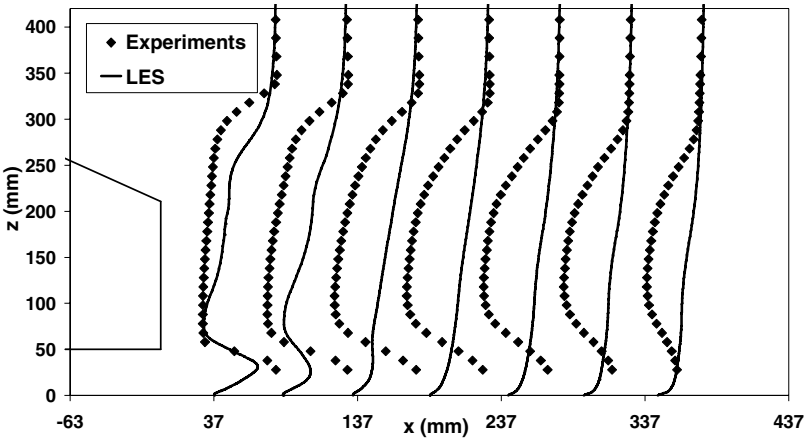

Fig. 6 Comparison between the velocity profiles obtained on the body with LES by Chalmers at Re = 200,000 and the experimental data of Lienhard and Becker (2003)

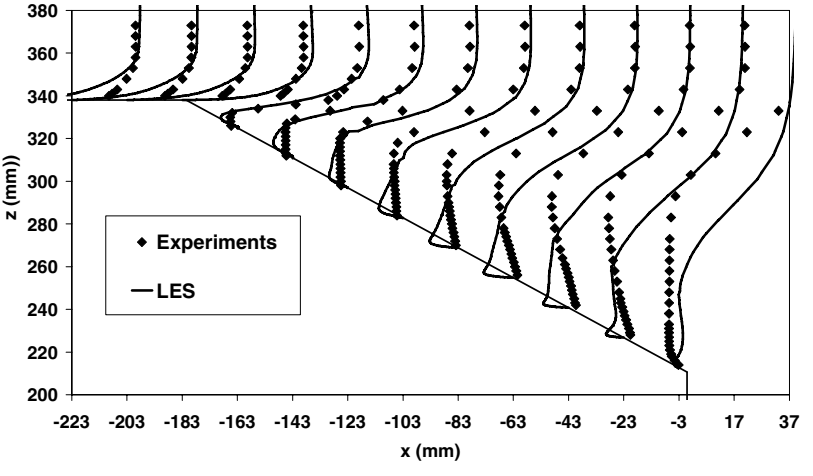

Fig. 7 Comparison between the velocity profiles obtained in the wake with LES by Chalmers at Re = 200,000 and the experimental data of Lienhard and Becker (2003)

explanation is that the 35° slant angle influences the upstream flow in a way LES cannot represent.

4.5 Concluding Remarks

The Ahmed body test case has been and remains a challenging test case for steady computations and, from the results presented here, it appears to hold for unsteady simulations.

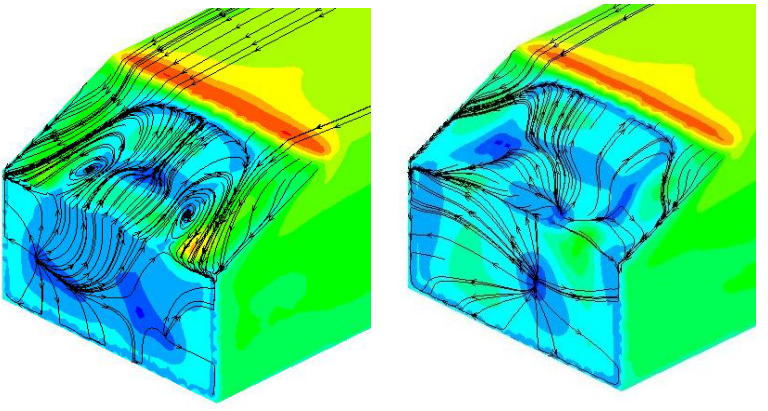

Fig. 8 Changes in instantaneous separation structure during the XLES simulation

The results obtained for the 25° slant angle case do not agree very well with the experimental data. Two of the simulations fail to predict the separation on the slant while the three others show a too large recirculation zone. The reason behind this failure is not clear and could be linked to several factors including grid inadequacy, strong influence of the underlying RANS model in the DES model, inaccuracy or sensitivity in the experimental data. An indication for the latter might be that the XLES simulation of DLR showed instantaneous "streamline" patterns at certain times which might results from moments of reattachment (or secondary separation) on the slant (see Fig. 8). This remains to be clarified. Nevertheless, it may well be that the 25 ° case is very sensitive to slight changes in the flow, i.e. small modifications of the slant angle or minor changes of the flow in the artificial tunnel which might result in earlier reattachment.

For the 35° case, only one LES computation was run and the results do not match very well with the experimental data. The reason for this divergence is also not clear and could be attributed to several factors including an influence of the Reynolds number or differences in boundary conditions (trip wires were used during the experiments).

5 Decay of Isotropic Turbulence

C. Mockett and F. Thiele

TUB

Abstract. This chapter presents and discusses a considerable volume of work that was invested by many partners into the validation of their models and numerical schemes for LES using the canonical test case of decaying, isotropic turbulence (DIT). Motivated by an increasing interest in hybrid RANS-LES, many partners have begun implementing LES and related methods into industrial CFD solvers originally intended for RANS simulations. Due to the central importance of low numerical dissipation in LES, and the inaccessibility of this to purely analytical approaches, an empirical calibration is considered an essential demonstration for new models and implementations. High quality spectra have been presented by most partners and the test case has furthermore provided a platform for secondary investigations by some. These are summarised together with a discussion of the various methods used to set up and run a DIT simulation.

5.1 Background and Motivation

Decaying isotropic turbulence (DIT) represents mathematically the simplest conceivable realisation of turbulent flow and is therefore a fundamental test case for new turbulence modelling and/or simulation techniques. The methods investigated in DESider all involve the inclusion of a degree of turbulence resolution, i.e. LES, into either new modelling frameworks or into CFD solvers for which previously only RANS models were implemented. Against this background the motivation of simulating DIT by the DESider project partners can be summarised as follows:

- DIT represents a basic and readily-verifiable test, at minimal computational cost, of the capability of the model/solver combination to *resolve* turbulent structures and to predict the energy cascade.
- Many of the methods developed and studied involve empirical parameters that must be calibrated (e.g. C_{DES} for DES, which is analogous to the Smagorinsky parameter in LES). DIT offers a basis for this.
- The level of numerical dissipation within a given solver can be established. In cases where this is excessive, steps must be taken to reduce it. The value of the model parameter can also be adjusted such that numerical and model dissipation is balanced pragmatically.

Demonstration of these basic LES capabilities and calibration of new model constants are considered an essential prerequisite to the implementation of a hybrid RANS-LES method. Although analytical methods may exist to derive the values of subgrid-scale model parameters (e.g. deriving an expression for C_{DES} in terms of the Smagorinsky parameter and other RANS model parameters), these can in

some cases be self-contradictory (Yan et al., 2005). Furthermore, such derivations do not take numerical dissipation into account.

To reflect this importance, the DIT case was declared "50% mandatory" within the project; each partner had to demonstrate their results with either the DIT case or the fully-developed turbulent channel flow. An exception was made in cases where two partners employed the same solver and models.

In addition to the primary goals of demonstrating LES capability and calibrating parameters, a variety of secondary uses have been exploited by some partners. These include the demonstration of the functionality of particular model features (e.g. the Ψ function used for DES with some models (Spalart et al., 2006), see Chapter II, Section 4) and a measure of the energy conservation of the numerical scheme using a "no-model" test (see also Chapter V, section 17).

Despite, or perhaps owing to its simplicity, real isotropic turbulence is seldom found in nature or practical applications. It is also a very difficult flow state to approximate in a wind tunnel. Nonetheless, its usefulness as a computationally-inexpensive and canonical turbulent flow for the purposes stated above is not diminished.

5.2 Flow and Test Case Description

The simulation of DIT is conducted in a cubic computational domain with three pairs of periodic boundary conditions in each spatial direction, to reflect the homogeneous and infinite nature of the flow. In experiments, the turbulence is generated at an upstream station by a grid, and the measurement reference frame moves with the mean convective velocity downstream to capture the decay of the turbulence in the absence of mean shear. A coordinate transformation from space to time is conducted for the simulation, such that the computational box is considered to be transported with the mean velocity. The experimentally spatial decay of turbulence is therefore tracked temporally in the simulation; the initial solution field is set with a suitable instance of isotropic turbulence, the decay of which is then solved in an unsteady manner.

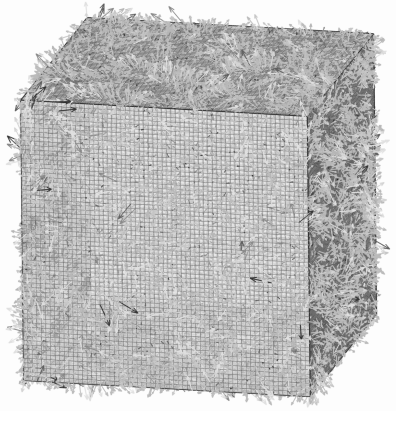

Fig. 1 Visualisation of the decaying isotropic turbulence test case (velocity vectors are shown on the surface of the 3D, periodic grid). An initialisation field from the DNS data of (Wray, 1997) re-sampled to 64^3 volumes is shown

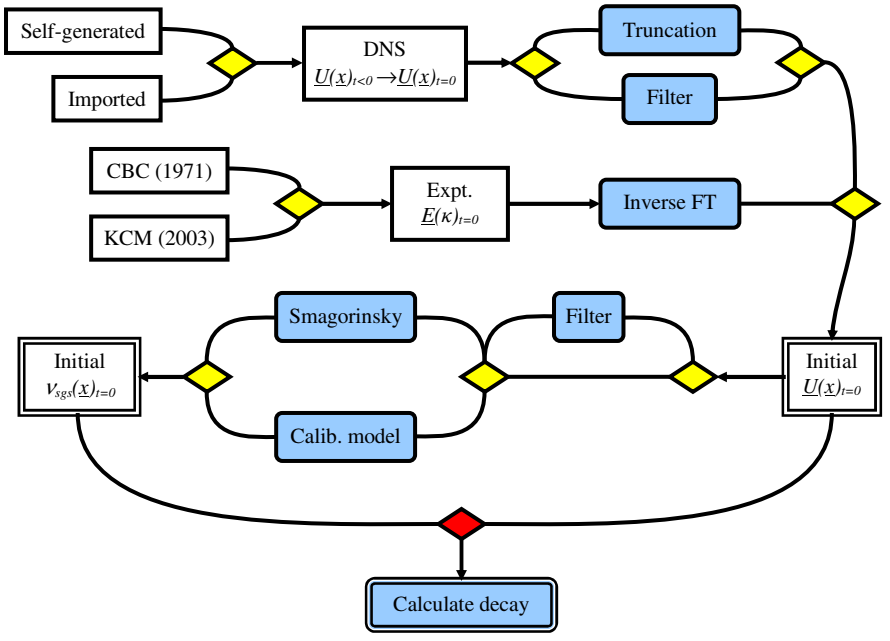

Fig. 2 "Road map" illustration of possible methods to generate the initial DIT solution fields. The yellow diamonds represent "OR" decisions, the red diamond an "AND" combination

The grids employed were all equidistant and cubic, with external dimensions of 2π and varying grid resolutions of usually 16^3, 32^3 or 64^3 cells (in some cases higher resolution of up to 128^3, or non-2^n point counts were applied). The lowest and highest resolved wavenumbers ($\kappa = 2\pi / x$) corresponding respectively to the largest and smallest resolved scales are therefore 1 and $N_x / 2$.

A range of alternative benchmark data is available for DIT, with various advantages and disadvantages. The experiment by (Comte-Bellot & Corrsin, 1971), referred to as CBC in the following, was conducted at a Reynolds number too low for an inertial sub-range to exist in the energy spectra. To address this shortcoming, a more recent experiment by (Kang, Chester & Meneveau, 2003), referred to as KCM, was conducted at a sufficiently high Reynolds number. Both experiments however have the disadvantage that the three-dimensional, unsteady velocity field cannot be measured. As a result, the initialisation velocity field for the simulation must be generated using an inverse Fourier transform of the upstream energy spectra. Although exhibiting the correct spectral distribution, such a velocity field does not contain physically valid spatial correlations. This disadvantage is alleviated by using benchmark DNS data, such as that of (Wray, 1997).

A variety of different techniques were applied by the partners to obtain the initial flow field required by their solvers and different benchmark data were used. In the majority of cases, these choices were demonstrated not to affect the principle outcome of the results in terms of calibrated model parameter values. One further technique adopted by some partners involved the application of an explicit filter

function to the initial velocity field. The majority of partners employed the method adopted in the FLOMANIA project (Haase et al., 2006), where the initial velocity field is obtained by inverse Fourier transform (using a tool written and provided by NTS (Shur et al., 1999)) from the CBC benchmark spectra. From these velocity fields the remaining solution variables (e.g. turbulence model parameters) were obtained by solving the "frozen" initial field in steady-state mode. A road map representation illustrating the possible initialisation methods is given in Fig. 2. An equivalent tool for performing the inverse Fourier transform but employing a the faster "FFTW" library was provided by EDF.

5.3 Table of Participants and Methods

Due to the high level of participation in this underlying flow regime test case, the list of partners and methods is naturally extensive. In total 12 partners tested 19 different modelling configurations on grids ranging from 16^3 cells to 160^3 cells. The contributions are summarised in Tab. 1. Due to the code-specific nature of such information, it proves impossible to summarise the different numerical schemes investigated in a tabular fashion. This information is therefore not included in the table, however many partners additionally investigated variations of numerical aspects with a fixed modelling framework.

Table 1 List of partners, methods and benchmark data used

Partner:	Model(s):	Grids:	Benchmark:
Alenia	EARSM-DES	32^3	CBC exp
Ansys-CFX	Smag., SST-SAS	32^3, 64^3	CBC exp
DLR	SA-DES, X-LES, SST-SAS, TRRANS	16^3, 32^3, 64^3	CBC exp
EDF	Smag., dyn.-Smag.	128^3, 160^3	KCM exp
FOI	Smag., no-model, SA-DES, *k*-DES, Yoshizawa (Dahlström), mod. Yoshizawa	32^3, 64^3	CBC exp
ICL	Dyn.-Smag., Yoshizawa (Dahlström), Yoshizawa	64^3	Wray DNS
IMFT	Smag., SA-DES	32^3, 64^3	CBC exp
NLR	X-LES	32^3, 64^3, 128^3	CBC exp
NTS	SA-DES, SST-DES (k-ε), SST-DES (k-ω), SST-SAS	32^3, 64^3	CBC exp
Numeca	SA-DES, Smag., SST-DES, SST-SAS	16^3, 32^3, 64^3	CBC exp
TUB	SALSA-DES, LLR-DES, CEASM-DES, Wilcox-DES1, Wilcox-DES2, Wilcox-DES3, no-mod.	32^3, 64^3	CBC exp, Wray DNS
UMIST	SST-DES	64^3	CBC exp

5.4 Results and Discussion

The energy spectra for a multitude of calibrated results based on the CBC benchmark data is shown in Fig. 3. The description "calibrated" means that these are the

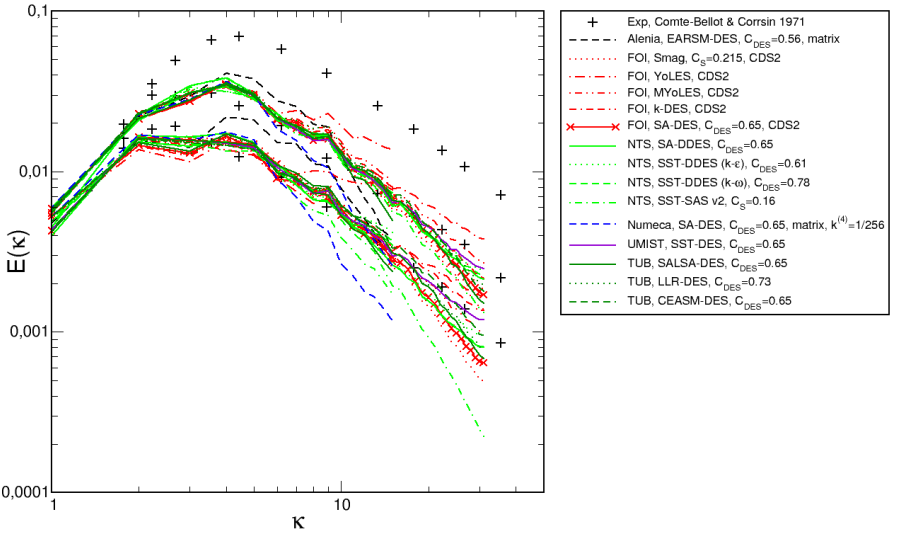

Fig. 3 Selected energy spectra for the calibrated partner results using the CBC data as benchmark

methods and setups that partners have declared to be used for the application test cases, rather than test versions or using numerical schemes that are unstable for complex applications. The amount of information in the figure is of course excessive, however it serves to illustrate that the majority of implementations deliver reasonable turbulent energy spectra for decaying isotropic turbulence.

Some highlighted results will be presented that allow more detailed discussion about some pertinent issues. Figure 4 shows some example results for the use of

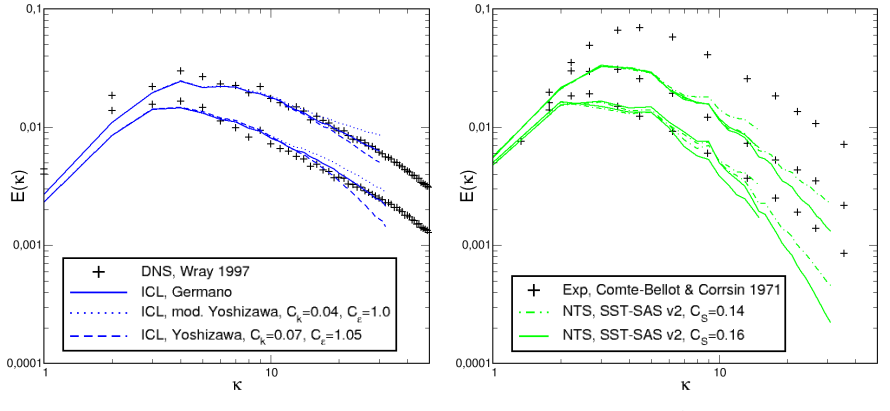

Fig. 4 Examples of DIT for model tuning purposes – *(a)* ICL tuning of Yoshizawa model parameters on the 63^3 grid against Wray DNS data, *(b)* NTS tuning of SST-SAS constant on 32^3 and 64^3 grids against CBC data

DIT in line with the primary purpose of tuning model parameters, as well as demonstrating the equivalence of different benchmark data sets for this purpose. ICL have tested a modified set of constants for the Yoshizawa one-equation SGS model (Yoshizawa & Horiuti, 1985), and NTS results are presented for a calibration that led to a modification of the SST-SAS model parameter from 0.16 to 0.14.

A central issue to LES-like simulation methods is the numerical dissipation; for the "classical LES" approaches considered in DESider (as opposed to "implicit LES"), models are derived for the unresolved scales that assume negligible numerical dissipation. Hence, a strong influence should be detected for the variation of the model parameter in DIT as shown by the FOI results with the low-dissipative 2nd order central difference convection scheme in Fig. 5. An interesting test of the energy conservation of the scheme can be carried out by considering inviscid flow with the model deactivated – i.e. all tangible sources of dissipation eliminated (Benhamadouche & Laurence, 2002, Benhamadouche et al., 2002). In this case a κ^2 gradient should develop in the spectra (Pope, 2000), as demonstrated by the FOI results for the no-model simulation with 2nd order CDS in Fig. 5 as well as by (Benhamadouche, 2006). Similar results are reported for TUB simulations with 2nd order CDS in Chapter V, Section 17. In contrast, when the upwind-biased MUSCL scheme is used for the convective terms, strong damping of the high wave-number scales is seen. This scheme is hence unsuitable for the LES-mode operation of a hybrid RANS-LES method.

For a certain class of density-based explicit solvers, artificial dissipation of the Jameson type must be added to guarantee numerical stability. The results of Numeca shown in Fig. 6(a) demonstrate the strong damping caused by scalar dissipation of this kind, with the side-effect that the results demonstrate negligible

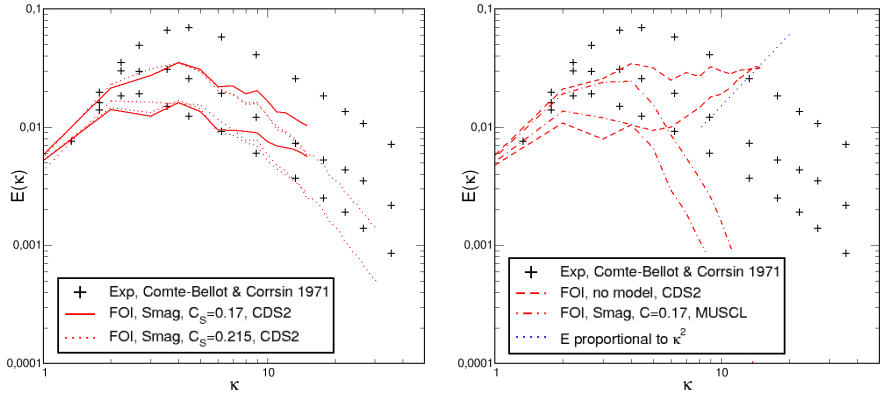

Fig. 5 Demonstration of sensitivity to model constants for a low dissipative scheme *(a)* – FOI results with the Smagorinsky model on 32^3 and 64^3 grids using a 2nd order central difference scheme and the CBC benchmark data. The effect of the high-dissipative MUSCL upwind-biased scheme and lack of SGS model on 2nd order CDS scheme *(b)* – FOI results on a 32^3 grid

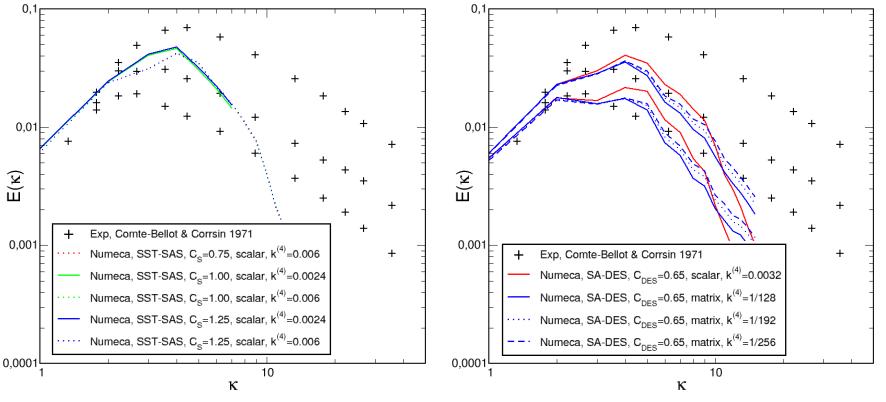

Fig. 6 *(a)* – Numeca SST-SAS results with scalar dissipation and variation of the model parameter, *(b)* – Improvement of results with matrix dissipation and dependency on $k^{(4)}$ coefficient for Numeca SA-DES results

sensitivity to strong variations in the SST-SAS parameter (compare this to the sensitivity seen to much smaller variations in Fig. 4(b)). Significant improvement could be obtained by switching to matrix dissipation (Fig. 6(b)), although a slightly excessive damping of the high wavenumbers is seen and a strong sensitivity to the k(4) damping coefficient remains. These observations have also been made by Alenia and the DLR (reported in Chapter V, Section 5), partners employing similar solver architectures.

An investigation into the issue of filtering in LES was conducted by EDF, employing DIT based on the KCM benchmark data. Initialisation with spectra truncated to the desired grid resolution was compared with initialisation using spectra filtered using a Gaussian filter (with $\Delta=2h$) and the results are plotted in Fig. 7 for 128^3 and 160^3 grids (for both of these grids, the cut-off wave number was shown to lie within the inertial sub-range). These indicate that the implicit filter imposed by the collocated numerical scheme is similar to a Gaussian filter of $\Delta=2h$, at least for these regular, Cartesian grids. Furthermore, the choice of filtering the initialisation spectra influences the calibration strongly in the case of the Smagorinsky model: the best spectra were returned by C_S=0.12 for the truncated spectra, whereas C_S=0.16 to 0.18 gave the best agreement for the filtered spectra. However, the C_S=0.12 computations delivered a non-physical value of the velocity derivative skewness. EDF therefore conclude that a filtering of the initialisation velocity field with a kernel approximating the grid filter is a necessary step in the calibration using DIT. Interestingly, the effect of truncation versus filtering is negligible for the computations with the dynamic Smagorinsky model, suggesting that this adaptively cancels the effect. Further investigation and consensus on this issue should be achieved in future studies. This investigation is described in more detail by (Benhamadouche, 2006).

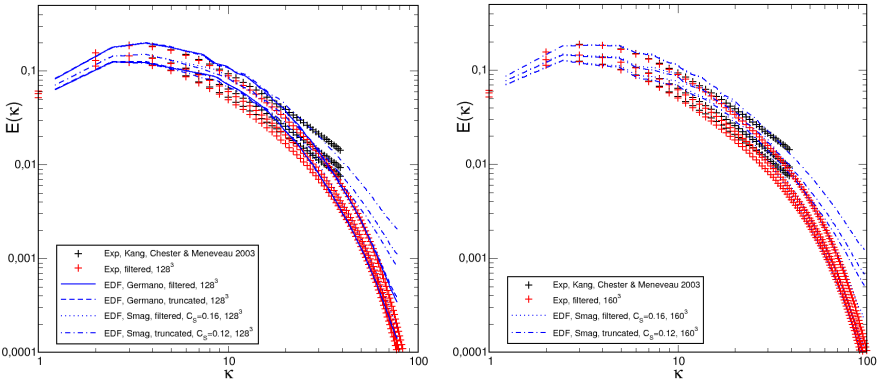

(a) *(b)*

Fig. 7 *(a)* – EDF results for the constant and dynamic Smagorinsky models, comparing truncated and filtered initial fields on a 128^3 grid, *(b)* – comparison of the filtered and truncated cases using the calibrated value of C_S in each case on a 160^3 grid

Finally, some examples of "secondary" investigations conducted using the DIT case are shown. Following the methodology developed by NTS for the correction of RANS model low-Reynolds number terms in DES (described in Chapter II, Section 4 and by (Spalart et al., 2006)), TUB derived a version of the model-specific Ψ correction function for their SALSA-DES implementation (Mockett et al., 2008). As shown in Fig. 8*(a)*, the function successfully prevents the undesired damping of eddy viscosity. In a separate investigation, TUB experimented with

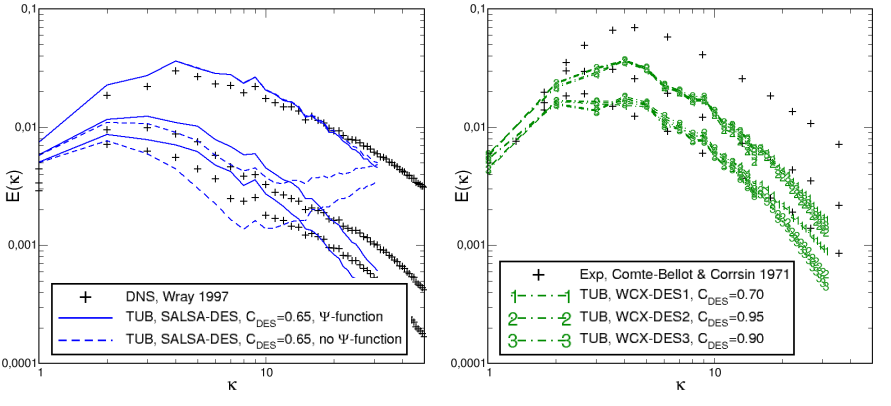

(a) (b)

Fig. 8 *(a)* – Effectiveness of the Ψ function derived for TUB's SALSA-DES (against Wray DNS benchmark), *(b)* – Calibration of C_{DES} for three alternative length scale substitutions for Wilcox-DES (TUB, CBC benchmark)

the substitution of the DES length scale in different terms of the Wilcox k–ω model (Yan et al., 2005). Strongly varying values of the C_{DES} parameter were required for the different formulations (denoted DES1, DES2 and DES3), and it was shown that these could not be rigorously determined by analytical means alone.

5.5 Conclusion

A large number of DESider partners have demonstrated fundamental validation work of the LES portion of their hybrid RANS-LES techniques on the basis of decaying isotropic turbulence. A representative selection of these copious results has been portrayed, which demonstrates the possibility of calibrating the parameters of novel methods or formulations for diverse solver types. The importance of checking the level of numerical dissipation has been underlined, and simple method for doing this presented. In cases where numerical dissipation is excessive, DIT serves to test modifications to the discretisation scheme aimed at addressing this. Hence, it is possible to demonstrate the fundamental ability of the model and solver combination to resolve turbulent flow. Additionally, the case serves as a simple demonstration of a number of new model features, as well as allowing an empirical investigation of modelling issues such as the DES length scale substitution method.

Despite all this, it must be acknowledged that the simplicity of the test case leads to a number of important factors being neglected – skewed or stretched meshes, the presence of mean flow shear etc. Hence DIT cannot in isolation be considered a full validation of a method for generic complex applications. Nonetheless, the failure to reproduce DIT does condemn a model/solver combination to failure in more complex applications. The consideration of DIT as an essential prerequisite test for new methods or implementations is therefore justified.

6 Three-Element Airfoil

S. Deck

ONERA

Abstract. New industrial needs in aerodynamics concern for example the noise control as well as the capability to predict dynamic loads so that the simulation of 3D unsteady turbulent flows is required. The main obstacle to practical use of LES in an industrial context which involves wall-boundary layers to take into account at high Reynolds number remains computational resources. Indeed, LES aims at capturing the scales of motion responsible for turbulence production which imposes severe demands on the grid resolution near solid-walls. Hybrid RANS/LES was invented to alleviate this resolution constraint in the near-wall regions (see the review by Sagaut, Deck and Terracol, 2006).

Especially, the numerical simulation of the flow field around a whole high-lift element with deployed slat and flap is a problem of outstanding importance. Indeed, the flow over a multi-element airfoil is inherently complex and exhibits a wide range of physical phenomena including large low speed areas, strong pressure gradients, unsteady flow regions, three-dimensional effects, confluence of boundary layers and wake. Each one of the aforementioned topics may constitute a very challenging issue for an hybrid RANS/LES method. The objective of this study is to assess the capability of a zonal-DES method to handle a complete high-lift configuration with deployed slat and flap. The approach is firstly explained before presenting the results obtained on the multi-element airfoil tested within the Europiv2 program. The recently developed Delayed Detached Eddy Simulation (DDES) is also briefly presented and assessed on this test case.

6.1 Test Case Description

6.1.1 Geometry and Conditions

This study concerns a three-element airfoil that was tested in the Low Speed Wind Tunnel (LWST) of Airbus Bremen (Germany) within the framework of the EUROPIV2 project (G4RD-CT-2000-00190) and used as a test case in the DESider European-project (AST-CT-2003-502842). The experimental results presented here were reported by Arnott at al. (2003) (see also Neitzke, 2003). Descriptions of the experimental apparatus and procedures are described in those publications. One of the goal of this experimental study was to investigate the flow over a slat/wing/flap model in high-lift configuration. The model is based on a RA16SC1 two-dimensional profile whose geometry is given in Figure 1. The slat and flap angles were set at one position with deflection angles of 30 and 40 deg. respectively. The reference chord is equal to c=0.5 m. The tests were performed at a freestream speed of U_0=54 m.s^{-1} in atmospheric conditions. The Reynolds number based on freestream velocity and chord length of the main wing is equal to 1.7 10^6.

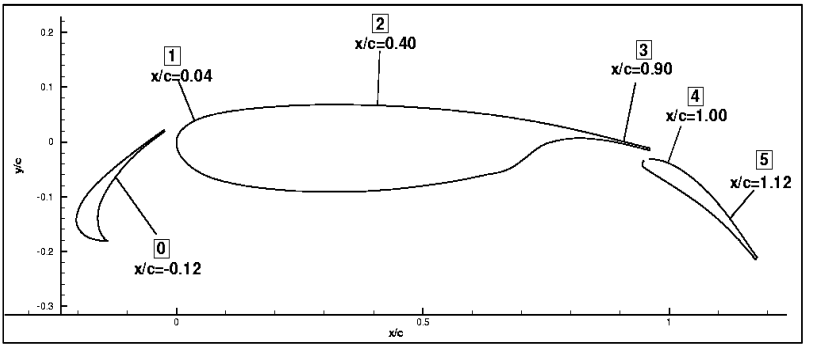

Fig. 1 RA16SC1 model

6.1.2 Grid

The present x-y grid has 250 000 points, and the spanwise grid has 31 points with $\Delta z/c=2.10^{-3}$. The zonal topology used for the present DES computations is also presented in Figure 2 which illustrates the two and three-dimensional domains. This strategy allows to save 2.10^6 nodes leading to a total number of $N_{xyz}=5.5\ 10^6$ nodes (instead of $N_{xyz}=7.5\ 10^6$). In addition, the normalized spanwise length of the grid is respectively equal to 100 Lz/c=6. The spanwise period appears small at first sight, but at this angle of attack, it should be compared with the chords of the slat and flap, rather than that of the airfoil. In addition, this figure shows the multi-domain decomposition where RANS and DES are preformed. Especially, the merging of the slat wake with the main body boundary layer is treated in RANS mode. The interest of this approach is that the user can focus his grid refinement on regions of interest (e.g. LES regions) without corrupting the boundary layer properties farther upstream or downstream. The focus regions are limited to the slat and flap coves as well as to the flow field over the flap.

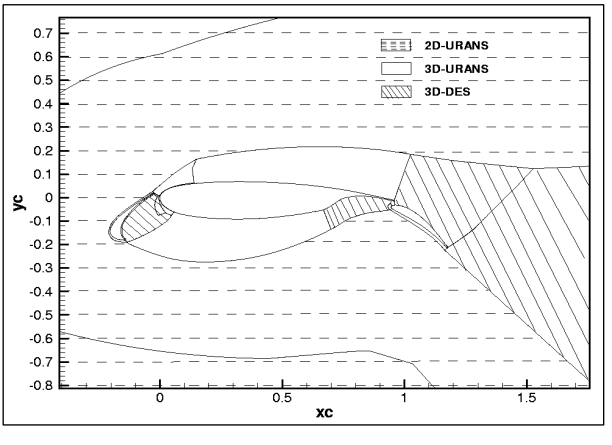

Fig. 2 Grid topology and Zonal-DES

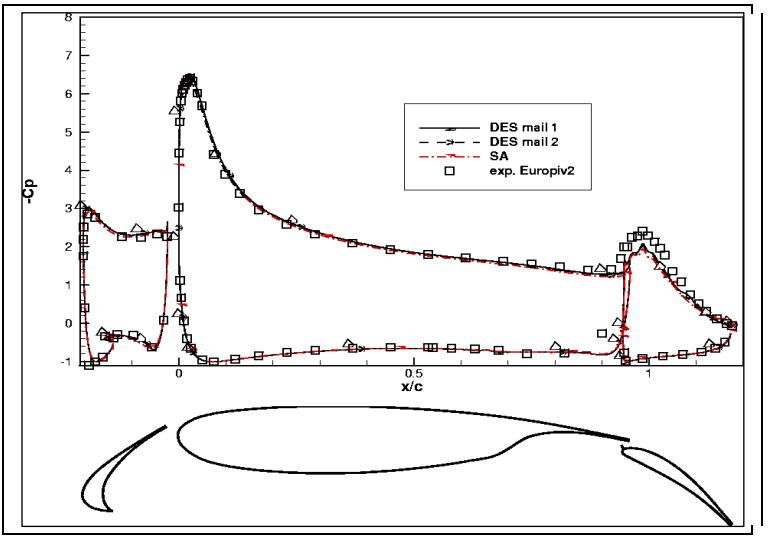

Fig. 3 Pressure coefficient around the airfoil

The presence of tunnel walls does affect the recirculation and thus the loading on the slat leading edge. To match the mean slat loading, the way we use the CFD calculation was an adaptation of the angle of attack to the suction peak at the main wing and slat. This adaptation is performed thanks to preliminary RANS calculations. Results presented in this paper were obtained with a 9 degree angle of attack (compared to 12 deg. for the experiment), which was found to yield the best assessment with the pressure distribution on the main wing. Figure 3 compares to the experiment the averaged pressure coefficient on each element. One can firstly notice that at this angle of attack, the main element bears the highest loads. Both RANS and zonal-DES compare favourably with experiment except on the flap. Indeed, the suction peak on the flap is not well-reproduced by calculations.

6.2 Computations and Models

6.2.1 Zonal-Detached Eddy Simulation (ZDES)

Detached Eddy Simulation is well understood in thin boundary layers where the model acts in RANS mode and in massive separation where the model degenerates toward a subgrid-scale model. The region corresponding to $d \approx \Delta$ where the model needs to convert from fully modelled turbulence (attached boundary layer) to mostly resolved turbulence (massive separation) is recognized as delicate. This situation happens when the switching to LES mode occurs inside the boundary layer, e.g., when the grid brings the $\tilde{d} = C_{DES}\Delta$ branch to intrude into the boundary layer. This practically results in lower eddy viscosity, but not weak enough to allow eddies to form which yields lower Reynolds stress levels compared to those

provided by the RANS model. Note that this issue was already addressed in the original paper presenting the method by Spalart et al. (1997) .

For complex geometries, the building of a DES grid appears to be a dilemma for the user. On one hand, the RANS part of the simulation requires a near wall grid spacing in tangential direction much larger than the boundary layer thickness at that location to avoid Modelled-Stress-Depletion (MSD, see Spalart et al. 2006). On the other hand, there is no reason why a DES calculation should accept a coarser grid than a LES calculation. Especially, an LES grid is locally refined in all direction since strongly anisotropic grids are inefficient. As a result, the grid is also refined in regions not intented to be handled by LES. This situation is practically unavoidable in structured grids where refinement is required in regions of high geometry curvature or in presence of thick boundary layers. Note that both features are encountered on a high lift device making it a challenging case for a hybrid RANS/LES simulation.

To avoid this problem, we developed a "zonal-DES" approach (Deck 2005a and 2005b) where attached boundary layer regions are explicitly treated in URANS mode no matter how fine the grid is. That means that, following the example of RANS/LES coupling methods, the user has to select individual RANS and LES domains. The interest of this approach is that the user can focus his grid refinement on regions of interest without corrupting the boundary layer properties farther upstream or downstream. The computational grid has then to be carefully designed. For example, in the LES region (e.g. outside boundary layers), the grid is designed to obtain nearly cubic cells in order to use the cube root $\Delta = (\Delta x \Delta y \Delta z)^{1/3}$ as "filter-width" for LES. This simple modification decreases drastically the level of predicted eddy viscosity since this latter is proportional to the square of the filter width. We also made the choice to remove the near wall functions in LES mode formulation (see also Breuer et al., 2003):

$$f_{v1}=1,\ f_{v2}=1,\ f_w=1.$$

This choice also avoids that the damping functions of the RANS model interpret the low eddy viscosity levels typical of resolved LES regions as closeness to the wall with corresponding fast non-linear drop of sub-grid viscosity. An alternative proposal that prevents the activation of the low Reynolds terms in LES mode has been made by Shur et al. (2003) by introducing a threshold function based on the ratio ν_t/ν.

6.2.2 Delayed-Detached Eddy Simulation (DDES)

Spalart et al. (2006) redefined the DES length scale in order to preserve the RANS treatment of the boundary layer (Spalart and Allmaras, 1994). The modification is analogous to that developed by Menter and Kuntz (2003) which uses the blending function F_2 of the SST model (Menter, 1994). The new length-scale is redefined as:

$$\tilde{d} = d_w - f^d \max\left(0., d_w - C_{DES}\Delta\right)$$

where f_d is a shielding function designed to be 1 in the LES region and 0 elsewhere. Therefore setting f_d to 0 yields RANS $\left(\tilde{d} = d_w\right)$ no matter how fine the grid is while setting it to 1 gives standard DES $\left(\tilde{d} = \min\left(d_w, C_{DES}\Delta\right)\right)$. The quantity $r_d = \frac{\nu_t + \nu}{\sqrt{U_{i,j}U_{i,j}}\kappa^2 d_w^2}$ is used as an argument to the function $f_d = 1 - \tanh\left(\left[8r_d\right]^3\right)$. The subscript "*d*" means "*delayed*" and this new version of the technique is referred to as *DDES* for *Delayed DES.*

Although the new definition of $\tilde{d}$ could appear as a mere adjustment within DES, there is however an essential change. Indeed, the DDES length scale does not depend only on the grid but also on the time-dependent eddy viscosity field.

6.3 Results and Discussion

6.3.1 ZDES

It is desirable to study the slat flow first because its effect is convected all the way downstream. The flow field over the slat is not well understood and is difficult to predict. Figure 4 shows a positive value of the Q-criterion coloured by the transverse velocity component. This figure clearly illustrates the roll-up of two-dimensional eddies in the free shear layer which progressively become three-dimensional when they impact the lower side of the slat. More precisely, after experiencing severe distortion at the reattachment point, some large and strong vortices are entrapped in the cove. Computed and experimentally statistical-averaged velocity magnitudes are also compared to the experiment in Figure 4 The time-averaged velocity magnitudes contours near the leading edge slat clearly display the acceleration of the local flow through the gap as well as the recirculation zone. This low speed recirculation area on the suction side of the slat is bounded

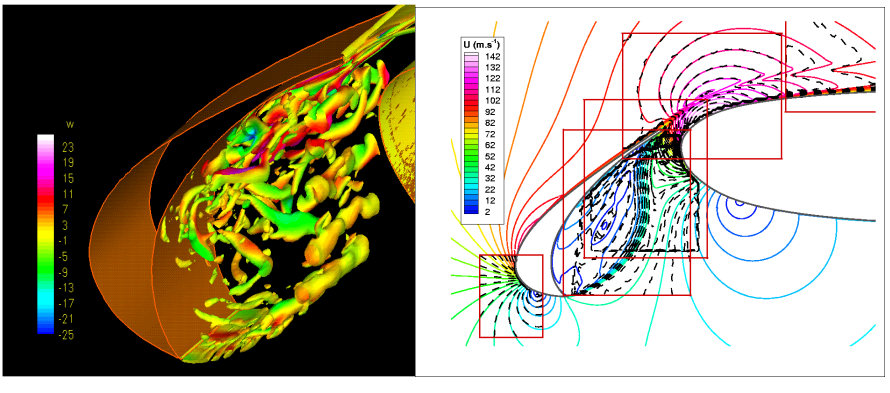

Fig. 4 Instantaneous flowfield (left) / Averaged velocity field (right) in the slat area (solid line: zonal-DES, dashed line: PIV)

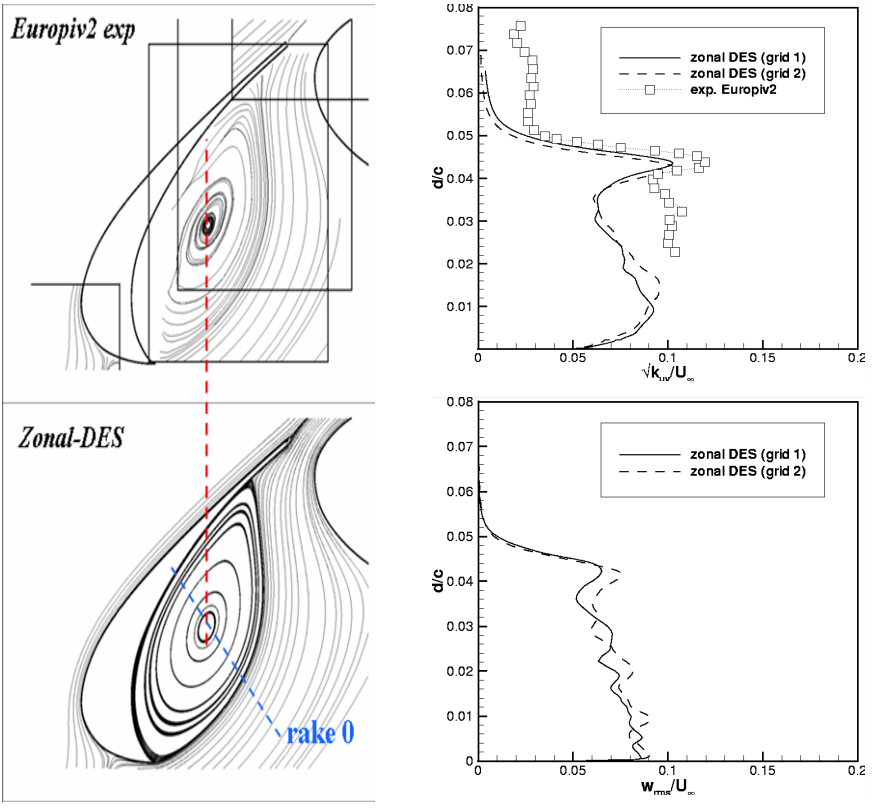

Fig. 5 Averaged streamlines (left) / Velocity fluctuation (right) in the slat area (rake 0)

by the mixing layer that develops in the shear layer. The flow acceleration through the slat/wing gap is particularly prominent. The development of the slat wake and gap flow is also evidenced. It is observed that the mean velocity fields obtained by zonal-DES as well as the size of the separation are in fair agreement with experiment. The velocity component fluctuations profiles are also shown. The highest levels of transverse velocity fluctuations up to 9% are observed in the vicinity of the lower surface. The levels of turbulent kinetic energy are also underestimated by the calculation (see Figure 5).

Computed and experimentally statistical-averaged velocity magnitudes around the main wing are compared to experiment in Figure 5 The time-averaged velocity magnitude contours near the leading edge flap display the acceleration of the local flow through the gap as well as the recirculation zone. Important stages such as merging of the slat wake and the main element boundary layer are depicted. Besides, the turbulent structures depicted in Figure 6 show the merging and turning effects of the wakes. In addition, this instantaneous field reveals that the vortices that do escape through the gap are severely deformed by the accelerating local flow in such a way that they become mainly longitudinal eddies. The spanwise

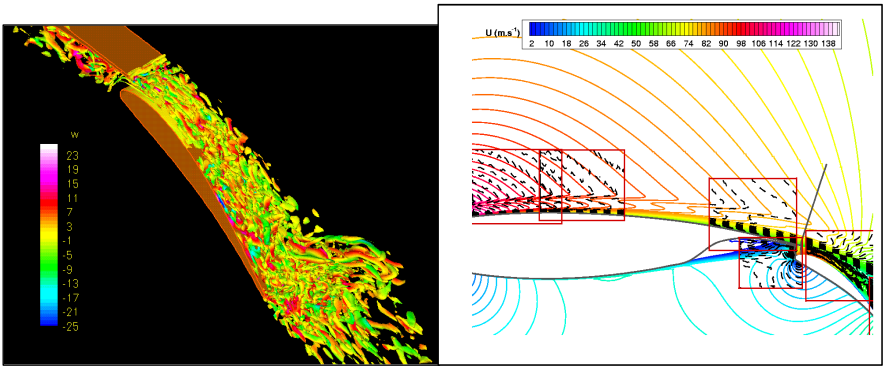

Fig. 6 Instantaneous flowfield (left / Averaged velocity field (right) in the flap area (solid line: zonal-DES, dashed line: PIV)

grid extension Δz has therefore to be small enough to allow the capture of these thin elongated eddies. It is also worth noting that the flow through the gap is unsteady and three-dimensional and that these features can not be reproduced by classical steady RANS calculations.

6.3.2 DDES

ONERA also contributed together with NTS to the development and validation of the Delayed Detached Eddy Simulation. Figure 7 presents the contours of spanwise

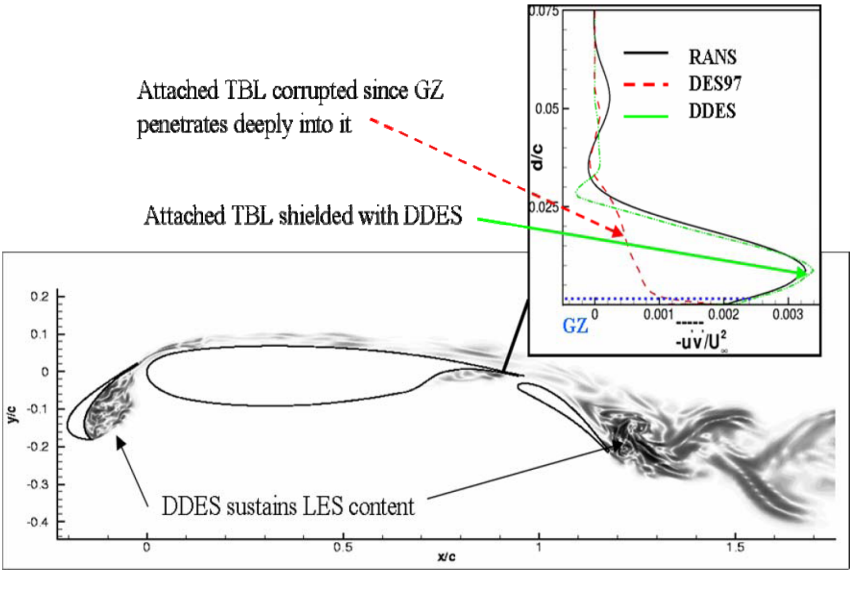

Fig. 7 Flow over a multi-element airfoil and DDES behavior

velocity and shows that the separated regions, namely the slat an flap coves as well as the wake over the flap sustain LES content while the attached boundary layer is shielded with DDES. This is confirmed by the same figure which presents the modelled stresses at location x/c=0.95 where the boundary layer has become very thick. The grey area penetrates deeply into the boundary layer and the modelled stress depletion is clearly evidenced when using standard DES (DES97). Conversely, the boundary layer is mostly shielded with DDES.

6.4 Conclusions

The numerical simulation of the unsteady flow field around a high-lift element with deployed slat and flap is a problem of outstanding importance but is a very difficult and challenging case for DES since it presents thick boundary layers. Such a complex simulation has been possible thanks to the use of a ”zonal-DES” (ZDES) method, allowing to reduce the cost of the simulation compared to a LES by limiting the extent of the DES zones while maintaining the desired level of accuracy in (U)RANS and focus regions. The results also provide an insight into the real unsteady nature of the flow around a three-element airfoil that cannot be reproduced by classical RANS models. Furthermore, it is worth to stress that acquisition of experimental PIV data like those performed in the EUROPIV2 project is crucial to validate hybrid RANS/LES methods and thus to improve the CFD methods that are used to design such high-lift systems. A first DDES has also shown that the RANS mode is maintained in thick boundary layers whilst switching to (and maintaining) the LES content after separation.

7 Simpson's 3D Hill Test-Case

S. Benhamadouche

EDF

7.1 Test-Case Description

The three-dimensional hill tested in the present work is from the experiments by Simpson et al (2002) and Byun (2004). The geometry of the computational domain is given in Figure 1. The body height is $H=0.078\ m$. The geometry of the hill is given by the following function,

$$\frac{y(r)}{H} = -\frac{1}{6.04844}\left[J_0(\Lambda) I_0\left(\lambda \frac{r}{a}\right) - I_0(\Lambda) J_0\left(\lambda \frac{r}{a}\right)\right].$$

where $\Lambda=3.1962$ and $a=2H$. J_0 and I_0 are respectively the Bessel function of the first kind and the modified Bessel function of the first kind. The Reynolds number, based on the maximum inlet velocity ($U_{ref}=27.5\ m/s$ in the experiment) and the hill height H is $Re=130\ 000$. The Hill is at a distance L_1 from the inlet and L_2 from the outlet. The channel has two lateral walls separated by a distance L_3 and a roof at a height of L_4 from the ground plane. In the experiment, the values are $L_1=3.03m$, $L_2=4,95m$, $L_3=0.91m$, $L_4=0.25m$. The tunnel free-stream turbulent intensity reported in Simpson et al (2002) is 0.1%. The boundary layer when the hill is not in place is equal to $39\ mm$ at the position of the hill. All the variables in the following are normalized by H and U_{ref}. Figure 2 shows the two planes where most of the measurements were made.

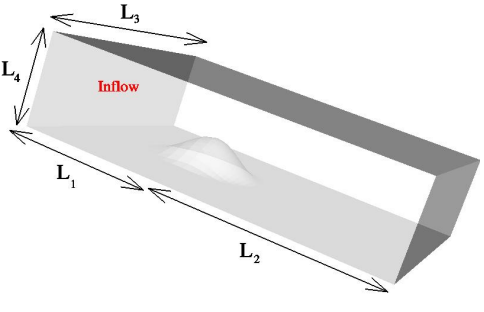

Fig. 1 Computational domain definition

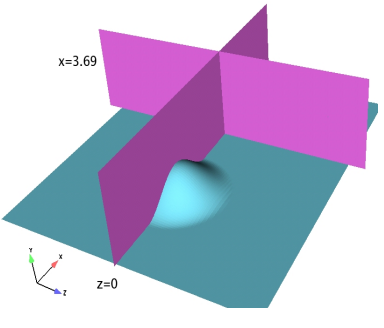

Fig. 2 Two major planes for post-processing

7.2 The Computations

The main simulation features by the different contributors are as follows:

7.2.1 Chalmers University

Three computations are reported herein. Note that the two hybrid simulations have been also performed with a fixed RANS/LES interface (using the gridlines) but gave very close results.

	Ch_LES_Fine15M_NoFl	Ch_Hyb	Ch_Hyb_NoFl
Turbulence model (TM)	LES	Hybrid RANS/LES	-
Specificities of TM	One equation	One equation for both. Interface defined with instant. streamlines	-
Number of nodes	15M	1.7M (162x82x130)	-
Inlet BC (mean)	experimental	-	-
Inlet BC (unsteady part)	No Fluctuations	Isotropic Synthetic Turbulence	No fluctuations
Maximum CFL	2	1.3	-
y+ max, lower wall		2	-
$T*U_{ref}/H$		580	410

"-" means the same options as in the previous computation are used.

7.2.2 FOI

Four computations are reported by partner FOI:

	FOI_kDES	FOI_Hyb_Smag	FOI_Hyb_k	FOI_Hyb_k_NoFl
Turbulence model (TM)	kDES	Hybrid RANS/LES	-	-
Specificities of TM	k eq. based on DES	RANS: zero equation LES: Smagorinsky Cs=0.12	RANS: zero equation LES: k eq.	-
Number of nodes	1M (128x80x96)	1.1M (144x80x96)	1M (128x80x96)	-
Inlet BC (mean)	experimental	-	-	-
Inlet BC (unsteady part)	Fluctuations recycled and rescaled from the outlet	Fluctuations recycled and rescaled from a downstream plane	Fluctuations recycled and rescaled from the outlet	No fluctuations
Maximum CFL	12	9	11	10.5
y+ max lower wall	0.17	0.36	0.3	0.2
$T*U_{ref}/H$	37	34	48	47

7.2.3 Imperial College

Although several computations have been carried out by Imperial College (Tessicini, 2007), only three of them are reported here:

	IC_LES_TL	IC_LES_Fine9M	IC_LES_Fine37M
Turbulence model (TM)	LES (Two Layer model)	LES	-
Specificities of TM	Dynamic (average in span-wise direction)	-	-
Number of nodes	3.5M (192x96x192)	9.6M (448x128x192)	36.7M
Inlet BC (mean)	Results from RANS calc.	-	-
Inlet BC (unsteady part)	quasi periodic recycling and re-scaling	-	-
Maximum CFL	0.2	0.2	
y+ max lower wall	20	5	
T^*U_{ref}/H	70	70	100

7.2.4 EDF

Two simulations are reported herein:

	EDF_LES_WF	EDF_LES_EWF
Turbulence model (TM)	LES Cs=0.065	-
Specificities of TM	Standard WF	Extended WF (meshless)
Number of nodes	3.7M (unstructured)	-
Inlet BC (mean)	RANS calculation	-
Inlet BC (unsteady part)	Vortex method	-
Maximum CFL	0.6	0.6
y+ max lower wall (during the simulation)	200	200
T^*U_{ref}/H	108	136

7.3 Discussion

Within the precursor FLOMANIA project, several partners have investigated the 3D-Hill flow with numerous RANS, LES and Hybrid RANS/LES models. Only the last two methods gave satisfactory results. None of the RANS computations

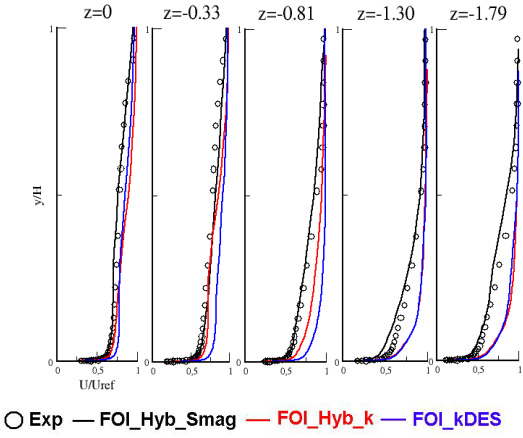

Fig. 3 Stream-wise velocity component in the plane x=3.69

gave a credible representation of the flow. During DESIDER 4 kinds of approaches for turbulence modelling have been used

1. DES (1 computation from FOI)
2. Hybrid RANS/LES (2 from Chalmers, 3 from FOI)
3. LES with wall treatment (1 from EDF, 1 from IC)
4. LES with no slip boundary conditions (1 from Chalmers, 1 from EDF, 2 from IC)

The kDES gives the worst results. This is shown for the stream-wise velocity in figure 3 where the results of kDES are compared to those of hybrid RANS/LES approaches. The velocity vectors projected on the planes z=0 and x=3.69 are given in figure 4 and compared to the experimental results. The recirculation region is too large and the secondary motion in the plane x=3.69 is not well predicted.

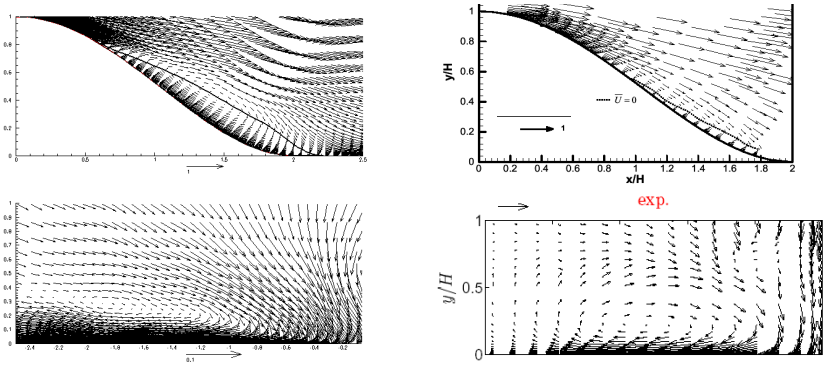

Fig. 4 The projection of the velocity vector in the planes z=0 on the top and x=3.69 on the bottom (left: FOI_kDES, right: Experiment)

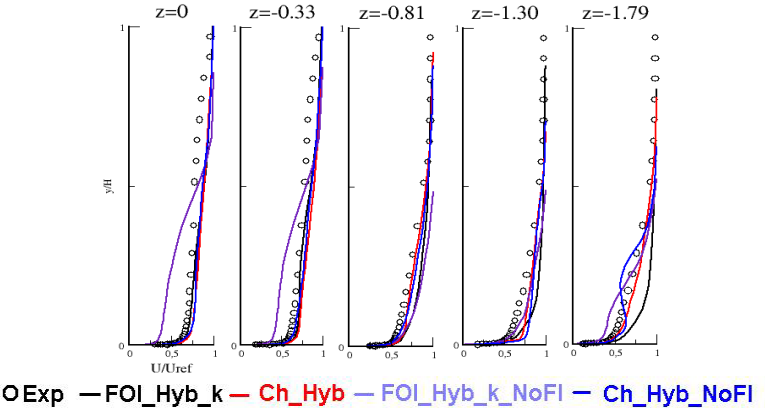

Fig. 5 Stream-wise velocity component in the plane x=3.69

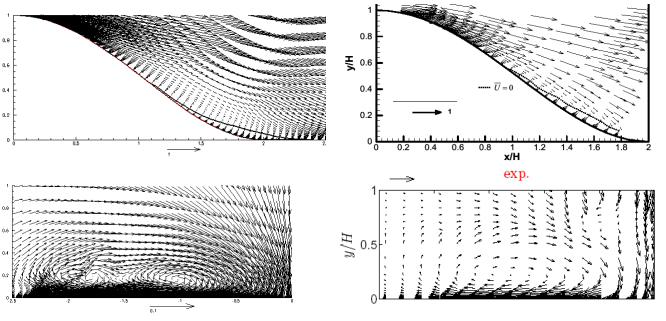

Fig. 6 The projection of velocity vector in the planes z=0 on the top and x=3.69 on the bottom (left: Ch_Hyb_NoFl, right: Experiment)

FOI calculations (FOI_Hyb_k and FOI_Hyb_k_NoFl) show also that it is mandatory to use fluctuating inlet conditions with hybrid-RANS LES approaches for the present test-case. This is confirmed by Hybrid RANS/LES calculations from Chalmers University with steady inlet BC (Ch_Hyb and Ch_Hyb_NoFl) which exhibit an unusual behaviour far from the symmetry plane (see figure 5). Figure 6 shows the projection of the velocity vectors on the planes z=0 and x=3.69 for Chalmers computation (Ch_Hyb_NoFl). One can clearly see that there are two counter rotating vortices in the plane x=3.69 instead of one.

The Hybrid RANS/LES simulations from FOI (FOI_Hyb_Smag and FOI_Hyb_k) and from Chalmers (Ch_Hyb) give reasonable results (see figures 7 to 10). Although the hybrid approach using a standard Smagorinsky model gives the best results in the cross section plane x=3.69, it predicts a too large recirculation zone in the symmetry plane. Note that no simulation managed to capture the wall normal velocity behaviour in particular at z=-0.33 (see figure 8). A global overestimation of the turbulent kinetic energy is also observed, in particular close

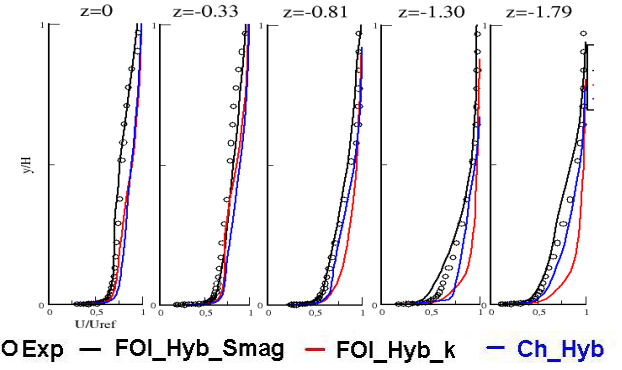

Fig. 7 Stream-wise velocity component in the plane x=3.69

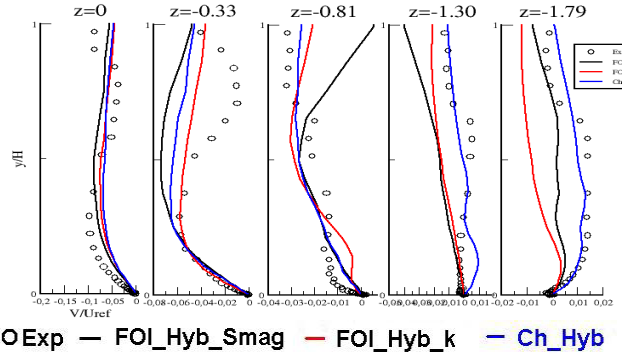

Fig. 8 wall-normal velocity component in the plane x=3.69

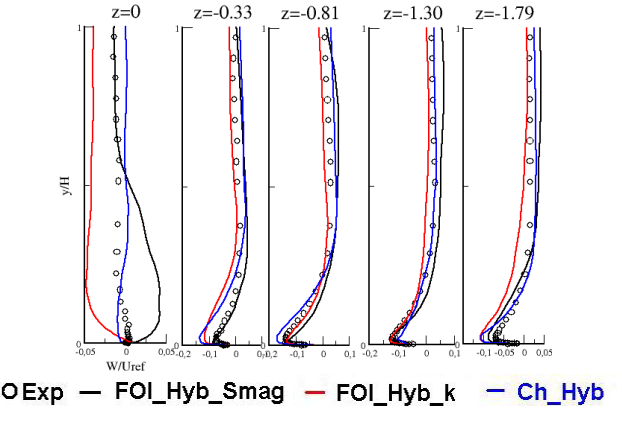

Fig. 9 span-wise velocity component in the plane x=3.69

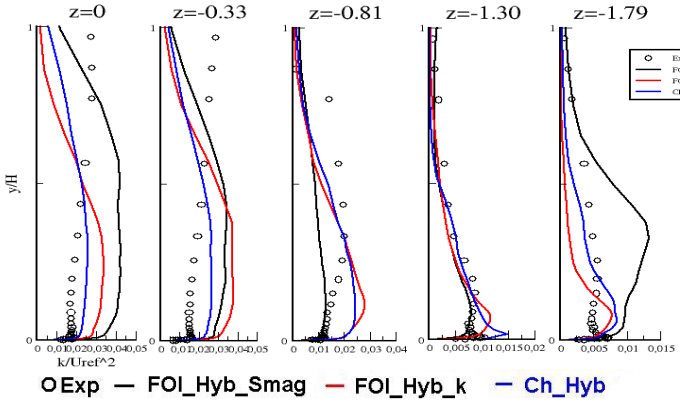

Fig. 10 kinetic energy in the plane x=3.69

to the symmetry plane (see figure 10). The recirculation in the symmetry plane z=0 is satisfactory with the two hybrid RANS/LES approaches which use a *k* equation for LES (FOI_Hyb_k and Ch_Hyb) but both fail in predicting the tangential structure of the flow in the plane x=3.69.

LES seems to be more adapted to give satisfactory results in the present test-case. Figures 11 to 14 give respectively the stream-wise velocity, the wall normal velocity, the span-wise velocity and the turbulent kinetic energy for the computations using pure LES as a turbulence model (the results are plotted when available). The Two Layer approach utilized by Imperial College agrees quite well with the experimental data. The recirculation region is still too large but a good agreement is observed for the secondary motion in the plane x=3.69 (see figure 15). The wall functions or extended wall functions used by EDF give satisfactory results (with slight differences between the two approaches) in the plane x=3.69 but the recirculation region is significantly too large (see figure 15).

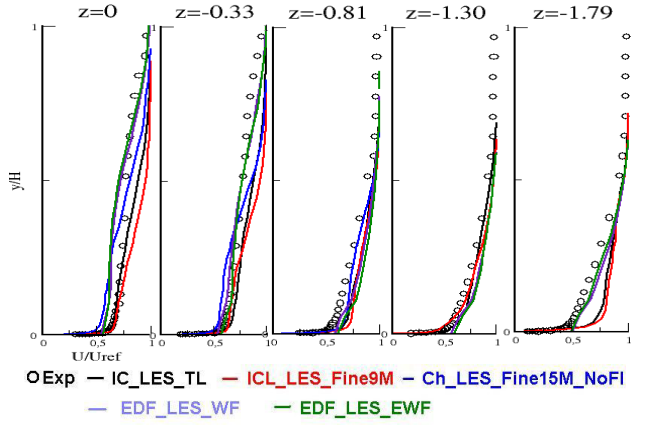

Fig. 11 Stream-wise velocity component in the plane x=3.69

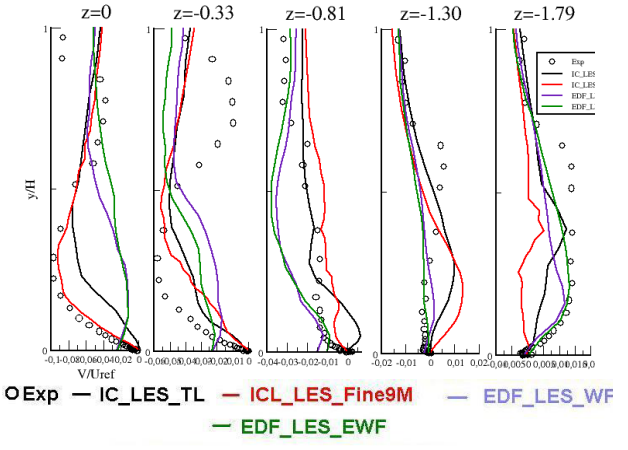

Fig. 12 wall-normal velocity component in the plane x=3.69

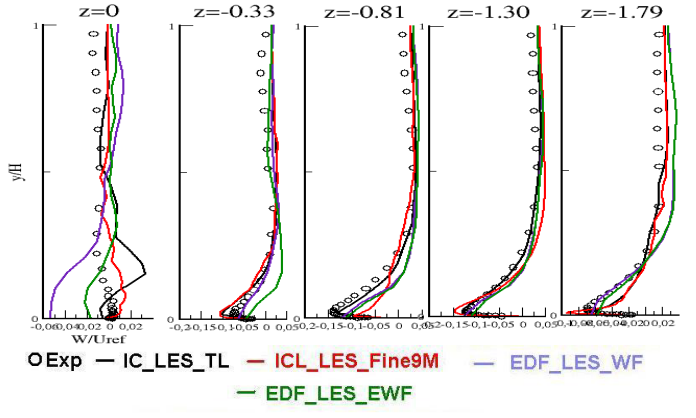

Fig. 13 Span-wise velocity component in the plane x=3.69

The Chalmers LES (Ch_LES_Fine15M_NoFl) computation did not use any synthetic turbulence or LES/DNS results at the inlet.

It shows satisfactory results (some profiles for this computations are not available). The question of the importance of inlet boundary conditions for pure LES is raised again for the present test-case. After a simulation with 9M cells, Imperial College concluded that the mesh has still to be refined. The finest mesh has 35M cells and seems to be the closest one to the experimental data (see figure 15). This is confirmed in the symmetry plane by the pressure coefficient in figure 16. A secondary motion has been observed in fine LES computations by Imperial College in the plane x=3.69 (see figure 17). This structure may be observed on both sides of the symmetry plane and should disappear in average but entails a very long averaging time.

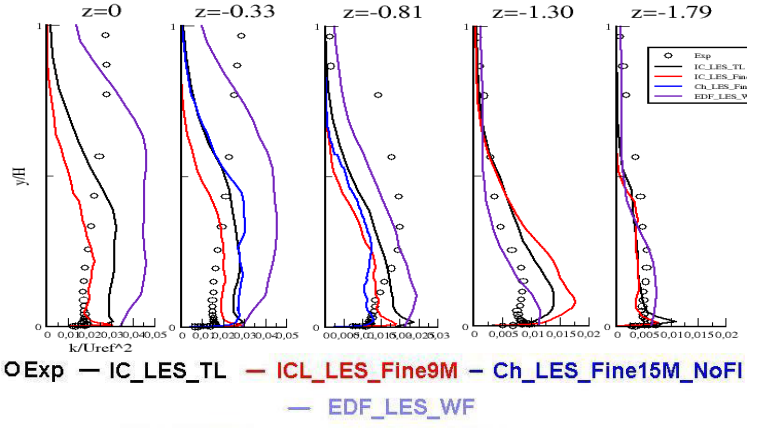

Fig. 14 kinetic energy in the plane x=3.69 - comparison between LES computations

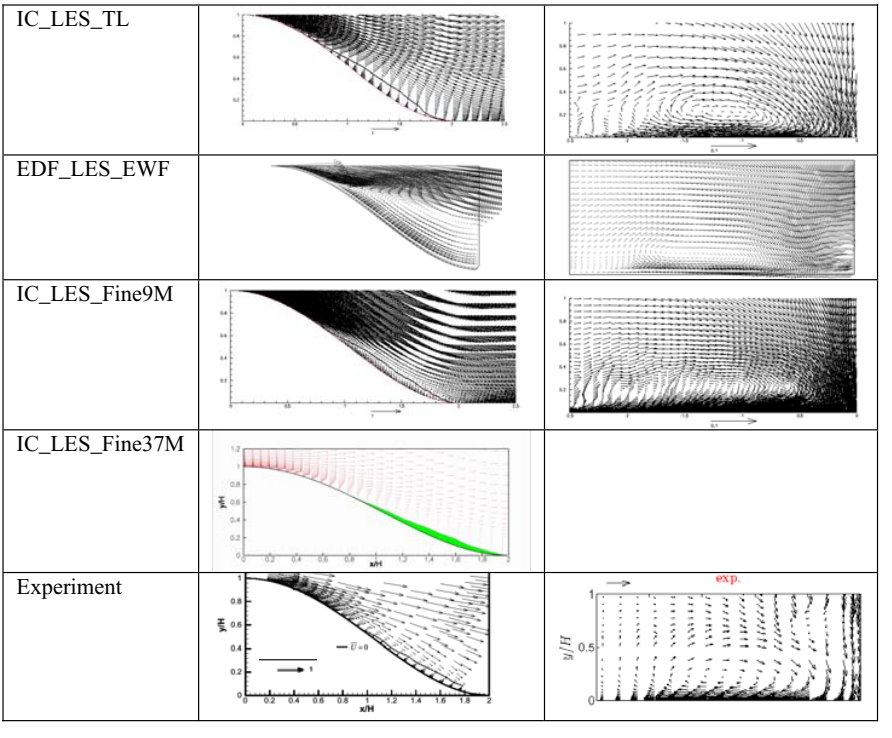

Fig. 15 The projection of velocity vector in the planes z=0 on the top and x=3.69 on the bottom

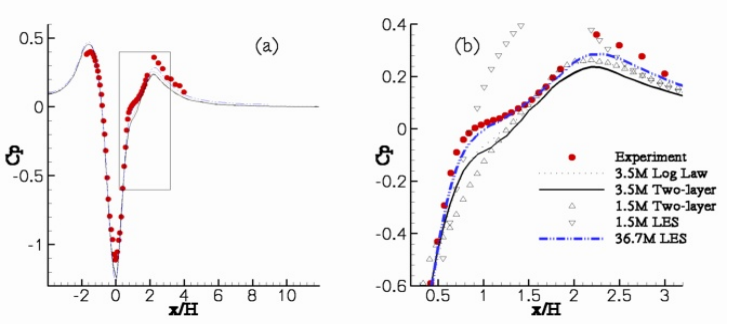

Fig. 16 Cp coefficient for various computations from Imperial College (including IC_LES_TL, IC_LES_Fine37M)

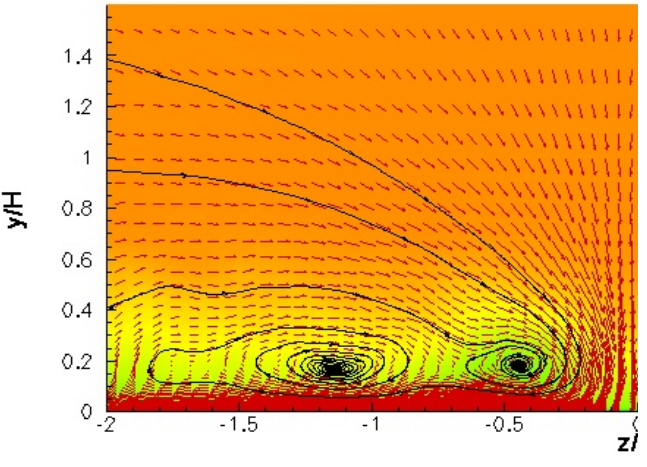

Fig. 17 The Wake structure in the plane x=3.69 with fine LES (IC_LES_Fine36M)

7.4 Conclusions

It is very difficult to draw definitive conclusions for the present test-case. It seems that the only approaches that may give satisfactory results are the one involving pure LES. None of the RANS or DES approaches managed to give satisfactory predictions for this test-case.

Hybrid RANS/LES approaches, LES with wall treatment, and LES with no-slip boundary conditions give better results. The question of the importance of unsteady boundary conditions is still open for pure LES. It has been clearly shown in the present report that the unsteadiness is mandatory for hybrid RANS/LES computations.

LES with no-slip boundary conditions seems to be the key for the present case. The LES from Imperial College with 37 million cells gave the best results but still shows that the mesh probably needs to be still finer.

8 Fully Developed Channel

L. Davidson

Chalmers

Abstract. Wall-resolved large-eddy simulation (LES) is an accurate method to predict both time-averaged and instantaneous (large-scale) wall-bounded flow. Unfortunately, LES requires too large computational resources at high Reynolds numbers. One way to circumvent this problem is to use wall models. This test case aims at evaluating different wall models. Two main types of models are used, namely low Reynolds number models and models.

This test case was 50% mandatory ($Re = 4000$, low-Re), meaning that partners could choose to do this test case or test case 5 (DIHT, Decaying of Isotropic Homogeneous Turbulence).

8.1 Low Reynolds Number Models

The boundary layer is resolved in the wall-normal direction down to approximately one viscous unit. A low-Re number model is used near the walls (most partners use a RANS model) and LES is used further away from the wall.

8.2 Wall Functions

The first cell is placed in the log-law region. Most partners used classical wall functions based on local equilibrium which are used in the same way as in RANS. The wall-adjacent nodes are located in the log-layer. The wall shear stress is then estimated using an empirical law, such as the log-law Deardorff (1970. The flow is by some partners covered entirely with LES whereas other partners use a mix between RANS (near the walls) and LES (outer flow). Although wall functions include a higher element of modelling compared to low-Re formulations, one big advantage is that the aspect ratio of the cell sides is more than one order of magnitude smaller on wall function grids compared to low-Re grids.

One partner, ICSTM, used a two-layer model. In two-layer models (Balaras et al 1996; Cabot, 1995; Cabot and Moin, 1999; Tessicini et al., 2007; Wang and Moin,, 2002) (also called “thin boundary layer equations”) the first node in the LES-simulations is located – as when using wall functions – in the log-region. Then a new fine near-wall mesh is created covering the wall-adjacent LES cell. This fine mesh may consist of 30 cells in the wall-normal direction and is the same as the LES mesh in the wall-tangential directions. On this fine mesh the boundary layer equations are solved. The wall shear stress is obtained from the the boundary-layer equations and is then fed back to the LES mesh as a wall boundary condition.

8.3 Technical Description

Three different Reynolds number have been investigated, $Re = u_\tau \delta / \nu = 4000$, 8000 and *Re*=16000. Since the flow should be fully developed periodic boundary conditions are used in both streamwise (x) and spanwise (z) directions. Both low-Re grids (first cell at $y^+ \simeq 1$) and grids for wall functions (first cell in the logarithmic region) were defined. In order to be able to use periodic boundary condition in the x-direction also for the pressure, it was recommended to add a driving constant forcing term per unit volume in the streamwise momentum equation,

$$S_U = \rho u_\tau^2 \delta V = 1 \cdot \delta V$$

The domain was defined as $(x_{max}, y_{max}, z_{max}) = (6.4, 2, 3.2)$ for all grids. This gives $(\Delta x/\delta, \Delta z/\delta) = (0.1, 0.05)$ for all grids and Reynolds numbers whereas the grid spacing in viscous units will depend on the Reynolds number.

8.3.1 Mandatory Low-Re Grid, $Re = 4000$

- $Re = 4000$, $64 \times 80 \times 64$ cells
- $(x^+, z^+) = (400, 200)$, 15% stretching in y-direction so that $(\Delta y^+_{min}, \Delta y^+_{max}) = (2.2, 520)$.

8.3.2 Recommended Low-Re Grids, $Re = 8000$ and 16000

- $Re = 8000$, $64 \times 96 \times 64$ cells. $(x^+, z^+) = (800, 400)$, 15% stretching in y-direction so that $(\Delta y^+_{min}, \Delta y^+_{max}) = (1.47, 1040)$.
- $Re = 16000$, $64 \times 96 \times 64$ cells. $(x^+, z^+) = (1600, 800)$, 18% stretching in y-direction the first 15 cells, then 15% so that $(\Delta y^+_{min}, \Delta y^+_{max}) = (1.85, 2090)$.

8.3.3 Recommended Wall-Model Grids, $Re = 4000$, 8000 and 16000

- $Re = 4000$, $64 \times 64 \times 64$ cells, $(x^+, z^+) = (400, 200)$, constant Δy so that $\Delta y^+_{min} = \Delta y^+_{max} = 125$.
- $Re = 8000$, $64 \times 64 \times 64$ cells, $(x^+, z^+) = (800, 400)$, 5.3% stretching in y-direction so that $(\Delta y^+_{min}, \Delta y^+_{max}) = (100, 500)$.
- $Re = 16000$, $64 \times 64 \times 64$ cells, $(x^+, z^+) = (1600, 800)$, 9% stretching in y-direction so that $(\Delta y^+_{min}, \Delta y^+_{max}) = (97, 1410)$.

8.4 Participants and Methods

The following partners have worked on this test case: Chalmers, EDF, FOI, Imperial College (ICSTM), NTS, TUB and UMIST. Below we summarize the methods different partners have used.

8.4.1 Chalmers

A hybrid LES-RANS approach is used in which a one-equation model is employed in both regions. Recommended grids are used. The matching line is prescribed along a constant grid line. Both forcing and no forcing are used. When using forcing, instantaneous turbulent fluctuations are added at the matching plane between the LES and URANS regions in order to trigger the equations to resolve turbulence. The turbulent fluctuations are taken from synthesized homogeneous turbulence assuming a modified von Kármán spectrum. More detail in Davidson and Billson (2006).

Simulations are also carried out using classical wall-functions (instantaneous log-law); in this case only “no forcing” is used.

8.4.2 EDF

Extended wall-function (pressure gradient is taken into account). LES is used in the entire domain.

8.4.3 FOI

A hybrid one-equation model. In the inner region, a RANS k equation is used and in the outer region a SGS k equation is employed. For more detail, see Peng (2005).

8.4.4 ICSTM

The LES Dynamic Model is used in the outer layer. The dynamic coefficient is averaged in the spanwise direction and filtering is applied in the periodic directions. The two-layer approach is used including all terms and 32 cells are used in the wall-normal direction. For greater detail, see Tessicini et al (2007).

8.4.5 NTS

Generalization of DDES approach to LES with wall modelling based on the SA and M-SST background RANS models. Recommended grids have been used. More detail can be found in Travin et al. (2006).

8.4.6 TUB

The model "CEASM-WMLES" (NTS method applied to CEASM-DES) is used on the recommended grids. CEAMS stands for Compact Explicit Algebraic Stress

Model and WMLES stands for Wall Modelling LES. Universal wall treatment is used (hybrid low-Reynolds/high-Reynolds wall function) allowing freedom of y^+ value of first point – defaults to low-Re B.C for mandatory grid.

8.4.7 UMIST

In Schumann's approach τ_{ij} is split into two parts

$$\tau_{ij} = -2\nu_a f(\overline{s}_{ij} - <\overline{s}_{ij}>) - 2\nu_r(1-f)<\overline{s}_{ij}>,$$

where $<\cdot>$ denotes averaging. The first part (locally isotropic part) corresponds to the fluctuating contribution to the SGS stress and the second part (inhomogeneous part) takes the wall effects into account. A blending function is introduced to achieve a smooth transition between the two parts, i.e.

$$\tau_{ij} = -2\nu_a f(\overline{s}_{ij} - <\overline{s}_{ij}>) - 2\nu_r(1-f)<\overline{s}_{ij}>$$

$$f = \tanh\left(\frac{0.46L_t}{2C_s\Delta}\right)^{1.3}$$

The first and the second term of the SGS stress correspond to the outer and inner region, respectively. The turbulent viscosity, ν_r, is obtained from mixing the length model, and ν_a is obtained from the Smagorinsky model. The averaged velocity is computed as a running average, i.e.

$$<U>=\alpha U^n + (1-\alpha)<U>^{n-1}$$

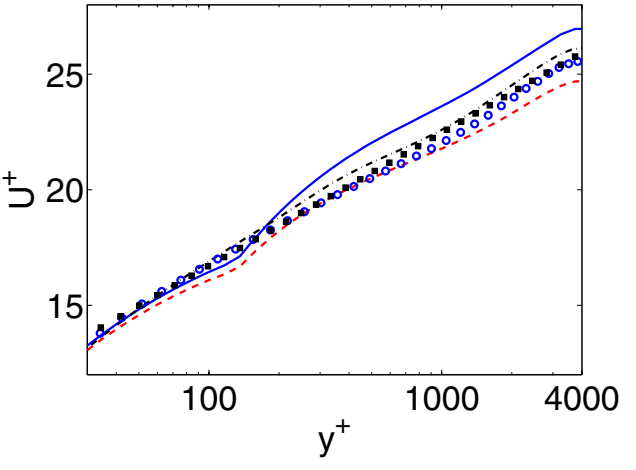

Fig. 1 *Re*=4000: Velocity profiles. Low-Re number models. Solid line: Chalmers, no forcing; dashed line: Chalmers, forcing; dash-dotted line: NTS, SST hybrid; circles: UMIST, Shuman's approach; black squares: log-law

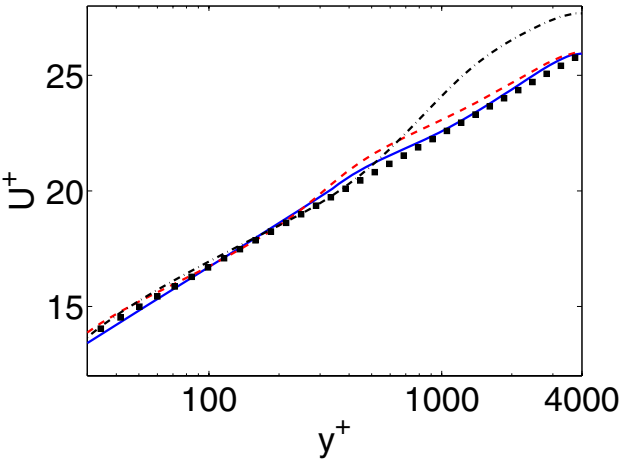

Fig. 2 *Re*=4000: Velocity profiles. Low-Re number models. Solid line: NTS, SA hybrid; dashed line: TUB, CEASM-WMLES; dash-dotted line: FOI, one-eq, black squares: log-law

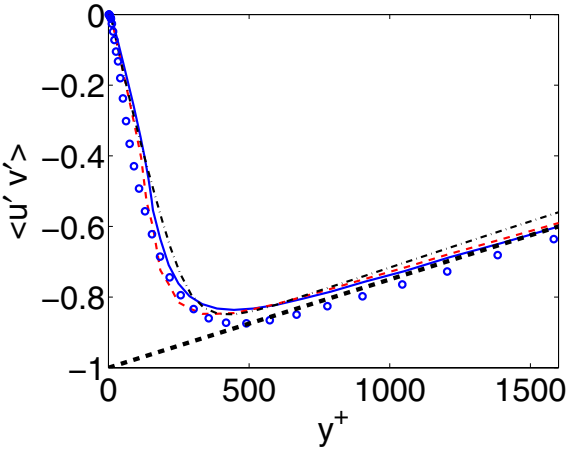

Fig. 3 *Re*=4000: Resolved shear stresses. Low-Re number models. Solid line: Chalmers, no forcing; dashed line: Chalmers, forcing; dash-dotted line: NTS, SST hybrid; circles: UMIST, Shuman's approach

8.5 Results

Figures 1–11 present the velocity profiles and the resolved and modelled shear stresses using either low-Re grids or wall function grids.

For the low-Re number grids, the predicted velocity profiles are – in general – in good agreement with the log-law. However, one-equation models (Chalmers, no forcing and FOI) give an over-prediction of the centreline velocity (or, rather,

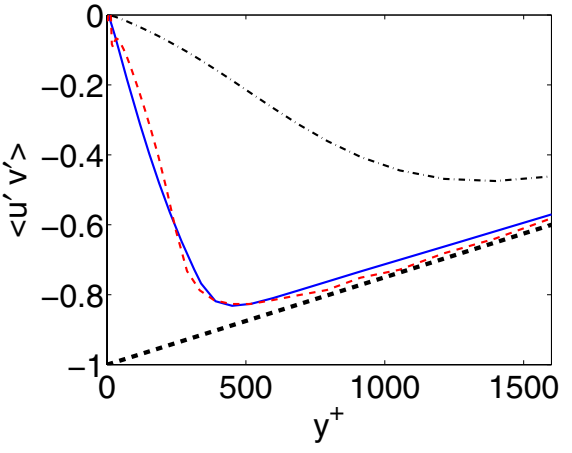

Fig. 4 *Re*=4000: Resolved shear stresses. Low-Re number models. Solid line: NTS, SA hybrid; dashed line: CEASM-WMLES, TUB; dash-dotted line: FOI, one-equ

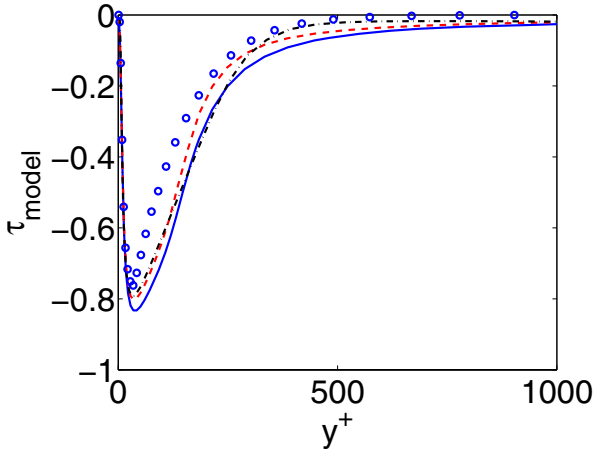

Fig. 5 *Re*=4000: Modelled shear stresses. Low-Re number models. Solid line: Chalmers, no forcing; dashed line: Chalmers, forcing; dash-dotted line: NTS, SST hybrid; circles: UMIST, Shuman's approach

over-prediction of the ratio of the centerline velocity and the friction velocity, $<\overline{u}>/u_\tau$), see Figs. 1, 2, 7a and 8a. The predicted resolved and modelled stresses are fairly similar for all models for *Re*=4000, with the exception of the one-equation model used by FOI. For this model the modelled part is much larger than for the others (Fig. 6) and, consequently, the resolved part is much smaller (Fig. 4). It can be noted that the results by TUB and the two results by NTS agree

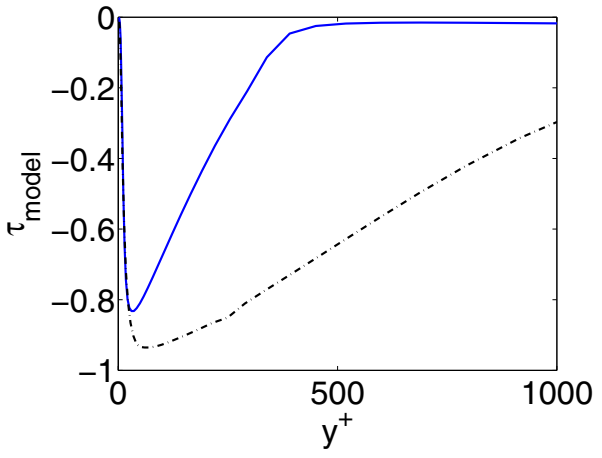

Fig. 6 *Re*=4000: Modelled shear stresses. Low-Re number models. Solid line: NTS, SA hybrid; dash-dotted line: FOI, one-equ

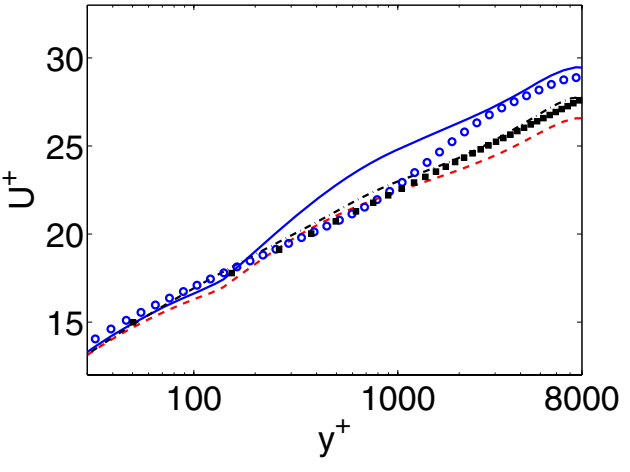

Fig. 7 *Re*=8000: Velocity profiles and resolved shear stresses. Low-Re number models. Solid line: Chalmers, no forcing; dashed line: Chalmers, forcing; dash-dotted line: NTS, SST hybrid; circles: FOI, one-equ

well with each other; the reason is that they are using the same DES but with different underlying turbulence models.

When the Reynolds number is increased (*Re*=8000 and 16000) it is clearly seen how the resolved part of the total shear stresses decreases, see Fig. 7b and 8b. Since the total shear stress must vary linearly as y-1, the modelled part consequently increases for increasing Reynolds number. For the largest Reynolds number, there is

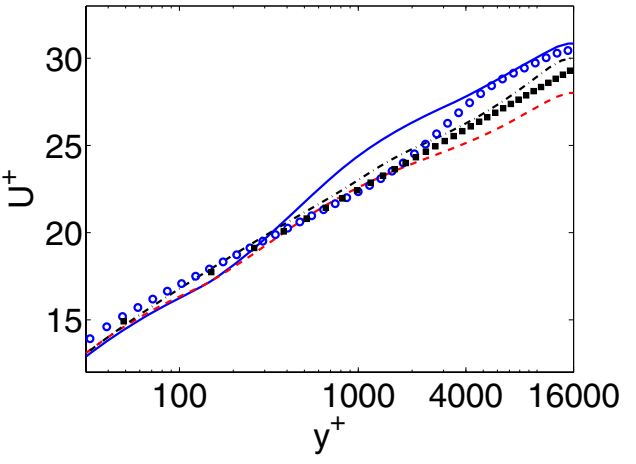

Fig. 8 *Re*=16000: Velocity profiles and resolved shear stresses. Low-Re number models. Solid line: Chalmers, no forcing; dashed line: Chalmers, forcing; dash-dotted line: NTS, SST hybrid; circles: FOI, one-equ

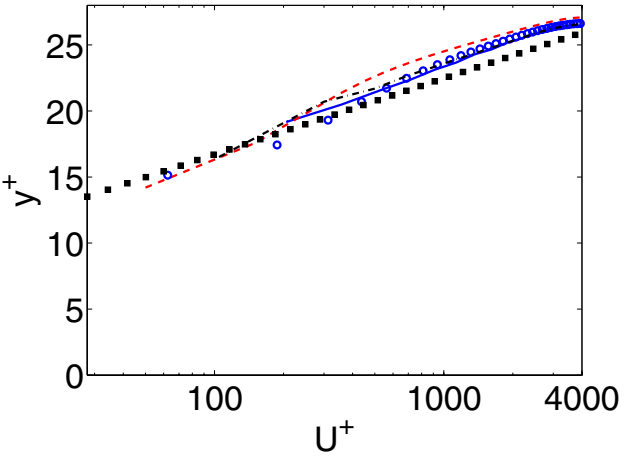

Fig. 9 *Re*=16000: Velocity profiles and resolved shear stresses. Wall functions. Solid line: ICSTM, two-layer model; dashed line: EDF, extended wall-functions; dash-dotted line: TUB, CEASM-WMLES with wall-functions; circles: Chalmers, wall-functions; black squares: log-law

a rather large difference in the predicted resolved shear stresses, see Fig. 8. The largest shear stresses are obtained with the one-equation model, with forcing. It is known that forcing increases the resolved fluctuations (Davidson and Billson, 2006). The SST hybrid model gives a smaller resolved shear stress than both one-equation models, which can be explained by the fact that the underlying turbulence

model is a RANS model. It can be noted that the difference in predicted resolved shear stresses between the one-equation model and the SST hybrid model is somewhat smaller for *Re*=8000 (Figs. 7b) and very small for *Re*=4000 (Fig. 3).

Turning to the wall functions, the predicted velocity profiles are in good agreement with the log-law for Reynolds number of 4000, see Fig. 9a. When the Reynolds number is increased, the agreement deteriorates. At Reynolds number 8000 (Fig. 10a), the wall functions (Chalmers and EDF) yield somewhat too small

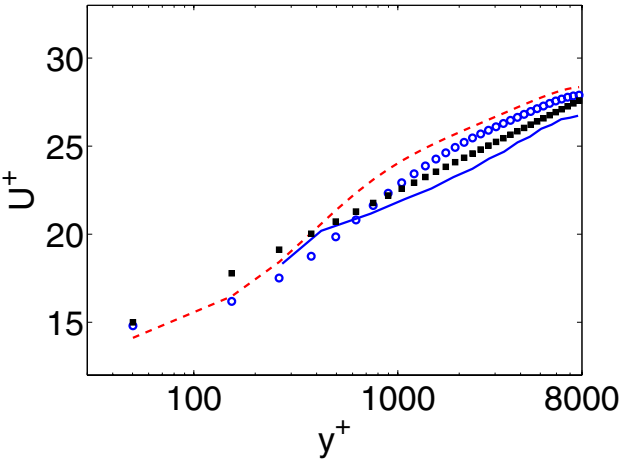

Fig. 10 *Re*=8000: Velocity profiles and resolved shear stresses. Wall functions. Solid line: ICSTM, two-layer model; dashed line: EDF, extended wall-functions; circles: Chalmers, wall-functions; black squares: log-law

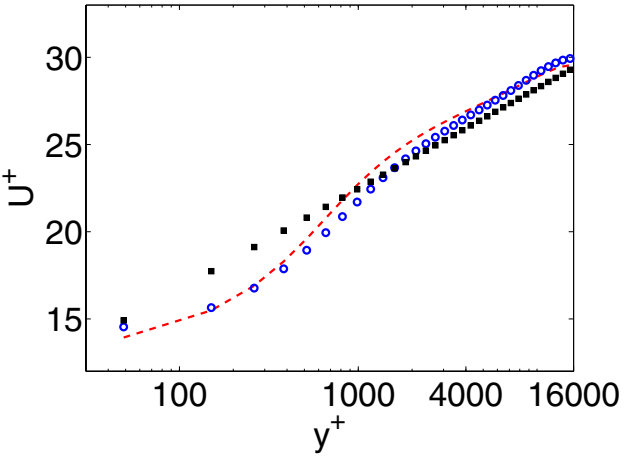

Fig. 11 *Re*=16000: Velocity profiles and resolved shear stresses. Wall functions. dashed line: EDF, extended wall-functions; circles: Chalmers, wall-functions; black squares: log-law

velocity in the inner region ($y^+ < 400$) whereas the two-layer model gives too low velocity in the outer region ($y^+ > 500$). The underprediction of the velocity in the inner region becomes slightly worse at Reynolds number 16000, see Fig. 11a, at which the velocity is too small for $y^+ < 1000$. The Reynolds number effect is clearly seen in the resolved shear stresses, Figs. 9b, 10b and 11b: the higher the Reynolds number, the smaller the resolved shear stress – and, consequently, the larger the modelled part – near the wall.

8.6 Concluding Remarks

A number of hybrid LES-RANS models and DES wall models have been evaluated for high-Reynolds number channel flow. Both low-Re grids and wall functions grids have been used.

- The DES approach proposed by NTS is found to give good results at all Reynolds numbers; the fact that another partner – TUB – has implemented the approach of NTS and obtained results that agree well with those of NTS further strengthens the conclusion.
- Most models behave reasonably when the Reynolds number is increased: the modelled content increases and the resolved content decreases.
- Classical wall functions based on the instantaneous log-law work surprisingly well, both when used in pure LES or in hybrid LES-RANS.

9 Bump in Square Channel (ONERA Experiment)

F.R. Menter and Y. Egorov

ANSYS Germany GmbH

Abstract. An experiment was conducted in the course of the DESIDER project by ONERA. The geometry is a diffuser with a low aspect ratio. The goal was to have a reference testcase with a large separation zone and a three-dimensional mean flow topology. This distinguishes this testcase from other cases, which have been set-up for nominally two-dimensional flow. Three-dimensionality was achieved in this experiment by a relatively low width to height ratio (10/3 at the inlet and 5/3 at the outlet). This experiment has been computed with a wide range of numerical methods and physical models. The results of the experiment and the simulations will be compared in this chapter.

9.1 Introduction

The bump shape and the flow parameters for this experiment were selected in a way, which resulted in a significant separation zone in the middle part of the channel at the bump end. Preliminary CFD simulations were carried out at ANSYS Germany in order to estimate the desirable bump shape. A flow solver ANSYS-CFX was used for these simulations. The main challenging tasks of the designed test case are the correct prediction of the separation location from a smooth curved surface, the fast development of the resolved turbulent content in the separated shear layer, and the adequate simulation of the influence of corner vortices on the separation zone in the middle. Figure 1 illustrates the flow structure with the mean stream lines and the mean separation zone boundary, as predicted with an ω-based Reynolds Stress turbulence model.

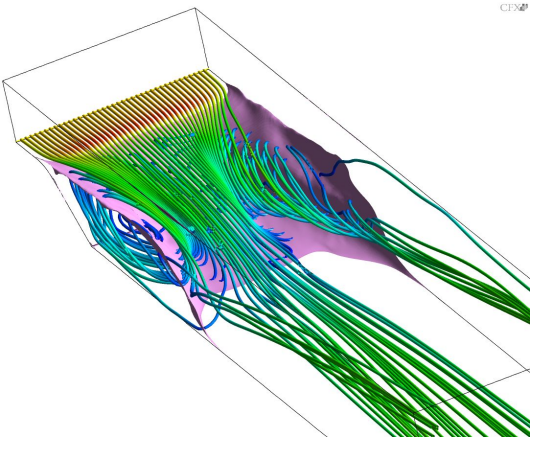

Fig. 1 Time-averaged flow configuration near the separation zone after the bump

This chapter summarises and compares the simulation results obtained by the test case participants: ANSYS, Chalmers University, FOI, NLR, NTS, Numeca, and TU Berlin. Details on the experiment are given in Chapter III.1.

9.2 Physical Properties and Boundary Conditions

According to experimental conditions, water with density of 997 kg/m3 and dynamic viscosity of 0.89·10-3 kg/m/s was used as work fluid. The following boundary conditions, corresponding to the experiment, were provided to all partners:

- Inlet: specified distributions of the Cartesian velocity components, and of the turbulence variables (k and ω provided by ANSYS see below).
- Outlet: specified averaged static pressure.
- Bottom, top, and side walls: no-slip boundary conditions.

The inlet plane is located at X=-0.367 m relative to the end of the bump. LDV-measured mean velocities U and V, as well as the Reynolds stresses $\overline{u'u'}, \overline{v'v'}, \overline{u'v'}$ have been provided by ONERA for this plane along nine lines Z=const and seven lines Y=const. In order to supply the boundary condition data the whole inlet plane, a special RANS simulation for the upstream part of the bump geometry was performed by ANSYS using the ω-based Reynolds stress transport model of the ANSYS-CFX solver. The resulting velocity distribution was then additionally multiplied by an analytic correction function f(y) to exactly match the measured velocity profile in the boundary layer and in the core flow in the central plane. Figure 2 (left) shows the velocity profiles along the central line Z=0 of the inlet plane. The calculated and then corrected velocity distribution fits well with the

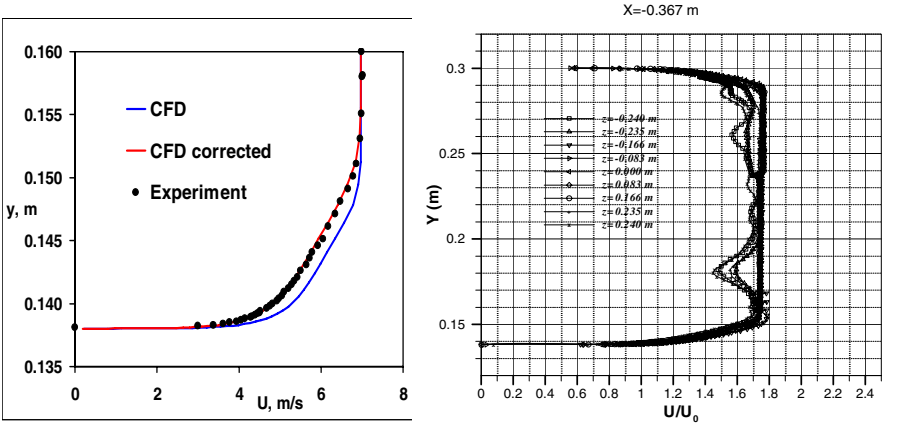

Fig. 2 Adjustment of the computed velocity profile on the bump surface to the LDV measurements (left). LDV-measured velocity profiles along the vertical lines z=const at the inlet plane (right)

measured profiles far from the side walls. Near the side walls, however, the measurements clearly indicate vortex traces, as shown on Figure 2 (right). Since the source of these vortices was not clearly identified, it was decided to ignore them when specifying the inlet boundary conditions. It should be kept in mind that the experimentally observed side vortices can in principle become a source of uncertainty.

9.3 Grid Information

A hexahedral grid of around 4 million nodes (221×121×150), provided by ANSYS, is shown on Figure 3. The grid is refined to all the walls providing for an average y^+ value of around one.

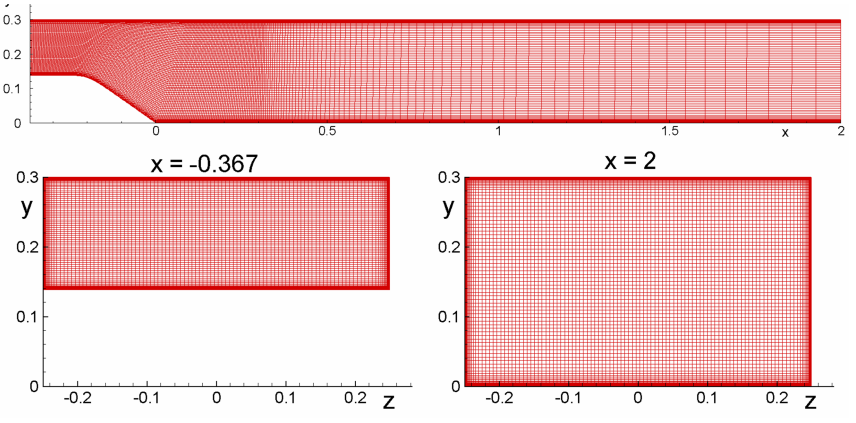

Fig. 3 Computational domain and grid

This grid was used by all partners except for NLR, although some of them slightly changed the number of nodes for the sake of the multi-grid methods. NLR has used a two times coarsened grid in each direction (110×60×76).

9.4 Participating Partners, Turbulence Models, and Simulation Details

Table 1 provides for a summary of the test case participants, the models used, as well as the time step information. Figure 4 gives a representative Courant number snapshot at the central plane, corresponding to the time step value of 1 ms.

In all simulations, except for the second simulation by Uni. Chalmers, steady inlet boundary conditions have been used according to the supplied inlet data arrays.

Table 1 List of participants, models, and time step information

Partner	Turbulence model	Time step, ms	Averaging time, s
Uni. Chalmers	HybridLES-RANS, steady inlet BC Hybrid LES-RANS, fluctuating inlet BC	0.42 0.42	12 10.9
FOI	Hybrid LES-RANS (zero-eq. HYB0 model)	0.4	6.5
NLR	X-LES	1.886	3.9
NTS	SST-DDES	0.465	2.8
Numeca	Spalart-Allmaras DES-97	1.0	3.2
TU Berlin	CEASM-DDES SAE-DDES SAE-WMLES	0.8 0.5 0.5	7.2 3.0 2.8
ANSYS	SST-SAS	0.5	7

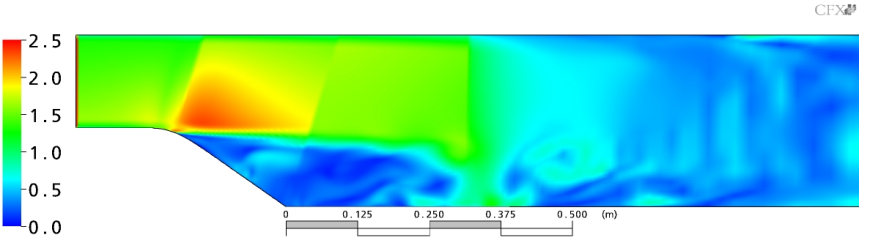

Fig. 4 Typical instantaneous distribution of the Courant number, obtained with the time step of 1 ms

9.5 Results of Simulations

The calculated results are compared to each other and to the measurements in the following paragraphs. The following results are included:

- Mean pressure distribution along the bottom central line z=0.
- Mean velocity profiles at the selected locations x=const on the central plane.
- Profiles of the principal Reynolds stress $-\overline{u'v'}$ at the same locations as the mean velocity profiles.
- Selected 2-D and 3-D plots: distribution of the resolved kinetic energy of turbulence over a central plane, mean streamlines in cross sections of the channel, instant resolved turbulent vortex structures.

9.5.1 Mean Pressure Distribution along the Bottom Wall

The time averaged pressure distributions are shown on Figures 5. The results of TU Berlin CEASM-DES, NTS, FOI and ANSYS agree well with one-another, but are shifted with respect to the experiments. The results from TU Berlin (SAE-DDES and SAE-WMLES), also agree with one-another, but are shifted even more upstream, which is probably due to the accuracy of separation prediction by the RANS part of these hybrid models. Note that an upstream shift in the cp-distribution indicates a reduced separation zone in the centre of the channel.

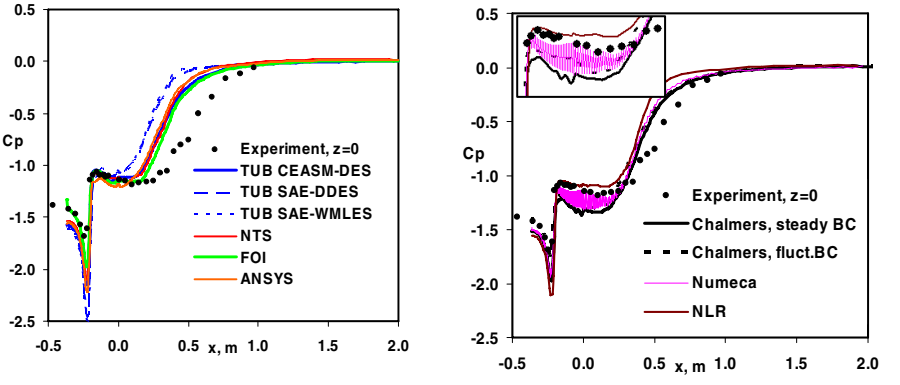

Fig. 5 Mean pressure distribution along the central line of the bottom wall

The second group of lines by Chalmers, Numeca and NLR are closer to the exp. data, as seen on Figure 5 (right). The grid oscillations on the result by Numeca indicate the too high weight of the central different scheme in the RANS region. The non-monotonous pressure curve, obtained by Chalmers with the steady inlet boundary conditions, reflects a local secondary separation near the corner towards the end of the bump.

A common trend in all simulations is the under-predicted length of the separation zone. The results of the second group are a bit closer to the experimental data, however from the pressure distribution alone one cannot draw any conclusion about the reason for this difference. The comparison will be continued in the next paragraphs, showing the profiles of the velocity and the principal Reynolds stresses.

9.5.2 Mean Velocity Profiles

The following four locations on the central plane were selected from the available measurement data: x=-7.9 cm, 15 cm, 25 cm, 35 cm (0 cm corresponds to bump slant junction with the bottom wall). More details can be found in Peng and Haase (2007).

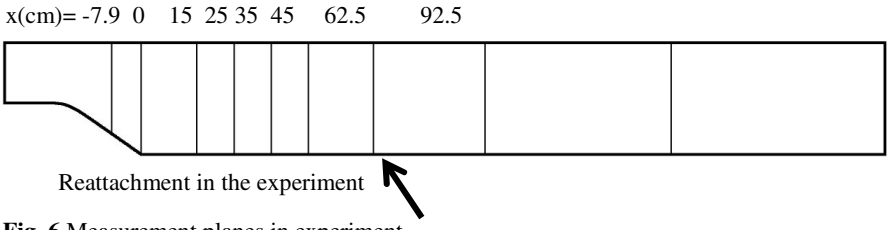

Fig. 6 Measurement planes in experiment

The measured reattachment point is located in the region 63 cm to 65 cm according to the LDV velocity profiles. As shown on Figures 7-8 below, all simulations predicted the reattachment much earlier, at around x=40 cm. The results are shown in two groups:

1st group : NTS, TUB, FOI
2nd group : Chalmers, Numeca, NLR, ANSYS

Most velocity profiles of the first group in Figure 7 correlate closely with each other, except for the two simulations by TUB performed with the Spalart-Allmaras based models. The over-predicted velocity defect at the upper wall in the result by FOI is probably caused by the LES influence on the RANS solution inside the boundary layer there. The second group of profiles are shown on Figures 8. The differences between the different simulations are clearly visible, with a tendency for larger separation bubbles in the second group. It is somewhat disturbing that the different solutions already differ significantly at the first measuring station.

9.5.3 Profiles of the Reynolds Stresses

Profiles of the computed total Reynolds stresses (resolved plus modelled) are compared here with each other as well as with the experimental results at the same locations on the central plane as those used for the velocity profiles in the previous paragraph. The measured profiles reveal a systematic deviation between the LDV and the PIV techniques, which is clearly visible in Figures 9-10. This deviation manifests itself as in the maximal stress magnitude (x=15 cm), as well as in the vertical displacement between the LDV and the PIV stress maxima (x=25 cm). For a discussion, see Chapter III.1.

As for the velocity profiles, the Reynolds stress profiles are shown in two groups:

1st group: NTS, TUB (only CEASM-DES), FOI
2nd group: Chalmers, Numeca, NLR, ANSYS

Only the best result by TU Berlin is included for the comparison here, since the two other simulations have delivered pressure distributions and velocity profiles too far from all the other simulations and also from the measurements.

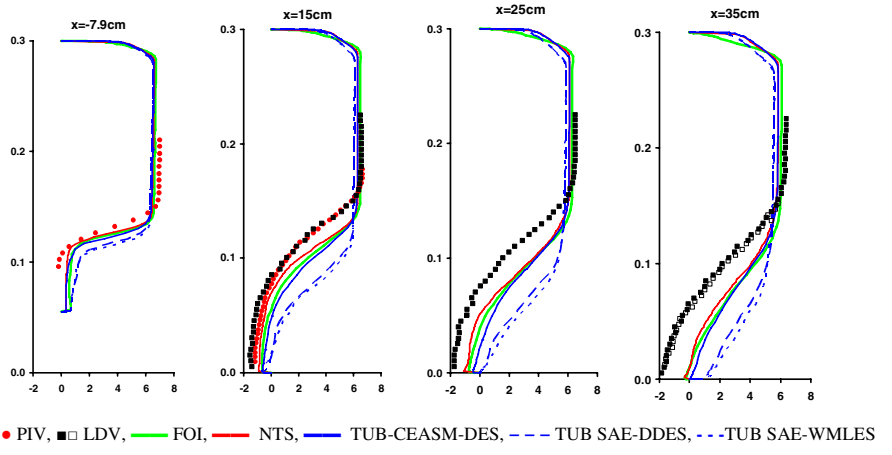

Fig. 7 Mean velocity profiles at the central plane, first group of results

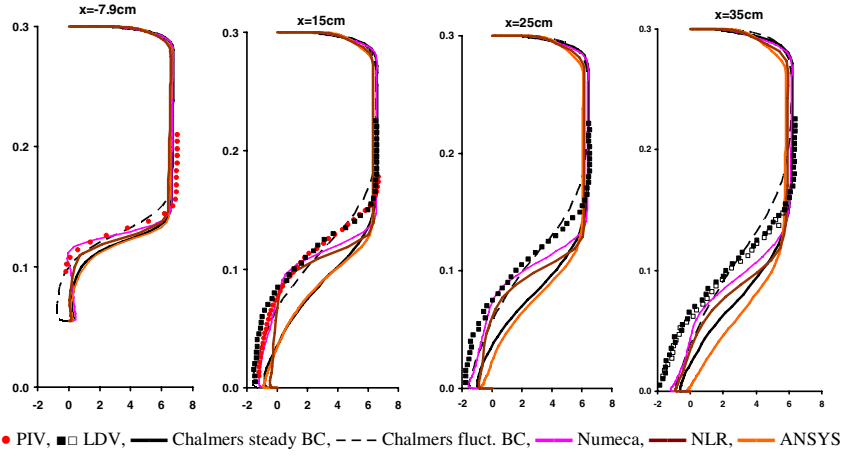

Fig. 8 Mean velocity profiles at the central plane, second group of results

In general, the profiles of the first group agree well with each other, see Figure 9. The difference between them is visually larger than the difference between the corresponding velocity profiles on Figure 7, because the Reynolds stress is a more sensitive quantity of the solution. A strong kink near the upper wall in the stress profile by TU Berlin at x=-7.9 cm was probably caused by a local numerical instability above the bump slant. The non-monotonous shape of the profiles by NTS may indicate an insufficient averaging time.

The second group of profiles is shown on Figure 10. The same common conclusion as that drawn from the velocity comparison applies also to the stresses.

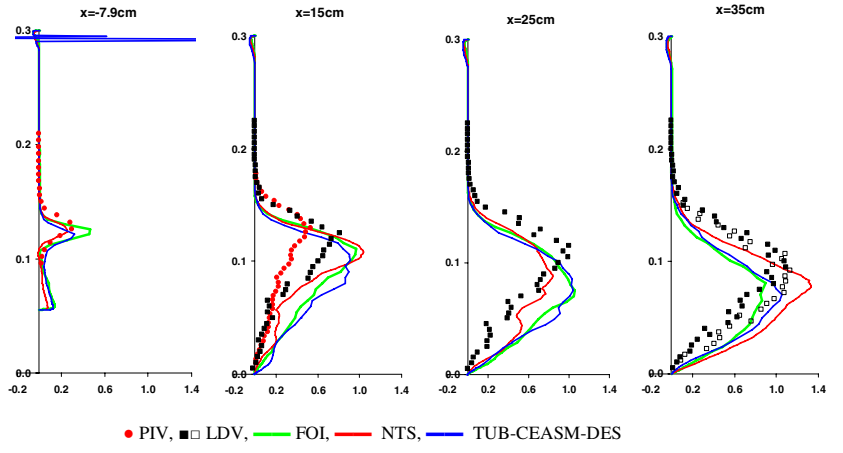

Fig. 9 Profiles of the Reynolds stresses (resolved plus modelled) at the central plane, first group of results

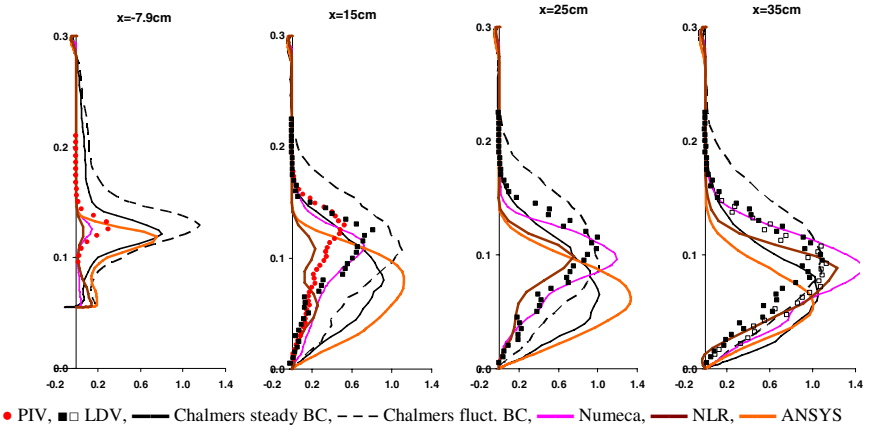

Fig. 10 Profiles of the Reynolds stresses (resolved plus modelled) at the central plane, second group of results

Namely, the disagreement between the different simulations does not normally exceed the deviation between the measured profiles. The result by Chalmers, obtained using the fluctuating inlet boundary conditions, appear different from all other results. Also the stress values by ANSYS noticeably exceed the other predicted stresses in the separation zone, locations x=15 cm and x=25 cm on Figure 10. This may be partially explained by the way of estimating the average modelled stress $\nu_t S_{ij}$. In the simulation by ANSYS the whole term was averaged rather than the eddy viscosity and the velocity gradients separately, as done by some of the other partners.

In general, compared to the experiment, the calculated location of the free shear layer is shifted down in most simulations. This is yet another indication of the too early reattachment in the simulation results.

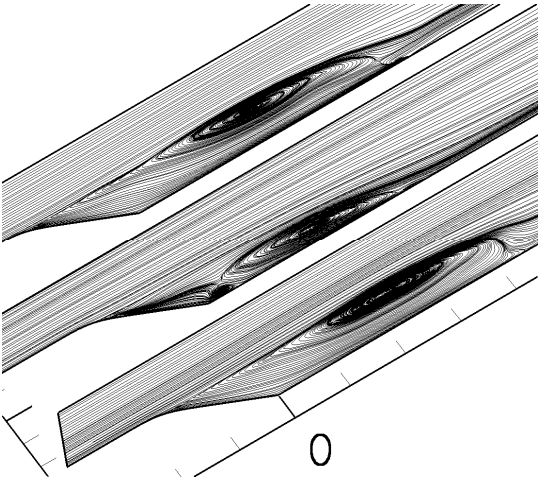

Fig. 11 Mean flow streamlines at central plane and planes z = ±20 cm, calculated by FOI

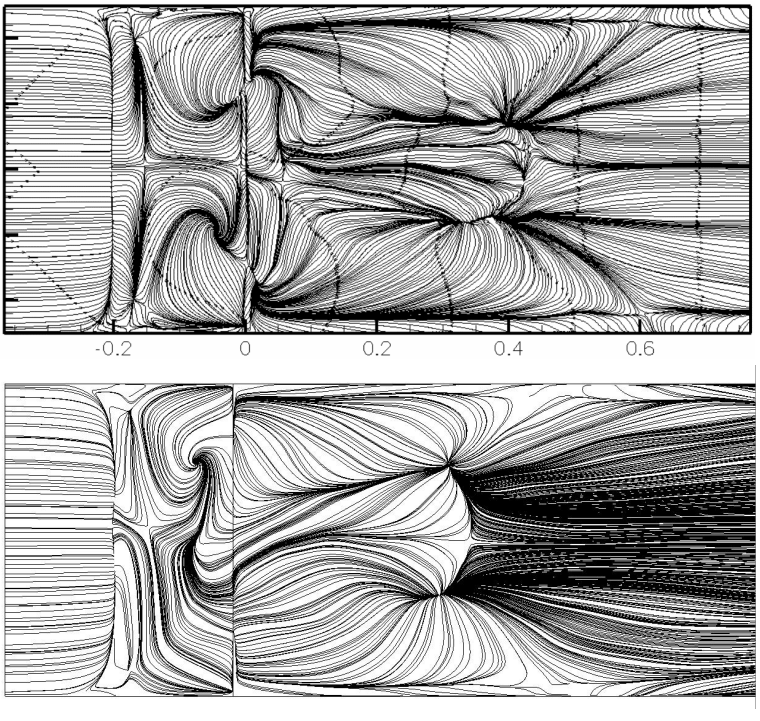

Fig. 12 Bottom wall skin friction pattern of the average flow, calculated by FOI (upper picture) and ANSYS (lower picture)

9.5.4 Two- and Three-Dimensional Visualisation

In this paragraph only few representative plots are shown, which illustrate the particular features of the simulation results.

The streamlines at the central plane show a secondary separation in the results by FOI, as seen from Figure 11. A small secondary separation zone is also produced by the NTS simulation. Liquid crystal visualisation indicated a secondary separation in the experiment. The meanflow fields by NLR, TU Berlin and ANSYS do not clearly show a secondary separation zone, although for some results this conclusion is not fully certain because of the insufficient transient averaging.

The 3-D structure of the mean flow is well illustrated by the skin friction pattern of the average flow on the bottom wall, see Figure 12. A 3-D secondary separation zone is clearly visible in the FOI results. It is important to point out that the primary separation line near the start of the bump is significantly three-dimensional near the side walls. This indicates that the flow separates earlier in the corner than in the middle of the channel in both simulations. Two strong counter-rotating vortices emanate from these corners at the onset of the bump. They have a dominating effect on the flow as they produce a downwash in the central plane.

Figure 13 shows the mean flow streamlines for four cross section planes for the NTS results (other models produced similar topologies):

- x=0cm – end of the bump;
- x=32 cm – shortly before the calculated reattachment in the middle of the channel;

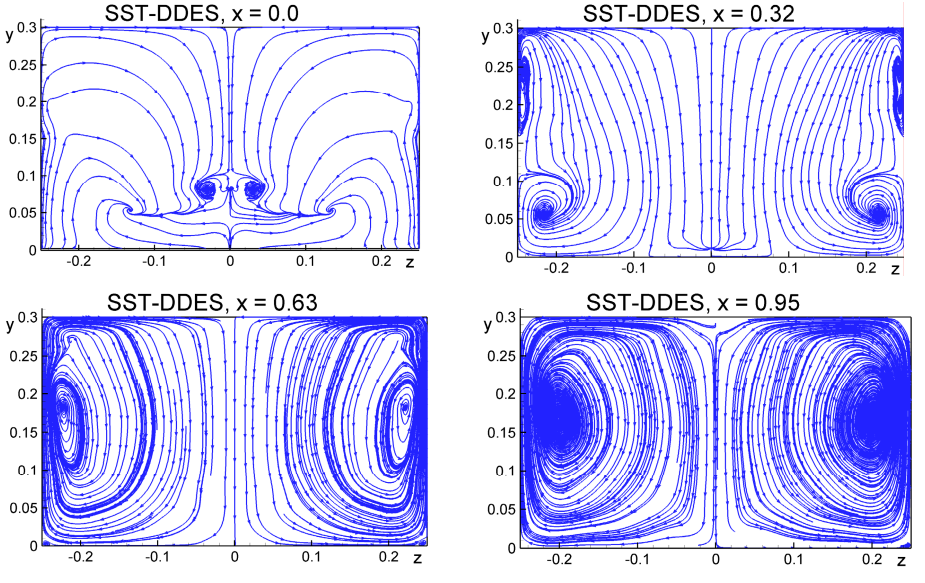

Fig. 13 Mean flow streamlines on the cross section planes – NTS

- x=65 cm – after the calculated reattachment;
- x=95 cm – recovery region.

Figure 12 shows the formation of two strong counter-rotating vortices, which produce a substantial downwash in the central portion of the domain.

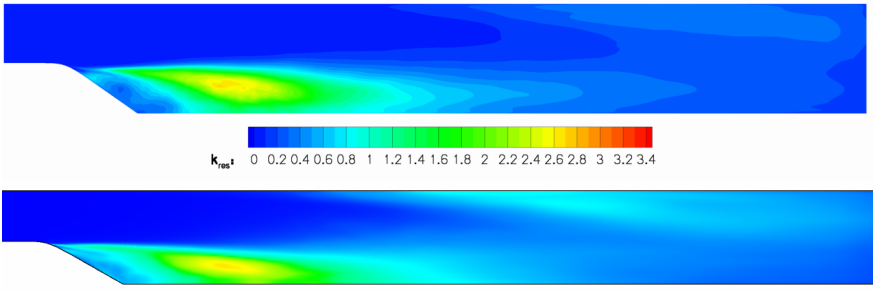

Fig. 14 Time-averaged resolved kinetic energy of turbulence: upper picture – DES by TUB, lower picture – SAS by ANSYS. The same colour scale applies to both pictures

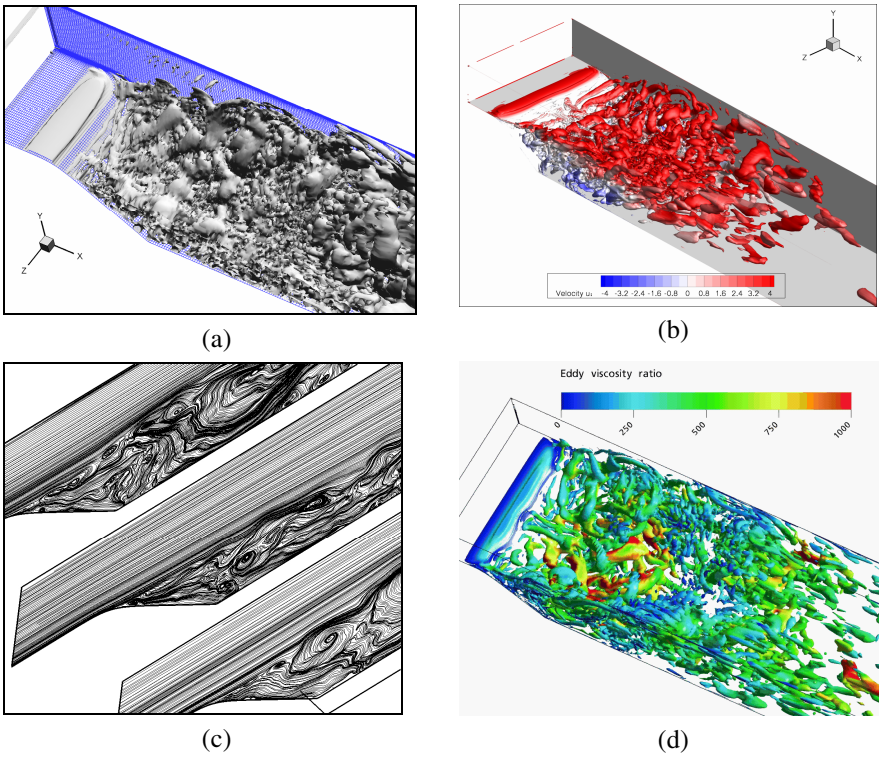

Fig. 15 Resolved instant turbulent structures: (a) – NTS, half of the domain, (b) – TU Berlin, (c) – FOI, (d) – ANSYS

In order to compare the turbulence resolving capabilities of DES and SAS, the time-averaged resolved kinetic energy is plotted in Figure 14 for the DES result by TU Berlin and the SAS result by ANSYS, using the same colour scale. These two plots show very close distributions, obtained on the central plane.

Finally, the instantaneously resolved flow structures for some selected results are shown on Figure 15.

9.6 Discussion

All simulations carried out for the full geometry show similar tendencies. They produce a shallower separation zone and underpredict the length of the separation in the central plane. It is interesting to point to a simulation carried out by Chalmers during the project, using modified boundary conditions. Instead of simulating the entire channel including the side walls, Chalmers performed a simulation with periodic conditions on the spanwise direction (see Peng and Haase, 2007). Interestingly, this simulation produced a markedly better agreement with the data than the full three-dimensional studies, as can be seen in the C_p distribution shown in Figure 16 (left). One of the main differences of a periodic simulation is that it does not produce the vortex pair seen in Figure 13, as these emanate from the side walls.

One could therefore argue that a possible cause of the observed deficiencies of the simulations with side-walls could come from an overestimation of the strength of these vortices. One reason could be that the models predict an early corner separation upstream of the bump (see the three-dimensional separation line in Figure 12). This is supported by the liquid crystal flow visualization of the experimental separation line also shown in Figure 16 (right), which is nominally two-dimensional. It is known that eddy-viscosity models cannot account for the momentum transfer by secondary flow into the corner (square duct). This deficiency can in turn cause early separation on corners. This could be the cause of a

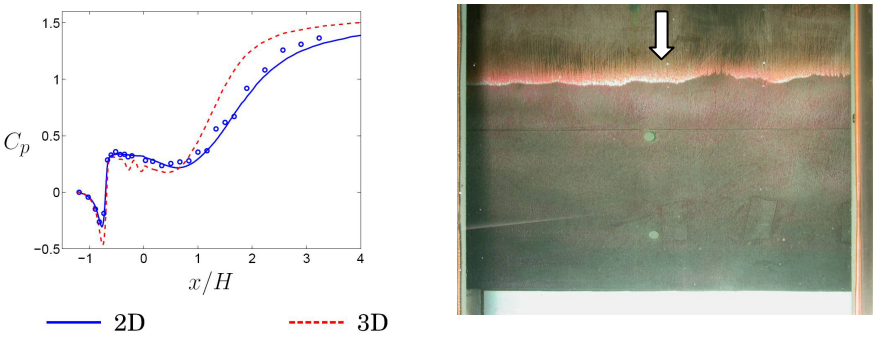

Fig. 16 Left: Wall pressure distribution (C_p) along centre line of bottom wall for quasi 2D (spanwise periodicity) and full 3D simulation from Chalmers. Right: Flow visualization of separation line in experiment

potential over-prediction of the strength of the corner vortices. In the current hybrid models, the primary separation line is computed by the RANS portion of the model (i.e. an eddy-viscosity model) making the results susceptible to such potential errors.

9.7 Conclusions

Ten transient simulations have been performed by seven project partners, using DES, SAS and hybrid LES-RANS models. Most of the results reveal satisfactory turbulence resolution quality of the separation zone in the middle of the channel. However in all simulations the separation zone length was under-predicted relative to the measurements. The two possible reasons for this trend are identified:

- Vortex traces in the experiment in the inlet plane, which have not been addressed by the inlet boundary conditions for the CFD simulations.
- Over-predicted strength of the side vortices behind the bump in CFD simulations. This can be caused by the insufficiently accurate calculation of the separation location at the side walls by the RANS parts of the hybrid models.

More definitive conclusions would require a very detailed experimental study of the inlet part of water tunnel. It would also be desirable to have more experimental information on the flow topology (oilflow measurements etc.). From the numerical side, grid refinement studies would be desirable. In general, the observed good correlation of different CFD results with each other is an indication of the consistency of the unsteady portion of all models used in the study. Following the argument in the discussion section, the differences to the experiments might result in the end from the RANS portion of the model formulations. This argument will have to remain speculative unless more detailed experimental data become available.

10 Supersonic Base Flow

A. Garbaruk, M. Shur, M. Strelets, and A. Travin

NTS

10.1 Introduction

A supersonic flow downstream of a blunt-based cylinder is characterized by a very complicated vortical structure of the base near wake, which includes a separated shear layer, recirculation zone, recompression region, and trailing wake subjected to strong compressibility effects. Other than that, the geometry is axisymmetric, which makes its computation more difficult in terms of both turbulence representation and numerics. Finally, this kind of flow is commonly found behind such objects as missiles, rockets, and projectiles, and the low pressure found behind the base causing "base drag" can be a sizable portion of the total drag. Thus, a capability of a turbulence model to predict the base pressure accurately is of significant practical importance. For these reasons, experimental data on such a flow obtained in the study of Herrin and Dutton (1994) present an attractive database for validation of innovative turbulence simulation approaches. All these and, also, availability of the experimental data in a digital form motivated including this flow in the list of DESider test cases.

10.2 Test Case Presentation

The flow is a near wake of a circular cylinder with adiabatic walls aligned with a uniform supersonic flow (see sketch in Fig.1). The flow parameters the experiments of Herrin and Dutton were performed at are presented in Table 1.

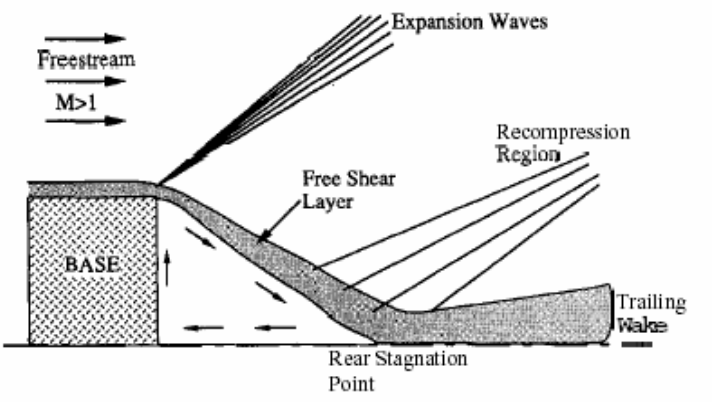

Fig. 1 Schematic of the supersonic flow in the near wake of the cylinder

Table 1 Major parameters of Herrin and Dutton (1994) experiment

Parameter	Notation	Value
Reynolds number	$\mathrm{Re}=U_\infty R/\nu$	$1.632\mathrm{x}10^6$
Cylinder radius	R	0.03175 m
Free stream Mach number	M	2.46
Stagnation Temperature	T_s	293 K
Free stream velocity	U_∞	564.2 m/s
Free stream temperature	T_∞	131 K

The flow quantities measured in the experiment and available for a comparison with results of computations include a radial distribution of static pressure over the cylinder base, $C_p(r)$, and velocity, Mach number, and Reynolds shear stress fields in the near wake.

10.3 Participants and Methods Used

A list of the partners who computed this flow and key-information on turbulence modelling approaches, numerical methods, and computational grids they used are presented in Table 2, and Figs.2-5 give an idea on the grids topology and size of the computational domain.

Table 2 Summary of simulations

Partner	Model	Numerics		Grid size and type	Time Step/Sample
		Space	Time		
DLR	S-A DES	AUSMDV	LUSGS	3.6, str. (NTS)	0.0935/37
FOI	RANS S-A	2nd ctr.	Impl.	0.9, unstr. (DLR)	Steady
	S-A DES		2nd Impl.		0.045/375
	HYB0				0.045/450
				1.8, str. (FOI)	0.0464/140
NTS	RANS S-A	3rd upw.	Impl.	1.8, str. (NTS)	Steady
	RANS S-A with Compressibility Correction				Steady
	S-A DES	3rd upw/ 4th ctr.	2nd impl.	1.8, str. (NTS)	0.01/200
	S-A DES			3.6, str. (NTS)	0.01/115
ONERA	Zonal S-A DES (C_{DES}=0.4)	AUSM+(P)	2nd Gear	14.0 (ONERA)	0.018/n.a.

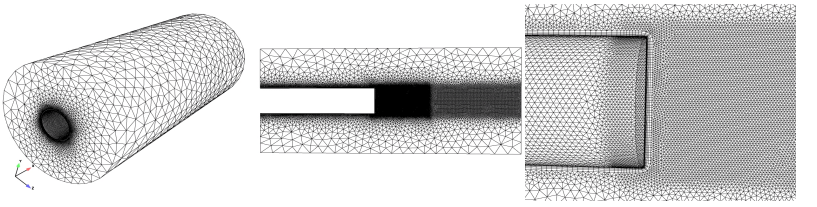

Fig. 2 DLR unstructured grid, 0.9 M nodes, 18 prismatic layers near the surface. Computational domain: L_x= (8R + 10R), L_r = 4.15R

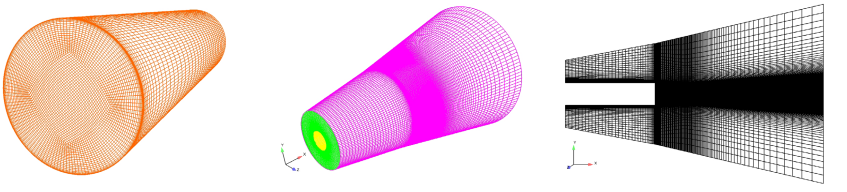

Fig. 3 FOI structured grid, 1.8 M nodes. Computational domain: L_x=(8R+15R), L_r=(3-8)R

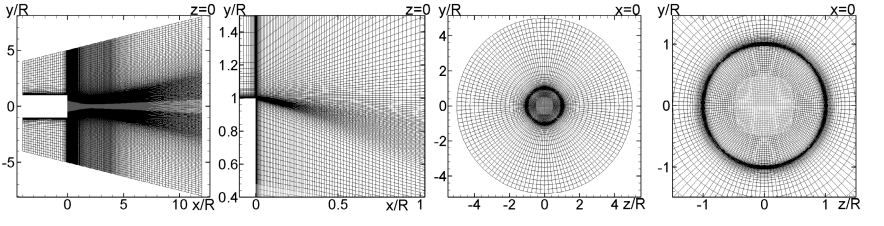

Fig. 4 NTS multi-block structured grids: coarse 1.8 M nodes; fine 3.6 M nodes. Computational domain: L_x=(4R+12R), L_r=(4-8)R. N_ϕ=128 in the outer block of the fine grid and 96 in the coarse one

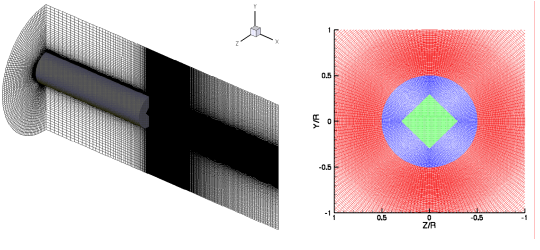

Fig. 5 ONERA structured multi-block gird, 14 M nodes. Computational domain: L_x=(8R+10R), L_r=4.15R. N_ϕ=180

The inflow boundary conditions include imposing streamwise velocity profile. In the simulations it has been adjusted to match the available experimental profile at x/R=-0.0315. Figure 6 shows to what extent different partners have reached this. One can see that in the simulation of FOI the inlet velocity profile noticeably

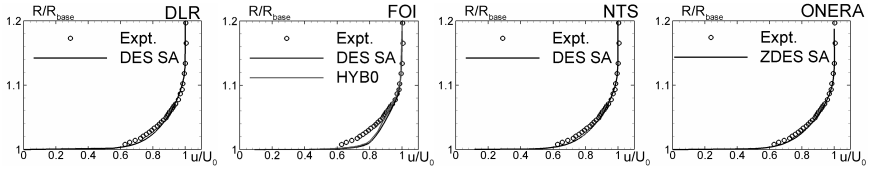

Fig. 6 Computed and experimental velocity profiles at x/R=-0.0315

deviates from the data. This should be kept in mind when analyzing results of the simulations presented below.

10.4 Results and Discussion

10.4.1 RANS Solutions

RANS computations of the flow were carried out by FOI and NTS with the use of the standard S-A model. In addition NTS carried out the computation with the use of the S-A model with the compressibility correction of Spalart (2000). Obtained RANS solutions are used as a baseline for evaluation of the turbulence-resolving approaches as applied to the base flow, since they permit to find out whether these, much more computationally expensive, approaches really overpass RANS-based modelling in terms of accuracy.

Figure 7 compares all the three solutions with each other and with the experimental data. It suggests that, despite somewhat different inlet velocity profiles (see Fig.6), results obtained by FOI and NTS with the use of the standard S-A model are close to each other, which supports a credibility of the model implementation in both flow solvers. Other than that, the figure clearly demonstrates a positive effect of the compressibility correction (dashed lines in the figure). However, even with this correction, the agreement of the RANS predictions with the data remains far from perfect, especially as far as the base-pressure is concerned: unlike virtually constant C_p in the experiment, RANS predicts a "wavy" C_p profile deviating from the data by up to 25%, which is typical of all the RANS computations of the massively separated flows over bluff bodies.

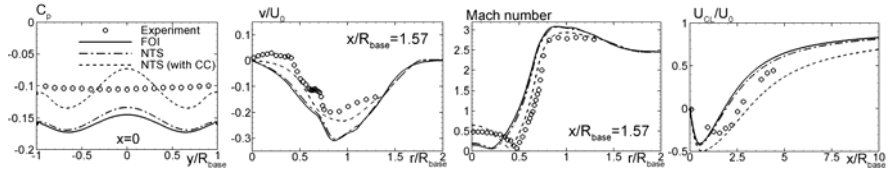

Fig. 7 RANS solutions obtained with different models and codes. (a): radial pressure distribution at the cylinder base; (b) and (c): radial velocity and Mach number profiles in the near wake; (d): streamwise velocity distribution along the wake centreline

10.4.2 Turbulence-Resolving Simulations

These simulations were carried out with the use of three approaches (see Table 2): the standard S-A DES (DLR, FOI, NTS), zonal S-A DES of Deck (2005), (ONERA), and an algebraic hybrid RANS-LES model HYB0 of Peng (2005), (FOI).

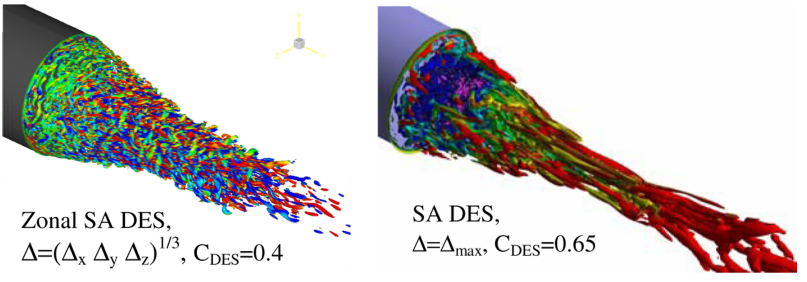

Fig. 8 Flow visualizations from zonal S-A DES of ONERA and S-A DES of NTS (fine NTS grid)

Figure 8 compares resolved turbulence structures from the zonal DES of ONERA and the S-A DES of NTS. One can see that both approaches provide for a realistic representation of the complex vortical structure of the considered flow. Also, it clearly demonstrates that the very fine grid used by ONERA provides for a resolution of much smaller eddies in the separated shear layer thus suggesting a severe need of a fine grid in this flow region. Note, however, that this effect (resolution of the much smaller eddies) is partially reached by the use of the cube root of the cell size and a smaller C_{DES} constant (0.4 versus 0.65) for the sub-grid scale in the LES zone of the ONERA simulation, which may cause some inaccuracy of turbulence representation.

A common feature of the DLR, FOI, and NTS simulations is that they suffer from some asymmetry of the mean flow. This is seen in Fig.9, where the contours of the time-averaged streamwise velocity at two wake's sections are presented from the NTS coarse and fine grid simulations. The figure shows also that with the restricted grid-refinement (2 times increase of the total nodes count) the asymmetry almost does not diminish. However, the simulation of ONERA with the much finer grid in the shear layer produces a virtually symmetric mean flow. Thus, exactly the insufficient resolution of the shear layer is responsible for the asymmetry of the DLR, FOI, and NTS mean flow predictions. Unfortunately, this asymmetry virtually rules out a consistent comparison of the mean flow calculations with the use of different approaches without averaging of the solutions over the azimuthal direction ϕ. This circumstance had not been foreseen in the beginning of the work on this test case, and so not all the partners saved the flow parameters needed for the averaging in the course of their simulations. For this reason, in the following discussion, if ϕ-averaged fields are not available, we were forced to present sectional fields.

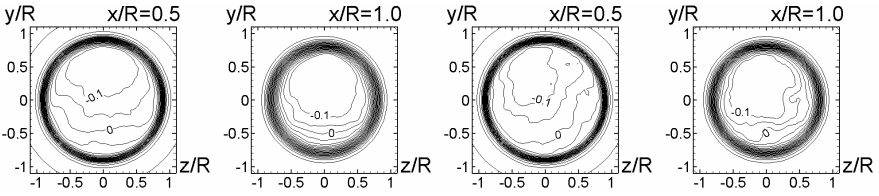

Fig. 9 Time-averaged streamwise velocity u/U_0 from NTS S-A DES on coarse (two left frames) and fine (two right frames) grids

The following figures give an idea on the effect of modelling approach, grid, and numerics on the quality of obtained solutions and their agreement with experiment.

Figure 10 shows the instantaneous vorticity fields from all the simulations. It suggests that independently of the modelling approach (either S-A DES or HYB0) the coarse unstructured DLR grid with 0.9 million nodes does not resolve any fine turbulent structures. With the fine NTS grid (3.6 million nodes), both DLR and NTS flow solvers permit to resolve much finer vortical structures, but NTS numerics are less dissipative. Same comment is true with regard to the FOI solver: the resolution it provides on the FOI structured grid, which is very close to the NTS coarse one, is quite a bit worse than that provided by the NTS solver. These findings are quite consistent with the expectations based on the general notion on the reaction of any turbulence-resolving approaches to a grid-refinement and lowering of numerical dissipation.

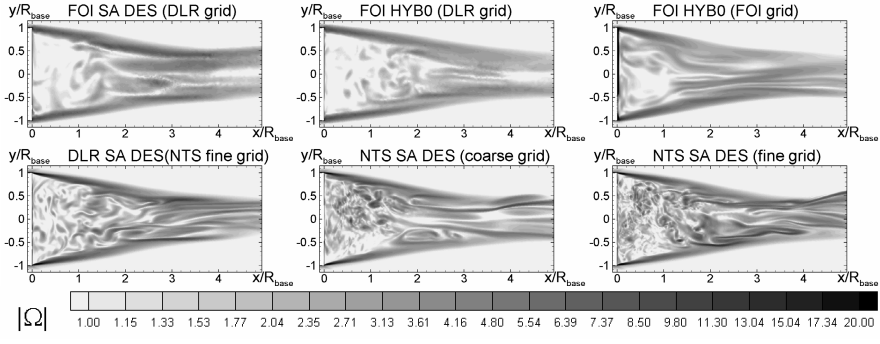

Fig. 10 Effect of modelling approach, numerics (flow solver), and grid on the instantaneous vorticity field

Figures 11-13 compare time-averaged solutions obtained with the use of the different modelling approaches, flow-solvers, and grids (upper parts of the frames present the experimental data and lower parts shows results of the simulations).

Major conclusions that can be made based on the analysis of these figures read:

First, all the simulations, except for the ONERA one carried out with the use of the very fine grid in the shear layer, significantly overestimate the length of the

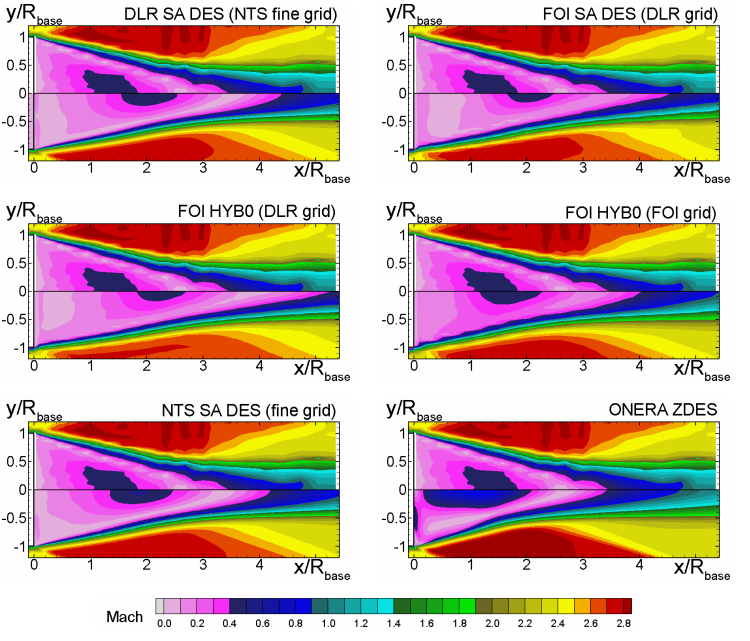

Fig. 11 Mean Mach number in meridian plane

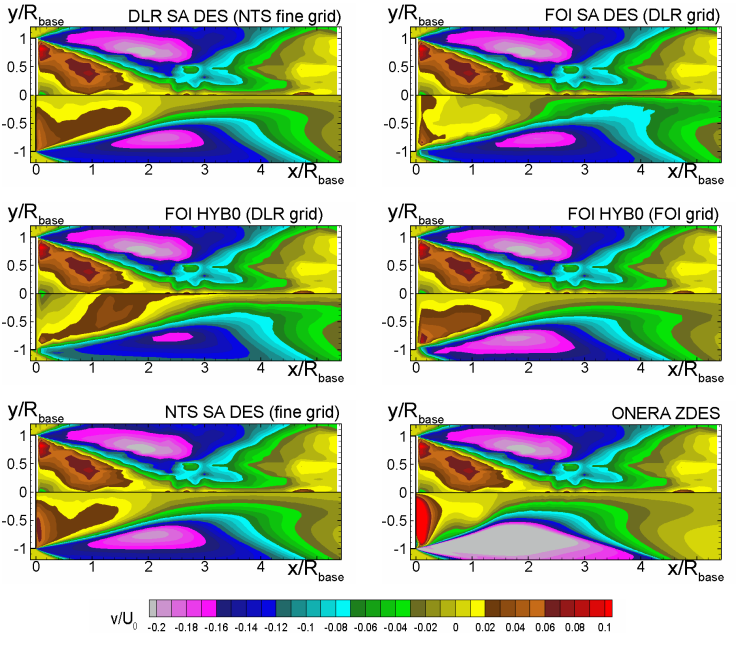

Fig. 12 Mean radial velocity in meridian plane

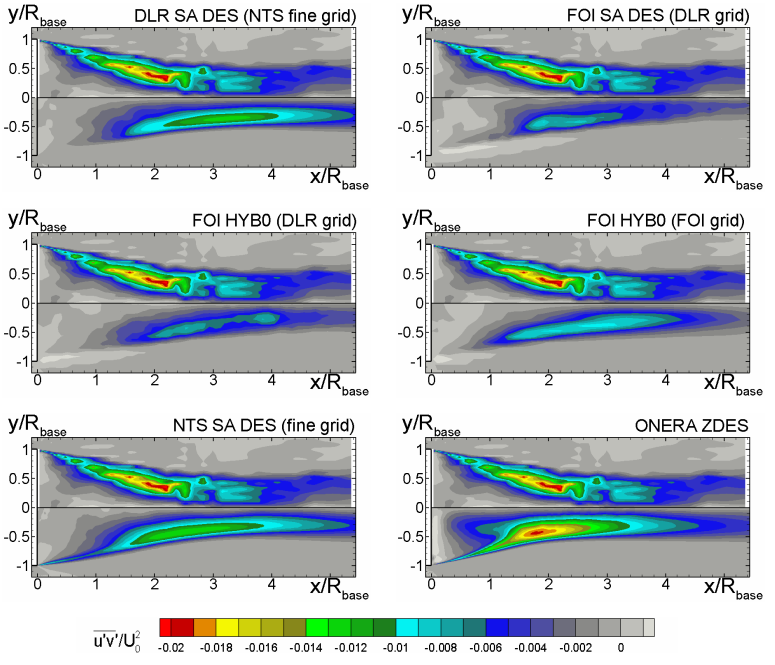

Fig. 13 Full (resolved plus modelled) shear stress in meridian plane

recirculation zone (Fig.11) and underestimate the level of the shear stress in the shear layer (Fig.13). The fine grid of NTS helps to weaken this flaw to some extent but obviously is still not sufficient.

Second, as expected based on the flow visualizations in Fig.10, the coarse unstructured DLR grid fails to provide a correct prediction of the flow independently of the modelling approach (either S-A DES or HYB0), whereas both the fine and coarse (not shown) NTS grids and the structured grid of FOI, which is close to the coarse NTS grid, provide quite an acceptable representation of all the flow features, except for the length of the recirculation zone and shear stress in the initial region of the shear layer. On the other hand, despite the very fine grid, the zonal S-A DES of ONERA results in a poor prediction of the flow *inside* the recirculation zone (Figs.11-13).

These observations are quantitatively supported by Figs.14-16. In particular, Fig.14 shows that the mean flow predictions obtained by the NTS on its coarse and fine grids are very close to each other. As has been noted, this does not mean, of course, that even the coarse grid is already sufficient for an overall (including the initial region of the shear layer) grid-independent solution: just neither the coarse nor the fine NTS grid provides for a sufficient resolution of this region.

Figure 15 compares HYB0 mean solutions obtained on the coarse unstructured DLR grid with that on the structured grid of FOI. Consistently with the above conclusion regarding the inability of the DLR grid to provide accurate turbulence

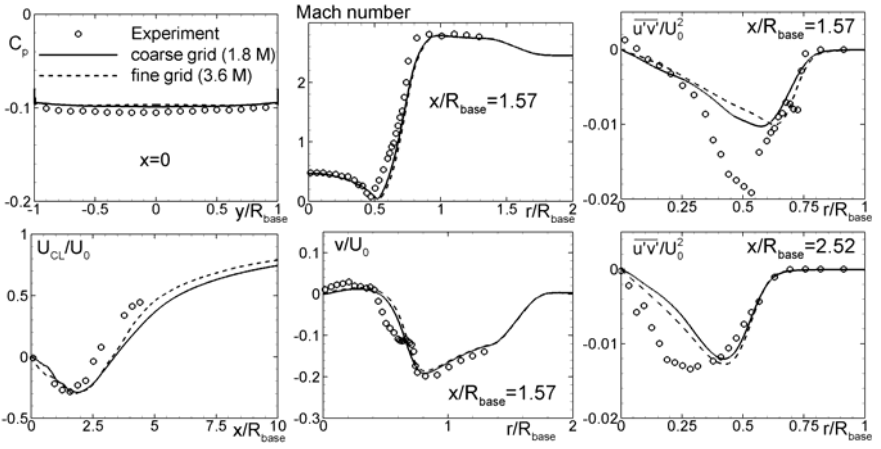

Fig. 14 Effect of grid on S-A DES prediction of the ϕ-averaged mean flow (NTS results)

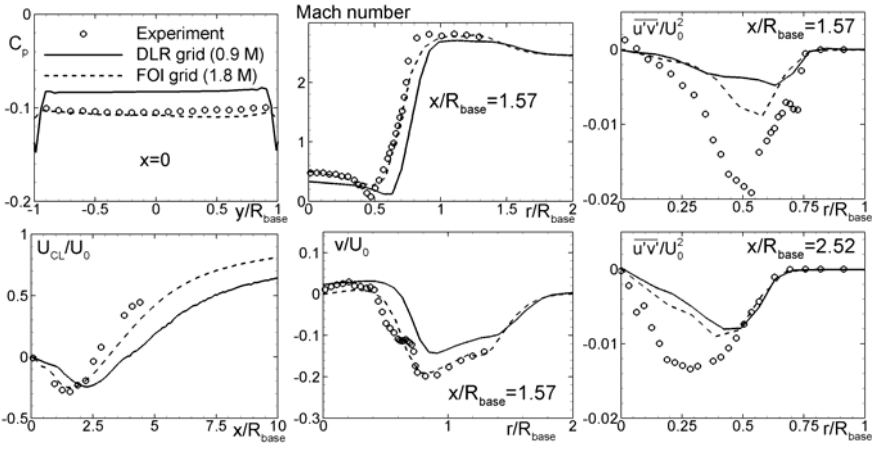

Fig. 15 Effect of grid on HYB0 prediction of the ϕ-averaged mean flow (FOI results)

representation, it turns out that it is insufficient for the mean prediction flow either. In contrast to this, with a finer grid HYB0 performs reasonably well, except for the prediction of the shear stress in the shear layer where, as mentioned above, a much finer resolution is needed.

Finally, Fig.16 compares performance of the three considered turbulence-resolving approaches (S-A DES, HYB0, and zonal S-A DES) on the finest available grids with each other and with the best available RANS solution (S-A with the compressibility correction). It suggests that the standard S-A DES and HYB0 predictions of DLR, FOI, and NTS are all close to each other, while the zonal DES is apart from these simulations and, as mentioned above, provides for a much better prediction of the shear layer but fails to predict the flow inside the recirculation

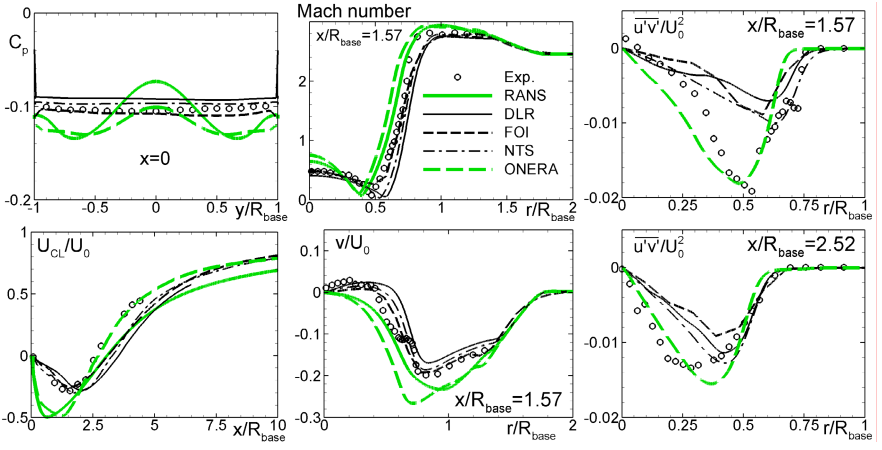

Fig. 16 Comparison of performance of turbulence-resolving approaches on the finest available grids with each other and with S-A CC RANS solution. DLR: S-A DES, NTS fine grid; FOI: HYB0, FOI structured grid; NTS: S-A DES, NTS fine grid; ONERA: zonal S-A DES (C_{DES}=0.55), ONERA very fine grid

zone. A reason of the latter deficiency of the zonal DES remains unclear. As already noted, one of possible explanations is the use of the "non-standard" subgrid length-scale definition $\Delta=(\Delta_x\,\Delta_y\,\Delta_z)^{1/3}$ and C_{DES} value.

10.5 Conclusions

In the course of DESider a series of simulations of the supersonic base flow is carried out with the use of different modelling approaches (S-A and S-A CC RANS, S-A DES, HYB0, and zonal S-A DES), CFD codes (DLR, FOI, ONERA, and NTS), and grids (unstructured and structured of different size, from 0.9 up to 12 million nodes). Comparison of results of these simulations with each other and with experimental data of Herrin and Dutton (1994) permits to make the following conclusions.

As far as the models performance is concerned, in accordance with the expectations, all the turbulence-resolving approaches turn out to be much more accurate than the S-A RANS, even if used with the compressibility correction, which results in some tangible improvements. However, all these approaches, except for the zonal S-A DES of ONERA, fail to provide accurate representation of the initial region of the separated shear layer. Analysis of the results suggests that this failure is caused by insufficiently fine grids in this region used in the simulations of DLR, FOI, and NTS. On the other hand, inside the recirculation zone, the zonal DES on the very fine grid demonstrates a "RANS-like" behaviour and, in particular, fails to reproduce the flat distribution of the base-pressure observed in the experiment, whereas both S-A DES and HYB0 model do this fairly well even with relatively coarse structured grids of about two million nodes. The only conjecture about a reason of this behaviour of the zonal DES we can suggest so far is that it is associated with the use of the non-standard C_{DES} value and of the cube root of cell-size rather than the maximum grid-spacing as the sub-grid length-scale.

11 Separated Flow behind an Aerofoil Trailing Edge without Camber

M.A. Leschziner and F. Tessicini

Imperial College London

11.1 Description of Test Case

This test case is the flow around a simplified airfoil with separation occurring from the curved upper side of the trailing edge. The rear portion of the airfoil and an instantaneous LES realisation are shown in Figure 1.

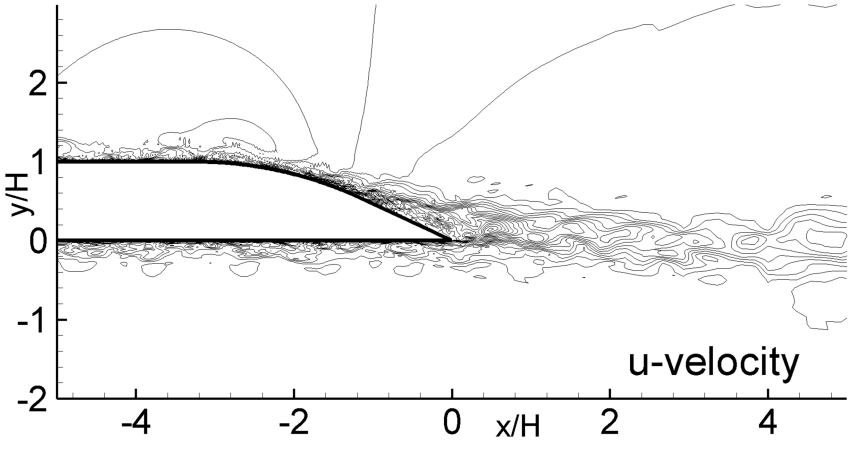

Fig. 1 Instantaneous realisation of flow over the trailing edge of a hydrofoil (Strelets et al, NTS)

The Reynolds number, based on free stream velocity U_∞ and the hydrofoil chord, is 2.15×10^6. The corresponding Reynolds number, based on hydrofoil thickness H, is 1.01×10^5, which is a more appropriate indicator of the resolution challenge this case poses. The flow was previously investigated experimentally by Blake (1975) and numerically by Wang and Moin (2002).

All simulations reported herein were performed over the rear-most 38% of the hydrofoil chord. The default computational domain recommended to all contributors is $16.5H \times 41H \times 0.5H$. The spanwise boundaries were treated as periodic. At the upper and lower boundaries, the streamwise velocity was prescribed to be at its free-stream value Inflow, while the boundary-normal velocity was set to zero. Inflow conditions were taken from Wang and Moin (2002), and these were made available via the DESider website. The conditions were generated in two parts: first, an auxiliary RANS calculation was performed over the full hydrofoil, using

Table 1 Computational grids

Case	Cell numbers	Remarks
Reference LES (Wang & Moin)	768x192x48	The C-topology grid actually used contained1536 x 96 x 48. However, this is equivalent, in resolution, to a 768x192x48 nodes
Hybrid RANS-LES grid	512x128x24	A H-topology, 2-part grid, designed to provide a slow expansion from the wall, with wall-nearest node at $y^+ = 1$
Zonal model LES grid	512x128x24	Similar to Hybrid grid, except that the wall-normal grid is more uniform and ends at $y^+ = 40$, from which location the near-wall zone is inserted

the *v2f* turbulence model by Durbin (1995); the unsteady inflow data were then generated from two separate LES computations for flat-plate boundary layers at zero pressure gradient. Discrete time-series of the three velocity components at an appropriate spanwise (y-z) plane were then saved. These data, appropriately interpolated, were fed into the inflow boundaries of the present simulations. The time step for the inflow, normalised with U_∞ and H, is $\Delta t^* = 0.02$ and $n = 3000$ time steps are saved (covering a total inflow time equal to 60 time units, H/U_o). The upper and lower boundaries are located at 41 hydrofoil thicknesses away from the wall, to minimize numerical blocking effects. At the downstream boundary, convective outflow conditions were recommended to be applied.

Table 1 lists the grid provided to all partners, by reference to the fine grid used by Wang and Moin. Two grids were provided, one for hybrid LES-RANS schemes that use a single computational domain, and the other for those using wall-function-type or zonal schemes. The two grids are similar, but the zonal scheme is more uniform in the wall-normal direction.

11.2 Partner-Specific Practices

Simulations contributed for this test case come from Imperial College London (ICL), New Technologies and Services (NTS) and the University of Manchester. (UMan) This section is not intended to present the simulation practices employed by the above contributors. These practices are documented in partner-specific sections contained in Chapter V. The statements provided below relate to specific issues pertaining to the application of the methods to the present test case.

11.2.1 Imperial College London (ICL)

Computation were performed by ICL with two different approaches: a hybrid LES-RANS scheme and a zonal scheme. Both schemes are fully documented in Tessicini et al (2006) and in Chapter V of this book. The grid used by ICL are those listed in Table 1.

The hybrid scheme solves the LES and RANS equations on a single, continuous mesh which is refined towards the wall to reach a y^+ of the wall-nearest node of order 1. The interface location can be defined, and in the computations performed, the location was prescribed by a chosen grid line, corresponding to y^+=60 and 120 in the boundary layer upstream of the curved trailing-edge region (denoted below by 'j12' and 'j19', respectively). The hybrid scheme employed herein combined the Yoshizawa-Horiuti (1985) SGS-energy transport model in the outer LES region with a low-Re k-ε model of Lien and Leschziner (1994) in the near-wall region. Experience arising from initial test computations for the present geometry has shown that the method is quite sensitive to the aspect ratio of the grid at the interface. Because the state at and around the interface region is close (or supposedly close) to a well-resolved LES state, the aspect ratio of the grid in this region must be relatively low, especially as the flow near the separation point varies rapidly in space and time in a complex fashion. Our observation has been, therefore, that placing the interface close to the wall, where the grid has a high aspect ratio, results in a suppression of separation. The model's performance improves as the interface is moved out into a region of lower aspect ratio.

The other method used by ICL involves two overlapping domains and grids: a LES grid that covers the whole flow and is not especially refined towards the wall. Hence, that grid is fairly uniform, of low aspect ratio, but is rather coarse at the wall, with y^+ near-wall value of the order 20 to 40. Between this wall-nearest node and the wall, a near-wall layer is inserted in which parabolized NS equations are solved, with convection ignored, pressure imposed upon the layer by reference to the LES solution and a mixing-length used to represent the turbulent viscosity. In effect, the near-wall layer is a wall-function-like region. The solution of the parabolized equation yields the wall-shear stress, which is the only quantity fed into the LES solution. This is a much simpler strategy, incorporating a simple algebraic turbulence model, requiring only 1D storage and thus being very economical. In the LES region, the dynamic Smagorisky model was used.

11.2.2 New Technologies and Services (NTS)

NTS has carried out the present computations of this test case with an extension of the DDES approach (DDES with improved wall modeling – or IDDES) presented in detail in Chapter V and in Travin et al (2006). This is a hybrid RANS-LES model, in which major new elements are a definition of the sub-grid length scale (along with the grid size it explicitly includes wall distance dependence) and a specific way of RANS-LES blending. The model reduces to the DDES in the case of no "turbulent content" (either artificially imposed or naturally generated) at the inflow boundary of the computational domain and functions as a Wall Modelled LES otherwise.

The computations are performed with the incompressible variant of the NTS code, which incorporates a 4th order centred approximation for the inviscid fluxes. The grid used by NTS is not identical to the recommended version indicated in Table 1. Rather, the particular three-block grid shown in Figure 2 was used. This contains about 1.5 million nodes with the near wall y^+ equal to 1.0 or less, with the

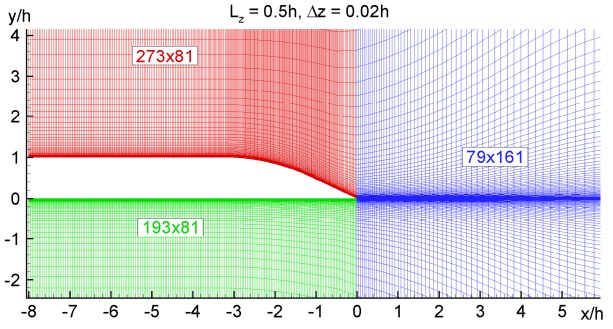

Fig. 2 NTS's computational grid in (x, y) plane

streamwise increment varying in the range from 0.02 up 0.04 hydrofoil thickness, *h* (i.e., about 1/10 of the boundary layer thickness), and the spanwise increment being 0.02*h*. A major point of difference between NTS's grid and the mandatory grid, is that the former offers a higher streamwise resolution around the curved trailing-edge portion. The wall-normal grid is also refined near the wall and in the wake line, while it coarsens in the outer portion of the wake, expanding away from the wake line. These differences necessarily pose a question mark against the comparisons to follow. In effect, the grid has been optimised, to some extent, to achieve an improved resolution in particular areas.

The inlet boundary conditions were not those provided to partners, but were generated by NTS in the course of the main simulation by a simultaneous simulation of a flat plate boundary layer with the same model used for the airfoil simulation.

11.2.3 University of Manchester (UMan)

To provide a reference point from which progress could be measured, UMAN first applied the conventional DES strategy, with the SST model serving as the RANS background model, together with the recommended "F1 blending function" to prevent grid-induced activation of the LES mode and spurious separation (Menter et al., (2003)). Next UMAN used its newly developed hybrid RANS/LES scheme, based on a "two velocity fields" concept documented in Chapter V of this book and in Uribe et al. (2007). This is itself based on an earlier idea by Schumann (1975) in which the strain rate is separated into fluctuating and averaged parts, the former contributing the subgrid-scale stress and the latter, multiplied by the RANS viscosity, contributing the mean stress. The mixing-length model or V2F model of Durbin are optionally used to determine the RANS viscosity, in combination with the mean strain field, obtained by an on-the-run integration of the LES solution.

Three solutions are included below, denoted by UMAN-DES, UMAN-HYB1 and UMAN-HYB2. All were obtained with the recommended hybrid mesh in Table 1. The difference between HYB1 and HYB2 relates to the specification of the inlet conditions: in HYB1, the default precursor data provided to contributors

were prescribed, while in HYB2, the Synthetic Eddy Method of Jarrin et al (2007) was used to generate the unsteady inflow conditions. The precursor data were also used for the DES simulation. This practice must be questioned, however, on the grounds that DES, in the form used by UMAN, is not intended or designed to accommodate unsteady inflow conditions, but is specifically designed to return a steady solution in attached layers.

11.3 Results and Discussion

Cross-plotted results are presented herein for the skin-friction coefficient, the mean-velocity magnitude and the r.m.s. velocity above the upper side of the aerofoil. Profile of velocity relate to the sections C-G identified in Figure 3. In addition, mean-velocity profiles are included for the wake region, at the streamwise locations y/h=0, 0.5, 1.0 and 2.0.

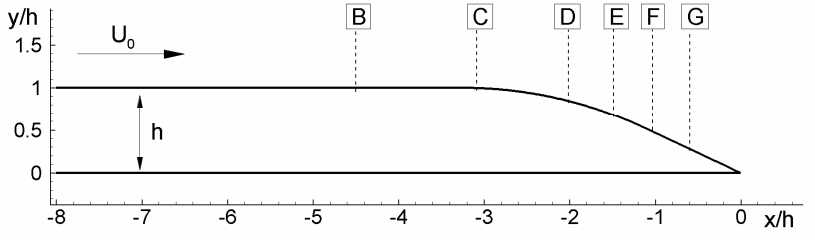

Fig. 3 Streamwise locations over the aerofoil at which profiles of mean and r.m.s. velocities are provided

An overall view of the mean field predicted by four of the six solutions contributed is given in Figure 4 in the form of stream-function contours. All solutions included are seen to capture the separation on the rear of the trailing edge, and this applies also to the two remaining solutions for which no stream-function plots are available. However, as is evident, there are significant differences in the details of the respective separation zones, some being relatively short (e.g. NTS-DDES) and others much longer (eg. ICL-hybrid).

The size of the recirculation is largely dictated by the position of separation, and this is one item of information that is conveyed by the skin-friction distributions shown in Figure 5. In particular, the close-up view of the rear portion of the suction side, given in the third plot of the figure, shows that IDDES predicts incipient separation (with very low, but positive C_f) over a significant distance ahead of the actual separation. This is thus consistent with the very short separated zone seen in Figure 4.

The solutions by ICL and that of UMAN with DES give early separation. The ICL-hybrid variation indicates, in addition, the presence of reattachment and secondary separation on the suction side, but it must be noted that the smoothness of C_f in the separation zone is especially sensitive to the time-averaging period,

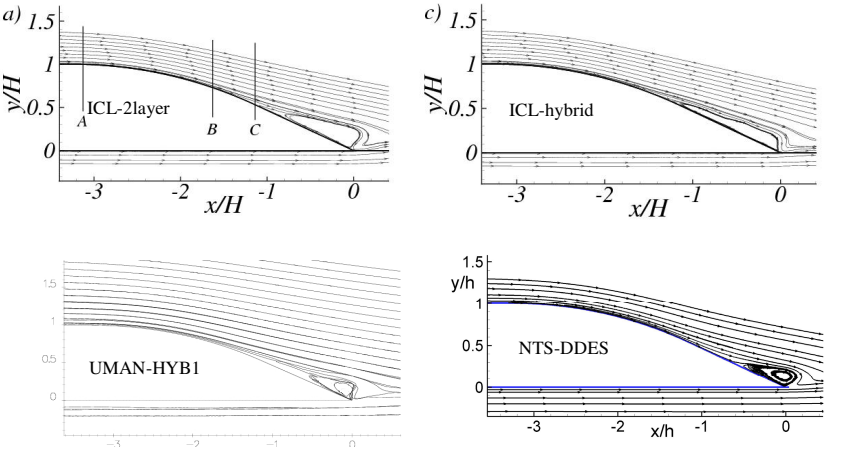

Fig. 4 Time-mean streamfunction fields

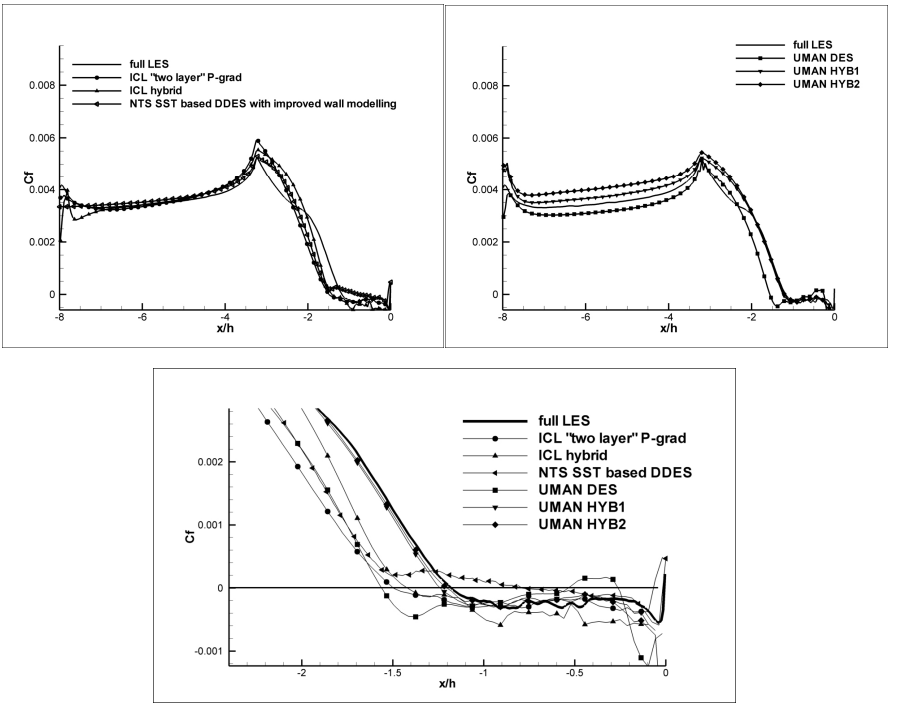

Fig. 5 Skin-friction coefficient on the suction side (with magnified view of separated trailing-edge region)

which explains the rather 'noisy' variations displayed by most solutions. UMAN's HB1 and HYB2 solutions agree exceptionally well with the reference LES, giving the correct separation point as well as friction level after separation. However, an exceptional feature of UMAN's method is that the near-wall mean flow is computed with a RANS model by reference to the time-averaged solution obtained on the run. Thus, the wall friction, in particular, is especially sensitive to the characteristics of the RANS model, rather than to the time-varying solution returned by the LES in the upper region above the wall. This weaker relationship between C_f and the unsteady field is also the reason for the relatively smooth variation of UMAN's skin-friction distributions in the separated zone.

While all simulations predict well the general features of C_f ahead of the separation point, none resolves the curious inflection just downstream, of the start of the curved suction-side portion returned by the reference LES. This inflection is not unrealistic, because a sudden imposition of convex wall curvature on a boundary layer is expected to result in relatively strong local deceleration, followed by a recovery, and this is precisely the behaviour shown by the reference simulation. The fact that none of the approximate solutions resolve this feature may be a consequence of insufficient streamwise-grid resolution downstream of the point at which the curved trailing-edge portion starts.

Profiles of velocity magnitude at the locations C to G identified in Figure 2 are shown in Figure 6. These give, arguably, a better view of the quality of the LES solutions than does C_f, because the latter is exceptionally sensitive to the minutiae of the modeling very close to the wall.

As might be expected, the DES solution provided by UMAN is seen to be rather poor, displaying an anomalous behaviour and a pronounced tendency towards early separation. This solution also gives the earliest separation, as seen in Figure 5. One likely major contributor to this poor behaviour is the fact that DES does not resolve the unsteady turbulence activity in the attached flow region upstream of separation. As will be shown by reference to the predicted turbulence

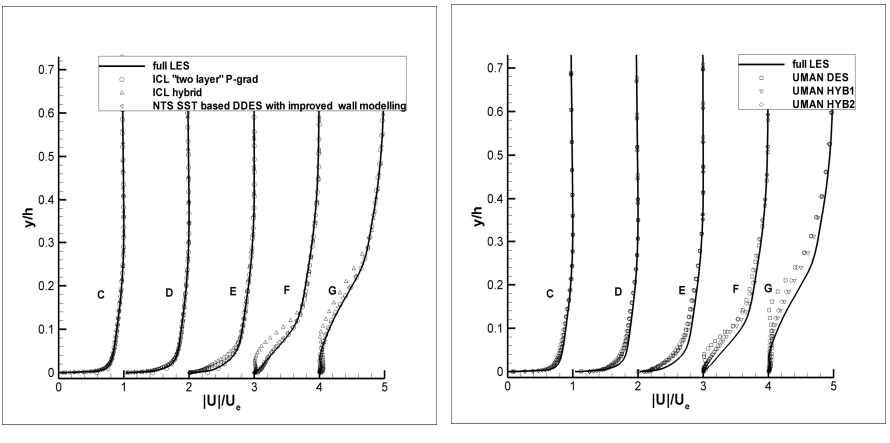

Fig. 6 Magnitude of mean velocity above the suction side

field to follow, this is so despite the (questionable) prescription of unsteady flow conditions at the inflow boundary above the suction side. Evidently, DES predicts an insufficient level of turbulence activity upstream, of separation and thus premature separation. The DES variant applied by UMAN addresses the issue of premature grid-induced separation by the use of the "F1 blending function", but this does not cure the defects observed in Figure 6. NTS's IDDES method is seen to give a much better representation of the velocity field, and this is probably due, principally, to the fact that, in this flow, the method effectively functions as a hybrid scheme for wall-modelled LES, rather than as a Detached Eddy Simulation in its generally understood sense.

The two-layer ICL method is seen to perform very well in respect of the velocity field, while the ICL hybrid scheme and UMAN's HYB1 and HYB2 profiles indicate excessive deceleration and early separation, although the C_f variations of the last two suggest that these two approximate methods return very accurate representations. Thus, here there is some evidence to support the earlier statement about the exceptional features of the UMAN's approach in its favouring an accurate representation of the skin friction, due to the dominant influence of the time-averaged near-wall solution to which the RANS model is linked.

Profiles of the r.m.s. of the streamwise (resolved) fluctuations are shown in Figure 7. Here, some substantial differences among the approximate representations, as well as between these and the reference solutions, come to light. The reference solution shows high near-wall peaks of fluctuations upstream of the separation zone, indicating that the viscous sublayer, at the edge of which the turbulence peaks, is very close to the wall. Of all approximate methods, only ICL's two-layer schemes resolves the near-wall variations with credible realism, and this is principally due to the fact that the near-wall layer over which the RANS equations are solved is thin (of order y^+=50).

The DES solution of UMAN shows, predictably, a negligible level of turbulence downstream of the inflow section, simply because DES is not designed to

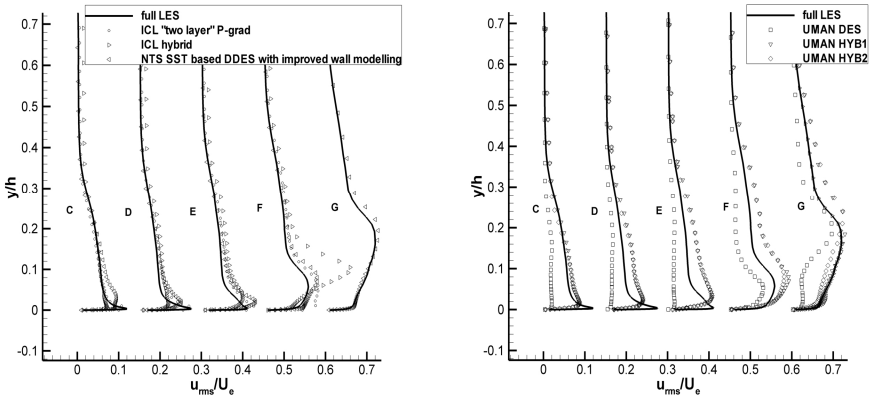

Fig. 7 Streamwise fluctuation intensity above the suction side

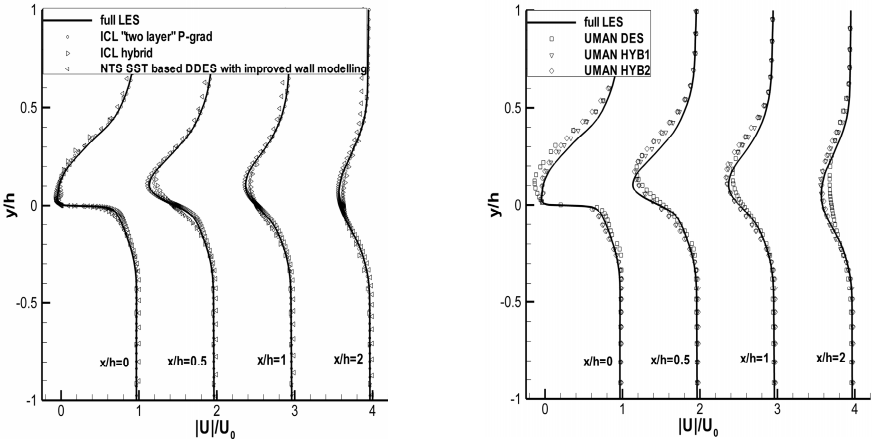

Fig. 8 Mean velocity in the wake region

resolve the unsteady turbulent motion in the attached region. Hence, the flow arrives at the separation region with too low level of turbulence activity, thus separating prematurely.

NTS's IDDES resolves, much like other conventional hybrid schemes, the unsteady turbulence in the attached region, thus giving a major improvement in performance relative to DES when applied to attached wall layers leading up to separation. UMAN's HYB1 and HYB2 models give very similar results and do not perform especially well, giving an excessively thick boundary layer (see also Figure 6) and a peak-turbulence position too far from the wall. ICL's hybrid method gives a behaviour similar to UMAN's HYB1 and HYB2 methods up to section G where the flow is fully separated. At this section, ICL's hybrid returns a much too large level of turbulence in the separated shear layer, but this is tied to the early separation and thus to the fact that this shear layer has evolved over a longer distance and is too far from the wall, encouraging a high level of turbulence.

Finally, Figure 8 shows velocity profiles in the wake region of the aerofoil. Subject to the flow conditions at the rear edge of the aerofoil being correct, the flow solution in the wake is dominated, principally, by the LES component and thus the grid-resolution quality behind the trailing edge. The comparisons in Figure 8 show that all methods, but UMAN's DES implementation return reasonable wake profiles. NTS's IDDES performs especially well, but this is likely to be partly linked to the higher cross-flow grid density used in the wake region, as is evident in Figure 2. UMAN's HYB1 and HYB2 methods give a wake that is inappropriately shifted upwards, and this is linked to the somewhat excessive thickness of the reverse-flow region and the shear layer above it.

11.4 Conclusions

No approximation of the near-wall region within a LES scheme that sacrifices full resolution will give an entirely satisfactory representation of this region, and this

statement also applies to the methodologies investigated in the present test case. The overall objective can only be to devise a method that will allow the simulation to maintain an adequate predictive realism in the outer flow and, thus returning an acceptable accuracy of the gross flow features.

Of the methods applied to the present case, DES is evidently inferior to the other methods, and this must be due mainly to the fact that it does not resolve the unsteady turbulent motion in the attached layer upstream of separation. Although the DES model was obtained with unsteady turbulent conditions (inappropriately) specified at the inlet, the fluctuations decay rapidly, so that a virtually steady flow approaches the separation point.

The other methods display a mixture of strengths and weaknesses. This fact, and the added uncertainties associated with NTS's use of an 'optimized grid, prevent an unbiased grading of the methods. Thus, the following comments merely highlight particular features of and differences among the solutions.

UMAN's HYB1 and HYB2 solutions are almost identical, thus illustrating that the Synthetic Eddy Method of Jarrin et al (2006) can be economically substituted for the precursor data provided to the contributors. Both variants return accurate results for the friction factor and separation point, but show weaknesses in respect of resolving the velocity and turbulence profiles. While the accuracy of C_f is commendable, as well as being highly desirable in some practical applications, the differences in the velocity profiles around the separation region suggest that the pressure field returned by the solution is not entirely correct.

NTS's IDDES, as applied to the present flow, is effectively a hybrid formulation, and it works in a manner similar to other hybrid methods. Its performance is generally good, but it shows a serious weakness in respect of representing the separation region. Specifically, it predicts a much delayed separation and a short recirculation zone.

ICL's hybrid method performs reasonably well, but predicts early separation, an excessively thick boundary layer upstream of separation (much like UMAN's HYB1 and HYB2) and excessive turbulence in the separated shear layer. ICL's two-layer scheme is simple and economical, and it gives a satisfactory representation of most flow features. This method gives the best representation of the turbulence profiles in the attached region, but returns moderately excessive levels after separation, relative to the experimental profiles, mainly because it predicts separation to occur too early. In the separated region, NTS's IDDES scheme performs best, but this is against the background of the seriously delayed separation it predicts, a defect that tends also to delay the steep rise in turbulence that is associated with separation.

12 FA-5 Configuration

S. Leicher

EADS-MAS

Abstract. While the flow physics of generic delta wings with sharp leading edges are largely understood, complex realistic configurations with round leading edges, canards and so on are still of scientific and industrial interest. The goal of test case 13 is the study of flow around a generic fighter type configuration at 15° angle of attack and high Reynolds number. A detailed comparison between the different simulations and the experimental wind tunnel results will be presented.

Four partners, ANSYS, DLR, EADS-MAS, and TUB have participated in this task, which was confidential because of its industrial importance. Structured as well as unstructured grids and codes are used as well as various URANS and DES models are applied.

12.1 Introduction

This industrial test case addresses the flow around a fighter type aircraft whose behaviour at high angle of attack is dominated by vortexes. The industrial goals are the computational efficiency and a reasonably exact prediction of the force coefficients and the relevant frequencies of their unsteady content in the range of manoeuvre as well as the structural interaction.

The problem is to model the unsteady turbulent phenomena of vortex dominated flows at high angle of attack. It turns out that URANS simulations give an insufficient description of the unsteady scales. Consequently a resolution of large scale flow fluctuations is necessary which can be better achieved by applying detached eddy simulations (DES). One hopes that DES modelling provides a better description of the vortex structure, and allows the identification of vortex burst and the identification and modelling of local unsteady effects in the flow field.

The flow conditions for this test case are a Mach number of 0.125 and an angle of attack of 15.0° and a Reynolds number of 2.8×10^6.

Table 1 Grids, codes and turbulence models used by the partners

	Structured	Unstructured	Code	RANS	DES or SAS
ANSYS		X	CFX		Menter SST-SAS
DLR		X	TAU		SA-DDES
EADS	X		FLOWer	Wilcox-kω EARSM RSM	SA-DES
		X	TAU		SA-DES
TUB	X		ELAN	SALSA	SALSA-DES EASM-DES

The partners in this test case are ANSYS, DLR, EADS-MAS and TUB. EADS-MAS started at the beginning of the project with computations employing a structured grid. This grid was made available for TUB. Both performed URANS and DES simulations and some results are shown further down.

In the second half of the project ANSYS, DLR and EADS-MAS performed DES and SAS computations on an unstructured grid generated by EADS-MAS also.

Table 1 summarizes the computations performed – a detailed code description of each partner can be found in the individual sections of chapter V.

12.2 Experimental Setup and Data

The experiments were performed by the TU Munich (Breitsamter 1997) in a wind tunnel with an open test section via Xwire. The main geometric features and a picture of the model in the wind tunnel are shown below.

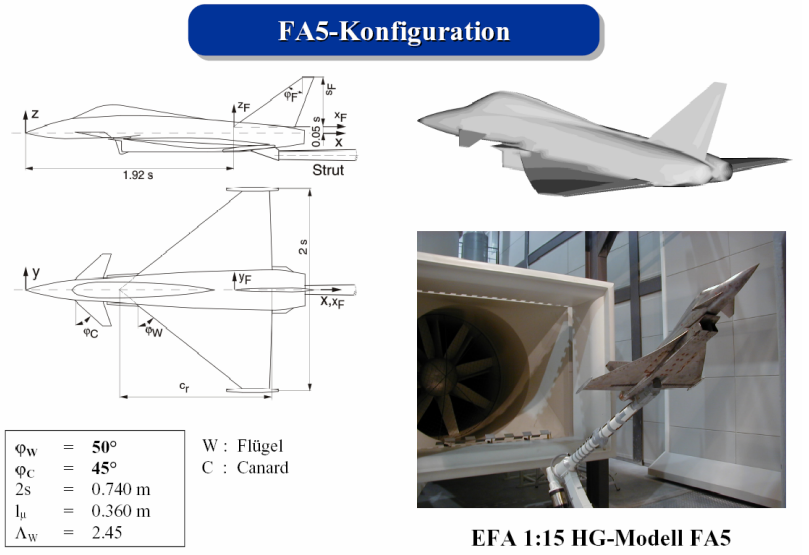

Fig. 1 Wind tunnel model and experimental setup

Experimental data available comprise mean velocity components, velocity RMS values, Reynolds stresses, vorticity magnitude and turbulent kinetic energy in twelve cuts.

12.3 Structured Grid

The CFD computations started at the beginning of the project with URANS calculations by EADS-MAS (Rieger, 2005) and first DES simulations by TUB

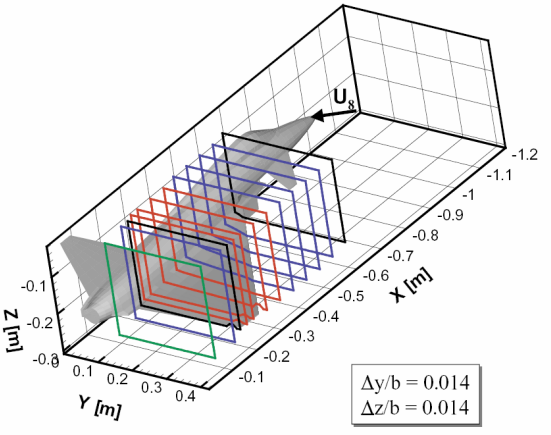

x/c_r	Punkte (Y x Z)
0.20	33 x 25
0.30	32 x 25
0.40	32 x 25
0.50	32 x 25
0.60	32 x 25
0.70	31 x 25
0.80	31 x 25
0.90	31 x 25
0.95	31 x 25
1.00	30 x 24
1.05	30 x 26
1.20	29 x 26

Fig. 2 Location of the experimental data planes

(Gurr, 2006). Both partners used in principle the same block structured grid generated by EADS-MAS, comprising 196 blocks with total grid size of 11.4 million points. TUB uses this grid on the medium level and only above the wing the resolution of the original fine grid is used, resulting in no pairing grid density at some block inter faces.

One geometry detail is included in all computational grids but not present with the wind tunnel model. This is the strake at the body side above the canard (see last figure). This strake generates an additional second vortex above the wing and along the side wall of the fuselage, which of course is not present in the experimental data.

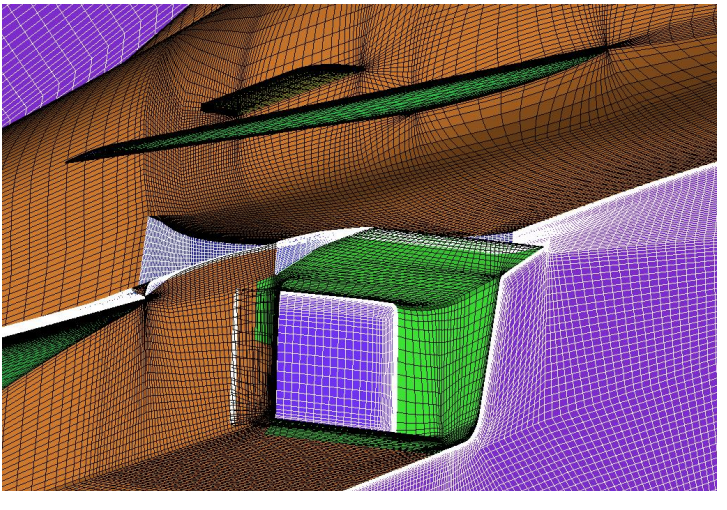

Fig. 3 Grid details of the structured grid

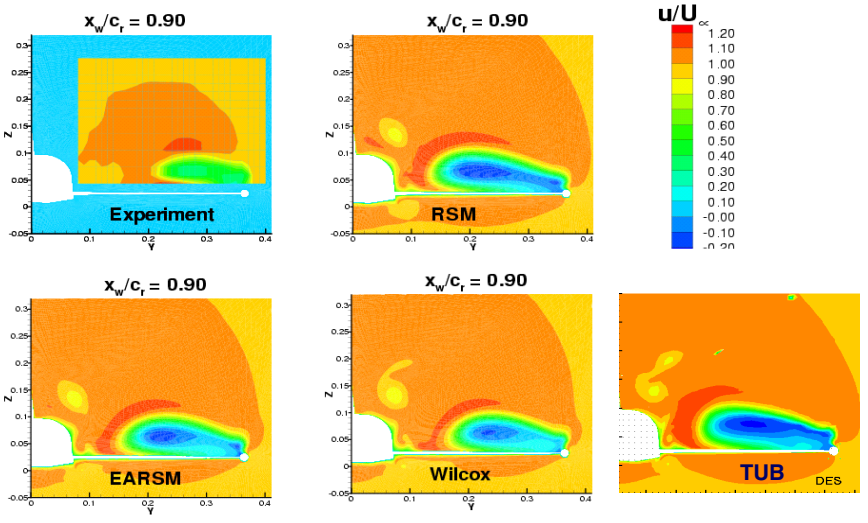

Fig. 4 Comparison of u-mean velocity URANS and SALSA-DES at x/C=0.90

EADS-MAS uses the FLOWer code applying the Wilcox-kω, the EARSM and RSM-SSG-ω turbulence model while the TUB uses their ELAN code in URANS, DES-SALSA and DES EASM mode.

The next figures show the comparison of the mean u-velocity at the station x/C=0.90, which is the last one and closest to the trailing edge. All CFD results show a negative u-velocity inside the vortex core while the experiment does not. The figure shows qualitatively the same structures. As the only one, the TUB SALSA-DES result seems to represent the second vortex above the body quite well.

The comparison of the RMS values, figure 5, shows qualitatively good agreement; the quantitative comparison is also acceptable, although the theoretical values are a little bit too low.

The TUB made a grid dependency study using the 2nd level of the grid and in the region of the vortex above the wing the fine grid resolution. The effect on the mean velocity components was very weak and did not improve the deficiency in the u-velocity very much.

But as the following picture, figure 6, shows a remarkable influence of grid refinement upon the RMS-values can be observed. A much higher resolution of the turbulence is obvious and the agreement with the experiment is improved a lot.

Figure 7 shows a typical comparison of the vortex structures between a URANS and a DES simulation, both using the SALSA model as the basic turbulence model. The DES result shows a strong expansion of the vortex system capturing the natural unsteadiness, while the SALSA URANS simulation presents a stable vortex up to the trailing edge and no unsteadiness is visible, at all. It turns out that the unsteadiness in the DES computation is depending upon the time step

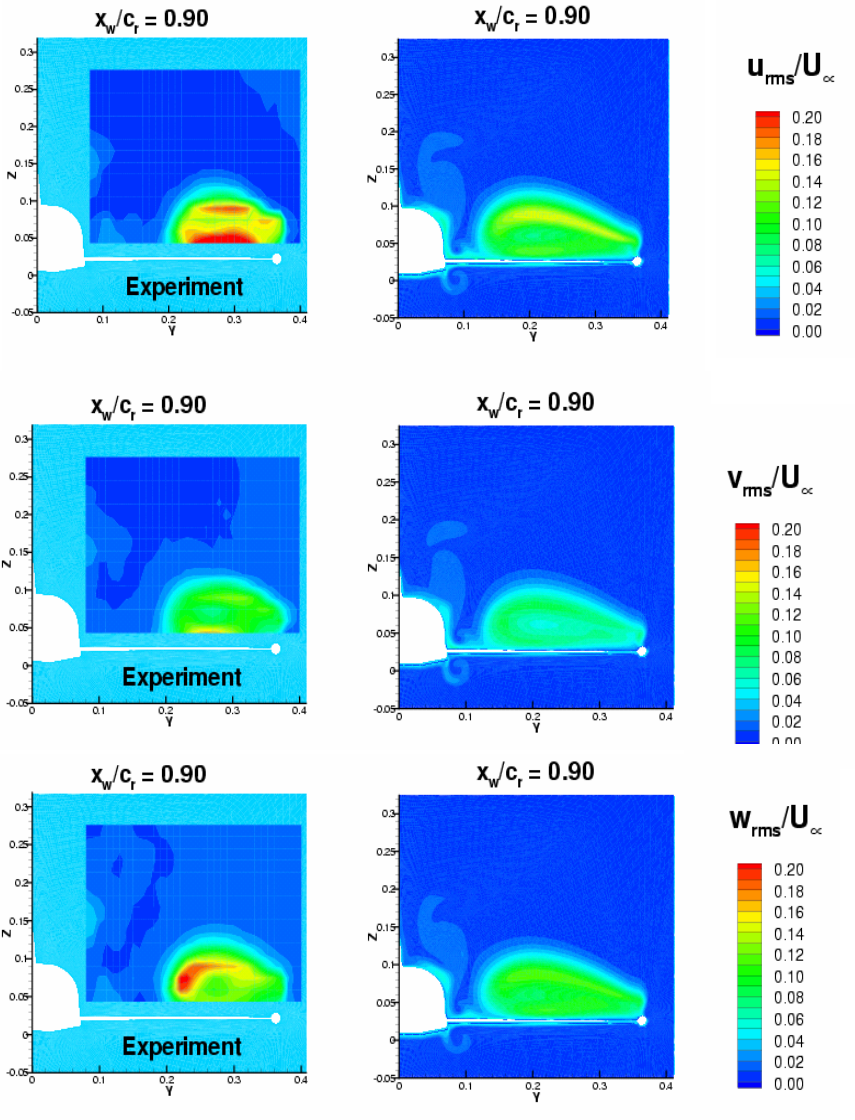

Fig. 5 Comparison of the u-, v-and w-rms distribution with the RSM-SSG-ω simulation

size, while the main features of the flow, like the location of the vortex burst seems not to be very sensitive to time step, turbulence model as well as spatial resolution. On the other hand URANS simulations show steady solutions regardless of the time step, with the main flow features depending more strongly on the turbulence model as well as on the grid resolution.

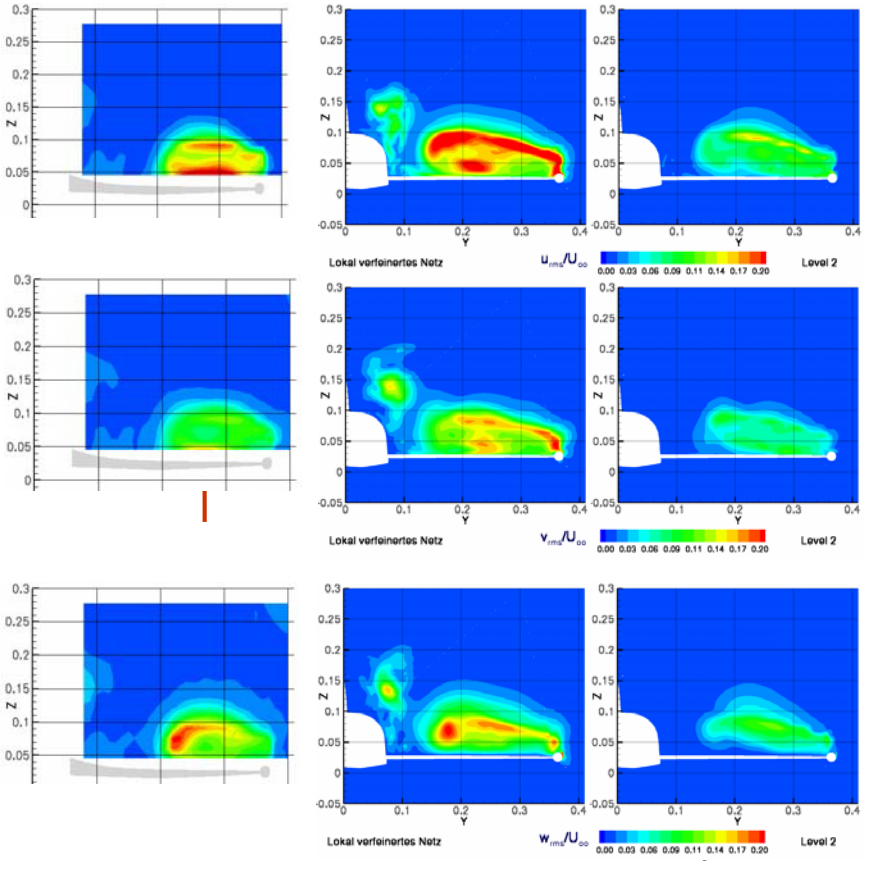

Fig. 6 TUB grid refinement study; SALSA-DES influence on RMS values at x/C=0.90

The effect of a time step reduction by a factor of 10 is shown in figure 8 above. Clearly visible are the much finer vortex structures appearing with the finer time step.

The influence of a second DES background model is shown in figure 9. The CEASM-DES model turns out to give a reduced region of reversal flow within the vortex and as a result a better agreement of the mean velocities especially for the u-component compared with the result of the SALSA model in figure 4. The RMS-values are also improved but not shown here.

The results in the structured grid indicated clearly that URANS is not able to reproduce the unsteadiness of this kind of flow correctly, regardless of the size of the time step. URANS calculations seem to depend strongly upon the model as well as the grid resolution.

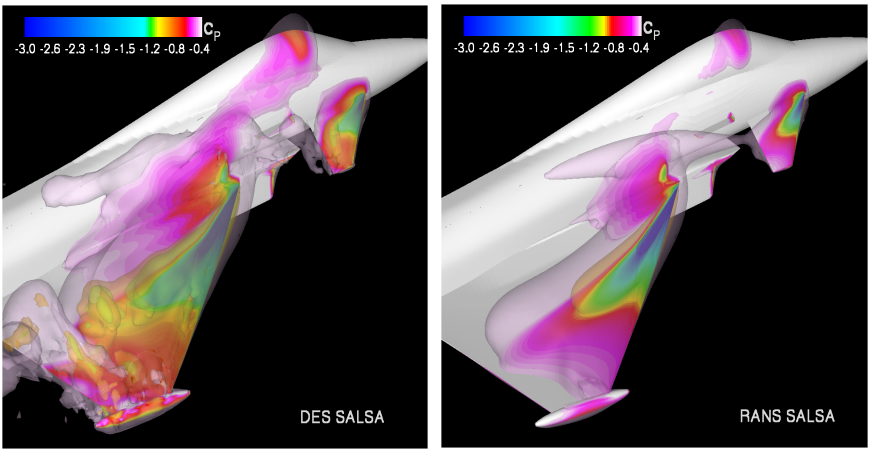

Fig. 7 Comparison of vortex structure between URANS and SALSA-DES

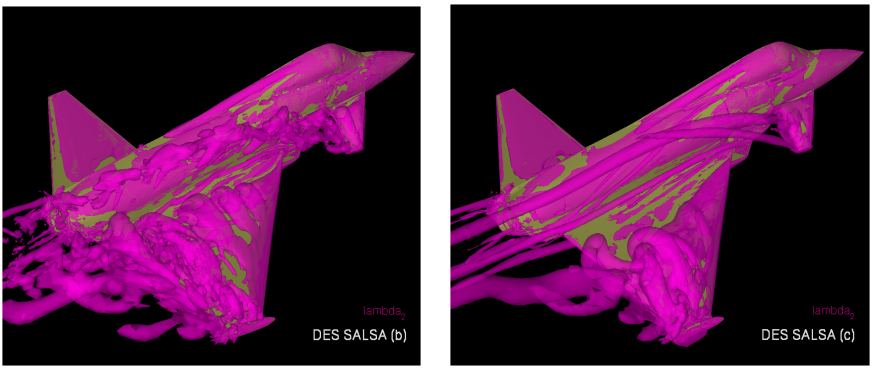

Fig. 8 The effect of reducing the time step by a factor of 10 upon the lamda2 criterion b) left: dt = 1. x 10^{-4} c) right: dt = 1. x 10^{-3}

DES on the other side offers the possibility to investigate such unsteady phenomena. The agreement with the experimental data is improved quite a bit. The magnitude of the unsteadiness resolved, by means of the RMS values, depends on the time step size, while its influence upon the main flow features seems to be smaller. The same remark can be made with regard to the grid resolution. The comparison between the SALSA DES and EASM DES points to high dependencies upon the background turbulence model.

The structured grid used here turns out still to be not fine enough. Therefore in the second phase of the project an unstructured grid is used which offers better control of the grid density and the possibility of future grid refinement.

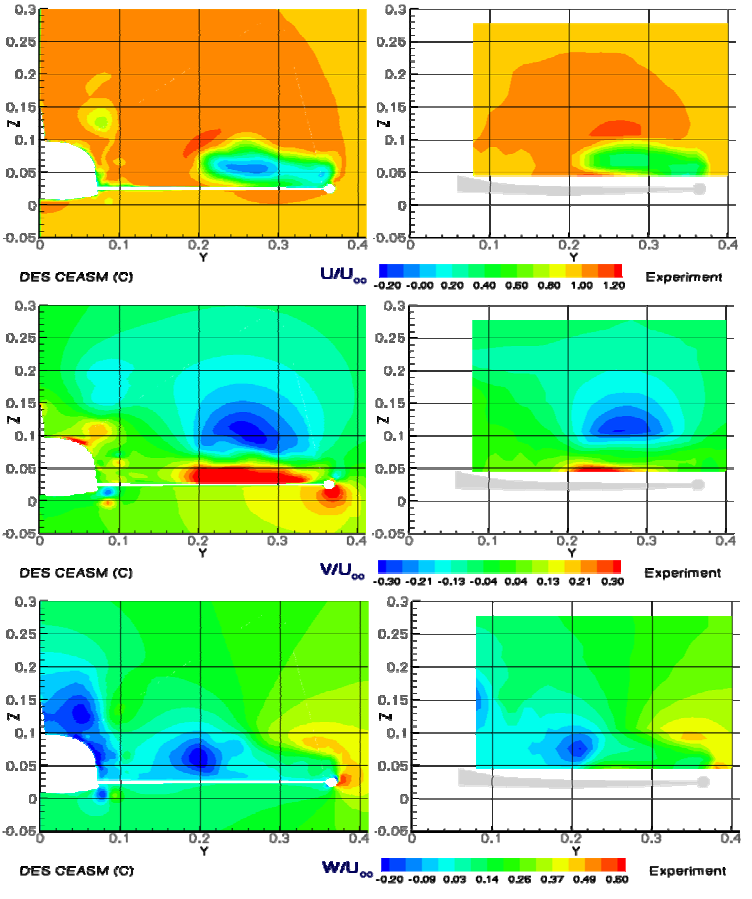

Fig. 9 Comparison of mean velocities EASM-DES and experiment at x/C = 0.90

12.4 Unstructured Grid Computations

The partners ANSYS, DLR and EADS-MAS participated in this part of the test case. All calculations are done by using the same unstructured hybrid grid with about 13 million nodes generated by EADS-MAS.

Both EADS-MAS and DLR performed their computations by using the TAU-code. While EADS-MAS applied the basic SA-DES turbulence model, based on the so-called DES97 model (Spalart 1997), DLR used the SA-DDES version, a recently derived Delayed DES model (Spalart 2006). The later model overcomes some ambiguous behaviour for extended boundary layers if the tangential grid spacing becomes inappropriate due to the solely grid dependent RANS-LES switching. ANSYS performed the computations with their commercial code CFX (ANSYS, 2007) using the SST-SAS turbulence model (Menter et al., 2005-2007).

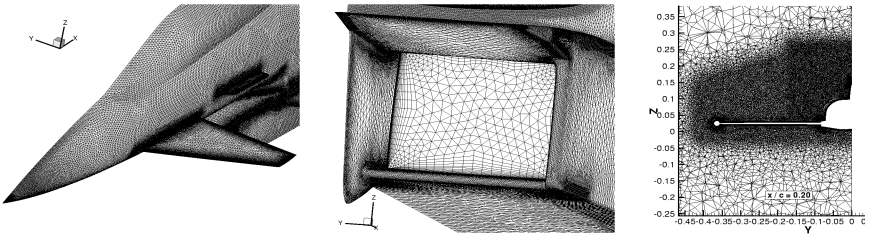

Fig. 10 Grid details

The resolution in time varies between the partners. EADS uses a time step of 5.0E-4, DLR one of 1.0E-4 and ANSYS 5.0E-5 seconds.

The time period monitored to collect statistic data was nearly one second in the case of DLR and EADS-MAS, while ANSYS, forced by the smaller time step, samples the data for about .30 seconds. The latter turned out to be a little too short because some data has not reached a fully settled mean for each value.

The comparison of the data with the experiments of the TU Munich was done in several cuts x=constant by means of mean velocities and RMS values of the velocities. The instantaneous ratio of turbulent to laminar viscosity and the average of the resolved turbulent kinetic is compared between the different simulations.

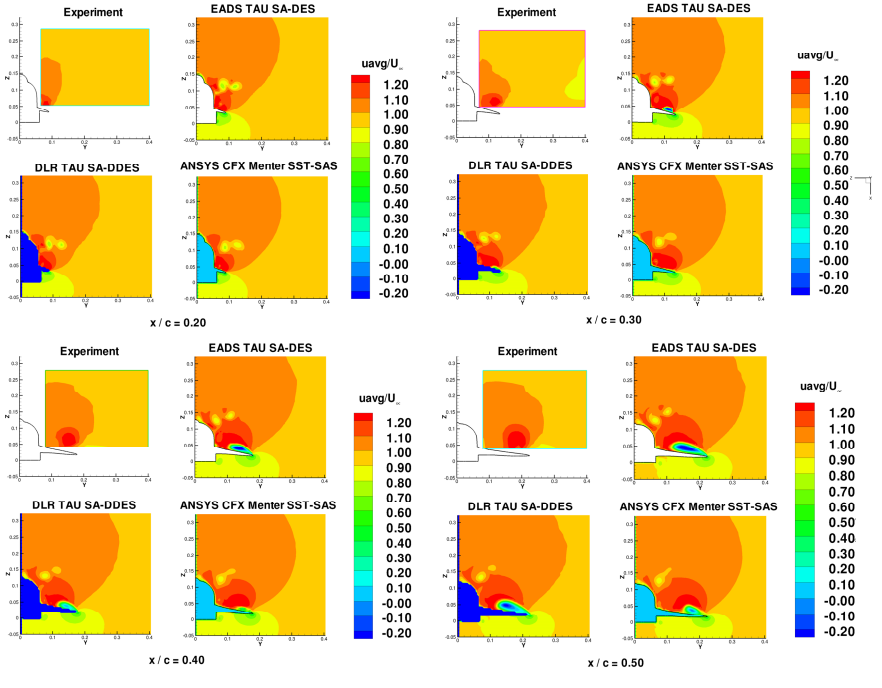

Fig. 11 Comparison of mean u-velocity in cuts x/C=0.2, 0.3, 0.4 and 0.5

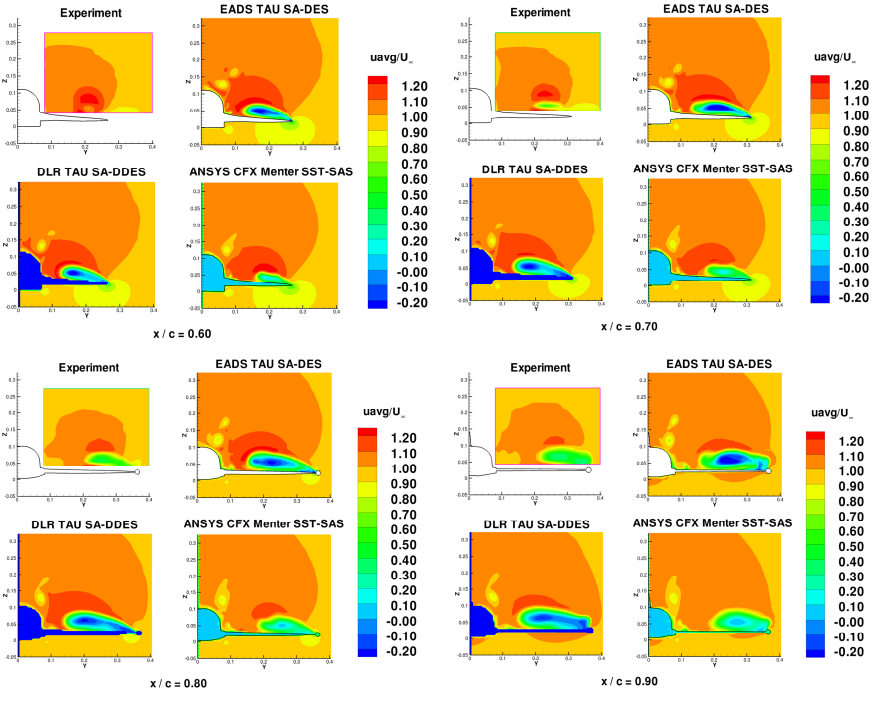

Fig. 12 Comparison of mean u-velocity in cuts x/C=0.6, 0.7, 0.8 and 0.9

Special attention was paid to the mean u-velocity field because in all former calculations using the structured grid the level inside the vortex core turned out to be negative. Here for both SA-models the velocity becomes also negative between x/C = 0.4 and x/C=0.5, figure 11, while the SST-SAS result from ANSYS stays positive downstream to the trailing edge and fits better the experimental behaviour.

This u-velocity difference can also be seen by a closer inspection of the values monitored in points 1, 9, and 19 situated near the trailing edge above the wing. Especially point 19, which is located most inboard, shows larger deviations.

Due to the larger extend of the vortex in the DES calculations the monitored u-velocity is lower than in the experiment (where point 19 is clearly outside the vortex). Accordingly, the amplitudes (also of the v- and w-component not shown here) are larger compared to the experiment or the SAS result, as there are no large fluctuations outside the vortex.

A comparison of the mean v- and w-velocity at the x/C=0.9 given below shows not such a great difference between the different results, although it can be noted that the SST SAS calculation seems to produce a smaller vortex size which is in accordance with the previous observations.

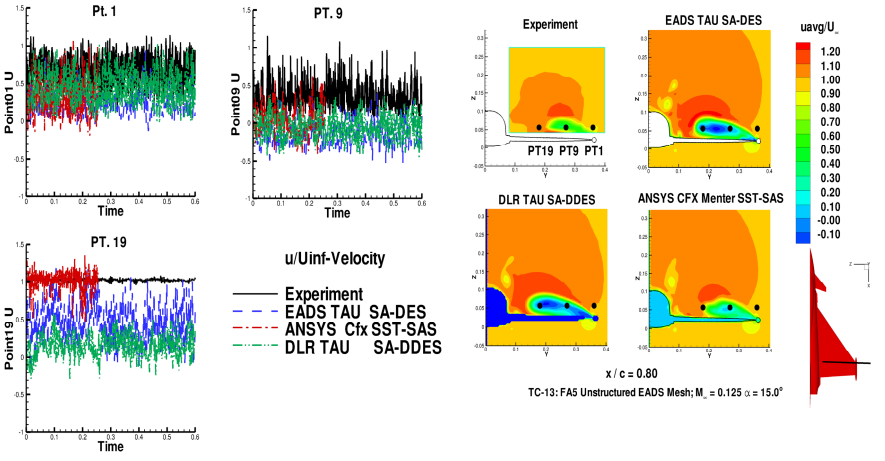

Fig. 13 Comparison of monitored u-velocity in discrete points

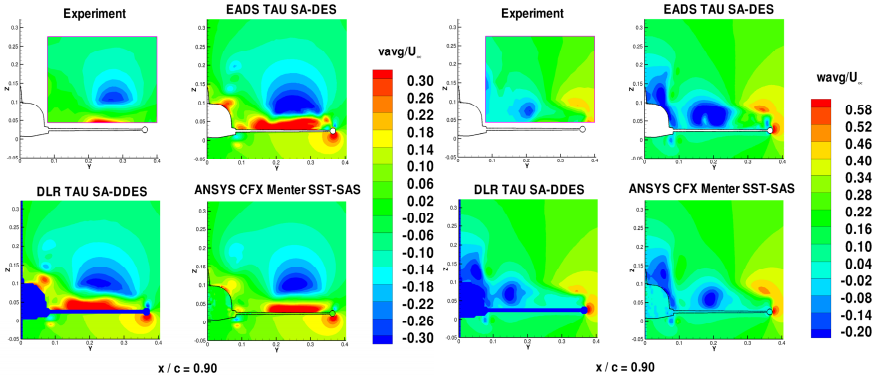

Fig. 14 Comparison of mean v- and w-velocity at x/C=0.90

Additionally included in the following figure 15, showing the power spectral density, is also an EADS-MAS FLOWer result on the structured grid using the same SA-DES model as for the TAU DES computations. The earlier drop-off of the PSD for the computational results compared to experiment is obvious and, at least to a certain degree, due to the time step size, which was the smallest for SAS. For point 19 the characteristic peak is located at the right frequency.

Furthermore standard-deviation data of u, v and w are given from the experiment. A comparison with the calculations for the cut x/C = 0.9 is shown in figure 16. All CFD results reproduce the observed turbulence anisotropy with Urms exceeding Vrms and Wrms values. However the absolute values of the velocity fluctuations are too high compared to the experiment, especially in the SAS result by ANSYS. Comparing both SA solutions the unsteadiness of the

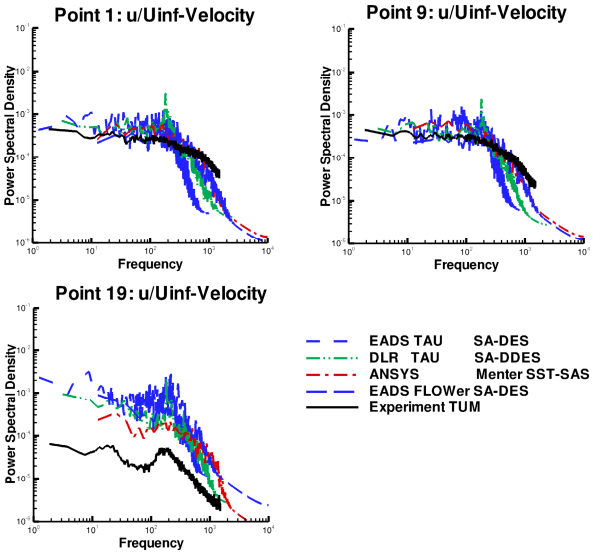

Fig. 15 Comparison of power spectral density of u-velocity in monitored points

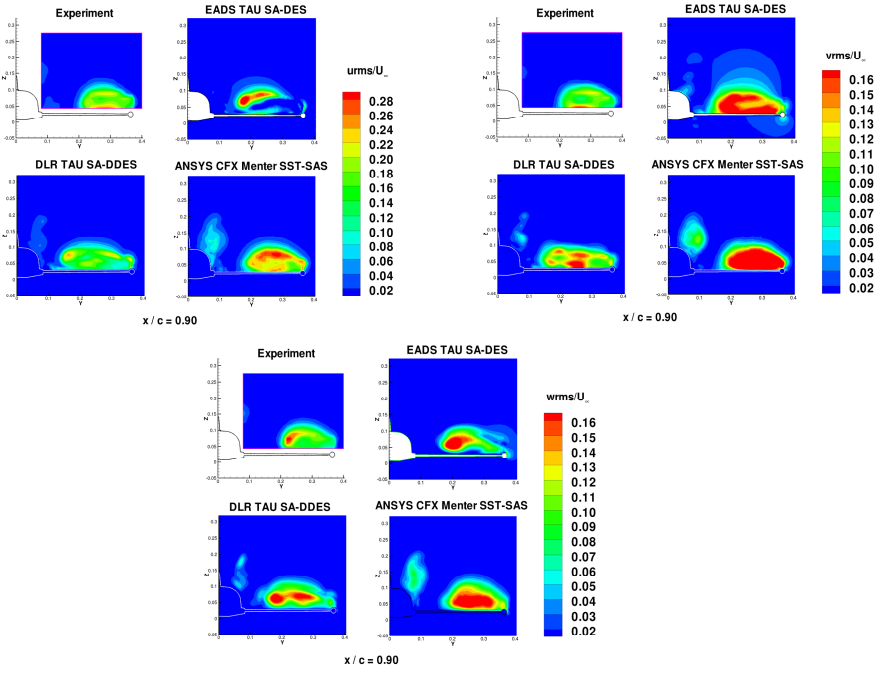

Fig. 16 Comparison of u- v- and w-rms values at x/C=0.90

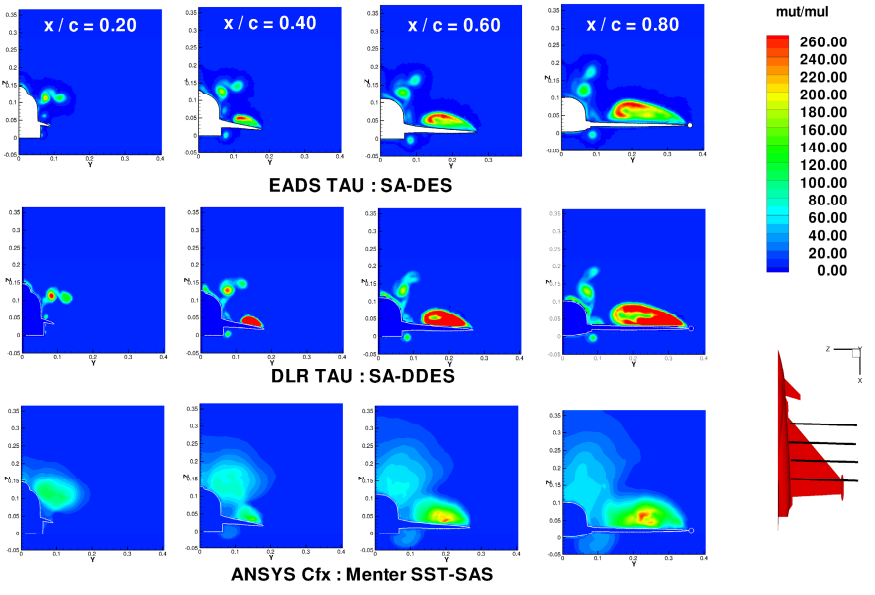

Fig. 17 Comparison of the ratio μt to μl of the theoretical computations

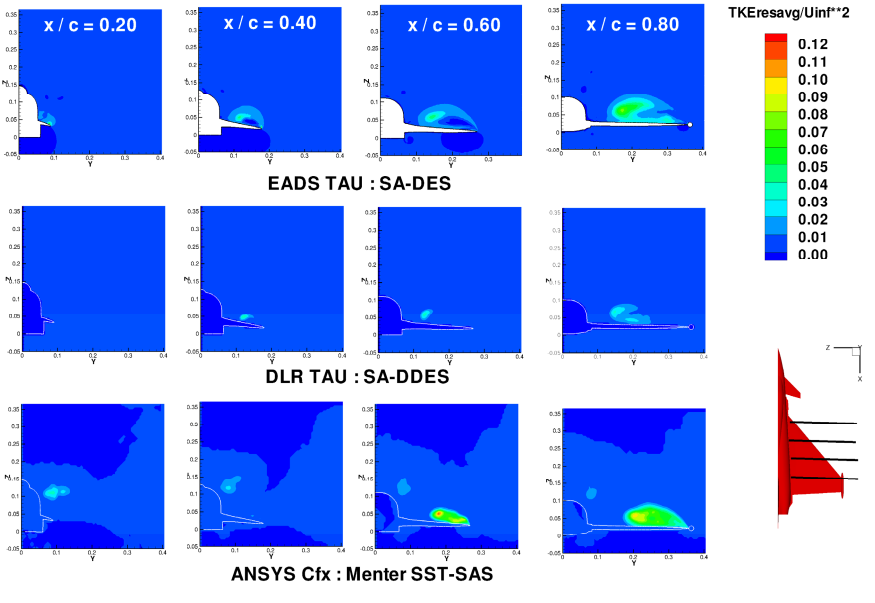

Fig. 18 Comparison of the resolved turbulent kinetic energy TKE

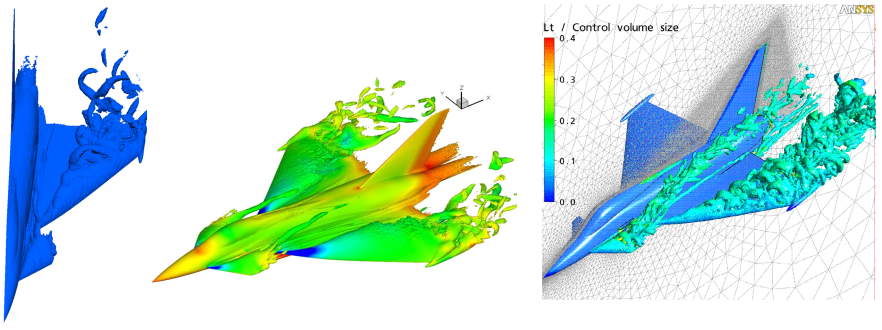

EADS-MAS **DLR Vorticity coloured with cp** **ANSYS Vorticity**

Fig. 19 3D Vortex structures

u-component shows a “blue spot" in DES result. The reason is not clear until now. Also the DES over predicts the rms-values of all components more than the DDES result. This might be an effect of the by a factor of five smaller time step size and the fact, that DDES prevents the LES region from developing instabilities close to the wall forced by grid spacing. This advantage is present especially near the wing tip, and important and appropriate for a physical behaviour.

The next two figures, 17 and 18, show comparisons of the distributions of the instantaneous ratio of μ_t to μ_l and the average of the resolved turbulent kinetic energy TKE. The μ_t to μ_l distribution presents very similar patterns for both, the SA DES and the SA DDES computation. You can observe the locations of the various vortices and a slightly higher level of the ration for the DDES compared to the DES solution. The ANSYS result looks quite different and seems to smooth out all discrete maxima. This is not understood and should be the topic of further investigations.

Looking at the TKE distribution remarkable differences between DES and DDES can be noticed. The DDES values are much lower. The ANSYS solution is similar to the DES one and is the only one that visualises the trace of the canard as well as the strake vortex by the given scaling.

Figure 19 shows the 3D vortex structures. Although the representation does not use identical criteria, one can conclude that the ANSYS flow field seems to contain more small details than the EADS-MAS or DLR result. This is probably a result of the finer time step size used, which is by a factor of ten or five smaller.

12.5 Conclusion

Within Task 13 various detached eddy simulations around the generic FA-5 fighter configuration has been performed, being a realistic test case of industrial relevance. In a structured grid mainly URANS computations by EADS-M applying three different turbulence models have been done and are compared with TUB DES computations, using two different background turbulence models, and the experimental data. All computations are basically using the same grid. The results

show the superior behaviour of the DES-models with regard to the description of the unsteady content of the flow. Also found is the strong dependency of the unsteadiness of the flow on the underlying turbulence model in DES mode as well as upon the size of the time step.

The last conclusion can also be drawn also from the calculations in the unstructured grid where an identical mesh is used by all partners. While the SA DES and SA DDES show more or less similar results the SST-SAS model shows a somewhat different behaviour coming closer to the experiment for some, but not all of the compared data. It has to be pointed out, that the chosen time step for the latter simulations was much smaller than for the other ones.

The SST-SAS model is the only one which predicts a still positive axial velocity at the trailing edge together with a vortex extension being closer to the experiments and giving a somewhat improved level of the power spectral densities of the velocities, while the rms- values are over predicted at the same time. This calls for more careful examination of both the DES and the SAS models for simpler vortex dominated configurations in order to come to sound conclusions for this type of flows.

13 Circular Cylinder on a Ground Plate

J.C. Uribe and D. Laurence

University of Manchester

Abstract. The case of a circular cylinder mounted on a ground plate is studied by three different partners, Chalmers, NTS and the University of Manchester. LES and DES and TRANS have been used. Each partner has created their own mesh. Results are compared to experimental values available. None of the simulations produces a reasonable agreement with the experiment and they miss important 3D features of the flow.

13.1 Overview

A cantilever cylinder with one end fixed and the other free is considered. The cylinder aspect ratios (AR) are 6 and 10 and the Reynolds number based on cylinder diameter and free stream velocity is Re= 20,000 for both cases. These cases are a continuation of the LES work of Frohlich and Rodi (2004), in which the authors tested a cylinder with an aspect ratio AR =2.5 and recommend testing of further AR cases at the same subcritical Reynolds number (Re) range. The availability in electronic format of experimental data from Park and Lee, 2000 made the test case quite attractive, but some inconsistencies were later discovered in the PIV velocity fields, while the Cp profiles around the cylinder seemed to vary significantly between publications. In addition, difficulties in finding agreement even between different LES, some as fine as 7 Million cells, tended to discourage other partners from participating to this test-case. Nevertheless a DES and Transient RANS simulations were attempted at an early stage, followed by several LES. The results of the finest, 15 Million cells LES were not yet fully available at the time of writing however.

The main observation is that the flow over the free end has a complicated three-dimensional structure, starting from a pair of delta wing type vortices from the sharp edges; with later a strong downwash from the free end of the cylinder almost all the way down to the floor and this downwash interferes strongly with the classical vortex shedding features expected from tall cylinders. The extent of the downwash and subsequent vortex shedding damping are features where most variations between different simulations are found.

13.2 Flow Geometry

The geometry consists of a finite circular cylinder vertically mounted on a flat plate with one end fixed and the other free (and other cases also allowed to

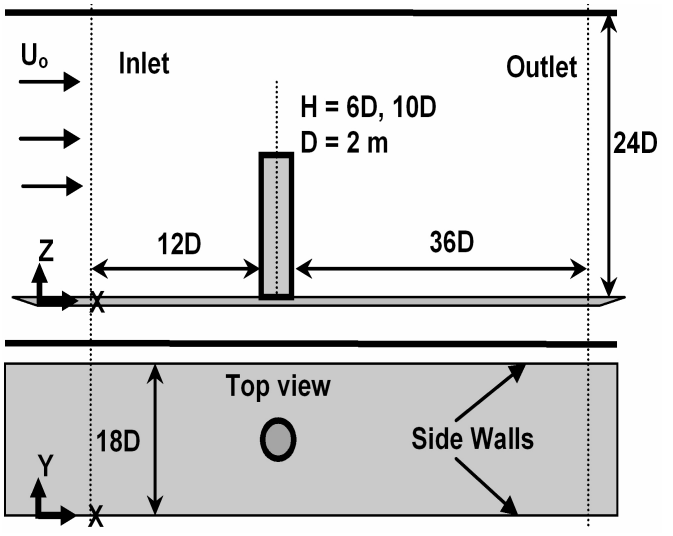

Fig. 1 Geometry under consideration of finite cylinder. Top: Cross sectional view in *XZ* plane. Bottom: Cross sectional view in *XY* plane

vibrate, but not considered here). The vortices that are shed from the cylinder, along with a strong downwash from its free end require a fairly long computational domain to capture the flow physics adequately. The downstream length is set at 36 diameters and the upstream length is set at 12 diameters, with the origin of the coordinate system located at the centre of the base of the cylinder.

The complete geometry is shown in Fig. 1, where a uniform flow enters from the left (other boundary layer thickness case are available). The blockage ratio defined as the ratio of the projected cylinder area to the cross sectional area of test section *(A/C)* is 1.38 % for *AR* 6 test case. However a little variation in this ratio is still acceptable; Frohlich and Rodi (2004) use a blockage ratio of 7.1% for all their simulations, still achieving decent results as compared to experiments. While understanding the tip flow effects special consideration should also be given to the height of the computational domain. In the present case this domain total height (H_{TZ}) is 24 diameters. Thus the ratio $H_{TZ}/H = 4$ for AR 6 case which is still sufficiently larger than the experimental (Park and Lee (2000)) ratio of 3.33.

13.3 Participants

The following table 1, see below, shows the partners involved in this test case and the details of the computations.

Details of the meshes used can be seen in figures 2, 3 and 4. All 3 groups use a cylindrical grid around the obstacle with a first cell width close to one in viscous wall units, then different strategies to match this inner grid to the rectangular computation domain mesh. NTS uses overset grids while Manchester uses non-conforming 1.5 refinements at block interfaces (2 cells facing 3 cells). Hence the

Table 1 Partners involved in this test case

Partner	Type of models used	Cells
Chalmers	LES	7 Million, block structured 15 Million, block structured
NTS	DES TRANS	2 Million, bloc structured (Chimera)
Manchester	LES	1.8 Million unstructured AR=6 3.4 Million unstructured AR=10

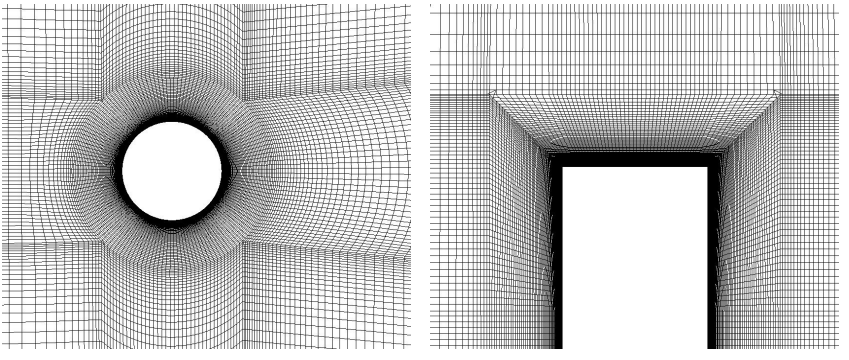

Fig. 2 Chalmers mesh

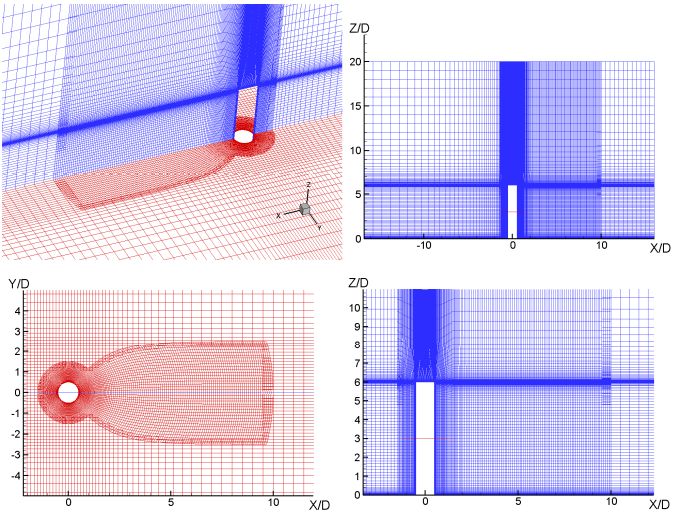

Fig. 3 NTS mesh

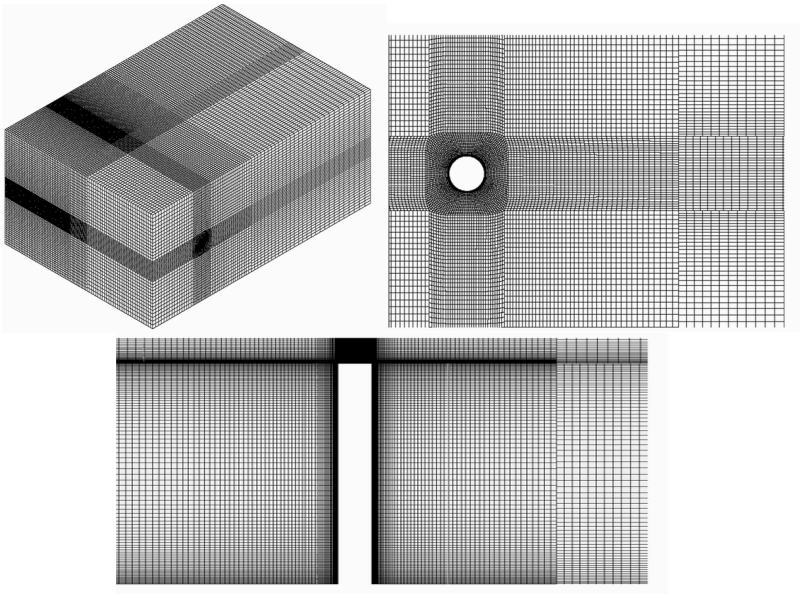

Fig. 4 Manchester mesh

near-cylinder meshes are more similar the total number of cells would suggest (2 M. for NTS and MaN, 7 M. for Chalmers).

13.4 Results

13.4.1 Pressure Coefficient

The comparisons for the pressure coefficient at four different locations can be seen in figure 5.

The LES results are in good agreement toward the middle height of the cylinder but they deviate from the experiments as the tip of the cylinder is approached. It is important to note that the results for the coarse LES from Chalmers are in better agreement than the fine LES implying either still a strong grid dependence, or a need for longer term statistics. The DES results overestimate the pressure coefficient in all instances and they are very close to the T-RANS results. The experimental results concerning Cp profiles and wake velocity at mid height significantly different from infinite cylinder case seem to confirm this but some discrepancies were noted and comparison is only qualitative. The TRRANS and DES predict Cp distributions and wake profiles close to each other and also showing a strong flow deflection and damping of the von Karman shedding. However, these predictions are tangibly away from those of the LES. It should be noted that the Park & Lee measurements of the pressure distributions do not seem to be reliable, since their Cp for the infinite cylinder differs a lot from the classic data of

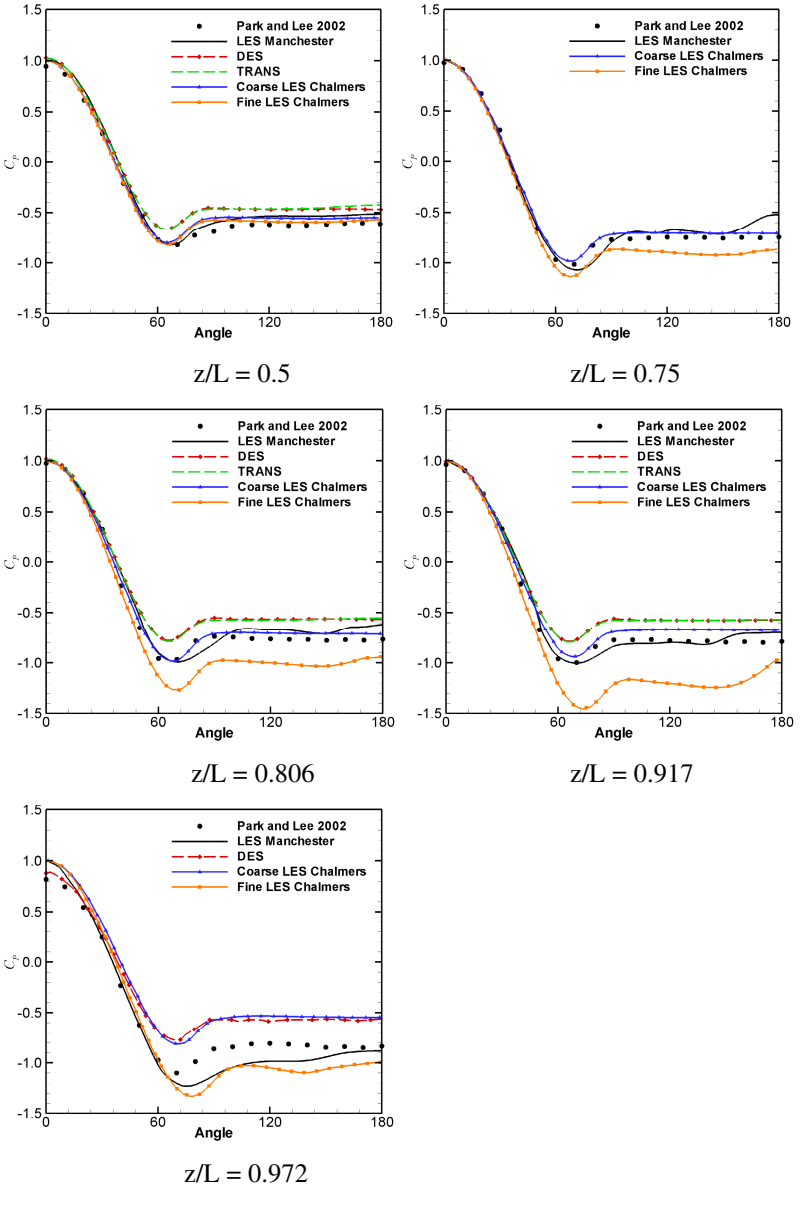

Fig. 5 Pressure coefficients around the cylinder at different locations

Cantwell and Coles, and in the case of the wall-mounted finite cylinder, Park & Lee data disagree with similar data of Luo et al. (Journal of Wind Engineering and Industrial Aerodynamics 59 (1996) 69-93).

13.4.2 Velocity Profiles

The velocity profiles can be seen in figure 6 at four different locations.

Here again the unstructured grid LES seems to be in agreement with the fine LES while the DES and T-RANS predict much higher values of velocity. The experiment on the other hand shows a surprisingly rapidly disappearing wake.

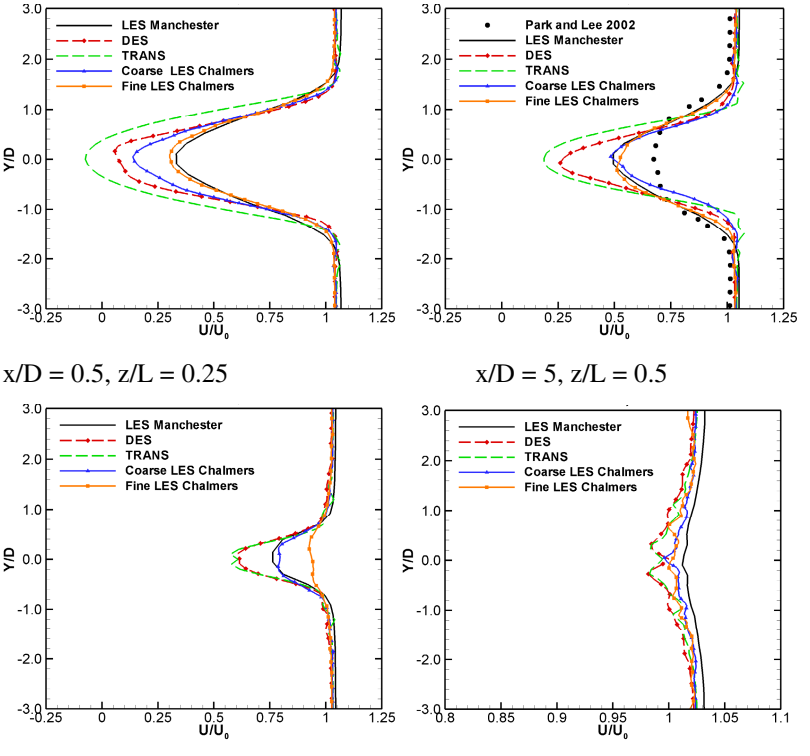

Fig. 6 Streamwise velocity profiles at different locations

13.4.3 Turbulent Intensity

Profiles of streamwise turbulent intensity at x/D = 5 and z/L = 0.5 can be seen in figure 7.

All calculations predict a high level of turbulence (25-30% TU) with a dip in the middle, which is not found on the experiments. As will be seen later this double peak distribution can be explained by the shedding of small vortices from the sides with a characteristic size of D/5 instead of D in the classical infinite cylinder case.

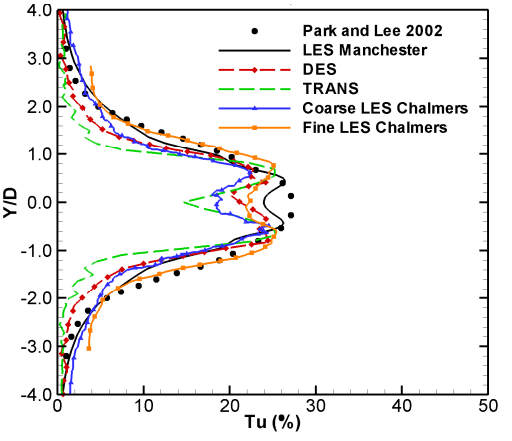

x/D = 5, z/L = 0.5

Fig. 7 Streamwise turbulent intensity

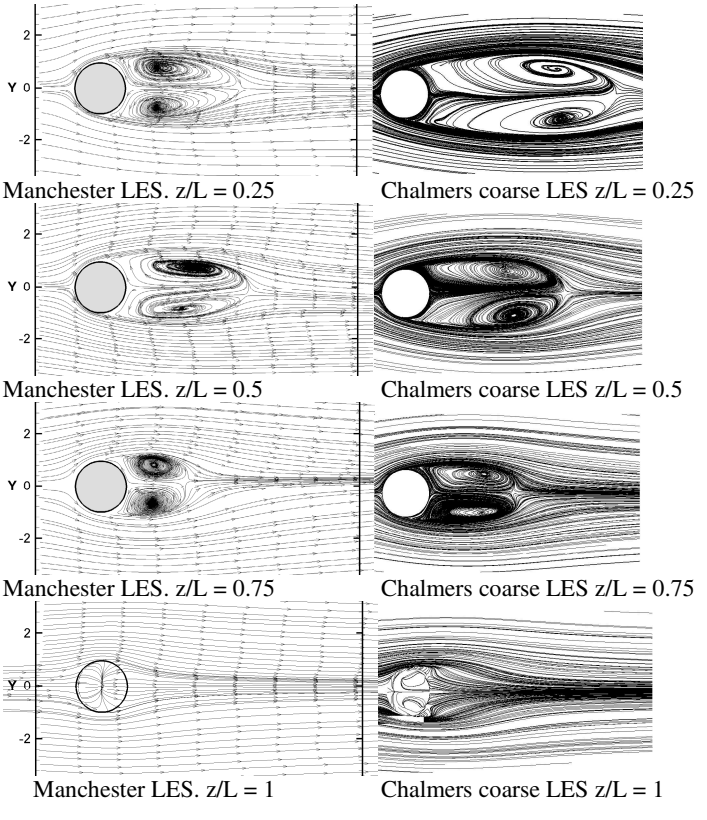

Manchester LES. z/L = 0.25 Chalmers coarse LES z/L = 0.25

Manchester LES. z/L = 0.5 Chalmers coarse LES z/L = 0.5

Manchester LES. z/L = 0.75 Chalmers coarse LES z/L = 0.75

Manchester LES. z/L = 1 Chalmers coarse LES z/L = 1

Fig. 8 Streamlines at different locations

13.4.4 Streamlines

In figure 9 the streamlines at the symmetry plane is shown and in figure 8 the streamlines at four different z planes (altitudes). Note in figure 8 the pair of very narrow or stream-wise elongated recirculation, which is a significantly different-pattern from the infinite cylinder case. In figure 9 a dense cluster of lines is generated just before the tip of the cylinder, which later highlights an "arc" shaped downwash, almost reaching the base plate. The location of this cluster of streamlines corresponds in figure 8 to the saddle points marking the end of the vortex pair. Thus the streamline divergence along the "arc" highlights the strong 3D effects. At the foot of the cylinder, in front, streamlines are seen to curve back towards the ground, just about suggesting a horseshoe vortex but this one is very shallow due to uniform inflow profile. Behind the cylinder at the cylinder plate junction a second vortex is seen resulting from the downwash all along the cylinder, but this one is fully embedded in the near wake and is unrelated to the horseshoe vortex.

The Chalmers and Manchester LES seem to agree with each other as concerns the top half of the flow, but less so nearer the floor. In particular from mid-height down to the floor, the Manchester results show a shortening and "rounding" of the mean flow vortex pair, which is interpreted as a re-appearance of the classical Karman Vortex street, while the Chalmers LES at z/L=0.25 still show a very elongated recirculation pair.

The "Fine LES" results of Chalmers herein correspond to results obtained in January 2007 on the 15 M. cells mesh, and may require further averaging. More detailed results are due to be presented at TSFP5 Munich August 2007. Further description of the Manchester LES, including mesh refinement studies and comparison of aspect ration 6 and 10, can be found in Afgan 2007.

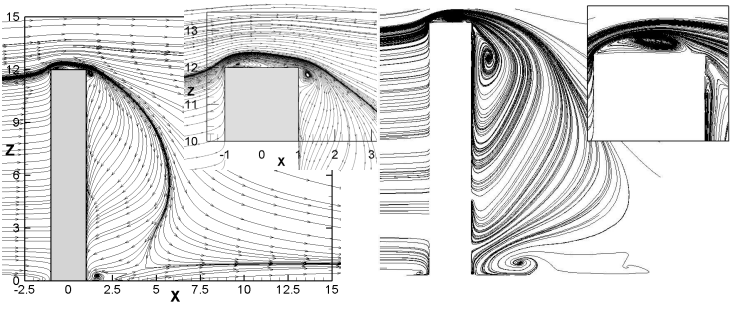

Manchester LES Chalmers coarse LES

Fig. 9 LES streamlines at y/D = 0

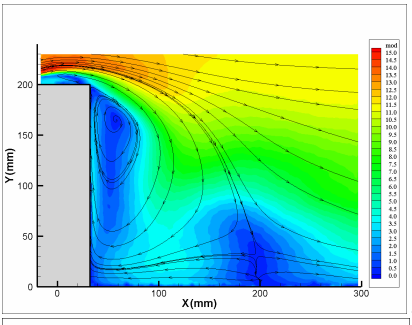

a) Symmetry plane

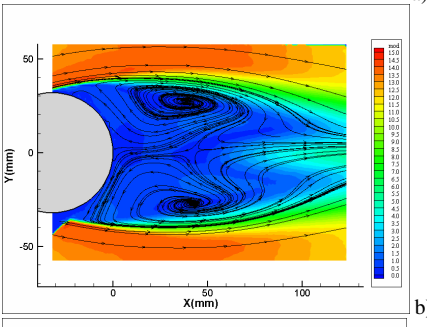

b) Z=150mm

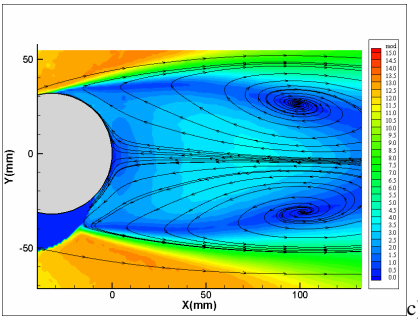

c) Z=20mm

Fig. 10 Streamlines from PIV of H/D=3 finite cylinder experiment at Re_D=4.26 10^6, by R. Manceau & L.E. Brizzi, (www.univ-poitiers.fr/lea)

13.5 Conclusions

The flow around a cylinder has shown many complex features. Despite the high aspect ratio, the flow over the cylinder is found to be strongly inhomogeneous along the height of the cylinder, i.e. highly three-dimensional and significantly more turbulent in the lower half of the wake. The roll up of the shear layer separation from the free end causes two counter rotating vortices near the free end of the cylinder leading to a strong downwash extending downstream nearly to the base. This downwash changes the flow evolution by interacting with the regular vortices being shed from the sides of the cylinder. This interaction causes changes in the pressure distribution in the wake of the cylinder and damping of the vortex shedding.

When comparing with the experimental results, all the simulation seem to miss important features of the flow field, both most importantly they do not agree well with each other. The lack of consistency of the results shows that this is a difficult case for which probably a higher mesh refinement is required.

Since even the LES do not agree with each other, and experimental data is too uncertain, it is certainly too early to use this test case for an evaluation of DES or hybrid models.

Nevertheless this type of geometry presents a very obvious interest for many industrial applications: aeroacoutics, flow induced vibrations of probes or towers (at higher Re!), and the experimental investigations must be pursued as well as modelling effort. The preliminary investigations performed within DESider have at least drawn the attention of the community toward this very challenging test case.

At the time of writing, R. Manceau & L.E. Brizzi from LEA, Poitiers provided a very detailed PIV set of results for similar Re number, but lower AR of 3 (private communication). The similarity of those PIV results shown in figure 10 with the previous LES streamline plots is quite striking. In particular a film generated from PIV data confirms clearly that the elongated recirculation pair seen is fig 10. c) is due to a number a quite small eddies being shed from the shear layer with their centre being convected along a straight line rather alternating as in a Karman street.

14 Fuel Assembly Industrial Test-Case

S. Benhamadouche

EDF

14.1 Introduction

The present work started during the Desider project and is still ongoing. Unsteady flow loading of fuel assemblies in PWR power plants is a potential cause of deformation and fretting wear damage (Rubiolo, 2006). Predicting the complex turbulent flow behaviour due to the grids, the vanes, the springs and the dimples, is a challenging task in the nuclear industry and this will remain the case for several years, if not decades, if one wants to compute a whole assembly.

CFD has been recently used to predict the flow behaviour along fuel rods (Seok et al, 2008, Chang et al, 2008 and Lee et al, 2007). The accurate prediction of such flows, and in particular their unsteadiness, is mandatory in order to carry out fluid/structure interaction calculations. Figure 1 shows the complexity of the real geometry. A real-life fuel assembly is composed of 17x17 rods (the diameter of a rod and its length are respectively around 1 cm and 4 m) maintained with around 8 mixing grids or grid assemblies. The mixing grids are not only used to maintain the rods but also to enhance the mixing and the homogeneity of the fluid and thermal distributions. The very long-term objective is to compute the instantaneous pressure loading to which the fuel rods are exposed during the exploitation in a nuclear plant for a whole assembly. Such an objective is very challenging as the computational domain is large and the physical phenomena are complex.

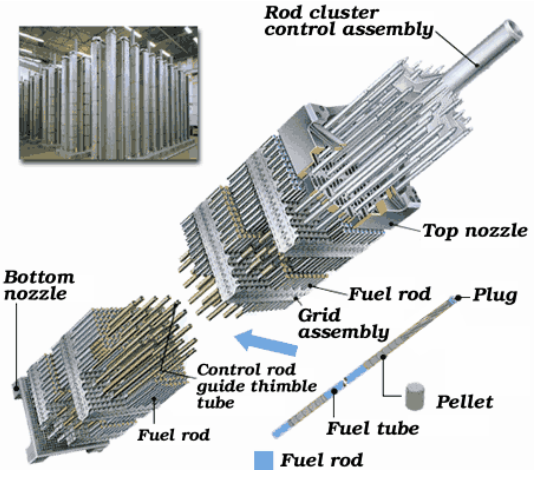

Fig. 1 General view of a fuel assembly

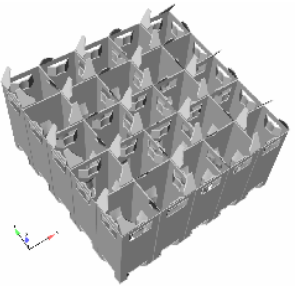

Fig. 2 5x5 grid assembly

Computing a whole assembly, even with less demanding turbulence models such as RANS, URANS or DES, is still impossible even with the most powerful existing computers as this will require grids of hundreds of billions of cells.

14.2 The Computational Domain

The aim is to obtain the instantaneous pressure loading along the tubes. The frequencies which are able to make the rods vibrating are in the range of 10 to 100 Hz. The only reasonable approach in this region is to utilize a pure Large Eddy Simulation approach. Although the Reynolds number in the reactor configuration is around 500 000, the known experiments of such configurations have Reynolds numbers around 40 000 to 50 000, which is considered reasonable for LES with wall functions. An intermediate objective is then to compute the axial flow along a bundle on a limited domain and at a reasonable Reynolds number.

Regarding the literature, a 5x5 fuel assembly with a typical grid such as the one represented in figure 2 with 2 m fuel rods is acceptable at a Reynolds number around 40 000. Even this restricted computational domain is still too big in order to perform simulations using pure LES. The present calculations are then limited to 4 sub-channels as shown on figure 3 with 40 cm fuel rods (which corresponds approximately to the space between two grids in a real-life fuel assembly). The dimensions of the computational domain are show in figure 4. The hydraulic diameter Dh is around 1cm and the length of a rod corresponds to 40 Dh. The upstream axial bundle has a length of around 2 Dh.

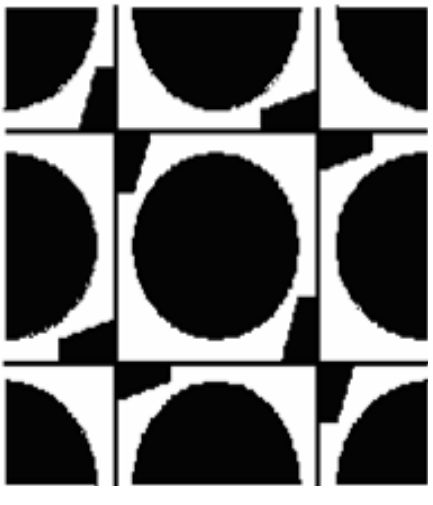

Fig. 3 The four sub-channels (the main flow in perpendicular to the higure)

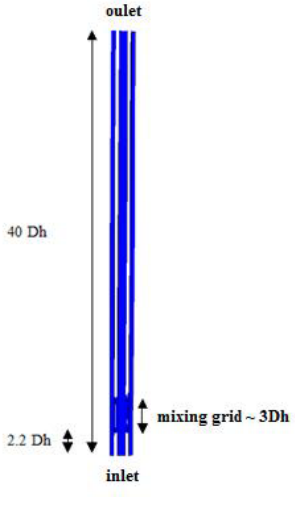

Fig. 4 The computational domain

14.3 Turbulence Modeling

The first idea was to use LES in the axial tube bundle region while using RANS in the mixing grids, as generating the mesh is complex in this region. One recalls that LES is very sensitive to non-orthogonal or non-conforming meshes (as the turbulent viscosity is very low compared to RANS one) and RANS is more adapted to the use of distorted and non-orthogonal computational cells. This aim has been postponed but the use of RANS/LES coupling or hybrid RANS/LES approaches will be probably mandatory for larger computational domains. Only pure LES or URANS approaches are presented herein.

14.4 Grid Generation

The use of LES incited us to create a fully hexahedral mesh. It took more than one year to obtain a satisfactory mesh for this configuration. The final grid has been obtained with the grid generator ICEM using the available blocking method. All the attempts with the other available mesh generators failed. Figures 5 and 6, respectively, show the interior of the mixing grid and the quality of the hexahedral cells which have been used. The mesh contains 8 million cells and has been used for all the computations on the four sub-channels configuration. Another mesh with 100 million tetrahedral cells has been built to test High Performance Computing (HPC) capacities at EDF (EDF made the acquisition of two Blue Gene machines, a BGL with 8 000 processors in 2007 and a BGP with 32 000 processors in 2008). Few words about these tests are given at the end.

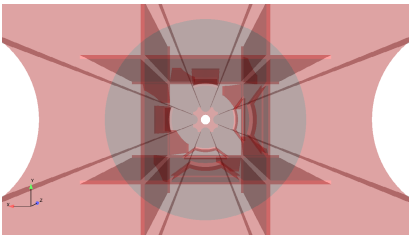

Fig. 5 Interior view showing the vanes, the springs and the dimples

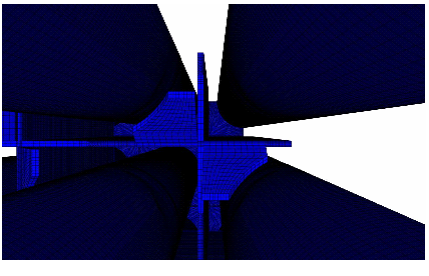

Fig. 6 The hexahedral mesh

14.5 URANS and LES Computations

EDF in-house open source CFD tool *Code_Saturne* is utilized herein for all the calculations. *Code_Saturne* is an unstructured collocated finite volume solver for incompressible flows using a SIMPLEC algorithm for pressure-velocity coupling with Rhie and Chow interpolation to avoid odd-even decoupling on structured meshes. Further details can be found in Archambeau (2004). It has been validated for cross-flows in tube bundles (Benhamadouche et al, 2003, 2005) with LES and

Table 1 The main parameters of the main computations

Turbulence model	Boundary Conditions	Dt (s)	CFL_{max}	No. time steps	No. passes	No. of passes for averaging
LES Cs=0.065	Cst	5.10^{-6}	0.8	700 000	30	8
SST	Cst	5.10^{-5}	7	120 000	45	30
SST	Dev	5.10^{-5}	7	50 000	20	4
SSG with SWF	Cst	5.10^{-5}	7	150 000	60	40
SSG with SWF	Dev	5.10^{-5}	7	75 000	30	10
SSG	Cst	5.10^{-5}	7	150 000	60	20

URANS approaches. LES technique provides the instantaneous velocity field whereas URANS approaches might give some unsteadiness but at low frequencies (one recalls that our main objective is to obtain the instantaneous pressure loading to carry out fluid structure interaction with these data).

A fine grid with 8 million cells is utilized to represent the restricted computational domain including 4 sub-channels along 40 hydraulic diameters and one mixing grid. The inlet bulk velocity and the hydraulic Reynolds number are respectively around *3 m/s* and 40 000. HPC calculations are carried out on 1024 or 2048 processors of BlueGene/L-P supercomputers, in particular with LES for which long physical time and small time steps are needed. For example, the LES computation ran during 40 days on 1024 processors for 40 flow through passes.

In addition to implicit reconstruction technique for non-orthogonal faces, all the computations use a fully centred scheme for the velocity components (without any up-winding). For LES, the time scheme is based on a Crank-Nicolson second order scheme. For URANS, the time scheme is an Euler implicit one, and the turbulent quantities are solved with a fully upwind convection scheme.

Table 1 gives the main computations and the main parameters for each of them. The highlighted computations are the one which have been deeply post-processed. There is no point in the present presentation to give all the details about the post-processing. The two main intermediate conclusions concerning the URANS approaches are: using constant or fully developed boundary conditions do not change the results and the use of Scalable Wall Function has no effect with the present mesh.

Available literature in the present field (see for example Seok (2008)) show that the turbulent intensity defines as the integral of $I = \frac{\sqrt{\frac{2}{3}k}}{U_{bulk}}$ on a plan orthogonal to the main flow, downstream of the mixing grid varies between 15% and 20%. Figure 7 gives the evolution of the turbulent intensity downstream the mixing grid for LES and the level of this intensity for the URANS approaches just downstream the mixing grid. It is clear that URANS (here the k-w-SST and the SSG with Scalable Wall Functions) are unable to reproduce a reasonable level of kinetic energy. This qualitative argument is sufficient to focus our attention and future efforts on pure

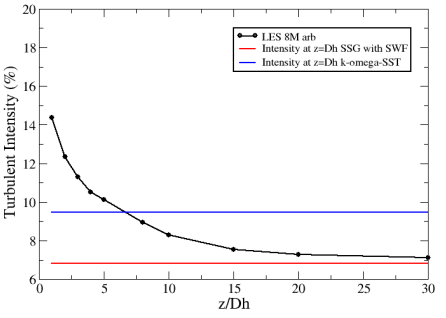

Fig. 7 Turbulent intensity

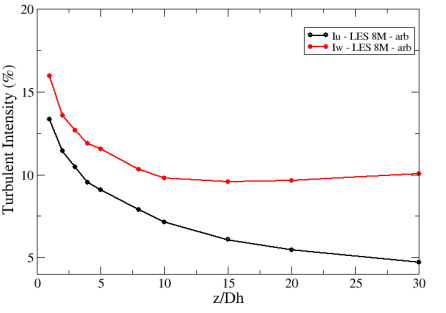

Fig. 8 Fluctuation intensities in the stream-wise (w') and span-wise directions (u')

LES simulations or on hybrid RANS/LES simulation. Figure 8 shows the evolution on the fluctuations of each velocity component downstream the mixing grid (for the component u, one has $I_u = \frac{\sqrt{u'^2}}{U_{bulk}}$). The level of the two intensities are comparable just at the exit of the mixing grid but the stream-wise velocity component becomes higher downstream as the near-wall gradient is the only term that produces turbulent energy. A swirling flow is created by the vanes. The intensity of this swirl can be estimated by the circulation given by $C = \frac{\sqrt{U^2 + V^2}}{U_{bulk}}$, where U and V are the tangential velocity components (in the plane orthogonal to the main flow). Figure 9 gives the evolution of this quantity downstream the mixing grid for LES computation. The decrease is, as it is the case for the turbulent intensity, natural. However, one can notice the high level of this quantity just downstream the mixing grid (around 35%). This may entail instantaneous circulations comparable to the inlet velocity (3 m/s). Figure 10 shows other qualitative

Fig. 9 Circulation evolution downstream the mixing grid for LES computation

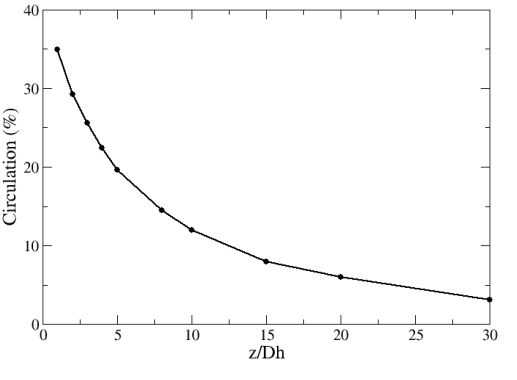

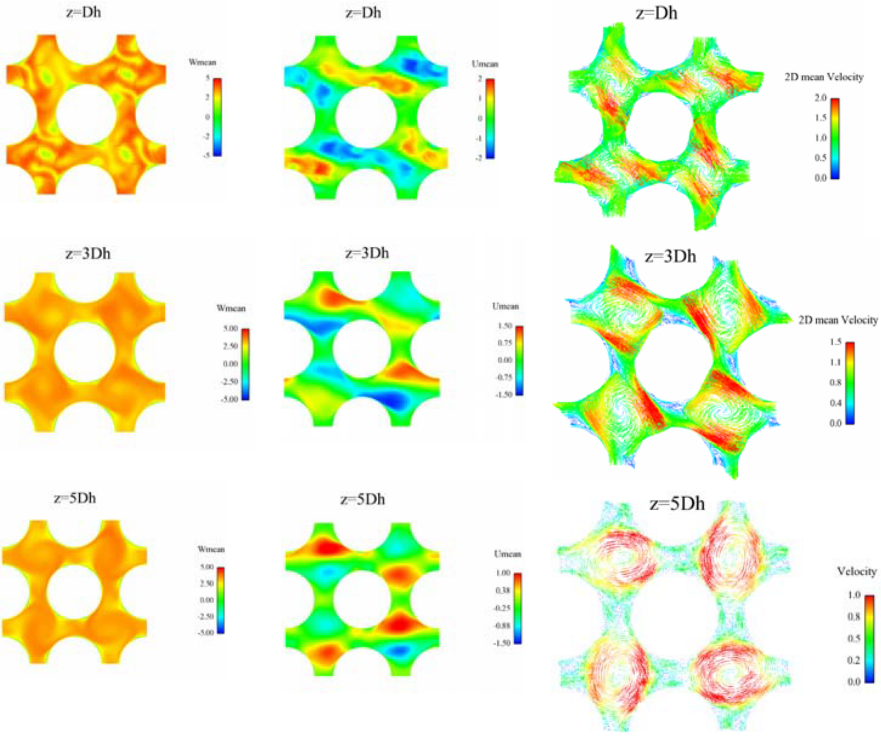

Fig. 10 Mean stream-wise velocity, mean tangential velocity and mean velocity vectors at three positions downstream the mixing grid

behaviour. The mean swirl is obvious. The form of the swirl is ellipsoidal at the beginning, the main axes of this ellipse turns depending of the position of the plan and becomes circular at some distance. All these qualitative estimations are in good agreement with the existing literature. The lack of experimental data does not allow us to have fine quantitative comparisons and an experimental program is being set up.

14.6 High Performance Computation (HPC) Tests (100 M Cells)

A tetrahedral mesh with 100 million cells has been used to perform HPC tests. Only the standard unsteady k-epsilon model with two layer wall functions has been tested. Figures 11 and 12 show respectively the velocity magnitude and the velocity streamlines at a given time. Although the fields seem physical, no quantitative variable has been deeply checked. This test allowed checking the performance of *Code_Saturne* on massively parallel machines such as the Blue Gene/L. The solver used up to 8192 processors with a very satisfactory speed-up.

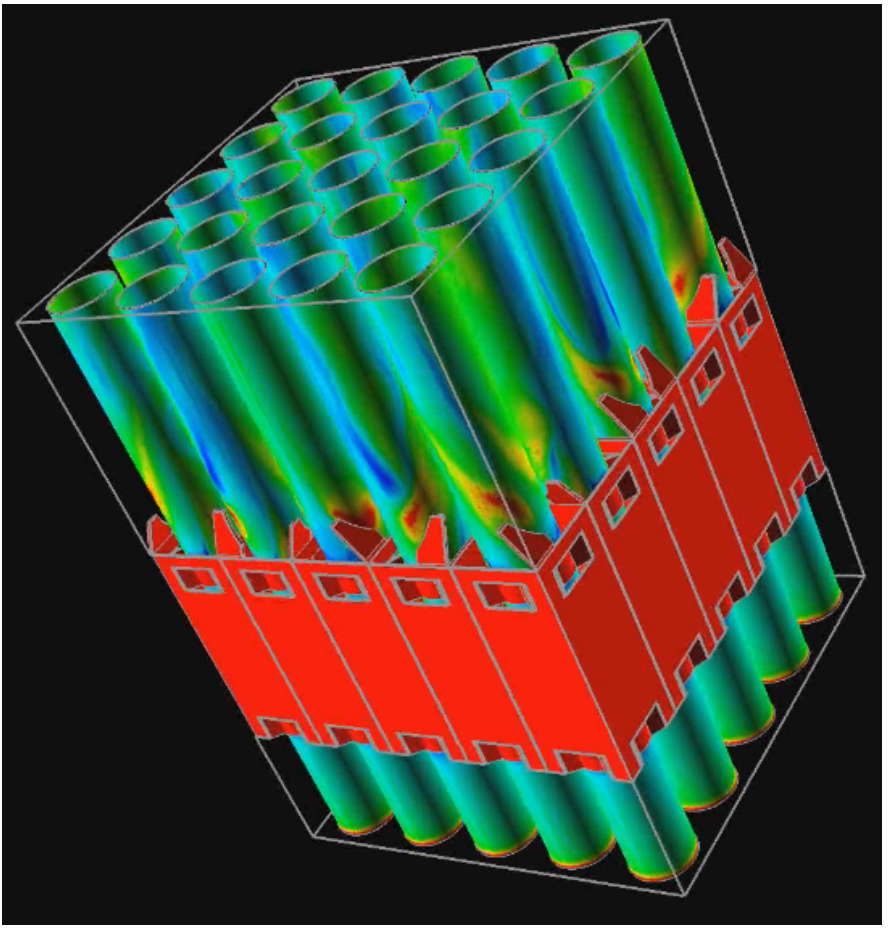

Fig. 11 Instantaneous velocity magnitude

14.7 Conclusions and Perspectives

More tests are needed in order to achieve the first objective which consists in simulating a 5x5 rod bundle. Although one can argue intuitively that the inlet conditions might not have an effect on this test case with LES because of the high and predominant production of energy through the mixing grid, one has to test the effect of a synthetic method such as the vortex method on this test-case. In addition, the sensitivity of the results to the mesh refinement is being tested with a finer mesh (19 M cells with a finer grid in the stream-wise direction). An experiment will also be carried out to have a fine database in order to evaluate the current numerical results. Finally, hybrid RANS/LES techniques should be tested in a

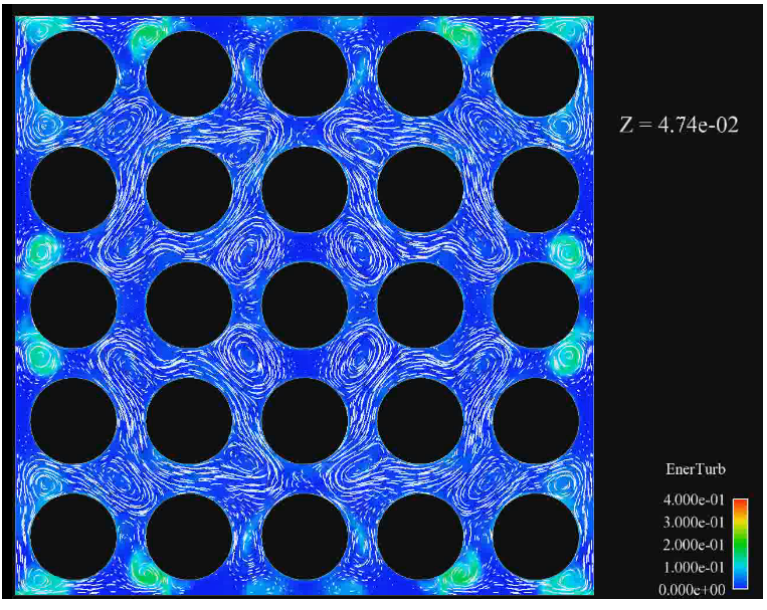

Fig. 12 Instantaneous velocity streamlines and the turbulent kinetic energy

near future to avoid wall refinement (in the perspective of an industrial application at a Reynolds number of 500 000).

15 EC145 Helicopter Fuselage – An Industrial Case

F. Le Chuiton[1], A. D'Alascio[1], G. Barakos[2], R. Steijl[2], D. Schwamborn[3], and H. Lüdeke[3]

[1] Eurocopter Deutschland GmbH
[2] University of Liverpool
[3] DLR

Abstract. The present report presents the technical achievements at Eurocopter Germany about a first industrial attempt to use DES-like methods to compute the wake behind a helicopter in forward flight. Three codes have been used: TAU (DLR), CFX (Ansys) and HMB (University of Liverpool) and four different turbulence models: standard SST and three of its unsteady extensions SAS, DES and XLES. Results for the loads, pressure distribution and skin-friction lines have been compared to each other and against wind tunnel experimental data. These more sophisticated models brought improvements over the base SST but not always markedly and consistently: the drag gets improved although the negative lift on the body departs further form the experimental value. The pressure distribution on the backdoor has been improved by one of the computation. Oil-flow visualisation results show that the mean flow in the region of the backdoor is qualitatively reasonably well captured.

15.1 Test Case Description

15.1.1 Geometry

The geometry is that of a wind tunnel model of the BK117-C2 helicopter fuselage (a precursor of the EC145 helicopter) including a support strut mounted underneath. The configuration is symmetrical with respect to the XZ-plane apart from the coloured components in Figure 1: fin, horizontal stabilizers and end plates. The latter are mounted with an angle to the right, so that they generate in cruise a force to the starboard side.

15.1.2 Flight Conditions

The flow conditions were chosen as

- upstream air velocity $V_\infty = 40$ [m.s^{-1}]
- angle of attack $\alpha = 0^o$
- angle of side-slip $\beta = 0^o$

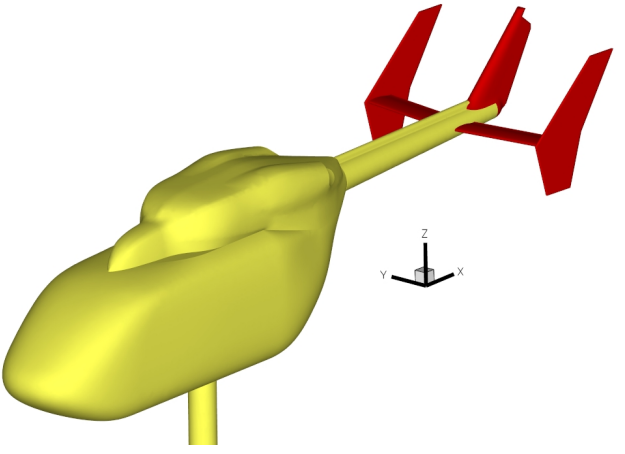

Fig. 1 BK117-C2 wind tunnel model

- upstream temperature $T_\infty = 295$ [K]
- upstream turbulence intensity $Tu_\infty = 0.4$ %

hence with

- Mach number $M_\infty = 0.11618$
- Reynolds number per unit length $Re_\infty = 2.480\ 10^6$ [m^{-1}]

15.2 Computation Challenges

This configuration proves to bear in it many challenging unsteady and vortical flow-field aspects, hereafter listed in the sequence of supposedly decreasing influence on the flow-field.

1. The flow field behind the backdoor obviously separates massively, thus inducing a strongly vortical wake that, in turn, impinges on the horizontal stabilizers. This is of particular significance for the study of the stability, static as well as dynamic, of the aircraft.
2. The flow behind the support strut also separates all the same massively and interacts with the backdoor separation. This is all the more important as this interaction conditions a good portion of the separation pattern on the backdoor and hence the vortical wake too.
3. The end plates may also experience flow separation on the front part of the suction side. This influences the side force exerted on the rear part of the configuration and hence the yaw stability of the complete configuration.
4. Since both engine exhausts are sealed, the flow naturally separates, thus creating a vortical wake that interacts with the main backdoor wake and influences the flow conditions in the region of the stabilizers and end plates.

5. The flow impinging on the nose of the engine fairing drives a horseshoe vortex to appear, the two arms of which then trails downstream on both sides of the cell and finally merge with the vortical backdoor wake.

15.3 Experiment

Through own funding, ECD has set up a wind tunnel campaign with an already existing model of the configuration described above. Measurement data, which have been used to compare against are:

- global force and moment coefficients (all three components); moments have been measured with respect to the centre of gravity;
- surface steady pressures at four sections: x=0.350, x=0.750, y=0.0 and z=0.280 [m];
- and oil flow pictures.

15.4 Partners, Numerical Tools, Grids and Computations

15.4.1 Partners and Numerical Tools

ECD and DLR used the flow solver of the unstructured simulation system TAU developed at DLR. TAU follows a finite volume approach with unknows located on grid nodes and control volumes built from the dual grid. For a thorough description of the present status of TAU please refer to Schwamborn *et al.*, 2006. For the present exercise the central scheme with matrix dissipation has been used. A second order accurate backward Euler formulation of the time derivative combined with the dual time-stepping approach has been retained for iterating in time. Low velocities have been accommodated for using a preconditioning technique, which also favoured the solution accuracy.

Additionally, ECD used the CFX solver by Ansys to run the SST-SAS computation; for details refer to Menter *et al.*, 2005.

The University of Liverpool used its in-house code Helicopter Multi-Block (HMB) for running the SST-DES computation. Convective fluxes are discretised using the scheme by Osher and a formally third order accurate MUSCL reconstruction method. Marching in time is done using a second order accurate backward Euler formulation of the time derivative. No low-velocity preconditioning has been used. Reference to Steijl *et al.*, 2006 can be made for further details.

15.4.2 Grids

An unstructured grid Figure 2 has been created by ECD with the Centaur grid generator of CentaurSoft with 2.2 million nodes, which was especially meant to be industry friendly because of the relative small number of points. The near wall region has been accommodated using 24 layers of prisms yielding a total thickness close to 8.5 [mm].

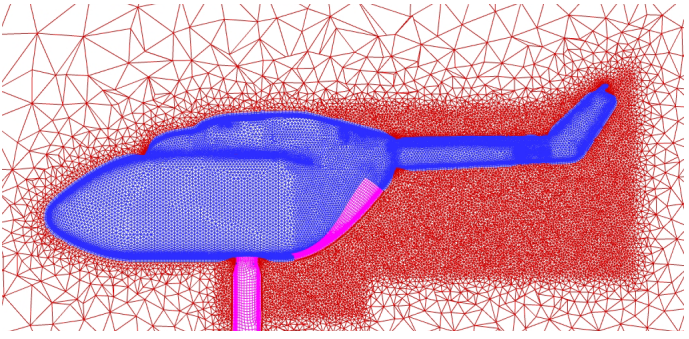

Fig. 2 Unstructured grid with 2.2 M nodes

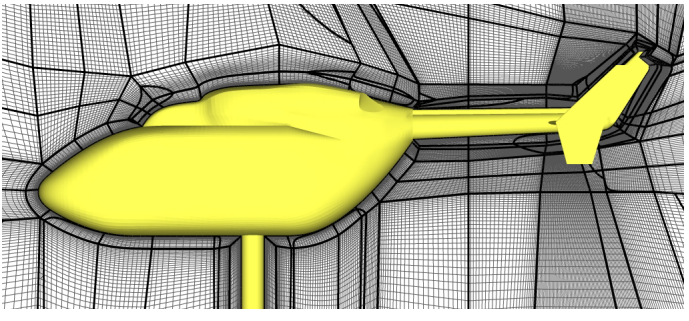

Fig. 3 Structured grid with 14.3 M nodes

The structured grid had been originally generated by ECD using the ICEM-Hexa software of Ansys with circa 10 million nodes, and was adapted to HMB by the University of Liverpool yielding approximately 14.3 million nodes and 2230 blocks (Figure 3).

15.4.3 Computations

The computations that have been carried out are summarised in Table 1 below. To be noted is that all five runs used the k-ω turbulence model as a basis and that, for the sake of comparing models, all three unsteady extensions used three different approaches: XLES, SAS and DES. One of the benefits of the unsteady DES-like modelling consists in highly reduced values of the turbulence eddy viscosity compared to pure RANS-modelling; refer to the line "max. μ_T/μ_L". Also note under "max. y^+" that all simulations yielded maximum values of y^+ around 2, which is fairly acceptable in an industrial context.

Unfortunately the time-step has not been chosen consistently over the three unsteady computations. In that respect, comparisons of the DES-content of the flow solutions may be unfair, especially for run 4 where the time-step seems to be clearly too large. For run 2, the LES-resolved area included 85% of the grid nodes;

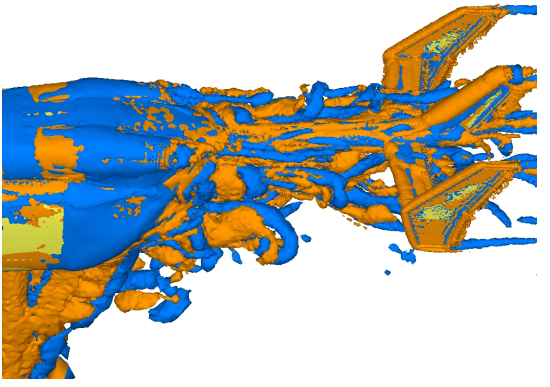

Fig. 4 TAU XLES, contours for two values of the λ_2 criterion

see Figure 4. As for run 4, the domain fore the model support strut was resolved by the RANS part of the model, while aft of it the LES-resolved region included 85% of the cells; see Figure 5.

For the purpose of post-processing, global loads as well as loads per component and surface output files also have been averaged either over iterations (steady mode) or time-steps (unsteady mode); this is indicated in Table 1.

Table 1 Runs and results matrix

identifier	1	2	3	4	5
partner	ECD	DLR	ECD	ECD	Uni.Liv.
code	TAU	TAU	CFX	CFX	HMB
turbulence model	kω-SST	kω-TNT-XLES	BSL-kω-SST	BSL-kω-SST-SAS	kω-SST-DES
grid	unstruct.	unstruct.	unstruct.	unstruct.	structured
nb. points	2.2 10^6	2.2 10^6	2.2 10^6	2.2 10^6	14.3 10^6
run mode	steady	unsteady	steady	unsteady	unsteady
integration	31000 (it.)	2.38 (s)	4808 (it.)	2.0 (s)	0.1625 (s)
time-step	---	0.2 (ms)	---	1.0 (ms)	0.025 (ms)
max. μ_t/μ_l	2430	150	5570	490	390
max. y^+	2.0	2.0	2.0	2.0	2.0
global loads	averaged over 21000 iterations	averaged over 3400 time-steps	averaged over 2700 iterations	averaged over 1000 time-steps	averaged over 6 values
loads per component	final	final	averaged over 2700 iterations	averaged over 1000 time-steps	averaged over 6 values
profiles of cp	averaged over 100 output files	averaged over 80 output files	final	averaged over 41 output files	averaged over 5400 time-steps
friction lines	averaged over 100 output files	averaged over 80 output files	final	averaged over 41 output files	---

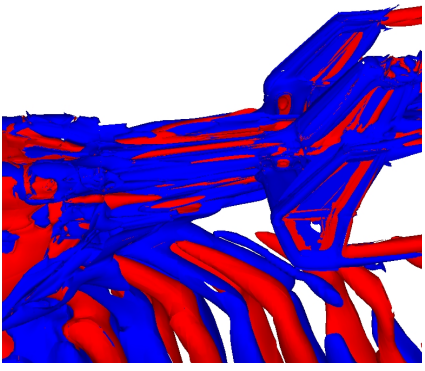

Fig. 5 HMB DES, contours for two values of the λ_2 criterion

It can be seen on Figure 2 that grid refinement for the wake of the support strut has been taken into account but unfortunately not enough: the refined region extends hardly down to the end of the back-door. Outside of it, the coarser grid area generates too high a numerical dissipation and causes the wake to completely fade away; see Figure 4. On the contrary, the structured grid allowed for the resolution of the wake of the support strut along its entire path downstream; see Figure 5.

15.5 Results

15.5.1 Global Loads

As illustrated in Figure 6 and with respect to the SST model, all XLES, SAS and DES models brought some improvement in the prediction of global loads on the fuselage. Overall both XLES and DES computations are closer to the experiment than the other ones, with a better force agreement for the DES simulation and a better moment agreement for the XLES computation.

Although all force and moment components are important for the study of the stability of the fuselage, the drag force is of particular interest. In that respect, the closest agreement to the experimental value is achieved by the DES computation, which was done on a structured grid.

Surprisingly, the negative lift is predicted with too large a magnitude by these two computations. This can be traced back to too large a contribution on the cell alone as evidenced on Figure 7. Considering the vertical force coefficient (CFz) and comparing runs 1 and 2 on the one hand and runs 3 and 4 on the other hand seems to indicate that the unsteady modelling modifies the flow structure in the direction of negative lift. Otherwise and apart from the right horizontal stabiliser, the lift coefficient is comparable between all computations.

15.5.2 Cp-Distribution

On Figure 8 is displayed the pressure coefficient distribution in the symmetry plane of the model. As expected all simulations capture equally well the pressure

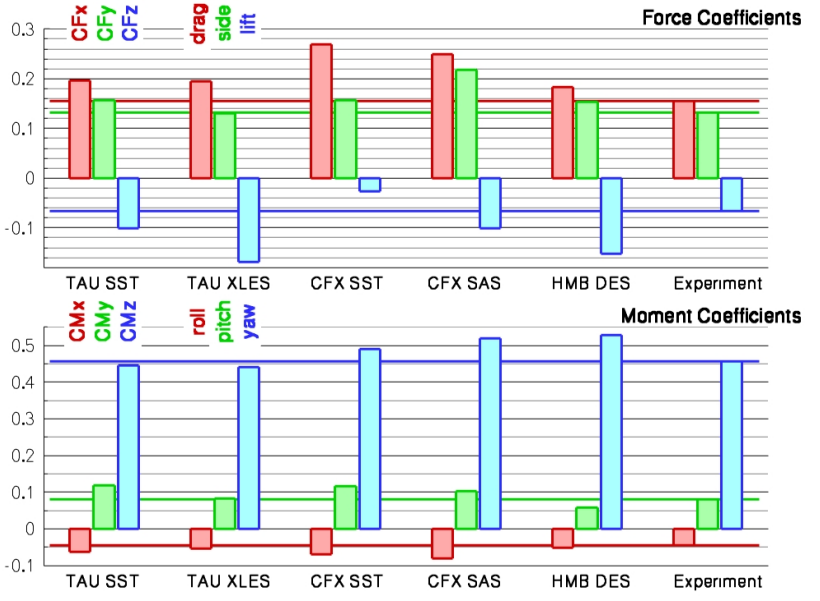

Fig. 6 Global force and moment coefficients

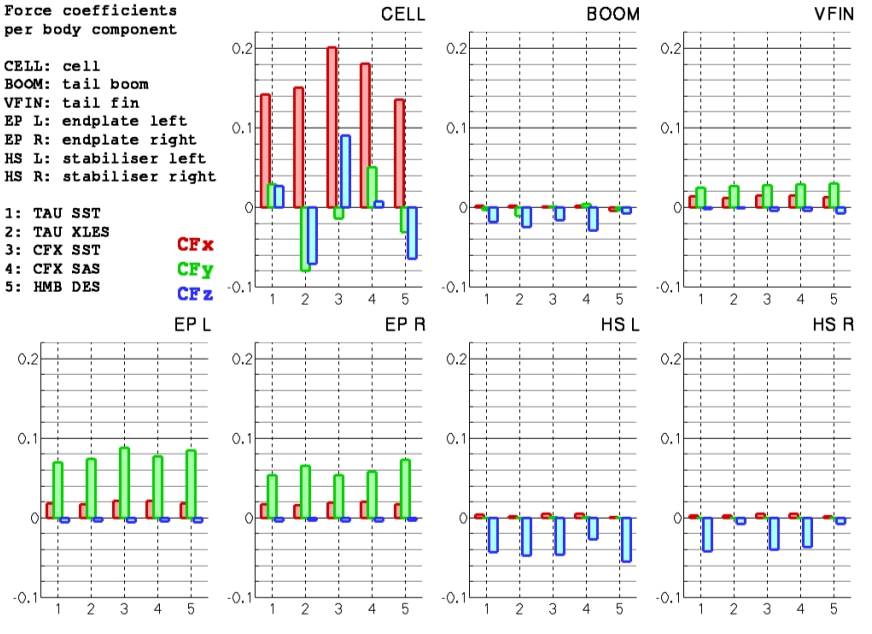

Fig. 7 Force coefficients per body component

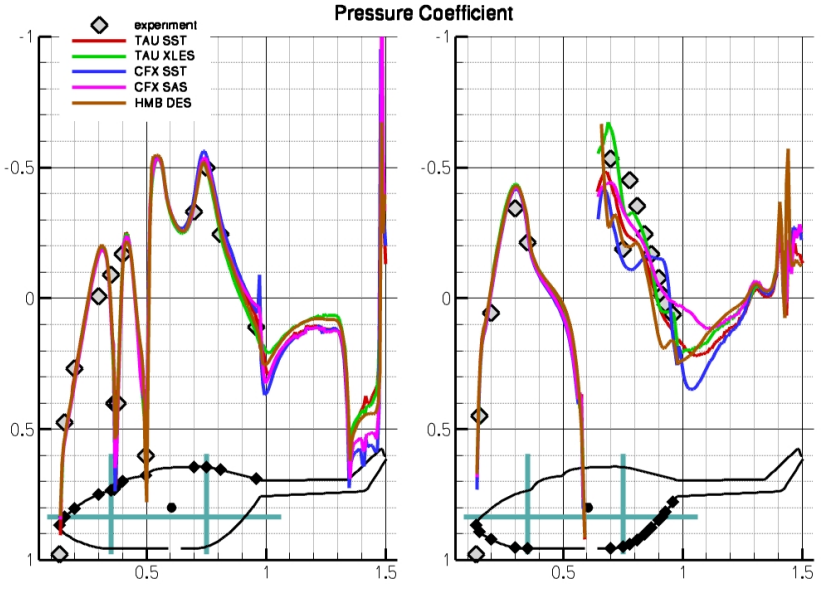

Fig. 8 Distribution of cp in the symmetry plane y=0 [m]

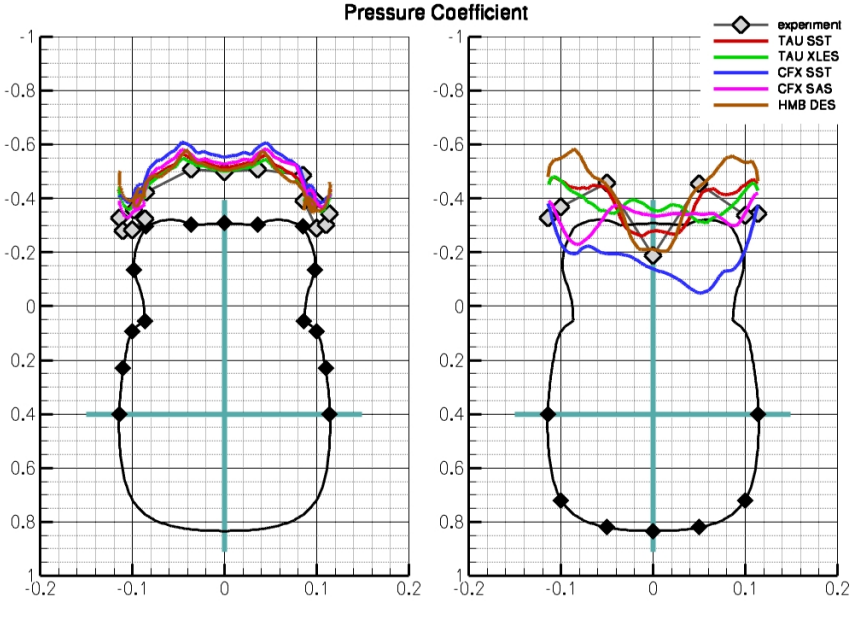

Fig. 9 Distribution of cp in the cross-section x=0.75 [m]

distribution on the top centre-line, apart form the tail boom where both the XLES and the DES computations, in accordance to each other, predict a somewhat lower pressure. On the bottom symmetry line, the front part doesn't raise any problem either, but discrepancies between the various solutions occur in the region of the backdoor. Almost all simulations render correctly the pressure rise on the top part of the backdoor close to the junction to the tail boom. On the opposite, close to the support strut, the agreement could be better: all but the XLES simulation overestimate the pressure, while the XLES underestimates it.

Figure 9 displays the pressure distribution on a cross-section just behind the support strut in the region of massive separation. Again the top part of the section is no problem for the flow solvers, except for a slight almost systematic underestimation of the pressure. The bottom part of the section is more interesting where apparently only the DES computation is able to show the pressure rise in the middle at the intersection with the symmetry plane. Surprisingly, the XLES solution doesn't perform better than its SST counterpart. This may be connected to the insufficient grid refinement of the unstructured grid in the wake of the support strut. Indeed, as seen at the end of the previous section, the strut wake is too much dissipated in the XLES computation.

Overall and when compared to the SST model, all three XLES, SAS and DES models do indeed improve the correlation with the experimental points.

15.5.3 Oil Flow

Figure 10 to Figure 15 show the surface flow pattern of both TAU computations: steady SST and unsteady XLES, while Figure 16 shows the unsteady CFX-SAS

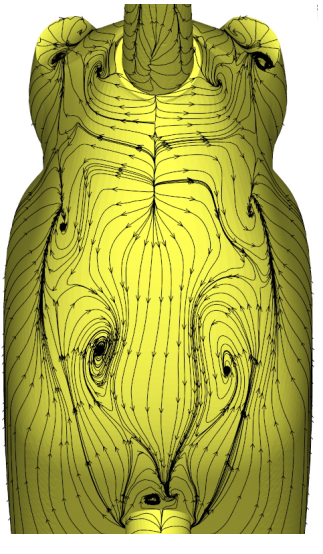

Fig. 10 TAU SST

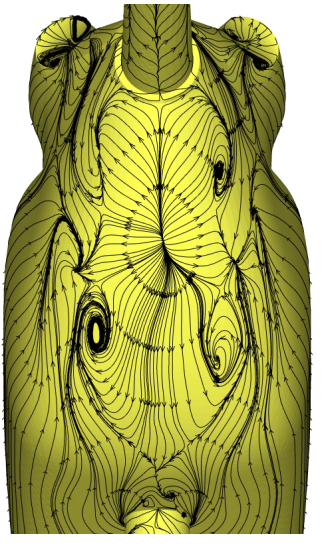

Fig. 11 TAU XLES

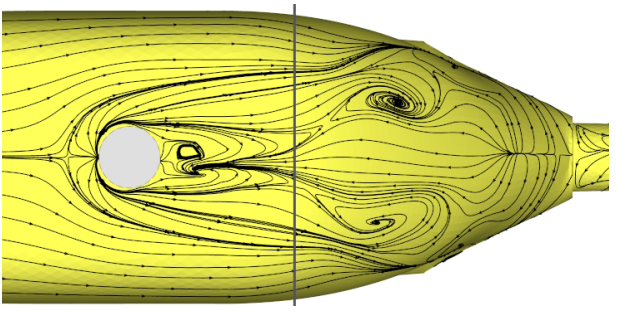

Fig. 12 TAU SST

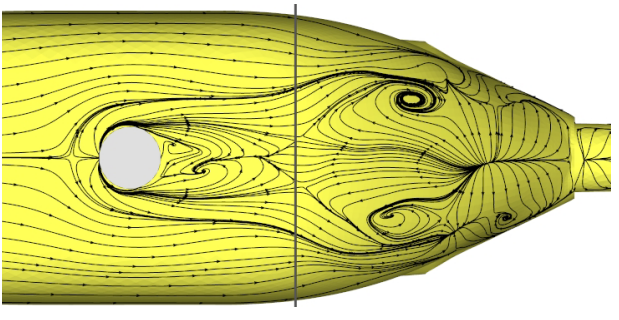

Fig. 13 TAU XLES

run and Figure 17 an oil flow picture from the wind tunnel experiment. For better eye-checking with pressure profiles, the location of the section x=0.75 [m] is displayed on Figure 12 and Figure 13. Please keep in mind the indications in Table 1 for the various averagings.

While maintaining the flow topology on the backdoor, the major effect of the XLES-modelling is to make the separated region more slender as it is with SST; compare Figure 12 and Figure 13. It also appears that the unsteady modelling has

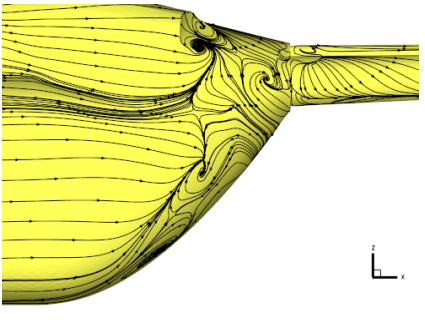

Fig. 14 TAU SST

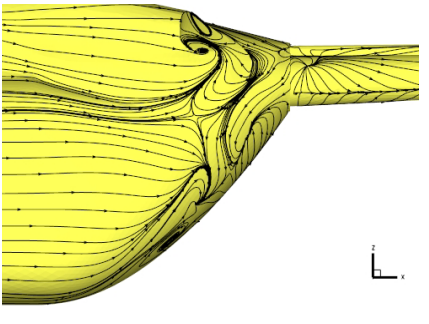

Fig. 15 TAU XLES

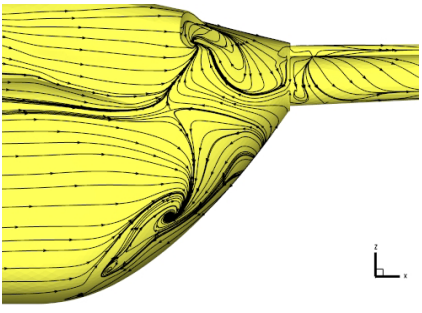

Fig. 16 CFX SAS

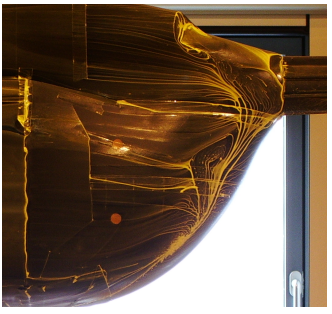

Fig. 17 oil flow, left view

reduced the time-averaged trace of the strut wake on the fuselage surface, which results in a reduced pressure rise for the TAU-XLES computation in comparison to the TAU-SST one; compare with Figure 9.

Figure 14 to Figure 16 show a left view of the surface flow pattern on the back-door area, corresponding to computations 1, 2 and 4 (unsteady SAS) respectively. The flow singularity where the oncoming flow separates into upward and downward parts is well captured although slightly too high located for TAU and also too upstream for CFX.

15.6 Conclusion

The wind tunnel model of the isolated fuselage of the BK117-C2 has been computed at zero angle of attack using three different codes: TAU, CFX and HMB, and four different models: SST, SAS, XLES and DES. Global loads, surface pressures and skin friction patterns have been compared to experimental data. All more sophisticated models: SAS, XLES and DES have brought some improvement over the base SST turbulence model (although not always markedly and consistently) in particular as regards the force and moment coefficients, which is of primary interest for the helicopter manufacturer.

Certainly, getting a better agreement would deserve dedicated studies about grid density and refinement, integration and averaging times and the size of an acceptable time-step. Also, it would be interesting to know a priori the major frequencies present in such a wake in order to be able to pre-tune the mesh so as to avoid unnecessarily too fine a grid.

But the challenge of the present test-case was to examine how far this kind of simulation is nowadays affordable in the industrial context of Eurocopter Germany. Although these techniques aren't yet affordable because of too high computation times, the trend points unambiguously to ever more simulation of flight conditions with high angles of attack and of side-slip – not to mention the normal cruise flight – where such turbulence models are thought to be most valuable.

16 Oscillating Airfoil NACA0012 at 15° – A Basic Case for Aero-Elasticity

T. Knopp, K. Weinman, and D. Schwamborn

DLR Göttingen

Abstract. The present chapter is dedicated to the test case for the forced harmonic pitching motion of the NACA0012 airfoil at deep-stall conditions. The partner contributions are from ALENIA, ANSYS, DLR, EADS, ECD, IMFT, and TUB.

16.1 Test Case Description

16.1.1 Dynamic Stall

Dynamic stall refers to the delayed stall process of an airfoil whose angle of attack is changing rapidly, e.g., at sinusoidal pitching oscillations or ramping (McCroskey and Fisher, 1972), (Carr and Chandrasekhara, 1996). The onset of stall can be delayed to angles of attack beyond the static stall angle and generate lift in excess of the maximum static lift. The predominant feature is the formation and shedding of the so-called dynamic stall vortex from the leading edge, which induces a strong suction peak. As this vortex propagates downstream along the chord, the centre of pressure is shifted which produces a large nose-down pitching moment called "moment stall". During pitch down, the flow over the airfoil remains stalled until at small angle of attack the flow starts to reattach from the leading edge. These processes cause substantial hysteresis behaviour of unsteady lift, drag and pitching moment coefficients.

Dynamic stall is of major interest for the helicopter industry, as it limits the helicopter flight envelope. The airspeed of the retreating blade slows down as the helicopter forward speed increases. The lift produced by the retreating blade must be increased such that it equals the lift produced by the advancing blade. This is achieved by locally increasing the blade pitch angle. The combination of the geometrical twist of the blade, the blade twist deformation and the induced flow generated by the preceding blades may lead, at some blade airfoils, to an effective angle of attack which goes beyond the airfoil static stall angle of attack. This leads therefore to dynamic stall conditions. From the industrial point of view, the large variations in pitching moment are of major interest. In fact they cause impulsive excitations on the pitch-link-rod, thus transferring strong vibratory loads to the pilot. Furthermore the impulsive excitation is dimensioning the fatigue life of the rotor.

16.1.2 Flow Conditions

The flow around a NACA0012 airfoil at so-called deep stall conditions, where a fully developed vortex is formed during the oscillation cycle, was investigated experimentally by (Mc Alister et al., 1982). The airfoil performs a forced

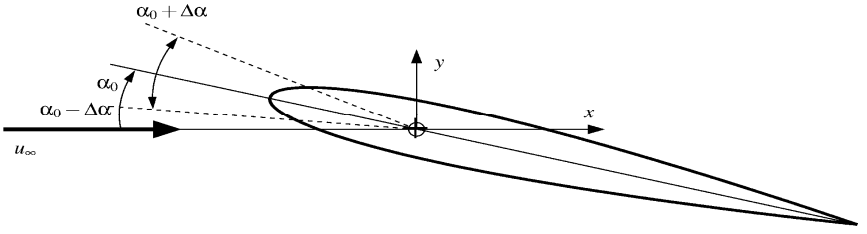

Fig. 1 Sketch of NACA0012 at forced harmonic pitching motion

harmonic pitching motion around the quarter-chord point where the time-dependent angle of incidence is given by $\alpha(t)=\alpha_0 + \Delta\alpha \sin(\omega t)$ with mean angle of attack $\alpha_0=15°$, amplitude $\Delta\alpha=10°$ and pitching frequency ω, see also Figure 1.

The reduced frequency k_f, which is the characteristic similarity parameter of the airfoil movement, is based here on the half chord length and defined by $k_f = \omega c/(2U_\infty)$, where c is the airfoil chord length and U_∞ is the free-stream velocity. In the experiment, measurements were performed for different Mach numbers. The flow parameters considered here are $Re = 0.98 \cdot 10^6$, Ma = 0.072, $k_f = 0.1$ and free-stream turbulence level Tu = 0.01.

16.1.3 Experimental Data

Pressure data were obtained from 26 Kulite differential pressure transducers, 16 located on the upper surface and 10 located on the lower surface, at a rate of 200 samples per cycle. Results are ensemble averaged over at least 50 pitching cycles. The pressure was integrated to give axial (chord) and normal forces, which were used to calculate lift and drag. Viscous forces were not measured, but their contribution to lift and drag can be assumed to be negligible small for the present case of deep-stall oscillations, where pressure forces are dominant. However, for the time-dependent moment coefficients no error bars are available, which would give a measure for the average spreading of the results in particular during downstroke.

From the hot-film skin-friction gauge data it can be seen (for the same case at Ma=0.3) that the flow at x/c=0.1 is fully turbulent over the entire pitching period, whereas at x/c=0.025 the flow might be laminar for smallest angles of attack, see Figure 4 in (McAlister et al., 1982), Volume 3. As only probes at six streamwise positions on the entire upper side were used, there are no detailed experimental data for the time-dependent transition locations. For the NACA0012 at similar flow conditions, heat-flux gauge measurements by (Chandrasekhara and Wilder, 2003) showed the existence of a small laminar separation bubble at the leading edge, and the dynamic stall onset was supposed to occur from the bursting of the laminar bubble.

The unsteady boundary layer measurements in (McAlister, 1982) clearly show significant variations in the angle where flow reversal occurred between one cycle and the next. Such random like behaviour of flow details during pitch-down has also been observed in other experiments on dynamic stall, e.g. (Pailhas et al. 2006).

16.1.4 Assessment of the Experimental Data

The experiment was performed in the 2m x 3m atmospheric-pressure, solid-wall wind tunnel at the U.S. Army Aerodynamics Laboratory. The model chord was 0.61m and the model spanned the 2.13m vertical dimension of the wind tunnel. A gap of approximately 2mm existed between the ends of the model and the wind-tunnel walls. In order to shed some light on the influence of the wind-tunnel side walls and the spanwise extent of the airfoil, it is worthwhile to consider also the data obtained by the same authors in the same wind tunnel but with a model whose chord was twice as large in a previous measurement (McAlister et al., 1978). During upstroke motion but before dynamic stall begins, C_L was larger for the model with smaller aspect ratio by approximately 10%, see Figure 35 in (McAlister et al., 1982), which is close to the differences for the corresponding static data. The peak in the unsteady lift curve was more pronounced for the model with smaller aspect ratio, and the reattachment of the boundary layer during downstroke occurred earlier. Therefore the spanwise extent of the domain can be supposed to have a significant influence on the organized vortex-shedding phenomena in dynamic stall.

It is well-known for static airfoils that even for a much larger ratio of spanwise extent to chord, the influence of the wind tunnel side walls on the development of three-dimensional flow structures for airfoils close to and beyond stall is significant, see e.g., (Schewe, 2003). Therefore it cannot be ensured that the spanwise extent of the configuration in (McAlister et al., 1982) is large enough to ensure that there is no influence of the wind-tunnel side walls.

The present data are with free transition. In order to investigate the influence of laminar-turbulent transition, McAlister and co-workers also fixed transition using a boundary layer trip at the leading edge, albeit only for Ma=0.18 and Ma=0.3. The effect on the maximum static lift and on the maximum lift under deep stall conditions is small. On the other hand, for a given angle of attack, the transition onset location is shifted towards larger x/c when decreasing the Mach number (Chandrasekhara and Wilder, 2003).

16.2 Computations

16.2.1 Computational Grids

Computations are performed on individual meshes by the partners, as shown in Table 1. For all grids, the numbers of mesh nodes in streamwise and spanwise directions are of comparable size, and we remark that the ALENIA grid is locally refined in the region of the dynamic stall vortex.

Due to the large computational costs for this test case it was not possible to perform a grid convergence study for the DES simulations. Instead, knowledge on grid requirements from the test case NACA0021 at 60 degree angle of attack was used as a guideline. We also remark that different boundary conditions in spanwise direction are used by different partners.

Table 1 Details of computational grids used by the partners

Partner	Type	Lx/c	Ly/c	Lz/c	Spanwise boundary condition	(Nx x Ny) x Nz
ALENIA	unstruct.	20	20	0.8	Periodic	(13390) x 42
DLR	unstruct.	100	100	1	Periodic	(25325) x 32
EADS	C-type	~15	~20	1	Symmetry	(35953) x 82
ECD	Ch-type	30	30	3	Periodic	(340 x 73) x 40
IMFT	O-type	15	15	1	Symmetry	(285x185) x 40
TUB	C-type O-type	10 15	13 15	1 1	Periodic	(347x100) x 42 (165x281) x 60

16.2.2 Computational Details

All partners used a similar number of time steps per period, except DLR who increased the number of time steps per period to 4000 for DES in order to ensure stability of the method during vortex shedding. The partners used different schemes for the discretization of the inviscid fluxes. EADS used the central scheme but observed spurious oscillations close to lift stall as inner iterations did not converge sufficiently. Similar stability problems were observed for the simulations on an unstructured mesh by DLR, who used therefore the MAPS+ upwind-scheme. ANSYS-CFX computations are performed using a 2^{nd} order upwind scheme and TUB used the hybrid CDS-TVD scheme. Due to convergence problems with the compressible solver, DLR performed computations at Ma=0.2. Comparison with URANS results for Ma=0.072 shows that the resulting differences are small but not negligible. This is also supported by the experimental data on the impact of compressibility in dynamic stall in (Carr and Chandrasekhara, 1996), as for Ma=0.2 sonic velocities in the suction peak region may occur. Details of the computations can be found in Table2.

16.2.3 Results for URANS

First the URANS results are considered, see Figure 2. DLR performed URANS simulations using the Spalart-Allmaras model with Edwards modification (SA-E) and the SST-kω model for more than twenty pitching cycles showing that the solutions of different cycles collapse perfectly and there is no randomness in the vortex shedding for these URANS models. However, special care has to be taken to avoid a pseudo-random character in the solution during downstroke caused by numerical errors and hence to ensure a sufficient number of time steps per period and an appropriate number of iterations within each time step.

The results by TUB (Frederich et al., 2007) for the SA model predict maximum lift, lift stall and the behaviour of lift during the first part of pitch-down in very good agreement with the experimental data. The agreement in drag is also very good. The SALSA model predicts lift stall somewhat too early but gives the best behaviour during pitch-down. The SA-E result by DLR predicts lift stall a little too late and the solution looks similar to the SA-result by TUB during downstroke.

Table 2 Details of the computations. The following abbreviations are used for the discretization schemes of the inviscid fluxes: 2nd order central with 4th order scalar dissipation (Central); Hybrid scheme using a blending of CDS and TVD 5th order depending on local flow conditions (Hybrid CDS-TVD). The ANSYS-CFX computations used the incompressible solver

Partner	Solver	Model	Periods	Time steps per period	Discretisation of inviscid fluxes
ALENIA	UNS3D	kω EARSM kω EARSM DES	2	1152	Central
DLR	TAU	SA-E, SST kω SA-DES	20-30 5	960 4000	Central(URANS) MAPS+ (DES)
EADS	TAU	SA-DES	5	960, 1920 (last period)	Central
ECD	ANSYS-CFX	SST kω (2D) SST-SAS	5 5	600 1200	2nd order upwind scheme
ANSYS	ANSYS-CFX	SST-SAS	6	3000	2nd order upwind scheme
IMFT	NSMB	OES	3	~15000	Roe 3rd order upwind scheme
TUB	ELAN	SALSA, LLR-kω, CEASM- kω, Wilcox kω and corresponding DES models	10	300 resp. 600	Hybrid CDS-TVD

While the results for the Wilcox k-ω model by TUB give good prediction of maximum lift and lift stall, the results for the SST model by DLR and ECD differ significantly. For the DLR results lift stall is predicted too early, which was confirmed by performing a convergence study for the inner iterations per time step. For the ECD results, lift stall is predicted too late, but oscillations in the lift curve which are apparently more pronounced for other periods not shown here suggest that the results might be influenced by a numerical error due to insufficient convergence in inner iterations. From the results of all partners it might be concluded that the reattachment behaviour for small angles of attack is better predicted by SA-type models than using k-ω type models.

16.2.4 Results for DES

The DES results for the aerodynamic coefficients shown in the sequel are for certain individual pitching cycles which differ from one cycle to another. In contrast the experimental data are averaged of several pitching periods.

The results for k-ω model based DES are considered first, see figure 3. The results for k-ω EARSM based DES and SST-SAS both predict lift stall discernibly too late. With increasing incidence lift falls down rapidly, once lift-stall has occurred in the experiment, and then shows a small second local maximum until finally lift breaks down due to subsequent full stall. Instead, after lift-stall occured,

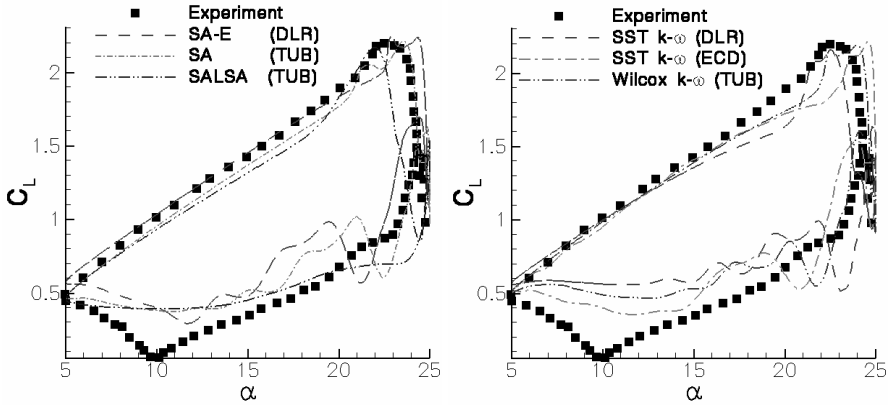

Fig. 2 URANS results for C_L vs. α

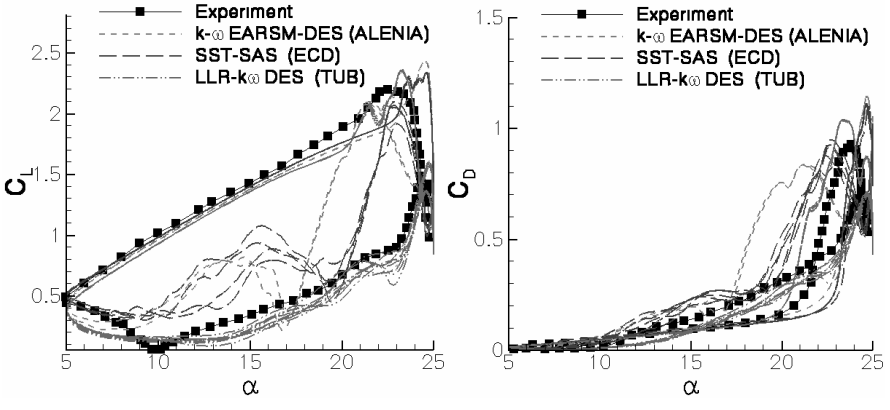

Fig. 3 DES results for C_L vs. α (left) and C_D vs. α (right)

k-ω EARSM based DES and SST-SAS predict a large second maximum in lift at a level comparable to the maximum lift in dynamic stall. Moreover both models show large fluctuations in the unsteady lift coefficient during down-stroke.

The LLR k-ω model based DES predicts the lift stall very accurately, and also the behaviour of lift during pitch-down movement is in good agreement with the experimental data, albeit a small deviation can be observed for the reattachment for small angles of attack. However, the simulation for LLR k-ω model DES used only 300 time steps per period, and for smaller time step sizes, an excessive secondary vortex shedding is observed, as for the two other k-ω based models, cf. (Frederich et al., 2007). Moreover, the excessive secondary vortex shedding causes a much larger drag during pitch-down than observed in the experiment.

The results for OES and SA-DES are shown in figure 4. The OES predicts a double lift-stall, the second at too large incidences, and a vigorous vortex shedding

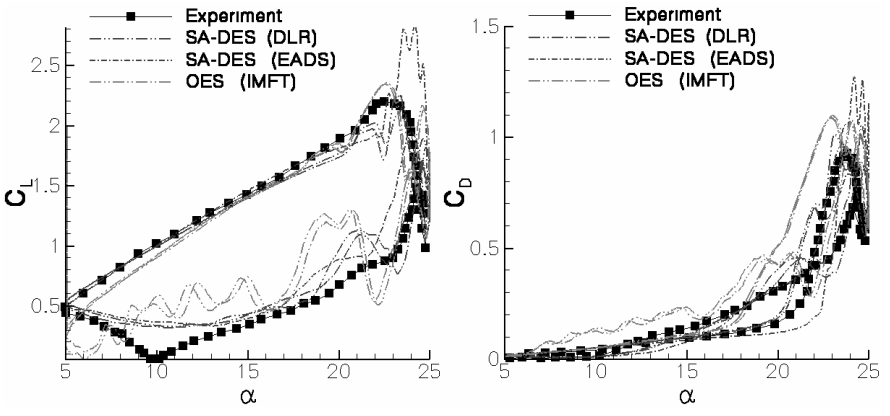

Fig. 4 DES results for C_L vs. α (left) and C_D vs. α (right)

during down-stroke. Moreover, lift recovery is predicted at too small incidences. The SA-DES results by DLR and EADS are obtained on different meshes, with different flux discretisation schemes and using a different number of time steps per period and inner iterations per time step. The central scheme used by EADS gives a better prediction during pitch-up until formation of the dynamic stall vortex near the leading edge. Near maximum lift, the scheme suffers from poor convergence and the numerical error causes a lift-overshoot and a too late prediction of lift stall. Using the MAPS+ upwind scheme stability of the numerical method can be ensured and the angle, at which lift stall is predicted, occurs a little early when compared to the experiment. During pitch-down, the MAPS+ upwind scheme predicts less secondary vortex shedding than the central scheme, and lift-coefficient is in fair agreement with the experiment.

For the SALSA-DES on the C-type mesh, the incidence at which lift stall is predicted is almost the same as for the SA-DES by DLR, albeit the predicted maximum lift is a little larger. Near maximum lift, the SALSA-DES solutions for different oscillation cycles almost collapse whereas the SA-DES results for different cycles differ. This might stem from the fact that the SALSA-DES results used only 600 time steps per period, which might be not sufficient to resolve the downstream motion of the dynamic stall vortex which is the predominant flow feature near moment and lift stall. For the O-type mesh, a visible lift-overshoot is obtained, and the secondary vortex shedding is larger than on the C-type mesh. On the other hand, the predictions on both meshes are very close to each other during pitch-up and for reattachment at small incidences.

Of strong industrial interest is the prediction of the abrupt variation of pitching moment coefficient and in particular the level of the minimum (nose-down, and therefore negative) pitching moment. From figure 6, it can be seen that the minimum pitching moment is overpredicted by 100% for all models and hence all DES-type approaches considered cannot be claimed to give quantitatively satisfying results, at least from the present results. Comparing the results for SA-URANS and SA-DES by DLR, the minimum C_M is reduced by 10% for DES.

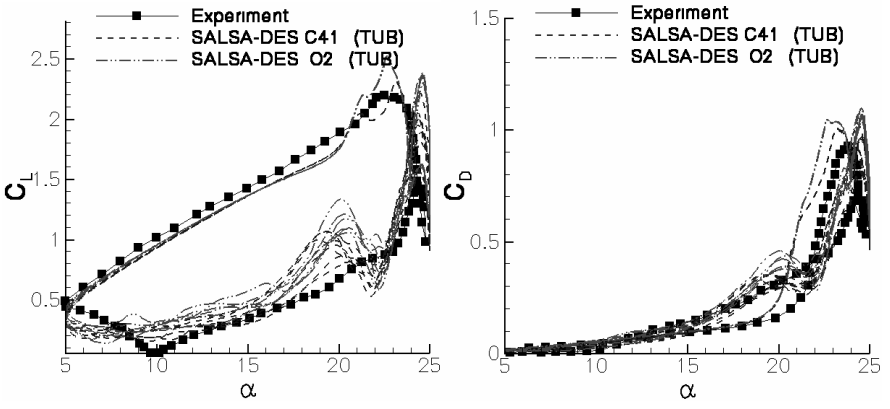

Fig. 5 DES results for C_L vs. α (left) and C_D vs. α (right)

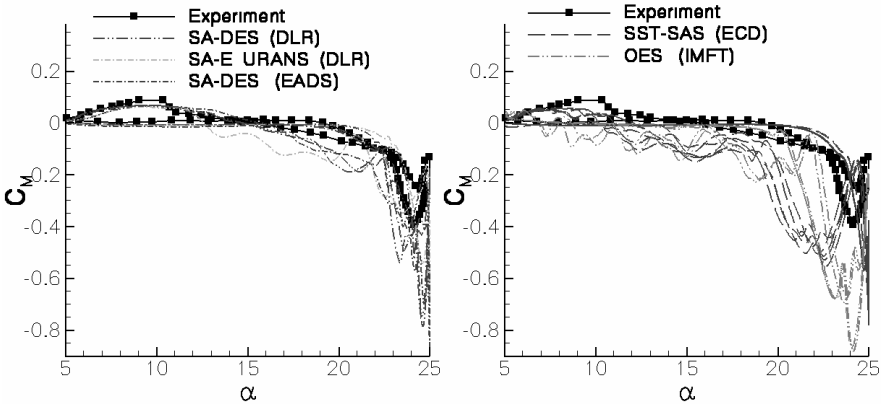

Fig. 6 DES results for C_M vs. α

On the positive side, during the entire pitch-up movement until moment stall occurs, the time-dependent C_M for SA-DES is very close to the experimental data and much better than for the SA-URANS solution by DLR. Moreover, during the second part of the pitch-down movement, the predicted C_M is much closer to the experimental data than the URANS model, indicating that SA-DES gives significant improvement of the results during reattachment. OES predicts moment stall much too early and the behaviour of C_M during pitch-down is far from the experimental results. The SAS results by ECD predict moment stall significantly too late and also show large deviations in C_M during pitch-down.

16.3 Conclusion

At the present stage of the investigation, there are indications that the DES approach is a new step towards the successful numerical prediction of the very

challenging phenomenon of dynamic stall. In contrast to URANS, DES allows to predict solutions which differ slightly from period to period and exhibit a random-like vortex shedding near lift and moment stall and during down-stroke similar to the observations in experiments. However, the question whether it is worth spending the large additional computational costs compared to URANS cannot be answered positively yet.

The delay of stall when the airfoil rapidly passages the static stall angle is of practical relevance to enhance the manoeuvrability of fighter aircrafts and increase the life of the rotor and reduce the vibrations of modern helicopters. The SA- and SALSA based DES models seem to have the tendency to give slightly improved prediction of maximum lift and lift stall compared to the corresponding URANS models.

On the other hand, from the point of view of the helicopter industry, the large variation in pitching moment coefficient is of major interest. Despite the tendency that the predicted negative pitching moment is reduced by about 10% using DES compared to URANS, the negative pitching moment is still overpredicted of about 100%. However, from the comparison of the present results with the ten year old URANS results summarized in (Ekaterinanis and Platzer, 1997) one can conclude that DES gives improved predictions for pitching moment coefficient during downstroke.

There are two major problems regarding dynamic stall test cases. First, there is access only to a limited number of test cases and the present one suffers from several uncertainties. On the one hand, the influence of the wind tunnel side walls cannot be estimated. Moreover, no measurement of the laminar-turbulent transition line was carried out during the wind tunnel experiment. Therefore no detailed information on the time-dependent transition location is available. All computations were consequently run fully turbulent and it is well known that this can have a large impact on the position of the separation and on the global results (Ekaterinanis and Platzer, 1997), (Pailhas et al., 2006). Additionally, there are no time-dependent field data, e.g. PIV, on location, size and behaviour of the small laminar separation bubble at the leading edge and on the dynamic stall vortex for assessing the physics resolved by the simulations.

Secondly, the number of simulations which can be performed is limited due to the very large numerical costs of this test case, and therefore the influence of the spanwise extension of the domain and of the spatial and temporal resolution required could not be studied in detail. The major computational hurdle is the large number of pitching cycles to be computed. After a transient period of several non-dimensional time units, averaging over up to 50 cycles as in the experiment is probably required for obtaining meaningful time-dependent integral coefficients, but this exceeds the available computing power of all partners to date. This, however, is a necessary prerequisite for giving a final assessment of the turbulence models for this test case.

17 M219 Cavity Flow

Shia-Hui Peng

Swedish Defence Research Agency, FOI

17.1 Introduction

The flow past an open cavity is often characterized by *statistically* unsteady motions due to instabilities of the mixing layer, which emanates from the upcoming boundary layer being detached from the cavity leading edge and, subsequently, contained by the cavity. The behaviour of the "detached" flow depends essentially on the freestream flow conditions and the geometry of the cavity. The cavity flow in this test case is of an open-cavity type characterized by unsteady shear-layer mode. The interaction between the shear layer and the cavity aft wall causes self-sustained pressure oscillations inside the cavity and, consequently, resulting acoustic excitation. With open cavities, high-intensity acoustic tones may be developed at discrete frequencies, which can be empirically estimated by the Rossiter formulation (1964). A typical example of cavity flows in aerodynamic applications is the landing-gear housing well, where the flow-generated aeroacoustic noise has been frequently addressed as part of the airframe noise. Other examples include weapons-bays and pressure vents in the space shuttle's cargo bay, where pressure oscillations may entail structural fatigue along with aero-acoustic excitations.

The success of a CFD simulation of a turbulent aeronautic cavity flow rests in the modelling of the flow physics of the incoming boundary layer, the shear-layer instabilities over the cavity opening and the turbulent motions inside the cavity. With URANS, DES and other hybrid RANS-LES methods, a typical cavity flow has been studied in the DESider project, which aims at assessing the involved modelling methods in an "aero-acoustic environment", a large part of work has thus been dedicated to the analysis of the pressure oscillation in the cavity, which is regarded as being the major noise source for cavity acoustic resonance.

17.2 Description of Test Case

The test case is based on an existing experimental measurement by QinetiQ for an open rectangular cavity (Henshaw et al., 2002). A detailed description of the experiment and its use for computational unsteady aerodynamics can be found in Henshaw et al. (2002) and Peshkin (2002).

The experiment was conducted in a transonic wind tunnel with freestream flow conditions of $M_\infty = 0.85$, $P_\infty = 6.21\times10^4$, $T_\infty = 266.53K$ and $\mathrm{Re} = 13.47\times10^6$ per meter. The open cavity is contained in a flat plate of length 72 inches (in the x-direction) and width 17 inches (in the y-direction). The rectangular empty cavity has dimensions of L = 20 inches in length, D = 4 inches in depth (namely, in the z-direction) and W = 4 inches in width, giving an aspect ratio of $L:D:W = 5:1:1$.

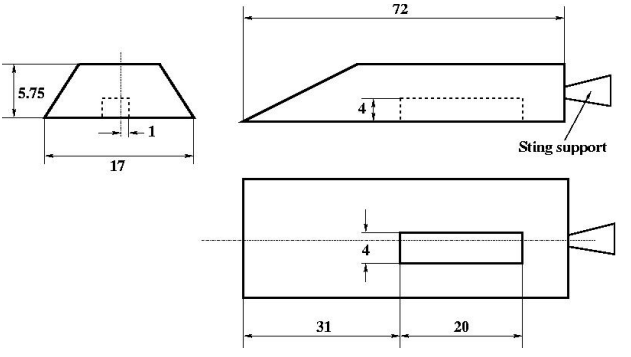

Fig. 1 Sketch of the experimental configuration (length unit: inch)

The cavity rig model used in the QinetiQ experiment is shown in Figure 1. Note that *x*-axis is not located along the centreline of the cavity. The origin for $y = 0$ is thus placed with distances of 1 inch and 3 inches, respectively, to the side walls of the cavity. The time histories of surface pressures were measured at a number of positions located on the wall surface prior to the cavity leading edge, the after-cavity downstream wall and the cavity wall surfaces.

The cavity can be fitted with removable bay doors. The presence of bay doors, set at 90^o above the cavity side-walls, is expected to have a constraining effect on the cavity flow, making it less three-dimensional than the "door off" case (Peshkin et al., 2002). For the present test case, the "door-off" case has been made mandatory in the modelling. Since the main purpose is to investigate the modelling performance for the acoustic tonal modes resulting from the pressure oscillations inside the cavity, a sample of the pressure fluctuations has been taken in the computations at all the 10 measured locations on the cavity floor (at $z = -D$). These are given in Table 1. In addition, full-resolved LES data for the mean flow field by Larcheveque et al (2004) can also be used for comparison.

Table 1 Transducer positions on the cavity floor for pressure measurements

Kulite	**x** (inches)	**y** (inches)	**z** (inches)
k20	1.0	0.0	-4.0
k21	3.0	0.0	-4.0
k22	5.0	0.0	-4.0
k23	7.0	0.0	-4.0
k24	9.0	0.0	-4.0
k25	11.0	0.0	-4.0
k26	13.0	0.0	-4.0
k27	15.0	0.0	-4.0
k28	17.0	0.0	-4.0
k29	19.0	0.0	-4.0

The recommended computational domain, shown in Figure 3, has dimensions of $L_x \times L_y \times L_z = 18D \times 9D \times 17D$, where D is the depth of the cavity. The upstream distance from the leading edge of the flat plate to the front wall (at $x = 0$) of the cavity is $7.75D$. The downstream distance from the cavity aft wall (at $x = 5D$) to the trailing edge of the plate is $5.25D$. The recommended boundary conditions are: adiabatic no-slip condition on all wall surfaces, symmetric conditions on the side (spanwise) boundaries at $y = 4.5\ D$ and $y = -4.5D$, and far field condition on the inflow, outflow and upper boundaries.

17.3 Information of Modelling Methods

In Table 2, the involved partners and related modelling methods are listed. In addition, the information of the computational grid, the time step (Δt) and the sampling time is also summarized.

In summary, the modelling approaches include URANS, DES, hybrid RANS-LES and LES methods. Besides the SA-model-based URANS, DES and DDES methods, other modelling approaches include the k-ω-EARSM-based URANS and DES model (Alenia), the SST-SAS model (Ansys), the k-ε based DES model

Table 2 Participants and related modelling methods

Partners	**Model**	**Mesh**	**Nodes** in cavity/**Total** ($\times 10^6$)	Δt (second)	**Sampling time** (second)
Alenia	k-ω-EARSM: URANS DES	Unstruct.	~ 0.50/**0.85**	3.61E-5	0.053 0.095
Ansys	SST-SAS	Struct.	0.083/**1.1**	2.0E-5	0.25
Dassault	k-ε DES SA-DES LES (selec.)	Unstruct.	1.11/**1.5**	2.0E-5 2.0E-5 1.0E-5	0.13 0.11 0.20
EADS-M	SA-DES [a] SA-DES XLES	Struct. Unstruct. Unstruct.	0.27/**1.26** 2.29/**6.2** 2.29/**6.2**	1.0E-4	0.5 0.5 0.5
FOI	SA-URANS SA-DES HYB0 HYB0	Struct. Struct. Struct. Unstruct. [b]	0.27/**1.26** 0.27/**1.26** 0.27/**1.26** 2.29/**6.2**	5.0E-6 1.0E-5 1.0E-5 2.0E-5	0.11 0.23 0.225 0.22
Liverpool	SA-DES ($C_{des} = 0.78$)	Struct.	0.5/**2.2**	9.1E-6	0.18
NTS	SA-DDES	Struct.	0.54/**3.0**	2.3E-6	0.10

[a] The SA-DES results by EADS-M on the structured grid are similar to the FOI SA-DES results (both have used the same structured grid generated by FOI). In the following summary, the SA-DES computation by EADS-M is referred to the solution computed on the unstructured grid, unless otherwise mentioned.

[b] The unstructured grid for the HYB0 modelling by FOI has been generated by EADS-M, and used in SA DES and XLES computations of EADS-M.

(Dassault), the XLES model (EADS-M) and a hybrid algebraic RANS-LES model (HYB0, FOI). In addition, a LES computation has been performed by Dassault with the selective SGS model. The smallest time step used in the computation is $\Delta t = 2.3\times10^{-6}$ second, while the largest takes $\Delta t = 10^{-4}$ second. Most of the partners have used a moderate time step between $10^{-5} - 4\times10^{-5}$ second. The effect of the time step has been demonstrated by Larcheveque et al. (2001) that the temporal resolution in full LES is negligible with a time step changing from 10^{-5} second to 2×10^{-5} second. A time step around $\Delta t = 2\times10^{-5}$ or smaller should be the most appropriate for this test case.

Several structured and unstructured grids have been adopted, of which the total number of nodes are ranging from 0.85 million to 6.2 million. Most of the partners have used the same or a similar computational domain as provided in the Test Case description, which is symmetric about the central section of the cavity. The EADS-M unstructured grid has however been generated on a much larger domain to simulate the wind tunnel test, with the cavity being embedded in a flat plate, as shown in the experiment set up in Figure 1. The computational domain is thus not symmetric about the cavity central section. The centreline of the plate-holder is biased one inch from the cavity central section. In addition, Dassault has conducted a grid-sensitivity analysis. The concluded best grid has been used in their computations, without resolving the wall layer and the first node is located at $y_1^+ = 200$ from the wall.

17.4 Results and Discussion

To avoid an "over-loaded" presentation with all detailed results, we have selected the results/illustrations that are most relevant to giving an indication of the modelling performance.

17.4.1 Unsteady Flow Features

It is noted that the figures below have been made by the partners for illustrating the unsteady/instantaneous flow features. If necessary, explanation has been made accordingly either in the figure caption or in the corresponding discussion.

URANS Modelling

Three URANS computations have been conducted using, respectively, a k-ω based EARSM model (Alenia), the SST-SAS model (Ansys), and the SA model (FOI). The SST-SAS model employs the von Karman length scale, which is able to resolve rich turbulence contents upon the grid resolution. Although not shown here, it is confirmed that both the EARSM and the S-A model are able to capture the statistically unsteady flow feature, with rather large modelled eddy viscosity though. A snapshot shows that the ratio of modelled eddy viscosity and the molecular viscosity, $R_t = \mu_t / \mu$, computed with the k-ω EARSM model (Alenia), may raise to the order of 10^4, and the SA model gives about a half of this value.

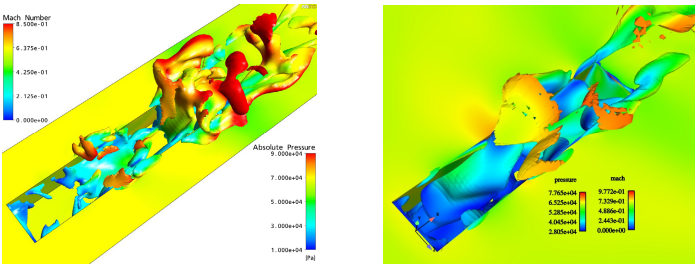

(a) SST-SAS (Ansys) **(b)** SA-URANS (FOI)

Fig. 2 URANS Modelling: Vorticity isosurface

Figure 2 demonstrates the URANS resolved/modelled vortex motion for the SST-SAS model (Ansys) and the SA model (FOI) with the iso-surface of the same vorticity magnitude. The SA URANS has enabled a representation of only a marginal amount of vortex structures, emanating usually from the edges of the cavity side walls. Note that, due to the inherent scale-adaptation feature, the SST-SAS model is able to render resolved turbulent contents. In spite of a rather coarse grid inside the cavity, the SAS model has produced relatively rich vortex motion, as compared to the SA modelling.

DES and Hybrid RANS-LES Modelling

A variety of DES and other hybrid RANS-LES models have been used. Unlike the URANS modelling, these modelling methods are able to resolve instantaneous turbulent structures due to inherent LES mode. Computations with all these approaches have indeed shown promising capabilities of capturing large-scale vortex motions for the mixing layer and for the flow inside the cavity. Some snapshots of instantaneous R_t (not shown here), computed by different DES and hybrid RANS-LES models, indicate that the modelled eddy viscosity is generally one order smaller in magnitude, as compared to the URANS modelling. In general, the finer the grid resolution, the smaller is the modelled eddy viscosity. For the XLES model, it is noted that this model may generate unreasonably intensive turbulent diffusion above the mixing layer, where the local length scale has probably switched back to the RANS length scale (in terms of k and ω).

Some illustrative examples provided by the partners are presented in Figure 3, which demonstrates the resolved instantaneous vortex motion resolved by different modelling approaches. These have been plotted for the iso-surface of the vorticity magnitude or the second invariant of velocity gradients. In line with the grid resolution used, the computations using DES and its variants, as well as the hybrid RANS-LES modelling, have attained a reasonable representation of resolved vortex motions for the mixing layer and inside the cavity. Comparing to the URANS modelling illustrated in Figure 2 (b), with the same grid (the FOI structured grid), the SA DES and the HYB0 models have produced much richer large-scale, instantaneous turbulent structures inside the cavity and over the cavity opening.

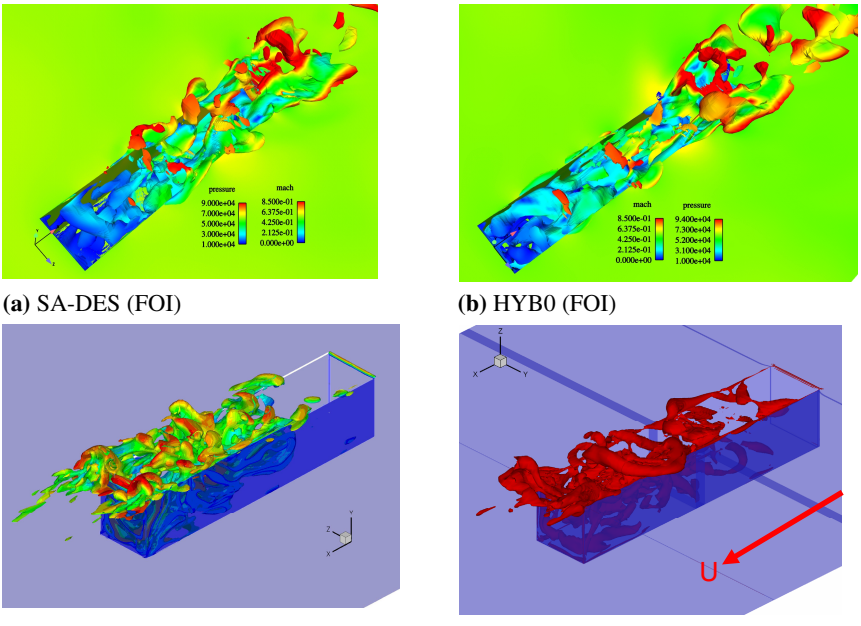

(a) SA-DES (FOI) **(b)** HYB0 (FOI)

(c) SA-DES (Liverpool) **(d)** SA DDES (NTS)

Fig. 3 DES and Hybrid RANS-LES modelling: Resolved vortex motion

17.4.2 Time-Averaged Mean Flow Features

In Figure 4, the time-averaged mean flow streamlines are illustrated on the cavity central section. As shown, all the computations have disclosed the mean recirculating motion inside cavity with two sub-recirculating centres. The large one is located near the cavity centre and the small one close to the cavity aft wall. Being different from the three computations in Figure 4 (b), (c) and (d) with, respectively, the k-ε DES (Dassault), the SA-DES (EADS-M) and the HYB0 model (FOI, with the EADS-M unstructured grid), the other computations have resolved a relatively weak reverse flow motion for the small sub-recirculation, of which the flow reverse orientation is parallel to the cavity floor and the centre is close to the floor. In these computations, the mixing layer is more deflected, when approaching the cavity aft wall. This is mainly due to a relatively coarse grid in the cavity. Referring to Table 2, this is indeed the case - the three aforementioned computations in exception are those using a rather refined grid resolution in the cavity (more than 1 million nodes, in general). The coarsest grid (by Ansys) has produced the smallest sub-recirculation near the rear wall. Some computations have used a relatively short averaging time, which has been reflected in Figure 4, for example, those in the k-ε DES modelling by Dassault, in the URANS modelling by FOI and in the DDES computation by NTS. This has made some time-varying motions not smoothed out sufficiently.

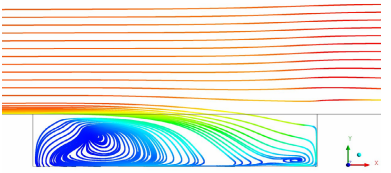

(a) SST-SAS (Ansys)

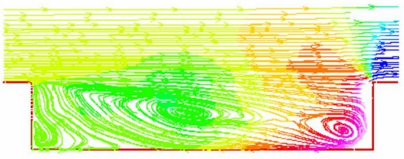

(b) k-ε DES (Dassault)

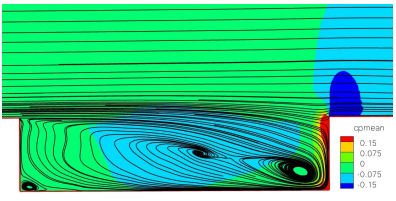

(c) SA DES (EADS-M)

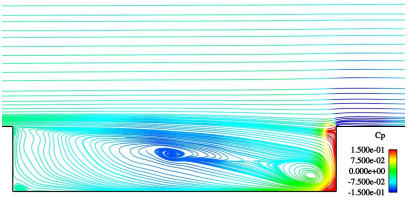

(d) HYB0 (FOI, with unstructured grid)

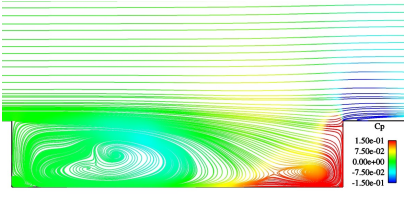

(e) SA URANS (FOI)

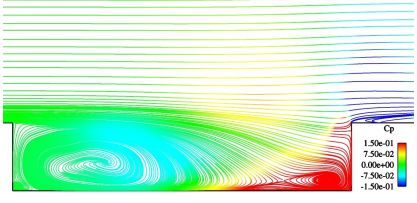

(f) SA DES (FOI)

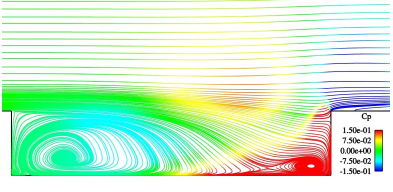

(g) HYB0 (FOI)

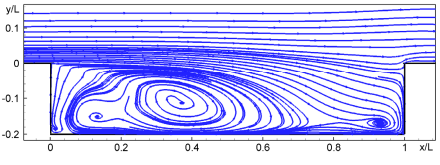

(h) SA DDES, NTS

Fig. 4 Time-averaged mean flow streamlines plotted on the cavity central section

The mean pressure distribution along the cavity floor is shown in Figure 5. All the computations have shown an adverse pressure gradient with different degrees. When a relatively coarse grid is used, the adverse pressure gradient becomes significantly large, starting generally at a location of $x/L < 0.4$. With a relatively fine grid, computations with the SA-DES (EADS-M), the SA- and k-ε (hereafter KE) DES (Dassault), as well as with the HYB0 (FOI, with the EADS-M unstructured grid) model, indicate a relatively small adverse pressure gradient in a small part near the cavity rear wall. The LES (Dassault) gives relatively large negative values of C_p, suggesting that the predicted recirculation bubble in the front part of the cavity has a relatively extensive reverse flow (strong recirculation with lower static pressure in the recirculation region).

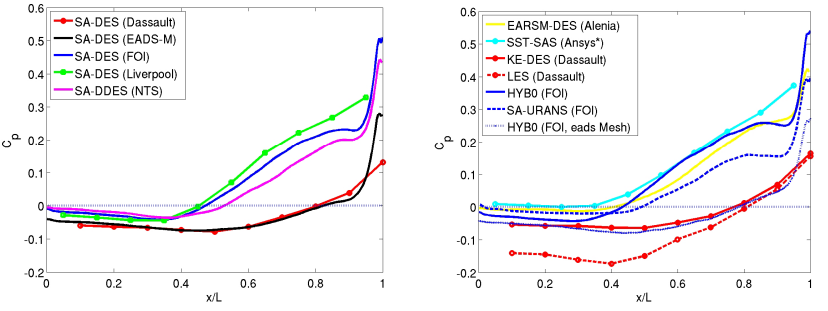

Fig. 5 Mean pressure distribution along the cavity-floor centreline. The lines with symbols have been plotted along a line deviated from the centreline by 0.25W

The mean flow and resolved turbulence statistics are compared below with the full LES for the same cavity flow by Larcheveque, et al. (2001). The distributions have been extracted from the central plane of the cavity.

Figure 6 shows a comparison of the mean streamwise velocity profiles plotted at locations x/L = 0.1, 0.3, 0.5 and 0.7, respectively. In the front part of the cavity

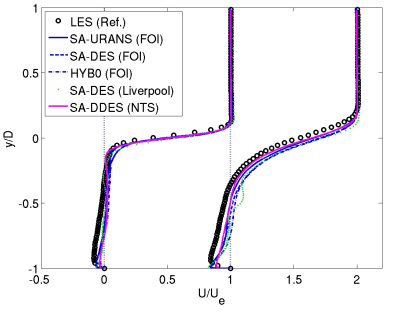

(a) At x/L = 0.1 (left) and 0.3 (right).

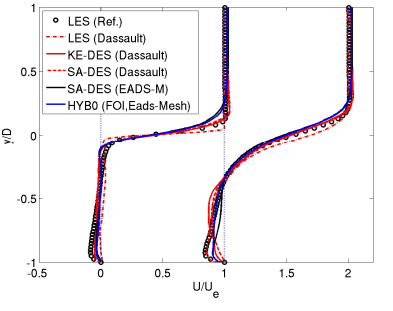

(b) At x/L = 0.1 (left) and 0.3(right).

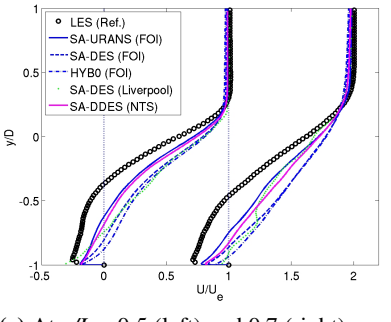

(c) At x/L = 0.5 (left) and 0.7 (right).

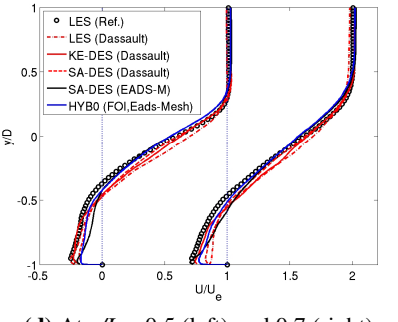

(d) At x/L = 0.5 (left) and 0.7 (right).

Fig. 6 Streamwise velocity on the cavity central section at x/L = 0.1, 0.3, 0.5 and 0.7

(at x/L = 0.1 and 0.3), all the models have produced reasonable comparison with the reference LES data. In the middle and rear part (at x/L = 0.5 and 0.7), however, the predictions are degraded when the grid resolution is decreased, no matter which model has been used. This observation is consistent to the mean flow pattern illustrated in Figure 4. In spite of a relatively fine grid, the SA-DES computation by Liverpool presents significant discrepancies from the LES data. With the same FOI structured grid, the SA-DES and the HYB0 model give similar results, under-predicting the reverse flow and over-estimating the deflection (diffusion) of the mixing layer. The FOI SA-URANS modelling has rendered predictions similar to the SA-DDES simulation by NTS on a relatively fine grid with the node number doubled in the cavity. Although the wall layer is not resolved with the Dassault grid, all the three computations by Dassault, with the KE-DES, SA-DES and LES methods, respectively, have produced reasonable predictions in comparison with the reference LES data. With the EADS-M unstructured grid, the predictions for the mean flow are overall improved by both the SA-DES (by EADS-M) and the HYB0 model (by FOI), slightly better than the Dassault prediction in the shear layer below the cavity opening.

In view of the above comparison, it is clear that the grid resolution (for the mixing layer and in the rear half of the cavity) plays a significant role in the simulations to attain improved predictions. Coarse grids usually make the predicted mixing layer more diffusive and being deflected earlier towards the cavity floor (prior to the impact on the cavity aft wall). Moreover, based on the Dassault simulations, which do not resolve the wall layer, it seems to imply that the unsteady flow features in the cavity are predominated by the mixing layer motion (with relatively large and energetic structures) more than by the near-wall turbulent structures. This is also partly reflected by the FOI SA-URANS computation, of which the predicted mean flow is in somewhat better agreement with the reference LES data than those obtained from the SA-DES and HYB0 computations with the same grid. Note that large structures usually have large time scales. The reasonable SA-DES results by EADS-M, which have been obtained with a relatively large time step, may also support plausibly the observation that an appropriate resolution of large-scale structure over the mixing layer is an essential ingredient to attain accurate modelling of this cavity flow.

The turbulent structure in the mixing layer is more energetic than in the near-wall flow structure, particularly in the rear half of the cavity. This can be further scrutinized with the resolved turbulent kinetic energy, k_{res}, in comparison with the reference LES data, as shown in Figure 7. For this comparison, only contributions from Dassault, FOI and NTS are available. It is interesting to note that the node number in the cavity with the four grids used by the partners is (roughly) doubled subsequently, from the coarsest FOI structured grid to the NTS grid, and the Dassault grid to the finest EADS-M unstructured grid (used by FOI with the HYB0 model). With the coarse FOI structured grid, the SA-DES and the HYB0 model have resolved the turbulence energy at similar levels with a distribution tendency similar to the LES result. Using the finest EADS-M unstructured grid, the HYB0 model has produced in the mixing layer generally reasonable peak values for k_{res} at similar locations, as compared to the reference LES data. The coarse grids have

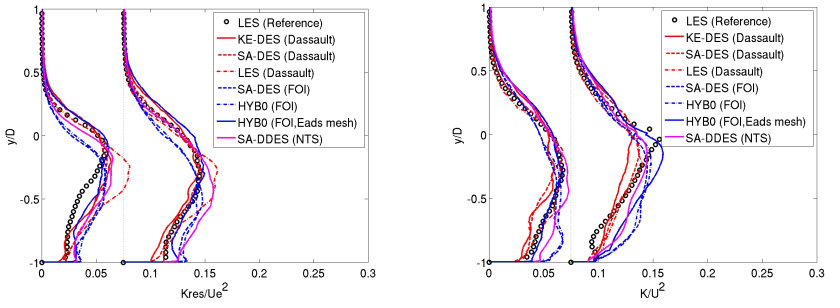

Fig. 7 Resolved turbulent kinetic energy, at x/L = 0.5 and 0.7 (Left) and x/L = 0.9 and 0.995 (right)

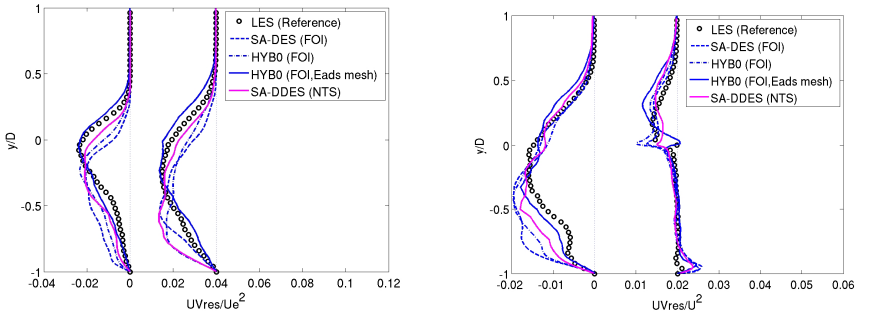

Fig. 8 Resolved turbulent shear stress, at x/L = 0.5 and 0.7 (Left) and x/L = 0.9 and 0.995 (right)

pronounced the k_{res} peak at a relatively low location from the cavity opening with a larger peak value (except for the profile at x/L = 0.995 close the cavity rear wall).

The resolved turbulent shear stress is compared in Figure 8, where only FOI and NTS contributions are available. The significance of grid resolution has been further underlined in predictions of the shear layer and its evolution towards the cavity aft wall.

17.4.3 Acoustic Tonal Modes Due to Pressure Oscillations

This cavity flow renders tonal acoustic resonance at discrete frequencies, being entailed by self-sustained pressure oscillations in the cavity. All the partners participating in this test case have sampled the pressure fluctuations at the ten locations on the cavity floor, as given in Table 1. In order to distinguish the tonal modes from the unsteady pressure pattern, the pressure fluctuations have been transformed into Power Spectral Density (PSD) as a function of frequency using the Burg method. The Sound Pressure Level (SPL) can then be estimated by

$$SPL = 10\log\left(\frac{PSD}{p_{ref}^2}\right) \tag{1}$$

In Equation (1), $p_{ref} = 2\times10^{-5}$ Pa. The pressure fluctuations from the QinetiQ experimental data base are transformed with the same method. The "mean" overall SPL (OASPL) is also estimated, for which the r.m.s. of pressure fluctuations, p_{rms}, is used to replace the PSD in Equation (1), namely,

$$SPL = 20\log\left(\frac{p_{rms}}{p_{ref}}\right) \tag{2}$$

In order to compare with the Rossiter frequency for each tonal mode, the empirical Rossiter formulation is also used, viz.

$$f_n = \frac{U_\infty}{L}\frac{n-\gamma}{M_\infty + 1/\kappa}, \tag{3}$$

where U_∞ and M_∞ are respectively the freastream flow velocity and Mach number, n is the mode number, and the values to the two empirical constants, κ and γ, are given by $\kappa = 0.57$ and $\gamma = 0.29$ (Larcheveque et al., 2001).

In Figures 9 and 10, the SPL is plotted as a function of frequency, f, at two typical positions, k21 and k28, located respectively in the front and rear part of the cavity floor. Based on the experimental data, four tonal modes can be identified at, respectively, f_1 = 135 Hz, f_2 = 350 Hz, f_3 = 590 Hz and f_4 = 820 Hz. The 2nd and 3rd modes are the dominant ones. As shown, all the computations have confirmed the appearance of discrete tonal modes, with different accuracies in comparison with the experimental data. The resolution of the tonal modes (both frequency and magnitude) is generally in line with the accuracy attained in predictions for the mean flow, indicating close coupling between the flow and the pressure pattern. A general observation is that the predicted 2nd and 3rd modes are more distinguishable than the other two modes identified, respectively, at the lowest and the highest frequencies. With refined grids, the predictions of the tonal modes have been improved, noticeably, by the SA-DES and LES computations of Dassault, the SA-DES and XLES computations by EADS-M and the HYB0 modelling by FOI (with the EADS-M unstructured grid) and, fairly satisfactorily, by Alenia EARSM-based DES modelling and Dassault KE-DES modelling. The frequency to the 2nd mode has been somewhat over-estimated by most of computations. Nearly in all computations the 1st mode has been only marginally resolved, which is less distinguishable than the other predicted modes. With the SA-DES model and LES on the Dassault gird and SA-DES model on the EADS-M grid, the magnitude to the 3rd mode is over-predicted. In addition, some specific observations can also be made. With a relatively coarse grid, the EARSM-based DES modelling by Alenia is able to reasonably resolve the 2nd and 3rd modes, better than the NTS SA-DDES modelling with a similar grid resolution (inside the cavity). This may be attributed

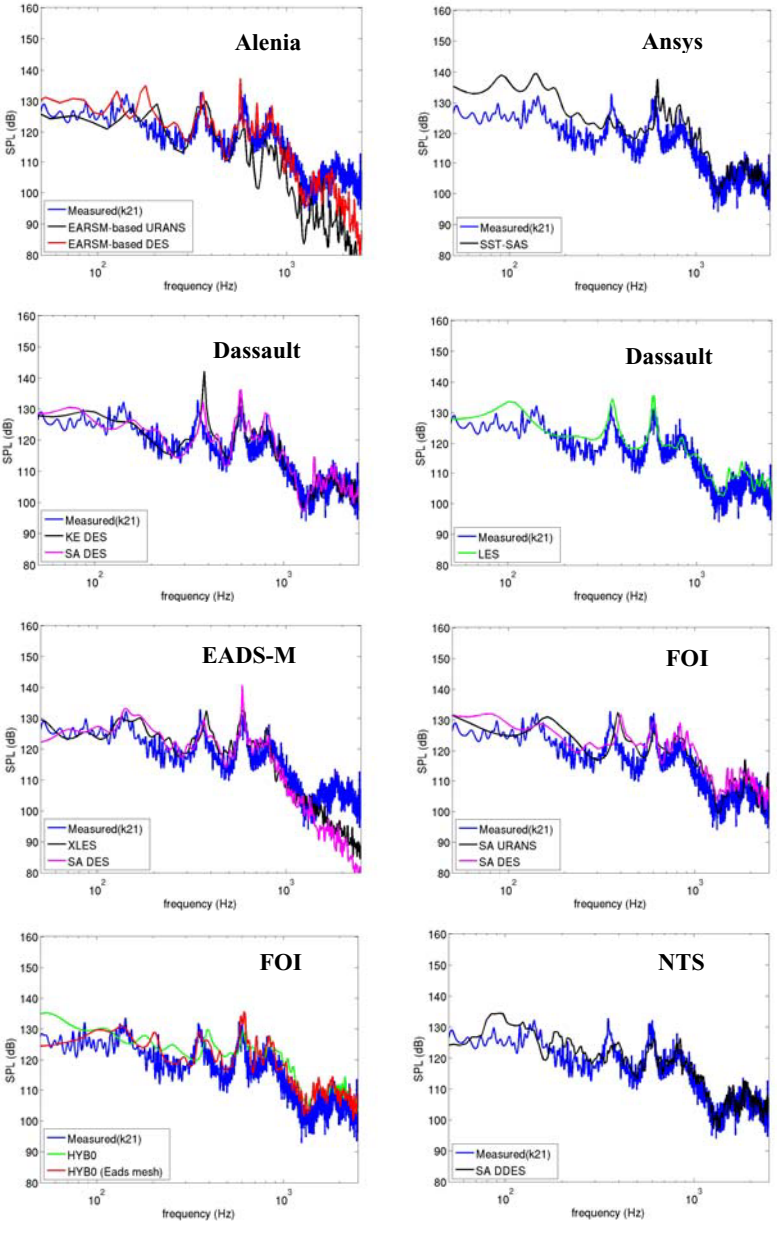

Fig. 9 Sound pressure level (SPL) at location, k21, on the cavity floor

to the EARSM formulation, which is more sophisticated than a linear eddy viscosity model. For the Alenia EARSM URANS computation, the 2nd mode is well represented though, the sampling time is too short to justify other modes. It is

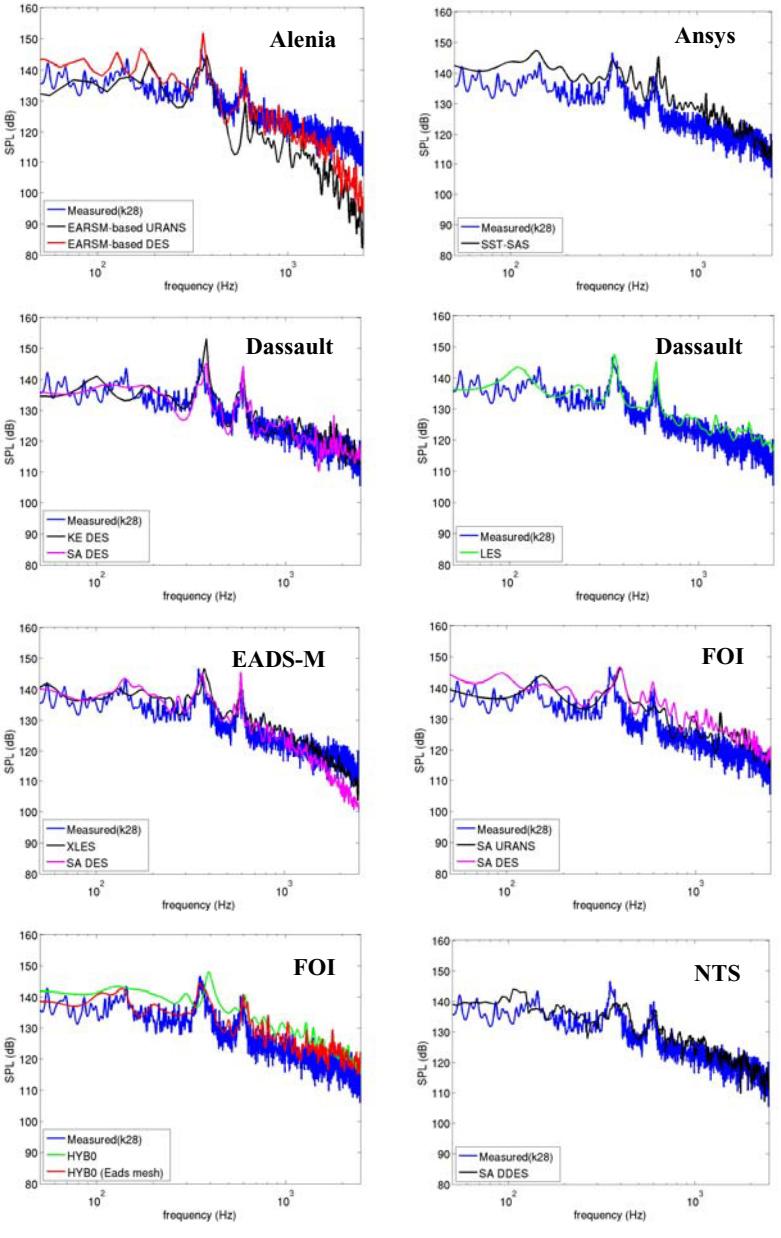

Fig. 10 Sound pressure level (SPL) at location, k28, on the cavity floor

noted here that Alenia has used a somewhat large time step, the SPL at large frequencies has thus been significantly damped. Similar outcome can be observed from the EADS-M results with an even larger temporal resolution. These may

Table 3 Comparion of predicted frequencies of the four tonal modes

Modes Frequency (Hz)		Mode 1	Mode 2	Mode 3	Mode 4
QinetiQ Experiment		135	350	590	820
Rossiter's formula		148	357	566	775
Alenia	k-ω-EARSM-based URANS	206	373	599	880
	DES	180	360	570	834
Ansys	SST-SAS	155	361	619	810
Dassault	k-ε DES	100	380	590	805
	SA-DES	145	375	590	815
	LES	105	365	595	840
EADS-M	SA DES	138	363	590	803
	XLES	152	378	593	785
FOI	SA-URANS	165	394	586	842
	SA-DES	136	392	598	830
	HYB0	158	390	591	842
	HYB0 (unstr. grid)	134	352	594	830
Liverpool	SA-DES	131	389	589	852
NTS	SA DDES	116	386	600	845

have also been induced additionally by too large numerical diffusion, which usually diminishes high-frequency oscillations.

With the coarsest grid in Ansys SST-SAS modelling, the resolved tonal modes are not so distinguishable, while the general tendency of the SPL as a function of frequency has been represented fairly reasonable. In the DDES modelling by NTS, the predicted magnitude for the 2nd mode (and even slightly for the 3rd mode) has been somewhat smeared. With the FOI structured grid, the SA-URANS, SA-DES and HYB0 modelling by FOI have produced similar results. Using the refined EADS-M grid, however, the FOI HYB0 modelling has greatly improved the predictions for all the four tonal modes with good agreement with the experimental data.

In Table 3, the predicted frequencies of the tonal modes are summarized in comparison with the experimental values and the Rosstiter frequencies.

In Figure 11, a cross comparison is made for the overall sound pressure level (OASPL) estimated from Eq. (2). The OASPL prediction is in line with the prediction of SPL shown in Figures 9 and 10, that is, the modelling gives better resolved tonal modes and SPL amplitudes has enabled better predictions of OASPL. Nonetheless, all the computations have over-estimated the OASPL in the range of 1-6 dB, in comparison with experimental data. Moreover, it should be noted that the change of the OASPL along the cavity implies also corresponding pressure patterns captured. It is thus desirable that a good prediction gives not only OASPL values close to the measurements, but also a shape of the OASPL-curve similar to the experimental curve changing in the same tendency along the cavity floor. The most sensible difference is observed due to the KE-DES computation by Dassault, which has pronounced decreasing OASPL in the range of $0.45 < x/L < 0.65$ in contrast to the increasing tendency of the experimental values.

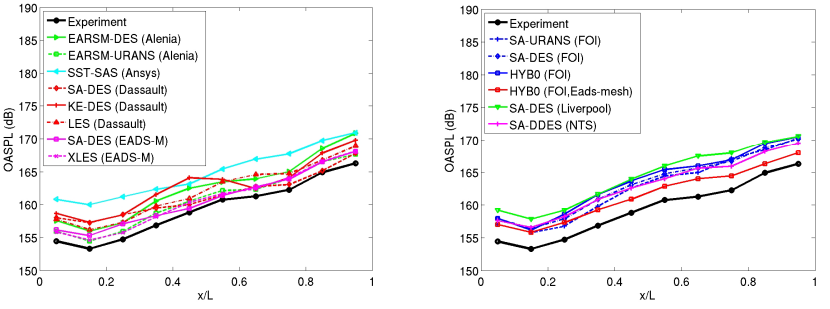

Fig. 11 Overall sound pressure level (OASPL) along the cavity floor

17.5 Concluding Remarks

The test case has been studied by 15 available computations on 7 different grids with URANS, DES, hybrid RANS-LES and LES modelling, contributed by six partners and one *observer* (Alenis, Ansys, Dassault, EADS-M, FOI, NTS and *Liverpool*). In comparison with available measurements (for unsteady pressure modes) and with full-resolved LES data (for resolved mean flow and turbulence statistics), a sensible span of different modelling accuracies can be observed in the predictions, due largely to various grid resolutions employed by different partners.

Nonetheless, in view of the resolved unsteady motions, all the computations have produced reasonable representation in line with the type of modelling approaches employed. The statistically unsteady flow feature has made the URANS modelling (both the ERASM k-ω model and the SA model) able to model unsteady large-recirculating motions in the cavity, but does not resolve rich vortex motions as by DES, hybrid RANS-LES modelling and the SST-SAS model.

Grid resolution is significantly important for accurate predictions of this flow, particularly for the mixing layer and inside the cavity. Coarse grids (and/or large numerical diffusion) may pronounce a too diffusive mixing layer, causing an earlier deflection of it towards the cavity floor prior to the impact on the cavity aft wall. As a consequence, the prediction of the cavity mean flow may become erroneous and, moreover, too large amplitudes of pressure fluctuations are generated on the cavity floor, giving inaccurate predictions of tonal modes. Furthermore, nearly all the coarse grids have predicted a large pressure gradient over the cavity. Based on the computations, it is justified that a grid with one million or more nodes in the cavity should be used to attain improved predictions for this specific case. In addition, the temporal resolution, as well as the numerical diffusion, has shown to play an important role in resolving high-frequency tonal modes and broadband resonances. A too large time step and/or too large numerical diffusion tend to dampen physical, high-frequency signals, for example, the 4th mode at a frequency of f_4 = 820 Hz may become smeared.

Most of the computations have responded to the two dominant tonal modes (the 2nd and 3rd modes), with different degrees of accuracy in terms of the mode magnitude and frequency. On the other hand, the 1st mode has been smeared or only

marginally resolved by many computations. With the same grid, the Dassault modelling has disclosed that the LES (with the selective SGS model) and the SA-DES model have performed somewhat better than the KE-DES model. On the same FOI structured grid, which is rather coarse, the SA-DES model and the HYB0 model have shown very similar behaviours. With the refined EADS-M grid unstructured grid, the FOI HYB0 modelling has produced a slightly better prediction of the mean flow than the SA-DES modelling by EADS-M, but the latter has employed a larger temporal resolution.

Due to fairly sparse resolutions in space and in time, as invoked by different partners, no superiority can be justified for any modelling approach in terms of modelling accuracy. Nonetheless, it is worth mentioning that the EARSM-DES computation by Alenia has presented a sensible capability of capturing the dominant tonal modes (the 2^{nd} and 3^{rd} modes) on a relatively coarse grid, due possibly to a sophisticated EARSM formulation inherent. Moreover, it should be noted that the HYB0 model is an algebraic hybrid RANS-LES model, which does not solve any additional turbulence transport equation. Enabling very similar predictions, the HYB0 model may entail a saving of CPU time in the computation by about 15-20%, as compared with a one-equation DES model.

In general, the computations conducted for this test case have reasonably demonstrated the capability of involved modelling approaches in predicting the acoustic source generated by turbulent flows. With appropriate grid and temporal resolutions, it is concluded that, the DES and different variants, the hybrid RANS-LES approach, as well as the SST-SAS model, are able to attain reasonable flow analysis in an “aero-acoustic environment” for this and similar turbulent cavity flows.

18 Appendix for M219 Cavity Flow: Computations with and without Bay Doors

S.J. Lawson[1], G.N. Barakos[1], and P. Nayyar[2]

[1] University of Liverpool
[2] ARA Ltd.

18.1 Introduction

Along with the mandatory computation for the "door-off" case, Liverpool has been the only participant in this test case, who has also made computations for the "door-on" configuration. Apart from some results contributed by the current authors included in the preceding summary (Section 18), this Appendix presents further a brief comparison of the Liverpool computations for the cavity flow with and without bay doors. The focus is placed on the prediction of the tonal modes using different models.

With the same cavity configuration as shown in Section 18, the bay doors were attached at 90° to the horizontal and each had a depth of half the cavity. Experimental data was provided by QinetiQ (Nightingale *et al.*, 2005).

The experimental data were sampled at either 6 or 31.25 kHz, for approximately 3.4 seconds. The numerical computations were sampled at a higher rate, but only for 0.1 seconds. Therefore, when comparing experimental and numerical data sets, 0.1 seconds of the experimental data were used and the computations were down-sampled to match the experimental sampling rates.

Figure 1(a) shows that the energy spectra differ between the doors-off and doors-on cases. For the doors-on case, the second mode is the dominant mode, with the first and third modes only just visible above the broadband noise level. For the doors-off case, the second mode is identified as still being the dominant mode, although the second mode is much smaller and the third mode much larger in magnitude than in the doors-on case. Also, the frequencies of all the modes shift to slightly lower values for the doors-off case.

The frequencies predicted by Rossiter's formula were not in perfect agreement with experiments and so for the SPL of each mode a window of 200 decibels was used. Extracting data in different frequency ranges aided in identifying which modes contributed most to the overall spectrum across the length of the cavity.

Figure 2(a) shows that the energy content of the first mode across the cavity length was very similar in both doors on and doors off cases. The shape of the second mode was also very similar for both cases, although as stated earlier the magnitude was higher in the doors on case. Also, since the magnitude of the dominant second mode was much greater than any other mode in the doors on case, the curve in Figure 2(b) was almost the same as the doors on curve for whole

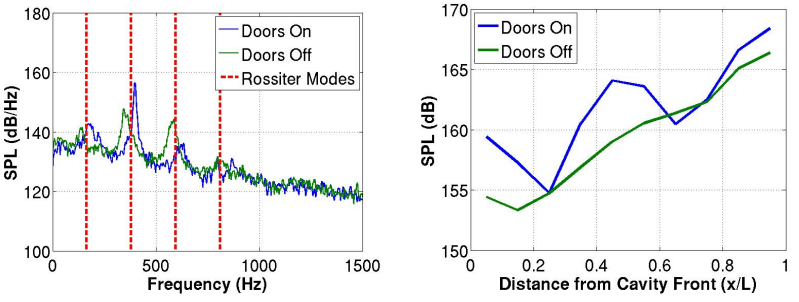

(a) PSD (b) SPL

Fig. 1 Power Spectral Density (PSD) at the cavity rear (x/L = 0.95) and Sound Pressure Levels (SPL) along the cavity floor with experimental data from Nightingale *et al.* (2005)

frequency range (Figure 1(b)). The SPL curves for the third mode had a similar shape, although the doors off curve had a higher SPL across the whole length and the magnitude of the SPL at the rear of the cavity was almost the same as the first mode at the same location. For both cases, the fourth mode did not have any distinctive shape, although it is worth noting that the cavity without bay doors had a slightly higher magnitude along most of the cavity length.

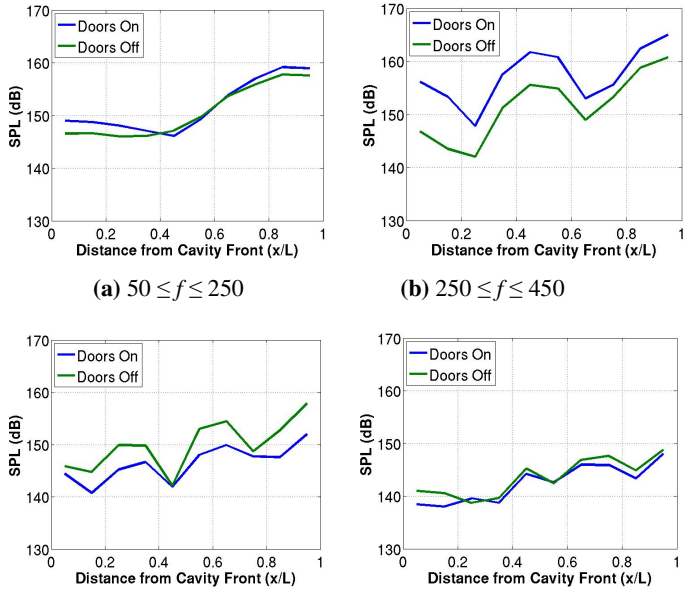

(a) $50 \leq f \leq 250$ **(b)** $250 \leq f \leq 450$

(c) $500 \leq f \leq 700$ **(d)** $700 \leq f \leq 900$

Fig. 2 Windowed SPL plots encapsulating the first four Rossiter modes for doors on and doors off. Plots taken along the cavity floor using data from Nightingale *et al.* (2005)

18.2 Results and Discussion

All the computations were performed using a 3D multi-block structured solver which solves the Navier-Stokes equations in the 3D Cartesian frame of reference (Nayyar *et al.*, 2007). The standard DES was used (Spalart *et al.*, 1997), and for LES the Smagorinsky SGS model (Smagorinsky, 1963) was employed. These were performed at a Mach number of 0.85 and a Reynolds number of one million (based on the cavity length). The Reynolds number was reduced from the value used in experiments since this does not change the fundamental physics within the cavity (Nayyar *et al.*, 2007). This was also compared to URANS results using Menter's Baseline k-ω turbulence model (Menter, 1994). Table 1 shows the details for two of the finest LES/DES calculations and compares with a 3D URANS calculation.

The computations were conducted in a domain with dimensions of 7.6L in the streamwise, 5L in the vertical and 4.85L in the spanwise directions, respectively, where L is the cavity length. The cavity was embedded in a flat plate (shown in Section 18, but without the sting support here), which was placed in the middle of the bottom boundary of the computational domain.

Table 1 Details of the computations undertaken

Calculation Details	**3D URANS**	**DES-SA**	**LES**
Cavity Configuration	Doors On	Doors On	Doors Off
Grid Size	1.5×10^6	4.5×10^6	8.5×10^6
Processors	19	320	256
CFD Time-step	1.81×10^{-5}	1.81×10^{-6}	1.81×10^{-6}
Unsteady Tolerance	0.005	0.001	0.001
Pseudo-steps/CFD Time-step	39	6	7
CFD Time-Steps/min	0.425	9.72	2.57
Total CFD Time-steps	5506	50200	18546
Total CPU Hours	3121	28100	39936
Signal Duration	0.1 s	0.1 s	0.034 s

18.2.1 Rossiter Mode Frequencies

]As with the experimental data, the PSD of the pressure fluctuations was computed. The frequencies for each of the first four modes were found by taking bands around each mode and finding the local maximum amplitude. Figure 3(a) shows that for the doors on case, none of the computational methods could accurately predict the frequencies of all four modes. The URANS results under-predicted the frequency of the second mode and over-predicted the third mode. For the first and fourth modes, there were no tones evident above the broadband spectrum. Both DES and LES results over-predicted the frequency of the dominant second mode. All computational models faired a little better for the doors off case. Figure 3(b) shows that the first two modes, were reasonable well predicted by all computations. The third and fourth modes were over-predicted by DES and

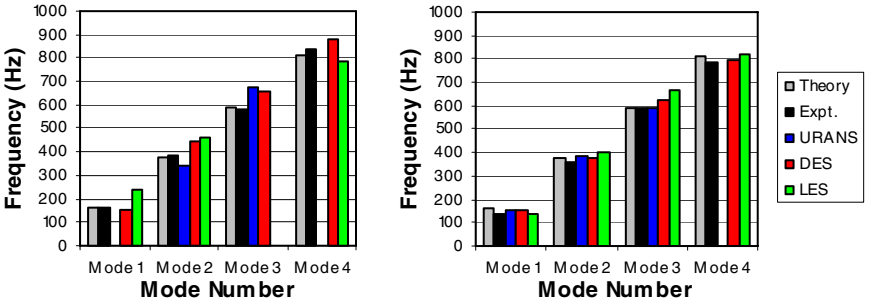

(a) Doors on (b) Doors off

Fig. 3 Frequencies of the first four Rossiter modes predicted by URANS (Menter's Baseline k-ω), DES (S-A) and LES (Smagorinsky SGS) at location x/L = 0.95

LES. URANS captured the third mode well, but failed to predict the fourth. It can also be seen that, as with the experimental data, the computational models predicted the modes to shift to lower frequencies for the doors off case.

18.2.2 Sound Pressure Levels (SPL)

The 2D cavity was thought to be a good representation of the full 3D cavity with doors-on as the doors restrict movement of the flow to the width of the cavity. Therefore 2D results using the SST model (Menter, 1994) were also compared with the 3D doors-on results. Figure 4 shows the SPL for both doors on and off cases. For the doors on case, the 3D URANS predicted the shape of the curve better than the LES and DES, although overall the magnitudes were better predicted by the LES and DES models. The 2D case predicted the shape of the SPL curve, but over predicted its magnitude.

For the doors off case, URANS predicted a 'W' shaped curve for the SPL across the cavity floor and under predicted the magnitude. However, LES and DES correctly predicted the shape shown by the experimental data, although the magnitudes for both were over predicted by 2 to 4 dB.

Band-limited SPL plots for the first (Figure 5) and second (Figure 6) modes revealed the limitations of the URANS model. In the doors on case, 3D URANS predicted the dominant second mode well but had difficulty in capturing the other modes, which were substantially under predicted. For the doors off case, URANS under predicted the magnitudes of both the first and second modes, but still captured the shape of the second mode well.

DES and LES were much better in predicting the shapes of the SPL curves in both cases, although the magnitude of the second mode was under predicted for the doors on case and slightly over predicted for the doors off case.

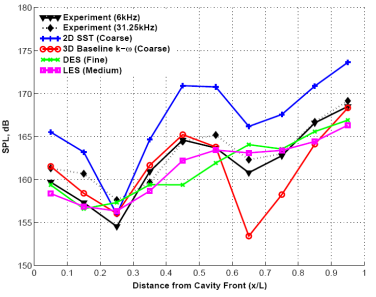

(a) Doors on

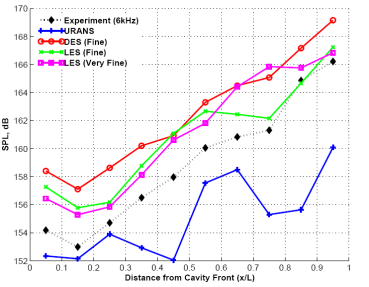

(b) Doors off

Fig. 4 Overall SPL plots, comparing URANS (Menter's Baseline k-ω), DES (S-A) and LES (Smagorinsky SGS). Plots taken at z/W=0.25 and along the cavity floor

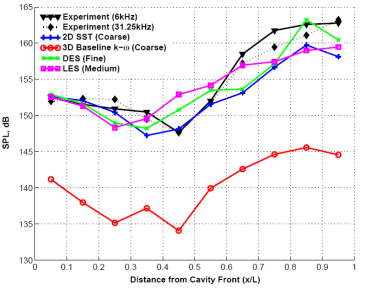

(a) Doors on

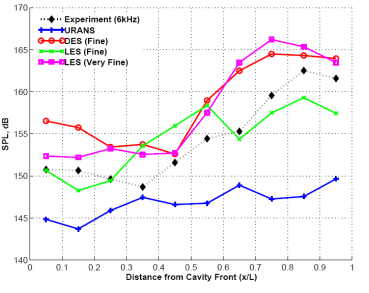

(b) Doors off

Fig. 5 Band-limited SPLs for the first mode ($50 \leq f \leq 250$ Hz) comparing URANS (Menter's Baseline k-ω), DES (S-A) and LES (Smagorinsky SGS) results with experiment. Plots taken at z/W=0.25 and along the cavity floor

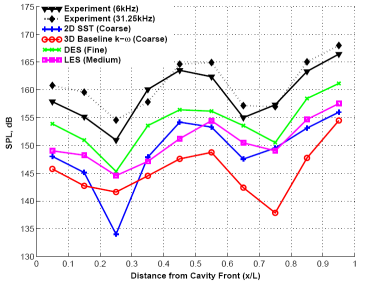

(a) Doors on

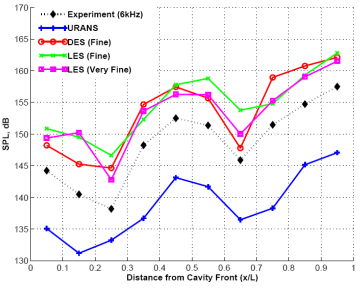

(b) Doors off

Fig. 6 Band-limited SPLs for the second mode ($250 \leq f \leq 450$ Hz) comparing URANS (Menter's Baseline k-ω), DES (S-A) and LES (Smagorinsky SGS) results with experiment. Plots taken at z/W=0.25 and along the cavity floor

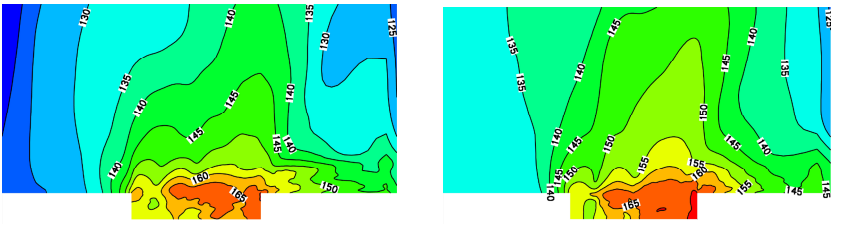

Fig. 7 SPL distributions calculated from the R.M.S pressure for the doors-on (left) and doors-off (right) cavity configurations using DES (S-A). Slices taken at cavity centreline

To highlight the differences in acoustic wave propagation between the doors-on and off configurations, Figure 7 shows the SPL distributions at the cavity centreline.

The SPL distributions (Figure 7) verify that the acoustic waves in the doors-off case were stronger and could travel further than those of the doors-on case. This could be mainly attributed to the very high SPL (170 dB) that is generated over the whole aft wall. It can be seen that at any point in the far-field, the SPL is almost 5dB less in the doors-on case. As with the iso-surfaces of acoustic pressure, there are similarities between the two cases in how the waves propagate throughout the domain. However, the levels in the doors-on cavity are generally lower inside the cavity as well as in the far-field.

18.3 Summary of Conclusions

Interrogation of the experimental data revealed that, with the bay doors attached, the second Rossiter mode was the dominant tone, with the magnitude of the other modes being much smaller. In contrast, without the doors the other modes contributed much more to the overall acoustic signature. The magnitude of the second mode was greatly reduced and the magnitude of the third mode increased.

The employed URANS model could not predict the higher or lower frequency tones than occurred in the flow regime under investigation. In both cases, the dominant Rossiter mode was predicted well in qualitative terms, although the modes were still under predicted in magnitude.

Computations using DES and LES had a good level of qualitative agreement with experimental data. The shapes of the SPL curves were predicted well in both cases, which indicated that the essential flow physics was captured. However, both DES and LES still had difficulty in predicting the magnitude of each mode. SPL distributions showed that stronger acoustic waves were generated in the doors-off case and so more noise was propagated outside the cavity.

The present results indicate that DES is a good alternative to LES for this flow and a much more reliable tool than URANS for cavity flow analysis.

19 Car Side-Mirror – An Aero-Acoustics Case

C. Mockett and F. Thiele

TUB

Abstract. The flow past a generic representation of an automobile side mirror has been simulated by 4 partners using a range of modelling approaches (pure LES, DES and SAS) and a range of grid resolutions (from 1.7 million to 11.8 million cells) and types (structured and unstructured with various cell geometries). The test case is representative of the simulation of aero-acoustic noise sources generated in the wake of bluff bodies. The investigation is a continuation of the study carried out in the precursor FLOMANIA project (Rung et al., 2006) and addresses some of the open questions posed therein. In particular, it emerges that the doubts cast upon the experimental data are in fact a consequence of modelling and grid resolution issues. A general tendency of increasing resolution of high-frequency content with grid refinement is observed, as is a similarity in the predicted levels of low-frequency sound. No direct comparison of LES and DES on the same grid has been carried out, however an apparent equivalence of DES and SAS on similar grids is observed.

19.1 Background and Motivation

The test case consists of a generic geometry intended to capture the characteristics of the flow around car wing mirrors. As well as a source of drag and fluctuating forces, the principle interest is in the sound sources created by the mirror. The motivation from an automobile industry perspective is primarily passenger comfort, with internal noise caused by pressure fluctuations transmitted through the window and vehicle side. Sound radiated into the far-field is considered less important as tyre noise is usually dominant. The test case could also represent applications involving a blunt protrusion from a smooth body (e.g. deployed air brake in aerodynamic applications).

19.2 Flow and Test Case Description

The geometry represents an idealised car wing mirror mounted on a flat plate, intended to represent the side window. The mirror consists of a half cylinder of diameter D=0.2m and height H=0.2m, which is topped with a quarter-sphere of the same diameter. The mirror is arranged with its curved side facing into the oncoming flow such that the wake forms behind the flat rear surface. The flat plate is 3m long and 1.6m wide. The Mach number of M=0.11 allows the flow to be considered incompressible and the Reynolds number is $Re_D=5.2\times10^6$. The experimental data (Höld et al., 1999), (Siegert et al., 1999) consists of time-averaged and unsteady signals at a range of pressure tappings on the mirror and plate. The

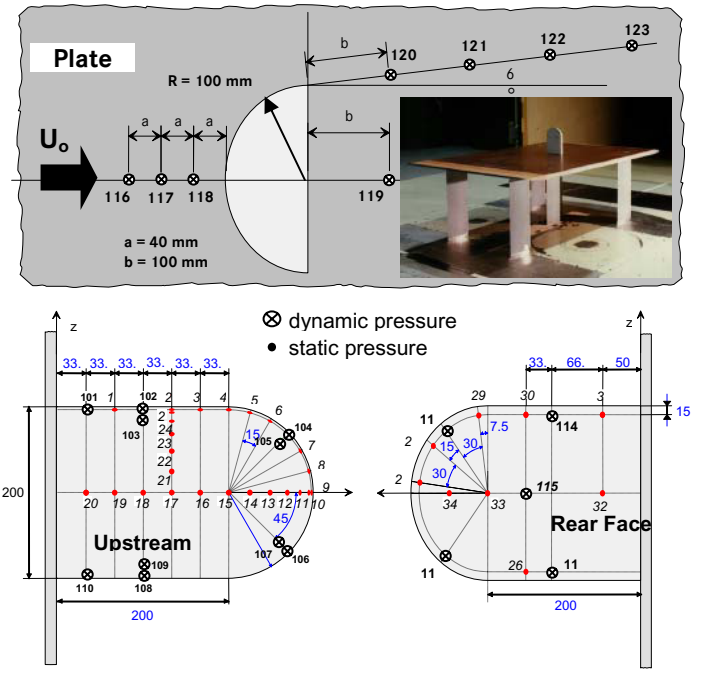

Fig. 1 Experimental setup and location of pressure probes

configuration and location of the sensors are shown in Fig. 1. The probes numbered 1-34 were used for time-averaged measurements and the second set, numbered 101-123 provided instantaneous signals at a sampling rate of 20kHz. This is available in the form of spectra with a bin width of around 10Hz. To avoid spurious noise sources, no transition tripping was applied in the experiments and a laminar separation has been observed 0.15*D* upstream of the rear face of the mirror.

19.3 Summary of the FLOMANIA Study

This test case was previously studied in the FLOMANIA project (Rung et al., 2006), for which URANS and DES97 computations were carried out by Bombardier Transportation (BT) and the Technische Universität Berlin (TUB). The following summarises the outcomes of the previous study:

- Considerable improvement was reported for the DES calculations in comparison to URANS with the same grid and time step.
- The DES overall sound pressure levels (SPL) agreed well with experiments at most measurement locations, those of URANS were under-predicted by typically 20dB.
- The laminar boundary layer separation was not reproduced by the fully-turbulent URANS and DES computations.

- No significant difference was seen between the different background RANS models for the DES results.
- It was not understood why such high SPL were returned from experimental tappings near the upstream horseshoe vortex whilst the simulations were fairly quiet.
- No information was available as to the window function applied in the experimental spectral analysis. Due to excellent agreement with the DES without a window function, it was suspected that none was applied to the experimental data.

In the continuation within DESider, the investigation has benefited from a greater number of partners, greater computational capacity allowing finer grids and the comparison with pure LES. Some of the conclusions from FLOMANIA are hence reassessed.

19.4 Partners Contributing, Numerical and Modelling Setup

An interesting blend of turbulence approaches, numerical methods, and grid strategies have been computed by the four partners involved, which are summarised in Tab. 1.

Table 1 Participants and methods

Partner:	Turbulence treatment:	Solver:	Δt:	Grid:
BT	SA-DES97, k-ε-DES97	Star-CD, flux blending convection (95% 2nd order CDS, 5% UDS)	1×10^{-5} $0.00195T_0$	BT
CFX	SST-SAS	CFX, hybrid convection (local between 2nd order CDS and 2nd order UDS)	2×10^{-5}s $0.0039T_0$	CFX
TUB	SALSA-DES97, LLR k-ω-DES97	ELAN, hybrid convection (local between 2nd order CDS & higher order TVD)	1×10^{-4}s $0.0195T_0$	TUB
Volvo	SA-DES97, Smagorinsky LES, dynamic LES	Fluent, 2nd order UDS and bounded central (BCD) convection	2×10^{-5}s $0.0039T_0$	Volvo-hex and Volvo-Cart

The pure LES simulations aim to exploit the laminar nature of the mirror boundary layers and the subordinate importance of the turbulent flat plate boundary layer to achieve a reasonable reproduction of the dominant flow features at modest cost – the flat plate boundary layer was under resolved in all cases. The extensive computations by Volvo (Ask, 2008), (Ask et al., 2006) allow the effects of grid refinement to be studied for the Smagorinsky LES results. The dynamic LES results by contrast were only computed on one of the grids, as some numerical instability issues were encountered (no averaging in homogeneous directions can be applied for this three-dimensional geometry).

In most cases low-dissipative convection schemes based around 2nd order central differences were applied, using various methods to achieve stability in coarser

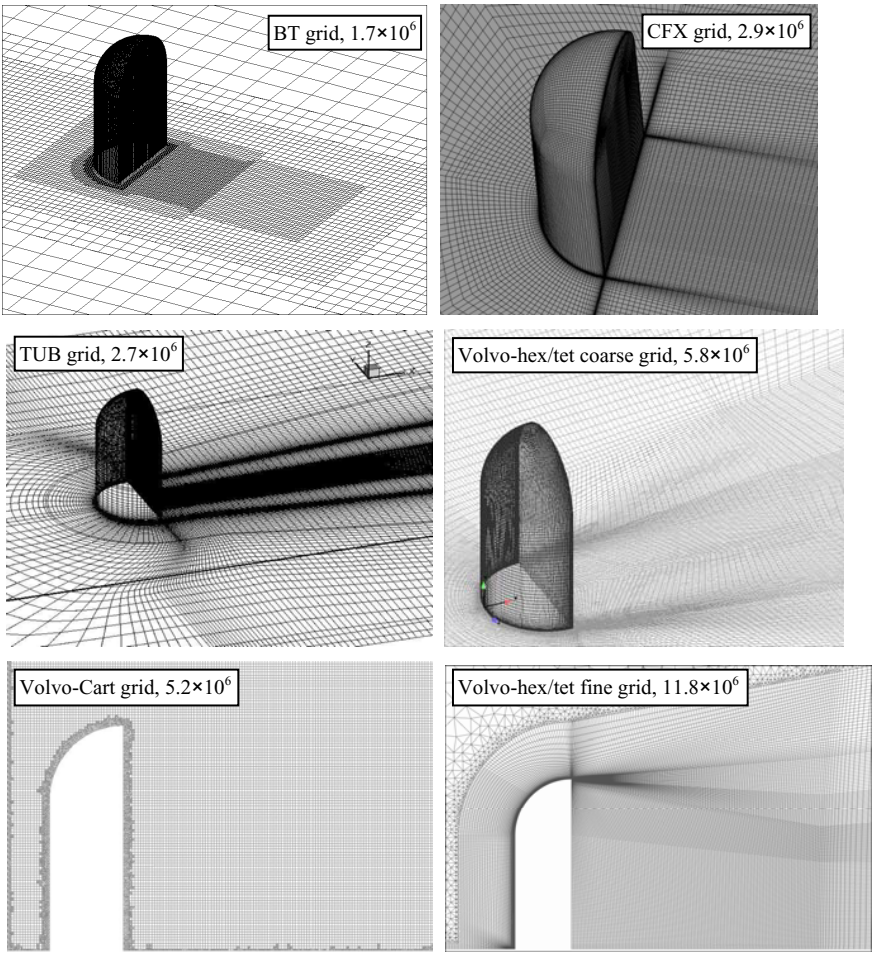

Fig. 2 Visualisations of the computational grids used

grid regions (a global 5% UDS blend for the BT calculations; UDS application on the basis of a "wiggle detector" by Volvo; local flux blending variation depending on the solution field by CFX and TUB). The exception is the SA-DES97 calculations by Volvo, for which pure UDS was applied throughout the domain.

A variety of grid generation strategies has been explored by the partners. Traditional block-structured hexahedral grids have been employed by CFX and TUB, allowing resolution of all boundary layers and refinement in the vicinity of the early separated shear layers. The unstructured mesh of BT employs a Cartesian dominant grid with local refinement achieved using hanging nodes. A similar methodology was applied in the Volvo-Cart grid, although the refined region is much more extensive. Volvo also applied a hybrid hexahedral/tetrahedral methodology whereby a structured near-wall and wake region grid is combined with a

tetrahedral meshing of the outer region. Whereas the Volvo-hex/tet grid allows wall-normal resolution of the boundary layers, wall functions were applied in the case of the Volvo-Cart grid.

All calculations were conducted at the experimental $Re_D=5.2\times10^5$, with an inflow velocity of U_0=39m/s. Steady-state inflow conditions were applied by all, as were symmetry boundary conditions at the lateral and upper domain frontiers. The calculation time steps range from between $0.00195T_0$ and $0.0195T_0$, where $T_0=D/U_0$.

19.5 Results

In the presentation of the results, a focus on the SPL spectra will be made, as these are the most relevant quantity bearing in mind the unsteady methods considered and the aero-acoustic motivation of the test case. Some comparison will also be made concerning the capability of the various methods to capture the laminar separation.

19.5.1 Processing of the SPL Spectra

It was shown in the FLOMANIA investigation (Rung et al., 2006) that the SPL spectra exhibit particular sensitivity to the signal processing details. The spectra presented in this investigation have therefore all been calculated using the original time traces from each partner by TUB, using the best practice method outcome of the FLOMANIA study. As such the maximum level of comparability between the partner spectra is ensured.

The time traces of pressure (in Pa) obtained at each probe location have been divided into overlapping windows of a 0.1s physical time length. These windows have been overlaid with a Hanning window function to remove aliasing effects and processed with a discrete Fourier transform. The window length of 0.1s is intended to deliver the targeted bin width of 10Hz observed in the experimental spectra. The resulting spectra have been averaged to achieve a smoother appearance and reduce the level of spurious noise. The fluctuation amplitudes are presented in terms of sound pressure levels (dB):

$$\mathrm{SPL} = 20\log_{10}\left(\frac{p'}{p_0}\right),$$

where p' is the pressure fluctuation away from the mean and the reference pressure $p_0 = 2\times10^{-5}$ Pa.

19.5.2 Comparison of LES, DES and SAS in the Wake Region

To obtain an impression of the comparability of results from different turbulence treatment methods, representatives of each have been selected based on the most similar grids available for calculations with low-dissipative numerical convection

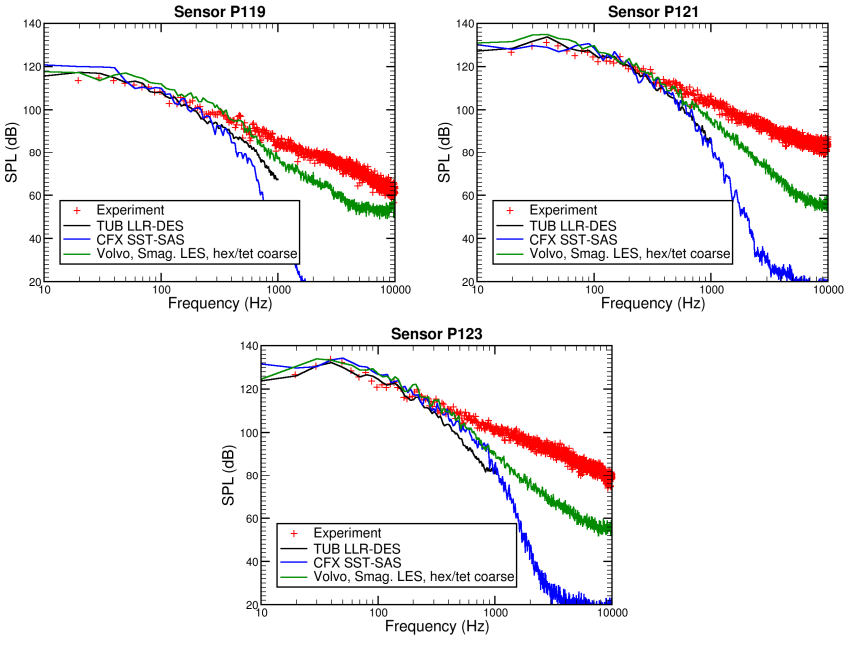

Fig. 3 SPL spectra for DES (TUB), SAS (CFX) and Smagorinsky LES (Volvo) at locations P119, P121 and P123

schemes. The selected data are the LLR-DES97 of TUB, the SST-SAS of CFX and the Smagorinsky LES of Volvo (on the hex/tet coarse grid).

The spectra for points P119 in the near wake and P121 and P123 along the shear layer path are plotted in Fig. 3 (the TUB spectra end at 1000Hz because the pressure was only recorded at every 5th time step). The agreement between the methods and with the experiment at lower frequencies is very good, particularly for the measurement points in the shear layers. At higher frequencies however, the Volvo LES results return a considerably higher SPL (and better agreement with the experiment), especially for the P119 location. For the DES and SAS, which were computed on very similar grids, these results can be interpreted as a strong similarity between the methods. The higher quality of the LES results can by contrast not conclusively be interpreted as an advantage of the method as the grid used was considerably finer. Unfortunately a direct comparison of LES with the other methods is not possible, as the SA-DES97 of Volvo on the same grid employed pure upwind numerics.

19.5.3 Effect of Grid Resolution

To examine the effect of grid resolution, the Volvo LES results with the Smagorinsky model will be compared, for which computations all employing the BCD convection scheme were carried out on the three different grids. The SPL spectra are again compared at the sensor locations P119, P121 and P123 in Fig. 4.

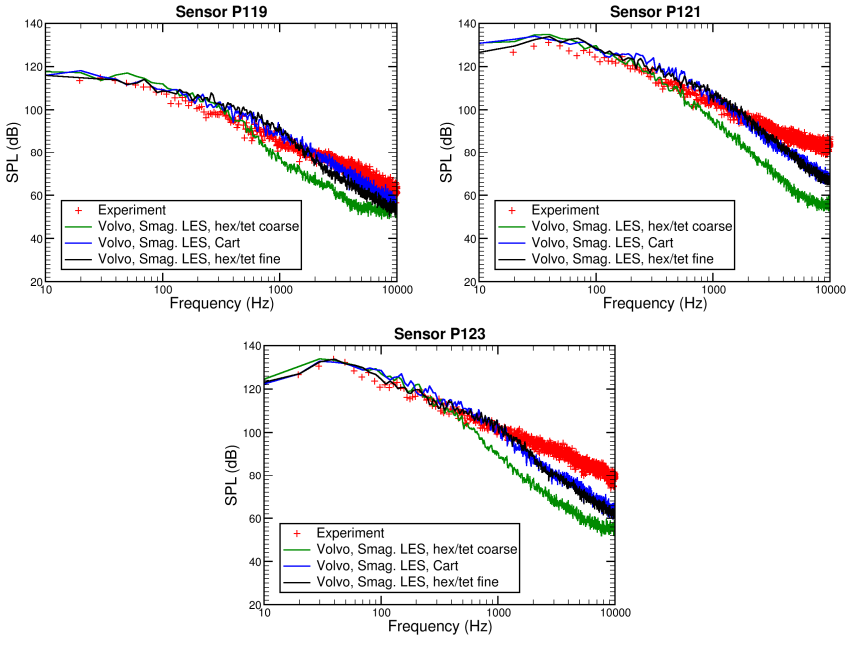

Fig. 4 SPL spectra for Smagorinsky LES (Volvo) on different grids at locations P119, P121 and P123

The effect of grid refinement is clearly an improvement in the agreement with the experimental spectra up to higher frequencies. In the published analysis, Volvo estimated the maximum resolvable frequency for each grid and measurement point based on the local grid resolution and velocity magnitude RMS (Ask et al., 2006), (Ask, 2008). A strong correlation was observed between these estimated values and the frequency at which the simulated spectra begin to decay below those of the experiment. This is therefore an illustrative demonstration of the effect of grid resolution: the good agreement of all results at lower frequencies demonstrates that the higher grid resolution does not improve the prediction of the larger, energy-containing structures. It furthermore suggests an equivalence of the methods and implementations for this flow.

Some comments about the grid strategies can also be made, based on the comparison of the hex/tet and Cartesian grids used (Fig. 2). The Volvo Cartesian grid is not body-fitted and employs wall-functions rather than resolving through the boundary layer in the wall-normal direction. The fact that these results are so similar to those from the hex/tet-fine grid is a reflection of the subordinate importance of the mirror and plate boundary layer prediction in this test case.

19.5.4 The Upstream Horseshoe Vortex

The interaction of the oncoming flat plate boundary layer with the upstream surface of the mirror leads to the formation of a horseshoe vortex. The measurement

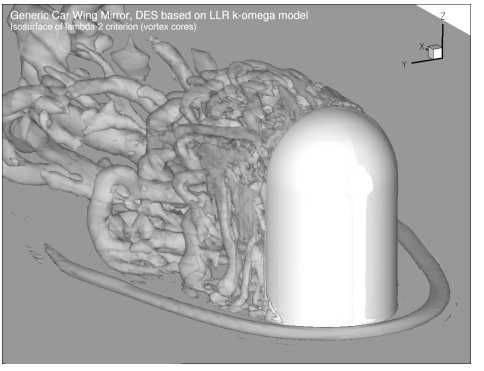

Fig. 5 Instantaneous snapshot of vortex cores (λ_2 criterion) for the TUB LLR-DES

point P116 is located in this region, and was the subject of some controversy in the FLOMANIA investigation (Rung et al., 2006). The horseshoe vortex is depicted in Fig. 5, in a visualisation of the instantaneous vortex core structures resolved in the TUB LLR-DES computation. It can be seen that this is very smooth, suggesting a very steady nature in comparison to the highly unsteady turbulent wake downstream of the mirror. For this reason, it was not understood why the experimental signals from P116 exhibited such high sound levels.

The spectra from the CFX SST-SAS and Volvo Smagorinsky LES computations at this measurement point are compared in Fig. 6. Whereas the SAS returns a very low SPL, the LES results show much higher levels, agreeing increasingly well with the experiment as the grid is refined. The LES is hence able to resolve some strong unsteady phenomenon in this region that the DES and SAS are not.

The answer indeed lies in the modelling methodology. Whereas DES and SAS target the application of RANS in attached boundary layers, the pure LES is intended for resolution of the energy-containing large eddies throughout the domain. Figure 7 portrays the instantaneous vorticity magnitude and tangential streamlines at a slice through the symmetry plane in the vicinity of the mirror foot. The DES exhibits a smooth and steady horseshoe vortex whereas that of the LES appears unsteady. Despite the insufficient resolution of the incoming boundary layer

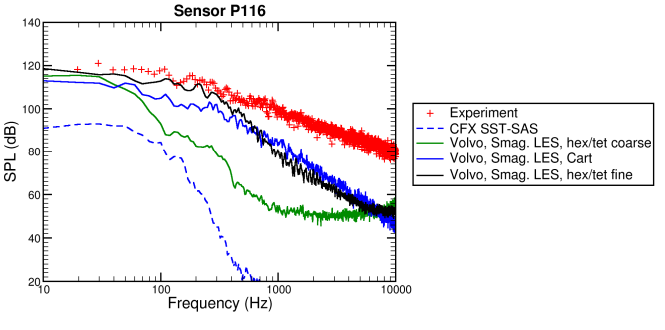

Fig. 6 SPL spectra for SAS (CFX) and Smagorinsky LES on different grids (Volvo) at the upstream P116

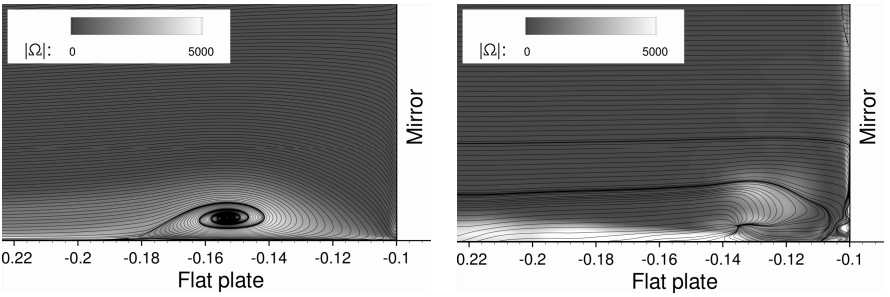

(a) TUB LLR-DES *(b) Volvo Smag. LES, hex/tet-fine*

Fig. 7 Instantaneous contours of vorticity magnitude and streamlines at a slice through the symmetry plane in the vicinity of the horseshoe vortex

turbulence, the LES appears to capture something approximating a bimodal horseshoe vortex instability (Devenport et al., 1990). Such an instability was found by (Paik et al., 2007) to be damped by eddy viscosity when the oncoming boundary layer is handled entirely using RANS.

Although the methodologies appear to be equivalent in the massively-separated wake region, the inherent inability to capture the unsteady behaviour of the horseshoe vortex (and the relative importance of this as a sound source) corresponds to a disadvantage of DES and SAS for this aeroacoustic application. Although proper resolution of the flat plate boundary layer would be prohibitively expensive for pure LES, it appears as if an approximation of the horseshoe vortex dynamics can nonetheless be captured on "under-resolved" grids.

19.6 Conclusions

A continuation of the FLOMANIA investigation of this test case has been carried out, with additional computations delivering new insight concerning the equivalence of methods and grid resolution issues. Some of the FLOMANIA conclusions contained doubts about the validity of the experimental data in two respects: the suspicion that the spectra were processed without a window function, and the "inexplicable" loudness of the horseshoe vortex region. These points have been reassessed in the light of the new computations by CFX and Volvo, as a consequence of which the question marks concerning the experimental data must be retracted. The agreement with the experimental data at high frequencies has been significantly improved by higher grid resolution as demonstrated by the Volvo computations. A physical explanation for high sound levels near the horseshoe vortex is provided with reference to studies of a bimodal instability in the literature. This instability cannot be captured by DES and SAS, which treat the attached boundary layer and horseshoe vortex in RANS mode. Despite insufficient resolution of the flat plate boundary layer, the LES simulations are able to reproduce an approximation of the horseshoe vortex instability.

Some caution is however advised in the extrapolation of these findings to more complex geometries. Although the damping of the horseshoe vortex by the RANS treatment of the boundary layers in DES and SAS is indeed a disadvantage for the aero-acoustic prediction, the disadvantages of the under-resolved LES treatment are suppressed by the simplified flat-plate geometry in this test case. More complex curved geometries are likely to occur in practice, for which an under-resolved LES could erroneously predict boundary layer separation and a corresponding distortion of the mean flow and aero-acoustic solution.

The importance of high quality grid resolution in the separated wake region has been demonstrated by the relative success of the Volvo simulation on the Cartesian grid with wall functions, which give comparable solution quality to the wall-refined grid with roughly half the number of grid points. Again, in the case of more complex flows where the boundary layers play an important role, this conclusion may not apply.

The similarity of the DES and SAS solutions on similar grids and with low-dissipative numerical schemes suggests an equivalence of the methodologies for this application. The higher quality of the LES solutions cannot however be interpreted as a fundamental superiority of LES as the grids used were considerably finer. The effect of grid refinement has been shown to be an increase in the maximum resolved frequencies in the SPL spectra. The spectra at lower frequencies by contrast agree well between grids and methods, implying that the large energy-containing scales have been reproduced to a similar level of quality.

20 Simplified Landing Gear Test Case

B.I. Soemarwoto, J.C. Kok, and H. van der Ven

National Aerospace Laboratory NLR

20.1 Introduction

During approach and landing, the noise originating from the flow around the airframe takes a significant portion of the overall noise, as the engine is operating in a low thrust. Reducing flow-induced airframe noise is still a challenging task. Significant noise is generated by the high-lift devices and the landing gear. A test case addressing the massively separated flow around the landing gear is therefore highly industrially relevant. The test case concerns a four-wheel configuration representing a 31% scale of a simplified Boeing 757's landing gear (see Figure 1). This configuration was measured in the Basic Aerodynamic Research Tunnel (BART) at NASA Langley Research Center. The mean flow DPIV experimental data (on the so-called PIV plane) are available for the free-stream velocity of 29 m/s and Reynolds number of 600,000 based on the wheel diameter (Lazos, 2000, 2002)). Within DESider, the test case is participated by NLR and NTS.

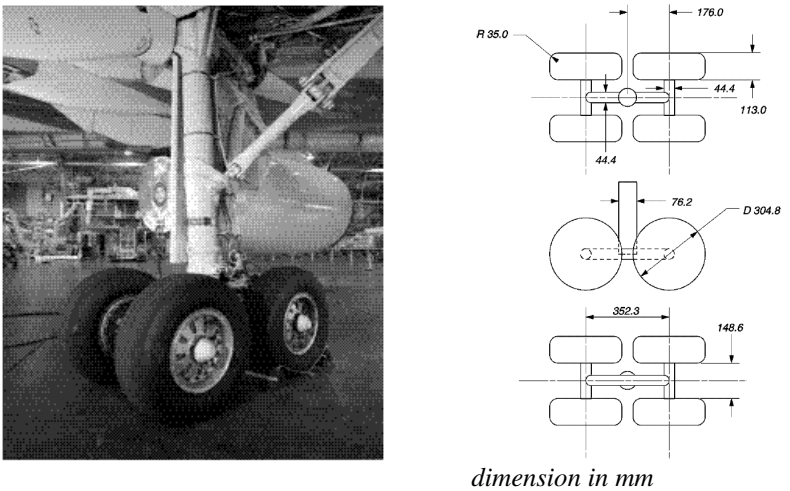

Fig. 1 Simplified four-wheel landing gear configuration (Lazos, 2002)

20.2 Computational Setup

NTS employs an overlapping grid of 13 blocks consisting of about 3 million nodes. NLR employs structured grids in a multi-block topology with a point-to-point

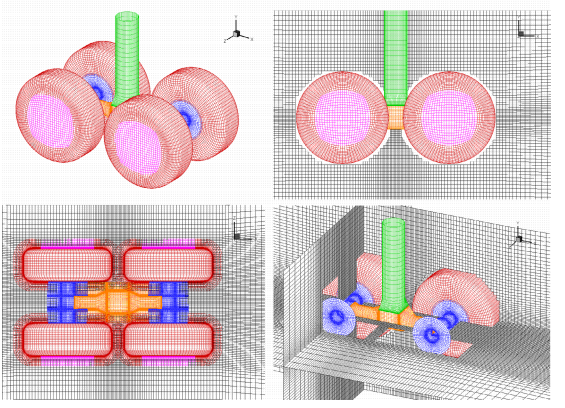

(a) NTS overlapping grid (3e6 nodes)

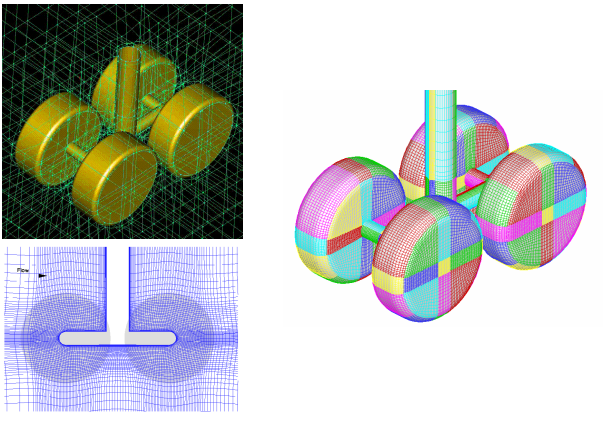

(b) NLR multi-block structured grid (2e6 cells)

Fig. 2 Impression of the computational grids

connection consisting of about two million grid cells. An impression of the grids is given in Figure 2. The methods used are SA-DDES (NTS) and X-LES (NLR), which are described in Chapter 2.

Both NTS and NLR use the same non-dimensional time step of 0.01 based on the free-stream velocity and wheel diameter. In this time resolution, one convective time unit is covered by 100 time steps. The flow domain is bounded conforming the wind tunnel walls defining a test section area of 71 by 102 cm. The inflow (outflow) boundary is -5D and -4D (+15D and +8D) in the NLR and NTS case, respectively, where D is the wheel diameter. The wind tunnel walls are treated as an inviscid wall with a slip boundary condition. NLR employs a compressible flow solver with a low Mach number pre-conditioner. NTS treats the flow as incompressible. NLR opted to use a uniform flow with the free stream velocity as the initial flow, while NTS takes a non-converged solution of a steady RANS computation as the initial flow.

20.3 Results

Figure 3 shows the time history of the force coefficients. The uniform flow used by NLR as the initial flow has not yet led to an asymmetric flow (with respect to plane-z), giving a zero level of F_z. The levels of the force coefficient in the horizontal (F_x) and vertical (F_y) direction are roughly the same. The RMS of F_x in the NLR results is larger than that of the NTS results. NTS results show a lower level of F_y. For both NLR and NTS results, the transient is considered to have decayed after 30 convective time units. The sample sizes for obtaining the the mean flow are different, i.e. 20 convective time units for NLR results and 60 time units for NTS results.

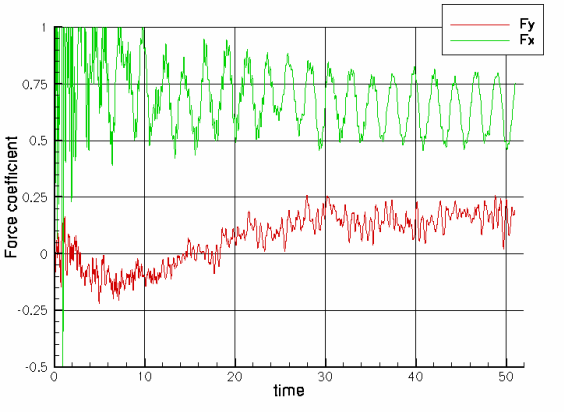

X-LES (NLR)

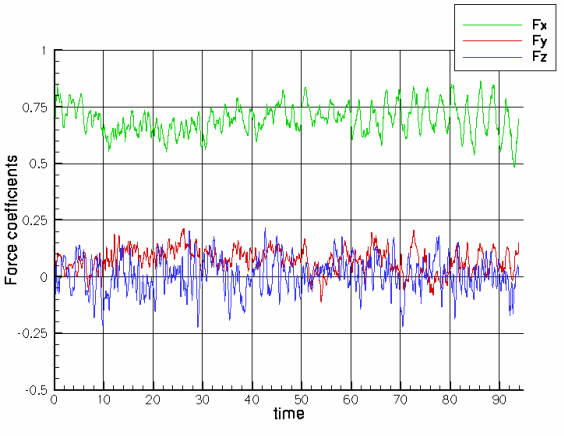

SA-DDES (NTS)

Fig. 3 Time history of the force coefficients

In the experiment, the flow alternates between two mean flows (Ref. 2), although the second one is less persistent than the first. Figure 4 shows the streamline patterns of the first mean flow in the PIV plane. The streamlines are coloured by the velocity magnitude. The streamlines in the experiment (Figure 4a) show two separation points, i.e. on the ground and wing sides of the fore wheel. The shear layers originating from these points attach on the rear wheel forming stagnation points on the corresponding sides. The streamlines branching from these stagnation points meet at a separation point near the centerline of the wheel. On the ground side, the separating streamline forms a vortex roll-up residing persistently near the fore wheel on the ground side. There is no PIV data available for the second mean flow. Nonetheless, it was reported (Ref. 2) that the second mean flow contains a vortex near the rear wheel under the location where the shear layer from the fore wheel impinges on the rear wheel.

In general the NTS results have captured the features of the first mean flow observed in the experiment (Figure 4d). There are only some minor discrepancies in the position of the separation points, the attachment points and the vortex core, and the level of the highest velocity is lower especially on the rear wheel. The NLR results capture the features of the first mean flow only on the wing side (Figure 4c), whereas the resulting mean flow does not contain the stagnation point

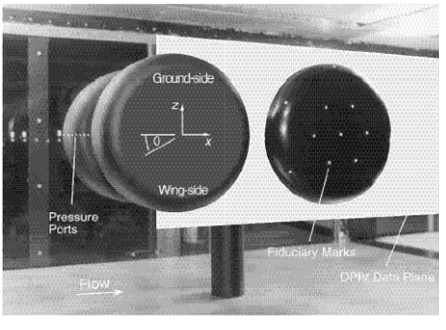

(a) Wind-tunnel and PIV plane setup

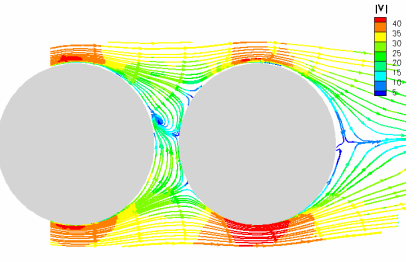

(b) Experiment

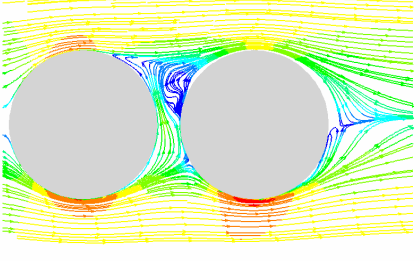

(c) X-LES (NLR)

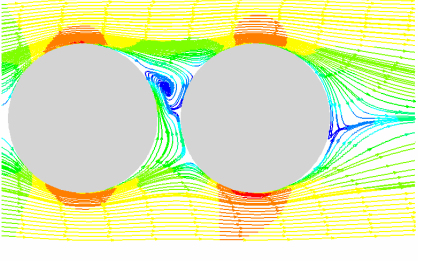

(d) SA-DDES (NTS)

Fig. 4 Pattern of the streamlines on the PIV plane (coloured by the velocity magnitude)

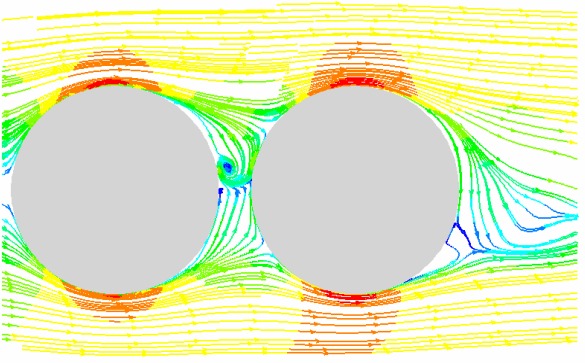

X-LES (NLR)

Fig. 5 Pattern of the streamlines observed shortly during the transient

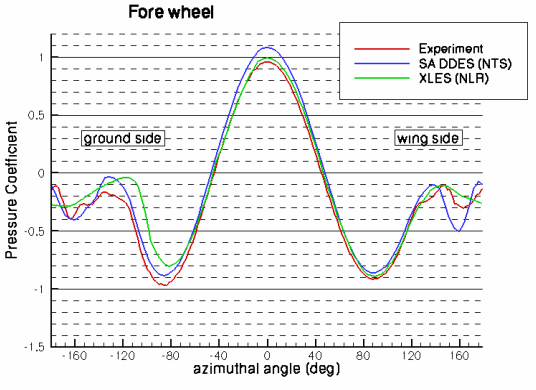

(a)

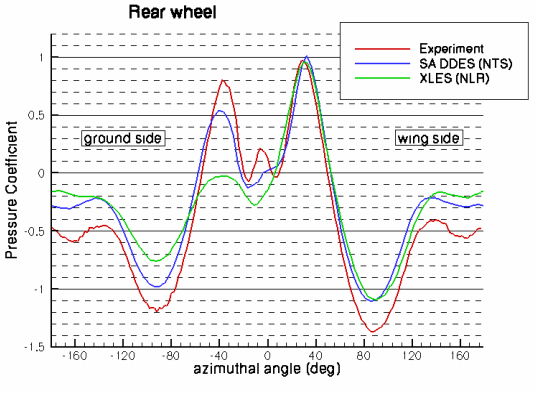

(b)

Fig. 6 Sectional pressure coefficient distribution on mid-plane of fore and rear wheels

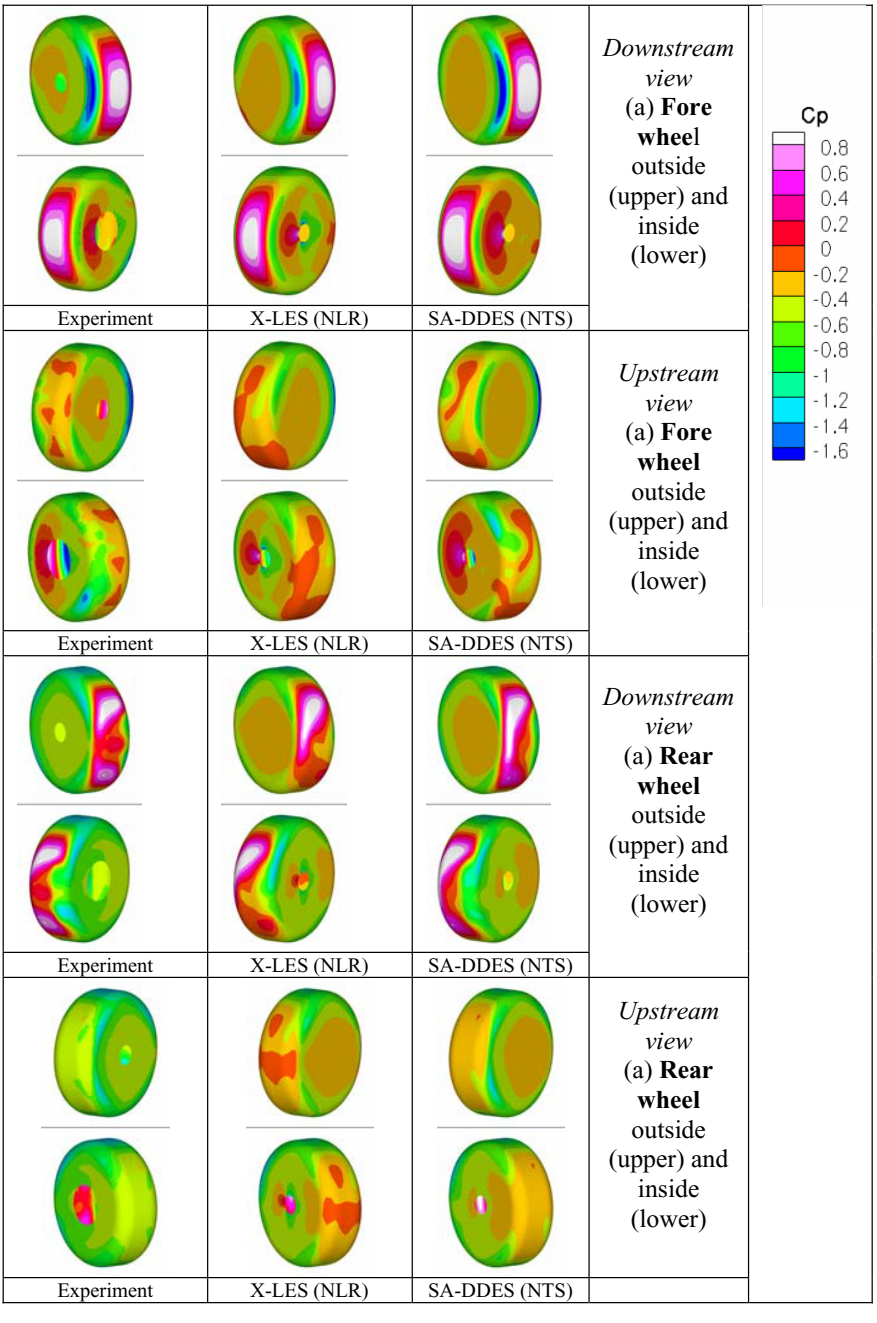

Fig. 7 Surface pressure coefficient distribution on the fore and rear wheels (upper: wing side, lower: ground side)

on the ground side of the rear wheel. Possibly, the NLR results are more consistent with the second mean flow, since on the ground side, a massive separation is indicated behind the fore wheel, and there is a vortical region residing in an area in front of the rear wheel. A similar mean flow was also reported in Ref. 3 where the flow in a DES simulation impinges only on the wing side.

It should be mentioned that in the NLR results, a flow feature is observed for a short period (about 1 convective time unit) during the transient (i.e. at around 10^{th} convective time unit) which closely resembles the first (more persistent) mean flow of the experiment in the area between the wheels, shown in Figure 5. This flow feature, however, does not materialize into a stable vortex roll-up. A possible explanation for this situation is that it is formed during the transient when disturbances are still large. Such disturbances may have induced an adverse pressure gradient on the ground side of the fore wheel, which may have implied a (premature) flow separation above the vortex roll-up. This flow separation makes the vortex unstable. Indeed, the vortex migrates progressively upwards exiting the region between the wheels, after which the flow becomes like the one shown in Figure 4c.

Figure 6 shows the mean pressure coefficient (Cp) on the intersection between the PIV-plane and the wheel surface. In general the NTS mean flow agrees with the mean flow features of the experiment, apart from discrepancies on the suction peaks and stagnation point pressures, and differences on the locations of the separation and attachment points. As the vortex roll-up is missing, the NLR results do not exhibit the wavy pressure distribution on the fore wheel near the centerline (azimuthal angle of around 180 and -180 deg.), see Figure 6a. The absence of the attachment point on the ground side of the rear wheel (near -40 deg.) in the NLR results is clearly reflected in Figure 6b. On the wing side of the rear wheel, the suction peak in the NTS and NLR results agrees closely, but there is a larger discrepancy with the experiment. In both NLR and NTS results, the flow leaves the rear wheel at about the same pressure level but at a considerably higher level than occurring in the experiment.

Figure 7 presents the pressure coefficient distribution on the wheel surface. Remarkable agreements are shown on the whole front side of the fore wheel and on the front-ground side of the rear wheel. Larger discrepancies with the experiment are shown on the back side (upstream view) of the wheels.

20.4 Conclusions

The flow around a simplified landing gear configuration has been computed using SA-DDES (NTS) and X-LES (NLR) on a moderate grid size of 2 – 3 millions cells. The flow on the ground side behind the fore wheel appears to strongly determine the mean flow features between the wheels and around the rear wheel. On the ground side, NTS results contain a vortex roll-up residing near the fore wheel and the attachment point on the rear wheel. NLR results indicate a susceptibility of the flow to a premature separation during the transient that leads to an unstable vortex roll-up.

V Technical, Partner-Related Reports – Methods, Models and Applications Performed

This chapter contains – partner by partner, in alphabetical order - brief descriptions of methods and tools used as well as highlights of work performed in and for the DESider project.

1 Contribution of Alenia Aeronautica: Main Results Obtained within the Project

N. Ceresola

Abstract. In this chapter the main outcomes of the activity made by Alenia in the framework of DESider project are outlined. The main technical achievements that have been obtained are:

1. Implementation in the company's CFD code UNS3D of a DES model;
2. verification of the consistency of the model using fundamental test cases;
3. application to more complex test cases as a necessary step toward the simulation of real-life problems.

1.1 Description of Numerical Techniques and Turbulence Models Implemented in Code UNS3D

1.1.1 The Code UNS3D

The computations have been performed using the code UNS3D. The solution algorithm is based on a finite volume, node centred approach operating on an hybrid unstructured grid. The artificial dissipation model is derived from the nonlinear scheme of Jameson, with no eigenvalue blending.

The Navier-Stokes equations are integrated in time with a second order backward difference and dual time stepping. A five stage Runge-Kutta scheme is used to drive toward zero the residual at each time step. With the use of residual averaging, a local CFL number of 4.9 could be employed in the multistage sub iteration process.

The Weiss and Smith version of low Mach number preconditioning is implemented in the code. A sensor depending on cell Reynolds number was also introduced to avoid applying the preconditioning inside boundary layers. For the computation of the present test case, its application was found to be beneficial in order to reduce numerical dissipation and enhance convergence in low-Mach number pockets.

W. Haase et al. (Eds.): DESider – A Euro. Effort on Hyb. RANS-LES, NNFM 103, pp. 309–431.
springerlink.com

1.1.2 URANS Turbulence Model

A k-ω turbulence model was employed, that has been developed by Hellsten3. The model constants have been calibrated requiring consistent behaviour near boundaries between turbulent and laminar flow, inside shear flows and for zero pressure gradient wall flows. In particular, the calibration have been considered taking into account a variable cμ , as it is the case if an algebraic stress model (EARSM) is included.

The Wallin-Johansson Explicit Algebraic Stress Model4 (WJ-EARSM) is implemented using Hellsten's k-ω as the basis RANS model. The model is an exact solution of the corresponding ARSM in two-dimensional mean flow. In three dimensions there still is a complete, while approximate, solution.

The full anisotropic version of the model is used, i.e. the anisotropic part of the Reynolds stress tensor is directly introduced in the momentum equations, while the isotropic part is taken into account in the form of an effective variable cμ..

1.1.3 DES Turbulence Model

The DES methodology essentially consist into using the k-ω-EARSM model as a subgrid scale model for LES in the regions where the grid resolution is sufficiently fine[5]. The DES length scale is therefore defined to be the minimum between the characteristic URANS length scale and a length related to the local grid, times an appropriate scaling coefficient:

$$l_{DES} = \min\{l_{RANS}, l_{LES}\} \tag{1}$$

where

$$l_{RANS} = k^{1/2}/(C_\mu \omega) \qquad\qquad l_{LES} = C_{DES}\Delta$$

and Δ can be the maximum distance between a cell vertex and the surrounding ones, $\Delta_i = \max_j\{l_{ij}\}$. In the case where very high aspect ratio cells are present in the LES region, it may be better to take the square root of the maximum surface between the cell faces, $\Delta_i = \sqrt{\max_j\{S_{ij}\}}$. C_{DES} is an adjustable constant, depending on the RANS model used and on its particular numerical implementation. In the present case, C_{DES} is derived analytically imposing identity between the eddy viscosities given by the present SGS model and the Smagorinsky model in equilibrium ($P^k = D^k$, $P^\omega = D^\omega$) conditions. It is given by

$$C_{DES} = \frac{C_{SMAG}\left\{F\left(\frac{\gamma_1}{\beta_1 c_\mu}\right)^{0.75} + (1-F)\left(\frac{\gamma_2}{\beta_2 c_\mu}\right)^{0.75}\right\}}{1-F} \tag{2}$$

where C_{SMAG} is the Smagorinsky constant, γ_1, γ_2 are k-ω constants and F is the Menter blending function, to be used as a "shield" to prevent the LES model switching on inside boundary layers.

The switch between RANS and LES was implemented expressing the kinetic energy dissipation in the k-equation in the following form:

$$\varepsilon = \rho k^{3/2} / \min\{l_{RANS}, l_{LES}\} \tag{3}$$

The modified length scale is also employed in the constitutive relations, to obtain the time scale τ used in the computation of eddy viscosity and also to normalize the vorticity and strain rate tensors. The eddy viscosity is

$$\mu = c_\mu \rho k \tau \tag{4}$$

where c_μ is given by the EARSM model and is a function of the scalar invariants of $\tau S_{ij}, \tau \Omega_{ij}$, and

$$\tau = \frac{\min(l_{RANS}, l_{DES})}{k^{\frac{1}{2}}} \tag{5}$$

It is worth noting that by this formulation, in LES regions the SGS model reduces effectively to a one-equation model.

1.2 Decay of Isotropic, Homogeneous Turbulence

The test case was computed using the SPTU method for initialising the flow field. The subgrid turbulence field initialisation was performed by computation with the model to be calibrated with frozen velocity field.

The DES constant used was C_{DES}=0.84, corresponding to C_{SMAG}=0.24 in equation (2). As a density-based code was used, compressible flow at Mach=0.05 was assumed. Low Mach number preconditioning and matrix dissipation were used for the computations. The geometry was a cube with 32^3 cells.

In Fig. 1 the computed energy spectra respectively at t=0.74 and t=200 is shown, in comparison with the experiment of Comte-Bellot and Corrsin.

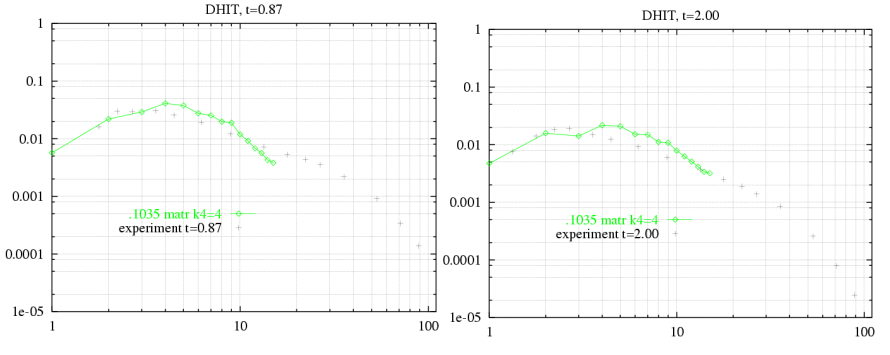

Fig. 1 Energy spectra at t=0.87 and t=2.00

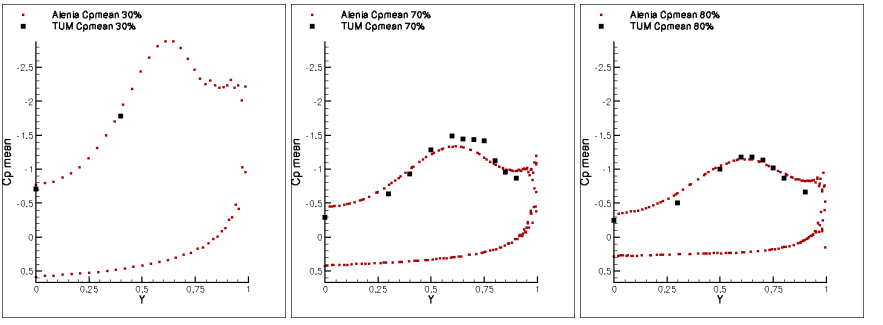

Fig. 2 Computed vs .experiment, Cp at x/c=0.3,0.7,0.8

1.3 TC 02, Delta Wing at High Incidence

Alenia generated an unstructured, hybrid grid with a relatively small number of points (5.84 10^5), that was flow adapted with point enrichment in the regions of vortex core and vortex sheet.

At α=35°, satisfactory results have been obtained in terms of mean pressure distributions: the location of vortex breakdown was also satisfactorily predicted (see Fig.2)

Concerning the fluctuating quantities, acceptable surface rms pressure distributions have been predicted up to x/c=0.7, but by far too high levels of pressure fluctuations were predicted toward the trailing edge, as shown in Fig.3.

The different fluctuating components predicted by the participants seemed not to have a relevant influence on the respectively computed mean values. The grid resolution in the vortex core appears to be the most relevant issue to be concerned.

1.4 TC E2 – Oscillating NACA0012 Airfoil

An automated grid refinement process was used during grid generation, using steady RANS computations at 15 and 20 degrees of incidence to compute the

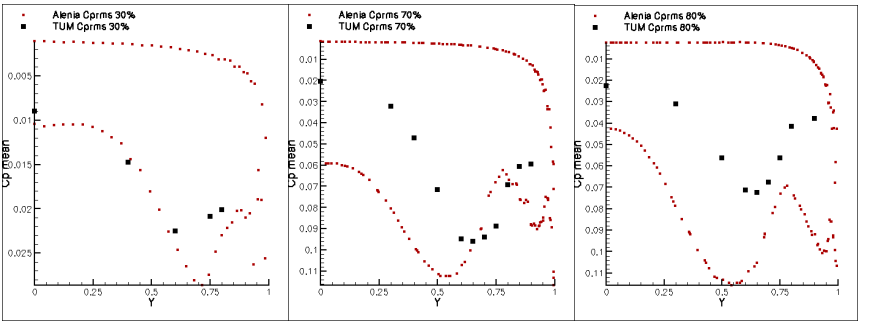

Fig. 3 Computed vs. experiment, Cp_{rms} at x/c=0.3,0.7,0.8

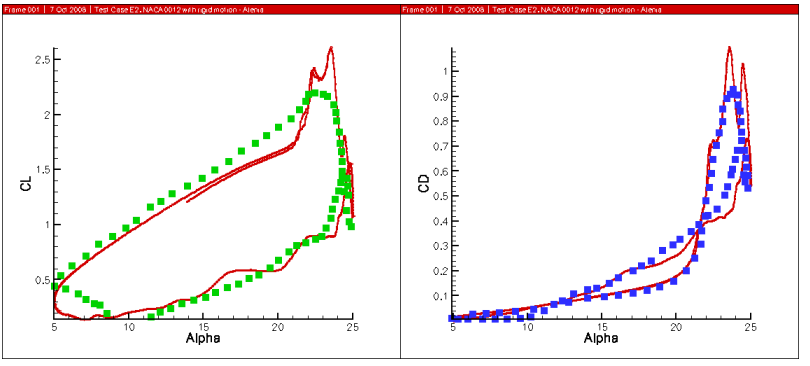

Fig. 4 Computed (solid) vs. experiment, lift and drag vs. angle of incidence during an oscillation cycle

adaptation sensor. The sensor, which is described in Flomania deliverable D5.2-27, is based on a function representing the local dissipation of energy. The final grid is made of 13390 points.

The 3D computational domain was defined to have a span of one chord length. The corresponding grid is made of 21 equally spaced 2D slices, for a total of 267800 mesh points.

The time histories of lift coefficient are shown in Fig. , in comparison with experimental data. The incidence at which Clmax occurs is well predicted as in general the lift history during most of the cycle. On the contrary, the computed value of Clmax is somewhat greater than in the experiment. The reason may be found in the unsufficient grid resolution on the leeward side of the airfoil, causing a greater vortical suction to take place at maximum lift conditions. The same holds for thre history of the drag coefficient, shown in Fig.4 .

1.5 TC A1, M219 Cavity Flow

For the Navier-Stokes computations, the cavity was considered to be mounted on a flat plate and the computational domain made of a parallelepiped. A hybrid grid was generated, starting from a wall surface triangulation made of about 25000 nodes and 50000 triangles. A wall proximity grid made of 25 prismatic layers and an external grid made of tetrahedrals have then been generated. The total number of points was about 700000, forming 1010000 prisms and 765000 tetrahedrals. The computation was made at a Mach number of 0.85 and a Reynolds number of 1.37 millions based on the cavity depth. A fixed time step $\Delta t=3.61\ 10\text{-}5$ sec was used, corresponding to 1/50 of the travel time of the cavity length at free stream speed. A CFL number of 3.5 was used for the dual time stepping computation, and 100 sub iterations were required to attain a drop in residuals between 1 and 2 orders of magnitude.

A quantitative comparison with experimental data is then made at the locations of four of the pressure probes, located respectively near the front of the cavity

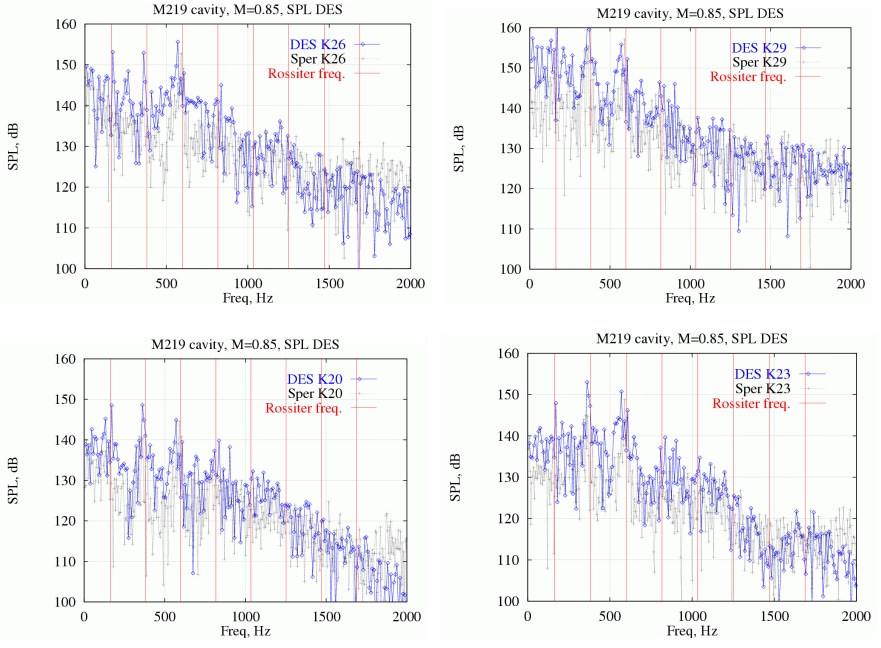

Fig. 5 SPL at four locations of cavity ceiling, DES computation vs. experiment

(K20), near its centre (K23, K26) and near the exit edge(K29). Comparison is carried out in terms of spectral analysis of the Sound Pressure Level (SPL).

In Fig.5 we can have a look at the sound pressure levels, in decibels, predicted with DES and compared with the experimental data. The vertical bars correspond to the Rossiter frequencies, as computed with the modified Rossiter formula.

The behaviour of SPL up to 1700 Hz is well predicted, and the first four resonance frequencies clearly result from the computed spectrum. At higher frequencies, an underprediction of sound levels is evidenced, possibly due to the numerical filtering made by unsufficient grid resolution.

The computation of two-dimensional sound radiation is performed on the vertical mid-plane (z=0). The convected wave equation is solved imposing as boundary conditions the fluctuating wall pressure computed with the DES simulation, along the flat plate and the cavity walls. No volume sources inside the domain, in the form of the Lighthill tensor, are taken into account. In this way the radiated acoustic field is only due to wall pressure fluctuations generated by the interaction of the vortical structures impinging on the walls.

In the present computations, the unstructured acoustic grid, composed by triangles and quadrilaterals, has about 30000 nodes, and the circular far-field boundary has a radius of 10 times the cavity depth.

The mean flow field is assumed to be composed by a uniform flow, with M=0.85, outside the cavity, and fluid at rest inside the cavity. 64 samples, equally spaced in time, for a period T=6.039 10^{-2} seconds, have been employed for describing the wall pressure fluctuations. The present amount of samples has been

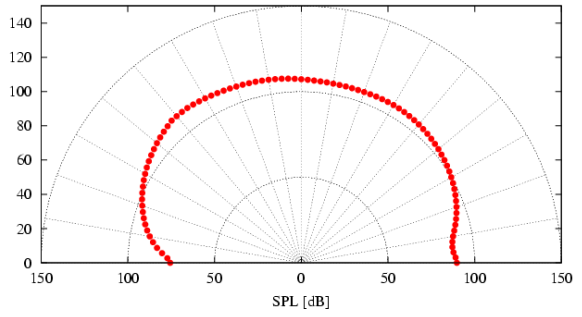

Fig. 6 Far-field sound directivity

found to correctly represent the noise radiation associated with the fundamental cavity modes.

In Fig. 6 the Sound Pressure Level, in dB, evaluated along a circle of ray 7.5D is shown. The directivity pattern is measured over the angular range of $0 \le \Theta \le 180^{\circ}$ the mean flow incoming direction corresponding to $\Theta = 0^{\circ}$. The levels range around 100 dB, with a peak radiation for Θ around 130°, showing the existence of a directivity effect of the acoustic radiation.

It can be seen in Fig.7 that the highest peaks of wall pressure fluctuations are located in proximity of the downstream cavity corner. In this location the impinging shear layer, strongly interacts with the wall. Consequently the corner acts as a strong dipole source of noise, with a well defined directivity.

Fig. 7 Instantaneous acoustic pressure field

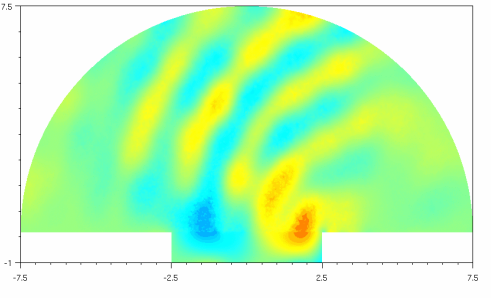

2 SAS Model Development and Validation Activity of the ANSYS Group in the DESider Project

F.R. Menter and Y. Egorov

ANSYS Germany GmbH

Abstract. This section provides a compact overview of the work done at the CFD development department of ANSYS Germany during the DESider project. Its main goals were the systematic development of a new Scale-Adaptive Simulation (SAS) turbulence modelling approach, the implementation of different SAS model variants in the commercial CFD solver ANSYS-CFX, the model validation by computing a series of the project test cases, as well as the collaboration with Project partners in testing the SST-SAS model with their own CFD solvers. The SAS model description is presented in Chapter II of this book, and the validation results can be found in the respective paragraphs of Chapter IV.

2.1 Model Development

At the beginning of the Project the SAS approach had been realised with a single-equation turbulence model. This model was based on a transport equation for the eddy viscosity [Menter, 1994], and the SAS capability of resolving a part of the turbulence spectrum was introduced in a rather phenomenological way by analysing the model behaviour with the different options for the length scale limiter, see [Menter et al., 2003]. A general systematic derivation and theoretical justification of the SAS method was undertaken via a series of the following steps:

- Critical assessment of the standard RANS models identified a main reason for the overly dissipative behaviour of these models in transient mode, when applied to flows with large separation zones. It was shown, that the model length scale was essentially an outcome of the diffusive transport of the turbulent kinetic energy through the shear layer, and must therefore correlate with the shear layer thickness.
- In order to model the length scale, which would be sensitive to the local flow instabilities, a length scale transport equation by Rotta [1972] was re-visited. It was shown by Menter [Menter, Egorov, 2004], that the second spatial derivative of the mean velocity must participate in the model source terms. The modified equation was re-formulated for $\sqrt{k}L$ as the transported variable. This equation possesses an own length scale, which is proportional to the von Karman length scale.
- The $\sqrt{k}L$ transport equation was combined with the turbulent kinetic energy transport equation to derive a new $k-\sqrt{k}L$ model. The model was calibrated using RANS arguments, including the near wall treatment. Correct RANS

functionality of the model was proven on a set of external and internal stationary flows. In transient mode the model revealed a capability of resolving turbulent fluctuations in large separation zones. With the adaptive switching to an LES-relevant non-dissipative discretisation and on the locally refined grids the new model delivered LES-like turbulence spectra. This capability resulted from the intrinsic model feature of reacting on the growing flow instabilities through the von Karman length scale.

- The $k-\sqrt{k}L$ model opened a new way for the hybrid RANS-LES simulation of complex industrial flows with the statistically stable attached regions and the transient separating flow zones. Unlike DES, this approach does not use the grid cell size information for switching to the LES mode and therefore does not suffer from the gray-zone uncertainty of DES.
- In order to benefit from the positive properties of the SST model in stable attached and mildly separated flow regions (Menter, [1993]), the $k-\sqrt{k}L$ model transport equations were analytically transformed to k and ω as the primary variables. It turned out, that the SAS capability of resolving the turbulent fluctuations was provided by an additional source term in the ω transport equation. This source term included the von Karman length scale and is automatically activated by transient flow instabilities outside the wall-attached region. The resulting SST-SAS model [Menter, Egorov, 2005a] combined the SAS properties with the ability to compute boundary layers, as inherited from the background SST model.
- A necessity to control the dissipative properties of the SAS models was identified in the course of implementing and testing the SST-SAS model in the CFD solvers by Project partners. A generic procedure of using the WALE-LES subgrid eddy-viscosity as a lower limit of the SAS eddy viscosity was suggested and recommended to achieve the appropriate model performance with different discretisation methods of the model source terms. During the implementation of the model in other codes, it was also found that the second derivative of the velocity field should be computed on a compact stencil (3 nodes in one-dimensional formulation)
- The SST-SAS model was implemented in a standard commercial version of the ANSYS-CFX. The $k-\sqrt{k}L$-SAS model and its single-equation $\sqrt{k}L$-SAS analogue are to be further studied and developed with a research solver version.

2.2 Model Validation

A set of the validation examples, used for the calibration and testing the SAS models in the DESider Project, included the underlying flow regimes tests:

- Decay of the isotropic turbulence
- Bump in a rectangular channel

as well as the complex flows identified as the application challenges:

- Airfoil at high incidence
- Delta wing
- Complete aircraft geometry

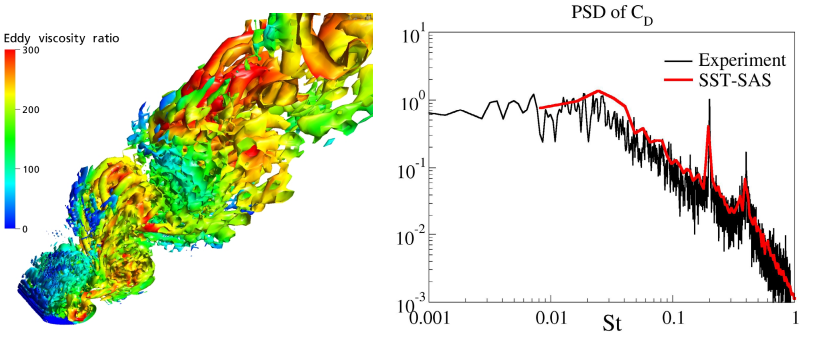

Fig. 1 NACA0021 airfoil at 60° angle of attack: left – resolved 3-D vortex structures, right – power spectral density of the drag coefficient

The last two cases address the aero-acoustic phenomena:

- Three-dimensional acoustic cavity
- Generic car mirror

Several representative results obtained using ANSYS CFX with the SST-SAS turbulence model are shown here: an airfoil beyond stall (Figure 1), complete aircraft geometry (Figures 2 and 3), three-dimensional acoustic cavity (Figure 4).

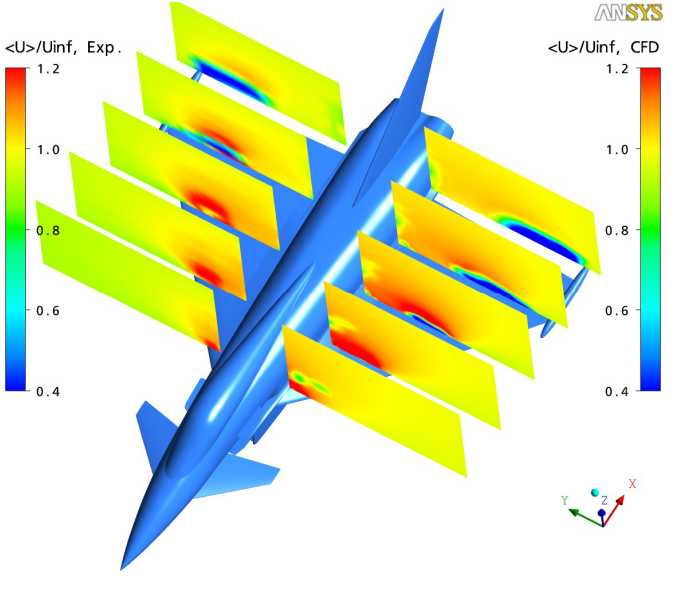

Fig. 2 Complete aircraft geometry FA5 at 15° angle of attack and Reynolds number of 2.8×106. Mean axial velocity distributions in cut planes: left – experiment, right – SST-SAS simulation using ANSYS CFX

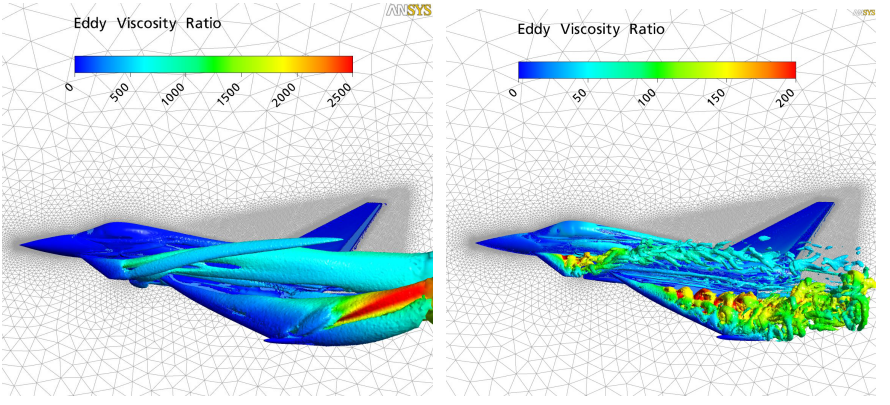

Fig. 3 Complete aircraft geometry FA5 at 15° angle of attack and Reynolds number of 2.8×106. Resolved vortex flow configuration: left – SST-URANS, right – SST-SAS

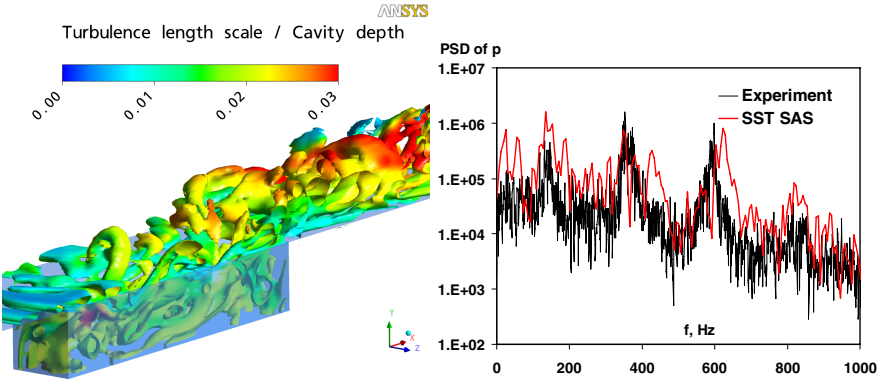

Fig. 4 3-D acoustic cavity: left – resolved turbulent structures, right – power spectral density of the transient wall pressure signal

3 Chalmers' Contribution

L. Davidson and S. Krajnović

Chalmers

Abstract. Chalmers has in the DESider project worked on fluctuating inlet boundary conditions for various flows. The SAS-SST model has been implemented and validated. Chalmers has also performed wall-resolved LES of the flow around a three-dimensional hill and a wall-mounted finite cylinder.

3.1 Inlet Boundary Conditions

A turbulent velocity field can be simulated using random Fourier modes. The velocity field is given by N random Fourier modes as

$$u'_i(x_j) = 2\sum_{n=1}^{N} \hat{u}^n \cos(\kappa_j^n x_j + \psi^n)\sigma_i^n \tag{1}$$

where $\hat{u}^n$, ψ^n and σ_i^n are the amplitude, phase and direction of Fourier mode n. The highest wave number is defined on the basis of mesh resolution $\kappa_{max} = 2\pi / (2\Delta)$. The wave number space, $\kappa_{max} - \kappa_1$, is divided into N=600 modes, equally large, of size $\Delta\kappa$. A modified von Kármán spectrum is chosen. The RMS of the inlet fluctuations is to 0.5, 1, or 2.

A fluctuating velocity field is generated each time step as described above. They are independent of each other, however, and their time correlation will thus be zero. This is unphysical. To create correlation in time, new fluctuating velocity fields are computed based on an asymmetric time filter.

$$(U'_i)^m = a(U'_i)^{m-1} + b(u'_i)^m \tag{2}$$

where m denotes the time step number and $a = \exp(-\Delta t/T)$. The time correlation of U'_i will be equal to $\exp(-\Delta t/T)$, and thus Eq. 2 is a convenient way to prescribe the turbulent time scale of the fluctuations. The inlet boundary conditions are prescribed as

$$\overline{u}_i(0, y, z, t) = U_{i,in}(y) + u'_{i,in}(y, z, t) \tag{3}$$

where $u'i,in = (U'i)^m$ and $U_{i,in}(y)$ denote the mean inlet profile.

The turbulent length scale and time scale are, except for the channel flows, $L_t = 0.1$ and $T_t = 0.05$, respectively, scaled with the boundary layer thickness and the friction velocity at the inlet.

Greater detail can be found in Davidson (2007c).

3.2 Channel Flow: Direct Numerical Simulations

The mesh has $256 \times 80 \times 64$ in the streamwise (x), wall-normal (y) and spanwise (z) directions, respectively. The size of the computational domain is $x_{max} = 8\pi$, $y_{max} = 2\delta = 2$ (geometric stretching of 12%) and $z_{max} = 0.5\pi$. Fluctuating inlet velocity boundary conditions with different time scales, length scales and amplitudes are investigated.

The velocity profile and the resolved shear stresses using inlet time scale $T_1 / 12$ and inlet length scale L_1 are shown in Fig. 1. The profiles are shown for $x = \delta$, $x = 10\delta$ and $x = 24\delta$. The velocity profiles agree very well with DNS data for both cases. The resolved shear stresses exhibit the correct linear variation at $x/\delta = 10$ and further downstream, although the profile close to the inlet ($x/\delta = 1$) is not yet fully developed. Still, the synthetic isotropic fluctuations do a remarkable job considering that the prescribed inlet shear stress is zero; they manage to trigger the equations to yield a reasonable shear stress profile even at $x = \delta$.

More results, both DNS and hybrid LES-RANS, can be found in Davidson (2007c).

3.3 3D Hill Flow

A 162x82x130 (x,y,z) mesh is used (1.7 million cells). The Reynolds number is 130 000 based on the hill height. The height of the domain is 3.2*H*. The inlet

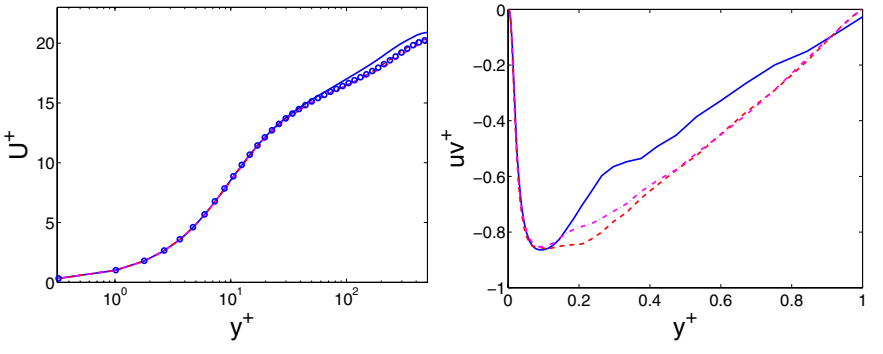

Fig. 1 Mean velocities (left) and resolved shear stresses (right). Synthesized isotropic inlet fluctuating velocities. $u_{in,rms} = v_{in,rms} = w_{in,rms} = 1.5$. Inlet time scale $T_1 / 12$ and inlet length scale L_1. $x/\delta = 1$; $x/\delta = 10$; $x/\delta = 24$

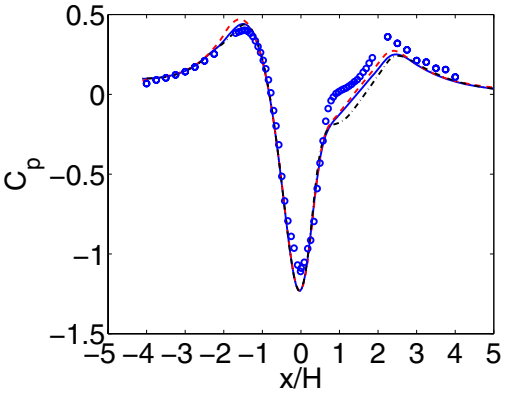

Fig. 2 3D hill: Pressure coefficient. $z = 0$. Dash-dotted line: $u_{rms,in} / u_\tau = 0.5$; solid line: $u_{rms,in} / u_\tau = 1$; dashed line: $u_{rms,in} / u_\tau = 2$; markers: experiments (Byun, Simpson, 2004)

boundary layer thickness is $\delta_{in} / H = 0.5$ at both the lower and upper wall. The grid resolutions at the inlet expressed in wall units are $\Delta x^+ = 280$ and $\Delta z^+ = 120$, which correspond to $\Delta x / \delta_{in} = 0.12$ and $\Delta z / \delta_{in} = 0.051$, respectively. The first near-wall cell centre is located at $y^+ = 1.5$. The matching line is defined along an instantaneous streamline; for more detail, see Davidson and Dahlström (2006). The time step is $9.3 \cdot 10^{-4} U_{in}/H$. This gives a maximum instantaneous CFL number of approximately 2.3 which occurs in the wall-normal direction; the maximum CFL number in the streamwise direction is approximately 0.75. Averaging was performed over approximately 30000 time steps.

Figures 2 and 3 present the surface pressure over the hill and the resolved shear stresses on the windside of the hill, respectively. As can be seen, the fluctuations in Case $2u_\tau$ seem to be too strong; an overshoot is seen in the pressure coefficient

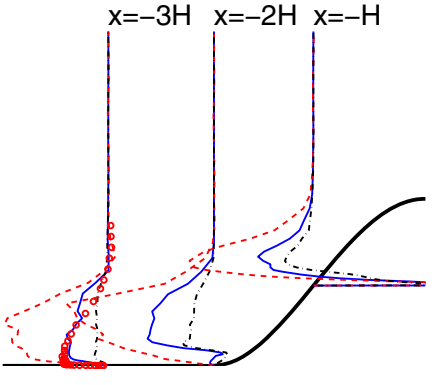

Fig. 3 3D hill: Resolved shear stresses. $z = 0$. For legend, see Fig. 2

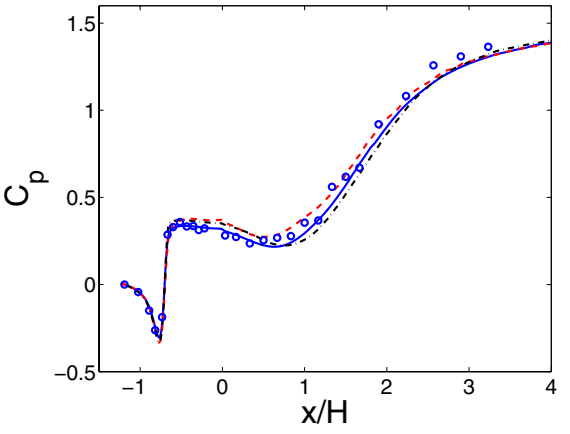

Fig. 4 Onera bump: Pressure coefficient. Lower wall. Dash-dotted line: $u_{rms,in}/u_\tau = 0.5$; solid line: $u_{rms,in}/u_\tau = 1$; dashed line: $u_{rms,in}/u_\tau = 2$; markers: experiments (Pailhas et al. 2008)

at $x/H = -1.5$ and the magnitude of the resolved shear stresses is too large. On the other hand, for Case $u_\tau/2$, the inlet fluctuations seem to be too small since only small resolved stresses are generated at $x/H = -3$. No difference is seen in the pressure coefficient between cases $u_\tau/2$ and u_τ. A small recirculation bubble is also formed at the foot ($x/H \simeq$-2) of the hill for Case $u_\tau/2$, which is not the case the other two cases.

More results for the flow around a three-dimensional hill as well for the asymmetric diffuser can be found in Davidson (2007a, b).

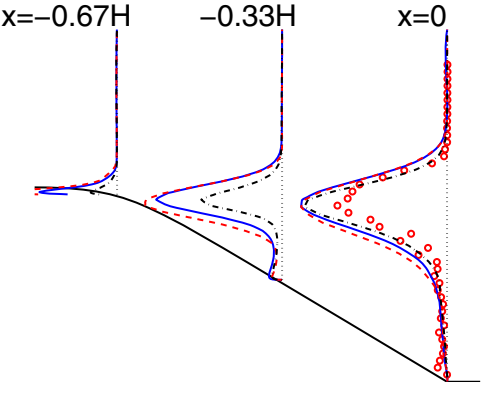

Fig. 5 Onera bump: Resolved shear stresses. For legend, see Fig. 4

3.4 Onera Bump

Measurements were carried out by ONERA in the DESider project (Pailhas et al. 2008). $Re_h = 0.93 \cdot 10^6$ based on the bump height, h. The simulations were carried out using only a slice in the central region and periodic boundary conditions in the spanwise direction. The extent of the domain in the spanwise direction is $-0.61/2 \le z/H \le 0.61/2$ and total length in the streamwise direction is $L/H = 8.86$. 32 cells are used in the z -direction and the grid in the x-y plane has 224x120 cells. The matching plane between LES and URANS is prescribed along fixed grid planes; the URANS region near the upper and the lower walls extends 12 wall-adjacent cells. The mean inlet boundary conditions are taken from URANS simulations of the entire bump using a zonal version of the Reynolds stress $-\omega$ model (Kuntz et al 2004); in the slice region the results of the URANS simulations match the experimental data.

The time step is $4.2 \cdot 10^{-4} s = 5.0 \cdot 10^{-3} U_b / H$ where U_b denotes the bulk velocity downstream of the bump. This gives a maximum instantaneous CFL number of approximately 2.3, which occurs in the wall-normal direction; the maximum CFL number in the streamwise direction is approximately 0.75. Averaging was performed over more than 30000 time steps and, of course, in the spanwise direction.

The grid is very coarse, expressed in both inner and outer scaling. This makes it a very demanding test case. Note, however, that this kind of resolution is relevant from an industrial point of view.

Figure 4 shows the pressure coefficient along the lower wall. As can be seen, the agreement with the experimental pressure coefficient is good for all three cases, at least up to $x/H = 2$. Further downstream, the pressure coefficients show that the experimental flow recovers faster than the predicted flow.

In Fig. 5 it can be seen that, for Case $u_\tau/2$, only very small resolved fluctuations are created for $x/H \le -0.67$. The peak is approximately 40% of that for Case u_τ. The peak for Case $2u_\tau$ is 50% larger than that for Case u_τ. For Case $u_\tau/2$ the resolved fluctuations are still too small at $x/H = -0.33$.

More results can be found in Davidson (2007a) and in Davidson (2007b) simulations of the full duct (not only a slice) are presented.

3.5 The SAS Model

The SAS model (Scale Adapted Simulation) was invented by Menter and co-workers (Menter et al 2003, 2004, 2005). The idea behind the SST-SAS k-ω model is to add an additional production term — the SAS term — in the ω equation, which is sensitive to resolved (i.e. unsteady) fluctuations. When the flow equations resolve turbulence, the length scale based on velocity gradients is much smaller than that based on time-averaged velocity gradients. Hence the von

Kármán length scale, L_{vK}, is an appropriate quantity to use as a sensor for detecting unsteadiness. In regions where the flow is on the limit of going unsteady, the objective of the SAS term is to increase ω. The result is that k and ν_t are reduced so that the modelled dissipation (i.e. the damping effect) of the turbulent viscosity on the resolved fluctuations is reduced, thereby promoting the momentum equations to switch from steady to unsteady mode.

The SST-SAS model and the standard SST-URANS are evaluated for developing channel flow. Unsteady inlet boundary conditions are prescribed in all cases by superimposing turbulent fluctuations on a steady inlet boundary velocity profile.

3.6 The Turbulence Model

The additional source term in the ω equation in the SST-SAS turbulence model reads

$$P_{SAS} = \tilde{\zeta}_2 \kappa \frac{L}{L_{vK,3D}}, \quad L_{vK,3D} = \kappa \frac{S}{U''}, \tag{4}$$

where S and U'' are generic first and second velocity derivatives, respectively.

The source term, P_{SAS}, includes the von Kármán length scale. This is interesting because the von Kármán length scale decreases when the momentum equations resolve (part of) the turbulence. When making unsteady simulations, the momentum equations are triggered through instabilities to go unsteady in regions where the grid is fine enough. With traditional turbulence models, high turbulent viscosity dampens out these instabilities. In many cases this is an undesired feature, because, if the flow wants to go unsteady, it is usually a bad idea to force the equations to stay steady. One reason is that there may not be any steady solution. Hence, the equations will not converge. Another reason is that, if the numerical solution wants to go unsteady, the large turbulent scales will be resolved instead of being modelled. This leads to a more accurate prediction of the flow.

The SAS term in Eq. 4 acts as follows: in regions of fine grid, resolved unsteadiness will appear. This gives a small $L_{vK,3D}$ and hence - through P_{SAS} - a large ω which gives a reduced k and ν_t and a reduced modelled dissipation, ε_M. Hence the resolved unsteadiness is not dampened, but instead part of the turbulence is resolved. This gives an increased accuracy since a smaller part of the turbulence is modelled.

In traditional turbulence models the opposite happens: when in regions of fine grid, resolved unsteadiness appears, the production term P_k increases which results in an increased turbulent viscosity. The resolved unsteadiness is dampened and the result is a reduced accuracy. Also, as mentioned above, perhaps no converged solution will be obtained at all.

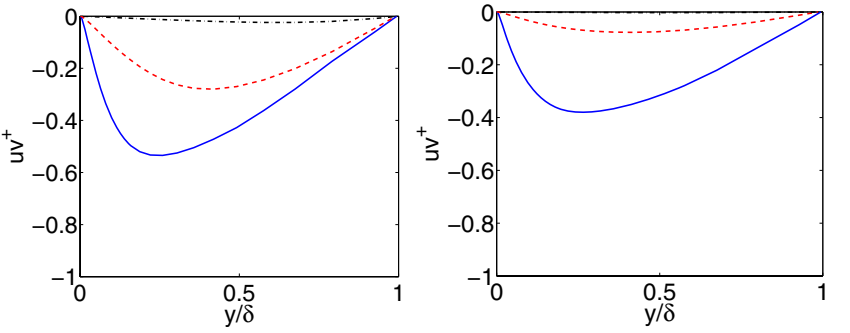

Fig. 6 Resolved shear stresses. Left: SAS; right: URANS. $x/\delta = 3.33$; $x/\delta = 23$; $x/\delta = 97$

3.7 Channel Flow

A 256x64x32 node mesh (*x*, streamwise; *y*, wall-normal; *z*, spanwise) was used. The size of the computational domain is $x_{max} = 100$, $y_{max} = 2$ (geometric stretching of 17%) and $z_{max} = 6.28$. The Reynolds number is $Re_\tau = u_\tau \delta / \nu = 2000$.

The results using the standard SST-URANS model and the SST-SAS model are presented. Figure 6 shows the predicted resolved Reynolds shear stresses. As can be seen, the stresses predicted by the SST-SAS model decay at a slower rate than those predicted by the SST-URANS model. The reason is that the turbulent viscosity is smaller with the SST-SAS model than with the SST-URANS model (Fig. 7), which makes the dissipation of the resolved fluctuations smaller with the former model. It can be noted that, at the end of the channel ($x/\delta = 97$), the turbulent viscosity obtained with the SST-URANS model is equal to the turbulent viscosity predicted in a one-dimensional channel using the SST-URANS model (see Fig. 7b) and that the resolved stresses are zero. Hence, the flow has returned to fully steady conditions.

The SAS model and more results can be found in Davidson (2006).

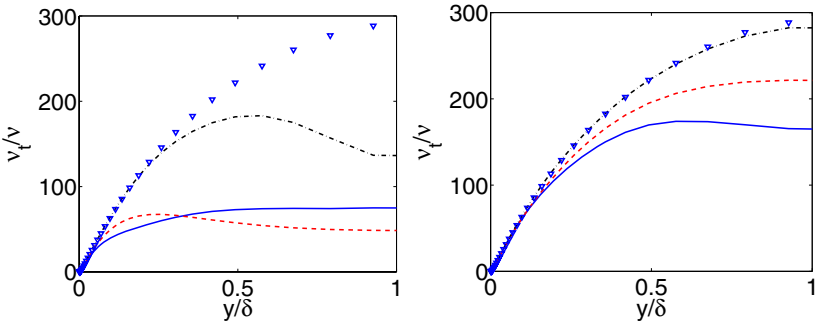

Fig. 7 Turbulent viscosity. Left: SAS; right: URANS. $x/\delta = 3.33$; $x/\delta = 23$; $x/\delta = 97$; from a 1D simulation with the SST model

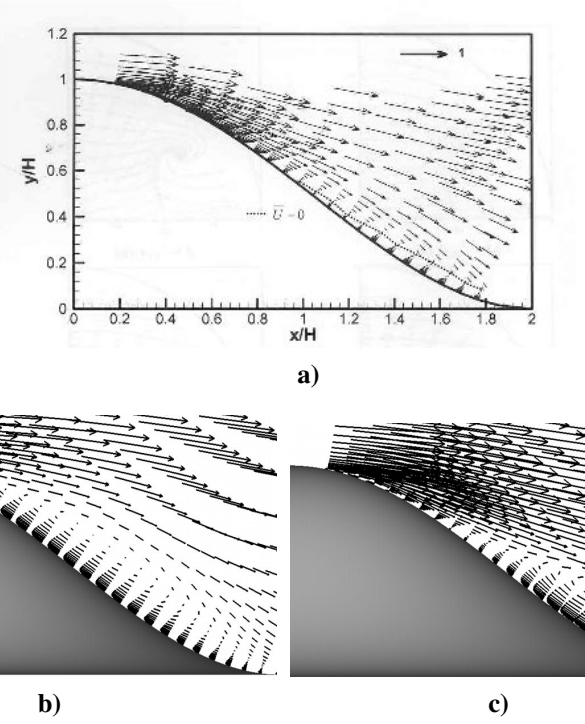

Fig. 8 Velocity vectors in the plane $z = 0$; a) LDV results by Byun and Simpson (2004), b) LES using coarse grid; b) LES using fine grid. Note that all three figures show the same part of the flow

3.8 LES of the Flow around a 3D Hill

Two simulations using two orthogonal grids are conducted. They contain $256 \times 96 \times 192$ and $256 \times 147 \times 387$ cells in the $x \times y \times z$ directions, respectively. Such grids resulted in a resolution in the spanwise direction of $\Delta z^+ \approx 200$ and $\Delta z^+ \approx 100$ at the inlet for the coarse-grid and the fine-grid LES, respectively. At the hill top the resolution was approximately $140 \le \Delta z^+ \le 250$ and $70 \le \Delta z^+ \le 130$ for the coarse-grid and the fine-grid LES, respectively. The distance of the first node from the wall in the wall-normal direction is $y^+ < 0.5$ in all simulations. The wall-normal grid curves are made orthonormal onto the wall of the hill and the bottom and the top walls of the channel. A time step of $\Delta t U_{ref} / H = 0.0038$ is used, resulting in a maximum Courant (CFL) number of around 2. The CFL number was larger than 1 in less than 200 cells during the entire simulations. The averaging time, tU_{ref} / H, in

the simulations is 103.8 ($27{,}000$ time steps) corresponding to approximately 8 flow-through times.

The LES use the Smagorinsky sub-grid scale model with the van Driest damping function and the constant of $C_S = 0.1$. LES equations are discretized using a 3D finite volume method for solving the incompressible Navier-Stokes equations using a collocated grid arrangement. Both convective and viscous plus sub-grid fluxes are approximated by central differences of second-order accuracy. Time integration is done using the second-order Crank-Nicolson scheme.

Results of LDV investigations of the flow above the hill were reported by Byun and Simpson (2004). Their resulting velocity vectors in plane $z/H = 0$ above the leeward side of the hill are shown in Fig. 8. The flow accelerates on the top and decelerates close to the bottom of the hill, producing a separation at $x/H = 0.96$. This is later than any of the LES produces. The coarse-grid simulation is completely incapable of resolving the upstream boundary layer, thereby producing too early a separation at the position directly after the top of the hill ($x/H = 0$). Although the fine-grid LES produces a noticeable improvement with the separation at approximately $x/H = 0.8$ it is still too early and the separation bubble is much thicker than the experimental one. One important observation is that the change of these structures between the two LES with steady and unsteady inlet boundary condition was negligible.

A comparison of the surface pressure coefficient, C_p, along the centre line of the channel floor and the hill is presented in Fig.9. The differences between the results from two LES with the fine grid are small, and only results from the simulation using transient inlet boundary condition are plotted in this figure. Both the coarse and the fine-grid LES predict the C_p in good agreement with the experimental data up to approximately $x/H = -2$. At this position the surface pressure is over-predicted in all LES to return to the experimental profile at the position slightly downstream. From this position and downstream, the C_p from the fine-grid LES follows the experimental curve all the way to the position at approximately $x/H = 0.8$, i.e. the approximate position of the separation of the flow on

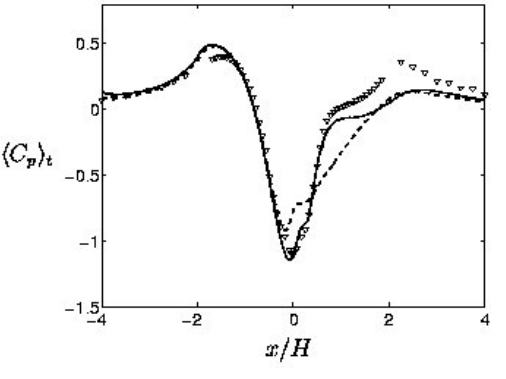

Fig. 9 Comparison of C_p along the line on the floor and plane $z/H = 0$: Solid line: LES with fine grid and transient inlet boundary conditions; dashed line: LES with coarse grid; markers: Experiments by Byun and Simpson (2004)

the leeward side of the hill found in the experiment. Downstream of the position *x/H*=0.8 the surface pressure coefficient in the fine-grid LES is under-predicted the entire distance to *x/H*=4 for which the experimental data are available.

More results from the LES around 3D hill can be found in Krajnović (2007a).

3.9 LES of the Flow over a Finite Cylinder

Two multi-block hexahedral meshes were used in our simulations. A grid topology was made using several *O* and *C* grids in order to concentrate most of the computational cells close to the cylinder. The large number of cells close to the surface is needed in order to resolve laminar boundary layer on the front part of the cylinder. Computational meshes contained approximately 7 and 14 million computational cells. The maximum CFL number was smaller then one for all time steps.

Our LES simulations used the Smagorinsky sub-grid scale model with van Driest damping function and the Smagorinsky constant of $C_S = 0.1$. LES equations are discretized using a 3D finite volume method for solving the incompressible Navier-Stokes equations using a collocated grid arrangement. Both convective and viscous plus sub-grid fluxes are approximated by a blend of 99.7% central differences of second-order accuracy and 0.3% of upwind differences. The time integration is done using the second-order Crank-Nicolson scheme.

The first impression of the resulting LES flow is that it contains wide spectrum of the length and the time scales. As the flow separates along the lateral sides of the cylinder, a large number of small-scale Kelvin-Helmholtz-like vortices (Fig. 10) is formed. These vortices are the result of the roll-up of the transition waves into the discrete eddies along the shear layer before becoming turbulent. Their origin indicates the separation line which is inclined in the streamwise direction as we move towards the free end of the cylinder. Another fully turbulent Kelvin-Helmholtz-like vortices are formed after the separation over the free end of the

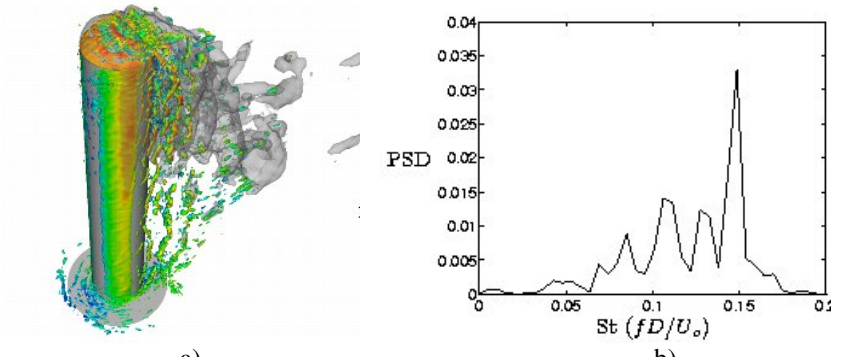

Fig. 10 a) Instantaneous flow from LES. An iso-surface of the second invariant of the velocity gradient Q=7000 coloured with the streamwise velocity and an iso-surface of low static pressure (grey). b) Power spectral density (PSD) distribution of the side force component signal

cylinder. As these vortices move downstream they form hairpin vortices and ones they reach the rear of the free end surface they decline and interact with the vortices coming from the lateral sides. This is only one of the flow mechanisms in this complex flow.

Experimental investigation by Park and Lee (2002) has revelled a vortex shedding frequency at 47 Hz corresponding to dimensionless frequency of St=0.141 (for inlet velocity of 10 m/s). We have here monitored the side force in time and used its time history to compute the power spectral density shown in Fig. 10b. The results shown in this figure are from the simulation using fine computational grid. Similar to the results of our colleges within the DESIDER project and their LES (Aftgan et. al., 2006) and DES (Streelets, 2005), our simulation using coarse computational grid resulted in a flow without any dominant frequency. However, as seen in Fig. 10b the spatial and temporal refinement in the resolution with the fine grid resulted in a very clear vortex shedding frequency at St=0.148 which is in a good agreement with the value found by Park and Lee (2002).

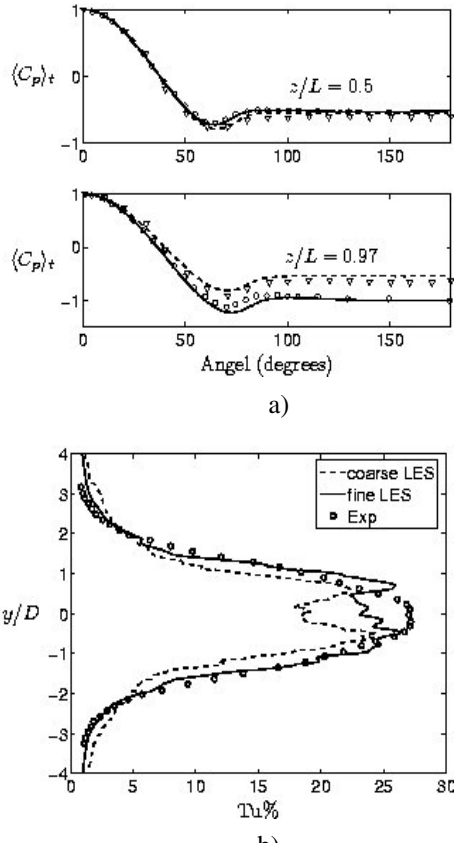

Fig. 11 a) Surface pressure coefficient at two z locations. Solid line: fine-grid LES; dashed line: coarse-grid LES; Triangles: Experiments by Park and Lee (2002); Circles: Experiments by Luo et. al. (1999). b) Turbulence intensity in the streamwise direction at position z/L=0.5 and x/D=5. Solid line: fine-grid LES; dashed line: coarse-grid LES; symbols: Experiments by Park and Lee (2002)

The time-averaged results from our LES were compared with the existing experimental data (Park and Lee (2002) and Luo *et. al.* (1999)) at several different positions in the domain. Due to the space constraints we shall present only selection of the results here.

Surface pressure coefficients at two positions along the cylinder are compared with the experimental data from both (Park and Lee, 2002) and (Luo *et. al.,* 1999) in Fig. 11a. Note that the reference pressure is chosen to produce Cp=1 at angle=0 at all positions z/L.

Streamwise turbulence intensity at the position z/L=0.5 and x/D=5 for which the experimental data exist is presented in Fig. 11b. Although both LES produce results in good agreement with the experimental data the grid refinement improves the agreement. However, both our LES as well as previous DES and LES results have a dip around the position y/L=0 which is different from the experimental data.

Additional results and discussion on our LES of flow over cylinder are available in Krajnović (2007b).

4 Contribution of Dassault to DESider

G. Petit and M. Mallet

Dassault Aviation

Abstract. The purpose of the work performed within this subtask is to develop or improve *DES*-capabilities based both on the *SST* two-layer k-ε model used everyday as a reference model at Dassault Aviation and the standard Spalart-Allmaras one equation model.

Our experience is that two-layer k-ε model is well-suited for most of our applications, and gives good predictions of the location and the size of separated area when tuned correctly. Thus, in addition to the *DES* based on the Spalart-Allmaras model, the capability to rely on a *DES* based on this model is a real improvement for design processes.

The code under consideration is our in-house code *AeTher*, whose numeric was shown to be able to capture *LES* features (see e.g. Marquez (1999), or work performed more recently by Levasseur (2007). The numerical method used is therefore well suited for *DES* applications.

4.1 Introduction

Work performed before the beginning of the DESider project shown both the ability of the in-house finite element *Navier-Stokes* solver *AeTher* to rely with turbulent unsteady features and that *DES* modelization based on Spalart-Allmaras was well adapted for flow fields with complex spectra like cavity ones.

Work performed within this project therefore aims at:

- implement and validate *DE*S method based on *SST* two-layer k-ε model to increase design process coherence
- increase the fields of application of *DES* methods in implementing well suited wall proximity treatment to make sure boundary layer is effectively treated in *RANS* mode and to preserve computations from *GIS* (Grid Induced Separation).

The validation process is presented as follow:

- presentation of unsteady features of the solver and the ability of implemented *DES* modelizations to perform with generic *DIHT* test case.
- implementation and validation of wall "blending functions" for both Spalart-Allmaras and *SST* two-layer k-ε based DES on generic flat plate & generic S-Duct test cases.
- application to aero-acoustics

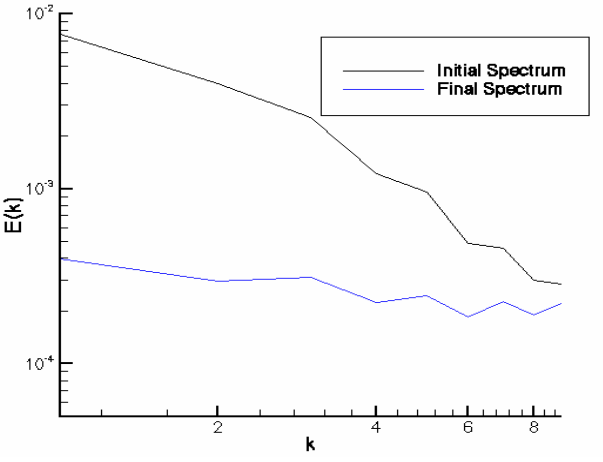

Fig. 1 Initial & Final spectrum of kinetic energy on 51^3 *DHIT* case

4.2 Presentation of Navier-Stokes Solver

AeTher solver relies on a semi-discrete Galerkin/Least-Square formulation of the symmetrized compressible *Navier-Stokes* equations (symmetrization enabled by the use of entropy variables). Time-integration is carried out using an implicit second-order backward difference scheme and piecewise linear elements are used for space discretization. Convergence of each time step is obtained by Dual Time Stepping (DTS) and solved by using the Generalized Minimal RESidual (GMRES) algorithm. Finite element approach enables the use of unstructured grids.

4.3 Validation of Numerics on DIHT Test-Case

Numerics described above are firstly validated on generic *DHIT* test case in particular to estimate numerical dissipation due to Galerkin/Least-Square (*GLS*) formulation. Numerical dissipation will effectively add itself to physical subgrid viscosity introduced in *LES* or *DES* features. We thus have to compute *DHIT* in "*Implicit LES*" mode to conclude on numerical viscosity level. Tests are done on 51^3 *DHIT* with no subgrid scheme, see Figure 1.

Without subgrid model, if the numerics are transparent in term of dissipation, computation of *DHIT* shows a k^2 slope of energy spectrum and a conservation of kinetic energy.

Figure 2 shows that Galerkin/Least-square formulation used in AeTher solver acts like a numerical dissipation implying a loss in kinetic energy during time of the simulation. Enstrophy is growing in the beginning of the calculation filling the spectrum until a final almost constant k^0 slope.

Galerkin/Least-square while acting as a real dissipation may not be considered as a relevant subgrid model for turbulent unsteady problem.

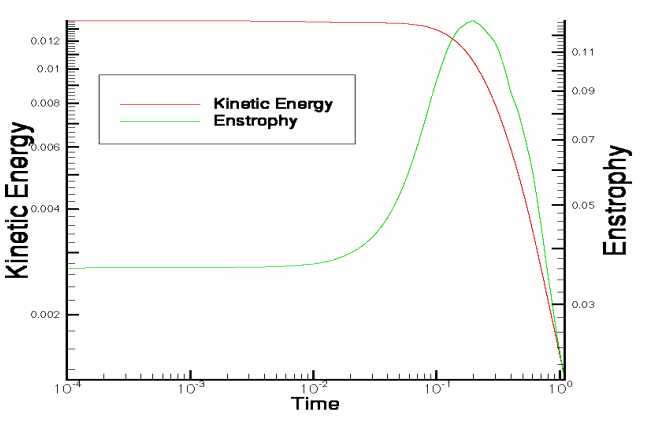

Fig. 2 Evolution of enstrophy & Kinetic energy during the computation

4.4 Implementation and Validation of DES Modelisation

4.4.1 Spalart-Allmaras Based DES

Academic Spalart based DES noticed now as "DES 97" has firstly being implemented in the *Navier-Stokes* solver Aether. The destruction term in the modified viscosity equation lead the behaviour of the model from *RANS* to *LES* mode. In a first attempt to prevent the model from switching to *DES* mode near the wall (ie force the model in *RANS* mode), only a minimum distance from the wall had been fixed to work in *LES* mode far from the boundary layer. Blending functions *fv* have been fixed to *0* or *1* depending on the *RANS* or *DES* mode. This way of working may be acceptable for fixed separation point like backward facing steps or cavity flows but is questionable for curved ducts or outflow fields like buffeting purposes.

The model reads:

$$\frac{D}{Dt}\rho\tilde{\nu} = c_{b1}\tilde{S}\rho\tilde{\nu} - \rho c_{w1} f_w \left(\frac{\tilde{\nu}}{\tilde{d}}\right)^2 + \frac{1}{\sigma}\left(\nabla.(\mu+\rho\tilde{\nu})\nabla\rho\tilde{\nu} + c_{b2}\rho(\nabla\tilde{\nu})^2\right)$$

Writing $\tilde{d} = \min(d, C_{des}\Delta)$ with C_{des} fixed at *0.65* according to bibliography.

4.4.2 k-ε SST Based DES

As the Spalart-based *DES*, a characteristic length-scale is needed to lead the way *DES* will modify the energy transfer between turbulence scales. The natural length-scale in *k-ε* is written:

$$l_{k-\varepsilon} = \frac{k^{\frac{3}{2}}}{\varepsilon}$$

The two-layer model reads:

$$\frac{\partial k}{\partial t} + div(\underline{U}.k) - div((\nu + \nu t)\underline{\nabla} k) = P_k - \frac{\varepsilon}{k}k$$
$$\frac{\partial \varepsilon}{\partial t} + div(\underline{U}.\varepsilon) - div((\nu + \nu t)\underline{\nabla} \varepsilon) = C_{\varepsilon 1}\frac{\varepsilon}{k}P_k - C_{\varepsilon 2}\frac{\varepsilon}{k}\varepsilon \qquad \text{if } Ry = \frac{y\sqrt{k}}{\nu} \geq 250$$

and

$$\frac{\partial k}{\partial t} + div(\underline{U}.k) - div((\nu + \nu t)\underline{\nabla} k) = P_k - \frac{\varepsilon}{k}k$$
$$\varepsilon = \frac{k^{3/2}}{L_\varepsilon} \quad with \quad L_\varepsilon = Cd(1 - \exp(-Ry/2C)) \qquad \text{if } Ry = \frac{y\sqrt{k}}{\nu} \leq 250$$
$$\nu t = C_\mu L_\mu \sqrt{k} \quad with \quad L_\mu = Cd(1 - \exp(-Ry/A))$$

DES based on the k-ε model is already available in the literature (see e.g. Travin *et al.*). The modification of the basic k-ε consists in the following modification of the destruction term in the k-equation:

$$D_k = \rho k^{3/2} / \tilde{l}$$

With $\tilde{l} = \min(k^{3/2}/\varepsilon, C_{DES}\Delta)$

The C_{DES} constant is to be calibrated on a *DHIT*. The value proposed by Travin *et al* is C_{DES}=0.61 and Δ is taken as the cubic root of the element volume. The calibration is presented latter in this document for this test-case. Since the part of the model where ε and μ_t are algebraic functions of k is in the inner part of the viscous layer, and since it is not a desirable feature of the model to switch in the *LES* mode in this area, our intention is to let this part of the model as it is. The only part that will be able to switch to the *DES* mode will be the high-*Re* part.

4.4.3 Calibration on DHIT Case

Both *DES* models have been calibrated on *DHIT* 51^3 test case and compared to Dynamic Smagorinsky subgrid model. Dynamic model is interesting for its adaptation to numerical viscosity leading to weaker Smagorinsky "constant" for subgrid model (*Cs≈0.11* compared to almost *0.18* for pure Smagorinsky).

Results of the calibration shows that reasonable values of *DES* constants are:

- C_{DES}=*0.4* for k-ε based *DES*
- C_{DES}=*0.65* for Spalart-Allmaras based *DES*

4.5 Implementation and Validation of Wall "Blending" Function

4.5.1 Spalart Based DES

Wall behaviour for Spalart based *DES* implemented is the proposed modification in the framework of DESider called *DDES* (Delayed Detached Eddy Simulation). Modified length-scale becomes:

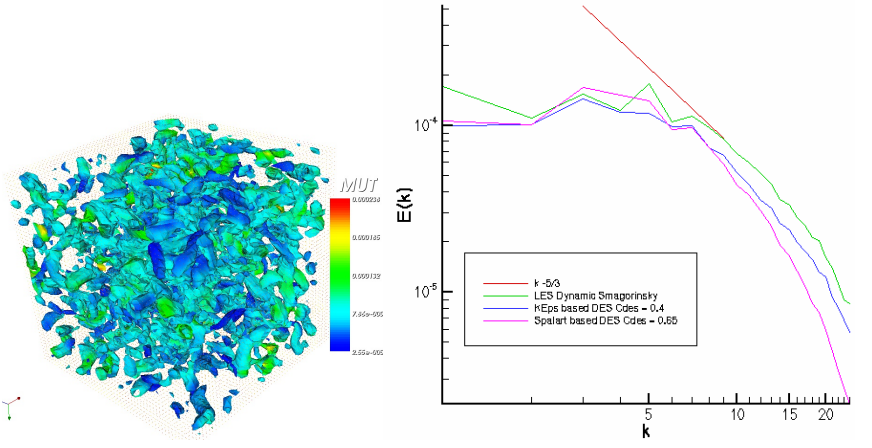

Fig. 3 Energy Spectrum for DHIT 51*3

$$\tilde{d} = d - f_d \max(0, d - C_{des}\Delta)$$

$$\text{with } f_d = 1 - \tanh\left(\left[8 r_d\right]^3\right) \text{ and } r_d = \frac{\tilde{\nu}}{\sqrt{U_{i,j}U_{i,j}}\kappa^2 d^2}$$

4.5.2 *k-ε SST Based DES*

For *k-ε SST* based *DES*, it has been chosen the blending function using one SST function *F2* that switch on only in boundary layer. Like in Spalart *DDES* length scale becomes:

$$\tilde{l} = \min(l_{k-\varepsilon}, \frac{C_{DES}\Delta}{1 - F_2})$$

4.5.3 *Validation on 3D Generic Flat Plate*

First validation of the wall formulation and the effectiveness against GIS is endeavoured on generic subsonic flat plate. *3D* mesh respecting *RANS* boundary layer refinement is generated:

- $\Delta x^+ \approx 250$
- $\Delta y^+ = 250$
- $\Delta z^+ = 2$

Figures below show the effect of DDES and Menter's F2 blending function on logarithmic law behaviour.

4.5.4 *Validation on Generic S-Duct*

Due to compressible features of AeTher code, validation of boundary layer separation under adverse pressure gradient is endeavoured on generic NASA S-Duct.

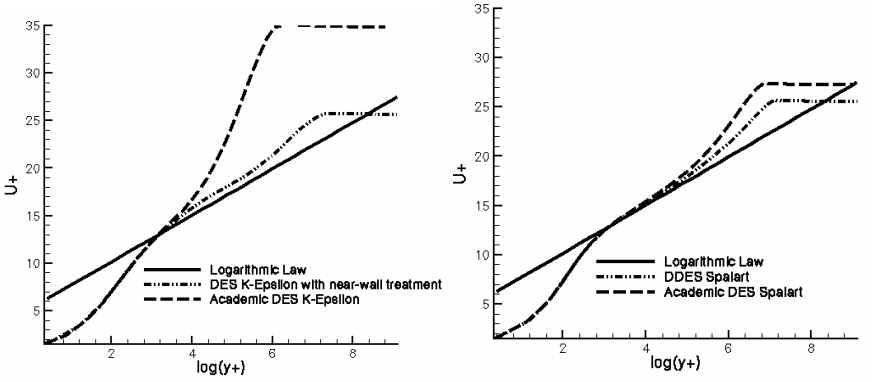

Fig. 4 Longitudinal velocities in wall values for different wall formulation

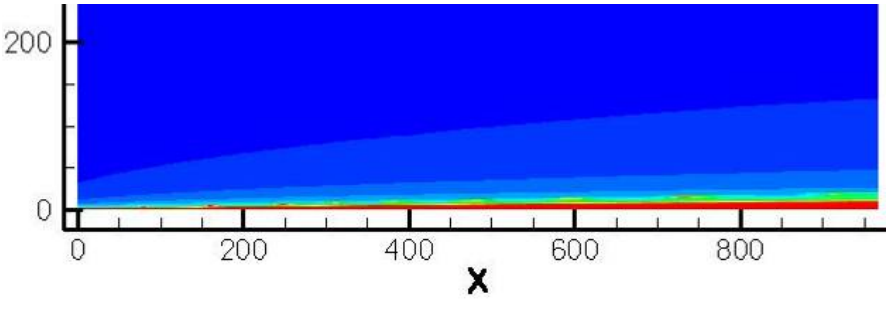

Fig. 5 *RANS* (red) & *LES* (blue) zone on generic flat plate (Spalart *DDES*)

Data from the experiment includes mean pressure coefficient on three iso-φ lines, separation and re-attachment point location, Mach and total pressure cartography on the CEP (Compressor Entry Plane), Total Pressure Recovery and Zonal Distortion parameter in the CEP.

Initial flow conditions are:

Pi	Ti	Mach	Mass Flow	δ
115400 Pa	307 K	0.6	7.135 kg/s^{-1}	4% de D1

The cartography of Pressure and Mach in the CEP are greatly improved by the use of *DES* showing a better mixing of low and high level of velocity and therefore a better distortion prediction. The same evolution is observed in *k-ε DES*. In this test-case, without *DDES* or Menter's formulation, a non-physical separation appears on the upper side of the duct where the boundary layer is thick, leading to high RMS values in the upper part of the CEP not seen in the experiment.

Both Spalart and k-*ε DES* showed rather good separation behaviour, but k-*ε* seems to predict better re-attachment point location *(s/D=4.69* compared to

Fig. 6 S-Duct Test-Case geometry

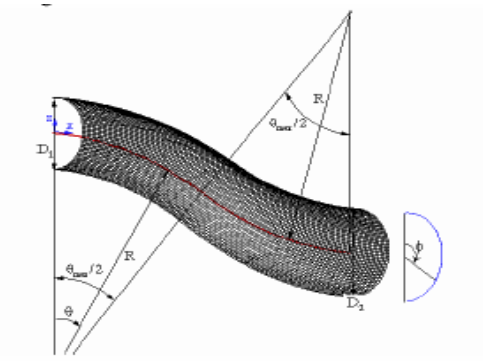

s/D=5.28 in Spalart *DDES* and *s/D=4.13* in the experiment), thanks to well suited length-scale computations (less directed by distance to the wall).

Nevertheless zonal distortion DC60 is better predicted in DDES modelization. Such controversial behaviour is still under investigation.

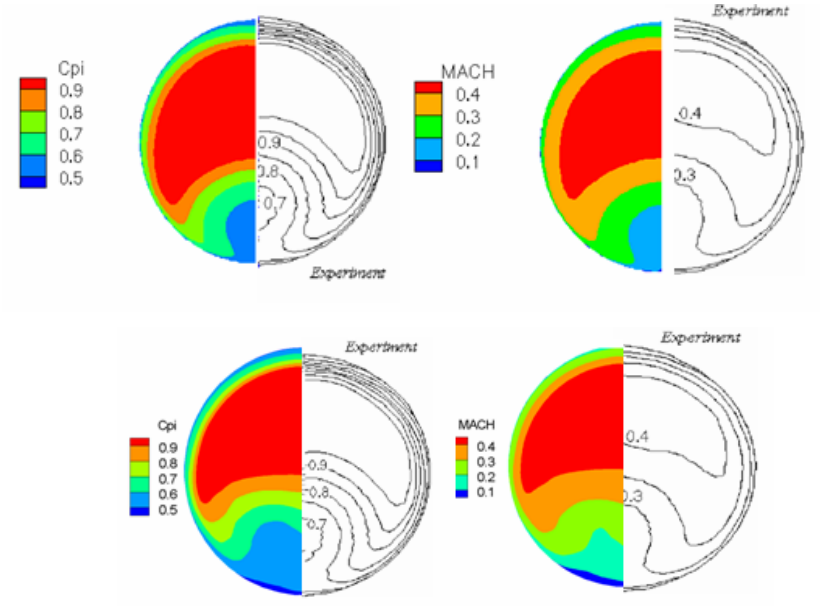

Fig. 7 Comparison of steady and unsteady fields in the CEP (Spalart vs Spalart DDES)

4.6 Application to Aero-Acoustics

A short presentation of work performed during "Application Challenges" Work Package of DESider project is presented below. The test-case is the M219 3D Cavity case with experimental data available from *DERA*.

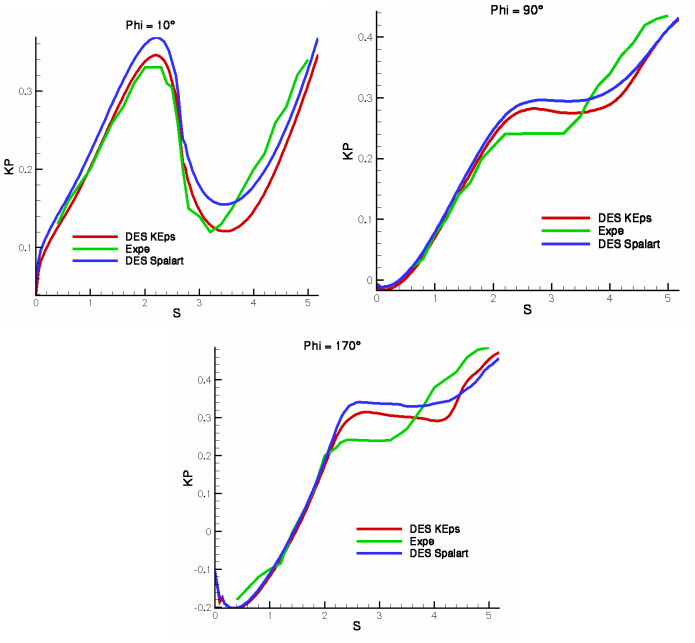

Fig. 8 Pressure coefficient on three iso-φ lines in the duct φ= 10° is the upper line of the duct φ=90° is the median line of the duct φ=170° is the bottom line of the duct (where the separation occur)

Table 1 Comparison of Pressure Recovery and Zonal Distortion in the CEP

	Pressure Recovery	DC60
Experiment	0.971	0.358
Steady Spalart	0.9815	0.479
DES Spalart	0.978	0.377
Steady k-ε	0.9816	0.478
DES k-ε	0.9804	0.403

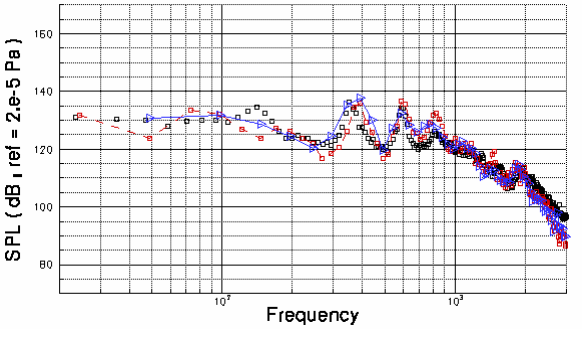

Fig. 9 Kulite K20

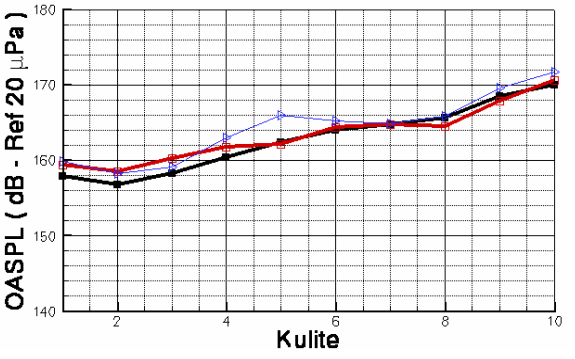

Fig. 10 OASPL Longitudinal evolution in the cavity

Only two spectrum and OASPL longitudinal evolution is shown below to complete the validation process.

The grid is unstructured with 1.5 .10 ^{6} points. Time step is $\Delta t=2.10^{-5}$ s for *DES* computations.

4.7 Conclusions

Unsteady purposes based on DES modelisations have been successfully implemented and validated both on generic and aerodynamic challenging test case, including pressure induced separation and broad band noise prediction. Reattachment prediction is said to be more accurate using k-ε based *DES*. Work performed in the framework of DESider, in particular on wall treatment, opens wide the field of application of such unsteady computation that are already included in the overall design process for next generation of airplane design.

5 Contributions of DLR in DESider

K. Weinman, T. Knopp, and D. Schwamborn

Abstract. This chapter presents a summary of DLR activities undertaken within the DESider project. Section 5.1 presents an overview of the numerical method used in the work. Section 5.2 contains a brief review of a grid convergence study for the NACA0021 test case undertaken jointly with NLR and TUB. Here we discuss some observations that have not been mentioned in the relevant case chapter. Section 5.3 presents work undertaken to improve numerical dissipation properties of the TAU code.

5.1 Numerical Method - The DLR TAU Code

The TAU code is a software system for prediction of viscous and in-viscid flows about complex geometries from the low subsonic to the hypersonic flow regime. The TAU system is designed to operate in a hybrid grid environment and full details on TAU can be found in (Schwamborn, 2006). Within DESider computations were performed using the dual-cell metric with implicit or explicit methods. The turbulence models implemented within the TAU code include linear and non-linear eddy viscosity models (EVM), Reynolds-stress models and hybrid RANS-LES models. The standard one-equation turbulence model used is the Spalart-Allmaras model which has been shown to yield highly satisfactory results for a wide range of applications whilst retaining good numerical robustness and stability. The two equation models are k-ω based, with the Menter SST model being most popular. Finally, there are options to perform Detached Eddy Simulations (DES) or Extra-Large Eddy Simulation (XLES) with various forms of GIS (gird induced separation) shielding which have been further extended and validated during the DESider project.

5.2 Work Undertaken during the DESider Project

The DLR participated in the assessment of the test cases given in the following Table 1, at the same time validating its DES implementations in TAU through additional comparison against the numerical results of the partners. These test cases are discussed in detail in the relevant chapters of this book. Note that XLES, SA-DES and SA-DDES (Travin et al., 1999) variants are used in this work.

Table 1 Models used

Test case	Description of Flow	Models used
2	FA5 aircraft	SA-DES, XLES
3	NACA0021 at 60° AoA	SA-DDES, XLES
4	Ahmed Body	SA-DDES, XLES
5	Decaying Isotropic Turbulence	SA-DDES, XLES, MSST-DES
11	Base Flow (M=2.46)	SA-DDES, XLES
18	NACA012 (Oscillating)	SA-DES, variety of URANS

5.2.1 DIT

An overview of the DIT test case is provided in Chapter 4, section 1. However, some additional points related to the DLR work are discussed here. The primary difficulty observed for this work was in the construction of the initial field for the compressible solver. In comparison to an incompressible problem, it is necessary to consider in detail the construction of two of the following fields: pressure, temperature or density. Failure to establish proper pressure and density fields can lead to un-physically high pressure gradients which create unphysical accelerations in the flow leading to an excess of turbulent kinetic energy while destroying the traditional turbulent kinetic energy cascade. Several suggestions are made in the literature as to how this problem can be resolved, for example (Samtaney, 2001). For the DLR work ideal gas constraints were used to estimate the pressure and density fields, and then the solution field was integrated in time whilst the velocity field was held constant. Typically hundreds to thousands of iterations were required before a fully converged field was established.

5.2.2 NACA0021

This test case is used to establish the validity of DES methods for flows with massive flow separation and large separation of turbulent scales. As noted by other authors, computational requirements are significant, with typically O(500-1000) convective time units being required for convergence of first order statistics. However it should be noted that WRLES requirements are significantly greater. Comparison of DES and URANS calculations show that integral coefficients are significantly improved when DES is used, most probably due to the improved resolution of the trailing vortex street which results in better estimations of the induced lift and drag components. This test case can be successfully computed even with relatively poor LES sub-grid scale characteristics. Differences between sub-grid scale models do not appear to be significant and the flow frequency response is improved when DES methods are utilised.

5.2.3 NACA 0012 (Oscillating at 15°AoA) - Basic Aero-Elasticity Case

The predominant feature of the flow around an airfoil in forced harmonic pitching motion at deep-stall conditions is the formation and shedding of a dynamic stall vortex from the leading edge, which propagates downstream along the chord during the down-stroke period. This causes a hysteresis type response in unsteady lift, drag and pitching moment coefficients. SA-DES gives slightly improved prediction of maximum lift, lift stall and during down-stroke compared to the SA-URANS model, although the assessment of the simulations by comparison with the experimental data requires further investigations due to the influence of the wind tunnel side walls and the lack of measurements of the laminar-turbulent transition.

5.2.4 Supersonic Base Flow at M=2.49

All relevant comments from the DLR regarding this case can be found in Chapter 4, section 11.

5.2.5 Ahmed Body

All relevant comments for the DLR regarding this case can be found in Chapter 4, section 4.

5.2.6 FA5 Aircraft

All relevant comments for the DLR regarding this case can be found in Chapter 4, section 13.

5.3 Additional Work Performed by DLR

Additional work performed by the DLR included a combined study with NLR and TUB related to grid convergence for DES calculations on the NACA0021 airfoil at 60° AoA, and a study on dissipation control for the TAU code.

5.3.1 Grid Convergence Study for NACA0021 at 60 °AoA

In this study grid convergence issues are considered between three levels of mesh refinement using three different flow solvers (each solver using a different numerical approach). DLR, TUB and NLR were involved in this study and some discussion of the results is given in chapter 4, section 3. This work is not completed yet and will be continued outside of DESider. Additional information relating to this work can be found in (Weinman et al., 2005) and (Weinman et al., 2006).

5.3.2 High Wave Number Dissipation Reduction in the TAU Code

It is known from work undertaken in the FLOMANIA project that standard TAU settings do not resolve the high wave number part of the energy spectrum for the DIT test case due to the too high numerical dissipation of the unstructured approach. The consequences are seen in comparisons of the resolved flow structure for the stalled NACA0021 at 60° AoA (see 4.3). The level of fine scale structure returned is significantly less than that returned by, for example, the higher order NTS code or the less-dissipative TUB ELAN code. As the TAU code operates in an unstructured environment the construction of an effective higher order stencil is non-trivial. Consequently, it was decided to seek methods of improving the DIT results based upon the central differencing scheme due to (Jameson et al.,1981), referred to as the JST scheme hereafter. Modifications of this nature should be easier to implement in standard industrial solvers.

The JST scheme augments a finite volume scheme by providing additional dissipative terms designed to suppress the tendency of odd-even oscillations and to

smooth oscillations near shocks. The scheme consists of a standard central difference formulation to which a second difference term, multiplied by a coefficient k(2), proportional to the absolute value of the pressure, is added. This term will approach zero if the pressure field is sufficiently smooth in regions where no discontinuities are present. In addition, Jameson observed that a fourth difference term was required to ensure convergence to a completely steady state. Near shock waves the fourth difference terms were shown to introduce spurious oscillations. This problem was overcome by subtracting k(2) from the coefficient of the fourth difference term k(4), so that contributions from the fourth difference contribution are inactive when the second difference terms are active. The formulation for the JST dissipation Dij is given below

$$D_{ij} = \varepsilon^{(2)}_{i+1/2,j} R_{i+1/2,j} \left(\phi_{i,j} - \phi_{i,j+1} \right) - \varepsilon^{(4)}_{i+1/2,j} R_{i+1/2,j} L(\phi_{i,j}),$$

where R is chosen to scale the dissipation terms correctly. Jameson notes that the spectral radius of the flux Jacobian provides the correct scale. Here L represents an estimate of the Laplacian operator. Consider a turbulent velocity which might exhibit a high degree of smoothness at very low wave numbers. As wave-number increases, the smoothness of the field will decrease on a finite grid stencil - higher resolved wave-numbers may appear as wiggles in the solution. The standard dissipation operator is designed to smooth these wiggles out of the solution. Furthermore, the influence of the second difference term can be accentuated through a non-zero $k^{(2)}$ coefficient in regions where a gradient is high. The poor high wave number properties of the standard JST scheme implemented in TAU can be traced back to inappropriate activation of the second difference term in the dissipation model.

From the above discussion it would seem that a mechanism to reduce the stabilising dissipation associated with the JST scheme is required. One idea is to implement a wiggle detector which decrements the stabilising dissipation in regions where unsteadiness appears, see for example (Ciardi et al., 2005). Another idea is to construct an operator which reduces the stabilizing dissipation terms by re-scaling the dissipation operator in response to the presence of unsteadiness. The dissipation operator is rewritten with two additional scaling terms $G_2(\ldots)$ and $G_4(\ldots)$ as follows:

$$D_{i,j} = A \left(G_2 (\ ) \varepsilon^{(2)} D \left(\phi_{i,j} \right) - G_4 (\ ) \varepsilon^{(4)} L(\phi_{i,j}) \right).$$

The functions $G_2(\ldots)$ and $G_4(\ldots)$ can be modified via a wiggle detector or can act as the wiggle detector itself. Concerning the wiggle-detector, the advection of smooth large scale structure through a control volume will result in the growth of the magnitude of the stabilising JST dissipation. If a small scale structure is then advected through the control volume, the high stabilising dissipation may damp higher flow modes present. Since the dissipation operator is implemented at a fixed point within an Eulerian reference frame, control of dissipation through a wiggle sensor cannot match exactly the optimal dissipation requirements for a fluid element which is Lagrangian in nature.

In regions near shocks the dissipation model coefficient are well established and the functions should not change the character of the JST scheme. In these

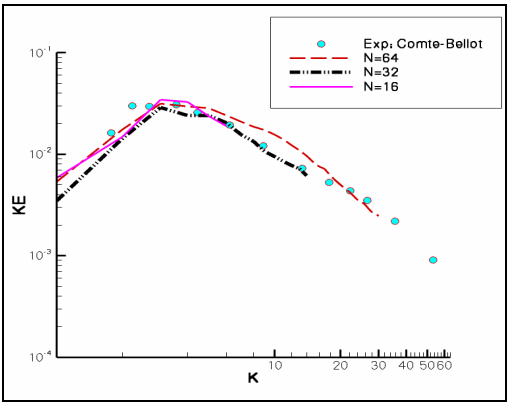

Fig. 1 DIT result of the modified JST scheme, using the matrix dissipation model on different meshes

regions the scaling functions should return a unity value, since the standard JST algorithm should not be damaged. In shock-free regions the magnitude of the JST dissipation model should decrease until stability boundaries are encountered. The definition of precise stability bounds for unstructured codes with complex topology is still an open question. In these regions the value of the scaling functions should be less than unity. These deliberations suggest that a suitable form of the scaling functions might be given by a hyperbolic tangent of the form

$$G\left(p,r\right) = \tanh(4.5\,p^{r}) \quad p < 0, r < 0$$

where p is an indicator of unsteadiness, and r is an exponent that can either be a scalar constant or solution functional. The coefficient 4.5 is chosen to ensure that the limits of the function are given by G(0,r) = H(0) and G(∞,r) = H(1) where H is the heavy side step function. Within the interval [0,1] the function is smooth and differentiable. For flows characterised by massive separation, tests have shown that a JST modification of this nature provides results which are superior to the standard JST scheme in LES mode. It should be noted that modifications that are similar to this form have been reported in the literature by (Ducross et al., 1999). At the present time work on this form of dissipation modification is ongoing, and the preliminary results presented here use the ratio of the local Mach number to a reference Mach number for p, and the value of r has been chosen through numerical experiment. Additionally, for DES calculations the G function values are weighted such that the original JST dissipation model is retained in the RANS mode of the DES, and the rescaled JST model is activated in the full LES region. The grid induced separation shield designed by (Strelets et al.) has also been coupled with the G functions to minimise possible problems in the grey zone between full LES and RANS modes. Decaying isotropic turbulence (DIT) is the first case examined using the modified JST scheme. The calculation is performed on three-dimensional hexahedral meshes of uniform aspect ratio and with an equal number N of points along each Cartesian co-ordinate axis. As rescaling of the scalar dissipation model was not fully successful, the modified JST scheme was applied also with Matrix dissipation.

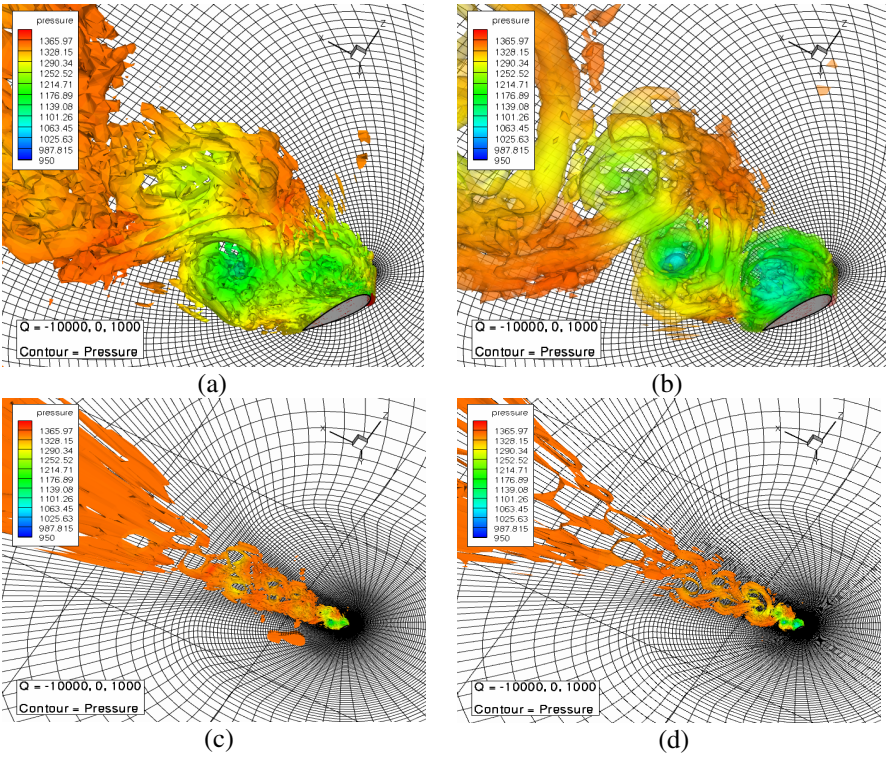

Fig. 2 DDES of the NACA0021 at 60° indicating the qualitative influence of the dissipation reduction. Computation with standard Central scheme and Matrix Dissi-pation (a), (c) versus modified central scheme with Matrix dissipation (b), (d)

Figure 1 illustrates that this combination resolves the energy spectrum correctly over the full range of wave numbers. This suggests that more meaningful flow physics content will be retained within the LES mode of DES by using this approach. It should be noted that when low Mach number preconditioning was applied, only a small amount of scaling for the fourth difference terms was required for the matrix dissipation model. These results are not shown here as the interaction between the low Mach number preconditioning and the modified JST scheme are still under investigation.

As noted earlier the modified dissipation model has been used successfully for the NACA0021 airfoil at 60° and will be further examined. Figure 2 illustrates the difference in DDES solution quality obtained on a coarse NACA0021 mesh with a unit span width. In the following structural coherence refers to the spatial cross-correlation of the flow field. Figure (b, d) shows that the modified JST scheme allows retaining structural coherence until the far-field boundary the LES mode. The standard scheme (a, c) looses coherence after about two chord lengths. However the integral aerodynamic coefficients are similar between both sets of calculations which support the point of view that for fully separated flows the quality of the sub grid scale mode in the LES mode of DES may not be significant.

6 EADS-MAS Methods and Applications

S. Leicher

EADS-MAS

Abstract. EADS main interest is in the performance with respect to the characteristics of high AoA flows with massive separation and vortex interaction effects in the subsonic and transonic flow region. Such cases contain flow features like separation, reattachment, high streamline curvature, vortex burst, shock boundary layer interactions and so on.

Also of primary interest for EADS-MAS are the aero-acoustic test cases of cavity-type flows which deserve as generic models for the aircraft bays opened during flight in any flow regime. The aim is to provide methods for prediction of relevant sound pressure levels generated by the aerodynamic flow field. The specific problem of EADS is related to the interaction of aerodynamic pressure fluctuations with the aircraft structure which could lead to fatigue damages. For all such test cases the unsteadiness of the flow field should be reproduced as accurate as possible offering a perfect field for application of the so called hybrid RANS-LES methods coming along with an acceptable effort within the daily industrial work.

EADS takes part in some basic test cases like the NACA0021, the delta wing, in the forced pitching motion of a NACA0012 airfoil as well as in complex applications containing real unsteady turbulent phenomena like the M219 cavity and the FA5 generic airplane.

6.1 Methods and Turbulence Models

Most of the simulations are performed using both the DLR unstructured flow solver TAU (Schwamborn at al. 2006) and the structured DLR FLOWer (Raddatz, Fassbänder, 2005) code.

The 3D FLOWer code is a parallel block structured second order finite volume solver for EULER as well as Navier-Stokes equations proceed from Jameson at al. (1981). Various numerical schemes like cell-centred, cell vertex and AUSM are implemented. A multistage Runge-Kutta scheme and additional implicit formulations drive the solution to a steady state. Local time stepping, implicit residual smoothing and full multigrid can be used to speed up the convergence. The dual time stepping scheme of Jameson (1991) is used as second order time integration for unsteady flow problems. This method is not limited to some smallest time step and all acceleration techniques mentioned above can be applied within the inner explicit loop. A lot of one and two equation turbulence models as well as RSM, EARSM and DES are applicable.

In most of the cases the hybrid RANS LES SA-DES model was used with both codes. For the Delta Wing case also normal URANS simulations were performed

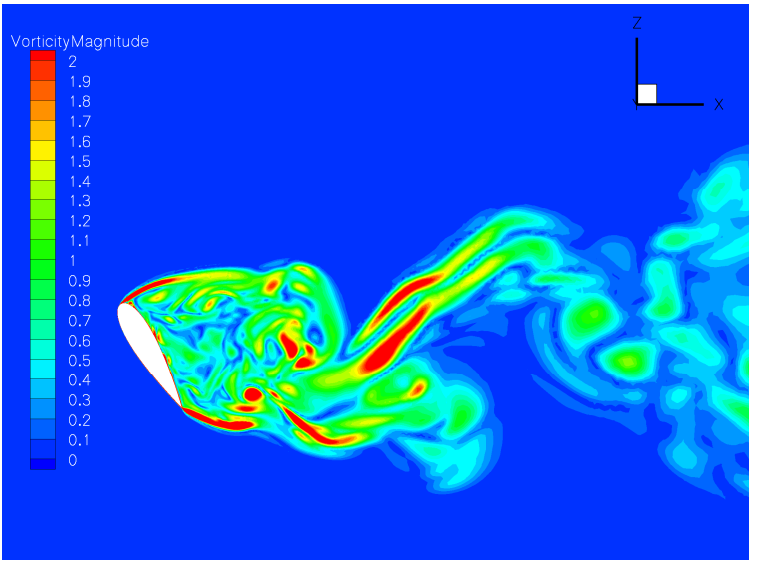

Fig. 1 NACA0021 Vorticity magnitude

using SAE, Wilcox-kω, EARSM, RSM SST-ω and SST model. Some of them were applied together with and without rotation correction according to Kok (2000).

For the cavity case beneath the SA-DES also a XLES (Kok, 2004) computation was performed.

6.2 NACA 0021

The NACA0021 test case is an airfoil at 60° degrees angle of attack with a large region with massive separated flow.

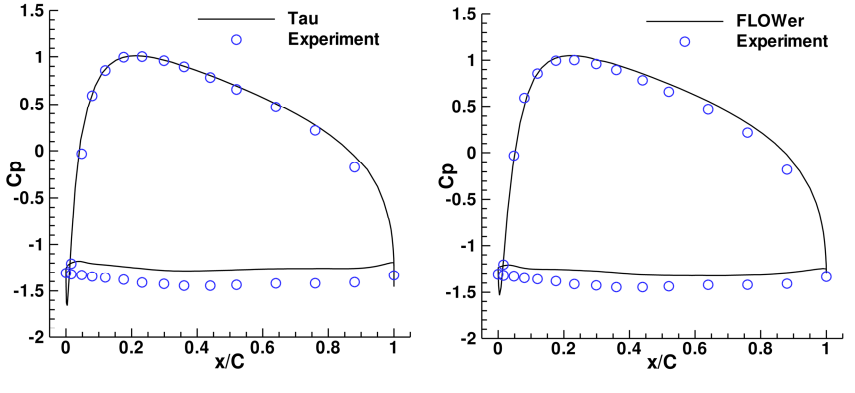

Fig. 2 NACA0021 comparison of mean cp-distribution

EADS performs calculations in structured and unstructured grids using the TAU and the FLOWer code. Best results were obtained in the very fine unstructured grid using the TAU code. Comparisons of the mean cp-distributions und the spectral analysis of the force coefficients are shown above.

6.3 Delta Wing

This test case is a delta wing with sharp leading edge at two angles of attack 25 o and 35o. It is a test case on vertical flow. A structured grid of 5 million mesh points was used because of the advantages in the discretization at sharp leading edges. Figure 4 provides on the left the mean cp comparison of the Spalart-Allmaras SA-DES results from Flower and TAU code with experiments performed by Breitsamter (1997). On the right the mean surface cp of the TAU computation and the experiment is shown.

Comparing the mean velocity components at 25^{o} and 35^{o} it is obvious that the concentrated vortex at 25^{o} is bursted at 35^{o}. The agreement between experiments and simulation is qualitatively good although quantitatively especially the level of the axial component is somewhat lower inside the vortex core.

6.4 FA5 Generic Airplane

The FA5 generic airplane test case is a delta wing configuration at Mach number of 0.125 and an angle of attack of 15.0° at a Reynolds number of 2.8×10^{6}.

The partners in this test case are ANSYS, DLR, EADS-MAS and TUB. Besides the structured approach (see chapter IV, section 13) EADS generates an unstructured grid and provided it to most of the partners. Used were hybrid RANS LES methods (DLR SA-DDES, EADS-MAS SA-DES) as well as the ANSYS SST-SAS model. The following figures shows a comparison of the standard deviations of the main velocity components by means of the RMS value compared to the experiment performed by Breitsamter (1997).

It turned out that the agreement is qualitatively acceptable but quantitatively the computed values are too high.

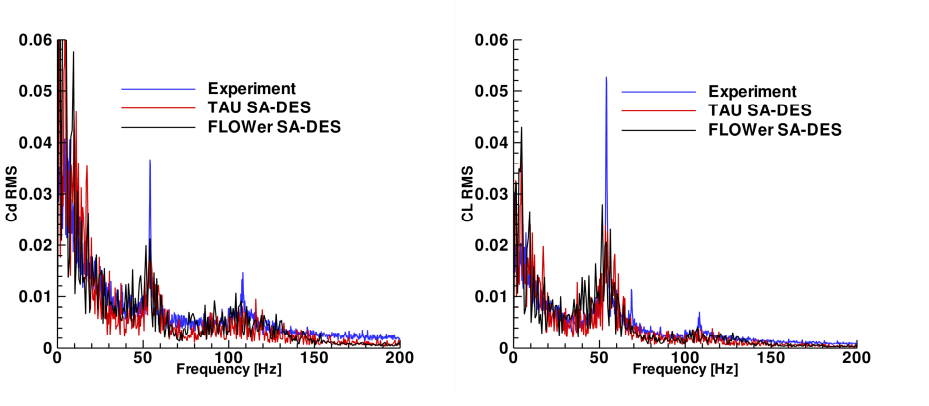

Fig. 3 NACA0021 spectral analysis of lift and drag coefficient

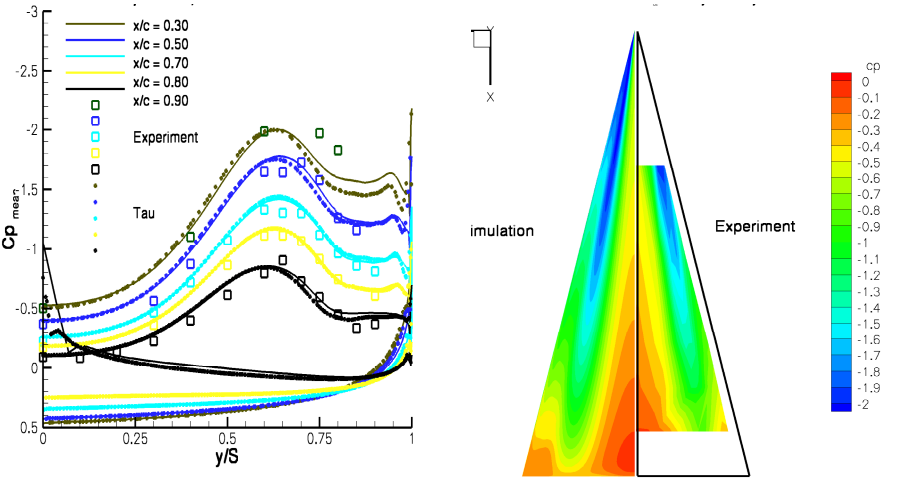

Fig. 4 Cp-comparison in cuts and on surface α=25°

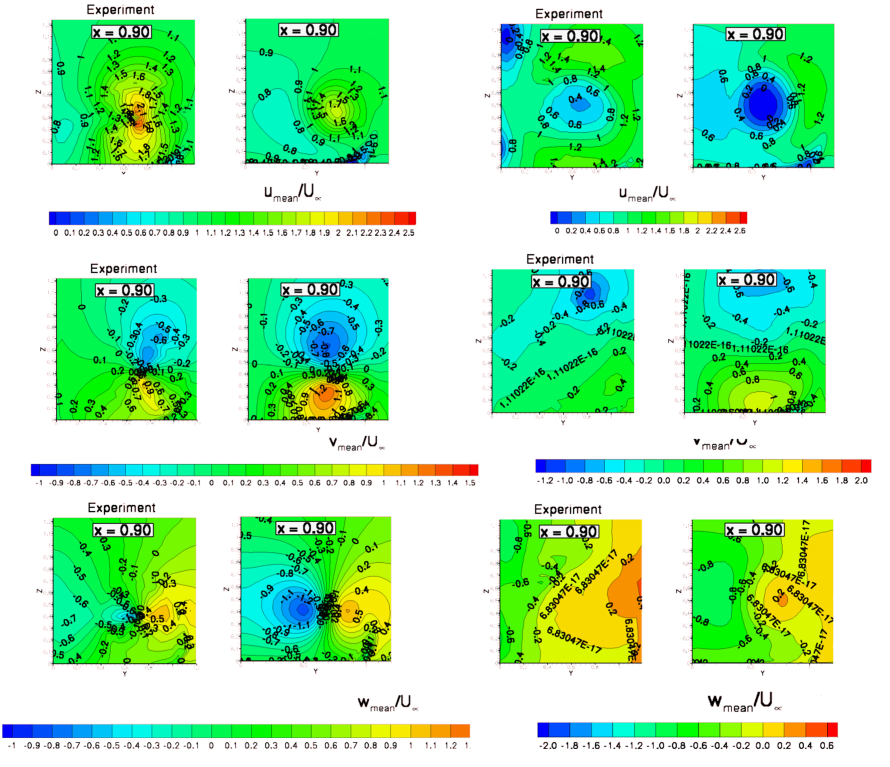

Fig. 5 Comparison of mean velocity components at 25° (left) and 35° (right) at x/C = 0.90

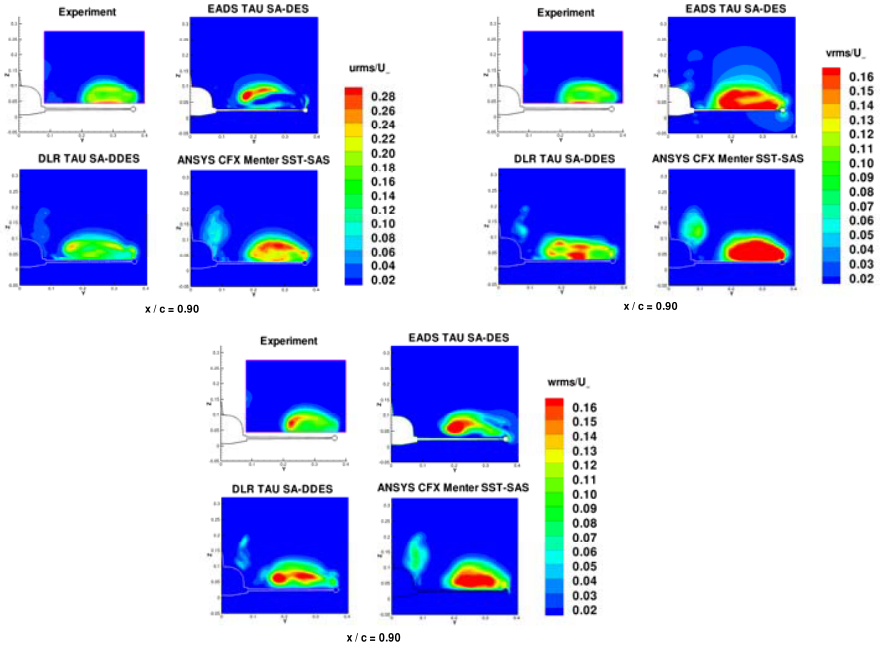

Fig. 6 Comparison of u- v- and w-rms values at x/C=0.90

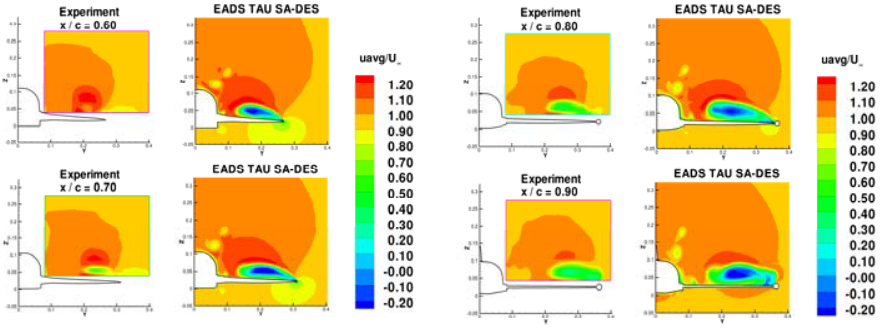

Fig. 7 Mean axial velocity

Looking at the mean axial velocity in figure 7 the level inside the vortex core is still too low although the higher density of the unstructured grid has improved the result.

An instantaneous flow field pattern shows quite nicely the complex flow structures.

6.5 M219 Cavity

As mentioned above cavity type flows are of primary interest for EADS-MAS. They deserve as generic models for the aircraft bays opened during flight. To

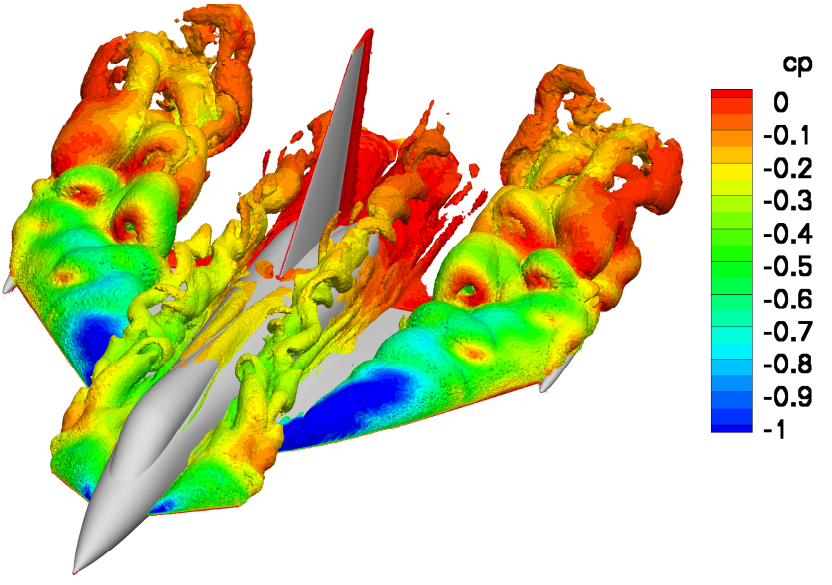

Fig. 8 Iso-vorticity surface coloured with cp

avoid fatigue damages at the aircraft structure the additional unsteady loads from the present pressure oscillations should be calculated as best.

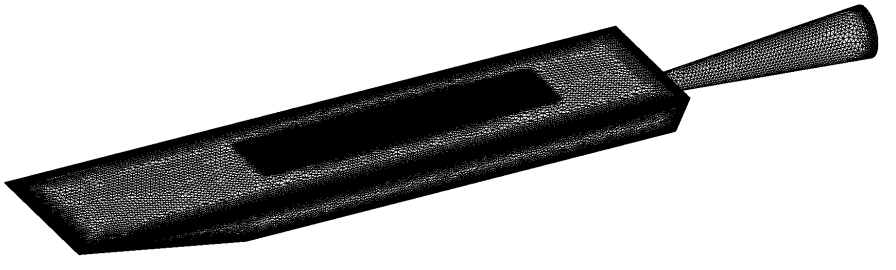

Fig. 9 Surface grid of unstructured EADS grid

EADS-MAS performed calculations in the structured grid provided by FOI as well as an unstructured grid generated by EADS. The structured grid, where the FLOWer as well as the TAU code were used, turned out to be too coarse to catch properly the unsteadiness of the flow while the 6.2 million hybrid grid do so. The EADS grid represents the original experimental geometry (figure 9) including the wind tunnel walls (Euler BC.). The grid was provided to FOI so that cross plottings of different codes using identical grid were done (chapter IV, section 18). The Mach number of this case is 0.86 and EADS-MAS applied the SA-DES as well as the XLES (Kok 2004) hybrid RANS LES turbulence model.

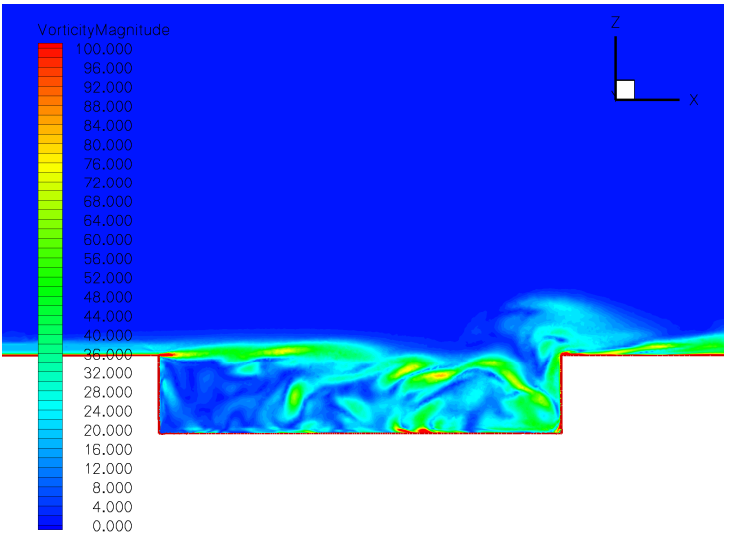

Fig. 10 M219 Cavity instantaneous vorticity field in symmetry plane

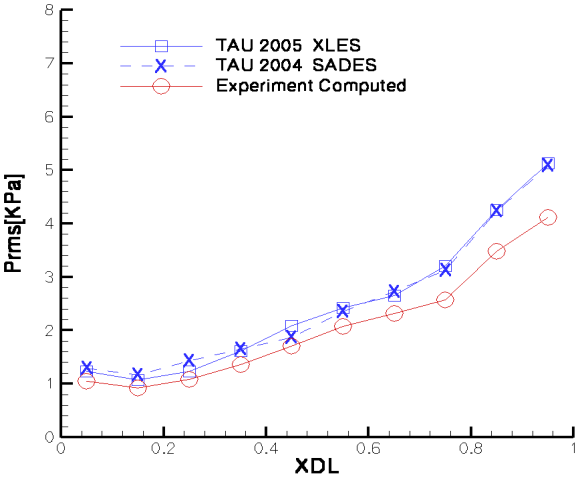

Fig. 11 M219 Cavity instantaneous vorticity field in symmetry plane

The flow features present in this case are separation, reattachment, free shear layer, LES part hitting boundary layer and acoustic resonance. The figure below presents the instantaneous vorticity field showing a lot of flow structures.

A comparison between experiment and SA-DES as well as XLES simulation for the over all standard deviation of the pressure by means of the RMS-value along the cavity bottom is given below. The agreement is quite satisfying.

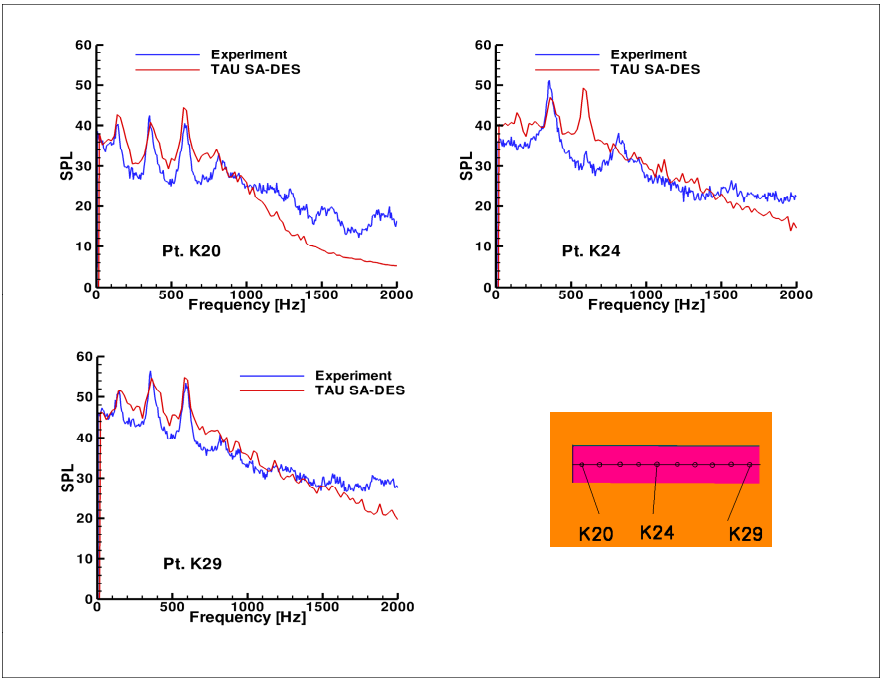

Fig. 12 Comparison of Sound Pressure Level

The spectral analysis for three points near the front, in the middle and at the end of the cavity shows that the first three dominant frequencies are found although the amplitudes are a little bit too high.

7 A Look Back on DESider at Eurocopter Germany

F. Le Chuiton and A. D'Alascio

Eurocopter Deutschland GmbH

Abstract. Dealing with highly separated flows at Eurocopter is almost a necessity due to the complexity of the configurations studied. Although no direct benefit of DESider could be translated in the daily design process, the project proves to be of value, in that a realistic perspective for solving such flow cases has been opened. Potential applications of DES at Eurocopter are recalled before methods and models used for the two test-cases considered are shortly outlined (oscillating NACA0012 aerofoil at 15° mean incidence and isolated fuselage of the BK117-C2 wind tunnel model). Subsequently, facts and lessons learnt are presented showing the difficulty to use advanced turbulence modelling for the first time in an industrial context. Finally, test-cases and models are commented on, stressing the necessity of modern experiments designed for in-depth comparison with CFD.

7.1 Numerical Aerodynamics at ECD

7.1.1 Potential Applications

A non-exhaustive but representative list of frequent and possibly prone to the use of DES-like modelling applications at ECD is given below:

1. Rotor Design (Performance and optimisation). Isolated rotor in hover flight, whereat not only the aerodynamically active part of the blade is accounted for but also the blade roots and cuffs. Besides the normal exercise of computing thrust and power (*i.e.* the field of induced velocities), the main objective is to determine the effects of the additional non-aerodynamic elements on thrust and power in view of their potential optimisation.
2. Rotor Design (Optimisation). Isolated rotor in forward flight with or without structural coupling. Here the challenge lies in the proper simulation of the dynamic stall phenomenon occurring on the retreating blade side, which can lead to excessive fatigue of control pitch rods.
3. Cell and Empennage Design (Stability). Isolated fuselage with or without rotor wake modelling through actuator discs. Focus is put on capturing the highly vortical wake separating behind the backdoor and convecting downstream till it impinges on the control surfaces of the empennage (horizontal stabilisers, end plates and fin).
4. Rotor Head Design (Vibration and Fatigue). Isolated rotor head in forward flight at different levels of geometrical modelling. The task lies in capturing the wake of the rotor head, which after downstream convection impinges on the tail fin and induces the so-called tail shake phenomenon, where eigenmodes of the empennage are excited.

As regards the second point, ECD was involved in the work package concerning the oscillating NACA0012 aerofoil at 15° mean angle of attack. This was meant as a two-dimensional simplification of the dynamic stall problem.

But more importantly, the third topic has been mainly addressed. This consisted in computing the flow-field about a wind tunnel model of the BK117-C2 helicopter fuselage (an intermediate version of the later EC145 helicopter) and to compare the numerical results with wind tunnel measurement data. It is here referred to the application report in Chapter 4 for thorough details on this activity.

7.1.2 Methods

During the DESider exercise, three codes have been used to assess the potentialities of DES-like turbulence modelling: the simulation system TAU from DLR, the CFX simulation platform by ANSYS and the research flow solver HMB of the University of Liverpool. For a description of these tools and the particular settings used for the exercise, the reader is referred to the application report in Chapter 4 and the references therein.

It is to be mentioned that, at present, out of these three simulation tools only the DLR-code TAU is installed and used at ECD on a continuing basis.

7.1.3 Models

For the sake of comparing modelling approaches, four different settings have been used: on the one hand a steady simulation using the k-ω-SST turbulence model and on the other hand three unsteady simulations using unsteady extensions of the previous model, namely the k-ω-TNT-XLES (TAU), the k-ω-SST-SAS (CFX) and the k-ω-SST-DES (HMB) models. All these models have been used as is without any special tuning; it is therefore referred to the general literature for technical details.

7.2 Facts and Lessons Learnt

From the point of view of ECD, the valuable achievements of the project are listed hereafter. First, on a general standpoint:

- The project provided the opportunity to draw the attention of the helicopter industry on advanced turbulence modelling, which is claimed to be able to cope with difficult aerodynamic cases such as those listed in the first section, and thus ensure knowledge transfer from research centres and universities to industry.
- Thanks to the project, contacts have been established with the development team of Ansys-CFX and experience has been gained on the SAS modelling.
- Results and knowledge from the DESider project are already being made available in the frame of the twined projects SHANEL (French-German binational) and SHANEL-L (German national), where highly separated flows are considered too; to name a few: fuselage wake, dynamic stall, rotor head wake.

Next, on a technical standpoint:

- ECD initiated a wind tunnel measurement campaign, the results of which have been used within the activities of test-case 16 "EC145 helicopter fuselage". Thus a sound reference was offered for comparison with computational results. Indeed it has been shown that DES-like modelling can, at least partly, improve agreement between numerical and experimental data.
- The unsteady flow-field about the isolated fuselage of the BK117-C2 wind tunnel model has been simulated, hence providing reference computational results that can be used for comparison in future studies.

Finally, on the "lessons learnt" topic:

- ECD also participated to test-case 17 "Oscillating NACA0012 at 15°", which was meant to assess whether dynamic polars of aerofoils can be substituted to static polars in the aerodynamic module of the helicopter comprehensive code HOST of ECD. Computations have shown that this is still unrealistic: first, because of too high computational costs while computing dynamic polars (in an industrial context) and, second, because the computed hysteresis cycles for the moment coefficient do not feature enough smoothness, which prevents using a stability criterion for dynamic stall. Generating acceptable dynamic polars would require unaffordable grid sizes and hence computing costs.
- Concerning the simulation of the isolated fuselage, it turned out that the grid resolution of the complete wake of the support strut, and not only a small portion close to the fuselage surface, is an important factor for successful comparison with experimental data on the backdoor. This entails of course additional grid nodes and thus increased computing times.
- The selection of an appropriate time-step is not that an easy task since making it too small induces (industrially) unacceptable computing times and choosing it too large impairs both the validity of the modelling approach and the quality of the flow solution.
- Overall, although DES-like modelling has much appeal for the computation of highly separated turbulent flows, it is still unaffordable in an industrial context with limited computing resources such as at ECD. Nevertheless, the need for such modelling techniques is particularly high as it can be seen from the list of potential applications in section 1. Therefore, ECD is of course to keep surveying the state of developments of DES and, more generally, of other approaches to turbulence modelling.

7.3 Notes

7.3.1 Test-Cases

When computing a test-case, it is important to be able to compare with fully documented and trustable measurement data. Earlier experimental campaigns were not necessarily conducted with a possible comparison with CFD in mind, which unfortunately often led to non-documented significant aspects of the experiment.

As regards the oscillating NACA0012 aerofoil, the following difficulties turned out to be particularly acute:

- The definition of the profile trailing edge has been left unspecified: some partners closed the aerofoil with a rounded trailing edge, others with a truncated one. This has a non-negligible influence on the dynamic stall phenomenology.
- The hysteresis cycles for the lift, drag and pitch moment coefficients didn't include uncertainty (error) bars. Such a confidence interval would have made the numerical to experimental data comparison much easier. In particular, it is known that the data spreading on the down-stroke part of the cycle can be fairly large.
- Also, using visualisation of the flow-field itself (e.g. with PIV measurements) contributes to a modern validation exercise.

Again, concerning the isolated fuselage test-case the following can be stated:

- The lack of flow-field visualisation hindered, to some extent, comparing numerical and experimental data.
- The frequency content of the fuselage wake at selected locations should have been used for validation of the combination: grid density and turbulence resolving capability of the models.

Nevertheless, the latter test-case is of high importance to the helicopter manufacturer and is to remain one of the favourites at ECD. Moreover, the related experimental database is being expended beyond the frame of DESider.

7.3.2 Models

From the industrial point of view, implementations of advanced turbulence models should care: for user-friendliness (very few more input necessary, if at all, as for common RANS models); if possible, for laminarity to turbulence transition (especially important for rotor performance prediction and for dynamic stall); and of course for as low computational costs as possible (which, in the light of today's applications, remains a challenging hope).

7.4 Conclusion

Although the DESider project didn't bring direct benefit in the daily design process at Eurocopter, the outcome is of value, in that a new realistic perspective for tackling difficult highly separated flow cases has been opened. Be it only on grounds of validation of CFD-methods about industrial applications, it is hoped, that real-world conditions will leave room for using such modelling capabilities.

8 EDF Achievements in Desider

S. Benhamadouche

EDF

8.1 Introduction

Coupling a code with itself using overlapping grid techniques allows performing computations that can be hardly done or are impossible with just one computational domain. Two examples can be mentioned; the use of moving meshes for Fluid Structure Interaction (FSI) with large displacements; RANS/LES coupling. The latter might allow performing a RANS calculation in a very large computational domain with a relatively coarse mesh while using LES in a small portion to get richer information of the fluid motion. One can imagine the whole vessel of a nuclear plant computed with a two second moment closure approach while computing the mixing grids with a LES technique to predict the fluid forces along the fuel rods. The reader might consult the articles by Schlüter et al (2005), Tang et al (2003) and Wang et al (2000), describing methods similar to the one presented herein. The developments have been made in the EDF open source CFD tool *Code_Saturne* Archambeau (2004) which is available on the web (http://www.code-saturne.org/). These developments allow to couple n executables of which run on n computational domains using different turbulence models. Some movies of the capabilities of the present developments can be found the following TWiki:

http://cfd.mace.manchester.ac.uk/twiki/bin/view/Main/Sturm4Gallery.

8.2 General Overview of the Overset Grid Technique

Figure 1 gives a general sketch for coupling two domains. One has to couple two domains Ω1 and Ω2 which use different turbulence models. The frontiers of the two domains are respectively called ω1 and ω2. Ω=Ω1 ∩ Ω2, ω21= Ω1 ∩ ω2 and ω12=Ω2 ∩ ω1. Navier-Stokes equations are solved separately in Ω1 and Ω2. there are two zones of coupling: Ω which is the overlapping domain, ω21 and ω12

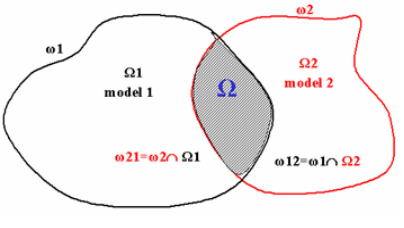

Fig. 1 General sketch for coupling two computational domains

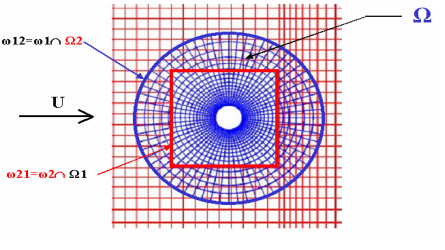

Fig. 2 Example of coupling two computational domains

which are parts of the frontier of a coupled domain which belongs to the other one. Ω might be empty. The two domains Ω1 and Ω2 are discretized and an unstructured collocated finite volume technique is used. Figure 2 gives an example for coupling two domains in the test-case of an infinite cylinder. Equations are solved at time step number *n+1,* assuming that φ is a variable known from the previous time step.

8.2.1 Coupling Boundary Faces

Figure 3 gives the sketch of a boundary face belonging to the coupled zone and to the domain Ω2. The computational cell Ω_I belonging to the domain Ω1 contains the centre F of the boundary face. After preliminary tests, the following interpolation has been implemented (*O'* is the centre of *I'J'*):

$$\varphi_F^{n+1} = \varphi_{O'}^n + (\underline{\nabla\varphi})_{O'}^n . \underline{O'F}$$

$$\varphi_{O'}^n = \frac{1}{2}\left(\varphi_{I'}^n + \varphi_{J'}^n\right) = \frac{1}{2}\left(\varphi_I^n + \varphi_J^n + (\underline{\nabla\varphi})_I^n . \underline{II'} + (\underline{\nabla\varphi})_J^n . \underline{JJ'}\right)$$

$$(\underline{\nabla\varphi})_{O'}^n = \frac{1}{2}\left((\underline{\nabla\varphi})_I^n + (\underline{\nabla\varphi})_J^n\right)$$

The values of φ and its gradients at *J* and *I* are explicit. These values might be made implicit by introducing inner iterations in order to reach a fix-point:

$$\varphi_F^{k+1} = \frac{1}{2}\left(\varphi_I^k + \varphi_J^k + (\underline{\nabla\varphi})_I^k . \underline{II'} + (\underline{\nabla\varphi})_J^k . \underline{JJ'}\right) + \frac{1}{2}\left((\underline{\nabla\varphi})_I^k + (\underline{\nabla\varphi})_J^k\right) . \underline{O'F}$$

For *Neumann* condition, one writes: $(\nabla\varphi)_F^{n+1} . \underline{n} = \frac{1}{2}\left((\underline{\nabla\varphi})_I^n + (\underline{\nabla\varphi})_J^n\right) . \underline{n}$

A Dirichlet condition is applied for the velocity components and the scalar values and a Neumann condition for the pressure.

8.2.2 Coupling with a Body Force in the Overlapping Region

Figure 4 gives a general sketch of a cell Ω_J belonging to the domain Ω2 with the corresponding cell Ω_I in the domain Ω1. The cell centre *I* is the closest one to *J*. One wants to impose a body force at the point *J*;

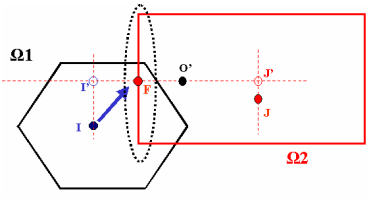

Fig. 3 general sketch for coupling a boundary face

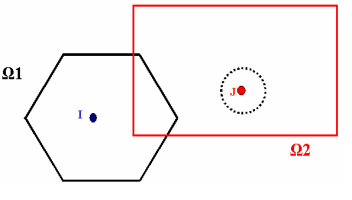

Fig. 4 General sketch to impose a body force

$$\left.\frac{\partial \varphi}{\partial t}\right|_J^{n+1} + \ldots = \ldots + \frac{1}{\tau_J}(\psi_J^n - \varphi_J^n) \cdot$$

ψ_J^n is an interpolated value coming from the domain Ω1 and τ_J is a relaxation time ($\psi_J^{n+1} = \varphi_I^n + (\underline{\nabla\varphi})_I^n . \underline{IJ}$). After few tests with constant relaxation time (τ=*100*Δt), a dynamic procedure to evaluate this quantity has been tested successfully. If m_{KJ} stands for the mass flow at F in the computational domain Ω2, $\tau = \rho_J vol(\Omega_J) / \sum_{m_{KJ}>0} m_{KJ}$.

ρ_J and $vol(\Omega_J)$ are respectively the density and the volume of the cell Ω_J.

8.3 RANS/LES Coupling Examples

8.3.1 The Back-Step Facing Step Test-Case – Normal RANS/LES Coupling

The first results obtained by coupling RANS and LES on the backward facing step are presented. LES deals with the regions where the phenomena are complex (detachment and re-attachment) and RANS (k-ω-SST) is mainly used in the inlet and the outlet (re-developing region). Figure 6 gives the detailed boundary conditions used in the present case. The computed configuration is from Le et al. (1992). The Reynolds numbers based on the maximum inlet velocity and the step height *h* is equal to 5000. Figure 5 gives the dimensions of the global computational domain. *h* is the step height is. The inlet of the domain is half a channel (*4h* is the half height of the channel). The length is the span-wise direction is equal to *4h*. Three computational domains are coupled (Figure 5). The first RANS domain (on the left) is not "really" coupled to the LES one. It provides RANS quantities to the LES inlet (called in figure 5 SEM) for which, by using a Synthetic Eddy Method, (Jarrin, 2008), unsteady conditions are generated. The "inlet" faces (left) of the second RANS domain (right) are coupled to the LES one. The mean values and the kinetic energy are estimated from the LES domain and imposed in the RANS "inlet".

Figure 6 shows the meshes. Only one cell is used in the span-wise direction for the RANS domain. LES uses standard wall function. The maximum CFL number

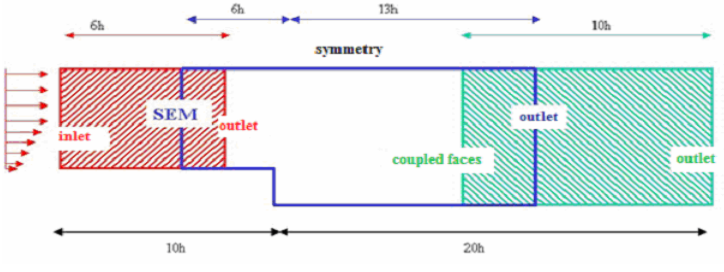

Fig. 5 RANS and LES subdomains (red and green : RANS, blue : LES)

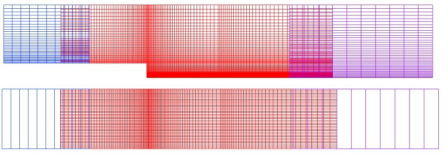

Fig. 6 view of the three meshes

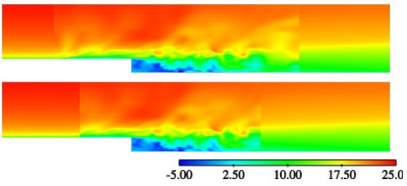

Fig. 7 Instantaneous stream-wise velocity component (top: LES on top, bottom: RANS on top)

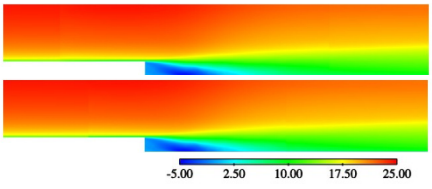

Fig. 8 Mean stream-wise velocity compo-nent

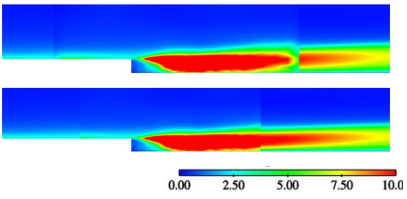

Fig. 9 Turbulent kinetic energy component

is equal to 0,6 in LES computation. Body forces are used in the overlapping regions. In LES simulation, this relaxation time is averaged in time.

In figures 6-9, the whole computational domain is shown, with alternatively the LES domain on the top (RANS on the background), and then the RANS one on the top. LES mean values are obtained by averaging in time (12 flow passes) and in the span-wise direction. The RANS calculation is stationary (although an unsteady algorithm is used). Figure 7 shows the instantaneous stream-wise velocity. It is clear that the SEM allows generating fluctuations at the inlet of LES. The mean stream-wise velocity is also shown on Figure 8. The continuity of the velocity is satisfactory; this is enforced by the body-force introduced in the momentum equations. Figure 9 shows the turbulent kinetic energy k. One assumes that the major part of k is resolved in LES. It is obvious that the SEM provides a sufficient amount of turbulent kinetic energy to LES in the near-wall region and that the flow develops rapidly departing from the inlet. A certain continuity of k is observed, although this is not the case if one considers k coming from the overlapping region from LES domain. Figure 10 gives the mean velocity field in the LES domain. Both the recirculation zone and the secondary recirculation are well predicted. Figure 11 provides the velocity at the first computational cell at the wall. Finally, results of the present calculation are compared to those obtained without body forces. The first computation gives a recirculation length around 6h, which is in accordance with the literature. Removing body forces results in a shorter recirculation (5h). This confirms the importance of body forcing when an overlapping region exists.

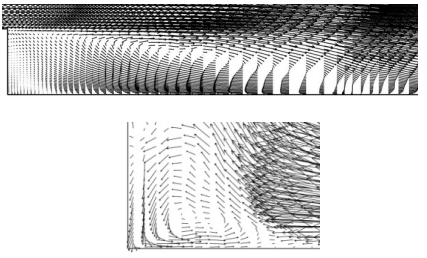

Fig. 10 Mean velocity field from LES

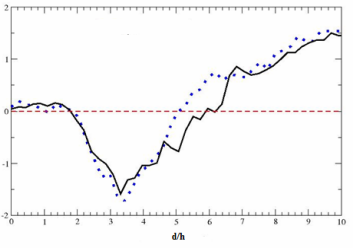

Fig. 11 Stream-wise component atthe wall (—: with body forcing, … : without)

8.3.2 Tangential Coupling – Channel Flow

The SEM is used in the present case to test its ability to handle tangential coupling. The Reynolds number based on the friction velocity is equal to 395. Implicit periodic boundary conditions are used in the stream-wise and span-wise directions. Figure 12 shows the meshes. The central mesh uses LES and the two others RANS (k-ω-SST). The RANS meshes go up to y+=150 (there is only one cell in the RANS meshes in both the stream-wise and span-wise directions). The LES mesh starts at y+=50.

Figure 13 gives the mean velocity and the Reynolds stresses profiles in the RANS and LES domains compared to DNS data from Kim et al (1987). The velocity is satisfactory and the log region is well predicted. A peak is observed for the diagonal stresses in LES while approaching the boundaries (y+=50). This behaviour is similar to the one obtained if there was a wall at y+=50. This is widely observed while using wall functions for example or when a Dirichlet condition is used (which is the case herein). This problem is dramatic as it probably comes from artificial streaks created in the near-boundary region and affects the instantaneous behaviour although the mean velocity profile is satisfactory. This

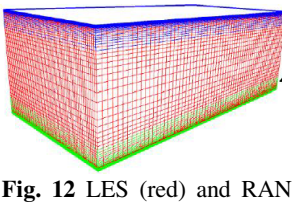

Fig. 12 LES (red) and RANS meshes

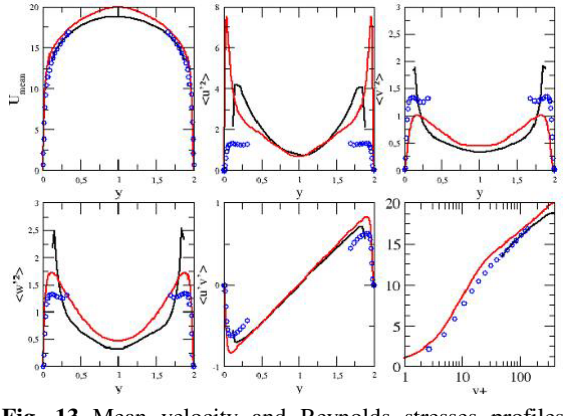

Fig. 13 Mean velocity and Reynolds stresses profiles (black: LES, red: DNS, Symbols: RANS)

makes this method very hazardous and this approach will be abandoned. In addition, it hard to conceive a general synthetic method able to reproduce the turbulent structures in the near wall region (inclined structures).

8.3.3 *Use of Code/Code Coupling for Wall Treatment (RALEWA Method)*

Figure 14 shows the meshes used with RALEWA approach (« *RAns LEs for WAll treatment* »). LES computational domain goes up to the wall with a high Reynolds cell at the wall. The RANS mesh goes from the wall to the first computational cell at the wall in the LES domain. LES mesh is n_x and n_z times finer than the RANS one in the stream-wise and span-wise directions. RANS meshes are well refined at the wall (the low-Reynolds k-ω-SST model is used herein). Thus, each parallel face to the wall in the RANS domain corresponds exactly to n_x x n_z cells in LES domain. Figure 15 gives a sketch of the RALEWA method. LES provides the RANS calculation with a mean value obtained by averaging in time and locally using the n_x x n_z cells. After performing a time-step with the RANS model on the RANS mesh, a mean friction velocity, denoted by $u_{\tau,RANS}(\underline{x})$ is obtained. The n_x x n_z LES cells receive this value. It is important to have a friction velocity that varies in time for LES. If $u_{\tau,LES}(\underline{x},t)$ and $\overline{u}_{\tau,LES}(\underline{x})$ stand respectively for the instantaneous mean friction velocity obtained with a standard wall function and its mean value in time, one can write: $u_\tau(\underline{x},t) = u_{\tau,RANS}(\underline{x}) \frac{u_{\tau,LES}(\underline{x},t)}{\overline{u}_{\tau,LES}(\underline{x})}$. At the end, one obtains $\overline{u}_\tau(\underline{x}) = \overline{u}_{\tau,RANS}(\underline{x})$.

This method has been tested on the channel flow at high Reynolds numbers (Re*=4000, 8000 and 16000). Figure 16 gives the mean velocity profiles compared to the one obtained with the Extended Wall Function (EWF) described by Montfort (2008), using the same LES meshes (these wall functions are close to TBLE). The results using EWF are standard. The log law is predicted but with a transition far from the wall (this behaviour appears at high Reynolds numbers). RALEWA approach shows a better behaviour with a wider log region. This method is promising but still needs investigations concerning mesh generation.

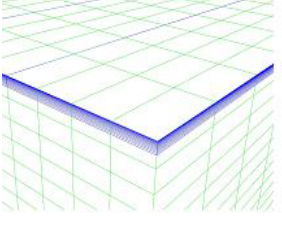

Fig. 14 RANS and LES meshes (green: LES, blue: RANS)

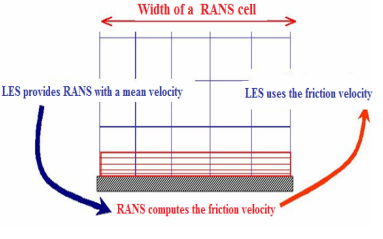

Fig. 15 Principle of the RALEWA method

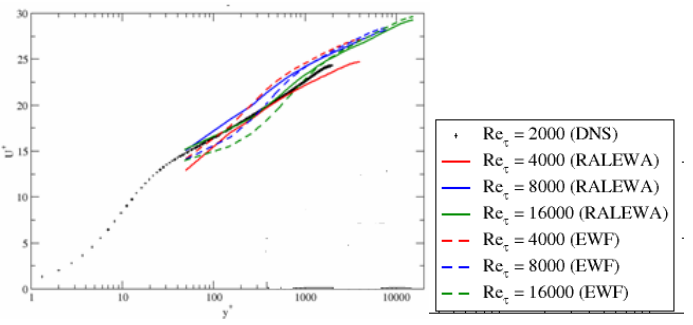

Fig. 16 Velocity profile at different Reynolds numbers, comparisons with EWF

8.4 Conclusions

A general method for Code/Code coupling has been presented. This method has been applied for RANS/LES coupling using separate computational domains for RANS and LES with overlapping regions. It has been shown that normal coupling can be utilized with a Synthetic Eddy Method. However, the use of this method for tangential coupling to simulate the wall is not satisfactory. While using RANS/LES coupling, special care has to be given to the regions where LES and RANS are applied. Finally, the coupling has been used by solving RANS equations up to the first LES computational cell (this takes into account naturally a the pressure gradient or buoyancy forces) and providing a friction velocity for LES. This method gives promising results on the channel flow.

9 Towards Efficient and Accurate Hybrid RANS-LES Modeling for Aerodynamic Applications

Shia-Hui Peng

Swedish Defence Research Agency, FOI

Abstract. This section presents some major scientific contributions and achievements made by FOI in the DESider project. FOI has worked on the implementation and validation of the URANS and DES models, the development and calibration of new DES and hybrid RANS-LES approaches, as well as on their applications to both underlying-flow-regime and industry-relevant test cases. In addition, effort has also been made on the implementation of effective numerical methods for unsteady aerodynamic computations. The emphasis in this summary is nonetheless placed on the algebraic hybrid RANS-LES model developed in the project with its applications to some test cases.

9.1 Introduction

Modelling of turbulent aerodynamic flows has often stemmed from fundamental research, mostly in the academic world, and incorporated subsequently into engineering applications. In spite of numerous existing turbulence models developed in different hierarchies, ranging from the simplest algebraic model to the most sophisticated differential Reynolds stress model in RANS and, further, to the SGS model of different types in LES, only a few have survived in the routine use by aerodynamic industries. It is obvious that a model with a well-balanced compromise of *simplicity*, *efficiency* and *accuracy*, is favoured in industrial applications. As a research organization, one of the principal roles of FOI is to bridge upstream academic research and downstream industrial applications.

Keeping this in mind, the FOI work in the DESider project has been driven towards implementation and development of efficient and accurate methods in terms of numerical schemes and turbulence models. To improve computational efficiency for modelling unsteady aerodynamic flows, FOI has implemented and tested the Recursive Projection Method (RPM) by Shroff and Keller (1993), which is an iterative procedure for accelerating convergence. For LES, DES and other hybrid RANS-LES modelling of turbulent internal flows, FOI has tested a recycling and rescaling method to approximate turbulent inflow conditions. In modelling flow physics, FOI has proposed a formulation of curvature and rotation correction for eddy-viscosity RANS models based on previous work (Wallin and Johansson, 2002). To attain a feasible RANS-LES interface for embedded LES modelling, the possibility has been explored using the dissipation rate of turbulent kinetic energy as a sensor, for which a preliminary work has been

undertaken for a channel flow with LES mode embedded in the wall layer. All these and other FOI work has been reported in details in various Deliverables of the DESider project.

This summary will focus only on the development of DES and hybrid RANS-LES modelling approaches accomplished in the FOI work, with a particular emphasis on the algebraic hybrid model and its validation and applications.

9.2 DES and Hybrid RANS-LES Modelling

A brief description of the development of a DES approach and two hybrid RANS-LES models is given here. The detailed formulation of these models should be referred to Peng (2005) and Peng (2006a), respectively.

9.2.1 DES Based on the k-Equation Model (k-DES Model)

The proposed DES model has been formulated using a scale-adaptation formulation for the RANS-LES matching similar to the S-A DES model (Spalart et al, 1997). Instead of using an empirically assembled transport equation, nonetheless, the transport equation for turbulent kinetic energy, *k*, has been invoked as the base model (hereafter the **k-DES** model). The exact *k*-equation exists, for which its modelling may be made physically profound. Moreover, to reach correct asymptotic behaviour, the modelled *k*-equation has been justified to accommodate the effect of near-wall viscous damping, which reads

$$\frac{D\rho k}{Dt} = -\tau_{ij}\frac{\partial u_i}{\partial x_j} + \frac{\partial}{\partial x_j}\left[\left(\mu + \frac{\mu_t}{\sigma_k}\right)\frac{\partial k}{\partial x_j}\right] - C_\varepsilon \rho \frac{k^{3/2}}{L_\varepsilon} \tag{1}$$

where τ_{ij} is the turbulent stress tensor, L_ε is a turbulent length scale and μ_t is the turbulent eddy viscosity. An additional length scale, L_μ, is used to formulate μ_t, namely, $\mu_t = C_k \rho \sqrt{k} L_\mu$ with $L_\mu = \kappa C_\mu^{1/4} f_\mu d / C_k$, where $\kappa = 0.418$, $C_\mu = 0.09$, $C_k = 0.05$, and *d* is a length-scale quantity which will be further addressed below. The damping function, f_μ, takes the form of

$$f_\mu = \tanh\left(\frac{\sqrt{R_d} + R_d}{95}\right) \tag{2}$$

where $R_d = \rho\sqrt{k}d/\mu$. The length scale, L_ε, is formulated by $L_\varepsilon = \kappa C_\varepsilon C_\mu^{-3/4} f_\varepsilon d$ with $C_\varepsilon = 1.8$. The function, f_ε, takes the same form as in the two layer model by Chen and Patel (1988), giving

$$f_\varepsilon = 1 - \exp\left(\frac{-R_d}{A}\right), \text{ and } A = 2\kappa C_\varepsilon C_\mu^{-3/4} \tag{3}$$

In its RANS form, the length-scale quantity, d, is specified as the local wall-normal distance, d_w.

The k-equation in Eq. (1), is adjusted to model SGS turbulence kinetic energy, by replacing, d, with a SGS turbulence length scale, Δ_l. In the development of the k-DES model, we have calibrated the k-equation SGS model in LES for decaying, homogeneous, isotropic turbulence, where the conventional filter width has often been taken from the control volume of a local node, i.e., $\Delta_l \propto \delta V^{1/3}$. In LES for the DHIT case, we have assumed that $\Delta_l = C_{kdes}\delta V^{1/3}$, where C_{kdes} is a k-DES model constant, which is calibrated with $C_{kdes} = 0.62$ in LES of DHIT to give the best prediction of energy decay (Peng, 2006b).

In computations for flows with wall shear, the SGS length scale has been further calibrated viz. $\Delta_l = C_{kdes} l_{sgs}$, and

$$l_{sgs} = \frac{2\delta V^{1/3}\Delta_{\max}}{\left(\delta V^{1/3} + \Delta_{\max}\right)} \tag{4}$$

where $\Delta_{\max} = \max\left(\Delta_x, \Delta_y, \Delta_z\right)$, being the maximum cell size. For unstructured mesh, $\Delta_{\max}$ takes the maximum edge size of the local node. The k-DES model invokes a length-scale adaptation of $d = \min\left(d_w, C_{kdes} l_{sgs}\right)$ with $C_{kdes} = 0.62$. Furthermore, to justify possible over-dissipation of SGS turbulence energy, an additional turbulent length scale is introduced, viz. $l_s \equiv \sqrt{k}/|S|$. The length scales, L_μ and L_ε, in the k-equation model are replaced, with Γ_μ and Γ_ε, respectively, with $\Gamma_\mu = \min\left(L_\mu, \alpha\sqrt{k}/|S|\right)$ and $\Gamma_\varepsilon = \max\left(L_\varepsilon, \beta\sqrt{k}/|S|\right)$, where $\alpha = \beta = 6.0$.

Figures 1 presents the k-DES result for the turbulent channel flow at $\mathrm{Re}_\tau = 2000$ in comparison with the LES data by Piomellio et al (2003).

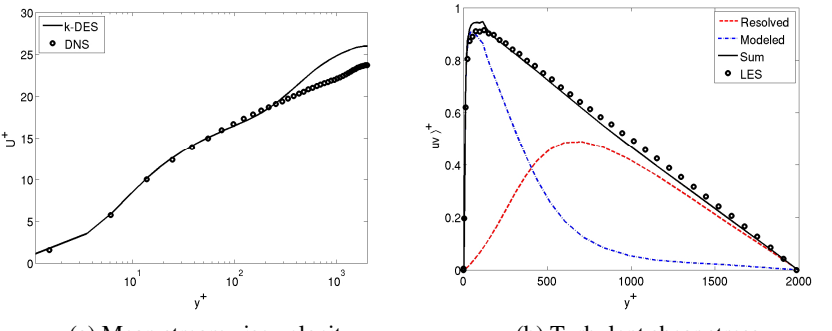

(a) Mean streamwise velocity (b) Turbulent shear stress

Fig. 1 k-DES modeling for turbulent channel flow at Re_τ = 2000, in comparison with full LES by Piomellio et al (2003)

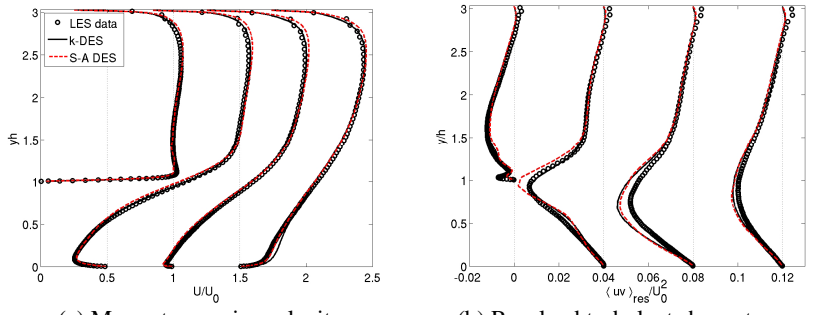

(a) Mean streamwise velocity (b) Resolved turbulent shear stress

Fig. 2 k-DES modeling for turbulent periodic hill flow at locations x/h = 0, 2, 4 and 6 (from left to right in each figure)

The k-DES model has been validated further in computations of a periodic hill flow, for which wall-resolved LES data are available (Temmerman et al, 2004). In Figure 2, a comparison is presented for the mean streamwise velocity and the resolved turbulent shear stress at locations x/h = 0, 2, 4 and 6, respectively. It is shown that both the SA-DES and k-DES models give similar predictions for these quantities, as compared with the LES data. The modelling for this test case demonstrates encouraging performance of the k-DES model to represent appropriately the size and location of the separation bubble and the flow properties in the free shear layer downstream of the hill crest.

The work performed in the DESider project has shed a light on the k-DES formulation and its validation for fundamental flows. Continuous effort is required for further modelling validation and improvement.

9.2.2 Hybrid RANS-LES Modelling

In the framework of DESider project, two hybrid RANS-LES models have been developed and examined. Both models are stemmed from the eddy viscosity concept. The first approach, termed the **HYB0** model, employs an algebraic formulation, in which a near-wall mixing-length RANS mode is hybridized with the Smagorinsky SGS model away from the wall. The RANS-LES matching is accomplished by an adaptation of the length scale over the interface zone. The second approach, termed the **HYB1** model, adopts the transport equation for the turbulence kinetic energy, k, in both the RANS and the LES regions. The RANS-LES matching is accommodated through the length scales in the definition of the eddy viscosity and the dissipation rate of k, respectively. The detailed formulation of the HYB0 and HYB1 models can be referred to Peng (2005).

Both models have been extensively calibrated and validated in simulations of a number of fundamental turbulent flows, by which the modelling capabilities have been explored. In the validation of the models, it has been noticed that the HYB0 model enables generally superior performance as compared with the HYB1 model (which has shown very encouraging and good performance though). The emphasis below is placed on the presentation of the HYB0 model.

The reasoning of using algebraic formulation in the HYB0 model lies in the fact that a well-developed simple algebraic RANS model is able to effectively model attached boundary layers and, on the other hand, many existing SGS models have been cast in a relatively simple form, based on a presumable argumentation that the unresolved SGS turbulence tend to be isotropic and thus its modelling is relatively amenable. In LES one of the most commonly used models is the Smagorinsky SGS model, which is of mixing-length type. Indeed, simple but robust modelling approaches are particularly appreciated in industrial CFD applications.

With the HYB0 model for both incompressible and compressible flows, the turbulent stress tensor, τ_{ij}, is modelled using the eddy viscosity concept for both RANS and LES modes in the form of

$$\tau_{ij} = -2\mu_h\left(S_{ij} - \frac{1}{3}\delta_{ij}S_{kk}\right) + \frac{1}{3}\delta_{ij}\tau_{kk} \tag{5}$$

where μ_h is the hybrid eddy viscosity and S_{ij} is the strain rate tensor. Note that, for incompressible flows, the isotropic part of the stress tensor is usually absorbed into an effective pressure, and the trace for the strain rate tensor is zero due to continuity. For compressible flows, the isotropic part in the LES mode may be modelled as $\tau_{kk} = 2C_I\rho\Delta^2|S|^2$, where Δ is the LES filter width and $|S|$ is the magnitude of the flow strain rate tensor. For the near-wall RANS mode, the turbulent kinetic energy, k, may be estimated by $k \propto \left[\mu_h/(\rho l_\mu)\right]^2$, where l_μ is a turbulent length scale. Based on a number of calibrations, we have set $C_I = 0$. In addition, for modelling compressible flows, the transport equation for the total energy, E, is solved, in which a model for the turbulent heat flux vector is incorporated. We have adopted the eddy diffusivity model for both the RANS and LES modes, namely,

$$h_{k\theta} = -\frac{\mu_h}{\mathrm{Pr}_h}\frac{\partial T}{\partial x_k} \tag{6}$$

where Pr_h is the turbulent Prandtl number and $\mathrm{Pr}_h = 0.4$. This value is commonly used as the SGS Prandtl number in LES for turbulent thermal convection flows. For the near-wall RANS mode, the mixing-length concept is used to formulate the eddy viscosity by $\tilde{\mu}_t = \rho\tilde{l}_\mu^2|S|$, where the length scale, $\tilde{l}_\mu$, is proportional to the wall distance d, reading $\tilde{l}_\mu = f_\mu\kappa d$ and $\kappa = 0.418$ being the von Karman constant. To avoid the awkwardness of using wall-shear related parameters in the formulation when modelling separating flows, the empirical damping function f_μ is formulated in the form of $f_\mu = \tanh\left(R_t^{1/3}/2.5\right)$ as a function of the RANS turbulent Reynolds number, $R_t = \tilde{\mu}_t/\mu$. In the LES region, the Smagorinsky SGS model is employed, *viz.* $\mu_{sgs} = \rho(C_s\Delta)^2|S|$, where $C_s = 0.12$ and $\Delta = \sqrt{\left(\Delta_{\max}^2 + \delta V^{2/3}\right)/2}$. Note that δV is the local control volume, $\Delta_{\max}$ is the local maximum cell size, $\Delta_{\max} = \max\left(\Delta_x, \Delta_y, \Delta_z\right)$, or the local maximum edge size for unstructured grids.

The matching between the RANS and LES modes is accomplished by modifying the RANS length scale into $l_\mu = \tilde{l}_\mu f_s$ so that $\mu_t = \rho l_\mu^2 |S|$ for the RANS mode, where f_s is a function of $R_s = \tilde{\mu}_t / \mu_{sgs}$ and

$$f_s = \frac{1}{2}\left\{\exp\left(-\frac{R_s^{0.75}}{4.75}\right) + \exp\left(-\frac{R_s^{0.3}}{2.5}\right)\right\} \tag{7}$$

The use of the function, f_s, is to achieve a smooth transition for the RANS-LES length-scale adaptation, which makes the near-wall RANS mode produce interfacing turbulence that is comparable to the resolve-turbulence in order to attain a realistic matching with the LES mode. The eddy viscosity for the HYB0 model, μ_h, is computed by $\mu_h = \mu_{sgs}$ if $\tilde{l}_\mu \geq \Delta$, and $\mu_h = \mu_t$ otherwise.

As done for the k-DES model, the RANS mode and the LES mode inherent in both the HYB0 and HYB1 models have been calibrated, respectively, against fundamental flows, including turbulent channel flow (RANS and LES) and the decaying homogeneous, isotropic turbulence (DHIT) (LES). Figure 3 presents the calibration of the LES mode in the simulation of the DHIT case in comparison with the experiment by Comte-Bellot and Corrsin (1971). Figure 3 (a) illustrates the result for the SA DES model with two meshes using $C_{des} = 0.65$, as identified by Spalart et al (1997). In Figure 3 (b), the constant, $C_{kdes} = 0.62$, is calibrated for the k-DES model on a 32×32×32 mesh, in which the constant used for the Smagorinsky model is $C_s = 0.215$. The calibration for the *k*-equation SGS mode in the HYB1 model is presented in Figure 3 (c) on a 32×32×32 mesh, which is extracted from a previous work (Peng, 2005).

9.3 Examples of Application Using the HYB0 Model

Along with extensive calibration and validation for fundamental turbulent flows, the performance of the HYB0 model has been examined in a number of test cases, some of which are briefly outlined below.

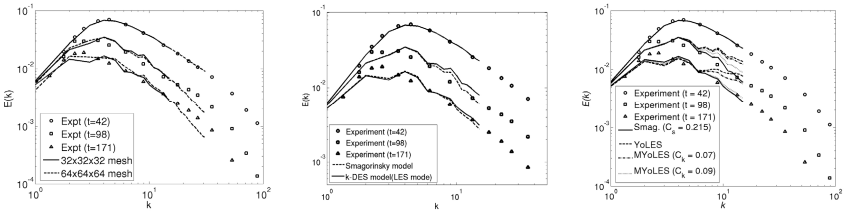

(a) k-DES model (b) SA DES model (c) HYB1 model

Fig. 3 Modeling calibration for decaying homogeneous, isotropic turbulence. In (c), YoLES indicates the *k*-equation SGS model by Yoshizawa (1985), MYoLES and MYoLES0 are the LES mode hybridized in the HYB1 model calibrated with different model coefficients

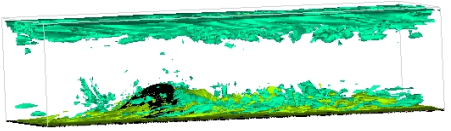

(a) Resolved near-wall flow structure

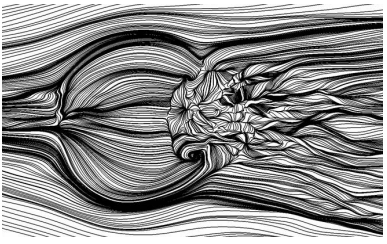

(b) Snapshot of streamlines above the hill

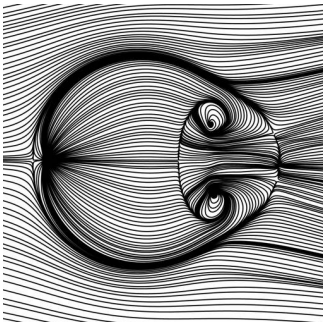

(c) Time-averaged streamlines above the hill

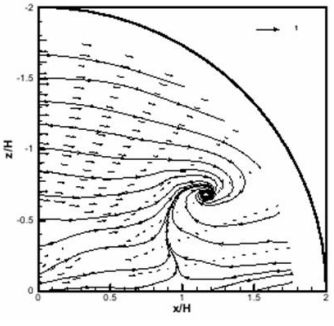

(d) Expt. on the upper recirculation eye

Fig. 4 Simulation of the 3D hill flow with the HYB0 model: resolved instantaneous and time-averaged near-wall flow structures. The flow is from the left to the right

9.3.1 Flow over a Three-Dimensional Hill

The flow over a 3D hill has been experimentally studied by Simpson et al. (2002) and Byun and Simpson (2005). The Re number, based on the hill height, h, and bulk velocity, U_b, is Re = 130000. The computational domain has a size of $(4.11+8.2)h \times 3.205h \times 11.67h$, meshed with $128 \times 80 \times 96$ cells. Figure 4 presents some results computed with HYB0 model. It is shown that the model is able to resolve reasonably the fundamental flow features of this separated flow.

It is known that the simulation is very sensitive to the inflow condition. A study has thus been performed on the effect of inflow turbulent conditions (Peng, 2006a). To approximate the inflow turbulent fluctuations for the velocity, a recycling and rescaling method is employed in the form of

$$u_{i,\text{in}} = u_{i,\text{expt}} + \frac{u_{i,rms,\text{expt}}}{\sqrt{\left(u_{i,\text{loc}} - \left\langle u_{i,\text{loc}} \right\rangle_z\right)^2}} \left(u_{i,\text{loc}} - \left\langle u_{i,\text{loc}} \right\rangle_z\right) \tag{8}$$

where $\left\langle u_{i,\text{loc}} \right\rangle_z$ is the plane-averaged velocity (over the spanwise z-direction at each time step) at a section far from the hill. The subscript "expt" indicates the quantities measured from the experiment by Simpson et al. (2002).

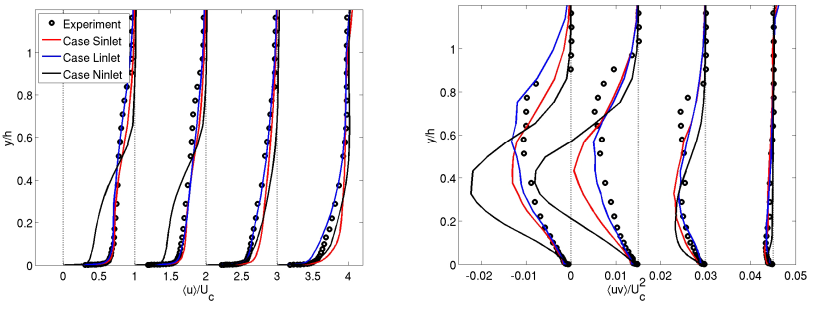

Fig. 5 Simulation of 3D hill flow with the HYB0 model. Distributions of resolved streamwise velocity and turbulent shear stress at $x/h = 3.69$ downstream of the hill

In one computation (Case Sinlet), $u_{i,\mathrm{loc}}$ has been taken from the outflow section, while another computation (Case Linlet) takes the recycling section at an upstream location, $x = 8.2h$, from the hill. These computations have been compared with the computation (Case Ninlet), which does not superimpose any turbulent fluctuations on the measured mean inflow. A comparison is presented in Figure 5, where the time-averaged streamwise velocity and the resolved turbulent shear stress are compare with the measured data over the transverse direction at a downstream location ($x = 3.69h$) from the hill. The result for the Linlet case agrees very well with the experimental measurements, while the prediction is rather erroneous without turbulent fluctuations specified at the inflow section (Case Ninlet) .

9.3.2 Supersonic Base Flow

The supersonic flow over a cylinder is characterized by flow separation and recirculation immediately after the cylinder base accompanied with expansion waves and strong recompression and, further, by near and trailing-region wakes, as shown in Figure 6. This flow is measured by Herrin and Dutton (1994) at a freestream Mach number of $M_\infty = 2.5$.

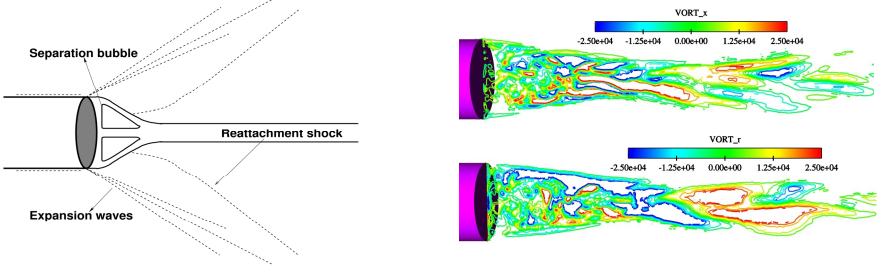

Fig. 6 Schematic of supersonic base flow over a circular cylinder

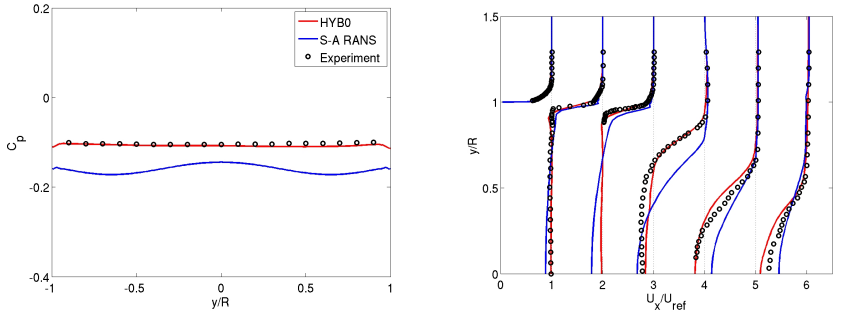

Fig. 7 Simulation of supersonic base flow with the HYB0 model. Left: Base pressure; Right: Mean streamwise velocity at different stations at the base and downstream over the separation bubble and in the trialing wake

This flow has been computed with the HYB0 model using two different grids with about 0.9 million and 1.8 million nodes, respectively. As an example, the result presented below has been computed with the fine grid. Figure 7 presents the results for the base pressure and the time-averaged streamwise velocity on different stations at the base and downstream over the separation bubble and in the trialing wake. For reference, the results from the SA RANS model are also presented with the same grid. The superiority of the hybrid modeling over RANS is obvious in comparison with experimental data by Herrin and Dutton (1994).

9.3.3 M219 Cavity Flow

The M219 cavity flow was measured by QinetiQ (Henshaw, 2002) in a transonic wind tunnel at $M_\infty = 0.85$ for a 5:1:1 (length/depth/width) rectangular cavity. The cavity flow is characterized by statistically unsteady motions due to instabilities of the mixing layer, which emanates from the incoming boundary layer being detached from the cavity leading edge and, subsequently, contained by the cavity. The success of a turbulence model for this cavity flow rests with the modelling of the flow physics of the incoming boundary layer, the shear-layer instabilities over the cavity opening and the turbulent motions inside the cavity.

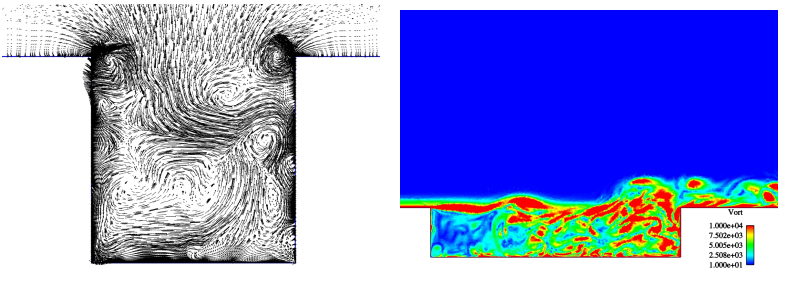

Fig. 8 Simulation of cavity flow with the HYB0 model. Left: resolved flow field on the transverse section in the middle of the cavity length; Right: Resolved vortex motion on the central symmetric section of the cavity

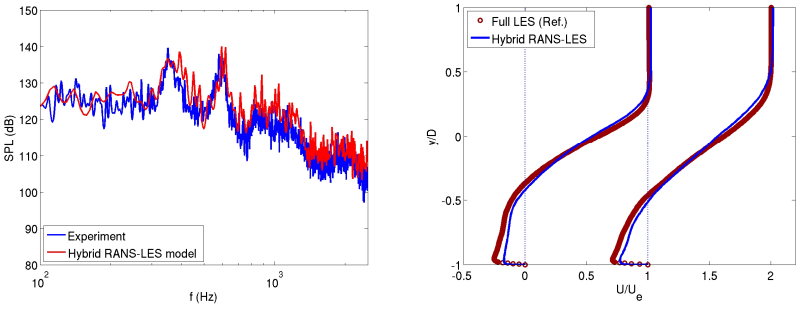

Fig. 9 Simulation of 3D cavity flow with the HYB0 model. Left: Sound pressure level, SPL, probed at a sampling point on the cavity floor; Right: Mean streamwise velocity on the mid-section of the cavity at locations x/L = 0.5 and 0.7 (L is the cavity length), respective, from the left to the right

The results presented here have been computed using an unstructured grid with about 6.2 million nodes in a large domain containing a flat plate where the cavity is embedded. Figure 8 illustrates some resolved instantaneous flow and vortex motions over the cavity opening and inside the cavity. The capability of the HYB0 model is highlighted in resolving instantaneous large-scale structures. A comparison is further given in Figure 9, where the sound pressure level, SPL, is compared with the experiment measurement, as a function of frequency, f, due to pressure fluctuations at a sampling point on the cavity floor. Also presented in the figure is the mean streamwise velocity on the mid-section of the cavity at locations x/L =0.5 and 0.7 (L is the cavity length), in comparison with the LES data by Larcheveque et al. (2004). It is shown that the modelling results agree well with the experiment for the SPL and with the LES data for the velocity. More details on the modelling of this flow can be found in Peng (2006c) and Peng and Leicher (2008).

The HYB0 model has been implemented in the general-purpose CFD solver, Edge, at FOI. Apart from the DESider project, this model has been exploited by other applications. As an example, Figure 10 presents some illustrations computed with this model for the flow around the CAWAPI F-16XL aircraft (Görtz and Jirásek, 2007) for M_∞ = 0.29 at an incidence of α = 13°. The prediction is compared with experimental data and with the SA DES modelling for the velocity near the leading edge and C_p at 39% of wing span. The simulation has highlighted the reasonable performance of the HYB0 model for industrial aerodynamic flows.

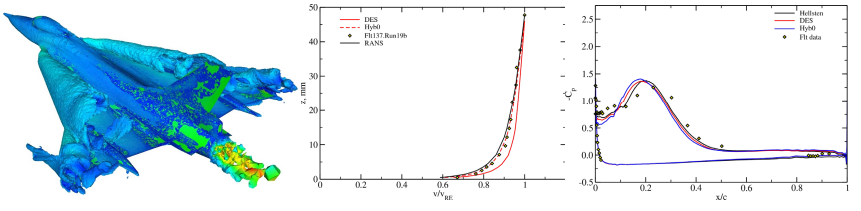

Fig. 10 Simulation of flow around F-16XL aircraft with the HYB0 modell (A courtesy from A. Jirasek, FOI)

9.4 Summary and Outlook

Some main work conducted in the DESider project has been reported, with an emphasis on the presentation of new DES and hybrid RANS-LES modelling approaches. A particular focus is on the algebraic HYB0 model and its applications to some industry-relevant aerodynamic flows.

The proposed k-DES model has shown encouraging performance. The theoretical derivation of the k-DES model is consolidated on the basis of the transport equation for turbulent kinetic energy, which is well defined in terms of turbulent flow physics and amenable from an exact equation. The model equation has been formulated with correct asymptotic properties in the vicinity of the wall surface. Nonetheless, unlike the *matured* SA-DES method, the work performed in the DESider project has just set up a framework for the k-DES formulation. Continuous effort is required for further modelling validation and improvement.

The promising modelling performance is highlighted for the HYB0 model in simulations of several particular test cases for both compressible and incompressible flows. The modelling formulation invokes a simple mixing-length RANS mode in the wall layer hybridized with the Smagorinsky SGS model in the off-wall region. The RANS-LES interface is well accommodated by means of an empirical yet effective transitional function. Unlike the standard DES method, the solution with the HYB0 model presents much less sensitivity to the near-wall RANS-LES interfacing location. It is thus flexible to implement the model for complex aerodynamic flows. Due to the algebraic modelling formulation, moreover, the HYB0 model does not invoke any additional turbulence transport equation. It is thus more computationally efficient. Compared to the SA DES model, for example, the HYB0 model may save about 15-20% CPU time.

Of the FOI contributions to the DESider project, a major part has been dedicated to the development of efficient and accurate modelling approaches in line with the requirement of aerodynamic industries. Continuous effort will be driven in this direction on further development and improvement for modelling and simulation of aerodynamic flows.

10 Approximate Near-Wall Treatments Based on Hybrid RANS-LES and Zonal Methods for LES at High Reynolds Numbers

M.A. Leschziner, F. Tessicini, and N. Li

Imperial College London

Abstract. A hybrid LES-RANS scheme developed at ICL and a two-layer zonal scheme proposed by others are introduced, and their performance is described for a number of flows investigated within DESider. The emphasis is on two particular configurations: a statistically homogeneous flow over the rear portion of a hydrofoil, separating from the upper suction surface, and a three-dimensional flow, separating from the leeward side of a circular hill in a duct. Information is also included on the performance of both schemes in fully-developed channel flow, to illustrate the basic characteristics of the schemes.

10.1 Description of Schemes

10.1.1 Hybrid RANS-LES Scheme

The principles of the hybrid scheme are conveyed in Figure 1, which also indicates the numerical coupling between the RANS and LES portions.

The thickness of the near-wall layer may be chosen freely, although in applications to follow, the layer is simply bounded by a particular wall-parallel grid surface. The LES and RANS regions are bridged at the interface by interchanging velocities, modelled turbulence energy and turbulent viscosity, the last being subject to the continuity constraint across the interface,

$$\nu_{SGS}^{LES} = \nu_t^{RANS}$$

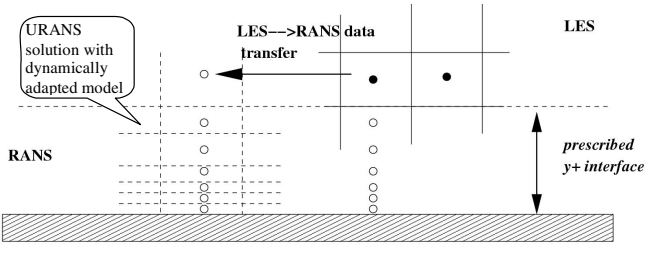

Fig. 1 Schematic of the hybrid LES-RANS scheme

The turbulent viscosity can be determined, in principle, from any turbulence model. In the case of a two-equation model,

$$\nu_t = C_\mu f_\mu \frac{k^2}{\varepsilon}$$

and matching the subgrid-scale viscosity to the RANS viscosity at the interface is effected by:

$$C_{\mu,\mathrm{int}} = \frac{\left\langle f_\mu \left(k^2/\varepsilon\right) \nu_{SGS} \right\rangle}{\left\langle \left(f_\mu \left(k^2/\varepsilon\right)\right)^2 \right\rangle}$$

where <…> denotes averaging across any homogeneous direction, or over a pre-defined patch, in case no such direction exists. An analogous approach may be taken with any other eddy-viscosity model. With the interface C_μ determined, the distribution across the RANS layer is needed. Temmerman *et al* (2005) investigate several sensible possibilities, and the one adopted here, based on arguments provided in the aforementioned study, is:

$$C_\mu(y) = 0.09 + (C_{\mu,\mathrm{int}} - 0.09)\frac{(1-e^{-y/\Delta})}{(1-e^{-y_{\mathrm{int}}/\Delta_{\mathrm{int}}})}$$

10.1.2 Zonal Scheme

As noted earlier, the objective of the zonal strategy is to provide the LES region with the wall-shear stress, extracted from a separate modelling process applied to the near-wall layer. The wall-shear stress can be determined from an algebraic law-of-the-wall model or from differential equations solved on a near-wall-layer grid refined in the wall-normal direction. The method is shown schematically in Fig. 2, was originally proposed by Balaras and Benocci (1994) and tested by Balaras *et al* (1996) and Wang and Moin (2002) to calculate the flow over the trailing edge of a hydrofoil with an immersed-boundary method.

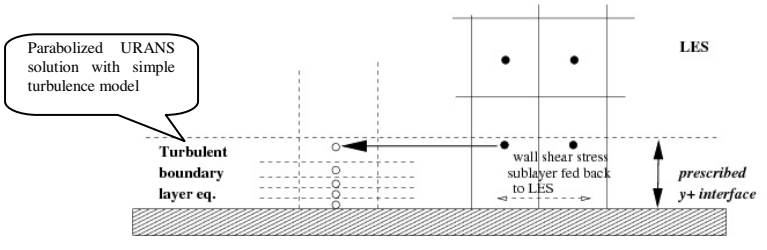

Fig. 2 Schematic of the two-layer zonal scheme

At solid boundaries, the LES equations are solved up to a near-wall node which is located, typically, at $y^+=50$. From this node to the wall, a refined mesh is embedded into the main flow, and the following simplified turbulent boundary-layer equations are solved:

$$\underbrace{\frac{\partial \rho \tilde{U}_i}{\partial t}+\frac{\partial \rho \tilde{U}_i \tilde{U}_j}{\partial x_j}+\frac{d\tilde{P}}{dx_i}}_{F_i}=\frac{\partial}{\partial y}\left[\left(\mu+\mu_t\right)\frac{\partial \tilde{U}_i}{\partial y}\right] \quad i=1,3$$

where y denotes the direction normal to the wall and i identify the wall-parallel directions (1 and 3). In most applications reported below only the pressure-gradient term been included in the left-hand side of the equation above, this left-hand side being identified later by F_i. However, more recently, the convection terms have been included, and related simulations will be included herein. The eddy viscosity μ_t is here obtained from a mixing-length model with near-wall damping:

$$\frac{\mu_t}{\mu}=\kappa y_w^+(1-e^{-y_w^+/A})^2$$

The boundary conditions for the equations governing the near-wall-layer are given by the unsteady outer-layer solution at the first grid node outside the wall layer and the no-slip condition at y=0.

10.2 Performance in Channel Flow

Extensive testing has been done for fully-developed channel flows, but much of this cannot be reported herein (see Temmerman *et al* (2005)). Some examples are shown in Figure 3, all results relating to flow at Re=42000 (Re_τ=2000). Figure 3(a) contains results arising from the hybrid scheme, with the RANS model based on either a one-equation k-l or a two-equation k-ε model, the zonal two-layer model and a reference simulation obtained with 512x128x128 grid, relative simulations with both near-wall approximations and a pure (under-resolved) LES with a 64x32x32.

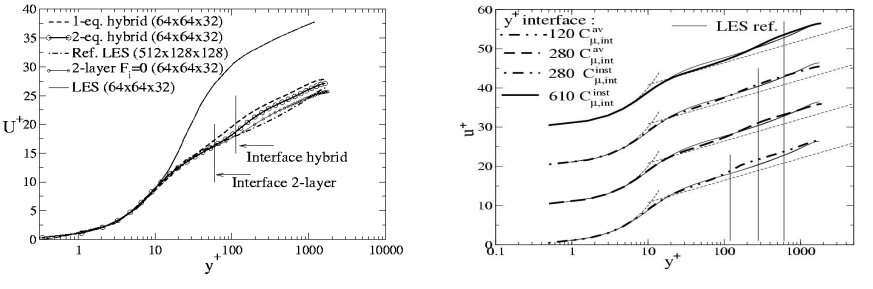

(a) (b)

Fig. 3 Velocity profiles in fully-developed channel flow at Re=42000; (a) dependence on scheme and near-wall RANS model; (b) dependence on 'spectral enrichment' at interface

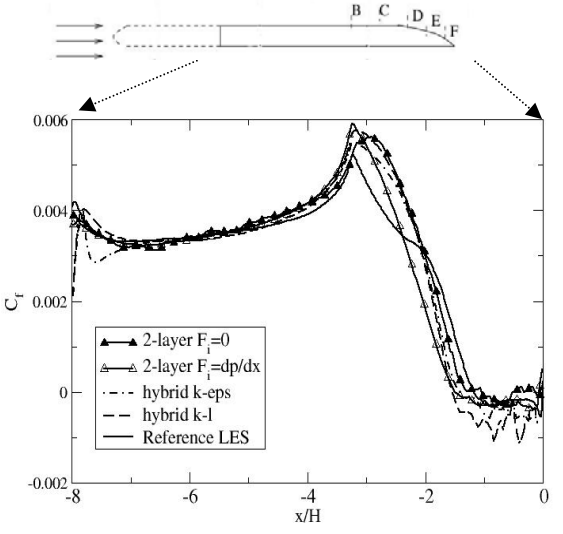

Fig. 4 Friction factor for a separated flow along the rear upper side of hydrofoil (F_i represents the convection and pressure terms that have been accounted for in the zonal implementation)

Figure 3(b) illustrates, for the hybrid RANS-LES scheme, a weak sensitivity to the location of the interface and the benefit arising from the use of the *instantaneous* interface value of the coefficient C_μ (i.e. C_μ^{inst}), relative to a spanwise-averaged value C_μ^{av}, the former constituting a form of 'spectral enrichment'. Results for channel flows at Re_τ up to 8000, obtained with the 'full' version of the zonal scheme, i.e. including all terms in the equations governing the near-wall layer, are reported in Leschziner et al (2007) and demonstrate that the inclusion of transport is of little benefit for this flow.

10.3 Separated Flow from a Hydrofoil

Selected results for a flow separating from the upper side of an asymmetric trailing edge of a hydrofoil, at a Reynolds number 2.15×10^6, based on free stream velocity U_∞ and the hydrofoil chord, are shown in Figure 4. These are taken from a paper by Tessicini *et al*. (2006). Simulations were performed over the rear-most 38% of the hydrofoil chord, using inflow conditions taken from Wang and Moin (2002), over a 512x128x24 grid, with the RANS-LES interface on the horizontal upper side at y^+=60 and 40 for the hybrid and zonal schemes, respectively. These are compared to a wall-resolved LES performed by Wang and Moin with a mesh of 1536x48x96 nodes.

It needs to be appreciated that the skin friction is an especially sensitive parameter, being linked to the velocity derivative at the wall. All formulations return reasonable agreement with the reference LES data, although there are some not

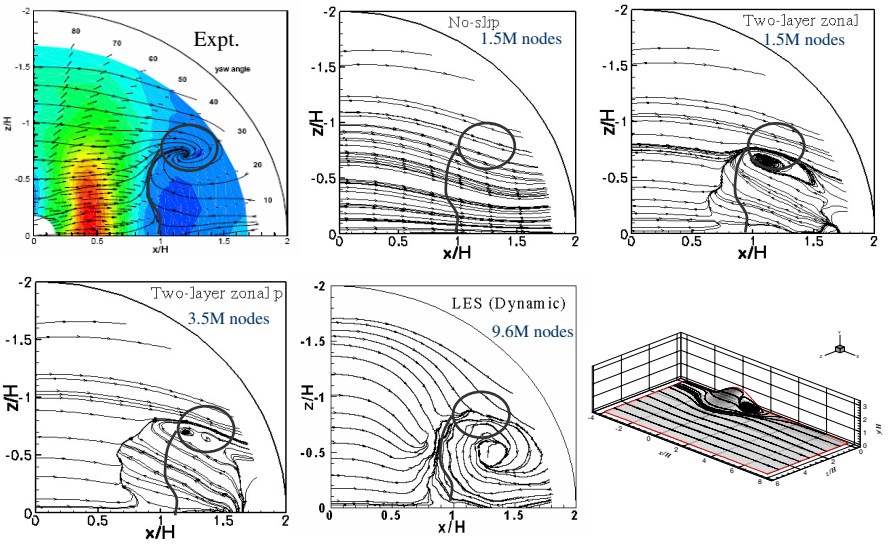

Fig. 5 3d-Hill-surface topology maps (on rear quarter of surface) computed with different grids, the coarser two using the zonal two-layer model

insignificant variations downstream of the start of the curved section, where wall curvature experiences a sudden change. Especially interesting is the observation that the inclusion of the pressure gradient in the zonal formulation (i.e. $F_i = \partial P / \partial x_i$) results in the effects of the sudden change of wall curvature being reproduced. Also, as might be expected, this formulation returns earlier separation relative to the implementation from which the pressure gradient has been omitted ($F_i = 0$).

10.4 Separated Flow over a Three-Dimensional Hill

The third application is a 3d circular hill, of height-to-base ratio of 4, is located on one wall of a duct, as shown in the inset of Figure 5. This flow, at a Reynolds number of 130,000 (based on hill height and duct velocity) has been the subject of extensive experimental studies by Simpson *et al* (2002) and Byun & Simpson (2005). Results reported here are taken from a broader exposition given in a recent paper by Tessicini *et al* (2007).

The size of the computational domain is 16*H* x 3.205*H* x 11.67*H,* with *H* being the hill height. The hill crest is 4*H* downstream of the inlet plane. The inlet boundary layer, at -4*H*, was generated by a combination of a RANS and LES precursor calculations, the former matching the experimental mean-flow data and the latter providing the spectral content. Simulations were undertaken with meshes containing between 1.5 and 9.6 million nodes, the finest-grid simulation approaching full wall resolution. Results from a fully wall-resolving 36.7 million-node simulation are reported by Li and Leschziner (2007). Coarser grids were used in conjunction

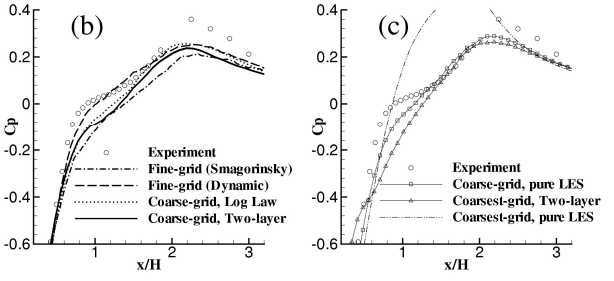

Fig. 6 Pressure-coefficient distributions on the centre-line in the leeward separation zone of the 3d hill

with the zonal scheme, wherein the interface was placed within y^+=20-40 and 40-60, using 3.5 and 1.5 million nodes, respectively. Fig. 6 shows predicted hill-surface topology maps, identifying the separation patterns that are returned by the various simulations. The designation "LES (Dynamic)" is to signify the use of the dynamic Smagorinsky model in the pure LES performed on the finest grid used. The designation "No-slip" indicates that no wall model was used on this coarsest-grid computation – i.e. this is again a pure LES computation, although one that is far from being wall-resolving. The inserted circles and connected curved lines indicate, respectively, the location of experimental focal point of the vortex and the separation line on the surface. The most important feature shown by Figure 5 is that no separation at all is predicted with the 1.5 million-node grid when a no-slip condition is applied, while a fair representation of the separation pattern is returned with the zonal scheme.

Figure 6 shows predicted surface-pressure-coefficient distributions along the hill centre line. "Coarse-grid" and Coarsest-grid" signify 3.5 and 1.5 million nodes, respectively, while "Log-Law" indicates that a log-law-based wall function has been used in the related simulation, included for comparison purposes. Most computed results agree fairly well with the experimental distribution, except the one arising from the 1.5-million-node solution with no-slip condition applied (i.e.

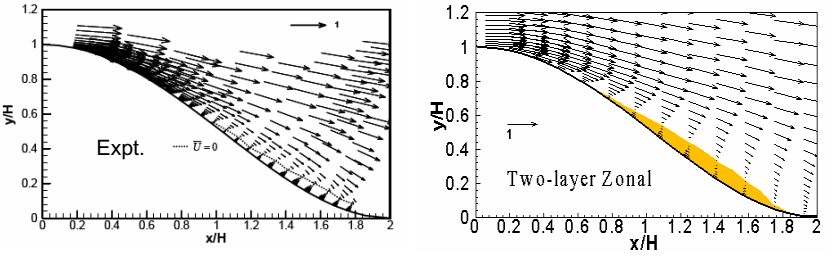

Fig. 7 Velocity field in centre plane bisecting the hill, prediction on lower plot with 3.5

million nodes (note thin reverse-flow region at the leeward side of the hill)
a pure LES on a grid that does not resolve the near-wall region). As shown in Fig. 5, this computation fails to resolve the separation, thus also returning entirely wrong pressure-recovery behaviour.

Finally, for this case, Figure 7 compares the experimentally recorded velocity field in the centre plane bisecting the hill with a simulation performed on the coarse (3.5-million-node) grid with the zonal model. A characteristic feature of the flow is a thin recirculation region located close to the hill surface, followed by reattachment close to the foot of the hill. Wang *et al* (2004) show that RANS models, at whatever level of sophistication, seriously over-estimate the size of and flow intensity in this region. As seen, the simulation with the zonal model returns a creditable representation of the reverse-flow region, and this is consistent with the favourable result for the pressure coefficient. Use of the no-slip condition on this grid results in a far too thin and short reverse-flow layer (not shown here).

10.5 Conclusions

Of the two methods examined, the hybrid approach is more expensive, but allows the interface to be placed further away from the wall and to provides a numerically consistent framework. In channel flow, the method was shown to yields results which are only weakly dependent on the location of the interface -- within reasonable limits, of course. However, in the much more complex trailing-edge flow, the solution is considerably more sensitive to the interface location, and this is a cause of some concern that needs to be explored further. In particular, it seems that the aspect ratio of the cells on the LES-side of the interface is an influential issue that needs to be examined. Relative to the earlier use of one-equation modelling in the near-wall layer, two-equation modelling does not seem to offer decisive benefits. Whatever model is adopted, small-scale (high-frequency) information is progressively lost as the near-wall layer is thickened, and this may require to be compensated for by some form of spectral enrichment.

The principal attraction of the zonal two-layer strategy lies in its economy and simplicity. It is, essentially, a method for generating, numerically, a solution in the near-wall layer, which is an improvement on the analytically prescribed log-law-based wall function. In fact, the two are virtually equivalent if pressure gradient and convection are omitted from the near-wall RANS equations. Inclusion of the pressure gradient and the results presented herein are clearly encouraging. On the other hand, the method does not allow thick near-wall layers to be prescribed without significant errors being provoked due to a serious deterioration in resolution. This also applies to wall-law-based approaches. Finally, it is arguable that the quasi-steady implementation, in which only the pressure gradient is included in the zonal scheme, is too simple. This may be appreciated upon noting that fluctuations in pressure gradient are balanced, at least to some extent, by inertial perturbations, even close to the wall. It thus follows that the transport terms may be influential, in general. However, somewhat surprisingly, initial studies for channel flow indicate that the inclusion of convection (including the unsteady term) is of little consequence, but this may reflect the particular conditions prevailing in this flow.

11 Statistical and Hybrid Turbulence Modelling for Strongly Detached Flows Around Fixed/Oscillating Bodies

R. Bourguet[1], M. Braza[1], R. El Akoury[1], G. Harran[1], Y. Hoarau[2], and G. Martinat[1]

[1] Institut de Mécanique des Fluides de Toulouse, UMR CNRS 5502
[2] Institut de Mécanique des Fluides et de Solides de Strasbourg

Abstract. IMFT has contributed in DESIDER with the application of the URANS/OES (Organised Eddy Simulation) modelling, as well as of the improved DES/OES modelling derived from DRSM-SSG for the 3D unsteady flows past a NACA0021 airfoil, around the Ahmed body and for the flow around a pitching NACA0012. This anisotropic OES approach strengthens turbulence stresses anisotropy in non-equilibrium regions. The results show improvements achieved by the OES approach in URANS and in DES.

11.1 Anisotropic OES Modelling – Tensorial Eddy-Viscosity Concept

To improve near-wall and near-wake behaviour of statistical and hybrid turbulence modelling approaches, the OES methodology can be considered (Bouhadji et al., (2002), Braza et al., (2006)), among other modelling approaches. It is briefly recalled that OES distinguishes the structures to be resolved from those to be modelled on the basis of their organised (resolved part) or chaotic character (modelled part), figure 1. This modelling can be achieved by reconsidered the URANS approach in respect of the modified shape of the energy spectrum, due to non-linear interaction of the coherent and random turbulence processes in the inertial range. This kind of modification, comparing to the equilibrium turbulence slope of -5/3 was studied by Perrin et al (2006), Braza et al, (2006). Therefore, modified turbulence scales are required for flow physics modelling of the turbulent stresses. The equations of motion in the time-domain are the phase-averaged (or ensemble – averaged) Navier-Stokes equations, (Hussain & Reynolds, 1975, Cantwell & Coles, 1983). Furthermore, by using Differential Reynolds Stress transport Modelling (DRSM) the eddy-diffusion coefficient C_μ used in OES two-equation modelling (Bourdet et al., 2007) was evaluated, by adopting the Boussinesq behaviour law as a first approximation, where turbulence stress and strain rate tensors were evaluated from DRSM. In the present, a tensorial eddy-viscosity concept has been developed, by taking into account physical characteristics of a *directional* stress-strain misalignment.

This approach is complementary to modifications of turbulence constitutive laws by means of scalar eddy-viscosity (Non Linear Eddy-Viscosity Models,

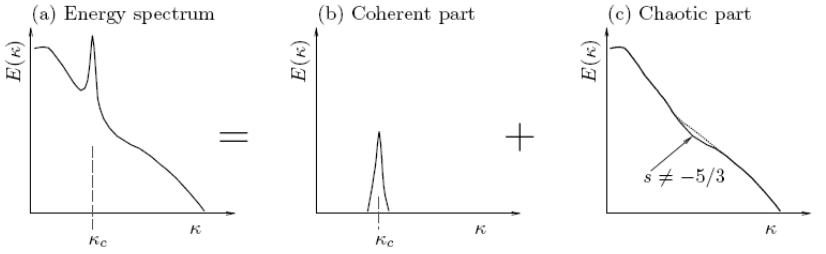

Fig. 1 Turbulence spectrum splitting in *OES*: (b): resolved part, (c): modelled part

NLEVM, or Explicit Algebraic Reynolds Stress Models, EARSM, (Pope, (1975) Shih et al., (1993), Gatski and Speziale, (1993), among other) and to the C_{as} model, (Revell et al, 2005, 2007) that suggested a scalar criterion of stress-strain misalignment derived from DRSM. Based on IMFT's circular cylinder test case, the angle between the turbulence anisotropy tensor α_{ij} and the phase-averaged strain-rate, S has been quantified by means of the 3C-PIV experimental data (described in the experimental data base contributions of the present book), figure 2.

To include these structural properties in the constitutive law, each directional contribution of the strain tensor is considered separately. A projection of the turbulence anisotropy tensor is performed onto the strain-rate principal matrices. This projection, $\hat{a}$, is investigated in the generic linear form:

$$\hat{a}_{ij} = -C_{V\alpha} V^{\alpha}_{ij} \quad \text{with} \quad C_{Vi} = -a_{\alpha\beta} V^{i}_{\alpha\beta} \quad \text{and} \quad V^{i}_{\alpha\beta} V^{j}_{\alpha\beta} = \delta_{ij} \tag{1}$$

V_i are 3 × 3 symmetrical tensors. C_{Vi} denotes the projection of −α onto V_i. Under a Boussinesq form of behaviour law, three tensors are considered, $V^i = V_i^S V_i^T$, where

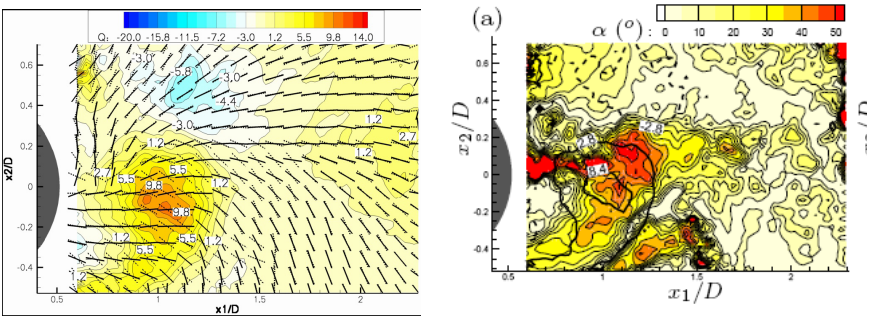

Fig. 2 (a): First principal directions between turbulence anisotropy tensor α (dashed) and strain rate S, as well as Q criterion (Hunt, 1988) iso-contours at phase angle ϕ= 50°. (b): iso-contours of the corresponding misalignment angle. Iso-lines of Q criterion (bold lines, dashed lines for Q < 0)

.T denotes the transposition. The corresponding projection coefficients are approximated by $C_{Vi} \approx 2\nu_t\lambda_t^S/k$. These matrices of rank *1* are called *S* principal matrices in the following. The coefficients C_{Vi} are predicted exactly as new state variables by DRSM-SSG transport equations, (Bourguet et al, 2007). The methodology suggested here aims at capturing directional properties of stress-strain misalignments leading to an anisotropic constitutive law. C_{Vi} projection coefficients allow identification of directional misalignments.

The suggested modelling (1) for the turbulent stress anisotropy tensor can be expressed as a tensorial eddy-viscosity model by means of a generalisation of the scalar eddy-viscosity concept towards a tensorial definition ν_{tt}:

$$(\nu_{tt})_{ij} = (\nu_{td})_\alpha V_{ij}^\alpha \quad \text{with} \quad (\nu_{td})_i = \frac{C_{V\,i}}{2\lambda_i^S} k \tag{2}$$

Transport equations for the prediction of $C\psi\eta\beta\psi$coefficients have been derived from the DRSM-SSG model (Bourguet et al, 2007). Morevover, the turbulent kinetic energy production term has the same form as in-DRSM:

$$P_k = -k\hat{a}_{\alpha\beta}S_{\alpha\beta} = -ka_{\alpha\beta}S_{\alpha\beta} \tag{3}$$

From (3), positive or even negative turbulent kinetic energy production regions can be predicted, that is not the case when using linear EVM (e.g. Carpy and Manceau (2006)). As a consequence of the projection subspace chosen here, the eigenvectors of $\hat{a}$ are also eigenvectors of the strain tensor. The linear EVM law can be generalised by means of (2) as follows:

$$-\langle u_i u_j \rangle + \frac{2}{3}k\delta_{ij} = 2S_{i\alpha}\,(\nu_{tt})_{\alpha j} = 2\,(\nu_{td})_\alpha\, S_{ij}^\alpha \quad \text{with} \quad S_{ij}^{mi} = \lambda_m^S V_{ij}^m \tag{4}$$

This anisotropic constitutive law involves the elements of a spectral decomposition applied to the mean strain-rate tensor, whose respective weights are determined by $(\nu_{td})_i$.

$$\frac{DU_i}{Dt} = \frac{\partial}{\partial x_\alpha}\left(\left(\nu\delta_{\alpha\beta} + (\nu_{tt})_{\alpha\beta}\right)\left(\frac{\partial U_i}{\partial x_\beta} + \frac{\partial U_\beta}{\partial x_i}\right) - \frac{2}{3}k\delta_{i\alpha}\right) - \frac{1}{\rho}\frac{\partial P}{\partial x_i} \tag{5}$$

The near-wall turbulence damping functions are the same as in Jin and Braza (1994).

11.1.1 DES Associated with OES

IMFT applied the DES/OES – Organised Eddy Simulation approach to predict the DESIDER test-cases. It is recalled that the turbulence length scale in the RANS part of DES can be modified according to OES.

$C_{\mu OES}$ was reconsidered either by means of the DRSM-LRR model and adopting Boussinesq behaviour law as a first approximation (Braza et al, (2006), Hoarau et al, (2006), or by means of the tensorial eddy-viscosity concept yielding a

directional eddy-diffusion coefficient as previously described, to strengthen the turbulence stress anisotropy. These aspects allow capturing non-equilibrium turbulence effects in the near-wall and near-wake detached flow regions. It has been shown that the adaptive C_μ coefficient reaches values of order 0.02 in non-equilibrium regions as in case of the Boussinesq-law OES two-equation modelling with a constant eddy-diffusion coefficient value. It was shown (Bourdet *et al*, 2007) that the velocity scale $k^{0.5}$ based on the turbulence kinetic energy, k is reduced by a factor of 4.5 that corresponds to a reduction of the DES l_{RANS} length scale, l_{OES} by 0.022 in the non-equilibrium regions and therefore to a consequent increase of the dissipation rate in the k transport equation, comparing with the use of the equilibrium turbulence length scale $l_{RANS} = k^{3/2}/\varepsilon$. Therefore, in DES/OES implementation of two-equation modelling, the eddy-diffusion coefficient is taken 0.02 in case of constant C_μ (scalar eddy-viscosity). Consequently the dissipation term in the k-transport equation, $D^k_{DES}=\rho k^{3/2}/l_{DES}$ is modified according to: $l_{DES}=\min(l_{OES}, C_{DES}\Delta)$. This has been used in the following test-cases presented DES computations. Furthermore, l_{OES} can be taken as the $\min(l_{i,\mathrm{OES}})$ corresponding to the $(\nu_{td})_i$ directions of the eddy-viscosity (4), in case of the tensorial eddy-viscosity law.

The above length scale replaces the RANS length scale in DES, according to the relation:

$$l_{DES} = \min(l_{RANS}, C_{DES}\Delta)$$

For example, in case of DES-k-ω model, $l_{OES} = k^{1/2}/C_{\mu,OES}\omega$.

Numerical method for all the test cases, IMFT has used the NSMB code (Navier-Stokes MultiBlock) where it included recent developments in DES/OES and DRSM modelling. Structured multiblock meshes have been employed as well as the third-order upwind Roe scheme (1981) for convection terms. Central second order spatial scheme has been used for the diffusion terms.Dual time stepping with constant CFL values of order 10-3 (dimensionless) with implicit second order time scheme has been employed.

11.2 Results

11.2.1 NACA0012 at Re=10^5, a=20° - "in House" Test Case

The present in house test case has been considered in 2D, as in the FLOMANIA research program, to first examine the predictive ability of the tensorial eddy – viscosity concept. A previously validated C-type mesh (256 × 81 nodes), Hoarau (2002), has been employed.

Table 1 Statistically averaged global parameters

	Experiment	k-ε Chien	k-ω SST 2D	OES k-ε 2D	OES k-ε 3D	A_OES
C_D	0.32	0.33	0.36	0.36	0.33	0.32
C_L	0.75	0.80	0.87	0.86	0.70	0.77

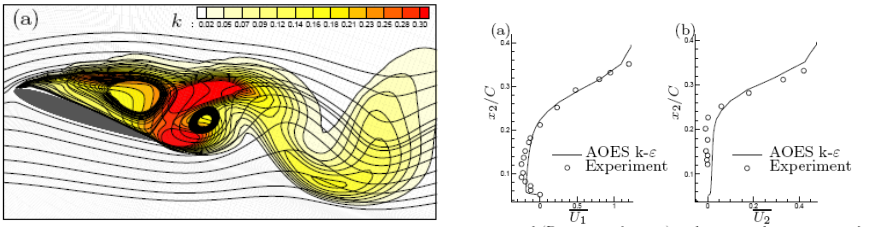

Fig. 3 Iso-contours of the angle between the first principal directions of –a and S at phase angle $\phi = 50^{o}$. Iso-lines of Q criterion (bold lines, dashed lines for $Q < 0$)

Comparison of global parameters with the experiment by Berton et al (UNSI European program) is presented in Table 1. In the following, the OES using the turbulence behaviour law with tensorial eddy-viscosity concept is designated by "AOES". An improved prediction of the aerodynamic coefficients is achieved. Comparison of the longitudinal and vertical velocity profiles with the experiment is provided in figure 3 (right). A good agreement is obtained. Figure 3 (left) shows

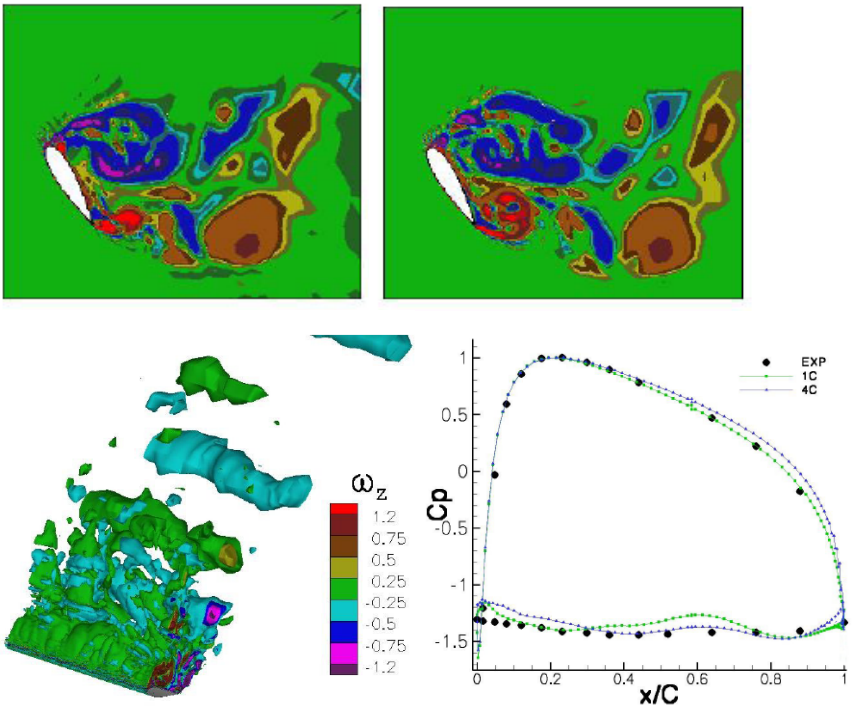

Fig. 4 Iso-vorticity contours and wall pressure coefficient; comparison between *1C* and *4C* spanwise lengths

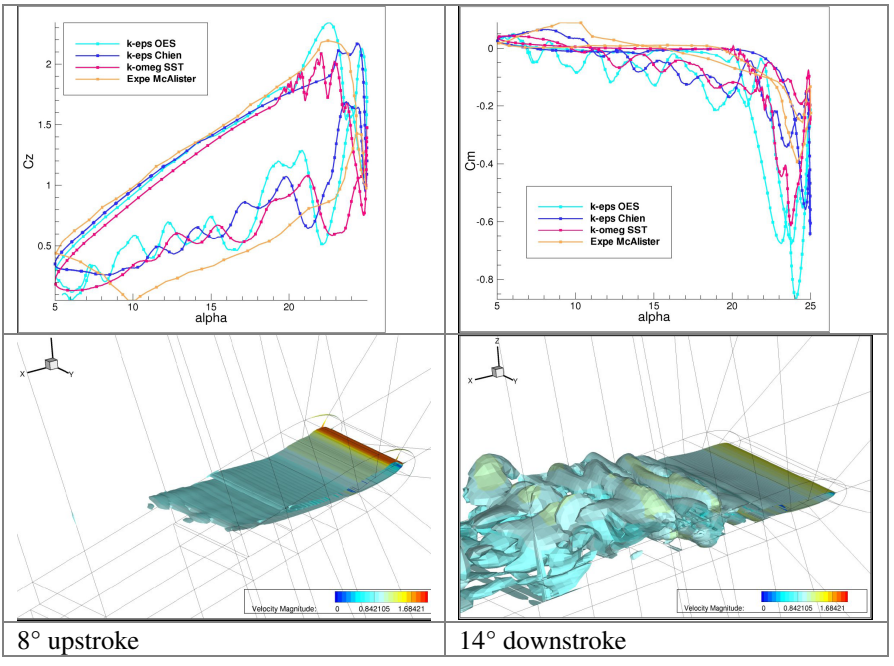

Fig. 5 Up: CL and Cm hysteresis loops, Mc Alistair test case. Down: 3D wake structure, Berton et al (2002) upstroke velocity, DES/CEASM (left); Iso-vorticity component ω_z, DES/OES (right)

phase-averaged iso-contours of the turbulence kinetic energy. By the present model the usually excessive rate of k around the leading edge region (Jin and Braza, 1994) that occurs in a number of two-equation URANS models is avoided.

11.2.2 NACA021 beyond Stall Test Case

The numerical grids are 148x104x35 for the *1C* spanwise chord length and 148x104x135 for the *4C* spanwise chord length.

The results discuss first the global parameters as well as the statistically averaged flow quantities compared with the experiment. Different kinds of eddies are captured by the DES/OES approach, the von Karman and Kelvin Helmholtz vortices, as well as the thin rotational/irrotational interface in the wake, downstram from the separation points (figure 4) that is an important feature for aeroacoustics use of the method (Hunt, 2008).

Table 2 shows comparison of the global parameters among different turbulence models. An improved prediction with the DES/OES model is achieved.

11.2.3 Pitching NACA0012 Airfoil

This test-case corresponds to the Mc Croskey & Mc Alistair (1978) DESIDER test case. The grid provided by TUB has been employed. In addition, results have

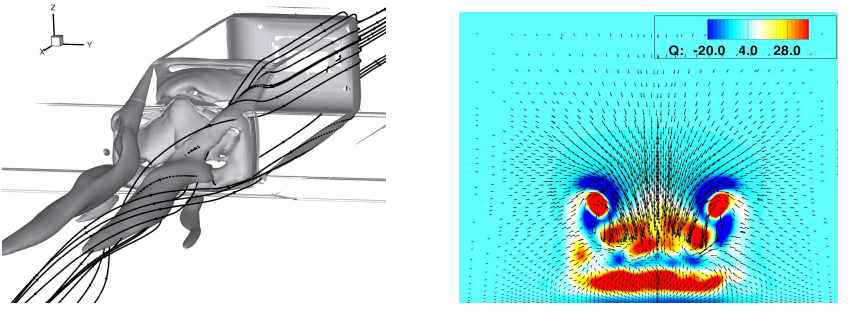

Fig. 6 Iso-surfaces of criterion Q=20; right: Iso-contours of *Q* criterion in transverse plan *X*=138 mm

Table 2 Global parameters according to different turbulence model

NACA0021	DES-SA	DES-*k*-ω	DES-OES-*k*-ω	Exp
CD	1.851	1.796	1.682	1.547
CL	1.106	1.093	1.002	0.931

been produced for the "in-house" pitching 3D flow test case by Berton et al (2002). Figure 5 shows the comparison of the aerodynamic coefficients hysteresis loops with the experiment. The oscillation amplitudes kept up by the OES modelling correspond to the unsteady dynamic stall vortices detachment as in DNS by Bourdet et al (2007). All models are found to overpredict (in absolute value) the negative *Cm* coefficient, a crucial parameter for rotorcraft design. A 3D view is provided corresponding to upstroke and downstroke phases of the pitching motion (Berton et al, 2002). It is noticeable that the downstroke phase of the motion only is characterised by strong 3D secondary instability of the deep dynamic stall, (Martinat et al, 2007).

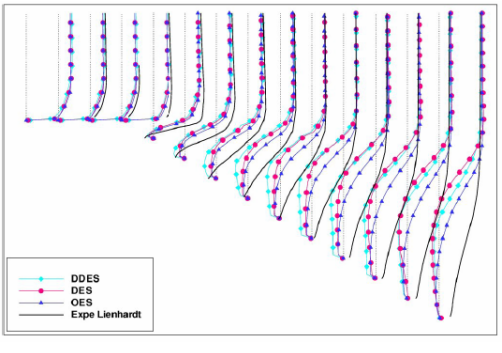

Fig. 7 Comparison of the velocity profiles (rear part) among different models and the experiment (Lienhardt, 2003)

11.2.4 The Ahmed Car Body

The numerical grid is provided by Chalmers Univ. It consists of 3.6 M points and is composed by 78 blocs. The near wake vortex structure is illustrated in figure 6 (OES model). Comparison of the velocity profiles among the different models used is given in figure 7. OES and DDES provide results closer to the experiment.

11.3 Conclusions

The presented developments indicate interesting predictive capabilities of the OES approach, including its tensorial eddy-viscosity version, as well as of the DES/OES approach, concerning the test-cases investigated. As an outlook, DES involving directly DRSM, as well as NLEVM associated with tensorial eddy viscosity concept merit to be examined.

12 Hybrid RANS–LES Simulations at NLR Using X-LES and a High-Order Finite-Volume Method

J.C. Kok, B.I. Soemarwoto, and H. van der Ven

National Aerospace Laboratory NLR

Abstract. This chapter highlights some of the work performed at NLR during the course of the DESider project. For hybrid RANS–LES computations, NLR has developed the X-LES method, which consists of a composition of a RANS k–ω turbulence model and a k-equation SGS model. To improve the numerical accuracy in the LES regions, a high-order finite-volume method has been developed. The method is strictly fourth-order accurate on smooth, non-uniform, curvilinear grids, preserves the skew-symmetry of the compressible convection operator, and has low numerical dispersion. The improved accuracy over a second-order method is shown by performing grid-convergence studies using a fixed filter width. Finally, the instability of shear layers in X-LES computations is briefly discussed.

12.1 X-LES Method

The X-LES formulation (Kok *et al*., 2004) is a particular DES method (Spalart *et al*., 1997) that consists of a composition of a RANS k–ω turbulence model and a k-equation SGS model. Both models use the Boussinesq hypothesis to model the Reynolds or subgrid-scale stress tensor, which depends on the eddy-viscosity coefficient ν_t. Furthermore, both models are based on the equation for the modelled turbulent kinetic energy k, which depends on its dissipation rate ε. Both the eddy viscosity and the dissipation rate are modelled using the turbulent kinetic energy as velocity scale together with a length scale l_t,

$$\nu_t = l_t\sqrt{k} \qquad \text{and} \qquad \varepsilon = \beta_k \frac{k^{3/2}}{l_t},$$

where l_t is defined as a combination of the RANS length scale $l = \sqrt{k}/\omega$ and the SGS filter width Δ,

$$l_t = \min\{l, C_1\Delta\},$$

with $C_1 = 0.05$. The RANS k–ω model is completed by an equation for the specific dissipation rate ω. The X-LES method will be in LES mode when the filter width (times C_1) is small compared to the RANS length scale. Note that in that case the SGS model is completely independent of ω.

12.2 High-Order Finite-Volume Method

In order to reduce the interference of numerical discretization errors with the SGS model, a high-order finite-volume scheme is employed. Details of this scheme are

given by Kok (2006, 2008). In particular, the high-order scheme is used to discretize the inviscid terms of the flow equations. The diffusion terms (viscous terms and terms due to turbulence model) as well as the transport equations of the k–ω model are discretized with a standard second-order finite volume scheme. The high-order finite-volume scheme has the following key properties:

- It is formally fourth-order accurate. The order of accuracy is maintained on non-uniform curvilinear grids, provided they are sufficiently smooth. The finite-volume method has been made fourth-order accurate by extending the approach of Verstappen & Veldman (2003), which uses Richardson extrapolation, from Cartesian to curvilinear grids.
- The numerical dispersion of the scheme is minimized by extending the dispersion-relation preserving approach of Tam and Webb (1993) to finite-volume schemes. Minimizing the numerical dispersion is equivalent to minimizing the implicit filter introduced by the numerical discretization, thus reducing the numerical errors relative to the SGS model.
- A central scheme is employed, containing no numerical dissipation. A small amount of sixth-order artificial diffusion is added explicitly to enhance stability. The artificial diffusion is scaled such that it introduces an error of only fifth order.
- The finite-volume approach leads to local conservation of mass, momentum, and energy.
- The discretization is based on the skew-symmetric form of the compressible convection operator in such a way that kinetic energy is exactly conserved by convection. For incompressible flow, this implies that the total kinetic energy cannot increase, ensuring numerical stability. For compressible flow, this is not the case (the total kinetic energy can increase due to work done by the pressure), but the advantage of the skew-symmetric form is that it does not lead to production or dissipation of kinetic energy interfering with the SGS model.

In order to test the capability of the high-order finite-volume scheme to accurately capture vortices without significant dissipation or dispersion, the convection of a 2D isentropic vortex in a uniform flow at $M_\infty = 0.5$ is considered. The vortex has a maximum induced velocity $u_A = 0.8\ u_\infty$, located at a radius b. Computations are performed on a strongly non-uniform (but smooth) grid over a time interval of 26 convective time units (based on u_∞ and b.) Using the new high-order method, the shape and location of the vortex is greatly improved compared to a standard second-order method (Figure 1). See Kok (2008) for details.

Although the high-order scheme is intended for the LES regions, it has been implemented throughout the complete flow domain. This means that the RANS region is also solved with the fourth-order scheme. In contrast, others have proposed hybrid numerical schemes (e.g., Travin *et al.*, 2002), in which a second-order upwind scheme is used in the RANS region. Because second-order accuracy is considered sufficient in the RANS region, no effort has been made to develop a fourth-order accurate boundary condition at solid walls. A second-order accurate boundary condition is used instead.

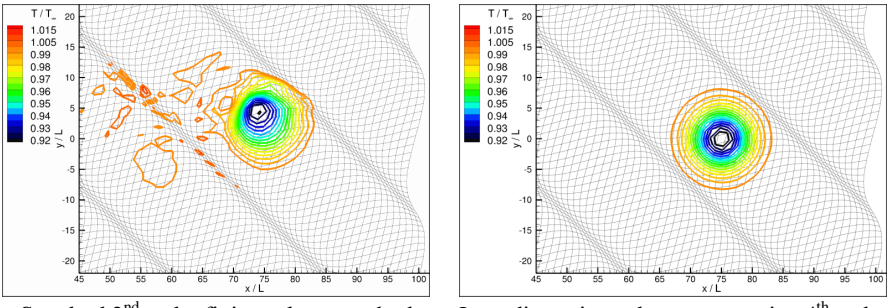

Standard 2nd-order finite-volume method

Low-dispersion skew-symmetric 4th-order finite-volume method

Fig. 1 Convection of isentropic vortex on strongly non-uniform grid. Vortex position after 26 convective time units

12.3 Grid Convergence

If a large-eddy simulation (LES) employs an explicit subgrid-scale (SGS) model, and one is interested in validating this model, then it is important to distinguish modelling errors from numerical errors. Typically, for a given numerical method, this is done by performing a grid convergence study. For LES, this requires that the SGS model is independent from the grid resolution, which can be obtained by fixing the filter width Δ. The mesh size h can then be varied relative to this fixed filter width. Second-order schemes typically require at least four grid cells per filter width, i.e., $h \geq \Delta/4$ (e.g., Vreman *et al.*, 1997). The advantage of the fourth-order finite-volume method is that it achieves at least the same accuracy with only two grid cells per filter width ($h = \Delta/2$). This has been verified by performing a grid-convergence study for the energy spectrum of isotropic homogeneous turbulence (Figure 2).

A grid-convergence study also has been performed for the NACA0021 airfoil at 60° angle of attack (see section IV.3 for a full description of this test case).

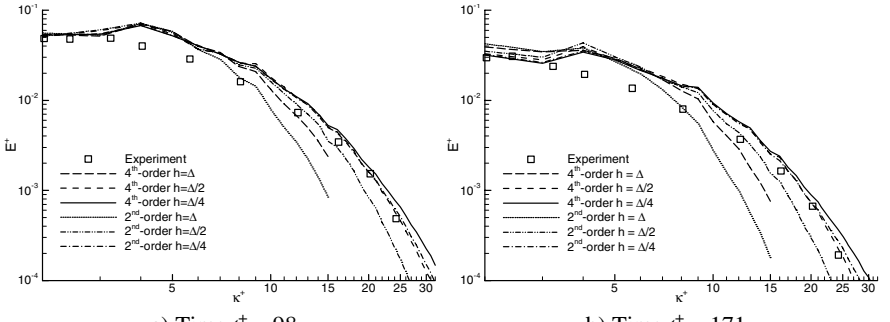

a) Time $t^+ = 98$

b) Time $t^+ = 171$

Fig. 2 Incompressible isotropic homogeneous turbulence: grid dependence of energy spectra for standard 2nd-order and low-dispersion skew-symmetric 4th-order methods

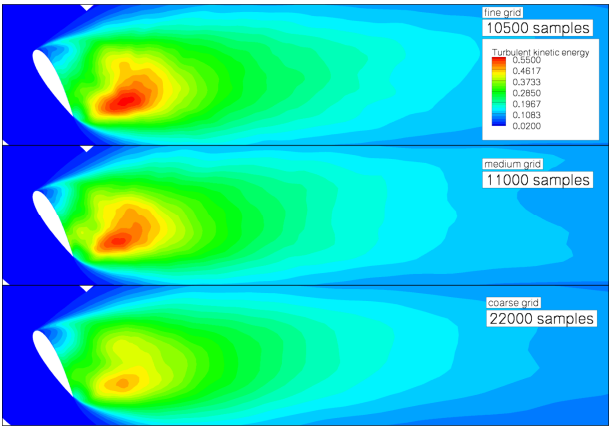

Fig. 3 NACA0021 airfoil at 60° angle of attack: Resolved turbulent kinetic energy of X-LES computations on a series of grids using high-order finite-volume method

Figure 3 shows the resolved turbulent kinetic energy on a series of three grids using the high-order finite-volume method. The filter width is defined as the maximum of the mesh size in the different computational directions on the coarse grid. At least the medium grid level, with one-and-a-half mesh sizes per filter width, is needed to have a reasonable grid-converged solution. A more detailed analysis of grid-convergence issues for this case is given by Weinman *et al.* (2006).

The effect of the high-order finite-volume method has also been tested for the turbulent, separated flow over a rounded bump in a square duct (so-called ONERA bump). This standard DESider test case is fully described in sections III.1 and IV.10. To study the grid dependence of the numerical schemes, a coarse and a fine grid are considered, with the coarse mesh size equal to twice the fine mesh size, where the fine grid has 284×120×152 cells. The filter width is defined as the maximum of the mesh size in the different computational directions on the coarse grid. In other words, per filter width, the coarse grid has one grid cell whereas the fine grid has two.

Profiles in the centre-plane of the time-averaged velocity are given in Figure 4. The grid dependence of the velocity profiles is clearly weaker for the fourth-order method than for the second-order method. In particular the second-order coarse-grid result deviates strongly from the other results. The fourth-order results are closer to the experiment, although a substantial difference remains. This case is discussed in more detail by Kok *et al.* (2007).

12.4 Shear Layer Instability

DES-type methods originally are intended for flows with massive separation. Usually, a shear layer develops downstream of the separation point. Shear layers are intrinsically unstable as their velocity profiles contain an inflection point. The spreading rate and turbulence levels in the shear layer may strongly influence the

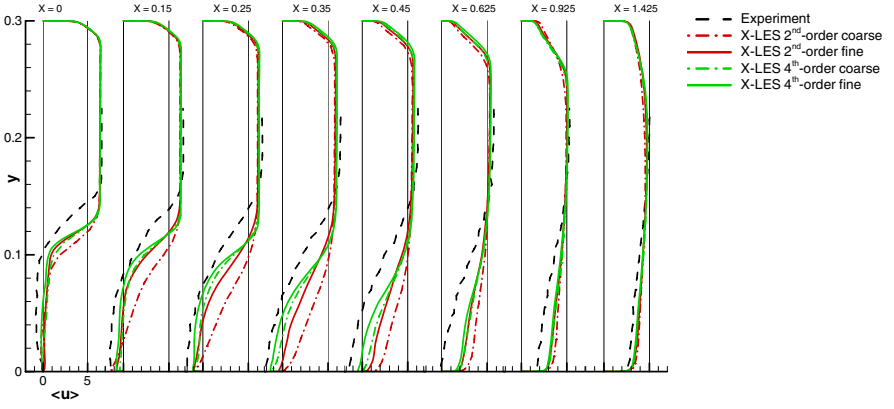

Fig. 4 ONERA bump: time-averaged velocity profiles (*x*-component) along cross sections in centre-plane for high-order X-LES computations

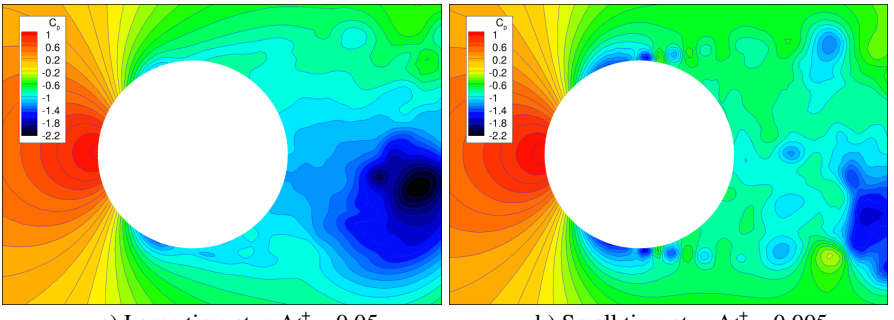

a) Large time step $\Delta t^+ = 0.05$ b) Small time step $\Delta t^+ = 0.005$

Fig. 5 Circular cylinder ($M = 0.3$, $Re = 5.4 \cdot 10^4$): Instantaneous pressure coefficient of high-order X-LES computations

separated flow region downstream. This means that the shear layer must be resolved with sufficient accuracy by the numerics. An example of the sensitivity of the shear layer to numerical parameters is given in Figure 5. For the flow around a circular cylinder, an initially stable shear layer becomes unstable if a time step is used that is substantially smaller than what is commonly used. This effect was also observed by Mockett *et al.* (section V.17).

In real life, the instabilities in the shear layer are triggered by external disturbances (free-stream turbulence, noise, ...), the so-called receptivity. Thus, the growth of instabilities in the shear layer will depend on the disturbance environment and therefore will be different in windtunnels or free flight. Such physical disturbances are normally not included in the numerical computations. If the computations also have a high numerical accuracy, as is the case when using

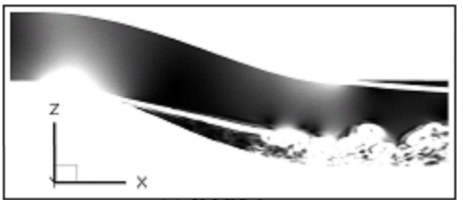

a) Instantaneous Schlieren-like plot for simplified high-offset engine inlet

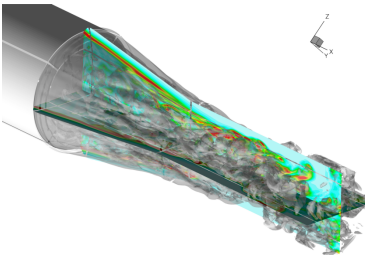

b) Instantaneous vorticity contours in wake of supersonic flow along circular cylinder

Fig. 6 Behaviour of shear layer for high-order X-LES computations

high-order schemes, then also numerical disturbances will be low (see Figure 1). As a consequence, the computations may show a long extent of the shear layer where the resolved turbulence is low, before becoming unstable. This is illustrated in Figure 6 for the flow inside a simplified engine inlet, where flow separation occurs due to the S-shape of the inlet, and for the supersonic flow along a circular cylinder, where the flow separates at the base of the cylinder. Such long 'stable' extents of the shear layer are typically not found in experiments due to higher disturbance levels. Reproducing experimental results may require introducing similar disturbances in the computations; a topic for future research.

12.5 Application

The X-LES method has been applied to simulate the flow around a simplified landing gear of the Boeing 757 (see Section 4.20). This configuration was measured in the Basic Aerodynamic Research Tunnel (BART) at NASA Langley Research Center. It was reported that during the experiment the flow alternates between two mean flows. Figure 7a shows streamline patterns of the first

ground side

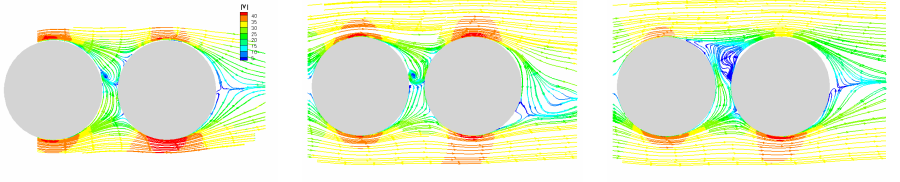

wing side

a) Mean flow pattern from experiment, streamlines coloured by velocity magnitude

b) Flow pattern observed shortly during the transient of the X-LES simulation

c) Mean flow pattern resulting from the X-LES simulation

Fig. 7 Pattern of the streamlines on the PIV plane (coloured by the velocity magnitude)

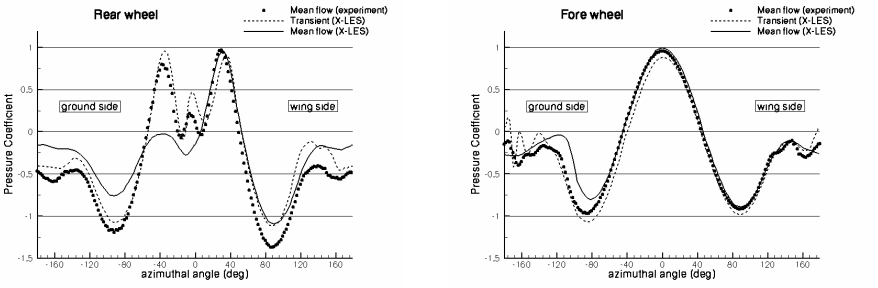

a) rear wheel b) fore wheel

Fig. 8 Sectional pressure coefficient distribution on mid-plane of fore and rear wheels

(more persistent) mean flow in the PIV plane. On the ground side, the separating streamline forms a vortex roll-up residing persistently near the fore wheel.

Figure 7b presents a flow feature observed for a short period during the transient of the X-LES simulation. This closely resembles the first mean flow and sectional pressure distribution of the experiment, shown respectively in Figure 7a and Figure 8a. It contains the same features occurring in the experiment, i.e. the separation point near the azimuthal angle of zero degrees and the attachment points around the azimuthal angle of +/- 40 degrees on the rear wheel. However, it does not materialize into a stable vortex roll-up. A possible explanation is that it is formed during the transient when disturbances are still large. For example, Figure 8b shows a wavy pressure distribution on the fore wheel near the azimuthal angle of around -160 degrees (i.e. a position above the vortex roll-up), which may be a manifestation of such disturbances. As a consequence, the vortex migrates progressively upwards exiting the region between the wheels, after which the flow becomes like one shown in Figure 7c. This mean flow may resemble the second mean flow of the experiment. Unfortunately, this cannot be confirmed because there is no PIV data available for the second mean flow. Nevertheless, such a susceptibility of the flow to disturbances during the transient has to be investigated in future research.

12.6 Conclusion

A high-order finite-volume method has been developed for hybrid RANS–LES computations using the X-LES method. Considering a fixed filter width, the fourth-order method substantially improves the grid convergence compared to a standard second-order method, obtaining the same numerical accuracy with two instead of four cells per filter width. A side effect of the high-order method is that the triggering of shear-layer instabilities by numerical disturbances is reduced. Future work will be directed at studying the receptivity of the shear layer to physical disturbances.

13 Contribution of NTS

A. Garbaruk, M. Shur, M. Strelets, and A. Travin

NTS

Abstract. A summary is presented of NTS activity in the framework of DESider project. Section 14.1 provides a general overview of the work performed. Section 14.2 contains some general comments on two enhanced versions of the original DES technique, Delayed DES or DDES and Improved DDES or IDDES, developed in the course of the project (their comprehensive presentation is given in Section 4 of Chapter II). It also presents numerical examples of application of these models highlighting their important features not reflected in test-cases chapter IV due to the space-limit. Finally, section 14.3 digests a validation activity of NTS in the project and formulates some conclusions based on this activity.

13.1 General Overview

NTS activity in DESider in the area of turbulence simulation has been focused on a further development of DES and DES-like hybrid RANS-LES approaches. This includes, first of all, improvement and enhancement of the original DES model aimed at increasing its reliability and widening application area. Other than that, relatively restricted efforts have been invested into development and testing of a simple k-ω URANS approach with turbulence resolving capabilities (Turbulence-Resolving RANS or TRRANS) and into implementation of SAS approach developed by ANSYS in the in-house NTS code. A comprehensive presentation of all these approaches is given in sections 4 and 5 of Chapter II and some additional material is presented in Sections 14.2, 14.3 below.

The directions of modelling activity defined a selection of test cases chosen by NTS for validation purposes. These cases can be divided into two groups.

The first group includes natural DES applications, i.e., massively separated flows (NACA 0021 airfoil at 60^o angle of attack, supersonic base, wall-mounted cylinder, 3D cavity, and simplified landing gear). The work of the DESiser Consortium on the two first of these flows was coordinated by NTS.

The second group includes attached and shallow separated flows (developed channel flow and separated flow behind an aerofoil trailing edge). One more computed flow is a mandatory test case “Bump in square duct” studied experimentally by ONERA within DESider. This flow belongs to a mixed type and includes both significant attached regions and a moderate separation area.

13.2 DES Enhancements

13.2.1 Delayed DES (DDES)

A major flaw of the original DES formulation of Spalart et al., 1997 (DES97) is an odd reaction to the “excessive” refinement of grid in the wall-parallel direction.

This deficiency known now under the names of Grid-Induced Separation or GIS (Menter and Kuntz, 2002) and Modelled Stress Depletion or MSD (Spalart et al., 2006) originates from the so-called "grey area" (an intermediate region between the RANS and LES domains of DES). Although considered as not being a real issue due to restricted computer power in 1997, it drew complaints already in the very beginning of the current century (Caruelle, 2000 and Deck, 2002). Not surprisingly, this had motivated a search for efficient and simple remedies and resulted in the "shielded" DES proposed by ANSYS for the k-ω SST-based version of DES already in the course of the EU Project FLOMANIA (Menter and Kuntz, 2002) and in the Delayed DES or DDES (Spalart et al., 2006), which is a derivative of the Menter and Kuntz proposal applicable to DES with whatever background RANS model developed by NTS in the framework of DESider in collaboration with ONERA and US colleagues. A detailed outline of the DDES is presented in Section 4.3 of Chapter II of this book. So here we dwell upon only the DDES calibration, which is not presented there but seems to be important for a better understanding of the model.

DDES formulation involves an empiric delay function $f_d = 1 - \tanh(8[r_d]^3)$, where r_d is the parameter borrowed from the S-A RANS model as an indicator of the boundary layer. The values 8 and 3 for the constants in this function are based on intuitive shape requirements for f_d and on DDES computations of the flat-plate boundary layer on a series of grids with fine wall-parallel spacing. The objective of the exercise was to choose such values of the constants, which ensure that in the attached boundary layers the RANS mode of DDES prevails and therefore the DDES solution is essentially identical to the RANS one, even if the wall-parallel grid spacing is much less than the boundary layer thickness.

An example of exactly such behaviour of the DDES is presented in Fig.1, which compares RANS, DES97 and DDES solutions in a boundary layer with the wall-parallel grid spacing about 1/10th of its thickness. This is a very severe test with the "ambiguous-grid" region penetrating deep into the boundary layer. The figure shows that, as expected, DES97 reduces the peak eddy viscosity by about 75% from the RANS prediction (corresponding reduction of the skin friction is

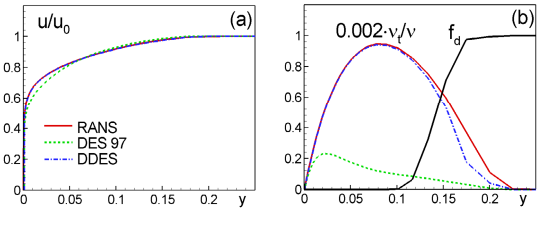

Fig. 1 Velocity (a) and eddy-viscosity (b) distributions in flat-plate boundary layer with unit Reynolds number 10^6 (Re_x=~1.2×10^7, Re_θ=~1.8×10^4) computed with the use of different approaches on a grid with $\Delta_{||}=0.1\delta$

19%). In contrast, DDES preserves the eddy viscosity almost fully, and its small deficit at the edge of the boundary layer is very acceptable. It could be eliminated by slanting the f_d function towards more "shielding" by a value of the constant larger than 8, but at some point it would suppress LES behaviour where such behaviour is best.

An important general comment concerning the DDES approach is that in spite of the outward simplicity and "cosmetic" character of the changes compared to DES97, they present a relatively deep change in philosophy of DES since the length-scale limiter in DDES depends on the solution, rather than only on the grid as in DES97. This, in particular, results in non-uniqueness (dependence on initial conditions) of the DDES equations applied as a wall-model in LES (see Spalart et al., 2006). However, DDES is aimed not at the derivative use of the DES formalism for WMLES (this issue is addressed by IDDES approach considered below) but at better fulfilling the original mission of DES, i.e., reliable prediction of massively separated flows. For such, natural, DES applications, DDES has been shown to be more reliable and user-friendly than DES97 in many studies both within (see Chapter IV) and outside DESider consortium and, therefore, today this DES version can be firmly recommended as the only working version of DES.

13.2.2 DDES with Improved Wall-Modelling Capability (IDDES)

The ambition of this approach is building a single set of formulas applicable to both natural (D)DES applications and WMLES uses, so that different flows or (more importantly) different regions inside a single simulation over a complex geometry can each be *automatically* treated by a very capable model. Moreover, in its WMLES mode, a remedy has to be found of the Log-Layer Mismatch (LLM) most available wall-modelling LES approaches suffer from. An approach that claims to possess these features developed by NTS in the course of DESider was named DDES with Improved Wall-Modelling capabilities or IDDES (Travin et al., 2006, Shur et al., 2008).

One of essential new elements of IDDES presented in detail in Section 4 of Chapter II is a definition of the subgrid length-scale, which, unlike the conventional definitions, explicitly involves not only the grid spacing but also the

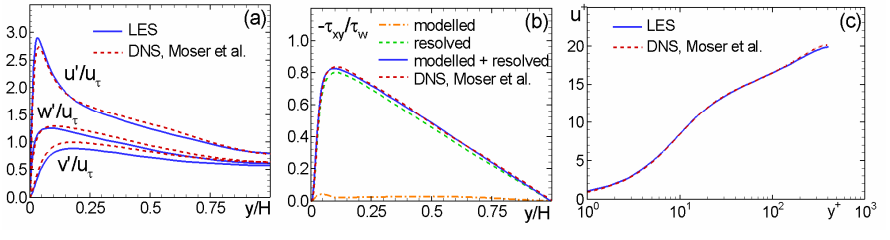

Fig. 2 LES of developed channel flow at Re_τ=400 with length-scale defined by eqn. (4.11) of Chapter II: (a)–resolved normal Reynolds stresses; (b) - resolved and modelled shear Reynolds stresses; (c) - velocity profiles

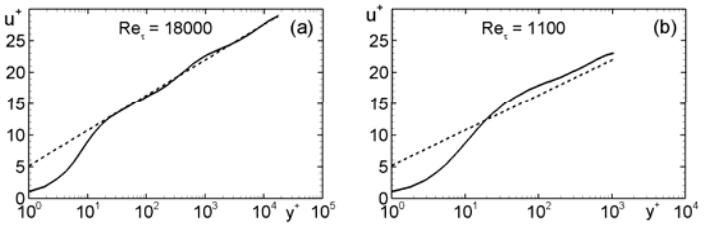

Fig. 3 Mean velocity profiles in developed channel flow at $\mathrm{Re}_\tau = 18{,}000$ and 1100 computed with the use of the algebraic DES model and subgrid length-scale defined by eqn. (4.11) of Chapter II. Dashed line – log law

distance to the wall. Some examples of plausible performance of this length-scale within IDDES are given in Chapter IV (Sections 9, 10, 12). However the definition turns out to be helpful also within both conventional well-resolved LES and pure DES models. This claim is supported by Figs.2, 3. In particular, Fig.2 compares results of the Smagorinsky well-resolved LES of developed channel flow at Re_τ=400 employing the proposed subgrid length-scale with the DNS of this flow by Moser et al., 1999. Note that the Smagorinsky constant in this simulation is equal to 0.2, i.e., has the value adjusted in simulations of DIHT with the NTS code. As far as DES is concerned, its performance with this length scale is demonstrated by Fig.3, which shows velocity profiles from the WMLES based on a simple DES model coupling the Prandtl - van Driest RANS and the Smagorinsky SGS models. As seen in the figure, at Re_τ=18000 the profile does not have any LLM and reproduces the log law fairly well. However at a moderate Reynolds number (Re_τ=1100), the model does not predict the velocity profile accurately enough. Thus, the subgrid length-scale alone is still insufficient for an accurate WMLES at arbitrary Reynolds number. As shown in Fig.4 and, also, in Chapter IV (Sections 9, 12), this issue is successfully resolved by the IDDES approach.

Finally, general IDDES capabilities are illustrated by performance of the approach as applied to the flow in a plane channel with the straight up and stepped down walls studied in experiments of Vogel and Eaton, 1985. Although not included into the DESider test-case matrix, this flow seems to be a perfect IDDES

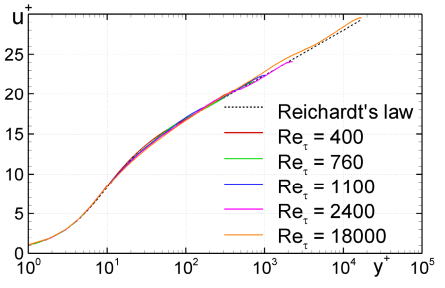

Fig. 4 Comparison of SST-based IDDES prediction of mean velocity profile in developed channel flow at different Reynolds numbers with Reichardt's empiric correlation

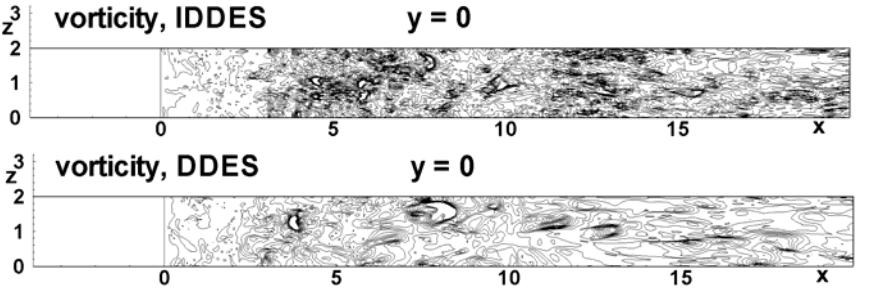

Fig. 5 Snapshot of vorticity magnitude on the stepped-wall of the Vogel and Eaton channel from IDDES and DDES

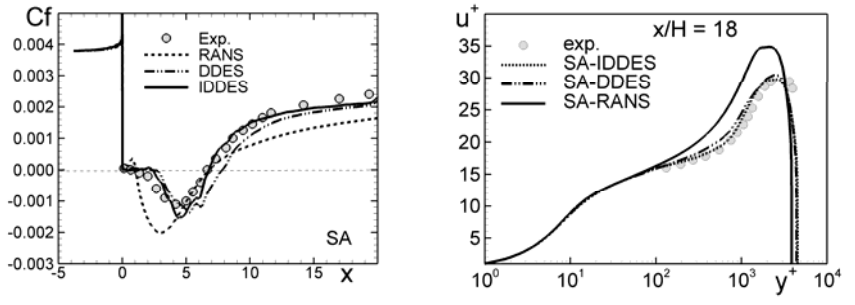

Fig. 6 Comparison of mean friction coefficient distributions along the stepped-wall and mean velocity profiles in recovery region predicted by RANS, DDES, and IDDES with Vogel and Eaton, 1985 data

"showcase" since it demonstrates simultaneous performance of all the three modes of the model (RANS, LES, and WMLES) in one flow. In particular, the RANS mode turns out to be active in the attached boundary layer on the upper wall of the channel and on its lower wall upstream of the step since these boundary layers do not have any inflow turbulent content. A full LES mode of the IDDES prevails in the separation zone, and, finally, a WMLES mode switches on in the reattached boundary layer on the stepped-wall, which inherits turbulent content from the upstream separation zone. As a result, as seen in Fig.5, in the vicinity of the lower wall, IDDES provides for a much better representation of turbulence (resolves much finer grained eddies) than DDES does which, in turn, results in a more accurate prediction of the mean flow characteristics in the reattached flow region known to be most challenging for both RANS and DDES (see Fig.6).

13.3 Digest of the Validation Activity

Nine test cases, which NTS has computed in the course of DESider, and simulation approaches used are listed in Table 1. Below we briefly summarise major lessons learned from the simulations.

Table 1 Test cases and simulation approaches

Test Case No.	Flow	Simulation Approaches
3	NACA0021 at 60^o incidence	DES97, S-A IDDES, k-ω TRRANS, SST SAS (versions 1 and 2)
5	Decay of isotropic, homogeneous turbulence (DIHT)	k-ω TRRANS; SST SAS (versions 1 and 2)
9	Fully developed channel flow at high Reynolds number	S-A and SST DDES
10	Bump in square duct	SST URANS and DDES
11	Base flow (M =2.46)	S-A RANS, S-A RANS with compressibility correction, S-A DDES
12	Separated flow behind an aerofoil trailing edge without camber	SST IDDES
14	Circular cylinder on a ground plate	DES97, k-ω TRRANS
A2	3D cavity flow (M =0.85).	S-A DDES
A4	Simplified landing-gear truck	S-A DDES

NACA 0021 at 60^o Incidence

This is a massively separated flow, i.e., a typical flow DES97 was designed for. Major conclusions based on the simulations of this flow performed by NTS are as follows.

As expected, on the relatively coarse grids used in the simulations DES97 and S-A based IDDES provide virtually identical solutions. The same is true with regard to the TRRANS and version 2 of SAS modelling approaches (see Section II.5 for more detail). In contrast to this, version 1 of SAS returned 3D URANS periodic solution with no fine-grained turbulence. One more important finding of the study is that, in order to obtain span- and time sample-independent solutions within turbulence-resolving approaches a span-size of the domain, L_z, should be rather large (at least 3 airfoil chords, c) and a time sample of simulations should be as long as 500-1000 convective time units, c/U_∞ (this conclusion is probably relevant to all the nominally two-dimensional bluff bodies). Finally, it turned out that the mean pressure distribution over the airfoil based on these solutions somewhat worse agrees with the data than that obtained in the domain with L_z=c.

Decay of Isotropic Homogeneous Turbulence (DIHT)

In the course of DESider NTS computed this flow aimed at calibration of the models with turbulence-resolving capabilities only with the use of URANS-type approaches, TRRANS and SAS, since the DES-like approaches had been calibrated earlier within FLOMANIA project (Haase et al., 2006). A major outcome of the computation is the value of the empiric constant involved in TRRANS and a conclusion on numerics-dependence of the empiric constant F_{SAS} (this finding stimulated ANSYS for searching a more robust implementation which resulted in version 2 of SAS).

Fully Developed Channel Flow at High Reynolds Number
This was a key test of IDDES in terms of its WMLES performance. The simulations have demonstrated quite accurate representation of the attached boundary layers provided by IDDES at arbitrary Reynolds numbers and, in particular, a complete elimination of the LLM in the mean velocity profiles.

Bump in Square Duct
This was a mandatory specially designed test case aimed at evaluation of different modelling/simulation approaches in terms of their ability to predict pressure-induced separation of the flow, its reattachment, and relaxation complicated by corner vortices. NTS computed the flow with the use of the SST URANS and DDES approaches. It turned out that the latter works as designed, i.e., the attached boundary layers upstream of the separation are sheltered from the LES mode and the separated shear layer instability is not damped so that the turbulent structures downstream of the separation are resolved fairly well. As a result DDES tangibly surpasses URANS in terms of the mean flow prediction. However it still significantly underestimates the length of the separation zone. At least partially this can be explained by the influence of the corner vortex in the inlet velocity field found in the experiments and not accounted for in the inflow boundary conditions specified based on the precursor RANS computations of ANSYS.

Base Flow (M =2.46)
Just as the stalled airfoil, this flow (supersonic flow downstream of a blunt-based cylinder) belongs to the natural DES application area. However, in this case the near wake is strongly affected by the compressibility effects, and therefore, the test permits to evaluate a capability of turbulence models to capture these effects adequately. Considering this, NTS has carried out the computations of this flow with the use of the standard S-A RANS model as a reference and also with the S-A model with the compressibility correction (CC) of Spalart, 2000, and with the DDES based on the standards S-A model. In general, the results of the study are encouraging in the sense that DDES turned out to be much more accurate than the S-A RANS, even if used with the CC. However DDES failed to provide sufficiently accurate representation of the initial region of the separated shear layer. Analysis of the results suggests that this is caused by insufficiently fine grid used in the simulation in this region.

Separated Flow Behind an Aerofoil Trailing Edge without Camber
This is a typical example of the flows with shallow separation, which computing with DES97 or DDES does not make much sense: in this situation the approaches, if used properly, should return effectively RANS solution. On the other hand, it is an attractive test case for the IDDES approach, which claims to an *automatic* switch to WMLES mode once an inflow turbulent content is available in the simulation and wall-parallel grid spacings are small enough for WMLES. Results of the simulation of this flow with the use of SST IDDES carried out by NTS turned out to be quite competitive with similar results obtained by ICL with the use of specialized WMLES approach, thus confirming that the claim is justified.

Circular Cylinder on a Ground Plate, Re_D=20,000

A peculiar feature of this flow is a strong interaction between the vortical flow separated from the free end of the cylinder with its wake. This interaction can drastically change not only the shedding pattern but also surface pressure distribution, especially for the cylinders with small and moderate heights (in the considered case it is equal to 6D). NTS has computed the flow with the use of TRRANS and DES97 on the same relatively coarse grid (about 2 Million nodes total). An outcome of the study turned out somewhat disappointing. First, in contrast to the infinite cylinder, where TRRANS provides not worse turbulence resolution and accuracy of the mean flow prediction than DES97 does, in this flow it turns out to be effectively URANS, i.e., resolves only large smooth vortices. This finding suggests that TRRANS turbulence resolving capability is rather flow-dependent and that a wider testing is needed to establish its ranges of validity. As far as DES97 is concerned, it performs better than TRRANS but also cannot be considered as "good enough" for the considered flow. This, however, is probably caused not by any fundamental deficiency of the approach itself but by the too coarse grid used in the simulation. This is confirmed by the LES study of the flow carried out by Chalmers within DESider and by a recent LES of a similar flow conducted by Rodi, 2007 who have shown that only a grid with about 22 million nodes provides a proper representation of the extremely complicated flow in the vicinity of the free end of the cylinder.

3D Cavity Flow (M =0.85)

This, aeroacoustic, test case has been computed by NTS with the use of S-A DDES. Specific features of the flow are strong pressure oscillations with high-amplitude tones caused by the instability of the shear layer and its interaction with the aft wall of the cavity. The simulation confirmed that the model does shelter the incoming boundary layers from MSD caused by a strong refinement of the wall-parallel grid in the vicinity of the cavity edges and turned out generally successful in terms of both turbulence resolution and pressure oscillation spectra.

Simplified Landing Gear

Although this is also an aeroacoustic test case, no unsteady experimental data are unfortunately available. So evaluation of accuracy of the simulation, which has been also carried out with the use of the S-A DDES, is possible only on the basis of the mean-flow characteristics. The comparison turned out to be fairly well. In particular, the model captures subtleties of the very complex topology of the flow and provides for a fairly accurate prediction of the mean pressure distribution over the landing gear surface. Note also that it somewhat surpasses a similar simulation carried out on the same grid with the use of DES97 (Hedges et al., 2002).

14 Contribution by NUMECA

L. Temmerman and Ch. Hirsch

NUMECA Int. S.A.

Abstract. As commercial code developer and engineering consulting company, NUMECA's interest in advanced modelling strategies is high and the DESider project is of direct benefit to the company. Indeed, design studies rely more and more on numerical tools for complex situations. Unfortunately, in some, if not many, of these cases, RANS has been unable to meet the challenge and has proven to be unable to capture some of the most important features. At the same time, the continuing increase in computing power has made the use of unsteady simulations feasible, although not on a day-to-day basis, for a growing number of applications.

14.1 Introduction

The present chapter reports thus NUMECA work and accumulated experience within the framework of the DESider project and is organized as follow. The next part is a short summary of the numerical methods used, directly followed by a Section on the modelling approaches that were implemented and tested. Selected results, ranging from the calibration test to the most complex test cases, are then shown. Some concluding remarks are then drawn, including a word of advice and recommendations.

14.2 Code Description

Both NUMECA's solvers (HEXSTREAM^{TM} – unstructured and EURANUS^{TM} - structured) have been used in the course of this project. Both codes use similar numerical methods and are based on a co-located finite volume method. The diffusive terms are approximated using a second-order central approximation. For the inviscid term, various numerical schemes are available: the central scheme with scalar dissipation of Jameson et al (1981), a central scheme with matrix dissipation (Swanson and Turkel, 1992) and the second order Roe scheme (Roe, 1981). The accuracy of the code can be increased by using a reconstruction procedure of the fluxes via a least-mean square approach. Time-accurate computations are done with a dual-time stepping method using a second order backward difference for the temporal derivative. Steady solutions are obtained using a fourth order Runge-Kutta method. The iterative process is accelerated using multigrid, local-time stepping and residual smoothing. For low-Mach numbers and incompressible flows, low-Mach number pre-conditioning techniques are used. RANS turbulence models available include the Spalart-Allmaras model (Spalart and Allmaras, 1994), the k-ε model of Yang and Shi (1993) and the SST model of Menter (1993).

14.3 Turbulence Modelling

Two different unsteady modelling strategies have been considered: the SAS approach from Menter and Egorov (2005) (a full description of the approach can be found in Chapter II.2 of the present book) and two variants of the DES approach. The first variant (Shur et al, 1999) is based on the Spalart-Allamaras RANS model (Spalart and Allmaras, 1994) while the second, proposed by Travin et al (2002) is constructed on the RANS SST model of Menter (1993). More information on the details of DES modelling can be found in Chapter II.4 of the present book.

14.4 Selected Results

14.4.1 Calibration and Validation

Industrial codes designed to provide steady RANS are often heavily dissipative so they guarantee the code robustness in all circumstances. It is therefore of paramount importance to evaluate the amount of numerical dissipation and eventually re-calibrate it so that the code can give LES contents whenever the part of the computational domain is to be simulated with a LES-like method.

This assessment is done by reference to the case of isotropic turbulence for which experimental data (Comte-Bellot and Corrsin, 1971) are available. A complete description of the test case and computational procedure can be found in Chapter IV.5.

The first step consists of evaluating the dissipative behaviour of the code without model and this is illustrated in Fig. 1 for two numerical schemes and three different grid densities. In its default configuration, the code was too dissipative and the parameters controlling the dissipation and the selection of numerical schemes needed to be changed. Fig. 1 shows that the parameter controlling the numerical dissipation is varying with the grid density and therefore not constant. Fig. 1 also shows the impact of using different schemes (central scheme with scalar dissipation vs. central scheme with matrix dissipation). Finally, it is shown that, by selecting a median value of the dissipation parameter, similar spectrum shapes can be obtained, independently of the grid density at the cost of a loss of

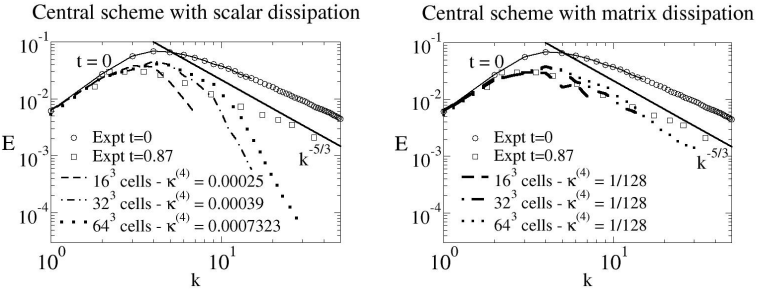

Fig. 1 Turbulence energy spectra for the central scheme with scalar dissipation (Left) and for the central scheme with matrix dissipation (Right). No DES model

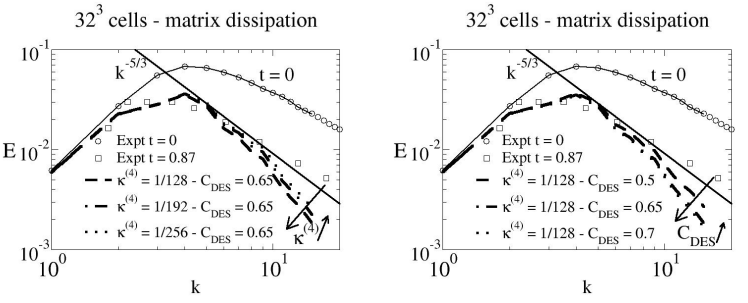

Fig. 2 Turbulence energy spectra for the central scheme with matrix dissipation used in conjunction with the SA-DES model. Left: influence of the fourth order dissipation parameter; Right: influence of the C_{DES} constant

accuracy in the prediction of the exact turbulence energy level. This is in line with the observations made by Garnier et al (1999).

The second part of the calibration process concerns the modelling strategies. The models (SAS and DES) are integrated in the code with the parameters as described by their authors. Fig. 2 shows the influence of the parameter controlling the numerical dissipation and the DES constant. For the other models, the observations are essentially the same. For the SAS-SST model, an additional phase is required and consists of assessing the model behaviour in steady circumstances i.e. that it returns the same steady solution as its underlying model, the SST model.

14.4.2 Aerofoil at a High Angle of Attack

The flow around a NACA0021 aerofoil with an attack angle of 60° and a Reynolds number of 270,000 is considered. The case corresponds to the experience of Swalwell et al (2004) and includes mean pressure, drag and lift coefficients and temporal histories for the lift and drag coefficients collected over 9000 time units. A complete description of the test case can be found in Chapter IV.3. This flow is representative of the applications for which DES was initially designed.

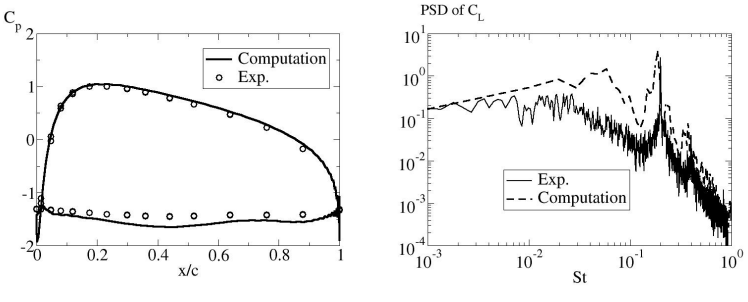

Fig. 3 Mean pressure coefficient distribution around the aerofoil (Left) and Power Spectra Density for the lift coefficient (Right)

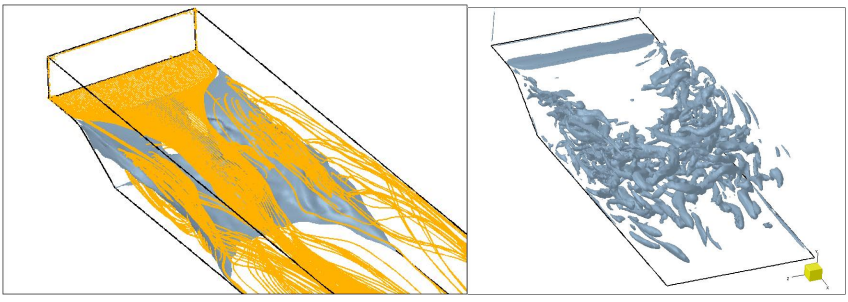

Fig. 4 Time averaged (Left) and instantaneous (Right) view of the flow over the DESider bump

The results shown here were obtained on a grid made of 140 x 100 x 36 cells and a spanwise extent of one chord length. The computation used the SA-DES model. Data were collected over a period of 177 flow units. Fig. 3 shows, on the right, the Power Spectrum Density for the lift (logarithmic scales) and, on the left, the distribution of the mean pressure coefficient along the profile. The computational data agree well with the experiment.

As pointed out in Chapter IV.3, for this case, a lateral extent of 4 chords and data sampling over a period of 400 flow units are recommended. This is however computationally very expensive, hence the somewhat smaller value used. Fig. 3 nevertheless shows satisfying results, considering the limitations just mentioned.

14.4.3 The DESider Bump

This flow was specifically designed for the DESider project (a full description of the test case is available in Chapters III.1 and IV.10). The computation shown here was run using the SA-DES (DES97) model and statistics collected over 3540 time-steps (1 time-step = 10^{-3} s).

Fig. 4, left, shows a time-averaged view of the flow with the grey surface representing the separation zone and the streamlines highlighting the strong three-dimensionality of the flow. The right picture shows an instantaneous view of the flow structures, identified by using the λ_2 criterion. The mean re-attachment point on the centre-plane on the lower wall is located at 0.47 m from the bump basis and this prediction thus over-estimates the experimental value of 0.625 m by about 15 cm.

Fig. 5 shows streamwise velocity and shear stress profiles at two different locations on the centre-plane, upstream and downstream of the reattachment point. Although the computation underestimates the recirculation bubble length, velocity and stress profiles compare reasonably with the experimental data, the differences agreeing with a too short recirculation zone.

14.4.4 The Ahmed Body

The final case considered is a generic ground vehicle with sharp edges at the rear and a slant inclined at an angle of 25°. This geometry was first studied by Ahmed et al (1984) and, more recently, by Lienhard and Becker (2003). A detailed

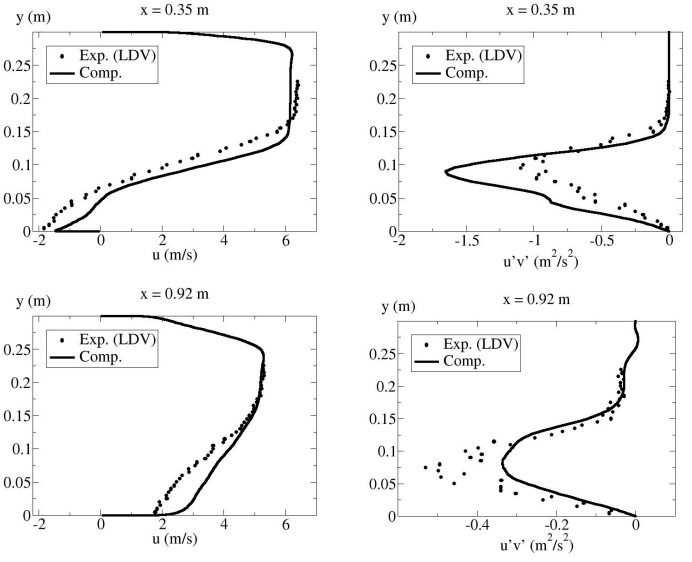

Fig. 5 Velocity and shear stress profiles at two different locations downstream of the bump basis on the centre plane

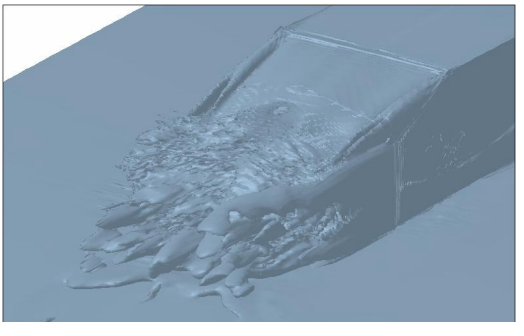

Fig. 6 View (instantaneous) of the rear part of the body showing iso-surface of the vorticity magnitude

description of the test case can be found in Chapter IV.4 of the present book. Two computations were performed: one with the SA-based DES and the other using the SST-based DES.

Fig. 6 shows a snapshot of the structures in the body wake. Fig. 7 compares the mean streamwise velocity profiles on the slant centre plane. Both models fail to predict the correct velocity distribution. The SA-DES model does not show any separation while the SST-DES version indicates a very large circulation. Annoyingly, this model seems to give a wrong prediction of the boundary layer upstream

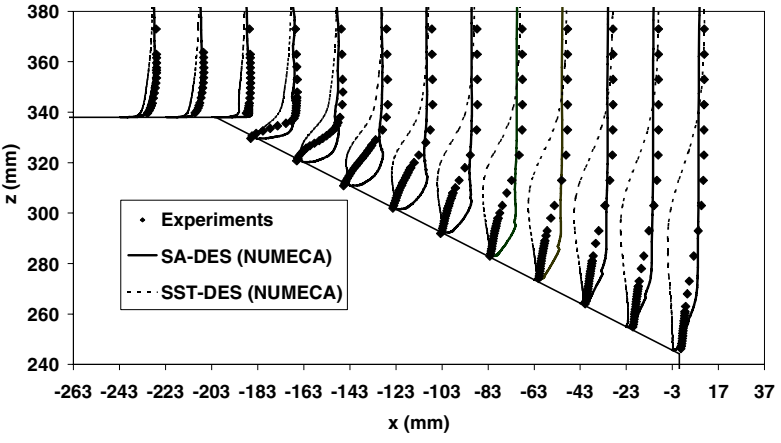

Fig. 7 Streamwise velocity profiles on the centre plane along the slant

of the slant. Possible sources for these differences may be the grid choice or the model choice. This is however not clear. It is to be noticed that results similar to those shown here have been obtained by other partners, as can be seen from section 5.4.

14.5 Concluding Remarks, Observations and Recommendations

NUMECA participation in the DESider project has resulted in the implementation of unsteady modelling strategies in its codes and the results obtained, allowed to gain a deeper knowledge of the working principle of unsteady models (SAS and DES) and their use on complex configurations. At the time of writing, this experience is being used in the UFAST project, an European project dealing with unsteady shock-boundary layer interaction.

Of paramount importance to achieve successful unsteady computations are the following parameters: code efficiency, grid adequacy, control of the numerical dissipation and pragmatism, these two latter being strongly linked. It was earlier demonstrated that artificial dissipation had to be “retuned” to guarantee that the code returns a LES-type solution. This tuning however is grid-dependent, scheme dependent and must guarantee code robustness. It should therefore be chosen as a medium value that guarantee all these aspects rather than being adjusted on a case by case basis.

15 Contribution by ONERA

B. Aupoix, P. Barricau, S. Deck, A. Gilliot, V. Gleize, I. Mary, J.C. Monnier, G. Pailhas, and Y. Touvet

ONERA

Abstract. This section summarises all efforts undertaken by ONERA in the framework of the DESider project. A main part was devoted to the bump experiment. Improved DES modelling was also addressed but this activity was stopped. DES was successfully applied to a high lift configuration. Future techniques were also investigated, as embedded LES on the A airfoil and hybrid LES.

15.1 Task 2.2: Measurements of Separating/Re-attaching Flows

As this experiment is described in detail in chapter III-1, the reader is referred to this chapter for further information.

15.2 Task 3.2: DES with Improved Modelling

The key problem with the classical DES approach is the grid induced separation. Attached boundary layers must be shielded to compute them in RANS mode.

In the framework of standard DES based upon the one-equation Spalart-Allmaras model, the idea is to get another length scale from the turbulence model. Many length scales can be formed from the available quantities, some of them being used by the model. Examples are $L = \dfrac{\tilde{\nu}}{\sqrt{\dfrac{\partial \tilde{\nu}}{\partial x_k}\dfrac{\partial \tilde{\nu}}{\partial x_k}}}$ or $L = \sqrt{\dfrac{\tilde{\nu}}{\sqrt{S_{ij}S_{ij}}}}$.

The followed approach is to derive the length scale from an explicit algebraic approach. Standard explicit algebraic models rely upon the assumption that the anisotropy tensor $a_{ij} = \dfrac{\overline{u_i' u_j'}}{k} - \dfrac{2\delta_{ij}}{3}$ does not change. Using a Reynolds stress transport model, the constant anisotropy assumption leads to an equilibrium relation from which the anisotropy tensor can be related to the non-dimensional mean strain and vorticity tensors. But, the knowledge of non-dimensional mean strain and vorticity tensor requires the turbulence time scale, which is provided by any two-equation model but not by the Spalart and Allmaras one-equation model. The problem was circumvented, for two-dimensional flows, using Pope's representation of the anisotropy tensor

$$\overline{u_i' u_j'} = \frac{2}{3}\delta_{ij}k + 2\nu_t S_{ij} - aT\nu_t\left(S_{ik}\Omega_{kj} - \Omega_{ik}S_{kj}\right) - bT\nu_t\left(S_{ik}S_{kj} - \frac{1}{3}S_{lk}S_{kl}\delta_{ij}\right)$$

where dimensional analysis leads to introduce two coefficients a, b and an unknown time scale T. Note that the turbulent kinetic energy is also unknown. Then, introducing this representation in a Reynolds stress transport model, projecting on the basis formed with the four tensors, four equations are obtained. The system analysis lead to relate the time scale T to the time scale provided by the turbulence model, $T_\nu = \left[\frac{1}{\nu_t}\frac{D\nu_t}{Dt}\right]^{-1}$. Thus, a third order equation for $\tau = \frac{aT}{T_\nu}$ is obtained. From its solution, it is possible to reconstruct all the unknown quantities such as the turbulent kinetic energy, its dissipation rate and hence the turbulence time and length scales.

It has been shown that this approach is equivalent to the one proposed for two-equation models by Wallin and Johansson (2000). The approach was validated first for homogeneous flows, and then for boundary layer flows (Aupoix and Grenard, 2005) and extended to three-dimensional flows.

This approach allows to locally determine a length scale, which could be used to shield the attached boundary layer. With the advent of the DDES approach, this work was however stopped to put more effort on task 2.2.

15.3 Task 3.3: Embedded LES – The Near-Future Approach

The A-Airfoil designed by Aérospatiale (Gleyzes and Capbern 2003) in a near stall configuration has been simulated with zonal RANS/LES method by ONERA to assess inflow turbulent condition for the LES domain. The Reynolds number, based on the upstream velocity (Uinf=50m/s) and the chord (c=0.6m), is equal to 2.1 million, whereas the angle of attack and upstream Mach number are set to 13.3 degrees and 0.15, respectively. Transition was triggered on the pressure side at x/c=0.3. Due to the strong adverse pressure gradient, transition occurs "naturally" on the suction side: there is a laminar separation bubble, which leads to a turbulent reattachment near x/c=0.12. After this position, the development of the turbulent boundary layer is characterized by an important thickening and by the presence of a second separation zone, which occurs between x/c=0.82 and the blunt trailing edge (its thickness is nearly equal to 0.5% of the chord). The inflow condition for LES domains are based on database. Unsteady three-dimensional database has been generated at ONERA for a turbulent boundary layer (TBL). Different rescaling have been assessed in order to adapt in terms of Reynolds and Mach number this database for the A airfoil test case. With the zonal coupling, average quantities are known. Therefore only fluctuating quantities must be determined for inflow conditions. The TBL is divided into inner and outer region. Assuming self-similarity for fluctuating fields, the fluctuating part can be written as:

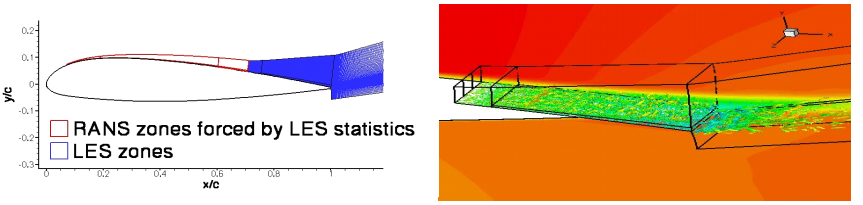

Fig. 1 Sketch of RANS/LES partitioning for the LES inflow condition assessment

$$\left(u'_i\right)^{region} = \phi_i^{region}\ f_i\left(\frac{y}{l_y^{region}}, \frac{z}{l_z^{region}}, \frac{t}{t^{region}}\right)$$

$$\left(T'\right)^{region} = \psi^{region}\ h\left(\frac{y}{l_y^{region}}, \frac{z}{l_z^{region}}, \frac{t}{t^{region}}\right)$$

$$\left(\rho'\right)^{region} = \chi^{region}\ g\left(\frac{y}{l_y^{region}}, \frac{z}{l_z^{region}}, \frac{t}{t^{region}}\right)$$

For both inner and outer regions, length and time scales are needed, as well as magnitudes for velocity components and thermodynamic variables. The viscous scale is used in the inner part and the boundary layer thickness in the outer part. A common time scale based on boundary layer thickness and the external velocity is retained. Four different scaling of the fluctuation intensity have been assessed:

$$\phi_i^{inner} = \phi_i^{outer} = u_\tau \qquad \textbf{Scaling 0}$$

$$\phi_i^{inner} = \phi_i^{outer} = \sqrt{k_{\max}} \qquad \textbf{Scaling 1}$$

$$\phi_i^{outer} = \sqrt{k_{\max}} \qquad \textbf{Scaling 2}$$

$$\phi_i^{inner} = U_{external}\ ;\ \phi_i^{outer} = \sqrt{k_{\max}} \qquad \textbf{Scaling 3}$$

The LES zone is described in the figure 1 below.

For practical case, scaling based on external quantities (TKE for instance) performs better, as can be seen from figure 2. Indeed scaling based on inner scaling are too dependent on geometry and flow condition and can lead to poor accuracy. The use of database for inflow condition seems to be a promising tool for zonal RANS/LES simulation, but it requires increasing the number of database (different Re, Ma) to obtain a practical tool box.

15.4 Task 3.4: Hybrid LES – A Step Forward

ONERA has worked on a zonal RANS/LES approach to deal with wall-bounded flow. The strategy is to use standard RANS model in a domain close to the wall. This domain plays the role of wall function for LES. The Spalart-Allmaras model

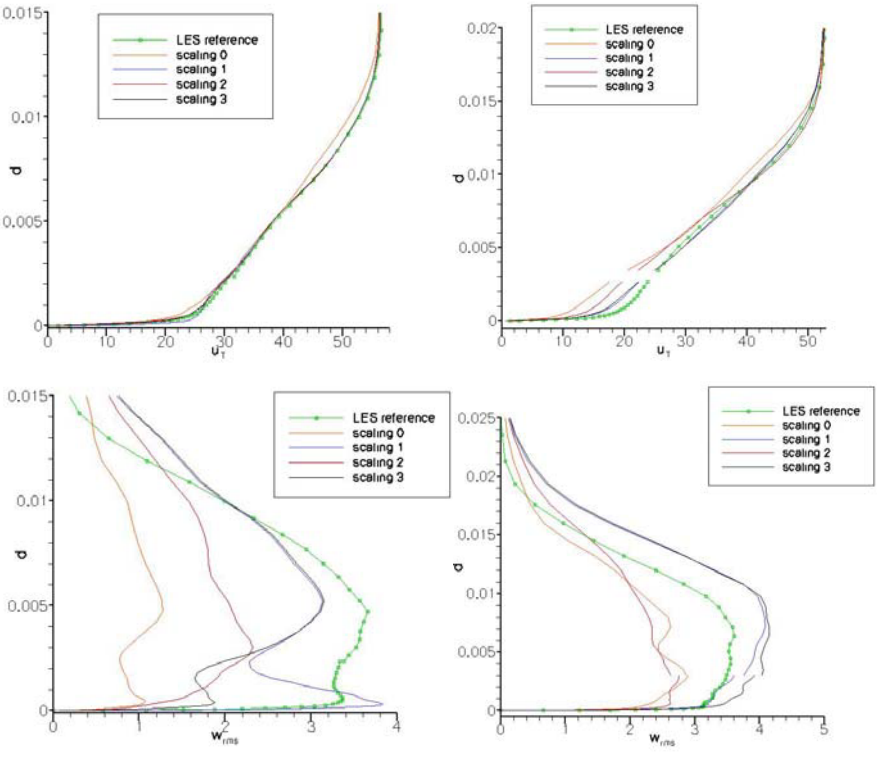

Fig. 2 Streamwise velocity profiles and spanwise velocity fluctuation profiles: Inflow plane left. 5δ downstream right

has been retained for the project. A LES domain is used in the upper part of the boundary layer. The main characteristics of the zonal RANS/LES method developed at ONERA are summarized in Nolin *et al*. (2005, 2006). RANS and LES overlapping grids are used in order that the whole computational domain is discretized by RANS method. In some places, where more accuracy or unsteady information is needed, LES domain with finer resolution is used and the underlying RANS values are defined from LES ones thanks to a space and time filtering in order to obtain an almost steady solution in the RANS domain.

In a previous study of Quéméré (2001), this technique was assessed for the periodic plane channel flow with a good success. But this test case is not relevant to develop zonal RANS/LES method, with a RANS zone used as wall model near the wall. Both teams have demonstrated that unsteady perturbation must be added at the interface of the LES zone to obtain satisfying results. In the case of periodic channel flow, the case is relatively simple, because perturbations are self-sustained in the center of the channel due to the periodicity condition in the streamwise direction. Moreover the interface is located at a fixed value of the wall in term of mm but also in wall unit. For a realistic flow configuration, these specific points cannot be used. Hence the location of the interface depends on the streamwise

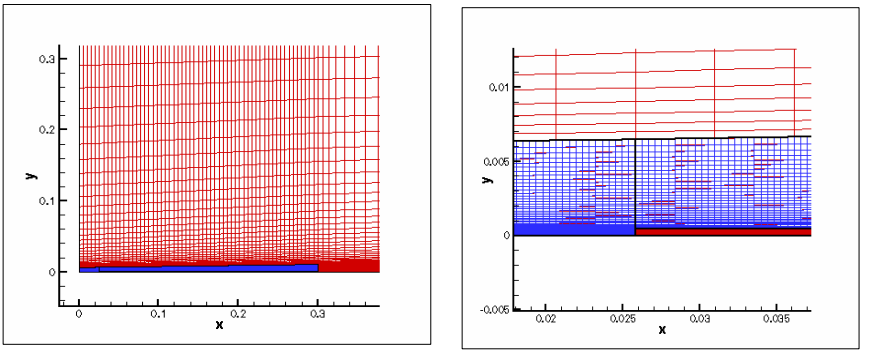

Fig. 3 Schematic view of LES and RANS domain for the flat plate simulation

direction and perturbations must be added at the inflow of the LES domain. Therefore the test case of a spatially evolving turbulent boundary layer has been retained to evaluate the method for a flow configuration, which is better representative of a real case than the periodic channel flow. The computational domain, employed to assess the method, is described in the figure 3. The whole is decomposed into 3 domains:

1. A 2D RANS covers the whole computational domain (red in figure 1).
2. At x=0, a LES domain is created (blue in figure 1). This domain goes to the wall (y=0) and stops at x=2.5cm. Laminar and steady inflow conditions are used at the inflow (x=0). This domain is used to trigger the transition to turbulence, which is enforced thanks to continuous forcing terms based on white noise. This domain allows to feed the inflow plane of the third domain with realistic and accurate turbulent vortices.
3. After x=2.5cm, a LES domain is located in the upper part of the boundary layer. At the bottom, this 3D domain is connected to the 2D RANS one.

At the inflow the inlet velocity, Ue is equal to 50m/s and the boundary layer thickness is close to 0.1cm. A first computation was realized without adding perturbations at the interface. Contrary to the channel flow simulation of Quéméré or Davidson, turbulence cannot be sustained in the LES domain, despite the use of the enrichment procedure of Quéméré. To overcome this bottleneck, turbulence analytical instantaneous vortices have been added at the interface of the LES domain. These vortices try to mimic the well known streaks of a turbulent boundary layer. The perturbations are added on the streamwise velocity component only

$$u' = 0.1 \times Ue \times \cos(0.5 \times Ue \times t - x/\lambda x) \times \sin(z/\lambda z)$$

The length waves, λx and λz, are determined in order that in wall unit, there are equal to 1000 and 50 respectively. The mean velocity profiles and resolved Reynolds stress profiles are compared in Figure 4 to the result of a reference LES. This reference LES solution is obtained by extending the LES domain up to the wall after x=2.5cm. Despite the improvement of the solution thanks to the

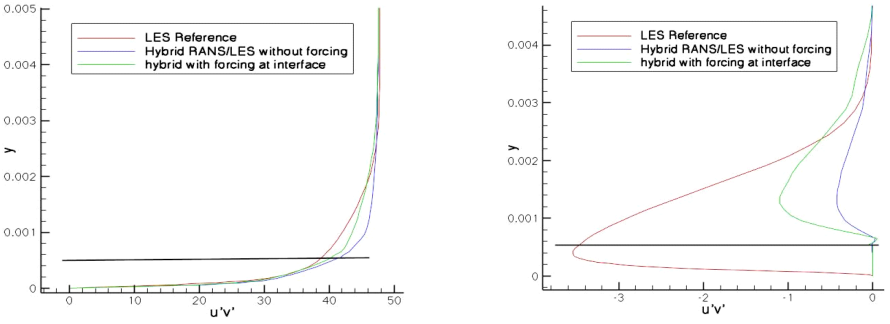

Fig. 4 Mean velocity profile and resolved Reynolds stress profile at x=0.1

perturbation, the results are not completely satisfactory. The idea to optimize the coefficient of the perturbation has not been tested. Indeed it is clear that the solution can be improved by this way. But this procedure will not be general. After assessment and reflection, it was concluded that it is very difficult to couple properly RANS and LES solutions at an interface parallel to a wall located in the boundary layer. Indeed the vortices go through this interface but in both ways.

15.5 Task 4.1.2: Application Challenges

ONERA worked on two methods aiming to protect attached boundary layers from Model Stress Depletion (MSD) which is a premature switching of a DES model to its LES mode inside the attached boundary layers. Both methods are assessed to handle a complete high-lift configuration with deployed slat and flap tested within the Europiv2 program (Arnott et al., 2003).

The first method is the Zonal-Detached Eddy Simulation (ZDES, [Deck, 2005]) approach where fully attached boundary layer regions are treated in RANS mode regardless to the grid resolution. That means that, following the example of RANS/LES coupling methods, the user has to define the RANS and LES zones. The interest of this approach is that the user can focus his grid refinement on

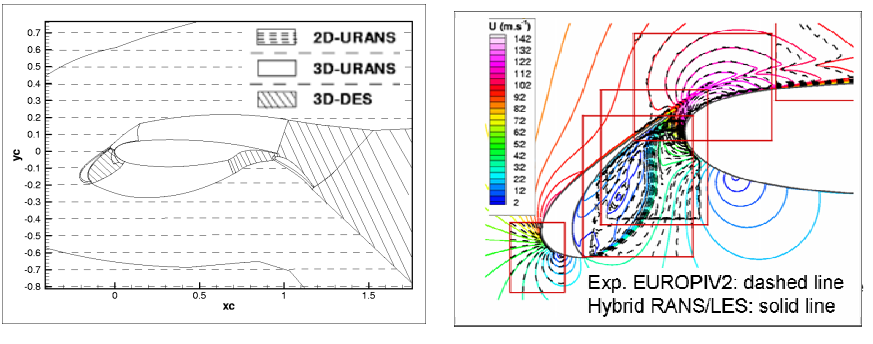

Fig. 5 ZDES decomposition (left) and time averaged velocity field in the slat area (right)

regions of interest (e.g. LES regions) without corrupting the boundary layer properties farther upstream or downstream.

ONERA also contributed together with NTS to the development and validation of the Delayed Detached Eddy Simulation (DDES, [Spalart et al., 2006]). Within DDES, the DES length scale is redefined in order to preserve RANS treatment of the boundary layer. This new length scale does not depend only on the grid but depends also on the time-dependent eddy viscosity field.

Within ZDES, the effort is geared toward detailed comparison of the numerical results with the Europiv2 experimental PIV data including both mean and fluctuating properties of the velocity field (see figure 5). The results also provide an insight into the real unsteady nature of the flow around a three-element airfoil that cannot be reproduced by classical RANS models. DDES has proven to maintain the RANS mode in thick boundary layers whilst maintaining LES content after separation.

16 DES Implementation, Validation and Application at TU-Berlin

C. Mockett, U. Bunge, B. Greschner, T. Knacke, R. Perrin, T. Reimann, J. Yan, and F. Thiele

TUB

Abstract. This chapter provides a summary of highlighted achievements at TU-Berlin (TUB) during the course of the DESider project. The TUB work has been focussed on the DES method, concerning which a comprehensive set of investigations have been conducted. These have involved assessments of the suitability of the TUB in-house flow solver, the implementation and validation of the latest DES formulations based on a range of RANS models as well as the assessment of a number of issues of relevance to industrial best practice. The DESider project work has furthermore provided important enabling technologies, with the DES methods implemented taking a central role in TUB's ongoing research activities in the fields of unsteady flow prediction, computational aero-acoustics and flow control (Mockett et al., 2008). To illustrate this, examples of such DES applications from other projects are included.

16.1 Modelling Developments

A summary of the DES variants implemented by TUB during the course of the DESider project is given in Table 1. The reader is referred to Chapter II, Section 1 for the acronyms and references for the background RANS models, as well as for descriptions of the DES97, DDES and IDDES formulations and Ψ low-Re term correction functions. The grey dots in the table refer to implementations existing at the DESider outset, which were a product of the preceding FLOMANIA project (Haase et al., 2006). An early model-specific shield function to protect against grid-induced separation (GIS) was developed for the CEASM-DES (Bunge et al., 2007), which is based on the methodology of (Menter & Kunz, 2004). This was later superseded by the generally-applicable DDES methodology (Spalart et al., 2006).

Table 1 DES versions implemented and studied

Model acronym:	DES97:	DDES:	Ψ:	IDDES:
SAE	•	•	•	•
SALSA	·	•	•	
WCX	•	•	not reqd.	
LLR	·	•		
CEASM	·	•		•

Table 2 Test cases computed and modelling variants applied

Test case:	Modelling approaches applied:
1. Circular cylinder flow	CEASM-DDES*
3. NACA0021 at 60° incidence	SALSA-DES97, LLR-DES97, CEASM-DES97
5. Decay of isotropic turbulence	All variants, with and without Ψ function
9. Fully-developed channel flow	SAE-IDDES, CEASM-DES97, CEASM-IDDES
10. Bump in a square duct	SAE-DDES, SAE-IDDES, CEASM-DDES*
13. FA-5 military aircraft config.	SALSA-DES97, CEASM-DES97
17. Oscillating NACA0012 at 15°	SALSA-DES97, LLR-DES97, CEASM-DDES
19. Car side mirror	SALSA-DES97, LLR-DES97

16.2 Test Cases

The test cases computed by TUB within DESider are summarised in Table 2, together with the modelling approaches applied (the notation CEASM-DDES* refers to the model-specific GIS-shield function mentioned above). The test cases span a wide range of flow phenomena, from bluff bodies to internal attached flows, and a wide range of geometric complexity from canonical to industrial.

16.3 DES Investigations

16.3.1 DES Validation for Massively-Separated Flows

A particular achievement has been the very detailed validation of the CEASM-DDES* formulation against experimental data for the IMFT circular cylinder test case (Chapter IV, Section 1). Figure 1 shows the complex three-dimensional wake behind the cylinder obtained by the DES, and a quantitative comparison with the experiment. Excellent agreement has been seen for the mean flow, velocity spectra and the phase-averaged field. The work has been published in (Mockett & Thiele, 2007), (Mockett et al., 2008), (Mockett et al., 2008a), (Perrin et al., 2007), (Perrin et al., 2008) and (Spalart, 2009).

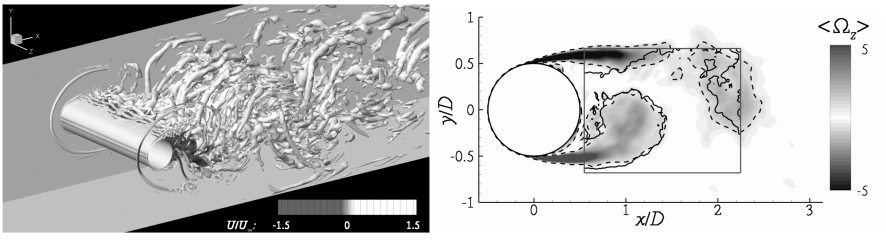

Fig. 1 CEASM-DES* computation of cylinder test case. Instantaneous vortical structures (*left*) and comparison of phase-averaged spanwise vorticity (contour and dashed lines: DES, solid black lines: experiment) (*right*)

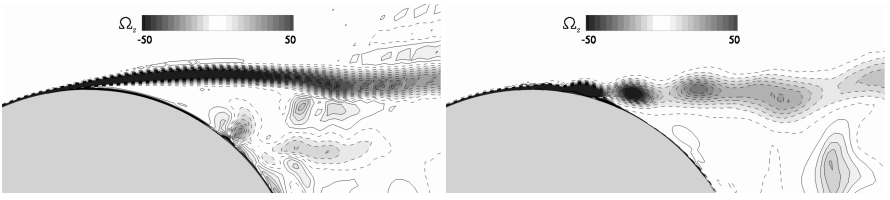

Fig. 2 Time filtering of vortices in the early shear layer, visualised with instantaneous contours of spanwise vorticity – coarse time step (*left*) and fine time step (*right*)

16.3.2 Time Step Sensitivity of DES

For the cylinder flow investigation discussed in the above section, two different time step sizes were computed, namely 0.03 and 0.05 non-dimensional time units (based on the free stream velocity and cylinder diameter). The finer of these was employed in the validation study above, and showed excellent agreement with experiments. The coarser time step however resulted in a dramatic deterioration of the solution quality, with a strongly over-predicted recirculation length, under-predicted drag coefficient and over-predicted shedding frequency. In an analysis of this sensitivity, published in (Mockett et al., 2008a), the principle mechanism was found to be time filtering of the early shear layer vortices (an impression of which can be obtained from Fig. 2). In this region, the CFL number was found to exceed unity in the coarse time step simulation, whereas values less than 1 prevailed throughout the domain with the finer time step.

The strength of this time step sensitivity emphasises the need for best practice guidelines for DES in industrial CFD, and evidence has been provided that a CFL type criterion could indeed represent a useful rule of thumb. It remains to be established whether a time step convergence has been achieved for the cylinder case, for which a still finer time step would need to be computed.

16.3.3 Dependency of DES on the Underlying RANS Model

The computation of some test cases with DES based on a variety of RANS models has enabled an assessment of the degree of model dependency of DES. For massively-separated flows with geometry-induced separation, the model dependency is observed to be negligible once sufficient time steps were collected for reliable statistics (e.g. for the NACA0021 test case, Chapter IV, Section 3). By contrast, for flows featuring the sensitive separation of turbulent boundary layers from smooth surfaces (e.g. the bump test case, Chapter IV, Section 10), the choice of background RANS model exerts a dominating influence on the solution. Dependent on the nature of the flow, DES can therefore be seen to inherit either the strong model-dependency of RANS or the comparatively weak SGS model dependency exhibited by LES.

16.3.4 Assessment of the Numerical Scheme

A variant of the decay of isotropic turbulence test case has been used to assess the level of numerical dissipation of different convection schemes implemented in the

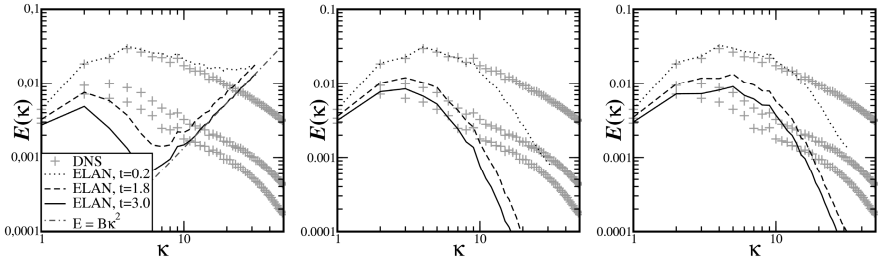

Fig. 3 Energy spectra for "no model" solutions of DIT with different convection schemes (64^3 grid), DNS benchmark data of (Wray, 1997). CDS (*left*), UDS (*mid*), TVD (*right*)

TUB in-house solver "ELAN". Assuming that the total dissipation of the solution is composed of model dissipation (i.e. subgrid-scale eddy viscosity), molecular dissipation and numerical dissipation, the numerical dissipation can be isolated by deactivating the subgrid-scale model and setting the molecular viscosity to zero. Initialising the simulation with the benchmark velocity spectra, in the absence of any dissipation an energy spectrum proportional to wave number squared should result. Figure 3 shows the energy spectra arising from the CDS, UDS and TVD convection schemes, and confirms that the numerical dissipation of CDS is indeed negligible (at least under these test conditions), whereas the UDS and TVD schemes exhibit very dissipative behaviour. The CDS scheme is therefore deemed suitable for LES simulations, such as in the LES-mode operation of DES.

16.3.5 Additional Length Scale Substitutions and the Grey Area Problem

The standard DES formulation for two-equation models involves a substitution of the DES length scale in the destruction term of the *k*-equation. However, rearrangements of the model terms reveal that the RANS length scale occurs also elsewhere, for instance in the expression for the eddy viscosity (Bush & Mani, 2001) (Kok et al., 2004). In an initial investigation by TUB (Yan et al., 2005) three alternative such formulations of the WCX-DES97 were compared on the basis of DIT and a NACA0012 airfoil at high angle of attack. Despite strong differences in the calibrated values of C_{DES}, no difference could be detected between the solutions for the massively-separated flow case. However, in later investigations of the application of DES for jet flow simulations (Yan et al., 2006) (Michel et al., 2007) (Mockett et al., 2008) (carried out within the CoJeN European project), the formulation employing an additional substitution of the DES length scale in the eddy viscosity expression revealed decisive advantages. With the additional substitution, the development of resolved turbulent structures in the early jet shear layer was strongly enhanced, indicating that such formulations may provide a route to alleviate some instances of the grey area problem of DES.

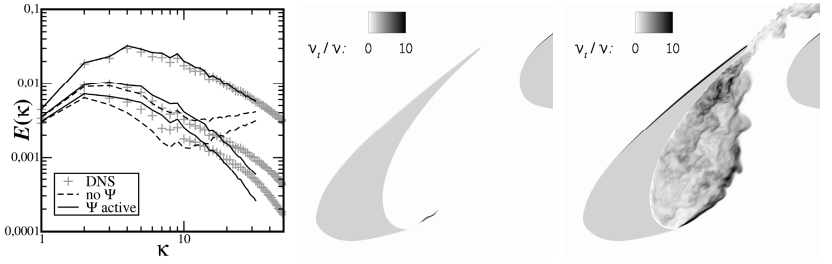

Fig. 4 DIT spectra demonstrating the functionality of the derived Ψ function for SALSA-DES (*left*); Eddy viscosity ratio plots for a SALSA-DDES simulation of a high-lift system without the Ψ function (*mid*) and with the Ψ function active (*right*)

16.3.6 Correction of RANS Model Damping Term Behaviour in LES Mode

Following the methodology developed by NTS (described in Chapter II, Section 4), the DES implementations at TUB were examined to establish the requirement for a Ψ correction function. This was found to be necessary and successfully derived for the SAE and SALSA variants and the effectiveness of the derived function for SALSA-DES is demonstrated on the basis of DIT in Fig. 4.

Figure 4 also shows the direct impact that the Ψ function can have on practical applications, with the example of a high-lift simulation using SALSA-DDES, carried out in the framework of an industrial cooperation (Mockett et al., 2007).

16.3.7 The IDDES Method for Wall-Modelled LES and Combination with Adaptive Wall Functions

The IDDES method proposed by NTS (Travin et al., 2006) (Shur et al., 2008) has been implemented on the basis of the SAE and CEASM models, although a tuning of the model-specific constants c_l and c_t (see Chapter II, Section 4) has not been carried out. Results for the fully-developed channel flow at $\mathrm{Re}_\tau = 4000$ are given in Chapter IV, Section 9, which exhibit highly satisfactory performance for such wall-modelled LES. The methodology has furthermore been coupled with a hybrid-adaptive wall boundary condition developed at TUB (Rung et al., 2000) (Schmidt et al., 2008), which allows any value of y^+ at the wall. This combination of approaches allows LES of boundary layer flows unlimited in terms of wall friction units both in the tangential and normal directions, vastly reducing the computational cost compared to fully-resolved LES. Figure 5 shows time-averaged velocity profiles for channel flow simulations for Re_τ varying between 590 and 100000, which were all carried out on the same cubic grid of resolution $\Delta x = \Delta y = \Delta z = \delta/20$. Very good agreement with the empirical correlation of (Reichardt, 1951) is achieved.

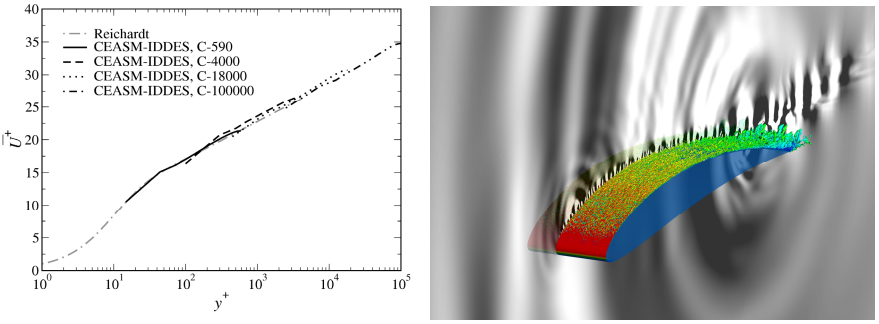

Fig. 5 Mean velocity profiles for CEASM-IDDES simulations of channel flow at Re_τ=590, 4000, 18000 and 100000 using the same cubic grid and hybrid-adaptive wall functions (*left*). Application of IDDES for airfoil aeroacoustic simulation (*right*)

For an example of the application of IDDES outside of DESider, the noise generated by an attached turbulent boundary layer and the trailing edge of a NACA5510 was simulated within the PROBAND European research project (Mockett et al., 2008). The Reynolds number was around one million and the grid consisted of around 5 million volumes. WMLES mode was activated on the upper surface, and RANS mode on the lower surface by targeted variation of the streamwise grid density. An instantaneous snapshot of the simulation is also given in Fig. 5.

16.4 Conclusions and Outlook

A summary of the highlights of TUB's research activities within the DESider project has been given, all of which address the DES family of hybrid RANS-LES methods. Through references to related work in other projects, it has been demonstrated how the DESider project has served as a key source of enabling technologies: The additional length scale substitution formulation has alleviated the grey area problem for jet simulations; The Ψ function methodology effectively solves the problem of erroneously damped eddy viscosity in some models; The DDES formulation represents a more robust method, immune to the perils of grid-induced separation in complex geometries; the IDDES method provides affordable access to the resolved large eddies in the outer boundary layer, of particular importance to aeroacoustic applications.

The investigations have also given a clear direction to future investigations, which will address: The strong time step sensitivity of DES and possible modifications to the formulation to reduce it; A thorough investigation of the early shear layer flow with respect to the balancing of spatial and temporal resolution, as well as the perspectives for alleviating the grey area problem; A study of the generality of the IDDES method for more complex flows; A tuning of the model-specific IDDES constants with the target of reducing the residual log-layer mismatch observed.

17 University of Manchester Contribution

A. Revell, N. Jarrin, J. Uribe, and D. Laurence

17.1 Introduction

The University of Manchester project partners focused on the development of three new approaches for the use of RANS and LES. The first is the URANS method based on a three-equation model to account for the strain – stress lag, following successful performance of the 7 equation second moment closures in predicting mean flows unsteadiness. The second is the Synthetic Eddy Method (SEM), which was developed to economically generate turbulent structures for LES boundaries using only RANS profiles. The third approached developed is a hybrid RANS-LES method based on two distinct velocity fields, one RANS one LES overlapping on the same mesh nodes. These methods have been already described in chapter 2 and here only a summary of their results is presented.

17.2 The Stress-Strain Lag Model

The flow around a circular cylinder in a square duct has been calculated in both 2-D and 3-D domains using URANS models and the DES approach. The standard SST model has been compared to the modified SST-C_{as} approach, which is sensitive to the lag between turbulent stress and the mean strain rate in the turbulent flow. The current form of the stress-strain lag model, SST-C_{as} was previously tested for several validation cases, including simple cyclic strain rates and the flow around a NACA0012 at 20^{o} (see Revell, 2006).

Figure 1 compares the 3-D URANS model predictions of the long-time averaged contours of streamwise velocity to experimental values from the data of Perrin et al. (2005). The recirculation length is under-predicted by the SST model and is improved upon, yet slightly over-predicted by the SST-C_{as} model. The point at which the flow is predicted to separate from the surface of the cylinder is still delayed, as noted above, due to the turbulent nature of the boundary layer, and the extent of the recirculation region in the normal direction is seen to be reduced, resulting in an under-prediction of the drag force.

Figure 2 displays two views of the iso-surfaces of the structure parameter, Q computed from the results of each of the three modelling schemes in the 3-D domain. This quantity is known to be an effective way to visualise the regions of coherent vorticity due to rotational motion (as opposed to those from shear), and should take a positive value. The lack of coherent structures is apparent in the results from the SST model, for the entire wake region except very close to the cylinder and the sidewalls. The process of vortex dislocation, which describes the bunching up of the von Kármán vortices, is not seen in the SST results, whereas those from the DES-SST and, to a lesser extent, the SST-C_{as} models clearly show these 'hairpin-like' structures. There are also significantly more spanwise structures than seen with the latter two models.

The SST-C_{as} model has been shown to improve the prediction of the mean flow field, relative to the standard SST model, and gives predictions similar to those from the DES-SST approach at a considerably lower cost.

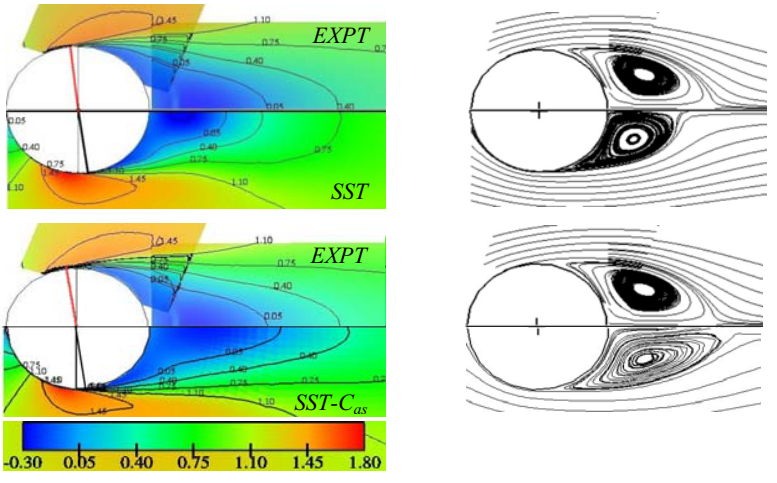

Fig. 1 (*Left*) Contours of averaged streamwise velocity, *U*. (*Right*) streamlines of the averaged flow. (*Top half:*) experimental data (*bottom half:)* URANS models

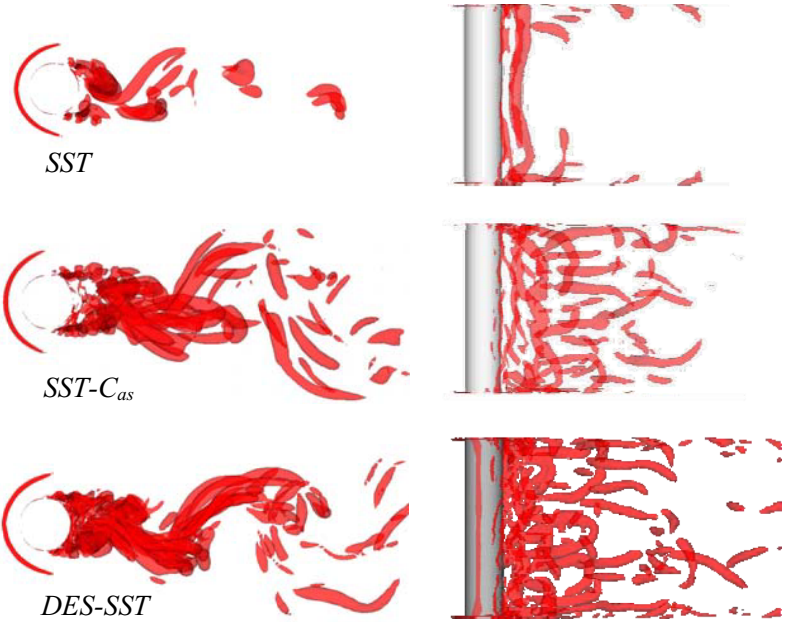

Fig. 2 Iso-surfaces of the structure parameter $Q=0.5$ are plotted for each model from the 3-D calculations. (*Left:*) view in –*Z* direction, (*right*) view in –*Y* direction

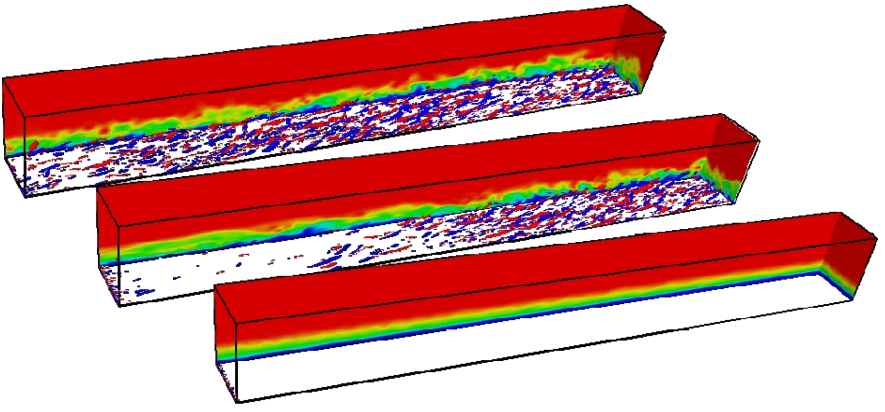

Fig. 3 *From top to bottom:* LES with SEM inflow, LES with Batten's (2004) spectral method, LES with uncorrelated random numbers. Instantaneous iso-surfaces of *Q=250* coloured by the instantaneous streamwise vorticity. Planes are coloured by the instantaneous streamwise velocity

17.3 Synthetic Eddy Method

The SEM was used to produce flow fields with turbulent flows based on averaged quantities such as those obtained by a RANS calculation. Hybrid RANS-LES simulations of a zero pressure gradient flat plate turbulent boundary layer were conducted in order to evaluate the method's performance. The RANS equations are solved in a domain of dimensions 35δx4δx3δ, where δ is the boundary layer thickness at the inlet of the domain. The RANS simulation generates its own inflow data by using the re-cycling re-scaling method of Lund et al. (1998), covering a Reynolds number range of Re_δ=750-1250 based on the momentum thickness. The LES domain begins at x=10δ and has dimensions 35δx4δx3δ. The LES grid uses 300x42x72 which is fine enough to accurately discretize the near wall turbulent structures. Three hybrid simulations are carried out with different inflow conditions for the LES region: a simulation with the SEM, one simulation with Batten et al. (2004) spectral method and one simulation using uncorrelated random numbers. Figure 3 shows instantaneous fields on the LES region for the three hybrid RANS-LES runs. It can be seen that the uncorrelated random numbers are unable to sustain vortical structures in the LES region whereas the Batten et al. (2004) method or the SEM manage, after an initial drop of the turbulent activity downstream of the interface, to regenerate the streaky self-sustaining vertical structures characteristic of the near wall region of boundary layers.

17.4 Hybrid RANS - LES Method

The same hybrid RANS-LES strategy has also been applied to several channel and pipe flows. Figure 4 shows the length of the transition region, computed from hybrid RANS-LES simulations. In all simulations, a steady upstream RANS

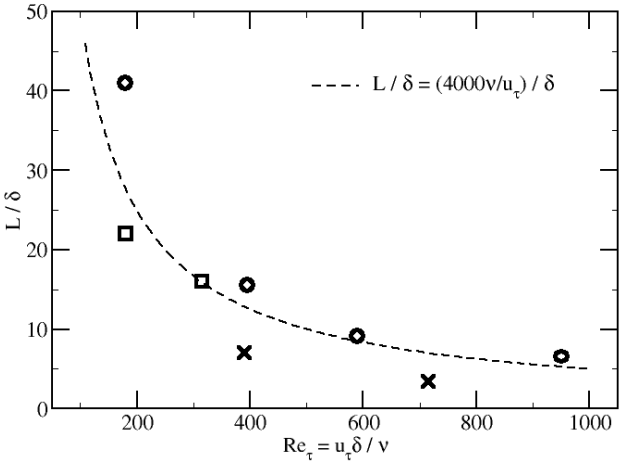

Fig. 4 Length of transition region for different wall flows computed using the hybrid RANS-LES with the SEM at the interface between the RANS and LES domains: channel flow simulations (×), pipe flow simulations ( ), boundary layer flow simulations (o)

solution is obtained using periodic or recycling streamwise boundary conditions, then used in the SEM to reconstruct turbulent velocity fluctuations at the inlet plane of the LES region.

From Figure 4 one can clearly see that the length of the artificial transition region decays as the Reynolds number increases for all the flows investigated. In other words, it scales with viscous wall units, rather than with the external length scale. This adaptation-transition length is on average $L^{+}=4000$ and independent of the Reynolds number, but can naturally be sensitive to the upstream RANS solution, on the inflow length scale, and the level of resolution of the LES Grid. The hybrid method described in Chapter 2 has been applied to channel flows at different Reynolds numbers and to the flow over a trailing edge case (see Chapter 4 sections 9 and 12).

Channel flow computations have been carried out at different Reynolds numbers using meshes that are too coarse for a standard LES to capture all the small scales and therefore the shear stress is usually under predicted which, in turn, produces an overestimation of the velocity magnitude. The hybrid model successfully blends the average shear stress and with the resolved one to produce the correct magnitude and therefore a better prediction of the velocity profile. The usual behaviour of overestimating the streamwise normal stress on coarse meshes by LES is corrected by the hybrid model. For all the different Reynolds numbers treated the velocity profiles follow the log-law (see Figure 5).

The instantaneous streamwise velocity contours on a plane at $y+=200$ can be seen in Figure 6 where it is clear that the DES model produces the "superstreaks" which are much larger than those which the grid can support.

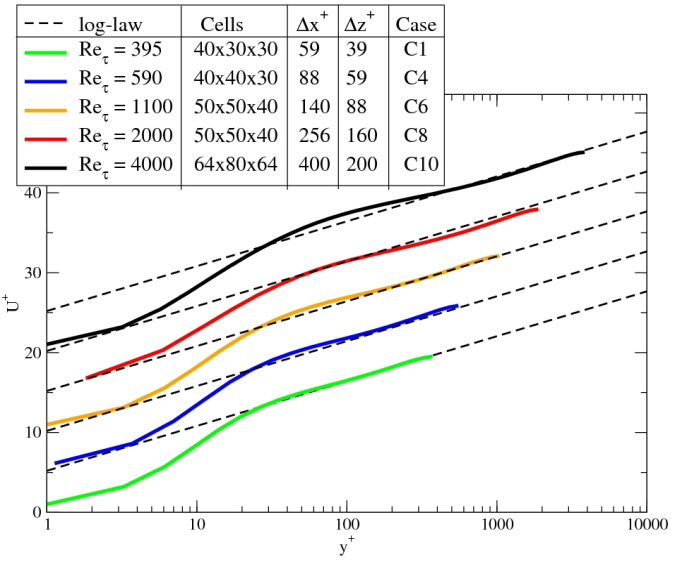

Fig. 5 Channel flow results at different Reynolds numbers

Simulations of the flow past an axisymmetric beveled trailing edge were also performed; described fully in chapter 4, section 11. Two simulations using the same mesh are presented; 1) DES using the SST model as the RANS background model, using the blending function F_1, to avoid grid induced separation and 2) the hybrid method presented above. The hybrid model presents a better agreement with the reference LES. DES simulation does not sustain the fluctuations from the inlet and by the time the flow reaches the station at $x = -3.125$, the resolved fluctuations are very small. This is the normal behaviour of DES in an attached boundary layer, since it is designed to be used in massively separated flows.

In general the structures are better resolved when using the hybrid model as the resolved stresses are able to develop independently from the RANS viscosity; i.e. the model associates the RANS viscosity with the mean flow only and the

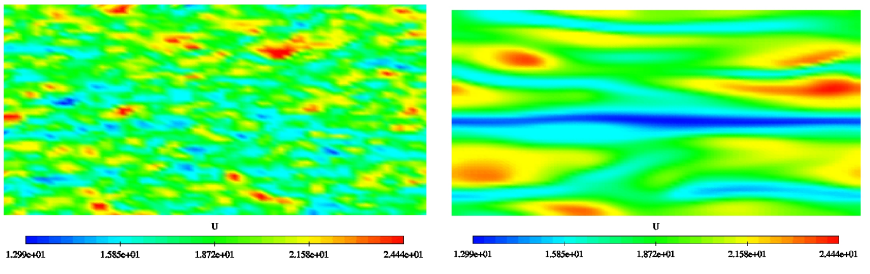

Fig. 6 Instantaneous streamwise velocity at $y^+ = 200$. Left: Hybrid. Right: DES

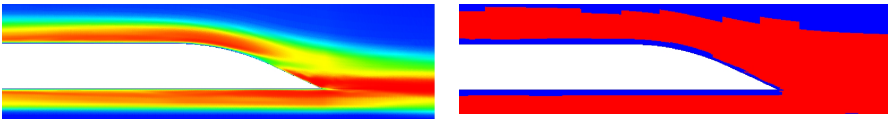

Fig. 7 Gradual blending from RANS (blue) to LES (red) in hybrid model (left) compared to the abrupt switch between length scales in DES (right)

resolved scale dissipation to the LES viscosity only. This is mainly due to the way in which each approach treats the boundary layer; DES uses RANS in a large zone near the wall, across much of the boundary layer, while the hybrid method only uses full RANS in a zone very close to the wall and there is then a transition zone where both approaches contribute via different velocity fields (see Fig. 7). In the same figure the corresponding analysis is shown for DES; the red region indicates where DES acts in LES mode, i.e. where the turbulent scale ($k^{3/2}/\varepsilon$) is larger that the filter length scale ($C_s\Delta$). In DES, the zone close to the wall is solved in RANS mode, therefore damping the fluctuations, whereas the hybrid model resolves the structures dictated by the size of the mesh, and introduces the effect of the wall via the averaged velocity.

17.5 Conclusions

Three methods to resolve unsteady flows were developed by the University of Manchester. The SST-C_{as} model has been shown to improve the prediction of the mean flow field, relative to the standard SST model, and gives predictions similar to those from the DES approach. While the level of unsteadiness from the SST-C_{as} model is far from what would be expected from LES or DES, the cost in terms of computational time and grid requirement is less for the SST-C_{as} model, and the reduction of viscosity is brought about in a physically justifiable manner, which could be exploited in a DES framework or a hybrid RANS-LES approach.

A method to generate synthetic turbulence either at an inlet plane or at an interface between RANS and LES was also developed. The methods create correlated structures in time and space which allows a fully turbulent flow to develop in shorter domains compared to other methods.

A new hybrid RANS-LES method which successfully blends the two approaches via two different velocity fields was also developed. The method has the advantage that does not suppress the turbulent fluctuations but it lets them develop via the fluctuating strain. This allows the method to return good predictions to attached boundary layer as well as separated flows.

VI Summary of Experience with Hybrid RANS-LES Methods and a Look Ahead

With the core activity on the development of CFD tools for aerospace applications, and the growing part of activities also oriented towards the area of fluid dynamics for industrial systems, all so-called "real-world" applications exhibit complex flow phenomena such as unsteady flow, (massive) separation, transition to turbulence and turbulence itself. All theses applications, exhibiting massive flow separation, need ideally the use of advanced turbulence models so as to capture the correct separation pattern and to resolve the frequency content of at least the mean flow. This is underlined by all test cases that have been carried out and properly investigated – see Chapter IV - during the course of the DESider project, and which at the same time allow to gain a good understanding of the pro and con's of the methods used and the way they interact with the numerical algorithms, but also with the grid properties and their effects on the computational effort required to attain satisfactory results. In general, the outcome can be taken as means for best practice guidelines and information on the accuracy of the numerical results, their cost and, thus, the area of applications for which these new methods should be considered.

There are now about 20 different approaches to the general problem of how to deal with near-wall modelling for LES at high Reynolds numbers, several emerging after DESider started. This reflects the importance the relevant academic and industrial communities attach to the subject. Indeed, it is no exaggeration to claim that a successful resolution of this problem is central to the exploitation of LES for a wide variety of flows that are strongly affected by walls. But at the same time, such a large number of approaches indicates a significant degree of uncertainty as to which is the best strategy. However, one positive overall conclusion that arises from many studies with hybrid RANS-LES schemes is that even very simple schemes tends to give much better results that a LES performed on a poorly-resolving near-wall grid – partly as a result of a much better prediction of the wall-shear stress (if not of the near-wall turbulence structure).

The (non-DES) hybrid schemes used in DESider vary considerable. With exception of the zonal two-layer strategy used by ICL, all employ a single numerical mesh and a single numerical strategy, applicable to the outer LES and inner RANS region. Some methods prescribe an explicit interface across which the nature of the model changes radically (e.g. a dynamic Smagorinsky SGS model is interfaced with a k-e RANS model). In one method by Chalmers University, 'spectral enrichment' is introduced by means of an injection of correlated fluctuations, derived from a separate DNS, to counteract stress depletion around the interface. In another, 'spectral enrichment' is produced by allowing a constant in the RANS model to respond instantaneously to the LES fluctuations at the interface, thereby introducing high-frequency components into the RANS layer close to the interface. In other approaches, a blending of two

W. Haase et al. (Eds.): DESider – A Euro. Effort on Hyb. RANS-LES, NNFM 103, pp. 433–436.
springerlink.com

models is effected with the aid of an empirical blending function. Despite all the efforts undertaken in the DESider project, and the positive aspects of

- encouraging experience (NTS and TUB) with newly developed hybrid models, like the IDDES model, which actually may replace DDES after a more careful validation, as well as the
- confirmation of an only marginal sensitivity of DES to the background RANS model,

it must be acknowledged that most hybrid models suffer from a number of common drawbacks, some listed below:

- The RANS equations arise from temporal integration, while the LES equations emerge from a filtering operation that excludes, in a pre-determined way, high-order components from the turbulence spectrum. Thus, the Reynolds stresses in the RANS equations are very different in nature from the subgrid-scale stresses in the filtered LES equations. However, in several RANS-LES combinations, especially those based on blending, the two are regarded as equivalent.
- The large majority of RANS models were formulated and calibrated by reference to steady, close-to-equilibrium conditions. Coupled to LES, these models have now to operate in an unintended, highly unsteady regime, in which turbulence is partly resolved and partly modelled. However, the models were designed to represent, statistically, the *totality* of turbulence effects, not an ill-defined, mesh-dependent 'filtered' portion thereof, and the combined resolved and modelled turbulence tends to be grossly excessive, unless constrained by ad-hoc limiters.
- Linked to the second bullet point above, even in the presence of modest unsteadiness, only very few RANS models would be expected to be physically tenable. In the context of hybrid RANS-LES schemes, "large eddies" frequently penetrate into the RANS layer and the RANS model is thus expected to account for severe non-equilibrium effects (rapid distortion, Lagrangian memory effects leading to dramatically increased stress-strain lag effects and occasionally negative production). Such extreme conditions have led RANS modellers towards the development of novel non-equilibrium turbulence models (UMan and IMFT) and the most advanced realizable Reynolds Stress Transport models (see in the past the EU FLOMANIA project, Haase et al (2006), but also the new ATAAC EU project, starting in 2009), but these models are complex to implement with problematic convergence characteristics, both features that negate the practicality and economy objectives of hybrid RANS-LES formulations.
- The basic rationale of using a RANS method in the near-wall region, within an overall LES strategy, is based on the observation that RANS computations of steady boundary-layer-type flows can tolerate very high near-wall aspect-ratio cells, but this is most definitely invalid in highly unsteady conditions in which unsteady wall-parallel advection is generally high. In any case, a need for very fine grid structures in the shear layers for an accurate flow prediction is evident.

- More generally, aside from large computational costs, selection of an adequate grid density and an appropriate time-step represents a non-negligible uncertainty – although this is a non-trivial statement. More specifically, a possible conclusion concerning mesh fineness is that for a correct simulation of rms quantities it is equally important to increase the grid resolution isotropically, which is coupled to the expensive need to provide the same resolution in both axial and radial/lateral directions, unlikely the way it is (or should be) done generating grids for (U)RANS computations.
- For vortical flows, grid resolution in the vortex core appears to be the most relevant issue to be addressed in order to correctly simulate the mean flow quantities - although the predicted fluctuating components do not have a relevant influence on the respectively computed mean values.
- There are a whole host of practical issues associated with numerical and model-related coupling or blending between the RANS and LES sub-domains. For example, some distance above the RANS-LES interface the solution should revert to full LES sense, but then the cell-aspect and expansion ratios must comply with LES constraints. This is often extremely difficult to realize in a general computational environment, and requires, at the very least, a complex dynamic adjustment of the interface location by reference to the local grid topology.
- Results obtained for aerofoils, like the NACA0021, led to findings concerning an extremely high sensitivity of DES of (so-called) two-dimensional bodies to the span size of domain (this is most probably true for LES as well) and the need of very long time samples needed for a reliable statistics for such flows.

An exceptional strategy is that of UMan, in so far as it is the only one to recognise the merit of using the RANS model in steady form to generate time-mean stresses in response to the time-averaged LES field being imposed on the model. Thus, in this approach, the RANS model operates within its intended applicability envelope. On the negative side, these stresses are then blended with the SGS stresses using an empirical function of wall distance. Not surprisingly, this model is found to give, in a separated trailing-edge flow, the best mean-separation location and, more generally, a very credible velocity field. Although the model has its faults, its performance is indicative of the basic validity of the concept of not using the LES near-wall model in unsteady form.

In other hybrid models, the RANS equations are subjected to high levels of unsteadiness at the interface, and this is aggravated by 'spectral enrichment'. This is, in itself, a recipe for error. An additional problem is that the interface has to be placed in a region in which the grid complies with LES constraints on cell-aspect ratio. Thus placing the interface close to the wall, may lead to an entirely wrong LES solution on the LES side of the interface, because the grid-aspect-ratio is intentionally increased rapidly as the wall is approached. Defects arising from this source have been observed by ICL.

An interesting outcome of the use of the zonal two-layer method by ICL is that this simple and cost-effective approach can give very respectable results, entirely equivalent to, if not better than, much more complex hybrid schemes. In part, this is because such models demand that the interface be placed fairly close to the wall

($y^+ \approx O(30)$). Another reason is that the LES grid, which extends to the wall, is allowed to maintain cell-aspect rations that comply with LES constraints. A third reason, linked to the first, is that, due to the proximity of the interface to the wall, the wall shear stress is (physically) fairly closely correlated with the interface conditions, so that a parabolised RANS solution is the thin near-wall layer readily results in a broadly correct wall shear stress, even if fluid advection is omitted in from the RANS solution.

There is a view among turbulence researchers concerned that the near-wall-turbulence structure is a "top-down" process, especially at high Reynolds number, i.e. that the outer flow dictates what happens close to the wall. The zonal scheme, as described above, is compatible with this concept. In fact, it suggests that what should be doing is to solve the RANS equations in steady-state mode, subject to time-averaged interface conditions, and that correlation functions should be use to derive wall-shear-stress fluctuations from fluctuation at the interface. Here again, however, the interface has to be fairly close to the wall.

Concerning inlet boundary conditions, it has been shown that *synthetic methods* are suitable for generating inlet boundary conditions in general flow situations – although in a variety of cases it is even sufficient to use steady inlet boundary conditions. In addition, the same synthetic methods can be used to generate an initial unsteady flow field and have also been successfully employed in zonal methods at the boundary separating a RANS field from an LES field, in what is also sometimes referred to as 'Embedded LES'.

It was also shown that complex 3D flows should be well aware of the need to use wall-resolved LES. Although, and unfortunately, high Reynolds numbers can not yet be treated because of the required extremely fine grids, which in turn underline the importance of DES and hybrid RANS-LES, investigated in DESider.

When improved (U)RANS modelling is concerned, the SAS model developed by ANSYS is essentially an improved URANS modelling concept which allows the formation and resolution of turbulent structures down to the grid limit under unstable flow conditions. This behaviour is based on the introduction of the von Karman length scale which allows the model to adjust to resolved flow features. For many unstable flows, the SAS model produced solutions similar to DES but without an explicit impact of the grid spacing on the RANS formulation. Due to its URANS characteristics, SAS will produce steady state solutions in stable flow situations, like channel flows, boundary layers or mildly separated flows.

Although the DESider project did open several ways for the use of hybrid RANS-LES methods, it did not (really) offer a direct benefit for the daily design processes, the industrial workhorse is still the (U)RANS approach, the outcome is of value, in that a new realistic perspective for tackling difficult highly separated flow cases was opened. Be it only on grounds of validation of CFD-methods for industrial applications, it is hoped, that "real-world" requirements clear the way towards hybrid RANS-LES modelling capabilities.

To a certain extent, a continuation can be seen in the – 2009 starting – EU proposal ATAAC, Advanced Turbulence Simulation for Aerodynamic Application Challenges, in general aiming at improvements to CFD methods for aerodynamic flows used in today's aeronautical industry. The reader is referred to the ATAAC Web site, www.cfd.mace.manchester.ac.uk/ATAAC/WebHome for further information.

References

Afgan, I., Moulinec, C., Laurence, D.: Large eddy simulation of flow over a vertically mounted finite cylinder on a flat plate. In: Conference on Modelling Fluid Flow (CMFF 2006). The 13th International Conference on Fluid Flow Technologies, Budapest, Hungary (2006)

Ahmed, S.R., Ramm, G., Faltin, G.: Some salient features of the time averaged ground vehicle wake. SAE paper no. 8403000 (1984)

ANSYS Inc. ANSYS CFX, Release 11.0 - Solver Theory Guide, Solver Modeling Guide (2007)

Archambeau, F., Méchitoua, N., Sakiz, M.: Code_saturne: a finite volume code for the computation of turbulent incompressible flows – industrial applications. Int. J. on Finite Volumes, Web based journal, only available electronically (Febuary 2004)

Arnott, K., Neitzke, K.P., Agocs, J., Sammer, G., Schneider, G., Schroeder, A.: Detailed characterization using PIV of the flow around an aerofoil in high lift configuration. In: EUROPIV2 Workshop on Particle Image Velocimetry, Zaragoza (2003)

Ask, J.: Prediction of aerodynamically induced wind noise around ground vehicles. PhD Thesis, Chalmers University of Technology, Gothenburg, Sweden (2008)

Ask, J., Davidson, L.: The Sub-critical flow past a generic side mirror and its impact on sound generation and propagation. In: 12th AIAA/CEAS Aeroacoustics Conference, Paper 2006-2558, Cambridge, Massachusetts, USA (2006)

Aupoix, B., Grenard, P.: Explicit algebraic modelling for eddy viscosity models. In: Fourth International Symposium on Turbulence and Shear Flow Phenomena, Williamsburg, Virginia (2005)

Aupoix, B., Barricau, P., Egorov, Y., Gilliot, A., Menter, F., Monnier, J.C., Pailhas, G., Perret, L., Stanislas, M., Touvet, Y.: The DESider Bump Experiment, ETMM7-Limassol, Cyprus, June 4-6 (2008)

Bailly, C., Juvé, D.: A stochastic approach to compute subsonic noise using linearized Euler's equations. AIAA Journal, 99–1872 (1999)

Balaras, E., Benocci, C.: Subgrid-scale models in finite difference simulations of complex wall bounded flows. In: Applications of Direct and Large Eddy Simulation, AGARD, pp. 2.1–2.6 (1994)

Balaras, E., Benocci, C., Piomelli, U.: AIAA Journal 34, 1111–1119 (1996)

Bechara, W., Bailly, C., Lafon, P.: Stochastic approach to noise modeling for free turbulent flows. AIAA Journal 32(3), 455–463 (1994)

Benhamadouche, S.: Large Eddy Simulation with the unstructured collocated arrangement. PhD Thesis, University of Manchester, Manchester, UK (2006)

Benhamadouche, S., Laurence, D.: Global kinetic energy conservation with unstructured meshes. International Journal for Numerical Methods in Fluids 40, 561–571 (2002)

Benhamadouche, S., Laurence, D.: LES, Coarse LES, and Transient RANS Comparisons on The Flow Across Tube Bundle. Int. J. Heat and Fluid Flow 4, 470–479 (2003)

Benhamadouche, S., Laurence, D., Jarrin, N., Afgan, I., Moulinec, C.: Large Eddy Simulation of flow across in-line tube bundles. In: The 11th International Topical Meeting on Nuclear Reactor Thermal-Hydraulics (NURETH-11) Paper: 405, Popes Palace Conference Center, Avignon, France, October 2-6 (2005)

Benhamadouche, S., Mahesh, K., Constantinescu, G.: Colocated finite-volume schemes for large-eddy simulation on unstructured meshes. In: Proceedings of the 2002 Summer Program, Center for Turbulence Research, Stanford University and NASA Ames, pp. 143–154 (2002)

Berkooz, G., Holmes, L., Lumley, J.L.: The Proper Orthogonal Decomposition in the analysis of turbulent flows. Ann. Rev. Fluid Mech. 25, 539–579 (1993)

Berton, E., Allain, C., Favier, D., Maresca, C.: Experimental methods for subsonic flow measurements. Notes on Num. Fluid Mech. and Multidisciplinary Design 81, 251–260 (2002); In: Haase, W., Selmin, V., Winzell, B. (eds) Progress in Computational Flow-Structure Interaction, UNSI European program, Sci. Springer, Heidelberg

Billson, M.: Computational Techniques for Turbulence Generated Noise. PhD thesis, Dept. of Thermo and Fluid Dynamics, Chalmers University of Technology, Göteborg, Sweden (2004)

Billson, M., Eriksson, L.-E., Davidson, L.: Jet noise prediction using stochastic turbulence modeling. In: AIAA paper 2003-3282, 9th AIAA/CEAS Aeroacoustics Conference (2003)

Blake, W.K.: A statistical description of pressure and velocity fields at the trailing edge of a flat strut. avid Taylor Naval Ship R&D Center Report 4241, Bethesda, Maryland (1975)

Bouhadji, A., Bourdet, S., Braza, M., Hoarau, Y., Rodes, P., Tzabiras, G.: Turbulence modelling of unsteady flows with a pronounced periodic character. Notes on Numerical Fluid Mechanics 81, 87–96 (2002); In: Haase, W., Selmin, V., Winzell, B. (eds) dedicated volume Progress in Computational Flow-Structure Interaction, Sci. Springer, Heidelberg

Bourdet, S., Braza, M., Hoarau, Y., El Akoury, R., Ashraf, A., Harran, G., Chassaing, P., Djeridi, H.: Prediction and physical analysis of unsteady flows around a pitching airfoil with the dynamic mesh approach in the context of fluid-structure interaction, Revue Européenne de Mécanique Numérique, 16/3-4, pp. 451–476

Bourguet, R.: Physical analysis and modelling of compressible turbulent unsteady flows around airfoils by high-fidelity and low-dimensional statistical approaches in fluid-structure interaction context, PhD thesis, University of Toulouse, Institut National Polytechnique, INPT (2008)

Bourguet, R., Braza, M., Perrin, R., Harran, G.: Physical analysis of an anisotropic eddy viscosity concept for strongly detached unsteady flows. In: IUTAM Symposium on Unsteady Separated Flows and their Control, Corfu, Greece, June 18-22 (2007); J. Fluids & Structures 24 (8) (2008)

Bourguet, R., Braza, M., Perrin, R., Harran, G.: Anisotropic eddy viscosity concept for strongly detached unsteady flows. AIAA J. 45(5), 1145–1149 (2007)

Braza, M., Faghani, D., Persillon, H.: Successive stages and the role of natural vortex dislocations in three-dimensional wake transition. J. Fluid Mech. 439, 1–41 (2001)

Braza, M., Perrin, R., Hoarau, Y.: Turbulence properties in the cylinder wake at high Reynolds number. J. Fluids and Structures 22, 757–771 (2006)

Breitsamter, C.: Turbulente Strömungsstrukturen an Flugzeugkonfigurationen mit Vorderkantenwirbeln. PhD thesis, Munich (1997)

Breuer, M., Jovicic, N., Mazaev, K.: Comparison of DES, RANS and LES for the separated flow around a flat plate at high incidence. International Journal for Numerical Methods in Fluids 41, 357–388 (2003)

Brunet, V., Deck, S.: Zonal Detached Eddy Simulation of of transonic buffet on a civil aircraft type configuration. AIAA paper 2008-4152 (2008)

Bunge, U., Mockett, C., Thiele, F.: Guidelines for implementing detached-eddy simulation using different models. Aerospace Science and Technology 11, 376–385 (2007)

Bush, R., Mani, M.: A two-equation large eddy stress model for high sub-grid shear. In: Proceedings of the 15th AIAA Computational Fluid Dynamics Conference, Anaheim, California, USA (2001)

Byun, G., Simpson, R.L.: Structure of three-dimensional separated flow on an axisymmetric bump. AIAA Paper 2005-0113 (2005)

Byun, G., Simpson, R., Long, C.H.: A study of vortical separation from three-dimensional symmetric bumps. AIAA Journal (4), 754–765 (2004)

Cabot, W.: Large eddy simulations with wall models. Annual Research Briefs, Center for Turbulent Research, Stanford Univ./NASA Ames Research Center, pp. 41–50 (1995)

Cabot, W., Moin, P.: Approximate wall boundary conditions in the large-eddy simulations of high Reynolds number flow. Flow, Turbulence and Combustion 63, 269–291 (1999)

Cantwell, B., Coles, D.: An experimental study of entrainment and transport in the turbulent near wake of a circular cylinder. J. Fluid Mech. 136, 321–374 (1983)

Carpy, S., Manceau, R.: Turbulence modelling of statistically periodic flows: Synthetic jet into quiescent air. International Journal of Heat and Fluid Flow 27, 756–767 (2006)

Carr, L.W., Chandrasekhara, M.S.: Compressibility effects on dynamic stall. Progress in Aerospace Science 32, 523–573 (1996)

Caruelle, B.: Simulations d'écoulements instationnaires turbulents en aérodynamique: application à la prédiction du phénomène de tremblement. Ph.D. Thesis, INPT/CERFACS (2000)

Chalot, F., Mallet, M., Ravachol, M.: A comprehensive finite element Navier-Stokes solver for low-and high-speed aircraft design. AIAA Paper 94-0814

Chandrasekhara, M.S., Wilder, M.C.: Heat-Flux Gauge Studies of Compressible Dynamic Stall. AIAA Journal 41, 757–762 (2003)

Chang, D., Tavoularis, S.: Simulations of turbulence, heat transfer and mixing across narrow gaps between rod-bundle subchannels. Nuclear Engineering and Design 238, 109–123 (2008)

Chauvet, N., Deck, S., Jacquin, L.: Zonal Detached Eddy Simulation of a Controlled Propulsive Jet. AIAA J. 45(10), 2458–2473 (2007)

Chen, C.H., Patel, V.C.: Near-wall turbulence models for complex flows including separation. AIAA Journal 26, 641–648 (1988)

Ciardi, M., Sagaut, P., Klein, M., Dawes, W.N.: A dynamic finite volume scheme for large-eddy simulation on unstructured grids. Journal of Computational Physics 210, 632–655 (2005)

Cid, E., Cazin, S., Drouin, V.: Validation de PIV stéréoscopique et application a un écoulement aérodynamique de sillage 3D. 8^{e} Congres Francophone de Vélocimétrie Laser (2002)

Coles, D., Wadcock, A.J.: Flying Hot-Wire Study of Flow Past an NACA 4412 Airfoil at Maximum Lift. AIAA J. 17(4), 312–329 (1979)

Comte-Bellot, G., Corrsin, S.: Simple Eulerian time correlation of full- and narrow-band velocity signals in grid-generated, isotropic turbulence. J. Fluid. Mech. 48, 273–337 (1971)

Craft, T.J., Launder, B.E., Suga, K.: Development and application of cubic eddy viscosity model of turbulence. Int. J. Heat Fluid Flow 17, 108–115 (1996)

Davidson, L.: HYBRID LES-RANS: Inlet boundary conditions for flows with recirculation. In: Advances in Hybrid RANS-LES Modelling. Notes on Numerical Fluid Mechanics and Multidisciplinary Design, vol. 97, pp. 55–66. Springer, Heidelberg (2008)

Davidson, L.: Evaluation of the SST-SAS model: Channel flow, asymmetric diffuser and axi-symmetric hill. In: ECCOMAS CFD 2006, Egmond aan Zee, The Netherlands, September 5-8 (2006)

Davidson, L.: Hybrid LES-RANS: Inlet boundary conditions for flows including recirculation. In: The International Symposium on Turbulence and Shear Flow Phenomena, Munich, Germany, 27-29 August, vol. 2, pp. 689–694 (2007a)

Davidson, L.: Inlet boundary conditions for embedded LES. In: First CEAS European Air and Space Conference, Berlin, September 10-13 (2007b)

Davidson, L.: Using isotropic synthetic fluctuations as inlet boundary conditions for unsteady simulations. Advances and Applications in Fluid Mechanics (1), 1–35 (2007c)

Davidson, L., Billson, M.: Hybrid LES/RANS using synthesized turbulence for forcing at the interface. International Journal of Heat and Fluid Flow 27(6), 1028–1042 (2006)

Davidson, L., Dahlström, S.: Hybrid LES-RANS: Computation of the flow around a three-dimensional hill. In: Rodi, W., Mulas, M. (eds.) Engineering Turbulence Modelling and Measurements, vol. 6, pp. 319–328. Elsevier, Amsterdam (2005)

Deane, A.E., Kevrekidis, I.G., Karniadakis, G.E., Orzag, S.A.: Low-dimensional models for complex geometry flows: Application to grooved channels and circular cylinders. Phys. Fluids A 3, 2337–2354 (1991)

Deardorff, J.: A numerical study of the three-dimensional turbulent channel flow at large Reynolds numbers. Journal of Fluid Mechanics 41, 453–480 (1970)

Deck, S.: Simulation numérique des charges latérales instationnaires sur des configurations de lanceur. Ph.D. Thesis, U. Orléans (2002)

Deck, S.: Zonal Detached Eddy Simulation of the Flow around a High-Lift Configuration. AIAA J. 43(11), 2372–2384 (2005)

Deck, S.: Numerical Simulation of Transonic Buffet over a Supercritical Airfoil. AIAA Journal 43(7), 1556–1566 (2005)

Deck, S., Thorigny, P.: Unsteadiness of an axisymmetric separating/reattaching flow: numerical investigation. Physics of Fluids 19(6) (2007)

Dervieux, A., Braza, M., Dussauge, J.P.: Scientific Editors of the volume: Computation and Comparison of Efficient Turbulence Models for Aeronautics. Notes on Numerical Fluid Mechanics, vol. 65. Vieweg (1998)

Devenport, W., Simpson, R.: Time-dependent and time-averaged turbulence structure near the nose of a wing-body junction. Journal of Fluid Mechanics 210, 23–55 (1990)

Ducross, F., Ferrand, V., Nicoud, F., Weber, C., Darracq, D., Gacherieu, C., Poinsot, T.: Large-Eddy Simulation of the Shock/Turbulence Interaction. Journal of Computational Physics 152, 512–549 (1999)

Durbin, P.A.: Separated flow computations with the $k - \varepsilon - v^2$model. AIAA Journal 55, 659–664 (1995)

Edwards, J., Chandra, S.: Comparison of eddy viscosity-transport turbulence models for three-dimensional, shock-separated flowfields. AIAA Journal 34(4), 756–763 (1996)

Egorov, Y., Menter, F.: Development and Application of SST-SAS Turbulence Model in the DESIDER Project. In: Proc. of 2nd Symposium on Hybrid RANS-LES Methods, Corfu, Greece, June 17-18 (2007)

Ekaterinanis, J.A., Platzer, M.F.: Computational Prediction of Airfoil Dynamic Stall. Progress in Aerospace Sciences 33, 749–846 (1997)

El Akoury, R.: Analyse physique des effets de rotation de paroi écoulements transitionnels et modélisation d'écoulements turbulents autour de structures portantes, PhD INPT, December 17 (2007)

El Akoury, R., Braza, M., Perrin, R., Harran, G., Hoarau, Y.: The 3D transition in the flow around a rotating cylinder. J. Fluid Mechanics 607, 1–11 (2008)

El Akoury, R., Braza, M., Hoarau, Y., Vos, J., Harran, G., Sevrain, A.: Unsteady flow around a NACA0021 airfoil beyond stall at 60° angle of attack. In: Procs. IUTAM Symposium on Unsteady Separated Flows and their Control, Corfu, Greece, June 18-22 (2007)

Ffowcs Williams, J.E., Hawkings, D.L.: Sound generation by turbulence and surfaces in arbitrary motion. Phil. Trans. R. Soc. A 264, 321–342 (1969)

Frederich, O., Bunge, U., Mockett, C., Thiele, F.: Flow Prediction around an Oscillating NACA0012 Airfoil at Re=1000000. In: Proceedings of the IUTAM Symposium on unsteady separated flows and their control, Corfu, Greece (2007)

Frohlich, J., Rodi, W., Kessler, P., Parpais, S., Bertoglio, J., Laurence, D.: Large eddy simulation of flow over circular cylinders on structured and unstructured grids. In: Hirschel, E. (ed.) Numerical Flow Simulation I. Notes on Numerical Fluid Mechanics, vol. 66, pp. 319–338. Vieweg (1998)

Frohlich, J., Rodi, W.: LES of flow around a circular cylinder of finite height. Int. J. of Heat and Fluid Flow 25, 537–548 (2004)

Garnier, E., Mossi, M., Sagaut, P., Comte, P., Deville, M.: On the use of shock-capturing schemes for large-eddy simulation. J. Comp. Phys. 153, 273–311 (1999)

Gatski, T.B., Speziale, C.G.: On Explicit Algebraic Stress Models for Complex Turbulent Flows. Journal of Fluid Mechanics 254, 59–78 (1993)

Gleyzes, C., Capbern, P.: Experimental study of two AIRBUS/ONERA airfoils in near stall conditions. Part I: Boundary layers, AST 7(6), 439–449 (2003)

Görtz, S., Jirásek: A Steady and Unsteady CFD Analysis of the F-16XL using the Unstructured Edge Code. AIAA-2007-678, Reno, Nevada (2006)

Graftieaux, L., Michard, M., Grosjean, N.: Combining PIV, POD and vortex identification algorithms for the study of unsteady turbulent swirling flows. Meas. Sci. Technol. 12, 1422–1429 (2001)

Gurr, A., Rieger, H., Breitsamter, C., Thiele, F.: Detached-eddy simulation of the delta wing of a generic aircraft configuration. In: New Results in Numerical and Experimental Fluid Mechanics V. Notes on Numerical Fluid Mechanics and Multidisciplinary Design, vol. 92, pp. 463–470. Springer, Heidelberg (2006)

Haase, W., Aupoix, B., Bunge, U., Schwamborn, D. (eds.): FLOMANIA - A European initiative on flow physics modelling. Notes on Numerical Fluid Mechanics and Multidisciplinary Design, vol. 94. Springer, Heidelberg (2006)

Hadžić, I., Hanjalić, K., Laurence, D.: Modeling the response of turbulence subjected to cyclic irrotational strain. Phys. Fluids 13(6), 1740–1747 (2002)

Hayakawa, M., Hussain, F.: Three-dimensionality of organised structures in a plane turbulent wake. J. Fluid Mech. 206, 375–404 (1989)

Hedges, L., Travin, A., Spalart, P.: Detached-eddy simulation over a simplified landing gear. J. of Fluids Engineering 124(2), 413–423 (2002)

de Henshaw, M.J.C.: M219 cavity case: Verification and validation data for computational unsteady aerodynamics. Tech. Rep. RTO-TR-26, AC/323(AVT)TP/19, QinetiQ, UK, 453–472 (2002)

Herrin, J.L., Dutton, C.J.: Supersonic base flow experiments in the near wake of A cylindrical afterbody. AIAA Journal 32, 77–83 (1994)

Hoarau, Y., Perrin, R., Braza, M., Ruiz, D., Tzabiras, G.: Advances in turbulence modelling for unsteady flows. In: Haase, W., Aupoix, B., Bunge, U., Schwamborn, D. (eds.) Flow Physics Modelling: an integrated approach. Dedicated volume in series Notes on Numerical Fluid Mech. and Multidisciplinary design, vol. 94. Springer, Sci., Heidelberg (2006)

Höld, R., Brenneis, A., Eberle, A.: Numerical simulation of aeroacoustic sound generated by generic bodies placed on a plate: Part I – Prediction of aeroacoustic sources. In: 5th AIAA/CEAS Aeroacoustics Conference, Paper AIAA-99-1896, Seattle, Washington, USA (1999)

Hunt, J.: The European Consortium For Mathematics In Industry - ECMI congress, London, 30 June- 4 July 2008. Springer, Heidelberg (2008)

Hunt, J.C., Wray, A., Moin, P.: Eddies, stream, and convergence zones in turbulent flows. Center for Turbulence Research Report S88 (1988)

Hussain, A.K.M.F., Hakayawa, M.: Eduction of large-scale organized structures in a turbulent plane wake. J. Fluid Mech. 180, 193–229 (1987)

Hussain, A.K.M.F., Reynolds, W.C.: Measurements in fully developed turbulence channel flow. J. Fluid Eng. 97, 568 (1975)

Jameson, A.: Time Dependent Calculations Using Multigrid with Applicarion to Unsteady Flows pat Airfoils and Wings, AIAA paper 91-1596 (1991)

Jameson, A., Schmidt, W.: Applications of Multi-Grid Methods for Transonic Flow calculations. In: Proceedings of the Multi-Grid conference, Koeln-Portz. Lecture notes in Mathematics, pp. 559–613. Springer, Heidelberg (1981)

Jameson, A., Schmidt, W., Turkel, E.: Numerical solutions of the Euler equations by finite volume methods using Runge-Kutta time-stepping schemes. AIAA Paper 81-1259 (1981)

Jeong, J., Hussain, F.: On the definition of a vortex. J. Fluid Mech. 285, 69–94 (1995)

Jarrin, N.: Synthetic Inflow Boundary Conditions for the Numerical Simulation of Turbulence, PhD Thesis (2008)

Jarrin, N., Benhamadouche, S., Laurence, D., Prosser, R.: A synthetic-eddy method for generating inflow conditions for large-eddy simulations. International Journal of Heat and Fluid Flow 27, 585–593 (2006)

Jarrin, N., Revell, A., Prosser, R., Laurence, D.: Reconstruction of Turbulent Fluctuations for Hybrid RANS/LES Simulations Using a Synthetic-Eddy Method, ETMM7, Limassol, Cyprus, June 4-6 (2008)

Kang, H., Chester, S., Meneveau, C.: Decaying turbulence in an active-grid-generated flow and comparisons with large-eddy simulation. Journal of Fluid Mechanics 480, 129–160 (2003)

Karweit, M., Blanc-Benon, P., Juvé, D., Comte-Bellot, G.: Simulation of the propagation of an acoustic wave through a turbulent velocity field: A study of phase variance. J. Acoust. Soc. Am. 89(1), 52–62 (1991)

Kim, J., Moin, P., Moser, R.: Turbulence statistics in fully developed channel flow at low Reynolds number. J. Fluid Mech. 177, 133 (1987) (category No. 25.6: full simulation, 192 x-points, b87-0149)

Klein, M., Sadiki, A., Janicka, J.: A digital filter based generation of inflow data for spatially developing direct numerical simulation or large eddy simulations. J. of Computational Physics 186(2), 652–665 (2003)

Kok, J.C.: Resolving the dependence on freestream values for the k–ω turbulence model. AIAA Journal 38(7), 1292–1295 (2000)

Kok, J.C., Brandsma, F.J.: Turbulence Model based on Vortical Flow Computations for a Sharp Edged Delta Wing in Transonic Flow using full Navier-Stokes Equations. NLR-CR-2000-342 (2000)

Kok, J.C.: A symmetry and dispersion-relation preserving high-order scheme for aeroacoustics and aerodynamics. In: Wesseling, P., Oñate, E., Périaux, J. (eds.) ECCOMAS CFD 2006, Egmond aan Zee, The Netherlands, 5-8 September 2006, NLR-TP-2006-525 (2006)

Kok, J.C.: A high-order low-dispersion symmetry-preserving finite-volume method for compressible flow on curvilinear grids. Journal of Computational Physics. NLR-TP-2008-775 (2008) (submitted)

Kok, J.C., Dol, H.S., Oskam, B., van der Ven, H.: Extra large eddy simulation of massively separated flows. In: Proc. 42nd Aerospace Sciences Meeting/Exhibit, Reno, NV, USA, AIAA paper 2004-264 (2004)

Kok, J.C., Soemarwoto, B.I., van der Ven, H.: Extra-large eddy simulations using a high-order finite-volume scheme. In: Peng, S.H., Haase, W. (eds.) Advances in Hybrid RANS–LES Modelling. Notes on Numerical Fluid Mechanics and Multidisciplinary Design, vol. 97, pp. 87–96. Springer, Heidelberg (2007); NLR-TP-2007-800

Kraichnan, R.H.: Diffusion by a random velocity field. Physics of Fluids 13, 22–31 (1970)

Krajnović, S.: Large Eddy Simulation of the Flow Over a Three-Dimensional Hill. Flow, Turbulence and Combustion (2007a) (accepted for publication)

Krajnović, S.: Flow Around a Surface Mounted Finite Cylinder: A Challenging Case for LES. In: Proceedings of Second Symposium on Hybrid RANS-LES Methods, Corfu island, Greece (2007b)

Kuntz, M., Menter, F., Egorov, Y.: Definition of bump shape. DESider project, Deliverable D2.2-01. ANSYS-CFX (2004)

Larcheveque, L., Sagaut, P., Le, H., Comte, P.: Large eddy simulation of a compressible flow in a three-dimensional open cavity at high Reynolds number. J. Fluid Mech. 301, 265–301 (2004)

Laskha, B., Ranke, H., Breitsamter, C.: Application of unsteady measurement techniques to vortical and separated flow. ZFW 19, 90–108 (1995)

Laurence, D., Uribe, J.C., Utyuzhnikov, S.: A robust formulation of the v2-f model. Flow, Turbulence and Combustion 73, 169–185 (2004)

Lazos, B.: The flow physics around a 4-wheel landing bogie associated with noise, Ph.D dissertation, Lehigh university (2000)

Lazos, B.: Mean flow features around the inline wheels of four-wheel landing gear. AIAA Journal 40(2) (2002)

Le, H., Moin, P.: Direct numerical simulation of turbulent flow over a backward-facing step, Stanford Univ., Center for Turbulence Research, Annual Research Briefs, pp. 161–173 (1992)

Lecordier, B., Trinite, M.: Advanced PIV Algorithms with Image Distortion - Validation and Comparison from Synthetic Images of Turbulent Flow. In: PIV 2003 Symposium Busan, Korea (2003)

Leder, A.: Dynamics of fluid mixing in separated flows. Physics of Fluids A 3, 1741–1748 (1991)

Lee, C.M., Choi, Y.D.: Comparison of thermo-hydraulic performances of large scale vortex flow (LSVF) and small scale vortex flow (SSVF) mixing vanes in 17x17 nuclear rod bundle. Nuclear Engineering and Design 237, 2322–2331 (2007)

Lee, S., Lele, S., Moin, P.: Simulation of spatially evolving turbulence and the application of Taylor's hypothesis in compressible flow. Physics of Fluids 4, 1521–1530 (1992)

Leschziner, M.A., Li, N., Tessicini, F.: Computational methods combining LES with approximate wall-layer models for predicting separated turbulent near-wall flows. ER-COFTAC Bulletin 72, 25–31 (2007)

Levasseur, V.: Simulation des grandes échelles en éléments finis stabilises: Une approche Variationnelle Multi-échelle or Large Eddy Simulation in Stabilized Finite Element environment: a Variationnal Multiscale approach, Université Paris VI (2007)

Li, N., Leschziner, M.A.: Highly-resolved large eddy simulation of separation from a three-dimensional hill. In: Proc. 11th European Turbulence Conference, Porto, June 2007, pp. 407–409 (2007)

Lien, F., Leschziner, M.: Computational modelling of 3D turbulent flow in S-diffuser and transition ducts. In: Rodi, W., Martelli, F. (eds.) Engineering Turbulence Modelling and Experiments, vol. 2, pp. 217–228. Elsevier, Amsterdam (1993)

Lien, F., Leschziner, M.A.: A general non-orthogonal collocated finite volume algorithm for turbulent flow at all speeds incorporating second-moment turbulence-transport closure. Comp. Meths Applied Mech. Eng. 114, 123–148 (1994)

Lienhart, H., Becker, S.: Flow and turbulent structure in the wake of a simplified car model. SAE paper no. 2003-01-0656 (2003)

Lighthill, M.J.: On Sound Generated Aerodynamically. I. General Theory, Proc. Roy. Soc. A 211(1107) (1952)

Lighthill, M.J.: On Sound Generated Aerodynamically. II. Turbulence as a Source of Sound, Proc. Roy. Soc. A 222(1148) (1954)

Lin, J.-C., Vorobieff, P., Rockwell, D.: Three-dimensional patterns of streamwise vorticity in the turbulent near-wake of a cylinder. Journal of Fluids and Structures 9, 231–234 (1995)

Lübcke, H., Rung, T., Thiele, F.: Prediction of the spreading mechanisms of 3D turbulent wall jets with explicit Reynolds-stress closures. In: Rodi, W., Fueyo, N. (eds.) Engineering Turbulence Modelling and Experiments 5, pp. 127–145. Elsevier, Amsterdam (2002)

Luo, S.C., Li, L.L., Shah, D.A.: Aerodynamic stability of the downstream of two tandem square-section cylinders. Journal of Wind Engineering and Industrial Aerodynamics 79, 79–103 (1999)

Manceau, R., Brizzi, L.E.: Presentation of PIV data for AR=3, (private presentation at EDF R&D Chatou, 13 June 2007) (2007), http://www.univ-poitiers.fr/lea

Marquez, B.: Simulation des grandes échelles d'écoulements compressibles par des méthodes éléments finis or Large Eddy Simulation of Compressible Flows using Finite Element Solver, PhD, INPT (1999)

Martinat, G., Braza, M., Harran, G., Sevrain, A.: Dynamic stall of a pitching and horizontally oscillating NACA 0012 airfoil. In: Procs. IUTAM Symposium on Unsteady Separated Flows and their Control, Corfu, Greece, June 18-22 (2007)

McAlister, K.W., Carr, L.W., McCroskey, W.J.: Analysis of the Development of Dynamic Stall Based on the NACA 0012 Airfoil. NASA TP-1100 (1978)

McAlister, K.W., Pucci, S.L., Carr, L.W., McCroskey, W.J.: An Experimental Study of Dynamic Stall on Advanced Airfoil Sections, NASA Technical Memorandum 84245, NASA Ames Research Center (1982)

McCroskey, J., Fisher, R.K.: Detailed aerodynamic measurements on a model rotor in the blade stall regime. Journal of American Helicopter Society 7, 20–30 (1972)

Menter, F.: Zonal two-equation k–ω turbulence models for aerodynamic flows. AIAA-Paper 1993-2906 (1993)

Menter, F.R.: Two-equation eddy-viscosity turbulence models for engineering applications. AIAA 32(8), 1598–1605 (1994a)

Menter, F.R.: Eddy viscosity transport equations and their relation to the k-ε model, NASA-TM-108854 (1994b)

Menter, F.R.: Eddy viscosity transport equations and their relation to the k-ε model. Journal of Fluids Engineering 119, 876–884 (1997)

Menter, F., Egorov, Y.: Revisiting the turbulent length scale equation. In: IUTAM Symposium: One Hundred Years of Boundary Layer Research, Göttingen (2004); Menter, F., Egorov, Y.: A scale-adaptive simulation model using two-equation models. AIAA paper 2005–1095, Reno, NV (2005)

Menter, F.R., Egorov, Y.: Revisiting the turbulent scale equation. In: Heinemann, H.-J. (ed.) Proc. IUTAM Symposium One hundred years of boundary layer research, Göttingen, Germany, 12-14 August, 2004. Springer, Heidelberg (2005a)

Menter, F.R., Egorov, Y.: A Scale-Adaptive Simulation Model using Two-Equation Models. AIAA Paper, AIAA 2005-1095 (2005b)

Menter, F.R., Egorov, Y.: Turbulence models based on the length-scale equation. In: Humphrey, J.A.C., et al. (eds.) Proc. Fourth International Symposium on Turbulence and Shear Flow Phenomena, Williamsburg, VA USA, June 27-29, 2005 (2005c)

Menter, F.R., Egorov, Y.: SAS turbulence modelling of technical flows. In: Proc. DLES-6 Conference, Poitiers, France, September 12-14 (2005d)

Menter, F., Kunz, M.: Adaption of eddy-viscosity turbulence models to unsteady separated flow behind vehicles. In: The Aerodynamics of Heavy Vehicles: Trucks, Buses and Trains. Lecture notes in applied and computational mechanics, vol. 19 (2004a)

Menter, F., Kuntz, M.: Adaption of eddy-viscosity turbulence models to unsteady separated flow behind vehicles. In: The Aerodynamics of Heavy Vehicles: Trucks, Buses, and Trains. Lecture Notes in Applied and Computational Mechanics, vol. 19. Springer, Heidelberg (2004b)

Menter, F.R., Egorov, Y., Rusch, D.: Steady and Unsteady Flow Modelling Using the $k-\sqrt{k}L$. In: Hanjalic, K., Nagano, Y., Jakirlic, S. (eds.) Proc. Turbulence, Heat and mass Transfer 5 (2006)

Menter, F., Kuntz, M., Bender, R.: A scale-adaptive simulation model for turbulent flow prediction. AIAA paper 2003–0767, Reno, NV (2003)

Menter, F., Kuntz, M., Langtry, R.: Ten yearts of experience with the SST model. In: Hanjalic, K., Nagano, Y., Tummers, M. (eds.) Turbulence, Heat and Mass Transfer 4 (2003)

Michel, U., Eschricht, D., Greschner, B., Knacke, T., Mockett, C., Panek, L., Thiele, F., Yan, J.: Simulation of the sound radiation of turbulent flows with DES. In: Proceedings of the West-East High Speed Flow Field Conference, Moscow, Russia (2007)

Mockett, C., Thiele, F.: Overview of DES for external and internal turbulent flow applications. In: Proceedings of the 5th International Conference on Fluid Mechanics, New Trends in Fluid Mechanics Research, Shanghai, China, pp. 79–82 (2007)

Mockett, C., Greschner, B., Knacke, T., Perrin, R., Yan, J., Thiele, F.: Demonstration of improved DES methods for generic and industrial applications. In: Peng, S.-H., Haase, W. (eds.) Advances in hybrid RANS-LES modelling. Notes on Numerical Fluid Mechanics and Multidisciplinary Design, vol. 97, pp. 222–231 (2007)

Mockett, C., Perrin, R., Reimann, T., Braza, M., Thiele, F.: Analysis of detached-eddy simulation for the flow around a circular cylinder with reference to PIV data. Journal of Flow, Turbulence and Combustion (2008a) (to be published)

Monfort, D., Benhamadouche, S., Sagaut, P.: Meshless approach for wall treatment in Large-Eddy Simulation. CMAME (accepted) (to appear, 2008)

Nayyar, P., Barakos, G.N., Badcock, K.J.: Numerical study of transonic cavity flow using Large-Eddy and Detached-Eddy simulation. The Aeronautical Journal 111(1115), 153–164 (2007)

Neitzke, K.P.: Using Advanced Measurements Techniques in High-Lift Validation Experiments. In: RAeS, Aerospace Aerodynamics Research Conference, UK (June 2003)

Nicoud, F., Ducros, F.: Subgrid-scale stress modelling based on the square of the velocity gradient tensor. Flow, Turb. Combust. 62, 183–200 (1999)

Nightingale, D.A., Ross, J.A., Foster, G.W.: Cavity unsteady pressure measurements - Examples from wind-tunnel tests. Technical Report Version 3, Aerodynamics& Aeromechanics Systems Group, QinetiQ (2005)

Nikitin, N., Nicoud, F., Wasistho, B., Squires, K., Spalart, P.: An approach to wall modeling in large-eddy simulations. Physics of Fluids 12(7), 1629–1632 (2000)

Noack, B., Afanasiev, K., Morzynski, M., Tadmor, G., Thiele, F.: A hierarchy of low-dimensional models for the transient and post-transient cylinder wake. J. Fluid Mech. 497, 335–363 (2003)

Nolin, G., Mary, I., Ta, P.: RANS eddy viscosity reconstruction from LES flow field for turbulent boundary layers, AIAA-paper 2005-4998 (2005)

Nolin, G., Mary, I., Ta, P.: LES inflow conditions for turbulent boundary layers of complex flows using database, AIAA-paper 2006-2888 (2006)

Norberg, C.: LDV-measurements in the near wake circular cylinder. In: Conference on Bluff Body Wakes and Vortex Induced Vibrations Presented at ASME Fluids Engineering Division (Annual Summer Meeting), Washington, DC (FEDSM98-5202) (1998)

Okajima, A., Kosugi, T., Nakamura, A.: Flow-induced in-line oscillation of a circular cylinder in a water tunnel. J. of Pressure Vessel Technology, ASME 124, 89–96 (2002)

Pailhas, G., Houdeville, R., Barricau, P., Le Pape, A., Faubert, A., Loiret, P., David, F.: Experimental investigation of dynamic stall. ONERA TP 2006-08 (2006)

Paik, J., Escauriaza, C., Sotiropoulos, F.: On the bimodal dynamics of the turbulent horseshoe vortex system in a wing-body junction. Physics of Fluids 19, 045107 (2007)

Pailham Barricau, P., Touvet, Y., Monnier, J.: Turbulent separated flow through a channel with a bump (to be presented). In: EWA-UFAST workshop, Prague (2008)

Park, C.W., Lee, S.J.: Free end effect on the wake flow structure behind a finite circular cylinder. J. of Wind Eng. and Ind. Aerodynam. 88, 231–246 (2000)

Park, C.W., Lee, S.J.: Flow structure around a finite circular cylinder embedded in various atmospheric boundary layers. Fluid Dynamics Research 30, 197–215 (2002)

Park, C.W., Lee, S.J.: Effects of free-end corner shape on flow structure around a finite cylinder. J. of Fluids and Structures 19, 141–158 (2004)

Peng, S.-H.: Hybrid RANS-LES modelling based on zero- and one-equation models for turbulent flow simulation. In: Humphrey, J., Eaton, J., Friedrich, R., Kasagi, N., Leschziner, M., Gatski, T. (eds.) The Fourth International Symp. on Turbulence and Shear Flow Phenomena, Williamsburg, Virginia, vol. 3, pp. 1159–1164 (2005a)

Peng, S.-H.: TC-A2 Description – Specification of Test Case A2 (TC A2): 3D Cavity Flow (2005b), DESider project website, http://cfd.me.umist.ac.uk/desider/

Peng, S.-H.: Hybrid RANS-LES modelling based on zero- and one-equation models for turbulent flow simulation. In: Proc. of 4th Int. Symp. Turb. and Shear Flow Phenomena, vol. 3, pp. 159–1164 (2005c)

Peng, S.-H.: Algebraic hybrid RANS-LES modelling applied to incompressible and compressible turbulent flows. AIAA Paper 2006-3910, San Francisco (2006a)

Peng, S.-H.: Towards detached eddy simulation modelling using a k-equation turbulence model. In: Wesseling, P., Oñate, E., Périaux, J. (eds.) Proceedings of the European Conference on Computational Fluid Dynamics ECCOMAS CFD 2006, Egmond aan Zee, The Netherlands (2006b)

Peng, S.-H.: Simulation of turbulent flow past a rectangular open cavity using DES and unsteady RANS. AIAA Paper 2006-2827, San Francisco (2006b)

Peng, S.-H., Haase, W. (eds.): Advances in Hybrid RANS-LES Modelling. Notes on Num. Fluid Mech. And Multidisciplinary Design, vol. 97. Springer, Heidelberg (2007)

Peng, S.-H., Leicher, S.: DES and hybrid RANS-LES modelling of unsteady pressure oscillations and flow features in a rectangular cavity. In: Peng, S.-H., Haase, W. (eds.) Advances in Hybrid RANS-LES Modelling. Notes on Numerical Fluid Mechanics and Multidisplinary Design, vol. 97, pp. 132–141 (2008)

Perrin, R., Braza, M., Cid, E., Cazin, S., Chassaing, P., Mockett, C., Reimann, T., Thiele, F.: Coherent and turbulent process analysis in the flow past a circular cylinder at high Reynolds number. In: IUTAM Symposium on Unsteady Separated Flows and their Control, Corfu, Greece, June 18-22 (2007)

Perrin, R., Braza, M., Cid, E., Cazin, S., Chassaing, P., Mockett, C., Reimann, T., Thiele, F.: Coherent and turbulent process analysis in the flow past a circular cylinder at high Reynolds number. Journal of Fluids and Structures 24(8), 1313–1325 (2008)

Perrin, R., Braza, M., Cid, E., Cazin, S., Thiele, F., Borée, J.: Time resolved Stereoscopic measurements in the near wake of a circular cylinder at high Reynolds number. In: 14th Int. Symp. on Applications of Laser Techniques to Fluid Mechanics, Lisbon, Portugal, July 07-10 (2008)

Perrin, R., Braza, M., Cid, E., Cazin, S., Barthet, A., Sevrain, A., Mockett, C., Thiele, F.: Obtaining phase averaged turbulence properties in the near wake of a circular cylinder at high Reynolds number using POD. Experiments in Fluids 43(2-3), 341–355 (2007)

Perrin, R., Braza, M., Cid, E., Cazin, S., Sevrain, A., Strelets, M., Shur, M., Hoarau, Y., Barthet, A., Harran, G., Moradei, F.: 3D circular cylinder (IMFT). In: Aupoix, B., Bunge, U., Haase, W., Schwamborn, D. (eds.) Flow Physics Modelling-an integrated approach. Dedicated volume in series Notes on Numerical Fluid Mechanics and Multidisciplinary design, vol. 94. Springer, Heidelberg (2006)

Perrin, R., Cid, E., Cazin, S., Sevrain, A., Braza, M., Moradei, F., Harran, G.: Phase averaged measurements of the turbulence properties in the near wake of a circular cylinder at high Reynolds number by 2C-PIV and 3C-PIV. Experiments in Fluids 42, 93–109 (2007)

Perrin, R., Mockett, C., Braza, M., Cid, E., Cazin, S., Sevrain, A., Chaissaing, P., Thiele, F.: Joint numerical and experimental investigation of the flow around a circular cylinder at high Reynolds number. Particle Image Velocimetry, New Developments and Recent Applications, Topics in Applied Physics 112, 223–244 (2008)

Peshkin, D.A.: TurMMAC application challenge test case specification: M219 cavity. QinetiQ/FST/CAT/WP020905 (2002)

Pope, S.B.: A More General Effective-Viscosity Hypothesis. Journal of Fluid Mechanics 72, 331–340 (1975)

Pope, S.B.: Turbulent Flows. Cambridge University Press, Cambridge (2000)

Quéméré, P.: Une méthode multidomaine/multirésolution avec applications au couplage LES/LES et RANS/LES, PhD thesis, Paris 6 University (2001)

Piomelli, U., Balaras, E., Pasinato, H., Squires, K., Spalart, P.R.: The inner-outer layer interface in large-eddy simulations with wall-layer models. Int. J. Heat and Fluid Flow 24, 538–550 (2003)

Raddatz, J., Fassbender, J.K.: Block Structured Navier-Stokes Solver FLOWer. In: Kroll, N., Fassbender, J.K. (Hrsg.) MEGAFLOW - Numerical Flow Simulation for Aircraft Design. Notes on Numerical Fluid Mechanics and Multidisciplinary Design, vol. 89, pp. 27–44. Springer, Heidelberg (2005); Closing Presentation DLR Project MEGAFLOW, Braunschweig (de), 10-11.12.2002, ISBN 3-540-24383-6

Reichardt, H.: Vollständige Darstellung der turbulenten Geschwindigkeitsverteilung in glatten Leitungen. Zeitschrift für angewandte Mathematik und Mechanik 31, 208–219 (1951)

Revell, A.: A stress-strain lag Eddy viscosity model for mean unsteady turbulent flows. PhD thesis, University of Manchester (2006)

Revell, A., Benhamadouche, S., Craft, T., Laurence, D.: A stress strain lag eddy viscosity model for unsteady mean flow. Int. J. Heat Fluid Flow 27, 821–830 (2006)

Revell, A., Craft, T., Laurence, D.: Turbulence modelling of strongly detached flows: the circular cylinder. Notes on Numerical Fluid Mechanics and Multidisciplinary Design, vol. 97, pp. 279–288 (2008)

Revell, A., Duraisamy, K., Iaccarino, G.: Advanced turbulence modelling of wingtip vortices. In: TSFP 5, Munich, Germany, August 27-29 (2007)

Reynolds, W.C., Hussain, A.K.M.F.: The mechanics of an organized wave in turbulent shear flow. Part 3. Theoretical models and comparisons with experiments, J. Fluid Mech. 54, 263–288 (1972)

Rieger, H.: First Experiences with Detached-Eddy Simulations in the Aeronautics Industry. In: Symposium on Hybrid RANS-LES Methods, Stockholm, Sweden, July 14-15 (2005)

Rodi, W.: LES of flow past 3D hill and finite-height cylinders. In: Book of abstracts of Colloquium LES for External Aerodynamics Flows. Imperial College, London, March 15-16 (2007)

Roe, P.L.: Approximate Riemann solvers, parameters vectors and difference schemes. J. Comp. Phys. 43, 357–372 (1981)

Roshko, A.: Experiment on the flow past a circular cylinder at very high Reynolds number. J. Fluid Mech. 10, 345–356 (1961)

Rossiter, J.E.: Wind tunnel experiments on the flow over rectangular cavities at subsonic and transonic speeds. Rep. Mem. 3438, Aeronautical Research Council (1964)

Rossow, C.-C., Kroll, N., Schwamborn, D.: The MEGAFLOW Project - Numerical Flow Simulation for Aircraft, DLR IB. 124-2005/1 (2005)

Rotta, J.C.: Über eine Methode zur Berechnung turbulenter Scherströmungen, Aerodynamische Versuchsanstalt Göttingen, Rep. 69 A14 (1968)

Rotta, J.C.: Turbulente Strömumgen. BG Teubner Stuttgart (1972)

Rubiolo, P.R.: Probabilistic prediction of fretting-wear damage of nuclear fuel rods. Nuclear Engineering and Design 236, 1628–1640 (2006)

Rung, T., Thiele, F.: Computational modelling of complex boundary-layer flows. In: Proceedings of the 9th International Symposium on Transport Phenomena in Thermal-Fluid Engineering, Singapore (1996)

Rung, T., Bunge, U., Schatz, M., Thiele, F.: Restatement of the Spalart–Allmaras eddy-viscosity model in strain-adaptive formulation. AIAA Journal 41(7), 1396–1399 (2003)

Rung, T., Lübcke, H., Thiele, F.: Universal wall-boundary conditions for turbulence-transport models. Zeitschrift für angewandte Mathematik und Mechanik 81(1), 1756–1758 (2000)

Rung, T., Eschricht, D., Yan, J., Thiele, F.: Sound radiation from the vortex flow past a generic side mirror. In: Proceedings of the 8th AIAA/CEAS Aeroacoustics Conference & Exhibit, AIAA/CEAS 2002-2549, Breckenridge, Colorado, USA (2002)

Rung, T., Wu, D., Bunge, U., Mockett, C., Thiele, F.: Analysis of sound sources for a generic car mirror. In: Haase, W., Aupoix, B., Bunge, U., Schwamborn, D. (eds.) (2005)

Sagaut, P., Deck, S., Terracol, M.: Multiscale and Multiresolution Approaches In Turbulence. Imperial College Press, UK, London, 356 pages (2006)

Samtaney, R., Pullin, D.I., Kosovic: Direct numerical simulation of decaying compressible turbulence and shocklet statistics. Physics of Fluids 13(5), 1415–1430

Schewe, G.: Reynolds-number effects in flow around more-or-less bluff bodies. Journal of Wind Engineering and Industrial Aerodynamics 89(14-15), 1267–1289 (2001)

Schlüter, J.U., Wu, X., van der Weide, E., Hahn, S., Herrmann, M., Alonso, J.J., Pitsch, H.: A python approach to multi-code simulations: CHIMPS. Center for Turbulence Research Annual Research Briefs (2005)

Schmidt, T., Mockett, C., Thiele, F.: Adaptive wall function for the prediction of turbulent flows. In: Kroll, N., Schwamborn, D., Becker, K., Rieger, H., Thiele, F. (eds.) MEGADESIGN and MegaOpt – Aerodynamic Simulation and Optimization in Aircraft Design. Notes on Numerical Fluid Mechanics and Multidisciplinary Design (2008) (to be published)

Schroff, G.M., Keller, H.B.: Stabilization of unstable procedures; the Recursive Projection Method. SIAM J. Num. Anal. 30, 1099–1120 (1993)

Schumann, U.: Subgrid scale model for finite difference simulations of turbulent flows in plane channels and annuli. Journal of computational physics 18, 376–404 (1975)

Schwamborn, D., Gerhold, T., Heinrich, R.: The DLR TAU-code: recent Applications in Research and Industry. In: European Conference on Computational Fluid Dynamics, Egmond aan Zee, ECCOMAS CFD 2006 (2006)

Seok, K.C., Sang, K.M., Won, P.B., Young, D.C.: Phenomenological investigations on the turbulent flow structures in a rod bundle array with mixing devices. Nuclear Engineering and Design 238, 600–609 (2008); Shih, T. B., Zhu, J., Lumley, J. L.: A realizable Reynolds stress algebraic equation model. NASA TM 105993, ICOMP 92-27, CMOTT 92-14 (1993)

Shur, M., Spalart, P.R., Strelets, M., Travin, A.: Detached-eddy simulation of an airfoil at high angle of attack. In: Rodi, W., Laurence, D. (eds.) 4th Int. Symp. On Engineering Turbulence Modelling and Measurements, Corsica, May 24-26, pp. 669–678 (1999)

Shur, M.L., Spalart, P.R., Strelets, M., Travin, A.: Modification of S-A subgrid model in DES aimed to prevent activation of the low-Re terms in LES mode. In: Proceedings of workshop on DES, St.-Petersburg, July 2–3 (2003), http://cfd.me.umist.ac.uk/flomania

Shur, M.L., Spalart, P.R., Strelets, M.K., Travin, A.K.: A hybrid RANS-LES approach with delayed-DES and wall-modelled LES capabilities. International Journal of Heat and Fluid Flow 29(6), 1638–1649 (2008)

Siegert, R., Schwarz, V., Reichenberger, J.: Numerical simulation of aeroacoustic sound generated by generic bodies placed on a plate: Part II – Prediction of radiated sound pressure. In: 5th AIAA/CEAS Aeroacoustics Conference, Paper AIAA-99-1895, Seattle, Washington, USA (1999)

Simon, F., Deck, S., Guillen, P., Sagaut, P.: RANS-LES Simulation of Supersonic Base Flows. AIAA J. 44(11), 2578–2590 (2006)

Simon, F., Deck, S., Guillen, P., Cayzac, R., Merlen, A.: Zonal Detached Eddy Simulation of Projectiles in the subsonic and transonic regimes. AIAA J. 45(7), 1606–1619 (2007)

Simon, F., Deck, S., Guillen, P., Sagaut, P., Merlen, A.: Numerical Simulation of the compressible mixing layer behin an axisymmetric trailing edge. Journal of Fluid Mechanics 591, 215–253 (2007)

Simpson, R.L., Hong, C.H., Byun, G.: Study of vortical separation from an axisymmetric hill. Int. J. Heat and Fluid Flow 23, 582–591 (2002)

Sirovich, L.: Turbulence and the dynamics of coherent structures. Parts I-III, Q Appl. Math. 45, 561–590 (1987)

Smagorinsky, J.: General circulation experiments with the primitive equations. Mon. Weather Rev. 91(3), 99–165 (1963)

Spalart, P.R.: Trends in Turbulence Treatments. AIAA Paper No. 2000-2306 (2000)

Spalart, P.: Detached-eddy simulation. Annual Review of Fluid Mechanics 41 (2009) (to be published)

Spalart, P.R., Allmaras, S.R.: A one-equation turbulence model for aerodynamic flows. La recherche aérospatiale 1, 5–21 (1994)

Spalart, P., Jou, W.-H., Strelets, M., Allmaras, S.: Comments on the feasibility of LES for wings and on the hybrid RANS/LES approach. In: Liu, C., Liu, Z., Sakell, L. (eds.) Advances in DNS/LES, pp. 137–148. Greden Press (1997)

Spalart, P.R., Deck, S., Shur, M., Squires, K., Strelets, M., Travin, A.: A new version of detached-eddy simulation, resistant to ambiguous grid densities. Theoretical and Computational Fluid Dynamics 20, 181–195 (2006)

Steijl, R., Barakos, G.N., Badcock, K.: A Framework for CFD Analysis of Helicopter Rotors in Hover and Forward Flight. Int. Journal of Numerical Methods in Fluids 51, 819–847 (2006)

Strelets, M.: Detached Eddy Simulation of massively separated flows. AIAA Paper 2001-879 (2001)

Swalwell, K.E.: The Effect of Turbulence on Stall of Horizontal Axis Wind Turbines. Ph.D. Thesis. Monash University (October 2005)

Swalwell, K.E., Sheridan, J., Melbourne, W.H.: Frequency Analysis of Surface Pressure on an Airfoil after Stall. In: 21st AIAA Applied Aerodynamics Conference, AIAA Paper 2003-3416 (2003)

Swalwell, R.C., Sheridan, J., Melbourne, W.H.: Frequency analysis of surface pressure on airfoil after stall. In: 21st AIAA Applied Aerodynamics Conference (2004)

Swanson, R.C., Turkel, E.: On central-difference and upwind schemes. Journal of Computational Physics 101, 292–306 (1992)

Tam, C.K.W., Webb, J.C.: Dispersion-relation-preserving finite difference schemes for computational acoustics. Journal of Computational Physics 107, 262–281 (1993)

Tang, H.S., Casey Jones, S., Sotiropoulos, F.: An overset-grid method for 3D unsteady incompressible flows. Journal of Computational Physics 191, 567–600 (2003)

Temmerman, L., Hadziabdic, M., Leschziner, M., Hanjalic, K.: A hybrid two-layer URANS-LES approach for large eddy simulation at high Reynolds numbers. Int. J. Heat and Fluid Flow 26, 173–190 (2005)

Temmerman, L., Leschziner, M.A., Mellen, C.P., Froehlich, J.: Int. J. Heat and Fluid Flow 24, 157–180 (2003)

Tessicini, F., Li, N., Leschziner, M.A.: Large eddy simulation of three-dimensional flow around a hill-shaped obstruction with a zonal near-wall approximation. Int. J. Heat Fluid Flow 28, 894–908 (2007)

Tessicini, F., Temmerman, L., Leschziner, M.A.: Approximate near-wall treatments based on zonal RANS-LES hybrid methods for LES at high Reynolds numbers Invited paper, Flow, Turbulence and Combustion. Int. J. Heat and Fluid Flow 27, 789–799 (2006)

Trapier, S., Deck, S., Duveau, P.: Delayed detached-eddy simulation and analysis of supersonic inlet buzz. AIAA Journal 46(1) (2008)

Travin, A., Shur, M., Spalart, P.R., Strelets, M.: On URANS solutions with LES like behaviour. In: Neittaanmäki, P., Rossi, T., Majava, K., Pironneau, O. (eds.) Congress on Computational Methods in Applied Sciences and Engineering ECCOMAS 2004, 24-28 July 2004. Jyväskylä, Finland (2004)

Travin, A., Shur, M., Spalart, P.R., Strelets, M.: Improvement of delayed detached-eddy simulation for LES with wall modelling. In: Wesseling, P., Oñate, E., Périaux, J. (eds.) Proceedings of the European Conference on Computational Fluid Dynamics ECCOMAS CFD 2006, Egmond aan Zee, The Netherlands (2006)

Travin, A., Shur, M., Strelets, M., Spalart, P.: Detached-eddy simulation past a circular cylinder. Flow Turb. Combust. 63, 269–291 (1999)

Travin, A., Shur, M., Strelets, M., Spalart, P.R.: Physical and numerical upgrades in the Detached-Eddy Simulation of complex turbulent flows. Fluid Mechanics and its applications 65, 239–254 (2002); Advances in LES of Complex Flows. In: Friedrich, R., Rodi, W. (eds.) Proc. Of EUROMECH Colloquium, vol. 412. Kluwer Academic Publishers, Dordrecht

Uribe, J.C., Jarrin, N., Prosser, R., Laurence, D.: Hybrid V2F RANS LES model and synthetic inlet turbulence applied to a trailing edge flow. Turbulence and Shear Flow Phenomena 5 2, 701–706 (2007)

Uribe, J.C., Jarrin, N., Prosser, R., Laurence, D.: Two Velocities hybrid RANS-LES of a trailing edge flow. In: IUTAM, International Symposium on Unsteady Separated Flows and their control (2007)

Verstappen, R.W.C.P., Veldman, A.E.P.: Symmetry-preserving discretization of turbulent flow. Journal of Computational Physics 187(1), 343–368 (2003)

Vreman, B., Geurts, B., Kuerten, H.: Large-eddy simulation of the turbulent mixing layer. Journal of Fluid Mechanics 339, 357–390 (1997)

Wallin, S., Johansson, A.V.: Modelling streamline curvature effects in explicit algebraic Reynolds stress turbulence models. Int. J. Heat and Fluid Flow 23, 721–730 (2002)

Wang, C., Jang, Y.J., Leschziner, M.A.: Int. J. Heat and Fluid Flow 25, 499–512 (2004)

Wang, M., Moin, P.: Dynamic wall modelling for large eddy simulation of complex turbulent flows. Physics of Fluids 14(7), 2043–2051 (2002)

Wang, Z.J., Parthasarathy, V.: A fully automated Chimera methodology for multiple moving body problems. Int. J. Numer. Meth. Fluids 33, 919–938 (2000)

Wallin, S., Johansson, A.: An explicit algebraic Reynolds stress model for incompressible and compressible flows. Journal of fluid mechanics 303, 89–132 (2000)

Welty, J.R., Wicks, C.E., Wilson, R.E.: Fundamentals of Momentum, Heat, and Mass Transfer, 3rd edn. John Wiley & Sons, New York (1984)

Weinman, K., Knopp, T., Mockett, C., Bunge, U., Thiele, F., Van der Ven, H., Kok, J.C.: A grid convergence study for DES-like simulations of a stalled Airfoil. In: Symposium on Hybrid RANS-LES methods, Stockholm (2005)

Weinman, K.A., van der Ven, H., Mockett, C.R., Knopp, T.A., Kok, J.C., Perrin, R.T.E., Thiele, F.: A study of grid convergence issues for the simulation of the massively separated flow around a stalled airfoil using DES and related methods. In: Wesseling, P., Oñate, E., Périaux, J. (eds.) ECCOMAS CFD 2006, Egmond aan Zee, The Netherlands, 5–8 September 2006. NLR-TP-2006-436 (2006)

Wilcox, D.: Reassessment of the scale-determining equation for advanced turbulence models. AIAA Journal 26, 1299–1310 (1988)

Wray, A.: Unpublished DNS data. Available on AGARD database Test cases for the validation of large-eddy simulations of turbulent flows (1997), ftp://torroja.dmt.upm.es

Xue, L.: Entwicklung eines effizienten parallelen Lösungsalgorithmus zur dreidimensionalen Simulation komplexer turbulenter Strömungen. Dissertation, Technische Universität Berlin (1998)

Yan, J., Mockett, C., Thiele, F.: Investigation of alternative length scale substitutions in detached-eddy simulation. Journal of Flow, Turbulence and Combustion 74, 85–102 (2005)

Yan, J., Tawackolian, K., Michel, U., Thiele, F.: Computation of jet noise using a hybrid approach. In: 10th CEAS. ASC Workshop, 1st Scientific Workshop X3 - Noise, Trinity College, Dublin, Ireland (2006)

Yang, Z., Shih, T.H.: A k-ε model for turbulence and transitional boundary layer. In: Speziale, C.G., Launder, B.E. (eds.) Near-Wall Turbulence Flows, R.M.C. So., pp. 165–175. Elsevier-Science Publishers B.V., Amsterdam (1993)

Yoshizawa, A.: Statistical theory for compressible shear flows, with the application to subgrid modeling. Phys. Fluids 29, 2152–2164 (1986)

Yoshizawa, W., Horiuti, K.: A statistically derived subgrid scale kinetic energy model for the large eddy simulation of turbulent flows. J. Phys. Soc. Japan 58, 2834–2839 (1985)

Notes on Numerical Fluid Mechanics and Multidisciplinary Design

Available Volumes

Volume 103: Werner Haase, Marianna Braza, Alistair Revell (eds.): DESider – A European Effort on Hybrid RANS-LES Modelling - Results of the European-Union Funded Project, 2004–2007. ISBN 978-3-540-92772-3

Volume 102: Rolf Radespiel, Cord-Christian Rossow, Benjamin Winfried Brinkmann (eds.): Hermann Schlichting – 100 Years - Scientific Colloquium Celebrating the Anniversary of His Birthday, Braunschweig, Germany 2007. ISBN 978-3-540-95997-7

Volume 101: Egon Krause, Yurii I. Shokin, Michael Resch, Nina Shokina (eds.): Computational Science and High Performance Computing III - The 3rd Russian-German Advanced Research Workshop, Novosibirsk, Russia, 23–27 July 2007. ISBN 978-3-540-69008-5

Volume 100: Ernst Heinrich Hirschel, Egon Krause (eds.): 100 Volumes of 'Notes on Numerical Fluid Mechanics' - 40 Years of Numerical Fluid Mechanics and Aerodynamics in Retrospect. ISBN 978-3-540-70804-9

Volume 99: Burkhard Schulte-Werning, David Thompson, Pierre-Etienne Gautier, Carl Hanson, Brian Hemsworth, James Nelson, Tatsuo Maeda, Paul de Vos (eds.): Noise and Vibration Mitigation for Rail Transportation Systems - Proceedings of the 9th International Workshop on Railway Noise, Munich, Germany, 4–8 September 2007. ISBN 978-3-540-74892-2

Volume 98: Ali Gülhan (ed.): RESPACE – Key Technologies for Reusable Space Systems - Results of a Virtual Institute Programme of the German Helmholtz-Association, 2003–2007. ISBN 978-3-540-77818-9

Volume 97: Shia-Hui Peng, Werner Haase (eds.): Advances in Hybrid RANS-LES Modelling - Papers contributed to the 2007 Symposium of Hybrid RANS-LES Methods, Corfu, Greece, 17–18 June 2007. ISBN 978-3-540-77813-4

Volume 96: C. Tropea, S. Jakirlic, H.-J. Heinemann, R. Henke, H. Hönlinger (eds.): New Results in Numerical and Experimental Fluid Mechanics VI - Contributions to the 15th STAB/DGLR Symposium Darmstadt, Germany, 2006. ISBN 978-3-540-74458-0

Volume 95: R. King (ed.): Active Flow Control - Papers contributed to the Conference "Active Flow Control 2006", Berlin, Germany, September 27 to 29, 2006. ISBN 978-3-540-71438-5

Volume 94: W. Haase, B. Aupoix, U. Bunge, D. Schwamborn (eds.): FLOMANIA - A European Initiative on Flow Physics Modelling - Results of the European-Union funded project 2002 - 2004. ISBN 978-3-540-28786-5

Volume 93: Yu. Shokin, M. Resch, N. Danaev, M. Orunkhanov, N. Shokina (eds.): Advances in High Performance Computing and Computational Sciences - The Ith Khazakh-German Advanced Research Workshop, Almaty, Kazakhstan, September 25 to October 1, 2005. ISBN 978-3-540-33864-2

Volume 92: H.J. Rath, C. Holze, H.-J. Heinemann, R. Henke, H. Hönlinger (eds.): New Results in Numerical and Experimental Fluid Mechanics V - Contributions to the 14th STAB/DGLR Symposium Bremen, Germany 2004. ISBN 978-3-540-33286-2

Volume 91: E. Krause, Yu. Shokin, M. Resch, N. Shokina (eds.): Computational Science and High Performance Computing II - The 2nd Russian-German Advanced Research Workshop, Stuttgart, Germany, March 14 to 16, 2005. ISBN 978-3-540-31767-8

Volume 87: Ch. Breitsamter, B. Laschka, H.-J. Heinemann, R. Hilbig (eds.): New Results in Numerical and Experimental Fluid Mechanics IV. ISBN 978-3-540-20258-5

Volume 86: S. Wagner, M. Kloker, U. Rist (eds.): Recent Results in Laminar-Turbulent Transition - Selected numerical and experimental contributions from the DFG priority programme 'Transition' in Germany. ISBN 978-3-540-40490-3

Volume 85: N.G. Barton, J. Periaux (eds.): Coupling of Fluids, Structures and Waves in Aeronautics - Proceedings of a French-Australian Workshop in Melbourne, Australia 3-6 December 2001. ISBN 978-3-540-40222-0

Volume 83: L. Davidson, D. Cokljat, J. Fröhlich, M.A. Leschziner, C. Mellen, W. Rodi (eds.): LESFOIL: Large Eddy Simulation of Flow around a High Lift Airfoil - Results of the Project LESFOIL supported by the European Union 1998 - 2001. ISBN 978-3-540-00533-9

Volume 82: E.H. Hirschel (ed.): Numerical Flow Simulation III - CNRS-DFG Collaborative Research Programme, Results 2000-2002. ISBN 978-3-540-44130-4

Volume 81: W. Haase, V. Selmin, B. Winzell (eds.): Progress in Computational Flow Structure Interaction - Results of the Project UNSI, supported by the European Union 1998-2000. ISBN 978-3-540-43902-8

Volume 80: E. Stanewsky, J. Delery, J. Fulker, P. de Matteis (eds.): Drag Reduction by Shock and Boundary Layer Control - Results of the Project EUROSHOCK II, supported by the European Union 1996-1999. ISBN 978-3-540-43317-0

Volume 79: B. Schulte-Werning, R. Gregoire, A. Malfatti, G. Matschke (eds.): TRANSAERO - A European Initiative on Transient Aerodynamics for Railway System Optimisation. ISBN 978-3-540-43316-3

Volume 78: M. Hafez, K. Morinishi, J. Periaux (eds.): Computational Fluid Dynamics for the 21st Century. Proceedings of a Symposium Honoring Prof. Satofuka on the Occasion of his 60th Birthday, Kyoto, Japan, 15-17 July 2000. ISBN 978-3-540-42053-8

Volume 77: S. Wagner, U. Rist, H.-J. Heinemann, R. Hilbig (eds.): New Results in Numerical and Experimental Fluid Mechanics III. Contributions to the 12th STAB/DGLR Symposium, Stuttgart, Germany 2000. ISBN 978-3-540-42696-7

Volume 76: P. Thiede (ed.): Aerodynamic Drag Reduction Technologies. Proceedings of the CEAS/DragNet European Drag Reduction Conference, 19-21 June 2000, Potsdam, Germany. ISBN 978-3-540-41911-2

Volume 75: E.H. Hirschel (ed.): Numerical Flow Simulation II. CNRS-DFG Collaborative Research Programme, Results 1998-2000. ISBN 978-3-540-41608-1

Volume 66: E.H. Hirschel (ed.): Numerical Flow Simulation I. CNRS-DFG Collaborative Research Programme. Results 1996-1998. ISBN 978-3-540-41540-4